Research Topics

Atmospheric physics, atmospheric environment, and atmospheric effects on human health

Edited by
Honglei Wang, Meng Gao, Duanyang Liu and Yi Li

Published in
Frontiers in Earth Science

ISSN 1664-8714
ISBN 978-2-8325-2570-8
DOI 10.3389/978-2-8325-2570-8

About Frontiers

Frontiers is more than just an open access publisher of scholarly articles: it is a pioneering approach to the world of academia, radically improving the way scholarly research is managed. The grand vision of Frontiers is a world where all people have an equal opportunity to seek, share and generate knowledge. Frontiers provides immediate and permanent online open access to all its publications, but this alone is not enough to realize our grand goals.

Frontiers journal series

The Frontiers journal series is a multi-tier and interdisciplinary set of open-access, online journals, promising a paradigm shift from the current review, selection and dissemination processes in academic publishing. All Frontiers journals are driven by researchers for researchers; therefore, they constitute a service to the scholarly community. At the same time, the *Frontiers journal series* operates on a revolutionary invention, the tiered publishing system, initially addressing specific communities of scholars, and gradually climbing up to broader public understanding, thus serving the interests of the lay society, too.

Dedication to quality

Each Frontiers article is a landmark of the highest quality, thanks to genuinely collaborative interactions between authors and review editors, who include some of the world's best academicians. Research must be certified by peers before entering a stream of knowledge that may eventually reach the public - and shape society; therefore, Frontiers only applies the most rigorous and unbiased reviews. Frontiers revolutionizes research publishing by freely delivering the most outstanding research, evaluated with no bias from both the academic and social point of view. By applying the most advanced information technologies, Frontiers is catapulting scholarly publishing into a new generation.

What are Frontiers Research Topics?

Frontiers Research Topics are very popular trademarks of the *Frontiers journals series*: they are collections of at least ten articles, all centered on a particular subject. With their unique mix of varied contributions from Original Research to Review Articles, Frontiers Research Topics unify the most influential researchers, the latest key findings and historical advances in a hot research area.

Find out more on how to host your own Frontiers Research Topic or contribute to one as an author by contacting the Frontiers editorial office: frontiersin.org/about/contact

Atmospheric physics, atmospheric environment, and atmospheric effects on human health

Topic editors
Honglei Wang — Nanjing University of Information Science and Technology, China
Meng Gao — Hong Kong Baptist University, Hong Kong, SAR China
Duanyang Liu — Nanjing Joint Institute for Atmospheric Sciences, Chinese Academy of Meteorological Sciences, China
Yi Li — Intel, United States

Citation
Wang, H., Gao, M., Liu, D., Li, Y., eds. (2023). *Atmospheric physics, atmospheric environment, and atmospheric effects on human health*. Lausanne: Frontiers Media SA. doi: 10.3389/978-2-8325-2570-8

Table of contents

frontiers | Frontiers in Earth Science

ORIGINAL RESEARCH
published: 15 August 2022
doi: 10.3389/feart.2022.935139

Intercomparison of Atmospheric Upper-Air Temperature From Recent Global Reanalysis Datasets

Yassmin H. Essa[1,2]*, *Chiara Cagnazzo*[1,3], *Fabio Madonna*[4], *Paolo Cristofanelli*[5], *Chunxue Yang*[1], *Federico Serva*[1], *Luca Caporaso*[1,6] and *Rosalia Santoleri*[1]

[1]*Institute of Marine Sciences, National Research Council of Italy, Rome, Italy,* [2]*Central Laboratory for Agriculture Climate, Agriculture Research Center, Giza, Egypt,* [3]*European Center for Medium Range Weather Forecasts, Reading, United Kingdom,* [4]*Institute of Methodologies for Environmental Analysis, National Research Council of Italy, Tito Scalo, Italy,* [5]*Institute of Atmospheric Sciences and Climate, National Research Council of Italy, Bologna, Italy,* [6]*European Commission–Joint Research Centre, Ispra, Italy*

Atmospheric temperature is a key variable to detect and attribute climate change. Due to the relative sparseness of ground-based observations and heterogeneity of satellite data, global atmospheric reanalysis products are considered valuable datasets for studying and monitoring the climate, since these usually ensure spatially complete and continuous temporal coverage. Consequently, evaluating differences among the existing reanalyses is key to identifying inconsistencies. To this aim, the current study intercompares the climatological mean, variability, and linear trends for upper air temperature provided from four recent atmospheric reanalysis products (ERA5, ERA-Interim, MERRA-2, and JRA-55) The Reanalysis Multi-Model Ensemble-mean (RMME) is used as a comparator. Radiosonde observations are included for comparison on the regional scale (tropics). The results reveal that all evaluated reanalyses provide a consistent reproduction of the upper-air temperature profile. Temperature differences from RMME within ±0.25 K are found in both the troposphere and lower stratosphere, except for a few specific regions. Larger differences (>± 1.5 K) and discrepancies among the datasets are found in the upper stratosphere. Agreement between reanalyses increased after 1998. Differences in the temperature time series and seasonal cycle at the regional scales are smaller in the Northern Hemisphere mid-latitudes than in the tropics and Southern Hemisphere. A robust cooling trend in the lower stratosphere during the period of largest ozone depletion (1980-1997) and a warming trend in the troposphere for the period 1998-2018 are clearly found, at the global level, in all the datasets. Temperature trends and variability in the tropics are consistent in all reanalysis datasets with the homogenized radiosonde records from the lower to middle troposphere and in the lower stratosphere. However, large differences are found in the upper troposphere, tropical tropopause layer (TTL), and middle stratosphere. The well-known temperature variability in the lower stratosphere associated with Quasi-Biennial Oscillation (QBO) is captured in both reanalyses and observational datasets. Among the reanalyses, ERA5 shows the smallest temperature difference with respect to homogenized upper-air radiosoundings records.

Keywords: upper-air temperature, vertical thermal structure, atmospheric reanalysis, radiosonde observations, climatology and variability, trend

Edited by:
Paulo Artaxo,
University of São Paulo, Brazil

Reviewed by:
Tercio Ambrizzi,
University of São Paulo, Brazil
Juan José Taboada,
Spanish National Research Council (CSIC), Spain

***Correspondence:**
Yassmin H. Essa
Yassmin.hesham@artov.ismar.cnr.it

Specialty section:
This article was submitted to Atmospheric Science,
a section of the journal
Frontiers in Earth Science

Received: *03 May 2022*
Accepted: *10 June 2022*
Published: *15 August 2022*

Citation:
Essa YH, Cagnazzo C, Madonna F, Cristofanelli P, Yang C, Serva F, Caporaso L and Santoleri R (2022) Intercomparison of Atmospheric Upper-Air Temperature From Recent Global Reanalysis Datasets. Front. Earth Sci. 10:935139. doi: 10.3389/feart.2022.935139

1 INTRODUCTION

Atmospheric temperature is a state variable, crucial to understanding and predicting the evolution of climate. It is especially important to identify climate change signals in the troposphere and stratosphere (Steiner et al., 2020). For example, the rising of the tropopause, resulting from the warming of the troposphere and the cooling of the stratosphere, has been indicated as one of the most robust fingerprints of anthropogenic climate change (IPCC, 2013; Pisoft et al., 2021), along with stratospheric ozone depletion affecting the temperature profile in the stratosphere (Polvani et al., 2011; Ivanciu et al., 2021).

The limitations of studying upper-air temperature are mainly due to the incompleteness and heterogeneity of satellite and ground-based atmospheric observations (Sterin et al., 2008). A valuable alternative solution to observational datasets is atmospheric reanalysis data (Baatz et al., 2021), which combines vast amounts of observations with numerical models using data assimilation techniques to provide a globally complete gridded and continuous temporal coverage dataset. However, the accuracy of reanalysis products varies strongly (Dee et al., 2011) especially for variables that are very sensitive to atmospheric dynamics and to the main parameters of the assimilation systems, such as the quantity and quality of the assimilated observations, the assimilation scheme (e.g., variational, Kalman filter), and the background forecast model, particularly the spatial and temporal resolutions (Simmons et al., 2004; Alghamdi, 2020; Gleixner et al., 2020). The usability of reanalyses data for long-term climate applications, including trend estimation, is controversial as discussed in the literature, for specific regions in previous reanalyses generations (e.g., Thorne, 2008; Thorne and Vose, 2010). Assessing both long-term temperature variability and trend using reanalyses proved to be challenging due to changes in the assimilation systems and observations that can introduce inhomogeneities, and to the documented difficulties with the representation of low-frequency variations (Simmons et al., 2017; Madonna et al., 2022).

Several intercomparison studies of upper air temperature were performed to assess the quality of the datasets since the first release of the reanalysis products (e.g., ERA15 & NCEP-R1: Pawson and Fiorino 1998, 1999; ERA40 & ERA15 & NCEP-R1: Randel et al., 2004; ERA40 & NCEP-R1 & R2: Manney et al., 2005). Major outcomes of these assessments showed that ERA products agree better with radiosonde observations and have better performance in resolving the low tropopause temperatures compared to NCEP temperatures that are more biased towards satellite-derived values (Pawson and Fiorino, 1998). Evident differences between datasets for temperature at specific regions and/or levels are also documented (e.g. polar lower stratosphere, temperatures near the tropical tropopause and the global stratopause).

In terms of variability and trends studies (Simmons et al., 2014), reasonable agreement is reported in the lower-middle troposphere and lower stratosphere, while larger variations accounted for the mid-upper stratosphere among the considered reanalyses (ERA-40, ERA-interim, MERRA, and JRA-55).

Recently the "Stratosphere-troposphere Processes And their Role in Climate (SPARC) Reanalysis Intercomparison Project (S-RIP)" devoted a notable effort in intercomparing different generations of reanalysis products (SPARC, 2022). Wide enhancements for the reanalyses in terms of model characteristics, physical parameterizations employed, assimilation schemes, and observations assimilated, have been archived as a function of their evolution in time (Fujiwara et al., 2017).

In this framework, particular attention was paid to intercomparing the climatology and variability of the atmospheric temperature and wind variables in reanalyses for the period 1979-2014 (Long et al., 2017), pointing out major improvements for the recent generation of reanalyses compared to the older versions. Discontinuities due to the changing in assimilation instrument(s) were also discussed revealing evident improvements both in the troposphere and in the lower stratosphere in the recent generation (e.g., ERA-Interim versus ERA-40; MERRA2 versus MERRA, JRA-55 versus JRA-25), while issues persist in the upper stratosphere–lower mesosphere.

SPARC project also evaluated the climatological and long-term tropical tropopause layer (TTL) temperature and tropopause characteristics in older and new generations of reanalysis datasets (Tegtmeier et al., 2020), revealing larger biases at TTL in the older reanalysis generations. The recent reanalyses (ERA5, ERA-Interim, MERRA-2, JRA-55, and CFSR) provide realistic representations of temperature structure within the TTL, and the vertical resolution of the involved products played a significant role in representing the temperature at the cold point and lapse rate at the tropopause.

As pointed out, comprehensive inter-comparisons between the old and new generations of reanalyses are provided in the literature. However, among the recent generations, the products' quality and suitability for a broad set of climate studies or applications are still under discussion or a few discussed for specific regions (e.g., Graham et al., 2019; Alghamdi, 2020; Keller and Wahl, 2021; Simmons, 2022). Furthermore, ERA5, the newest global reanalysis product and one of the most used reanalysis families, has not been extensively intercompared and discussed at the current time compared to the other products. Therefore, the main goal of this study is to investigate the vertical structure of the atmospheric temperature and the coherence among the most recent reanalysis products (ERA5, ERA-Interim, MERRA-2, and JRA-55), focusing on both global and regional scales, with particular attention to the variability and trends. The latter can significantly be influenced by the discontinuities associated with changing the assimilation instruments in reanalysis systems. The reanalyses multi-model mean (RMME) used as a comparator in this study, assuming it is able to minimize the discrepancy with the unknown true value, although it provides a smoother representation of climate variability. The upper-air homogenized observational datasets are also used as a benchmark at a regional scale. A set of diagnostics are used, highlighting the strengths and weaknesses of the presented reanalysis products.

The paper is organized as follows; the considered datasets and methodology are described in **Sections 2** and **3**. Time series and climatological differences from RMME, trend assessment, and comparison with observations are discussed in **Section 4**. Discussion and conclusions of the results are provided in **Section 5**. A list of all acronyms used in this paper is provided in the GLOSSARY section, some of the most important for the understanding of the paper are also introduced in the text.

2 DATASETS AND METHODS

2.1 Reanalysis Datasets

The datasets considered in this study include two datasets of European Centre for Medium-Range Weather Forecasts (ECMWF) reanalyses ERA5 (Hersbach et al., 2020) and ERA-Interim (Dee et al., 2011), NASA's Modern Era Retrospective Analysis for Research and Applications-2 (MERRA-2: Molod et al., 2015; Gelaro et al., 2017), and Japanese 55-years Reanalysis (JRA-55: Kobayashi et al., 2015). Climate Forecast System Reanalysis (CFSR) dataset has been excluded as it has changed in 2011 to CFSR-2 with higher resolution and upgrade to the forecast model, and assimilation scheme (SPARC Reanalysis Intercomparison Project (S-RIP), 2022), while the intercomparison of this study focuses on the recent reanalyses which are consistent in their system (i.e., used the same forecast model and assimilation scheme over the entire assessed period).

Older versions of the chosen datasets have been discarded (JRA-25, ERA-40, and MERRA), as they have been discontinued. Nevertheless, we decided to include ERA-Interim (discontinued in September 2019), because it is the former ECMWF reanalysis, recently replaced by ERA5, and it is crucial to understand the quality of this new product with respect to the predecessor version. It is known that reanalyses that span the whole 20th century with global coverage, like ERA-20C or NOAA's 20CR, are less accurate in the upper atmosphere, as they assimilate surface observations only (Fujiwara et al., 2017); therefore, they have been excluded from the comparison.

2.1.1 ERA5

ERA5 (Hersbach et al., 2020) is the fifth and latest version of atmospheric global reanalysis provided by the European Centre for Medium-Range Weather Forecasts (ECMWF). It is produced using a four-dimensional variational (4D-Var) data assimilation and model forecasts in CY41R2 of ECMWF's Integrated Forecast System (IFS) 2016 release, with a TL639 (~31 km) spatial resolution, and 137 hybrid vertical levels with the top level at 0.01 hPa. The data is available in the climate data store (CDS) in hourly temporal resolution, 0.25° × 0.25° spatial resolution, and interpolated to 37 pressure levels ranging from 1,000 hPa to 1 hPa. In addition to the use of an updated version of IFS in the dataset production and the higher spatial, temporal and vertical resolutions with respect to the preceding version ERA-interim, ERA5 assimilates a much larger number of reprocessed observational datasets that are expected to enhance the reanalysis products, and it depicts a better representation in the troposphere (Hersbach et al., 2020). ERA5 uses the data prepared for CMIP5 (van Vuuren et al., 2011; Lamarque et al., 2010) for representing the evolution of tropospheric aerosols. Volcanic sulfates (Sato et al., 1993) and ash (Tanré et al., 1984) are considered in the stratosphere. Carbon dioxide and trace gases are also treated based on CMIP5-recommended values (Meinshausen et al., 2011), with the extension of RCP3PD scenario after 2010 ("PD" stands for Peak and Decline).

A supplement dataset of the ERA5, called "ERA5.1", has been released by ECMWF in May 2020 covering the period from 2000 to 2006 to improve the reported cold bias in the lower stratosphere exhibited by ERA5 during the mentioned period (Simmons et al., 2020). ERA5.1 is a rerun of ERA5 from 2000 to 2006, using the background error covariances that were used to produce the ERA5 analyses for the years 1979–1999. It also includes the more restrictive ensemble assimilation of Solar Backscattered Ultra Violet (SBUV) ozone data that was employed in the production of ERA5 from 1979 to 1999. Therefore, in this work, the period 2000-2006 in the ERA5 data is replaced by ERA5.1.

2.1.2 ERA-Interim

ERA-Interim (Dee et al., 2011) is a global atmospheric reanalysis dataset covering the period from 1 January 1979 up to 31 August- 2019. The assimilation system is based on Cy31r2 of the ECMWF IFS model 2006 release, which includes a 4D-Var. The assimilation includes *in situ* observations of near-surface air temperature, pressure and relative humidity, upper-air temperature, wind, specific humidity, and rain-affected Special Sensor Microwave Imager (SSMI) radiances. The dataset provides 3 h (forecast) or 6 h (analysis) temporal resolution depending on the selected variable, and a spatial resolution of 0.75° (approximately 79 km) on 60 vertical levels from the surface up to 0.1 hPa. It uses climatological values for aerosols, carbon dioxide, trace gases, and ozone, while it takes prognostic information from the forecasting model for the water vapor and a suite of SST and sea ice data from observations and NCEP.

2.1.3 MERRA-2

The Modern-Era Retrospective analysis for Research and Applications, Version 2 (MERRA-2) provides data from 1980 to present (Gelaro et al., 2017), using an updated new version of the Goddard Earth Observing System Data Assimilation System Version 5 (GEOS-5, Molod et al., 2015) atmospheric general circulation model (AGCM) with a 4D-Var data assimilation scheme. Compared to the previous generation of MERRA reanalysis (Rienecker et al., 2011), the assimilation system in MERRA-2 has been updated. The new assimilation system enables the assimilation of modern hyperspectral radiance and microwave observations, along with Global Navigation Satellite System (GNSS) Radio Occultation (RO) datasets. MERRA-2 is the first long-term global reanalysis that assimilates space-based observations of aerosols and represents their interactions with other physical processes in the climate system (Gelaro et al., 2017).

MERRA-2 considered carbon dioxide following the IPCC RCP4.5 scenario, aerosol optical depths from satellites and AERONET are assimilated into the GEOS-5 GAAS (Buchard et al., 2015, 2017; Randles et al., 2017), and the reactive trace gases are specified according to steady-state monthly climatologies from the Goddard two-dimensional chemistry transport model (Rienecker et al., 2008).

The data are hourly fields produced with a horizontal resolution of 0.625° × 0.5° and 72 sigma vertical levels up to 0.01 hPa interpolated to 42 vertical levels from 1,000 hPa to 0.1 hPa available for downloading.

2.1.4 JRA-55

Japanese 55-years Reanalysis (JRA-55) (Kobayashi et al., 2015) is the latest reanalysis produced by the Japan Meteorological Agency (JMA) and released in 2013. It uses a sophisticated data assimilation system based on the operational system as of December 2009 with a 4D-Var scheme. The analysis period covers 55 years, starting from 1958 when regular radiosonde observation began on a global basis. JRA-55 uses *in situ* observation-based estimates of the COBE (Centennial *in situ* Observation-Based Estimates)-SST data and sea ice as boundary conditions. Daily values of carbon dioxide and reactive trace gases are assimilated in JRA-55 by interpolating from annual mean values. All species are treated as globally uniform, with sources that vary in time (Kobayashi et al., 2015; Table 7). Aerosols are represented using two aerosol profiles, one over land and one over sea (WMO, 1986), with AOD adjusted to a 2-dimensional monthly climatology (JMA, 2013). Interannual variations, such as those due to volcanic eruptions, are not considered (SPARC, 2022: chapter 2). The dataset spans the period from 1958 to present with 6-h temporal resolution, TL319 (~55 km) spatial resolution, and 60 vertical levels up to 0.1 hPa. Data interpolated to 1.25° × 1.25° spatial resolution and 37 vertical levels from 1,000 hPa to 1 hPa are available to download. Several issues addressed in the first version (JRA-25) are fixed. It is produced with a higher spatial resolution and a new radiation scheme, 4D-Var with Variational Bias Correction (VarBC) for satellite radiances, and introduction of greenhouse gases with time-varying concentrations.

2.2 Observational Datasets

2.2.1 Homogenized Radiosonde Records

Three upper-air homogenized data records are used in this study to better understand the performance of the reanalysis datasets: the Radiosonde Observation Correction using Reanalyses (RAOBCORE) (Haimberger, 2007), the Radiosonde Innovation Composite Homogenization (RICH) (Haimberger et al., 2012), and the Radiosounding HARMonization (RHARM) homogenized datasets (Madonna et al., 2022). RAOBCORE and RICH are both homogenized versions for upper air temperatures from the global radiosonde network. The adjustment approach of RAOBCORE/RICH is based mainly on two steps: first to identify the existing shifts in the radiosonde observation time series, then to estimate the size of the shifts through comparison with suitable reference series. A substantial difference between RAOBCORE and RICH in the method used for estimating the break size. RAOBCORE uses differences between the original radiosonde observations (obs) and background forecasts (bg) time series of an atmospheric climate data assimilation system used for reanalyses such as, the 40-years European Centre for Medium-Range Weather Forecasts (ECMWF) (ERA-40), ERA-interim, and currently ERA5, for estimating the break sizes, consequently, it is considered a not “independent” dataset for homogenization but it is influenced by satellite data and the assumptions made in the assimilating model. RICH estimates the break size by comparing the observations of a tested time series with observations of neighboring radiosonde time series (RICH-obs) or by comparing their background departures (RICH-τ). Although this approach is independent of satellite data, it remains influenced by breakpoint dates provided by RAOBCORE.

On the other hand, RHARM algorithm identifies breakpoints and estimates adjustments using a hybrid approach based on “reference measurements” (Thorne et al., 2017; Madonna et al., 2022). The RHARM algorithm works on each time series (i.e., station): data since 2004 (with starting time station-dependent) are obtained by post-processing each single radiosounding profile using a GRUAN-like algorithm (Dirsken et al., 2014); data before 2004 are homogenized at mandatory pressure levels using the cumulative sum test for detection of breakpoint and regulating trends using data after 2004 as a constraint. The approach is applied to 700 stations of Integrated Global Radiosounding Archive (IGRA)–Version 2 (Durre et al., 2018) and radiosoundings from ships.

The homogenized variables in RHARM are not influenced by cross-contamination of biases across stations (Sherwood, 2007) nor dependent on reanalysis data (Haimberger et al., 2012).

The three radiosonde datasets provide the temperature at 16 standard pressure levels (10, 20, 30, 50, 70, 100, 150, 200, 250, 300, 400, 500, 700, 850, 925, 1,000 hPa), and cover the common period between reanalyses, 1980–2018, for performing the inter-comparison.

3 METHODOLOGY

To inter-compare the atmospheric temperature from the global reanalyses shown in **Table 1** and quantify the consistency and discrepancy among these reanalyses, we first use the Reanalysis Multi-Model Ensemble-mean (RMME) as the benchmark. The observational datasets are used for tropics to compare the temperature variability related to the Quasi-Biennial Oscillation (QBO) and to study the vertical profiles of trends at mandatory pressure levels from the lower troposphere (850 hPa) to middle stratosphere (10 hPa).

The analysis is conducted for the longest available overlap period among the considered reanalysis datasets (1980–2018), and the common 34 pressure levels, ranging from the “lower” troposphere (1000 hPa) up to the “upper” stratosphere (1 hPa), are considered in the analysis (1,000 hPa, 975 hPa, 950 hPa, 925 hPa, 900 hPa, 875 hPa, 850 hPa, 825 hPa, 800 hPa, 775 hPa, 750 hPa, 700 hPa, 650 hPa, 600 hPa, 550hPa, 500 hPa, 450 hPa, 400 hPa, 350 hPa, 300 hPa, 250 hPa, 200 hPa, 150 hPa,

TABLE 1 | Summary of the main characteristics of the selected atmospheric reanalysis datasets.

Dataset (Institution)	Time Range	Temporal Resolution (h)	Model Horizontal Resolution	Model vertical Resolution	Model	Data Assimilation Algorithm	Main Reference
ERA-5 (ECMWF)	1979 - present (preliminary version: 1950-1978)	1	T639 (~31 km)	137 hybrid (σ – p) Top level (0.01 hPa)	IFS release 41r2 (2016)	4D-VAR	Hersbach., et al. (2020)
ERA-Interim (ECMWF)	1979–08/2019	6	T255 (~79 km)	60 hybrid (σ – p) Top level (0.1 hPa)	IFS release 31r2 (2006)	4D-VAR	Dee et al. (2011)
MERRA-2 (NASAGMAO)	1980–present	1	Cubed sphere grid, (~50 km)	72 hybrid (σ – p) Top level (0.01 hPa)	GEOS 5.12.4 (2015)	3D-VAR, with incremental update; Includes aerosol data assimilation, observation corrected precipitation forcing for land surface, and aerosol wet deposition	Gelaro et al. (2017)
JRA-55 (JMA)	1958–present	1	T319 (~55 km)	60 hybrid (σ – p) Top level (0.1 hPa)	JMA GSM (2009)	4D-VAR	Kobayashi et al. (2015)

100 hPa, 70 hPa, 50 hPa, 30 hPa, 20 hPa, 10 hPa, 7 hPa, 5 hPa, 3 hPa, 2 hPa, 1 hPa).

The monthly datasets have been bilinearly interpolated to a common grid and downgraded to the coarsest horizontal resolution grid resolution 1.25° × 1.25° for calculating the RMME. For each grid-point and pressure level, the RMME is therefore estimated as,

$$RMME(t) = \Sigma_k \frac{1}{N} (x_k(t))$$

where t is the time (monthly frequency), N is the number of ensemble members (N=4) and X(t) is an individual reanalysis product.

The global average temperature, calculated for the four considered datasets over the period 1980-2018, and the corresponding differences with RMME are first investigated. Temperature variability of the reanalysis datasets is examined through the time series and seasonal cycle differences diagnostics at regional scales, focusing on the Northern Hemisphere (NH) mid-latitude (25°N–60°N), Southern Hemisphere (SH) mid-latitude (25°S–60°S), and tropics (25° N–25°S).

Temperature trends are estimated using the ordinary linear least-squares fit to estimate the slope. The effect of the serial correlation (lag-1 temporal autocorrelation of the residuals) of the temperature from each dataset was removed. To determine the robustness of the results, the probability test of error (*p*-val) analysis was employed to calculate the confidence interval of the temperature trends.

Comparison with observations is finally performed by inspecting temperature anomalies time series from the considered datasets, focusing on the tropical stratospheric region where the signature of the QBO dominates in the lower stratosphere and TTL. Monthly anomalies are calculated for all the reanalyses and observations by first zonally averaging the monthly temperature (on land only for reanalyses) at 6 selected levels (100 hPa, 70 hPa, 50 hPa, 30 hPa, 20 hPa, and 10 hPa) for the region 10°N–10°S. Then, the difference between the temperature time series and its monthly climatology is generated. The vertical profile of the long-term temperature trend is also inter-compared across reanalyses at 13 standard pressure levels from the lower troposphere (850 hPa) to the middle stratosphere (10 hPa).

4 RESULTS

In the present section, we report the analysis of temperature climatology at the global scale ((**section 4.1**), temperature time series differences and seasonal cycle differences at two time frames 1980–2000 and 2001–2018 at the regional scale to highlight the main differences among the datasets and periods (**section 4.2**), the trend assessment (**section 4.3**) at the global scale and a regional case study (South Polar region). Finally, we compare the reanalyses with the homogenized radiosonde datasets (**section 4.4**).

4.1 Temperature Climatology

The vertical profiles of the zonal mean (latitude vs. pressure level) temperature difference (to RMME) are shown in **Figure 1**. From the lower troposphere to the middle stratosphere (10 hPa), air temperature climatology shows differences ranging within ±0.25 K except for a few atmospheric regions: the equatorial - mid and upper troposphere (0.5–1.0 K, MERRA-2 and JRA-55), the southern pole middle stratosphere (0.5–1.0 K, ERA5) and the equatorial mid-stratosphere (−1.0 to −0.5 K, ERA-Interim). The largest differences (more than 1.5 K) are found in the southern pole (ERA5, ERA-Interim, JRA-55) below 700 hPa. However, temperature values in this region are vertically extrapolated for all considered reanalyses, except for MERRA-2.

From the middle to upper stratosphere, the datasets show larger discrepancies in air temperature climatology. ERA5 (JRA-55) is ~3.5 K warmer (cooler) than RMME over the entire latitudinal range at the levels within 2–7 hPa, while below these levels (7–10 hPa), this signal is reversed. This reported strong warm (cold) tends to disappear between 1 and 2 hPa for both datasets. ERA-interim shows a warm signal over the

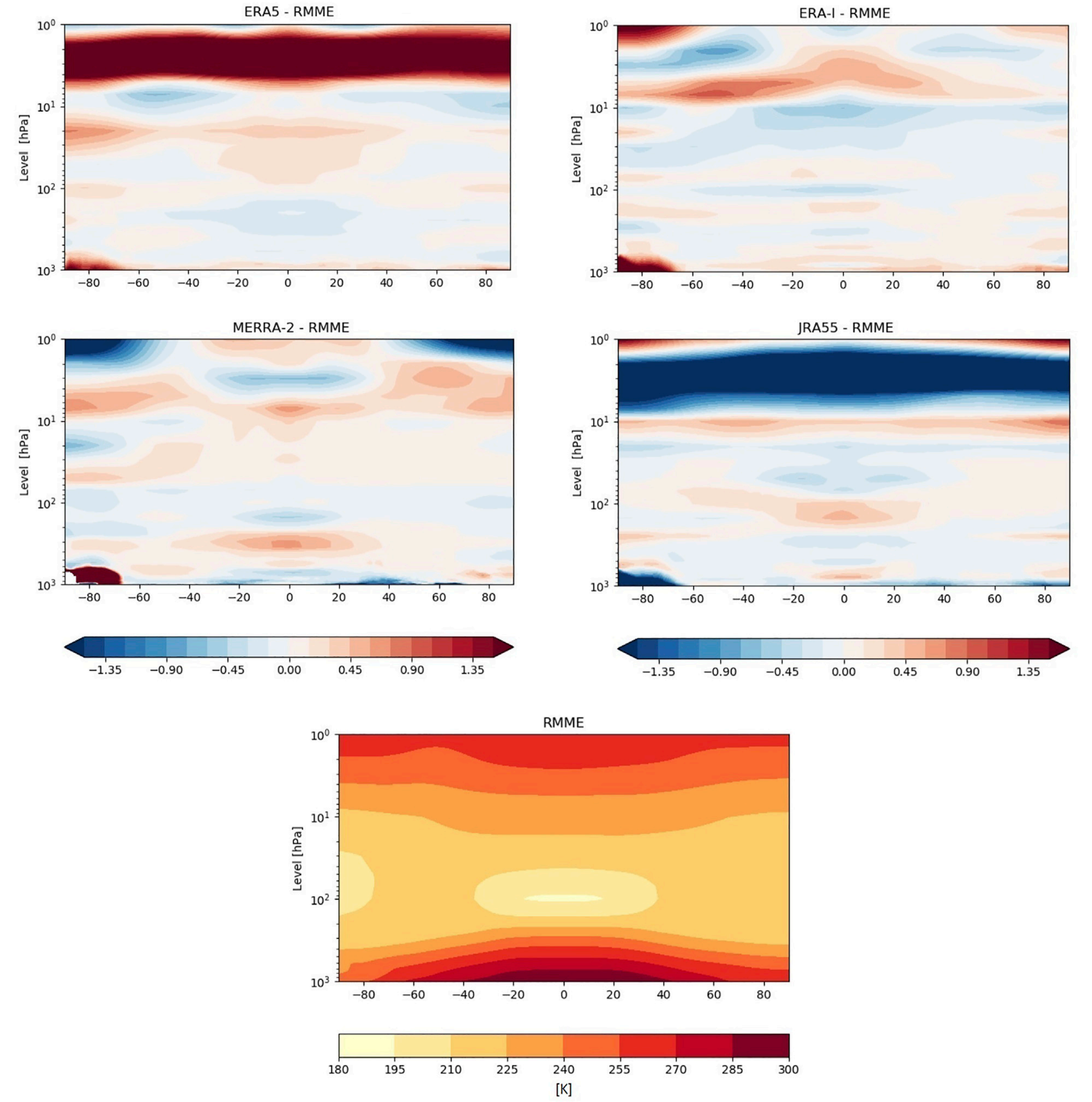

FIGURE 1 | Zonal mean of annual mean temperature difference between reanalyses and RMME for the period (1980–2018), and RMME zonal mean temperature map (bottom panel).

polar region between 1–2 hPa, and in the tropics between 3–7 hPa (extending to 90° S between 5–7 hPa). The opposite is found for MERRA-2 which shows a cooler signal at the same pressure levels and regions.

The reported smooth biases of ERA5 and JRA-55 at all latitudinal ranges are possibly due to the difference between the bias correction applied to the radiance in the assimilation model for each dataset. It is useful to highlight that only scan-angle adjustments to SSU-3 and/or AMSU-A14 (Advanced Microwave Sounding Unit for unit A) radiances are applied in ERA5 while a full adjustment to all SSU and AMSU-A channels are applied in JRA-55, as reported by Simmons et al., 2020. It is worth mentioning that a considerable warmer signal in ERA5 than ERA-interim has been also reported by Hersbach et al. (2020) in the monthly time series of the global mean increments between the reanalyses and first-guess fields, at both 0000 and 1200 UTC in the upper stratosphere due to a bias with respect to anchoring satellite observations that peak at those pressure levels, generating the evident warm signal of ERA5 at those levels.

4.2 Regional Time-Series and Seasonal Cycle Differences

The time series and seasonal cycle are also investigated for all the reanalyses on the regional scale, focusing on the NH mid-latitude (25° N–60° N), SH mid-latitude (25°S–60°S), and tropics (25°N–25°S). Differences between the monthly temperature time series of reanalyses and RMME for these regions are shown in **Figure 2**. The agreement among reanalyses improves after 1998 in the troposphere and lower stratosphere in all regions due to the transition from the TIROS Operational Vertical Sounder (TOVS) to the Advanced TIROS Operational Vertical Sounder (ATOVS). It is worth mentioning that an improvement in the data homogeneity at this atmospheric region in the recent reanalysis datasets compared to their previous generation versions, particularly after ATOV, is also reported by Long et al. (2017). Another evident improvement across reanalyses is found in the tropical upper troposphere after 2006, likely related to the assimilation of GPS-RO COSMIC data. For all considered reanalyses, the availability of the COSMIC mission data in 2006 significantly increased the number of GNSS-RO profiles available for assimilation (SPARC, 2022: **Figure 2**.17 in chapter 2).

Over the time-series 1980-2018, reanalyses datasets agree better in NH mid-latitude than SH and tropics where a smaller difference, within 0.25 K, is found for all reanalyses with respect to the RMME. In tropics, JRA-55 shows the largest bias at 100 hPa (TTL) within 0.5 K, while the ERA5 has the lowest bias in the same atmospheric region.

A more disagreement between reanalyses in the upper stratosphere (above 10 hPa) is found throughout the time period. The uniform bias of ERA5 and JRA-55, reported in **section 4.1**, is found in all regions and over all years. The change between TOV and ATOV is evident in ERA-interim dataset, causing a sudden change in the sign at 1–2 hPa. MERRA-2 also shows a substantial discontinuity around 1995 lasting until 2005 in all regions; afterward, improvement in the data homogeneity due to the assimilation of temperatures from Microwave Limb Sounder (MLS) is found.

Seasonal cycle (i.e., monthly climatology) differences between reanalysis products and RMME are examined for the same regions over two periods, 1980-2000 and 2001-2018 as reported in **Figures 3**, **4** respectively. The reason for dividing this analysis into two periods is to investigate the change in the temperature seasonal cycle before and after the notable

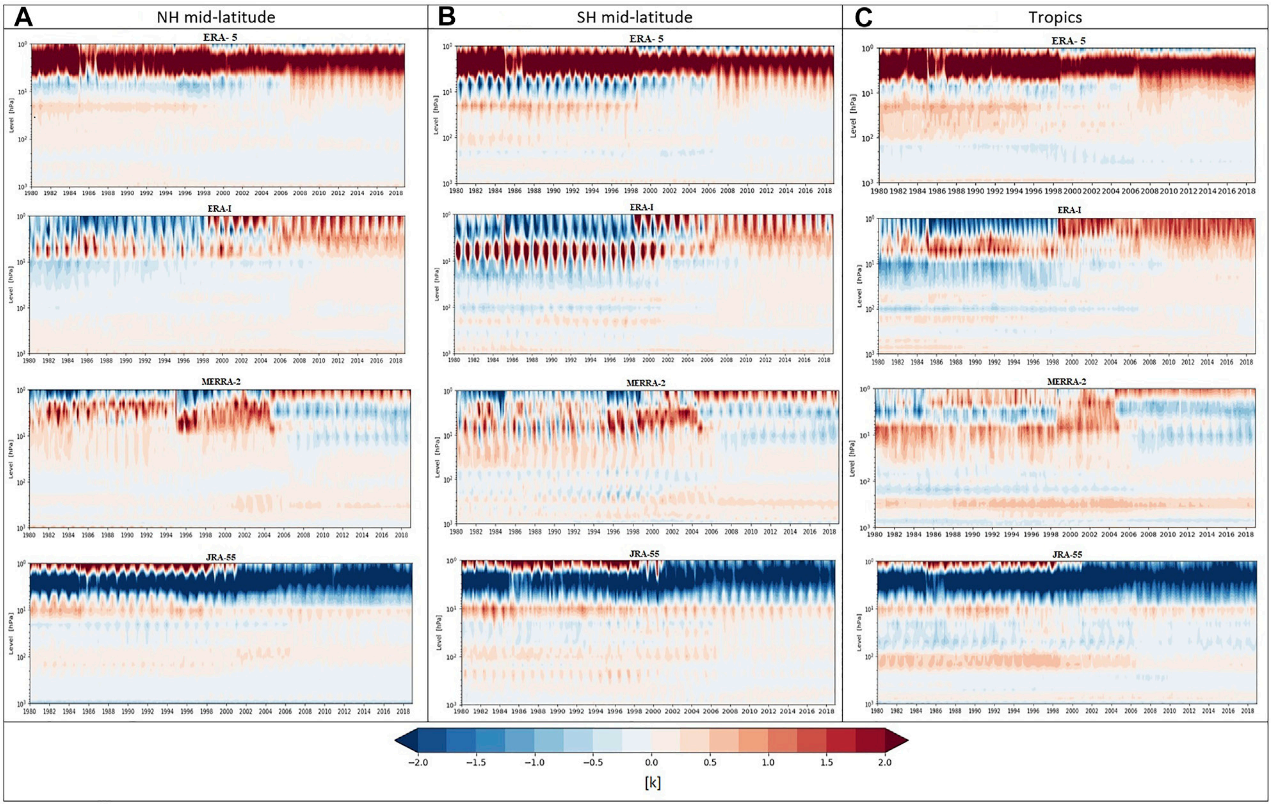

FIGURE 2 | Temperature time-series differences (in K) between reanalysis of time series and RMME in the (**A**-column) NH mid-latitude, (**B**- column) SH mid-latitude, and (**C**- column) tropics, spanning the period 1980–2018.

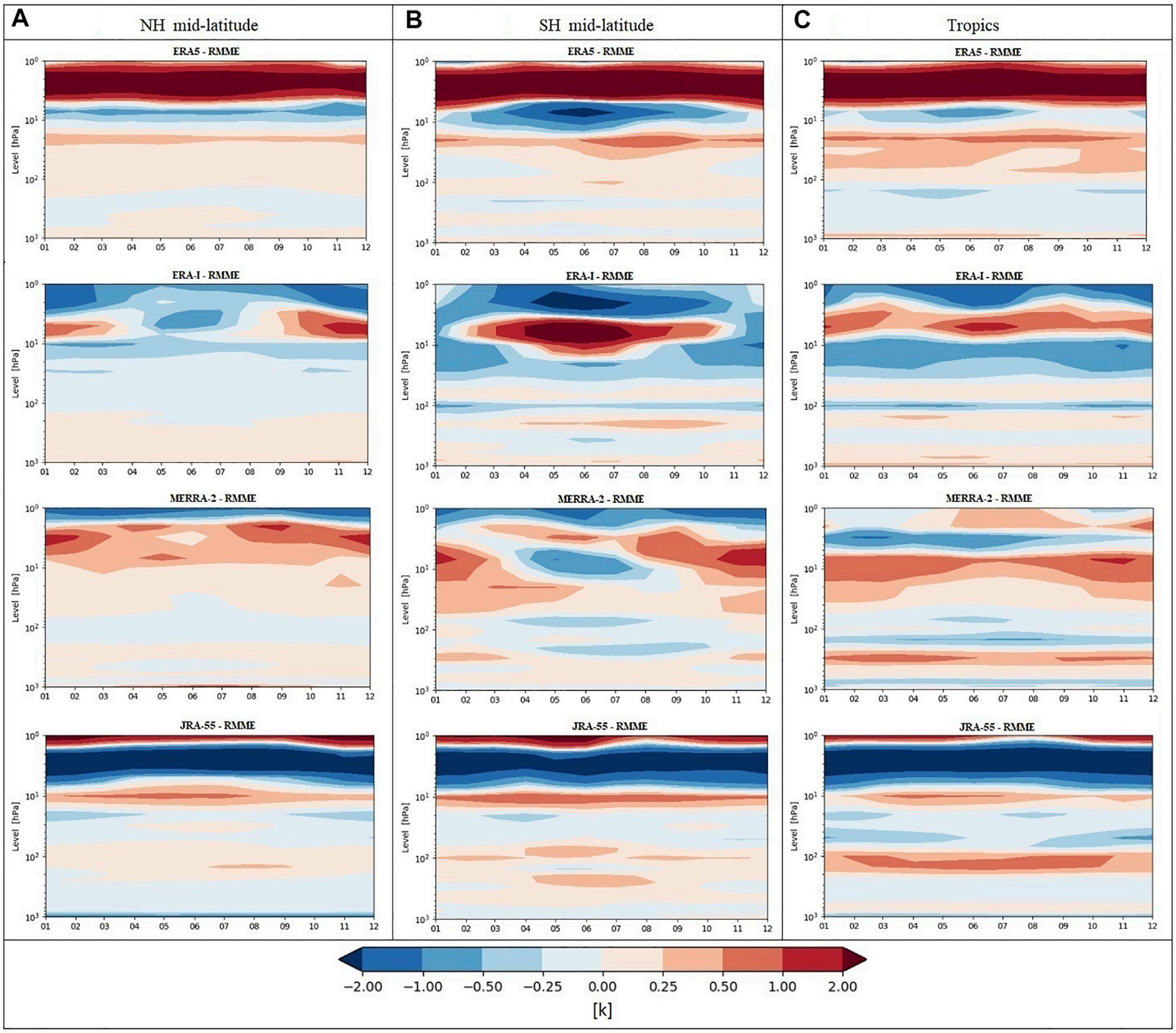

FIGURE 3 | Seasonal cycle difference (month vs. pressure level) differences (in K) between reanalyses and RMME in the (**A-**column) NH mid-latitude, (**B-** column) SH mid-latitude, and (**C-** column) tropics, spanning the period 1980–2000.

improvement in the time series after the availability of ATOVS. The results show a good agreement among all reanalyses which improves after 2000, likely due to the consistency in the assimilation of AMSU-A and AMSU-B radiances–so going from TOVS (1979–2006) to ATOVS (1998 to present), all reanalysis systems assimilate microwave and infrared radiance from these instruments. The improvement can be also due to that all the reanalyses, except for JRA-55, assimilate radiances estimated from the hyperspectral infrared sounders AIRS (2002–present), IASI (2008–present), and/or CrIS (2012–present). In addition, the increasing amount of assimilated observations and, in particular of GNSS-RO, can influence the data performance as pointed out for the tropics.

Among the examined regions, the difference in the seasonal cycle between reanalyses is pronounced in the SH mid-latitudes for the two periods but reduced in magnitude after 2000. In the upper stratosphere, ERA5 shows opposite sign of ERA-Interim at 5–10 hPa. Furthermore, ERA-Interim and MERRA-2 also show different signs in the tropics at the same atmospheric region. For the period 2001–2018, The differences have reversed the sign at 10 hPa for ERA5, and 20–30 hPa for ERA-Interim and MERRA-2.

Discrepancies between reanalyses in the upper stratosphere are controlled by different factors. In addition to the observations' paucity for the assimilation in this atmospheric region, mainly satellite data only, differences between reanalysis models and the treatments applied in the uppermost layers can play a relevant role in representing the temperature variability (Fujiwara et al., 2017).

The warm (cold) year-round bias of ERA5 (JRA-55) in the upper stratosphere found in the two periods and entire the

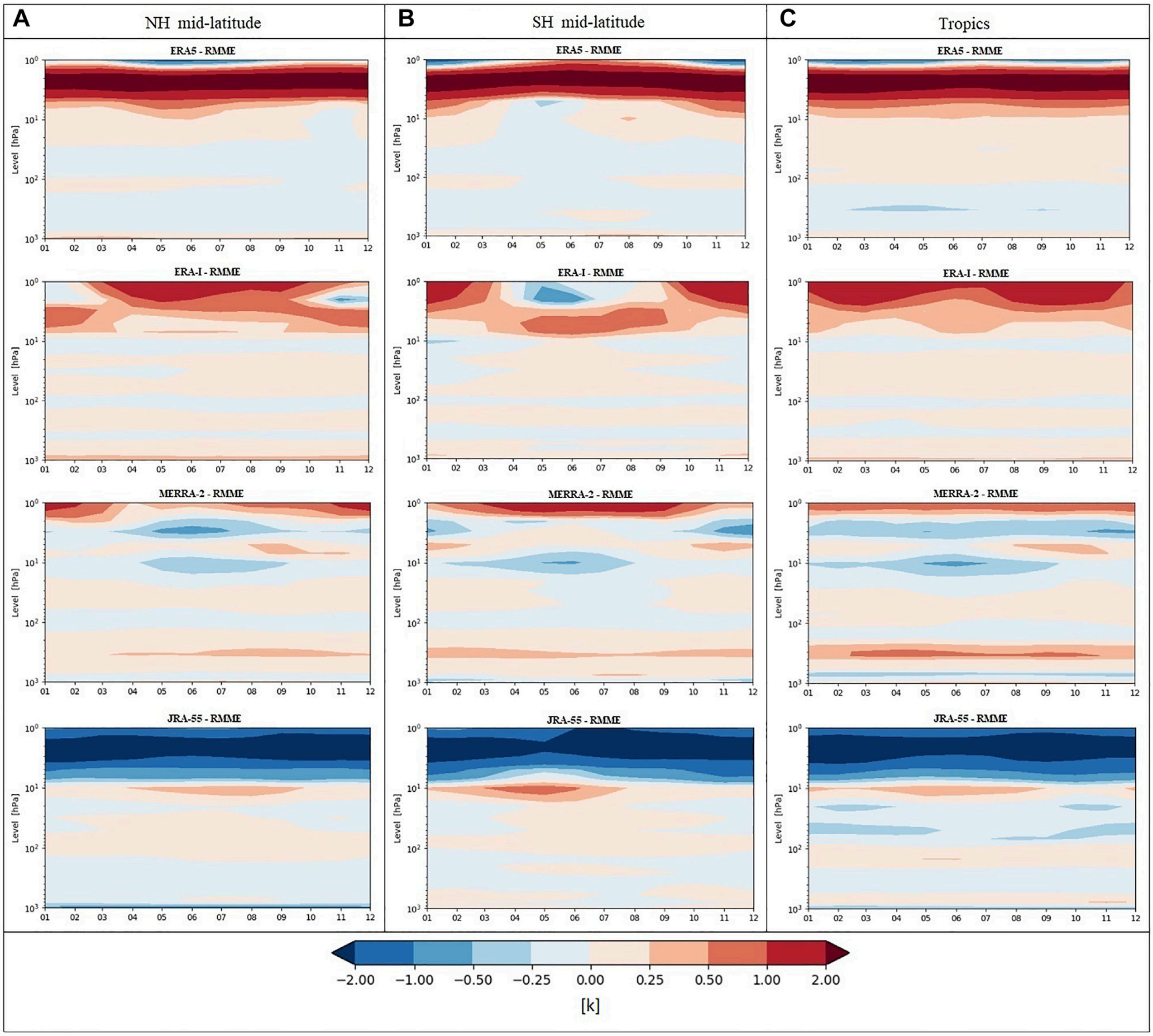

FIGURE 4 | Same as **Figure 3** but for the period 2001-2018.

investigated latitudinal ranges can possibly refer to the dominating role of the radiation representation in ERA5 and JRA-55 versus the role of representing the atmospheric circulation, dominant in ERA-Interim and MERRA-2.

4.3 Trend Analysis

Inaccurate climate trend detections may lead to deceptive conclusions about the current state and future evolution of climate. Despite the uncertainties affecting their estimations, trends are widely used to assess climate changes in both the scientific and stakeholders" communities. Regression methods represent a good relative diagnostic tool when different datasets are intercompared. Inhomogeneities in climate data records are one of the main issues affecting the reliability of the trends" estimation. For example, obtaining robust and consistent inferences about the long-term trend from different products that assimilate different types of observing systems can be challenging. Therefore, studying the coherence of trends for the reanalyses datasets can be crucial to assess the datasets" suitability for trend estimation.

In the next subsections, we investigate the ability of the considered reanalyses in defining the vertical profile of the global temperature trend; this diagnostic is considered as a fingerprint of climate change (Santer et al., 2013). The global zonal mean trend is also discussed along with the agreements/discrepancies between the considered datasets at different latitudes. Finally, we provide a case study on a regional scale at the southern pole, where the role of stratospheric dynamics in past changes of the Southern Hemisphere climate is evident (Cagnazzo et al., 2013).

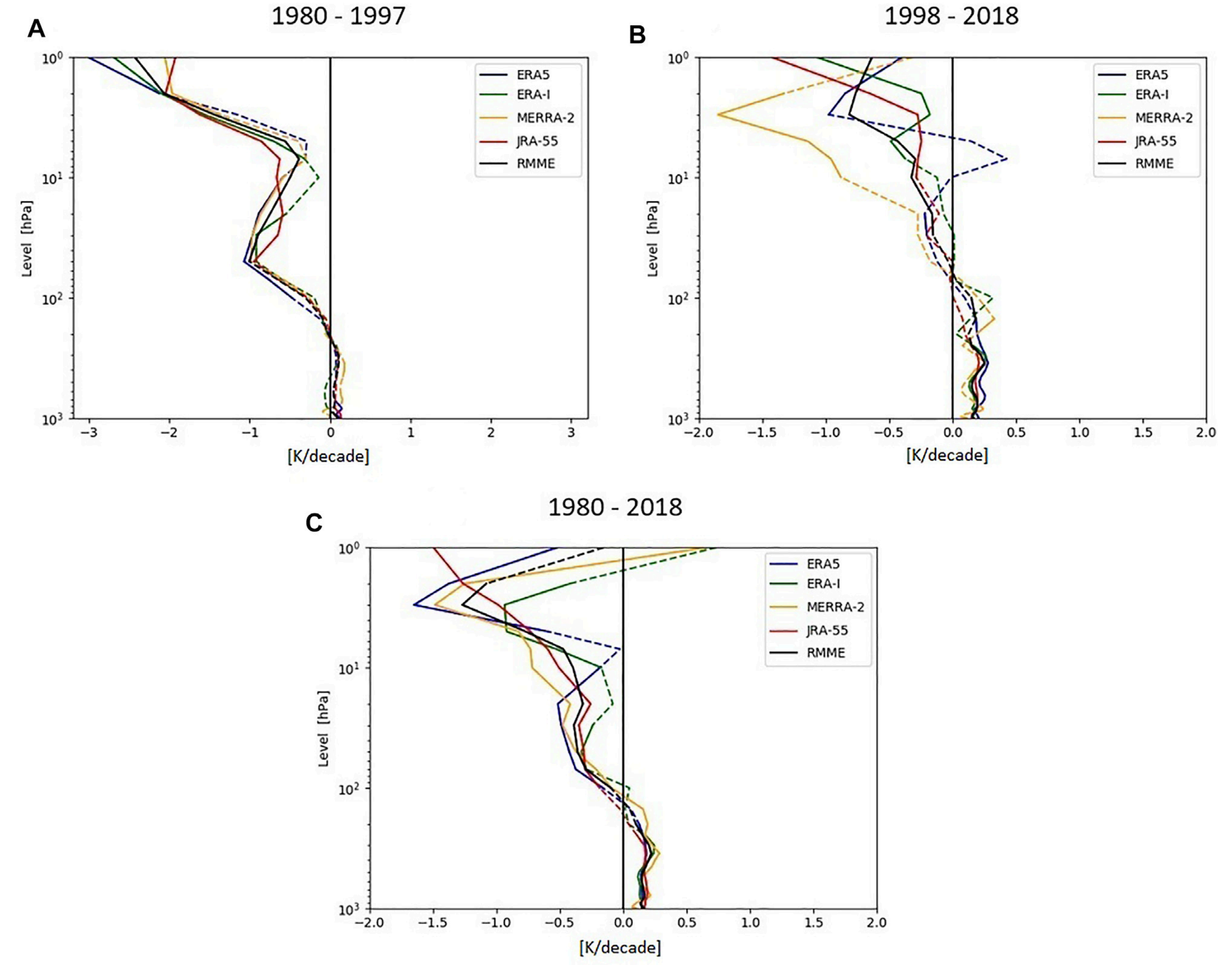

FIGURE 5 | Vertical profiles of global mean temperature trends (K/decade) in the four reanalysis datasets (colored lines), and the RMME (black line). Trends are calculated for **(A)** 1980–1997, **(B)** 1998–2018, and **(C)** 1980–2018. The solid lines represent trends at the confidence interval of 95% (*p*-val ≤ 0.05).

4.3.1 Vertical Profile of the Global Trend

The vertical trend profiles of global average deseasonalized temperatures over 1980–2018, 1980–1997, and 1998–2018, are shown in **Figure 5**. The two sub-periods (1980–1997 and 1998–2018) were selected to examine the weak stratospheric cooling that occurred in 1998–2018 compared to the period characterized by the large ozone depletion and associated cooling in 1980–1997 (Maycock et al., 2018).

Over 1980–1997, the ozone effect is evident in the period of maximum ozone depletion in the stratospheric layers (top-left panel of **Figure 5**), with the strongest cooling signal (~−3 K/decade) in the upper stratosphere near 1 hPa. A good agreement among the datasets is found for this period.

After 1997, the lower stratosphere cooling is dominated by the increase in GHGs (WMO Ozone assessment, 2018), and it becomes less robust for pressure levels below 20 hPa. This finding agrees with the reported stratospheric warming in the recent decades (Philipona et al., 2018). The results are less consistent among the datasets in the mid-upper stratosphere. For ERA-Interim, JRA-55, and MERRA-2, a stratospheric cooling with height up to 5 hPa is found, but with a magnitude smaller than within the preceding period (~−1.5 K/decade), instead, ERA5 shows a weakening of the cooling, and a non-robust warming signal is found at the levels 5–7 hPa. The temperature increase in the stratosphere is likely due to feedback related to the ozone layer recovery and to the changes in the concentrations of stratospheric halogen gases (WMO World Metrological Organization 2018), in analogy to what has been discussed in Randel et al. (2016).

Over the entire time period 1980–2018, the trends show a clear increase in the stratospheric cooling with height up to 20 hPa. This cooling is dominated by the known effect of carbon dioxide increase and ozone depletion on stratospheric temperatures before 1997 (Shine et al., 2003; Aquila et al., 2016; Steiner et al., 2020). Those effects result in maximum cooling into the lower stratosphere. Above 20 hPa, all datasets show a vertical weakening of the cooling trend, except for JRA-55 which shows a cooling up to 1 hPa. JRA-55 cooling is consistent with the reported temperature trends in the upper stratosphere for 1979–2018 using the SSU channels (Steiner et al., 2020).

In the troposphere, temperature trends behave differently through the considered periods. The tropospheric warming over 1980–2018 (order of 0.25 K/decade) is dominated by the 1998–2018 warming trends. Temperature warming trends in the upper troposphere are not robust, consistent with both large internal variability (Suárez-Gutiérrez et al., 2017) and with uncertainties associated with upper-air data in this atmospheric region (Dirksen et al., 2014; Madonna et al., 2020).

For 1980–2018, the warming (cooling) in the lower troposphere (stratosphere) is a robust trend. Although the separation in the two sub-periods has chosen to focus on stratospheric temperature trends, this choice is in line with the known controversy about the rate of tropospheric warming that was discussed since the 1990s (Spencer and Christy, 1990; Christy and Norris, 2004): global warming trends are indistinguishable from variability in the period 1980–1997 (for a few reanalyses trends are even negative) but become stable, positive and robust after 1998. In this study, the major volcanic signals are not removed from the full-time series, therefore, Pinatubo volcanic eruption that occurred quite late in the 1980–1997 period, causing warming in the stratosphere and cooling in the troposphere for several months following the event, may partially contribute to the weakening of tropospheric warming and stratospheric cooling during this period (Stocker et al., 2019).

4.3.2 Global Zonal Mean Trend

The global annual zonal mean of temperature trends is shown in **Figure 6**. In general, there is a good agreement among the examined reanalyses in both the warming and cooling patterns. For all the latitudes, the warming in the troposphere

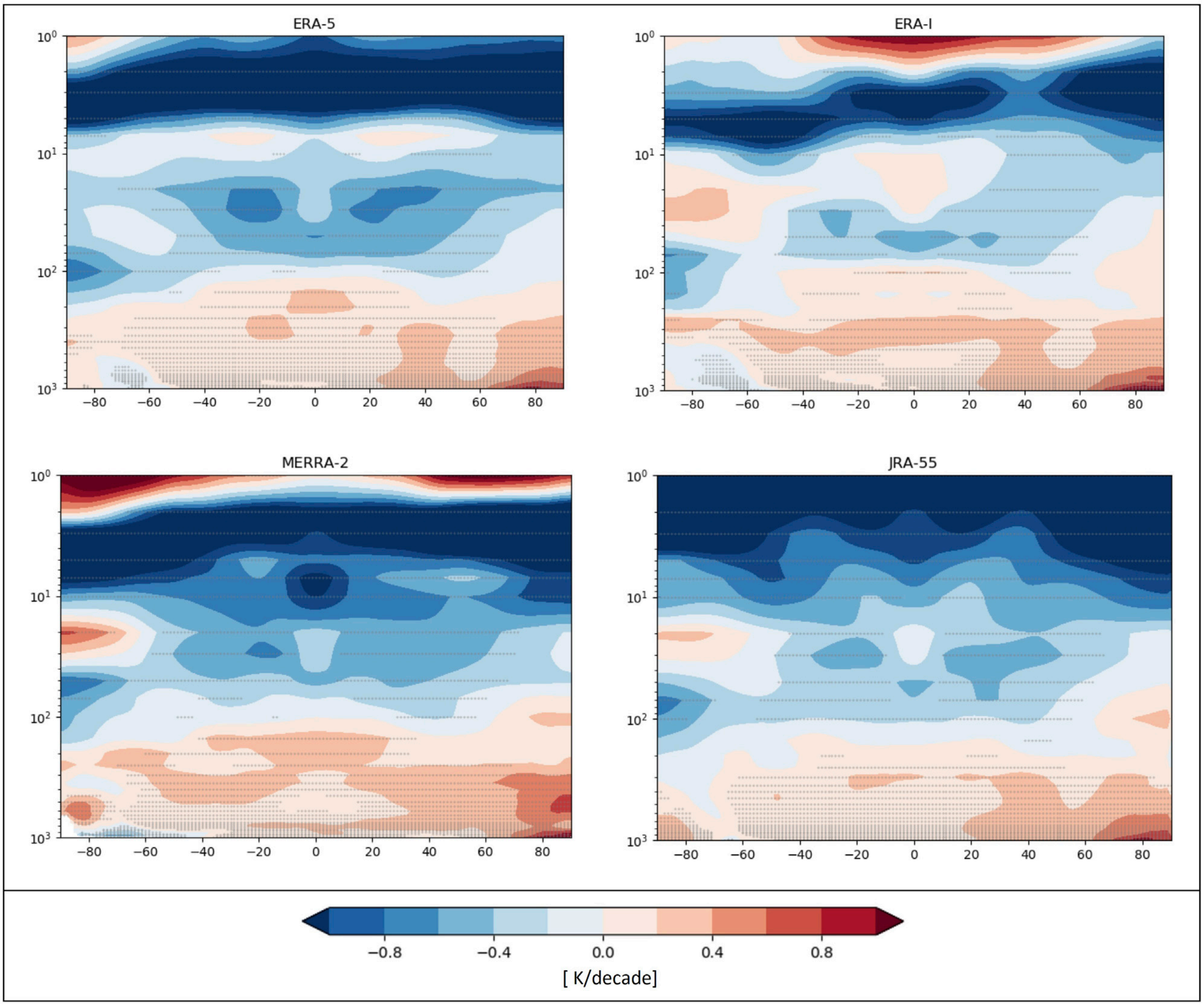

FIGURE 6 | Global zonal mean temperature trends [K/decade] of the period (1980-2018) for five reanalyses and the RMME. Gray dots represent confidence intervals 95% (p-val ≤ 0.05) of the trends.

and the cooling in the stratosphere are largely due to the radiative forcing associated with the increase in GHGs and with the decrease of stratospheric ozone (peaking in the Southern Hemisphere). The cooling in the stratosphere, concomitant to the warming in the troposphere, has been reported for the first time by Manabe and Wetherald (1967) and it is considered a typical fingerprint of increasing CO_2 in the extratropical regions (Santer et al., 2013). Meanwhile, the Arctic amplification, i.e., the large near-surface warming in the Northern Hemisphere high latitudes, is also evident in all datasets although with some difference in the magnitude.

In terms of differences, the southern pole warming (south of 60°S at around 20 hPa) is not reproduced in ERA5 dataset. MERRA-2 provides the largest warming trends in the mid-troposphere in the tropics (from 250 hPa to 300 hPa). A warming signal is detected by ERA-interim and MERRA-2 at the topmost stratosphere (1–3 hPa), albeit for ERA-interim is limited to the 50°S–70°N region. In general, the agreement in the sign of trends among the reanalyses shows a lower consistency in the tropopause, in the stratosphere at levels above 30 hPa, and in high southern latitudes.

4.3.3 Regional Trend: The Case of the Southern Pole

The global annual mean trends are dominated by changes in radiative forcing, nevertheless, trends in specific atmospheric regions and seasons also include signals due to changes in the atmospheric circulation and its dynamical forcing, especially in the stratosphere. In this section, we focus on the monthly temperature trends in the Southern Hemisphere (south of 60°S) for all the reanalysis datasets in the period 1980 to 1997.

As discussed in **section 4.3.2**, the observed temperature changes in this atmospheric region are dominated by the radiative forcing due to the increase of GHGs and the decrease of stratospheric ozone (due to increasing the ozone-depleting substances), but also feedback due to changes in the large-scale circulation (Screen et al., 2018).

In agreement with past studies, over the southern polar region, trends in the lower stratosphere peak in November, about 1 month after the maximum ozone depletion occurs in October (e.g., Trenberth and Olson, 1989; Randel and Wu, 1999). As shown in **Figure 7**, the obtained results of all reanalyses report the known seasonal evolution of stratospheric changes, with a cooling starting in September and lasting until March in the vertical range 30–200 hPa, reaching maxima in November and December. The peak cooling value is of -3.0 K/decade for all datasets. A consistent cooling trend, in order of −2.0 to −3.0 K/decade, has been reported by Thompson and Solomon (2002) using radiosonde data for the period 1969–1998. Part of this difference in the magnitude could be associated with a different dynamical response, across reanalyses, related to the representation of different processes in the reanalysis models (e.g., input to radiation scheme, feedback to large-scale stratospheric circulation, Brewer-Dobson circulation), similar to what is found for climate models (Cagnazzo et al., 2013; Rea et al., 2018). During the rest of the year, the stratosphere shows a general cooling (not fully evident in **Figure 7** because of the choice of contour levels), mostly associated with the radiative effect of increasing CO_2. At and below 300 hPa, all reanalyses show a marginally warming, in agreement with radiosonde analysis (though for a different period, Thompson and Solomon, 2002).

Above the large cooling, all considered reanalyses report a warming pattern in the mid-stratosphere, in agreement with what was reported in past studies, even if for a slightly different period (Cagnazzo et al., 2013; Rea et al., 2018). This warming has been diagnosed as a manifestation of the stratospheric dynamical response associated with changes in the residual circulation. The obtained results indicate that all considered reanalyses are able to capture the upper stratosphere circulation response and its feedback on temperature, with a signal that may be different in magnitude and in the time occurrence of peak values, although generally well represented.

4.4 Comparison With Upper-Air Radiosonde Observations

Comparison with observations is crucial for understanding the performance of reanalyses products. This section compares temperature variability and long-term trends estimated from reanalyses and homogenized upper-air radiosoundings data. Given the detailed characterization of the reanalysis datasets presented above, the comparison with upper-air observations is focused on the assessment of specific aspects of climate and atmospheric circulation in the tropics. This analysis aims to provide evidence of consistency among the datasets in a region where the representativeness error is smaller than at other latitudes.

Monthly temperature anomalies for the period 1980–2018 of the reanalyses (ERA5, ERA-Interim, MERRA-2, and JRA-55), RAOBCORE and RICH datasets for the region 10° N–10° S are shown in **Figure 8** at the pressure levels from 100 hPa to 10 hPa. The results show a good agreement for all considered datasets. The well-known variability associated with major volcanic eruptions (El Chichon 1982; Pinatubo 1991) is evident in all datasets, particularly between levels 20–30 hPa. Among the considered reanalyses, ERA5 shows the lowest differences with respect to the radiosonde data, while a notable difference in magnitude, within the range of 4 K, is found for ERA-Interim, MERRA-2, and JRA-55. For 10 hPa and 100 hPa levels, the datasets tend to show slightly larger differences compared to observations in a few years, within ±4 K and ±2 K respectively. However, similar patterns in all datasets are produced and this difference clearly decreases after 2000. It is worth mentioning that this intercomparison is not fully independent due to the fact that RAOBCORE adjustments have been used for radiosonde bias correction in ERA-Interim, MERRA-2, and JRA-55, and RICH is used in ERA5. Differences between reanalyses and RAOBCORE/

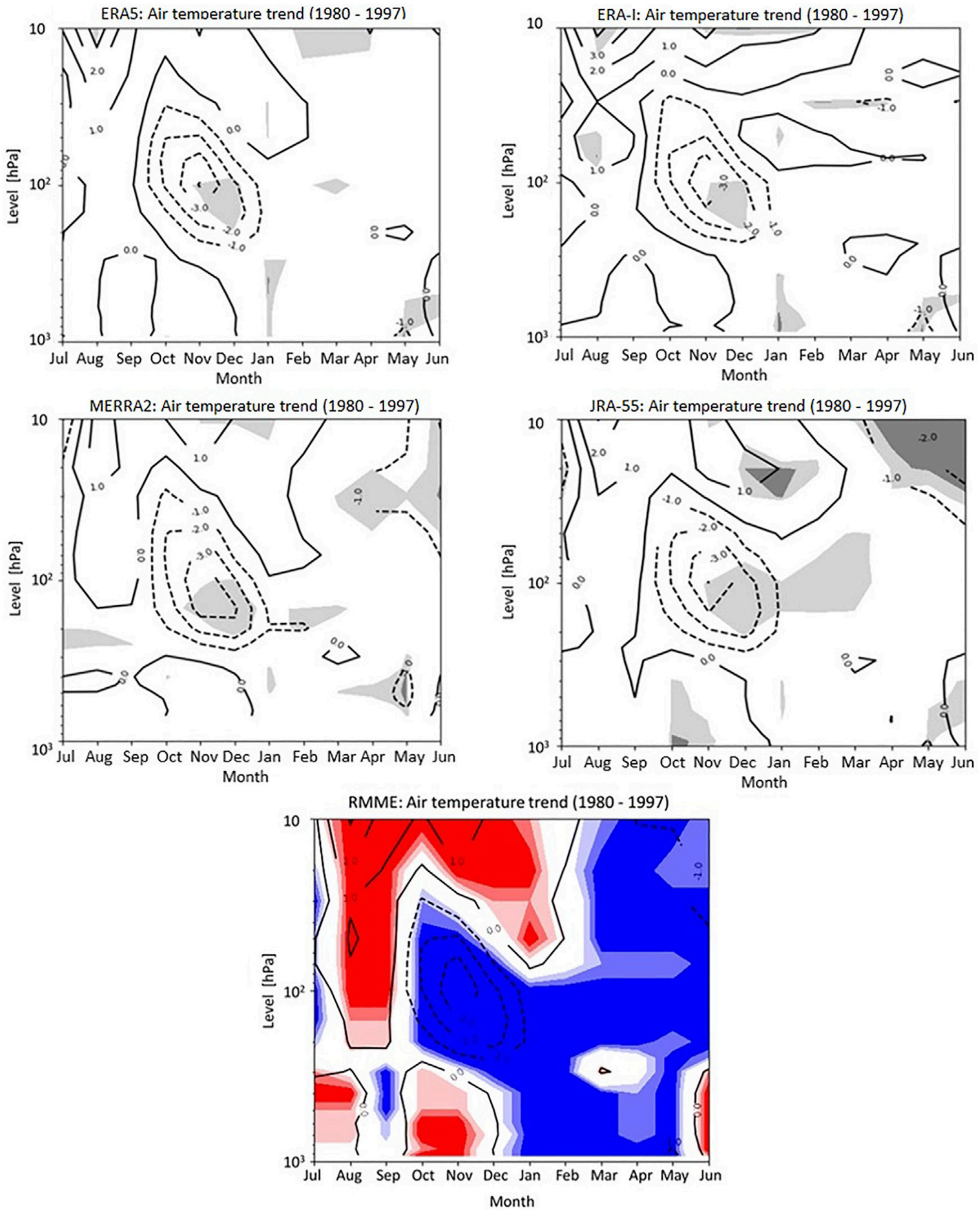
ERA5: Air temperature trend (1980 - 1997)

ERA-I: Air temperature trend (1980 - 1997)

MERRA2: Air temperature trend (1980 - 1997)

JRA-55: Air temperature trend (1980 - 1997)

RMME: Air temperature trend (1980 - 1997)

FIGURE 7 | Southern pole temperature trends for the period 1980–1997. Contour intervals are 1.0 K/decade. Trends at 95 and 99% confidence levels in reanalyses are shaded (light and dark grey, respectively). Agreement of sign between datasets in RMME are colored in blue (red) for cooling (warming) trend, and shades for number of datasets in agreement.

RICH are possibly due to differences in the datasets' characteristics (e.g., assimilation schemes, the model used, datasets resolution, spatial sampling, etc.).

Moreover, it is most notably that the resulted anomaly patterns for all considered reanalyses reflect a reliable representation of the atmospheric circulation in the tropical stratosphere, where the temperature is dominated by QBO signature in this atmospheric region; positive temperature anomalies correspond to westerlies and negative temperature anomalies correspond to easterlies (Pascoe et al., 2005; Yamazaki et al., 2020).

The vertical profile of the long-term trend of temperature, estimated using the linear least-squares method, is also intercompared for all reanalyses and observational datasets (RAOBCORE, RICH, and RHARM) in the tropics (25°N - 25° S) from the lower troposphere (850 hPa) to the middle stratosphere (10 hPa). As shown in **Figure 9**, all datasets are in very good agreement from the lower to middle troposphere

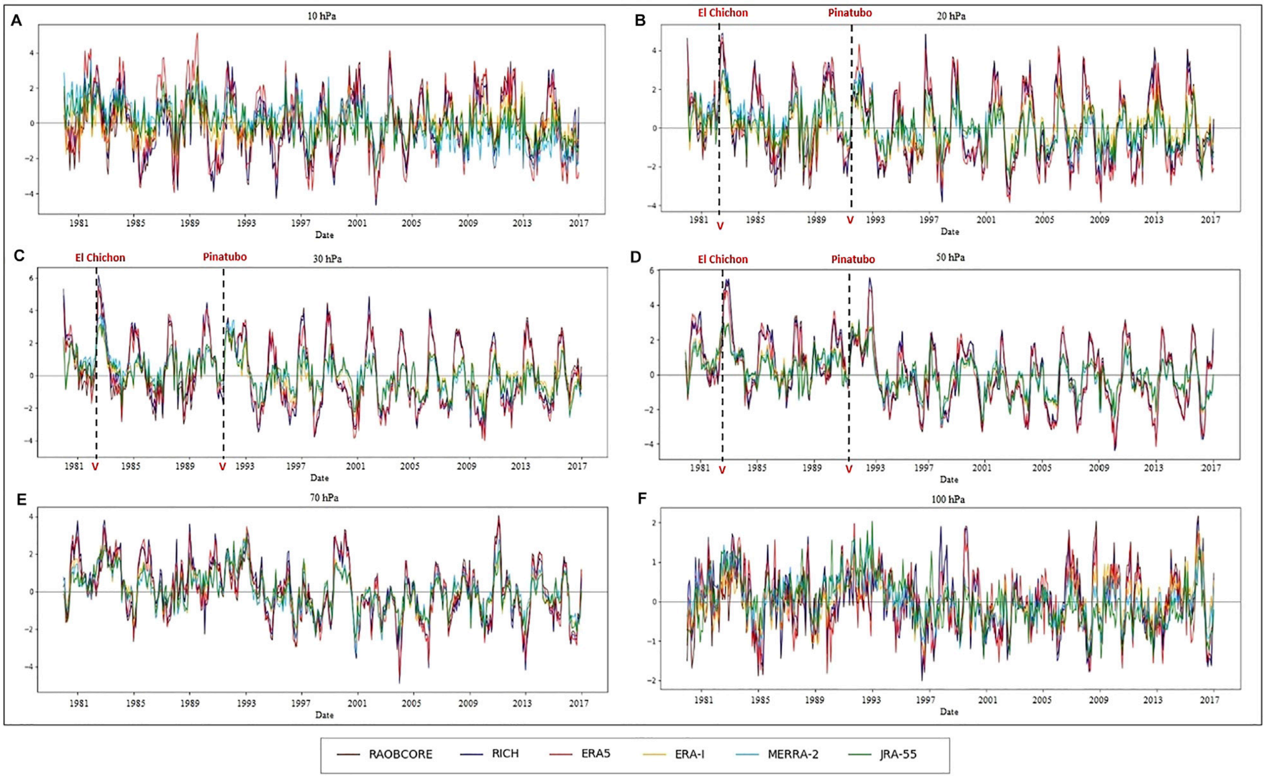

FIGURE 8 | Monthly temperature anomalies at the region 10°S - 10°N of the radiosonde observations (RAOBCORE and RICH) and the four reanalysis datasets (ERA5, ERA-Interim, MERRA-2, and JRA-55), for the vertical levels **(A)** 10 hPa, **(B)** 20 hPa, **(C)** 30 hPa, **(D)** 50 hPa, **(E)** 70 hPa, and **(F)** 100 hPa, over the period 1980–2018.

(250 hPa) for both the trend sign and magnitude. At and above 100 hPa, the reanalyses (except for ERA-Interim at 10 and 100 hPa) agree with observations in the sign although there are differences in the magnitude.

At the pressure levels between 100 hPa and 250 hPa, discrepancies in the trend results are evident not only between reanalyses and observational datasets but also among the observational datasets. RHARM is the only dataset that shows a cooling trend at the pressure levels 150–250 hPa, while RAOBCORE and RICH show a slight warming trend. It is worth mentioning that ERA5 and MERRA-2 show a warming trend with twice the magnitude of RAOBCORE/RICH datasets at these levels.

5 DISCUSSION AND CONCLUSION

The current study investigates and intercompares the upper air temperature provided by the recent generation of four global reanalyses datasets (ERA5, ERA-Interim, MERRA2, and JRA-55) in terms of their mean state, variability, and trends estimation.

The considered reanalyses are characterized by relatively high spatio-temporal and vertical resolution, and no missing data in space (except for MERRA-2 below at and below 700 hPa) and time over 4 decades. All datasets provide consistent reproduction of the upper air temperature although discrepancies are found, mainly due to differences in the reanalysis systems configuration.

The zonal mean of temperature differences agrees with RMME within ±0.25 K from the lower troposphere to the middle stratosphere (10 hPa), except for a few atmospheric regions, such as equatorial mid and upper troposphere, upper stratosphere south of 60°S, equatorial mid-stratosphere. Larger differences (within +3.5 K), instead, and less consistent results are found in the upper stratospheric levels.

Although the temperature data at the southern polar region (Antarctic) is vertically extrapolated and provided for ERA5, ERA-Interim, and JRA-55 below 700 hPa, the datasets largely disagree in this atmospheric region, possibly due to different extrapolation methods. Therefore, special care is strongly recommended to be used for climate studies or applications in this region.

The agreement between the considered reanalyses increased after 1998 owing to the transition from TOVS to ATOVS and the enhanced consistency between the data assimilation systems. At the regional scale, the reanalyses agree better in NH mid-latitudes than in tropics and SH mid-latitudes. The

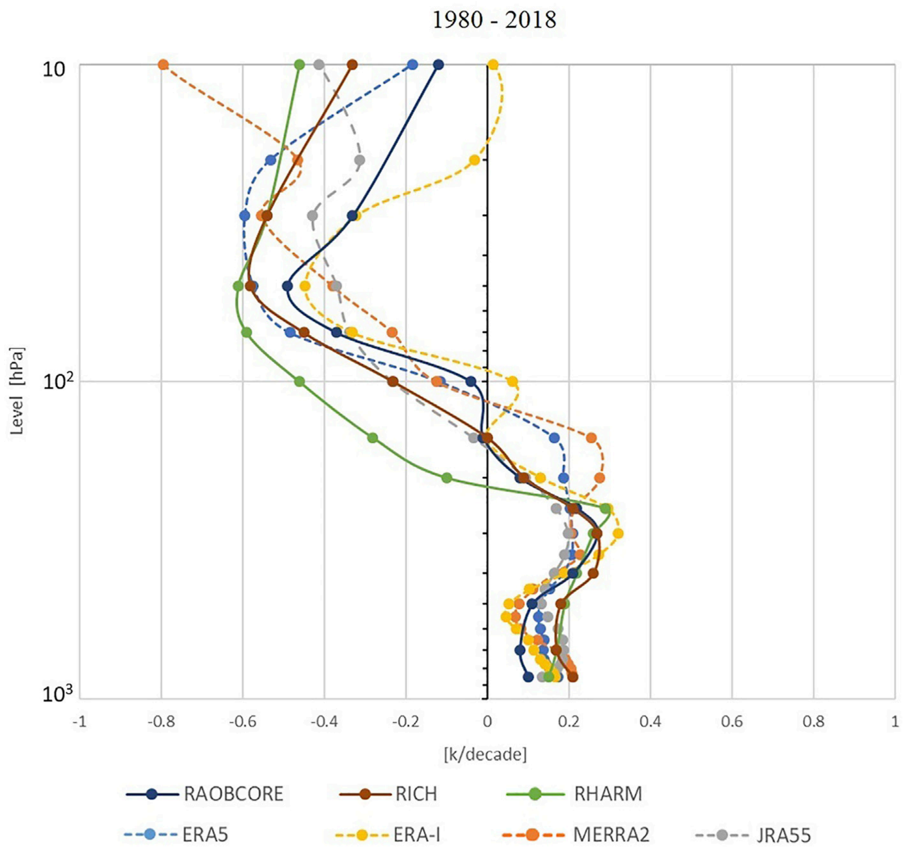

FIGURE 9 | Vertical profiles of temperature trends (K/decade) for tropics (25° N - 25° S) of radiosonde observations (solid lines) and the four considered reanalysis datasets (dashed lines), spanning the period 1980–2018.

differences among the datasets largely decrease in all regions after 2000, due to the increase in the amount of assimilated observations.

The tropospheric warming and stratospheric cooling are evident in the long-term temperature trend for all evaluated datasets. However, differences in the magnitude are found. Over the period 1980–1997, global temperature trends showed significant cooling in the lower stratosphere. The same is observed over the period 1998–2018 but only above 20 hPa and for specific datasets, consistently with the reported stratospheric warming after a decade of cooling by Philipona et al. (2018). A significant warming trend is found in the troposphere, in particular for the period 1998–2018. The large spread among the datasets indicates that caution needs to be deserved in estimating the trends above 30 hPa and at the tropopause level.

Comparisons of reanalyses and homogenized upper-air radiosounding data in the tropics reveal a reliable representation of the temperature variability and long-term trend for all reanalyses from the lower to the middle troposphere and in the lower stratosphere. Differences between datasets are evident in the upper troposphere, TTL, and middle stratosphere. Among the reanalyses, ERA5 shows the smallest bias in the monthly anomaly, on average, in the levels from 30 hPa to 70 hPa.

The findings of our analysis, including the recent ERA5 reanalysis and multiple *in-situ* observational datasets, are generally consistent with the major outcomes provided by the final S-RIP report (SPARC, 2022). The increase in the spatial, temporal, and vertical resolutions of the new generation of reanalysis allows to resolve a larger number of processes in the atmosphere, enhances performances, for example, of the trends with the homogenized upper-air data. Nonetheless, relevant issues are still present for all considered reanalyses mainly in the upper atmosphere, where caution is recommended, taking into account dataset-specific characteristics to avoid misleading data interpretations.

Researchers and reanalyses users are interested to know which dataset is the most suitable for their own study or applications. Although the obtained results in this study cannot provide a general answer to this question, specific suggestions and recommendations can be provided on the basis of the used diagnostics:

- For studies/applications that require the construction of long-term climatologies in the stratosphere, it is strongly

suggested to use data after 1998 (in all reanalyses systems presented here).
- For analysis focused on the TTL, it is recommended to use data from reanalyses systems with a high vertical resolution in their original grid.
- For the trend estimation, caution must be deserved in the mid-upper stratosphere (≤30 hPa, at the global level) and in Tropical Tropopause Layer (TTL)
- Although usage of multi-reanalyses of the same family is suggested to reduce the uncertainties, caution is recommended in the interpretation of trends driven by the assimilated data and the external forcing.

This study complements previous studies (e.g., Long et al., 2017) by including ERA5 which is most recent but, as a consequence, the less explored in the literature compared to other reanalyses, thus providing additional value to the scientific communities who are interested in using atmospheric reanalyses for their studies and applications.

DATA AVAILABILITY STATEMENT

The original contributions presented in the study are included in the article/supplementary material, further inquiries can be directed to the corresponding author.

AUTHOR CONTRIBUTIONS

YH contributed to designing the methodology, result analysis, and Writing the Original Draft Preparation. CC oversight and lead the planning of the work, designing the methodology, result analysis, and Review–Editing process of the manuscript. FM contributed to the designing the methodology, validation process, and Review; Editing process of the manuscript PC contributed to the designing the methodology, and the Review–Editing process of the manuscript. CY formulate overarching research goals and aims, and Review; Editing process of the manuscript FS contributed to the validation process, and Review–Editing process of the manuscript LC contributed to the Review and Editing process. RS Manage and coordinate the responsibility for the research activity planning, Writing and Review; Editing process.

FUNDING

This work is funded by European Copernicus Climate Change Service (C3S) implemented by European Centre for Medium-Range Weather Forecasts (ECMWF) under the service contract Independent Assessment on ECVs led by National Research council of Italy (CNR) with the service contract number as ECMWF/Copernicus/2017/C3S_511_CNR.

REFERENCES

Alghamdi, A. S. (2020). Evaluation of Four Reanalysis Datasets against Radiosonde over Southwest Asia. *Atmosphere* 1-1411 (4), 402. doi:10.3390/atmos11040402

Aquila, V., Swartz, W. H., Waugh, D. W., Colarco, P. R., Pawson, S., Polvani, L. M., et al. (2016). Isolating the Roles of Different Forcing Agents in Global Stratospheric Temperature Changes Using Model Integrations with Incrementally Added Single Forcings. *J. Geophys. Res. Atmos.* 121, 8067–8082. doi:10.1002/2015JD023841

Baatz, R., Hendricks Franssen, H. J., Euskirchen, E., Sihi, D., Dietze, M., Ciavatta, S., et al. (2021). Reanalysis in Earth System Science: Toward Terrestrial Ecosystem Reanalysis. *Rev. Geophys.* 59, e2020RG000715. doi:10.1029/2020RG000715

Buchard, V., da Silva, A. M., Colarco, P. R., Darmenov, A., Randles, C. A., Govindaraju, R., et al. (2015). Using the OMI Aerosol Index and Absorption Aerosol Optical Depth to Evaluate the NASA MERRA Aerosol Reanalysis. *Atmos. Chem. Phys.* 15, 5743–5760. doi:10.5194/acp-15-5743-2015

Buchard, V., Randles, C. A., da Silva, A. M., Darmenov, A., Colarco, P. R., Govindaraju, R., et al. (2017). The MERRA-2 Aerosol Reanalysis, 1980 Onward. Part II: Evaluation and Case Studies. *J. Clim.* 30, 6851–6872. doi:10.1175/JCLI-D-16-0613.1

Cagnazzo, C., Manzini, E., Fogli, P. G., Vichi, M., and Davini, P. (2013). Role of Stratospheric Dynamics in the Ozone-Carbon Connection in the Southern Hemisphere. *Clim. Dyn.* 41, 3039–3054. doi:10.1007/s00382-013-1745-5

Christy, J. R., and Norris, W. B. (2004). What May We Conclude about Global Tropospheric Temperature Trends? *Geophys. Res. Lett.* 31 (6), a–n. doi:10.1029/2003GL019361

Dee, D. P., Uppala, S. M., Simmons, A. J., Berrisford, P., Poli, P., Kobayashi, S., et al. (2011). The ERA-Interim Reanalysis: Configuration and Performance of the Data Assimilation System. *Q.J.R. Meteorol. Soc.* 137, 553–597. doi:10.1002/qj.828

Dirksen, R. J., Sommer, M., Immler, F. J., Hurst, D. F., Kivi, R., and Vömel, H. (2014). Reference Quality Upper-Air Measurements: GRUAN Data Processing for the Vaisala RS92 Radiosonde. *Atmos. Meas. Tech.* 7, 4463–4490. doi:10.5194/amt-7-4463-2014

Durre, I., Yin, X., Vose, R. S., Applequist, S., and Arnfield, J. (2018). Enhancing the Data Coverage in the Integrated Global Radiosonde Archive. *Journal of Atmospheric and Oceanic Technology* 35 (9), 1753–1770. doi:10.1175/JTECH-D-17-0223.1

Fujiwara, M., Wright, J. S., Manney, G. L., Gray, L. J., Anstey, J., Birner, T., et al. (2017). Introduction to the SPARC Reanalysis Intercomparison Project (S-RIP) and Overview of the Reanalysis Systems. *Atmos. Chem. Phys.* 17, 1417–1452. doi:10.5194/acp-17-1417-2017

Gelaro, R., McCarty, W., Suárez, M. J., Todling, R., Molod, A., Takacs, L., et al. (2017). The Modern-Era Retrospective Analysis for Research and Applications, Version 2 (MERRA-2). *J. Clim.* 30 (4), 5419–5454. doi:10.1175/JCLI-D-16-0758.1

Gleixner, S., Demissie, T., and Diro, G. T. (2020). Did ERA5 Improve Temperature and Precipitation Reanalysis over East Africa? *Atmosphere* 11, 996. doi:10.3390/atmos11090996

Graham, R. M., Hudson, S. R., and Maturilli, M. (2019). Improved Performance of ERA5 in Arctic Gateway Relative to Four Global Atmospheric Reanalyses. *Geophys. Res. Lett.* 46 (11), 6138–6147. doi:10.1029/2019gl082781

Haimberger, L. (2007). Homogenization of Radiosonde Temperature Time Series Using Innovation Statistics. *J. Clim.* 20 (7), 1377–1403. doi:10.1175/jcli4050.1

Haimberger, L., Tavolato, C., and Sperka, S. (2012). Homogenization of the Global Radiosonde Temperature Dataset through Combined Comparison with Reanalysis Background Series and Neighboring Stations. *J. Clim.* 25 (23), 8108–8131. doi:10.1175/jcli-d-11-00668.1

Hersbach, H., Bell, B., Berrisford, P., Hirahara, S., Horányi, A., Muñoz-Sabater, J., et al. (2020). The ERA5 Global Reanalysis. *Q.J.R. Meteorol. Soc.* 146, 1999–2049. doi:10.1002/qj.3803

Ivanciu, I., Matthes, K., Wahl, S., Harlaß, J., and Biastoch, A. (2021). Effects of Prescribed CMIP6 Ozone on Simulating the Southern Hemisphere Atmospheric Circulation Response to Ozone Depletion. *Atmos. Chem. Phys.* 21 (8), 5777–5806. doi:10.5194/acp-21-5777-2021

JMA (2013). Outline of the Operational Numerical Weather Prediction at the Japan Meteorological Agency. WMO Technical Progress Report on the Global Data-Processing and Forecasting System (GDPFS) and Numerical Weather Prediction (NWP) Research, JMA, Japan. available at: http://www.jma.go.jp/jma/jma-eng/jma-center/nwp/outline2013-nwp/index.htm.

IPCC (2013). *Climate Change 2013: The Physical Science Basis. Contribution of Working Group I to the Fifth Assessment Report of the Intergovernmental Panel on Climate Change*. Editors Stocker T. F., Qin D., Plattner G.-K., Tignor M., Allen S. K., Boschung J., et al. (Cambridge, United Kingdom and New York, NY, USA: Cambridge University Press), 1535.

Keller, J. D., and Wahl, S. (2021). Representation of Climate in Reanalyses: An Intercomparison for Europe and North America. *J. Clim.* 34 (5), 1667–1684. doi:10.1175/jcli-d-20-0609.1

Kobayashi, S., Ota, Y., Harada, Y., Ebita, A., Moriya, M., Onoda, H., et al. (2015). The JRA-55 Reanalysis: General Specifications and Basic Characteristics. *J. Meteorological Soc. Jpn.* 93, 5–48. doi:10.2151/jmsj.2015-001

Lamarque, J.-F., Bond, T. C., Eyring, V., Granier, C., Heil, A., Klimont, Z., et al. (2010). Historical (1850–2000) Gridded Anthropogenic and Biomass Burning Emissions of Reactive Gases and Aerosols: Methodology and Application. *Atmos. Chem. Phys.* 10, 7017–7039. doi:10.5194/acp-10-7017-2010

Long, C. S., Fujiwara, M., Davis, S., Mitchell, D. M., and Wright, C. J. (2017). Climatology and Interannual Variability of Dynamic Variables in Multiple Reanalyses Evaluated by the SPARC Reanalysis Intercomparison Project (S-RIP). *Atmos. Chem. Phys.* 17, 14593–14629. doi:10.5194/acp-17-14593-2017

Madonna, F., Kivi, R., Dupont, J.-C., Ingleby, B., Fujiwara, M., Romanens, G., et al. (2020). Use of Automatic Radiosonde Launchers to Measure Temperature and Humidity Profiles from the GRUAN Perspective. *Atmos. Meas. Tech.* 13, 3621–3649. doi:10.5194/amt-13-3621-2020

Madonna, F., Tramutola, E., Sy, S., Serva, F., Proto, M., Rosoldi, M., et al. (2022). The New Radiosounding HARMonization (RHARM) Data Set of Homogenized Radiosounding Temperature, Humidity, and Wind Profiles with Uncertainties. *J. Geophys. Res. Atmos.* 127, e2021JD035220. doi:10.1029/2021jd035220

Manabe, S., and Wetherald, R. T. (1967). Thermal Equilibrium of the Atmosphere with a Given Distribution of Relative Humidity. *J. Atmos. Sci.* 24 (3), 241–259. doi:10.1175/1520-0469(1967)024<0241:teotaw>2.0.co;2

Manney, G. L., Allen, D. R., Krüger, K., Naujokat, B., Santee, M. L., Sabutis, J. L., et al. (2005). Diagnostic Comparison of Meteorological Analyses during the 2002 Antarctic Winter. *Mon. Weather Rev.* 133, 1261–1278. doi:10.1175/mwr2926.1

Maycock, A. C., Randel, W. J., Steiner, A. K., Karpechko, A. Y., Christy, J., Saunders, R., et al. (2018). Revisiting the Mystery of Recent Stratospheric Temperature Trends. *Geophys. Res. Lett.* 45, 9919–9933. doi:10.1029/2018gl078035

Meinshausen, M., Smith, S. J., Calvin, K., Daniel, J. S., Kainuma, M. L. T., Lamarque, J.-F., et al. (2011). The RCP Greenhouse Gas Concentrations and Their Extensions From 1765 to 2300. *Climatic Change* 109, 213. doi:10.1007/s10584-011-0156-z

Molod, A., Takacs, L., Suarez, M., and Bacmeister, J. (2015). Development of the GEOS-5 Atmospheric General Circulation Model: Evolution From MERRA to MERRA-2. *Geoscientific Model Development* 8, 1339–1356. doi:10.5194/gmd-8-1339-2015

Pascoe, C. L., Gray, L., Crooks, S., Juckes, M., and Baldwin, M. (2005). The Quasi-Biennial Oscillation: Analysis Using ERA-40 Data. *J. Geophys. Res.* 110, D08105. doi:10.1029/2004jd004941

Pawson, S., and Fiorino, M. (1998). A Comparison of Reanalyses in the Tropical Stratosphere. Part 1: Thermal Structure and the Annual Cycle. *Clim. Dyn.* 14, 631–644. doi:10.1007/s003820050246

Pawson, S., and Fiorino, M. (1999). A Comparison of Reanalyses in the Tropical Stratosphere. Part 3: Inclusion of the Pre-satellite Data Era. *Clim. Dyn.* 15, 241–250. doi:10.1007/s003820050279

Philipona, R., Mears, C., Fujiwara, M., Jeannet, P., Thorne, P., Bodeker, G., et al. (2018). Radiosondes Show that after Decades of Cooling, the Lower Stratosphere Is Now Warming. *J. Geophys. Res. Atmos.* 123, 12. doi:10.1029/2018jd028901

Pisoft, P., Sacha, P., Polvani, L. M., Añel, J. A., de la Torre, L., Eichinger, R., et al. (2021). Stratospheric Contraction Caused by Increasing Greenhouse Gases. *Environ. Res. Lett.* 16 (6), 064038. doi:10.1088/1748-9326/abfe2b

Polvani, L. M., Waugh, D. W., Correa, G. J. P., and Son, S.-W. (2011). Stratospheric Ozone Depletion: The Main Driver of Twentieth-Century Atmospheric Circulation Changes in the Southern Hemisphere. *J. Clim.* 24 (3), 795–812. doi:10.1175/2010jcli3772.1

Randel, W. J., Smith, A. K., Wu, F., Zou, C.-Z., and Qian, H. (2016). Stratospheric Temperature Trends over 1979-2015 Derived from Combined SSU, MLS, and SABER Satellite Observations. *J. Clim.* 29 (13), 4843–4859. doi:10.1175/jcli-d-15-0629.1

Randel, W. J., and Wu, F. (1999). Cooling of the Arctic and Antarctic Polar Stratospheres Due to Ozone Depletion. *J. Clim.* 12 (5), 1467–1479. doi:10.1175/1520-0442(1999)012<1467:cotaaa>2.0.co;2

Randel, W., Udelhofen, P., Fleming, E., Geller, M., Gelman, M., Hamilton, K., et al. (2004). The SPARC Intercomparison of Middle-Atmosphere Climatologies. *J. Clim.* 17, 986–1003. doi:10.1175/1520-0442(2004)017<0986:tsiomc>2.0.co;2

Randles, C. A., da Silva, A. M., Buchard, V., Colarco, P. R., Darmenov, A., Govindaraju, R., et al. (2017). The MERRA-2 Aerosol Reanalysis, 1980 Onward. Part I: System Description and Data Assimilation Evaluation. *J. Clim.* 30, 6823–6850. doi:10.1175/jcli-d-16-0609.1

Rea, G., Riccio, A., Fierli, F., Cairo, F., and Cagnazzo, C. (2018). Stratosphere-resolving CMIP5 Models Simulate Different Changes in the Southern Hemisphere. *Clim. Dyn.* 50, 2239–2255. doi:10.1007/s00382-017-3746-2

Rienecker, M. M., Suarez, M. J., Gelaro, R., Todling, R., Bacmeister, J., Liu, E., et al. (2011). MERRA: NASA's Modern-Era Retrospective Analysis for Research and Applications. *J. Clim.* 24, 3624–3648. doi:10.1175/jcli-d-11-00015.1

Rienecker, M. M., Suarez, M. J., Todling, R., Bacmeister, J., Takacs, L., Liu, H., et al. (2008). *The GEOS-5 Data Assimilation System—Documentation of Versions 5.0.1 and 5.1.0, and 5.2.0. Technical Report Series on Global Modeling and Data Assimilation*, 27. Greenbelt, Maryland, 92. NASA/TM-2008-104606 https://ntrs.nasa.gov/search.jsp?R=20120011955.

Santer, B. D., Painter, J. F., Bonfils, C., Mears, C. A., Solomon, S., Wigley, T. M. L., et al. (2013). Human and Natural Influences on the Changing Thermal Structure of the Atmosphere. *Proc. Natl. Acad. Sci. U.S.A.* 110 (43), 17235–17240. doi:10.1073/pnas.1305332110

Sato, M., Hansen, J. E., McCormick, M. P., and Pollack, J. B. (1993). Stratospheric Aerosol Optical Depths, 1850–1990. *Journal of Geophysical Research* 98(D12), 22987–22994. doi:10.1029/93JD02553

Screen, J. A., Bracegirdle, T. J., and Simmonds, I. (2018). Polar Climate Change as Manifest in Atmospheric Circulation. *Curr. Clim. Change Rep.* 4, 383–395. doi:10.1007/s40641-018-0111-4

Shine, K. P., Bourqui, M. S., Forster, P. M. d. F., Hare, S. H. E., Langematz, U., Braesicke, P., et al. (2003). A Comparison of Model-Simulated Trends in Stratospheric Temperatures. *Q.J.R. Meteorol. Soc.* 129 (590), 1565–1588. doi:10.1256/qj.02.186

Simmons, A. J., Berrisford, P., Dee, D. P., Hersbach, H., Hirahara, S., and Thépaut, J.-N. (2017). A Reassessment of Temperature Variations and Trends from Global Reanalyses and Monthly Surface Climatological Datasets. *Q.J.R. Meteorol. Soc.* 143, 101–119. doi:10.1002/qj.2949

Simmons, A., Jones, P., da Costa Bechtold, V., Beljaars, A., Kållberg, P., Saarinen, S., et al. (2004). Comparison of Trends and Low-Frequency Variability in CRU, ERA-40, and NCEP/NCAR Analyses of Surface Air Temperature. *J. Geophys. Res. Atmos.* 109, 1–18. doi:10.1029/2004jd005306

Simmons, A. J., Poli, P., Dee, D. P., Berrisford, P., Hersbach, H., Kobayashi, S., et al. (2014). Estimating Low-Frequency Variability and Trends in Atmospheric Temperature Using ERA-Interim. *Q.J.R. Meteorol. Soc.* 140 (679), 329–353. doi:10.1002/qj.2317

Simmons, A., Soci, C., Nicolas, J., Bell, B., Berrisford, P., Dragani, R., et al. (2020). Global Stratospheric Temperature Bias and Other Stratospheric Aspects of ERA5 and ERA5. *1' Ecmwf Tech. Memo.* 859, 1–40. doi:10.21957/RCXQFMG0

Simmons, A. (2022). Trends in the Tropospheric General Circulation from 1979 to 2022. *Weather and Climate Dynamics*. doi:10.5194/wcd-2022-19

SPARC (2022). "SPARC Reanalysis Intercomparison Project (S-RIP) Final Report," in *SPARC Report No. 10*. Editors Fujiwara M., Manney G. L., Gray L. J., and WrighT J. S. WCRP-17/2020available at: www.sparc-climate.org/publications/sparc-reports. doi:10.17874/800dee57d13

Spencer, R. W., and Christy, J. R. (1990). Precise Monitoring of Global Temperature Trends from Satellites. *Science* 247 (4950), 1558–1562. doi:10.1126/science.247.4950.1558

Steiner, A. K., Ladstädter, F., Randel, W. J., Maycock, A. C., Fu, Q., Claud, C., et al. (2020). Observed Temperature Changes in the Troposphere and

Stratosphere from 1979 to 2018. *J. Clim.* 33 (19), 8165–8194. doi:10.1175/jcli-d-19-0998.1

Sterin, A., Khan, V., and Rubinshtein, K. (2008). "Upper-air Temperature Trends: Current Problems and Some Recent Results," in *Climate Variability and Extremes during the Past 100 Years*. Editors S. Brönnimann, J. Luterbacher, T. Ewen, H. Diaz, R. Stolarski, and U. Neu (Dordrecht: Advances in Global Change ResearchSpringer), Vol. 33.

Stocker, M., Ladstädter, F., Wilhelmsen, H., and Steiner, A. K. (2019). Quantifying Stratospheric Temperature Signals and Climate Imprints from Post-2000 Volcanic Eruptions. *Geophys Res. Lett.* 46, 12486–12494. doi:10.1029/2019GL084396

Suárez-Gutiérrez, L., Li, C., Thorne, P., and Marotzke, J. (2017). Internal Variability in Simulated and Observed Tropical Tropospheric Temperature Trends. *Geophys. Res. Lett.* 44, 5709–5719. doi:10.1002/2017GL073798

Tanré, D., Geleyn, J.-F., and Slingo, J. M. (1984). "First Results of the Introduction of an Advanced Aerosol-Radiation Interaction in the ECMWF Low Resolution Global Model," in *Aerosols and Their Climatic Effects*. Editors Gerber, H. E., and Deepak, A. (Hampton, VA: A. Deepak Publishing), 133–177.

Tegtmeier, S., Anstey, J., Davis, S., Dragani, R., Harada, Y., Ivanciu, I., et al. (2020). Temperature and Tropopause Characteristics from Reanalyses Data in the Tropical Tropopause Layer. *Atmos. Chem. Phys.* 20, 753–770. doi:10.5194/acp-20-753-2020

Thompson, D. W., and Solomon, S. (2002). Interpretation of Recent Southern Hemisphere Climate Change. *Science* 296, 5569895–5569899. doi:10.1126/science.1069270

Thorne, P. W. (2008). Arctic Tropospheric Warming Amplification? *Nature* 455, E1. doi:10.1038/nature07256

Thorne, P. W., Madonna, F., Schulz, J., Oakley, T., Ingleby, B., Rosoldi, M., et al. (2017). Making Better Sense of the Mosaic of Environmental Measurement Networks: A System-Of-Systems Approach and Quantitative Assessment. *Geosci. Instrum. Method. Data Syst.* 6, 453–472. doi:10.5194/gi-6-453-2017

Thorne, P. W., and Vose, R. S. (2010). Reanalyses Suitable for Characterizing Long-Term Trends. *Bull. Amer. Meteor. Soc.* 91 (3), 353–362. doi:10.1175/2009bams2858.1

Trenberth, K. E., and Olson, J. G. (1989). Temperature Trends at the South Pole and McMurdo Sound. *J. Clim.* 2 (10), 1196–1206. doi:10.1175/1520-0442(1989)002<1196:ttatsp>2.0.co;2

van Vuuren, D.P., Edmonds, J., Kainuma, M., Riahi, K., Thomson, A., Hibbard, K., et al. (2011). The Representative Concentration Pathways: An Overview. *Climatic Change* 109, 5. doi:10.1007/s10584-011-0148-z

WMO (1986). A Preliminary Cloudless Standard Atmosphere for Radiation Computation. *World Clim. Programme (WCP)* 112, 53. Available at https://library.wmo.int/index.php?lvl=notice_display&id=11668.

WMO World Meteorological Organization (2018). *Scientific Assessment of Ozone Depletion: 2018*. Geneva, Switzerland: Glob. Ozone Res. Ozone Res. Monit. Project–Report, 588. Available at: https://www.esrl.noaa.gov/csl/assessments/ozone/2018/downloads/2018OzoneAssessment.pdf.

Yamazaki, K., Nakamura, T., Ukita, J., and Hoshi, K. (2020). A Tropospheric Pathway of the Stratospheric Quasi-Biennial Oscillation (QBO) Impact on the Boreal Winter Polar Vortex. *Atmos. Chem. Phys.* 20 (8), 5111–5127. doi:10.5194/acp-20-5111-2020

Conflict of Interest: The authors declare that the research was conducted in the absence of any commercial or financial relationships that could be construed as a potential conflict of interest.

GLOSSARY

AGCM Atmospheric General Circulation Model.

ATOVs Advanced TIROS Operational Vertical Sounder

C3S Copernicus Climate Change Service

abrCDS Climate Data Store

CFSR Climate Forecast System Reanalysis

CMIP5 Coupled Model Intercomparison Project - Phase 5

COBE Centennial *in situ* Observation-Based Estimates

ECMWF European Centre for Medium-Range Weather Forecasts

ECV Essential Climate Variable

ERA ECMWF Re-Analysis

GEOS-5 Goddard Earth Observing System Data Assimilation System Version 5

GNSS Global Navigation Satellite System

GSM Global spectral mode

IFS Integrated Forecast System

JMA Japan Meteorological Agency

MERRA Modern-Era Retrospective analysis for Research and Applications

MLS Microwave Limb Sounder

RHARM Radiosounding HARMonization

RICH Radiosonde Innovation Composite Homogenization

RMME Reanalyses multi-model ensemble

RO Radio Occultation

RAOBCORE RAdiosonde OBservation COrrection using REanalyses

S-RIP SPARC Reanalysis Intercomparison Project

SPARC Stratosphere-troposphere Processes And their Role in Climate

SSMI Special Sensor Microwave Imager

TTL tropical tropopause layer

TOV TIROS Operational Vertical Sounder

VarBC Variational Bias Correction

frontiers | Frontiers in Earth Science

TYPE Review
PUBLISHED 23 August 2022
DOI 10.3389/feart.2022.934654

OPEN ACCESS

EDITED BY
Bin Yu,
Environment and Climate Change,
Canada

REVIEWED BY
Jin-Yi Yu,
University of California, Irvine,
United States
Shengping He,
University of Bergen, Norway

*CORRESPONDENCE
Robert V. Rohli,
rohli@lsu.edu
Gregg A. Snedden,
sneddeng@usgs.gov

SPECIALTY SECTION
This article was submitted to
Atmospheric Science,
a section of the journal
Frontiers in Earth Science

RECEIVED 02 May 2022
ACCEPTED 15 July 2022
PUBLISHED 23 August 2022

CITATION
Rohli RV, Snedden GA, Martin ER and DeLong KL (2022), Impacts of ocean-atmosphere teleconnection patterns on the south-central United States.
Front. Earth Sci. 10:934654.
doi: 10.3389/feart.2022.934654

Impacts of ocean-atmosphere teleconnection patterns on the south-central United States

Robert V. Rohli[1,2]*, Gregg A. Snedden[3]*, Elinor R. Martin[4,5] and Kristine L. DeLong[2,6]

[1]Department of Oceanography and Coastal Sciences, Louisiana State University, Baton Rouge, LA, United States, [2]Coastal Studies Institute, Louisiana State University, Baton Rouge, LA, United States, [3]United States Geological Survey, Wetland and Aquatic Research Center, Baton Rouge, LA, United States, [4]School of Meteorology, University of Oklahoma, Norman, OK, United States, [5]South Central Climate Adaptation Science Center, University of Oklahoma, Norman, OK, United States, [6]Department of Geography and Anthropology, Louisiana State University, Baton Rouge, LA, United States

Recent research has linked the climate variability associated with ocean-atmosphere teleconnections to impacts rippling throughout environmental, economic, and social systems. This research reviews recent literature through 2021 in which we identify linkages among the major modes of climate variability, in the form of ocean-atmosphere teleconnections, and the impacts to temperature and precipitation of the South-Central United States (SCUSA), consisting of Arkansas, Louisiana, New Mexico, Oklahoma, and Texas. The SCUSA is an important areal focus for this analysis because it straddles the ecotone between humid and arid climates in the United States and has a growing population, diverse ecosystems, robust agricultural and other economic sectors including the potential for substantial wind and solar energy generation. Whereas a need exists to understand atmospheric variability due to the cascading impacts through ecological and social systems, our understanding is complicated by the positioning of the SCUSA between subtropical and extratropical circulation features and the influence of the Pacific and Atlantic Oceans, and the adjacent Gulf of Mexico. The Southern Oscillation (SO), Pacific-North American (PNA) pattern, North Atlantic Oscillation (NAO) and the related Arctic Oscillation (AO), Atlantic Multidecadal Oscillation/Atlantic Multidecadal Variability (AMO/AMV), and Pacific Decadal Oscillation/Pacific Decadal Variability (PDO/PDV) have been shown to be important modulators of temperature and precipitation variables at the monthly, seasonal, and interannual scales, and the intraseasonal Madden-Julian Oscillation (MJO) in the SCUSA. By reviewing these teleconnection impacts in the region alongside updated seasonal correlation maps, this research provides more accessible and comparable results for interdisciplinary use on climate impacts beyond the atmospheric-environmental sciences.

KEYWORDS

El Niño/Southern Oscillation (ENSO), North Atlantic Oscillation (NAO), Arctic Oscillation (AO), Atlantic Multidecadal Variability (AMV), Pacific Decadal Oscillation (PDO), Pacific/North American (PNA) pattern, Madden-Julian Oscillation (MJO), climate impacts

Introduction

Ocean-atmosphere teleconnections—climate anomalies related to each other over large distances–and temporally-spatially defined climate modes link weather and climate variability occurring across time and space. Understanding such linkages can enhance skill in predicting weather and climate changes at seasonal and longer time scales, which in turn can be utilized by decision makers to anticipate the environmental, economic, and social impacts of such ocean-atmosphere variability, particularly in its extreme modes. At the synoptic scale, impacts of the major teleconnections as manifested on synoptic types (Sheridan and Lee, 2012; McGregor 2017) and hydroclimatic variability (McGregor, 2017) have been reviewed thoroughly. Regionally, similar work has been done recently for Australia (Frederiksen et al., 2014), the Horn of Africa (Bahaga et al., 2019), and the North Polar area (Bushra and Rohli, 2021). The objective of this research is to review the distinguishing features of the major modes of climate variability and their teleconnections that influence the atmospheric environment of the south-central United States (SCUSA)—defined here as the states of Arkansas, Louisiana, New Mexico, Oklahoma, and Texas—including a description of those impacts. While a literature review through 2021 is the primary tool for meeting the objective, the varying periods of analysis, data sets employed, and variables impacted complicates the comparison of previous work. Thus, this research also includes original maps of each teleconnection's degree and geographic extent of influence on temperature and precipitation, using the 1950–2020 averaging period and a modern, high-resolution data set, for comparison to the consensus of previous work on the impacts of major teleconnections on temperature and precipitation in the SCUSA.

Overview of the primary ocean-atmosphere teleconnections

Teleconnection research has a rich history since the identification of the Southern Oscillation (SO; Walker and Bliss, 1932) as the "see-saw" in surface atmospheric pressure anomalies between the western and eastern tropical Pacific Ocean. Related and concurrent extreme anomalies in the ocean have been known for centuries. Specifically, the El Niño phenomenon is characterized by weakening or even reversal of the easterly trade winds in both hemispheres that results in cooler surface waters and shallower thermocline in the western tropical Pacific Ocean concurrent with anomalously warm near-surface waters in the eastern tropical Pacific Ocean, that produce a reduced tilt in the equatorial Pacific thermocline and reduces upwelling along the South American west coast. By contrast, the La Niña phenomenon involves a strengthening of the trade winds and the Walker circulation in general that results in warmer near-surface waters and a deepening of the thermocline in the western tropical Pacific Ocean and increased tilt in the equatorial Pacific thermocline that promotes stronger upwelling and colder near-surface waters in the eastern tropical Pacific Ocean.

Mid-20th century technological advances in upper-air data collection, along with research emphasizing the connection of the SO to El Niño (ENSO; Bjerknes, 1969), led to advances in understanding the SO, such as the identification of its 2- to 7-year variability (Trenberth, 1976; Trenberth, 1984), its relation to extratropical weather (van Loon and Rogers, 1981), complexity and geographically-varying ocean-air feedbacks (Alexander et al., 2002), and nonlinearity of impacts (Hoerling et al., 1997; Hsieh et al., 2006) primarily through variability in surface heat and moisture fluxes and their transport (Deser et al., 2010). Meanwhile, research on identifying other teleconnections of variability in the ocean-atmosphere system at various spatial and temporal scales continued, including recognition of the importance of the surface energy fluxes (Deser et al., 2010). In particular, Barnston and Livezey (1987) provided a thorough description and analysis of teleconnections that explain significant low-frequency variability in atmospheric flow.

The spatial domains of the SO and the other modes of climate variability to be considered in this research, as represented by correlations of the respective climate mode index with SST or another key defining atmospheric variable, are depicted in Figure 1. Among the dozens of modes of climate variability identified since the SO, the Pacific-North American (PNA) pattern (Wallace and Gutzler, 1981; Barnston and Livezey, 1987; Leathers and Palecki, 1992) is among the most prominent for the SCUSA. The PNA index is obtained by obtaining the second rotated empirical orthogonal function mode of the 500 mbar geopotential height across 0°-90°N, and may be an atmospheric response to forcing by ENSO (Renwick and Wallace, 1996; Straus and Shukla, 2002) with the strength of the response differing across and within ENSO phases (Wang et al., 2021) associated with barotropic instability in the atmosphere (Simmons et al., 1983) or other forcings (He and Wang, 2013; Liu et al., 2017), and with the extratropical response to ENSO changing over time (Soulard et al., 2019). The PNA pattern is expressed in the form of variability in the amplitude and phase of the atmospheric Rossby wave train. More specifically, an enhanced mid-tropospheric ridge over the western cordillera of North America and concurrent trough over the southeastern United States (i.e., positive PNA phase) is more commonly associated with the El Niño phase of ENSO, and a dampened or reversed ridge-trough configuration over the same action centers (i.e., negative PNA phase) is more typical in the La Niña phase. The PNA pattern has long been linked to North American climatic variability, including through its

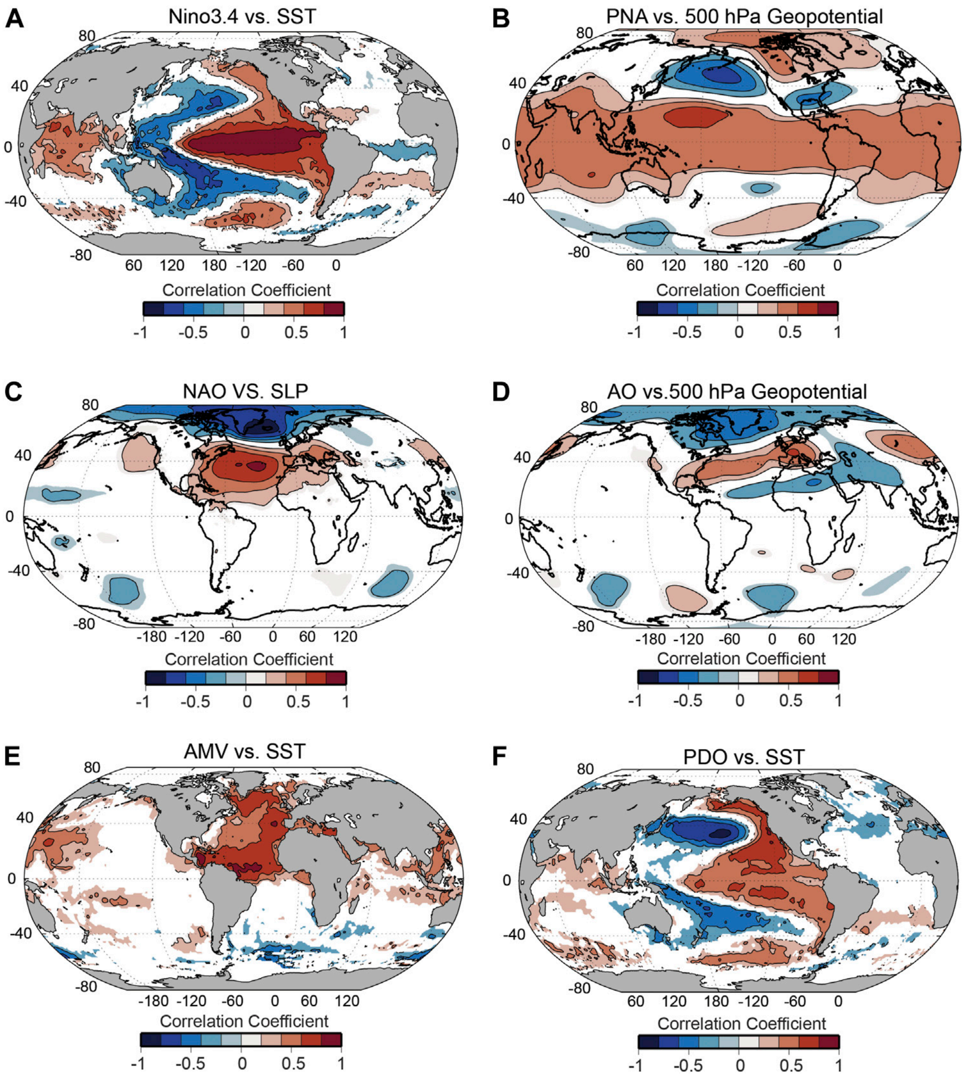

FIGURE 1
Centers of action for Nino3.4 **(A)**, AMV **(E)**, PDO **(F)**, identified by mapping their correlations with Hadley sea surface temperature (SST; https://www.metoffice.gov.uk/hadobs/hadisst/); NAO **(C)**, identified by mapping its correlation with sea-level pressure (ERA5; https://cds.climate.copernicus.eu/); and PNA **(B)** and AO **(D)**, identified by mapping their correlations with 500 hPa geopotential (ERA5; https://cds.climate.copernicus.eu/). Only regions where correlations were significant (alpha = 0.1) are shown on the maps.

connection to tropical variability (Mo and Livezey, 1986), regarding temperature (Loikith and Broccoli, 2014), precipitation (Henderson and Robinson, 1994; Liu et al., 2014), and extreme weather events (Bentley et al., 2019). Recent research has identified a causal relationship to sea surface temperatures (SSTs) less directly related to ENSO, in the South China Sea (Zhang and Liang, 2021).

The North Atlantic Oscillation (NAO; Rogers, 1984; Barnston and Livezey, 1987; Lamb and Peppler, 1987; Hurrell and van Loon, 1997; Marshall et al., 2001) came to prominence first, as an observed simultaneous dipole or “see-saw” in near-surface air temperature anomalies between Greenland and Europe (Loewe, 1966; van Loon and Rogers, 1978). The NAO has been recognized as a major forcing mechanism for transporting energy to the North Atlantic Ocean via the Atlantic Meridional Overturning Circulation (AMOC), with abundant air-sea energy exchange (Rodwell et al., 1999), and eventually affecting Northern Hemisphere multidecadal precipitation patterns (Zhang et al., 2021). The NAO-related (Wallace, 2000; Rogers and McHugh, 2002) Arctic Oscillation (AO; Thompson and Wallace, 1998; Thompson and Wallace, 2000) is also known as the Northern Hemispheric Annular Mode (NAM; Thompson et al., 2000), but was first described comprehensively by Lorenz (1951) and since has gained increasing attention as a prominent source of atmospheric flow variability in North America. The degree of coupling between the NAO and AO is now known to depend on temperature in the climate system (Hamouda et al., 2021).

The Atlantic Multidecadal Oscillation (AMO; Schlesinger and Ramankutty, 1994; Kerr, 2000) is an important and impactful, though enigmatic, ocean-atmosphere mode of climate variability in SST observed at multi-decadal time scales. The AMO had originally been named because of its characterization as an approximately 50- to 80-year cycle in which SST in the North Atlantic Ocean undergoes multi-decadal-scale variability of approximately 0.4 C° between the extreme phases after removing the global trend (Enfield et al., 2001). The AMO is now referred to as the Atlantic Multidecadal Variability (AMV) as recent evidence (Mann, 2021) suggests that it may not be a true oscillation. Paleoclimate reconstructions of the AMV reveal multi-decadal variability before the instrumental period, yet land- (Gray et al., 2004) and ocean-based reconstructions are misaligned in phasing and timing (Poore et al., 2009; Kilbourne et al., 2014), and the Loop Current in the Gulf of Mexico plays an important but complicating role (DeLong et al., 2014), leaving continued unanswered questions as to the AMO being a true oscillation that extends back in time. Knight et al. (2005) linked the AMV to thermohaline circulation variability, and Dima and Lohmann (2007) proposed more specifically that the AMV is modulated as freshwater variability causes a thermohaline circulation adjustment, which triggers subsequent SST response with sea ice and wind feedbacks. Clement et al. (2015) found that AMV variability is primarily a response to mid-latitude atmospheric forcing, with the AMOC and similar oceanic circulation responding in turn to the AMV rather than forcing it. The most recent AMV-related warming began around 1997 (Ellis and Marston, 2020). Interestingly, between 1995 and 2008, the Atlantic coast of the United States was one of the few places in the North Atlantic in which SSTs were not anomalously warm (Alexander et al., 2014). Debate continues as to the extent to which the AMV is driven by processes internal to the atmosphere-ocean system (Ting et al., 2009; Han et al., 2016; Deser and Phillips, 2021) related closely to the AMOC (Fang et al., 2021), natural external variability such as volcanic forcing (Wang et al., 2017; Mann, 2021), or anthropogenic external aerosol forcing (Booth et al., 2012). Several studies suggest that some combination therein appears likely (Ting et al., 2014; Qin et al., 2020), with the NAO also potentially playing a role in the relative contributions (Watanabe and Tatebe, 2019). Zhang et al. (2019) expressed hope for future improvements in the most recent climate models for more complete representation of the role of the AMOC on AMV and its impacts.

The analogous amorphous mode of low-frequency ocean-atmosphere variability in the Pacific Ocean initially gained widespread attention through analyses of SST in the mid-latitude and tropical Pacific (Davis, 1976). Specifically, North Pacific Ocean SST anomalies tended to display a simultaneous seesaw between near-coast Alaska and the central North Pacific. Rogers (1990) noted an atmospheric sea-level pressure (SLP; and therefore flow) seesaw in the northeastern Pacific near Alaska known as the North Pacific Oscillation (NPO). Gershunov and Barnett (1998) subsequently referred to the “NPO” as the SST (rather than the SLP) anomaly seesaw, and others have referred to a “North Pacific mode” (Tanimoto et al., 1993; Barlow et al., 2001) to refer to the same phenomenon. This North Pacific SST seesaw was shown to be an important modulator of within-ENSO impacts (Gershunov and Barnett, 1998). The collapse of fisheries off the Pacific Northwest coast of the United States in 1976 that corresponded to a shift in North Pacific SST anomalies led to the naming of the Pacific Interdecadal Oscillation (Mantua et al., 1997), which was shortened to the Pacific Decadal Oscillation (PDO; Mantua et al., 1997; Biondi et al., 2001; Mantua and Hare, 2002; Newman et al., 2003; Schneider and Cornuelle, 2005). The “warm phase” (“cold phase”) of the PDO is conventionally considered to be the phase in which SSTs near North America are anomalously warm (cold). The recent period of rapid global warming is also associated with the PDO’s warm phase, and the slower warming period is associated with the cold phase, as internal cooling by heat storage and circulation changes in the Pacific Ocean occurs (Meehl et al., 2013).

Another widely-used climate index used to represent the mode of whole Pacific Ocean variability is the Interdecadal Pacific Oscillation (IPO) (Salinger et al., 2001; Folland et al., 2002). Further research has found three centers of action for Pacific SST anomalies known as the Tripole Index (TPI) that combines the PDO, IPO, and Southern Hemisphere PDO (SHPDO; Shakun and Shaman, 2009) or South Pacific Decadal Oscillation (SPDO; Hsu and Chen, 2011; DeLong et al., 2012) as the tripole of variability (Henley et al., 2015). The North Pacific Gyre Oscillation (NPGO; Di Lorenzo et al., 2008; Ceballos et al., 2009; Di Lorenzo and Mantua, 2016; Tranchant et al., 2019) is related to the PDO but is a distinct mode of variability. In recognition that multiple Pacific atmospheric features are occurring, that an anthropogenic influence is likely (Bonfils and Santer, 2011), and that like the AMV, the PDO may not be a true oscillation, recent research now uses Pacific Decadal Variability (PDV; Deser et al., 2012) rather than the PDO, with several PDV modes interacting with each other and ENSO (Shakun and Shaman, 2009; Newman et al., 2016). Paleoclimate reconstructions that extend the observational record back more than 300 years with corals confirm these differing modes based on their geographic location—the IPO in the South Pacific Convergence Zone region (Linsley et al., 2008), the SPDO; Hsu and Chen (2011) or Southern Hemisphere Decadal Oscillation (SHPDO) in the southwestern Pacific Ocean (DeLong et al., 2012), and the PDO in the northern Pacific (Felis et al., 2010). Since 1976, the PDO/PDV has generally been in a so-called warm phase but currently appears to be shifting toward a cold phase, with the naming convention of the phases corresponding to the SST anomalies near Alaska.

The ocean-atmosphere variability patterns described briefly here (ENSO, NAO, PNA, AMV, PDV) all produce impacts to temperature, precipitation, and a variety of other atmospheric and environmental variables such as prevailing winds and runoff/ streamflow at varying locations and on a variety of time scales. Moreover, the changing influence of a teleconnection on local conditions (both across space and time), or non-stationarity, is an important influence (Stenseth et al., 2003). The variability patterns themselves can interact, increasing the complexity and capability for prediction, with compound impacts of multiple teleconnections (Swain et al., 2017) that can amplify or attenuate the signal. For example, Newman et al. (2003) described the relationship between ENSO and the PDO, and showed that the NPO-like atmospheric SLP signal is weaker than the oceanic signature in the form of ENSO- and PDO-related SSTs. Chiang and Vimont (2004) reported evidence of an interannual to decadal association in SST anomalies between the tropical Atlantic and Pacific near the ITCZ, which is linked to both ENSO and the NAO. Budikova (2005) found that AO-temperature relationship is modulated by the PDO. Mokhov and Smirnov (2006) described the nature of ENSO forcing of the NAO since the mid-20th century. Dong et al. (2018) showed the complicated influence of the IPO on ENSO- and PNA-pattern-related weather variability. Zhang and Delworth (2007) found that the AMV could contribute to variability in the PNA and the PDO and other similar Pacific patterns, independent of ENSO variability. Wu et al. (2011) concurred with the connection between the AMV and PDO, with PDO leading the AMV by 1 year. Most recently, Power et al. (2021) echoed that ENSO governs some, but certainly not all internal tropical Pacific decadal climate variability and change, as subtropical-tropical cells in the upper-ocean overturning circulation along with SST variability beyond the tropical Pacific are also important. However, even compounded and synergistic effects such as these may differ by teleconnection phase (e.g., Straus and Shukla, 2002). Assessment of the influence on complicated biological effects might be best characterized by the simultaneous influences of multiple teleconnections (Stenseth et al., 2003).

Teleconnections and the south-central United States

In recent years, the increased attention to the impacts of such ocean-atmosphere variability in environmental, economic, and social systems, especially at the regional and local scale (e.g., Steptoe et al., 2018), have made teleconnections an important part of our understanding of the climate system. One region influenced directly throughout natural and social systems is the south-central United States (SCUSA). Hopkinson et al. (2013) suggested that changes in hydrology during the coming century may be the most important impact of climate change on natural systems in the southeastern United States, which includes the eastern part of the SCUSA as defined here.

The SCUSA is an appropriate area of focus because of its expanding populations, diverse ecosystems, important agricultural and other economic sectors, significant potential for wind and solar energy generation, and geographic diversity (both highlands and lowlands, continental and coastal areas, arid West and humid East, water scarcity and water richness). The region also sits at the boundary of influences from the Pacific, Atlantic, and Gulf of Mexico, straddling the ecotone between humid and arid climates in the United States, with interplay between subtropical and extratropical circulation features and the influences of the Pacific and Atlantic Oceans and the adjacent Gulf of Mexico. These multiple influences lead to a lack of a dominant pattern of variability (e.g., ENSO, AMV), with projections for warming and drought looming (Naumann et al., 2018). This complicated environmental geography calls for the need to understand the climate variability in the SCUSA, particularly in light of the cascading impacts of these environmental influences through ecological and social systems.

The SCUSA is an understudied region vis-à-vis atmospheric variability and change that contains wide disparities in social vulnerability to environmental hazards (e.g., Mihunov et al., 2018). The SCUSA has a large proportion of vulnerable populations—in urban, rural, and borderlands, as well as indigenous nations, especially in Oklahoma but also in Louisiana (National Conference of State Legislatures, 2018), including the Biloxi-Chitimacha-Choctaw on Isle de Jean Charles. Moreover, despite its diverse ecoregions and lack of cohesiveness as a distinct hydroregion (Dethier et al., 2020), the region has relatively tight economic cohesiveness (Ó'hUallacháin, 2008), with hubs in Houston and the Dallas-Fort Worth metroplex, and major increases in urbanization at the expense of agricultural lands being forecasted (Ahn et al., 2002; Alig et al., 2004).

This research will focus on some important causes and effects of climate variability, specifically focusing on the SCUSA, but independently of that put forth in the Intergovernmental Panel on Climate Change (IPCC) Fifth and Sixth Assessment Reports (IPCC, 2014; IPCC, 2022). de Chazal and Rounsevell (2009) noted the importance of integrated analysis of biodiversity, land-use change, and climate change. Improvements in the understanding of linkages and feedbacks across the climate system in the SCUSA would provide tangible benefits, such as in agriculture (Klemm and McPherson, 2018) and fisheries management (Karnauskas et al., 2015).

Data analysis and methodology

One challenge to understanding teleconnection patterns and their relative importance across the SCUSA is a lack of

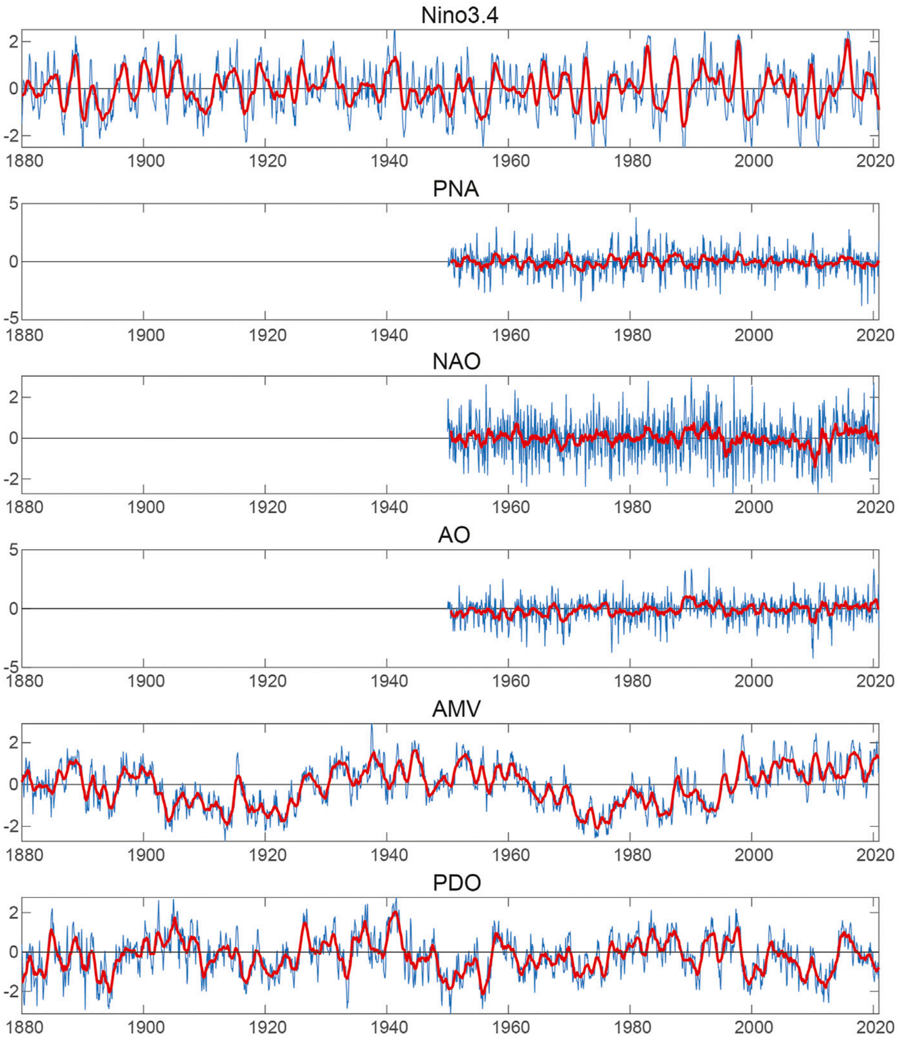

FIGURE 2
Time series of annual standardized climate indices for available periods of record (blue lines are monthly values, red are 13-month moving averages). NAO and AO indices are from the Climate Prediction Center; AMV and PDO indices are determined using the Extended Reconstructed Sea Surface Temperature (ERSST) data set version 5 (Huang et al., 2017). Source: https://climexp.knmi.nl/.

consistency in prior work between data sets and methods used. Thus, a uniform set of analyses of the relationship between climate modes (ENSO, PNA, NAO, AO, AMV, and PDO) and temperature and precipitation in each meteorological season—December-January-February (DJF), March-April-May (MAM), June-July-August (JJA), and September-October-November (SON)—is undertaken, using a consistent method and data set.

Each mode of climate variability (ENSO, PNA, NAO, AO, AMV, and PDO) is identified using a commonly-defined statistically standardized index, aggregated to monthly resolution, and displayed in Figure 2. To measure ENSO, the Niño 3.4 index (SST anomaly in the region bounded by 5°N to 5°S, from 170°W to 120°W), with values estimated back to 1877 (Bunge and Clarke, 2009) and 1856 (Kaplan et al., 1998), was selected over the SLP-based Southern Oscillation Index (Ropelewski and Jones, 1987), Multivariate ENSO index (Wolter and Timlin, 2011), or another indicator, owing to its direct reliance on SST in the central and Eastern Pacific (Trenberth, 1997; Trenberth and Stepaniak, 2001). Positive values correspond to the El Niño phase, with negative indices representing La Niña. The NAO was identified using the station-based NAO index (Hurrell, 1995), which measures the strength of the NAO as the difference between SLP in Portugal and Iceland. The PNA index (Barnston and Livezey, 1987) uses principal components analysis of SLP across the Northern Hemisphere. The AMV index (Enfield et al., 2001) uses SST across the North Atlantic, and the PDO index (Hamamoto and

Yasuda, 2021) is constructed using principal components analysis of SST across the North Pacific. Tree-ring-based reconstructions of the AMO (e.g., Wang et al., 2011) and PDO (e.g., D'Arrigo et al., 2001) have also been used to extend the record by hundreds of years. Statistically standardized time series of the indices are shown in Figure 2.

Monthly 2-m temperature and precipitation fields (preliminary/provisional from 1950 to 1978 and combined for 1979–2020) from the fifth-generation European Centre for Medium-range Weather Forecasts (ECMWF) Reanalysis (ERA5; Copernicus Climate Change Service, 2017) are aggregated into seasonal means (i.e., DJF, MAM, JJA, and SON) and correlated (separately) with each teleconnection index, for the 1950–2020 period. ERA5 is a reanalysis product that combines *in-situ* observations and numerical modeling and is available at 31-km horizontal resolution (Hersbach et al., 2020). Reanalysis products are typically used as gridded observations for synoptic- and large-scale atmospheric circulation and are adequate for pattern identification used herein. Each variable is linearly detrended at each grid point, and anomalies are calculated by removing the average monthly climatology. One area of caution in the interpretation of results is that current gridded data sets tend to suppress precipitation extremes in the SCUSA (Sun et al., 2019).

The relationship between each pattern of variability (e.g., ENSO) and each atmospheric variable (i.e., temperature or precipitation) is assessed for each season, such that a correlation analysis is conducted between the annual ENSO index time series and the (say) DJF temperature at each grid point across the continental U.S., although the focus here is on results for the SCUSA. DJF values were assigned to the year of their January-February components. Statistical significance at the 95 percent confidence interval is assessed by a two-tailed Student's t-test, taking into account serial correlation (Bretherton et al., 1999).

Impacts of enso in the south-central United States

The literature suggests that, while every ENSO event is different (Capotondi et al., 2015), ENSO generally has more prominent and well-understood impacts on the SCUSA than other climate modes investigated. Danco and Martin (2018) observed the influence of ENSO on the low-level jet stream that advects heat and moisture through the SCUSA toward the Great Plains. ENSO has been shown to have a predictable influence on both temperature and precipitation in the SCUSA (Wang and Robertson, 2019), although Zhou et al. (2016) cautioned that prediction of ENSO-induced precipitation tends to underemphasize extremes substantially. The El Niño phase has been linked to positive cold-season geopotential height anomalies in the southeastern United States (Horel and Wallace, 1981) and negative cold-season temperature departures across the United States. Gulf Coast and northern Mexico, especially in southwestern Texas and adjacent northern Mexico (Hurrell, 1996; Torbenson et al., 2019). EL Niño events have also been found to be generally associated with positive precipitation anomalies throughout the same area (Ropelewski and Halpert, 1986; Ropelewski and Halpert, 1987; Wise et al., 2015; Torbenson et al., 2019), but with significant clustering of precipitation "hotspots" over the Gulf of Mexico (Munroe et al., 2014). Summertime El Niño conditions also increase precipitation in the subsequent winter with La Niña summers suppressing the upcoming winter's precipitation in much of the SCUSA (Kurtzman and Scanlon, 2007). The La Niña phase is linked less conclusively to temperature and precipitation in the same area, but with tendencies for negative cold-season precipitation anomalies (Ropelewski and Halpert, 1989, 1996; Munroe et al., 2014).

Multiple causes of these anomalies have been noted. Vega et al. (1998) noted the importance of displacement of mid-tropospheric ridging near the SCUSA that supports ridging during La Niña events. Eichler and Higgins (2006) linked precipitation anomalies to displacements in storm tracks in North America and surrounding ocean environments. Sweet and Zervas (2011) emphasized the influence of an anomalously strong subtropical jet stream, which advects moisture (Sanchez-Rubio et al., 2011) that had been displaced eastward in the tropical Pacific Ocean during the El Niño event, with weakening of the subtropical jet and decreased cyclogenesis in the southeastern United States and SCUSA during La Niña events (Ropelewski and Halpert, 1986; Schmidt et al., 2001; McCabe and Muller, 2002). Bove et al. (1998) and Pielke and Landsea (1999) noted the decreases in upper-level vertical wind shear in the main hurricane development regions during La Niña events and increases during El Niño events, which can partially offset the "typical" anomalies during the early part of the cold season by increasing storm frequency during La Niña conditions and reducing storm frequency during El Niño conditions (Gray, 1984; Shapiro, 1987). The precipitation signature of ENSO is likely to be most important in the northern part of the SCUSA and the association with hurricanes is likely most influential in parts of the SCUSA where tropical cyclones represent an important part of the precipitation climatology, such as south coastal Texas and Louisiana, at the time of year when tropical cyclones may be a factor. However, ENSO's influence on tropical cyclone frequencies for the southeastern United States. Gulf of Mexico coast is likely to be reduced compared to that on the United States. Atlantic Coast (Smith et al., 2007).

Wide spatial and temporal variability in ENSO-forced temperature and precipitation anomalies are to be expected in the SCUSA as elsewhere (Deser et al., 2018), with the magnitude and even the sign of the winter temperature (Yu et al., 2012a) and precipitation anomalies affected by the location of the Pacific warm and cold pools during El Niño

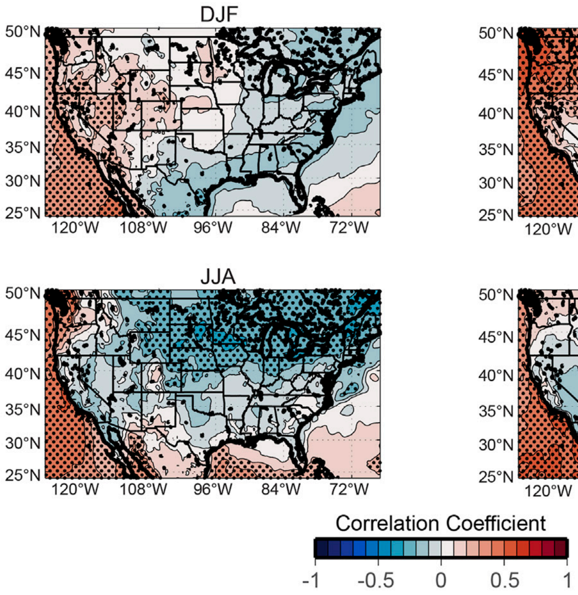

FIGURE 3
Correlation coefficients between the Niño 3.4 index and seasonal temperature across the continental United States (1950–2020); stippling indicates statistical significance ($p < 0.05$).

events (Zhang et al., 2012). Whereas conventional El Niño events are characterized by warming in the eastern tropical Pacific Ocean, the so-called El Niño Modoki events (Ashok et al., 2007), also known as central-Pacific El Niño events (Kao and Yu, 2009), have anomalously warm SSTs in the central Pacific Ocean flanked by cooler SST to the east and west. As Atlantic tropical cyclone landfall frequencies are suppressed less during Modoki events than during conventional El Niño events on the Gulf of Mexico coast and Central America (Kim et al., 2009), precipitation anomalies in the SCUSA may depend on the type of El Niño event. The diverging hydrometeorological responses by type of ENSO event (i.e., "conventional" vs. Modoki, or east-Pacific vs. central-Pacific), such as in above vs. below-normal spring Mississippi River basin precipitation, soil water hydrology, and streamflow (Liang et al., 2014), requires careful attention to the type of ENSO event to assess the impact. Flanagan et al. (2019) noticed the importance of central Pacific SSTs for producing precipitation anomalies in the southern Great Plains, including parts of the SCUSA. Nevertheless, "conventional" ENSO events tend to have a greater overall influence than Modoki events for the tropical Atlantic Ocean (Taschetto et al., 2016) westward in the SCUSA (Yu et al., 2017). Other studies have found that other weather phenomena across the United States respond to extreme ENSO phases, such as tornadoes being more frequent and intense in the SCUSA during winter and early spring (Cook et al., 2017). The observation of increased prevalence of Modoki El Niño at the expense of "conventional" or eastern Pacific El Niño (Yu et al., 2012b; Liang et al., 2015) may have implications for future ENSO impacts in the SCUSA.

Results, based on ERA5 for the 1950–2020 period, illustrate the relatively strong but complex spatial and seasonal differences in ENSO influence on temperature and precipitation in the SCUSA. The most prominent temperature relationship in the SCUSA is in Texas in spring, when anomalously cold conditions occur in the El Niño events and warm conditions occur in La Niña events (Figure 3). Precipitation anomalies are also most prominent in Texas during the spring, with El Niño events associated with anomalously wet conditions and La Niña with drier-than-normal springs (Figure 4). Our results of generally wet anomalies during El Niño events in SON (Figure 4) align with recent research that suggests a temporally decreasing influence of El Niño events on southeastern United States precipitation (Mo, 2010) and increasing autumn precipitation anomalies in the eastern SCUSA and adjacent Mississippi and Alabama related to El Niño events (Bishop et al., 2019).

The Great Plains low-level jet (GPLLJ), the Caribbean low-level jet (CLLJ), and extratropical wave trains America (Krishnamurthy et al., 2015) likely force the broader signals in the SCUSA during spring. Analysis of reanalyzes/observations demonstrate that ENSO has a significant impact on the strength of the GPLLJ, with a significant negative correlation in the spring and a significant positive correlation in summer (Schubert et al., 2004; Weaver et al., 2009; Muñoz and Enfield, 2011; Krishnamurthy et al., 2015; Danco and Martin, 2018). Muñoz

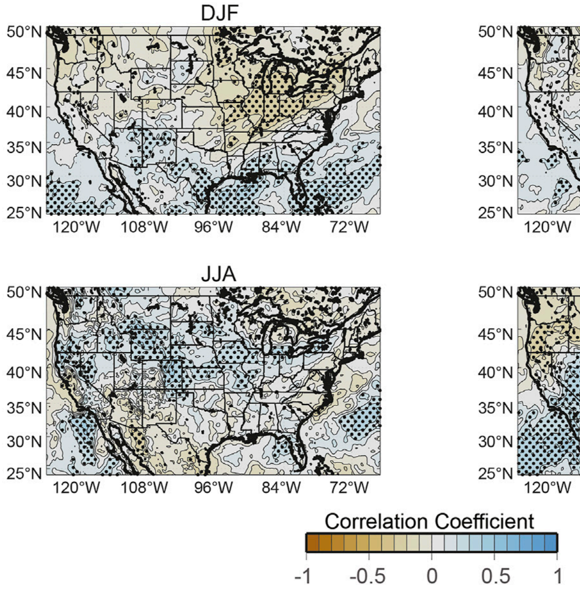

FIGURE 4
As in Figure 3, but for precipitation.

and Enfield (2011) discovered that colder SSTs in the Niño 3.4 region often result in a stronger GPLLJ in spring. Observations indicate wintertime La Niña induces high SLP anomalies over the Intra-Americas Sea the following spring through changes in the Walker and Hadley circulation. This leads to a strong CLLJ, which drives a stronger GPLLJ, with the GPLLJ and CLLJ significantly correlated in spring (Martin and Schumacher, 2011a). Lee et al. (2013) found that in April and May, cold SST anomalies in the Niño 4 region and warm SST anomalies in the Niño 1+2 region work together to result in increased moisture transport from the Gulf of Mexico, which could imply a stronger GPLLJ. Another study presented a similar pattern in the summer, with a Modoki (i.e., Central Pacific) El Niño weakening the GPLLJ and a conventional (i.e., East Pacific) El Niño strengthening it (Liang et al., 2015).

Going beyond traditional associations between ENSO vs. temperature and vs. precipitation, cascading socio-ecological connections to ENSO are also important in the SCUSA. For example, ENSO is an important control over "greenness," as represented by the Enhanced Vegetation Index, and explains 10 to 25 percent of variability in greenness in south-central Texas and adjacent western

Texas and eastern New Mexico (Swain et al., 2017). Mishra et al. (2011) and Konapala et al. (2018) identified linkages between ENSO and streamflow variability in Texas, with the latter finding strong but spatially and temporally inconsistent associations between El Niño events and drought in the subsequent summer, particularly in southern Texas (Rajagopalan et al., 2000). The Texas and Oklahoma floods of May 2015 have also been linked to El Niño events (Wang et al., 2015), and periodic Texas drought in the pre-instrumental period in the region have also been noted (Stahle and Cleaveland, 1988); such variability is likely associated with ENSO and potentially other teleconnections. El Niño events also lead to warmer SST in the Gulf of Mexico and Caribbean Sea (see Figure 1A) that can drive coral bleaching events that can impact fisheries in the northern Gulf of Mexico (Schmidt and Luther, 2002; Tolan, 2007; Piazza et al., 2010; Gomez et al., 2019).

ENSO has numerous cascading impacts on atmospheric circulation (Rasmusson and Carpenter, 1982) and precipitation-dependent human activities in the SCUSA. For example, the linkage of El Niño events to anomalously weak surface winds, and therefore reduced ocean waves along the major shipping routes in the northernmost Pacific Ocean (Chen et al., 2012), impacts North America including the SCUSA, particularly considering the temporally increasing volume of trade with Asia. ENSO-forced salinity fluctuations in Louisiana estuaries contribute to decreased brown shrimp abundance following El Niño events (Piazza et al., 2010). The SCUSA will undoubtedly be impacted if recent research (Cai et al., 2021) suggesting a widening ENSO-induced SST variability and therefore enhanced warm-phase-ENSO warming, along with an eastward shift and intensification of the ENSO-related PNA pattern and the Pacific-South American patterns, is realized.

The future of ENSO is far from certain, as some recent work suggests more extreme El Niño and La Niña (e.g., Cai et al., 2015; Liu et al., 2021) events, while other research (e.g., Callahan et al., 2021) suggests that CO_2 forcing will dampen ENSO events.

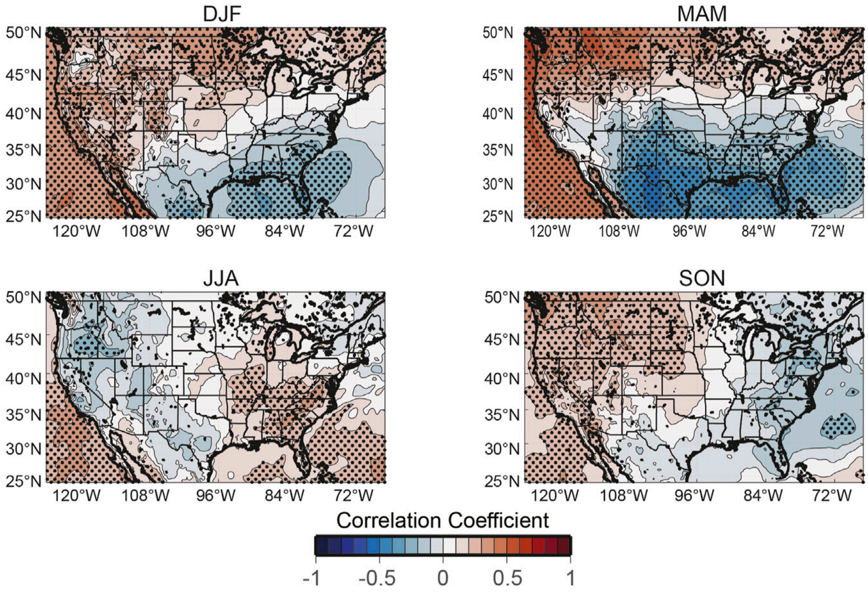

FIGURE 5
Correlation coefficients between the PNA pattern index and seasonal temperature across the continental United States (1950–2020); stippling indicates statistical significance ($p < 0.05$).

Nevertheless, any future changes in the dominance of conventional vs. Modoki (or central-Pacific) El Niño events are likely to affect SCUSA temperatures, particularly in the southeastern region (Yu et al., 2012a). Modoki have been projected to become more common in the future relative to the more conventional El Niño-defined SST anomalies (Yeh et al., 2009), perhaps because of the effect of weakened equatorial easterlies that in turn flatten the eastern tropical Pacific's thermocline (Ashok et al., 2007).

Impacts of the PNA pattern in the south-central United States

The PNA pattern has a substantial influence on both temperature and precipitation in the SCUSA (Wang and Robertson, 2019). Specifically, during the PNA positive phase, the SCUSA has been found to be anomalously cool (Hurrell, 1996) in all months except summer, when the PNA pattern is poorly defined (Leathers et al., 1991). Hardy and Henderson (2003) noted the proclivity for more frequent cold frontal passages in western Texas during the negative PNA pattern, thereby having implications on both temperature and precipitation. Dong et al. (2011) linked the PNA pattern causatively to cyclonic activity in the southwestern United States including much of the SCUSA, but they cautioned that the West Pacific teleconnection (Wallace and Gutzler, 1981; Barnston and Livezey, 1987) may provide an even more direct association. Somewhat wetter than normal conditions in the coastal SCUSA have also been found to occur during the positive mode (Wang and Robertson, 2019), although Leathers et al. (1991) had found only weak associations. Liu et al. (2014) observed a generally negative correlation between the winter PNA pattern and the oxygen isotope ratio ($\delta^{18}O$) of winter precipitation (including in nearly all of the SCUSA), showing the influence of moisture source and storm tracks on winter precipitation $\delta^{18}O$.

The ERA5-based analysis using the extended study period largely confirms results from the existing literature regarding the PNA-temperature relationship in the SCUSA, with generally negative correlations (i.e., anomalously low temperatures accompanying the positive PNA pattern, and vice versa) in meteorological winter and (especially) spring, and weak correlations in meteorological summer and autumn (Figure 5). Specifically, except for the extreme northern and western sectors, a negative relationship exists in meteorological winter (DJF) in the SCUSA, with the coastal southeastern corner following the pattern throughout much of the rest of the southeastern United States of significant negative correlations. By spring, the slight negative correlation in extreme northern and western SCUSA from winter is reversed, and nearly the entire SCUSA has significant negative correlation between PNA pattern and temperature. In summer, the pattern deteriorates, with the zero correlation line bisecting the SCUSA into western (negative) and eastern (positive) zones; only northeastern Arkansas joins much of the adjacent southeastern United States in displaying

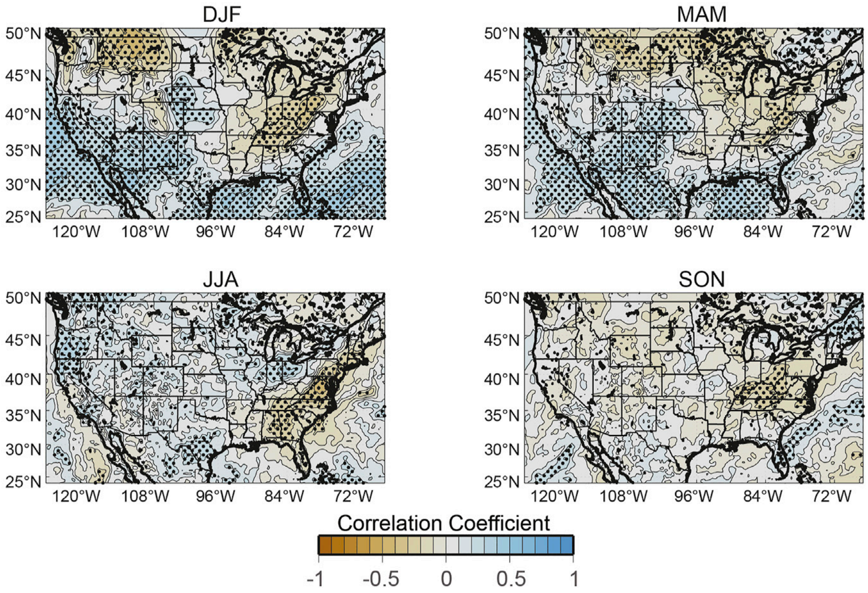

FIGURE 6
As in Figure 5, but for precipitation.

significant positive correlations. By autumn, even weaker relationships are found, not only across the SCUSA but also across the eastern two-thirds of the United States.

The PNA-precipitation spatial pattern in the SCUSA in the ERA5 for the extended period of years (1950–2020) is also largely similar to that described previously in the literature. Specifically, in winter and spring, relatively strong, significant positive correlations occur in much of the western and coastal SCUSA and adjacent Gulf of Mexico (Figure 6). A substantial zone of significant negative correlations exists to the northeast of the SCUSA, with its southwest-northeast orientation suggesting that the trough-to-ridge side of the Rossby wave characteristic of a negative PNA pattern brings anomalously wet conditions to the Ohio and Tennessee Valleys. However, that zone shrinks and moves eastward from winter to spring. In summer, the area of significant positive correlations in the SCUSA is largely confined to south-central Texas, perhaps due to the increase in albeit very weak cold frontal passages (Hardy and Henderson, 2003), with the zone of significant negative correlations

(i.e., PNA-induced trough leading to abundant precipitation) pushed well to the east of the SCUSA. In autumn, no areas of significance correlations are found in the SCUSA, with only isolated pockets of significant correlations elsewhere in the United States, such as over the Ohio and Tennessee valley and coastal Virginia and North Carolina (positive) and peninsular Florida and northern New England (negative).

Variability in the meridionality (i.e., north-to-south or south-to-north flowing) of the PNA-defined ridge-trough configuration, including both the temperature and precipitation anomalies shown here and previously in the literature, in turn contribute to fluctuations in other environmental and human systems in the SCUSA. For example, Rogers and Rohli (1991) and Rohli and Rogers (1993) linked PNA-induced variability to economic impacts to agriculture, including in the SCUSA. The PNA pattern has also been shown to have an important control over "greenness" in the western SCUSA, with particular importance in New Mexico and the Texas High Plains (Swain et al., 2017). Based on the relationships between the PNA pattern and temperature/precipitation shown here, many other primary and secondary impacts of the PNA pattern are likely to exist in the SCUSA. However, relationships between the PNA pattern and natural and human systems seem to be documented more thoroughly elsewhere, such as in the Great Lakes region (e.g., Rodionov and Assel, 2003; Yu et al., 2014).

Impacts of the NAO and NAM (AO) in the south-central United States

The seesaw in pressure anomalies between the northern and subtropical North Atlantic associated with the NAO produces a chain reaction of physical responses. The NAO contributes most dominantly to winter temperatures across much of the Northern Hemisphere (Barnston and Livezey, 1987; Hurrell, 1996). A northward displacement of the polar front jet stream during the NAO's positive (i.e., "warm" or "high") phase (Visbeck et al., 2001) generally contributes to anomalously warm and wet

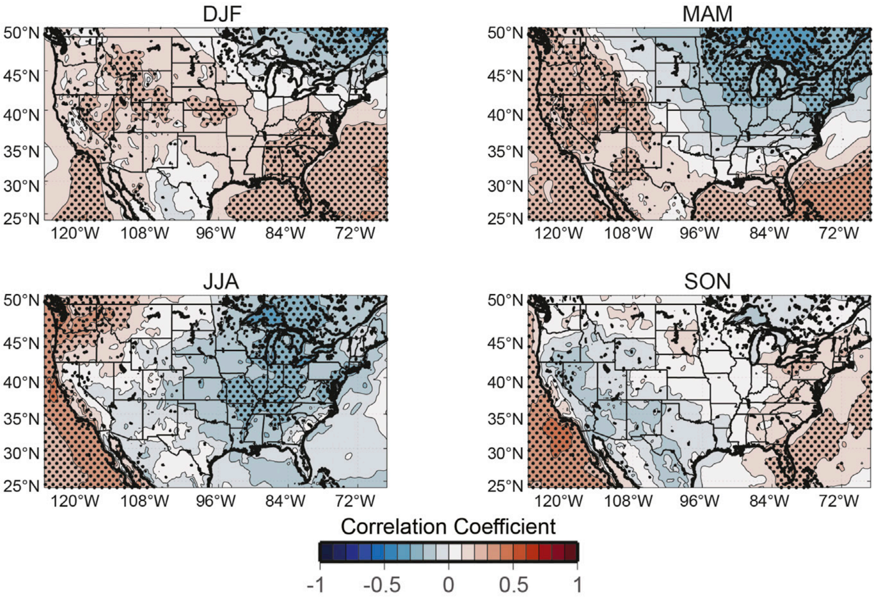

FIGURE 7
Correlation coefficients between the NAO index and seasonal temperature across the continental United States (1950–2020); stippling indicates statistical significance ($p < 0.05$).

conditions in the eastern United States (Tootle et al., 2005), but with warm (Hurrell, 1996) and varied precipitation conditions over the SCUSA (Ning and Bradley, 2016; Wang and Robertson, 2019). Such conditions and their impacts are generally amplified in the cold season (Folland et al., 2009). Consistent with colder conditions in the negative (i.e., "cold" or "low") phase of the NAO, Hardy and Henderson (2003) attributed their finding of increased cold frontal passages during the negative phase of the NAO in much of the SCUSA to troughing over the region and southerly displacement of the mid-latitude cyclone tracks. Negative phases of the NAO have also been shown to coincide with increased probability of cold air outbreaks across the United States (e.g., Walsh et al., 2001; Cellitti et al., 2006). Non-stationarity associated with the eastward shift of the NAO, particularly in summer (Sun and Wang, 2012), has likely been associated with changes in its influence over the SCUSA, and, similar to other teleconnections, temporally changing environmental, economic, and social impacts.

The inclusion of the ERA5 data over a longer period of time generally suggests that the correlation between temperature and the NAO index is typically insignificant in the SCUSA in all seasons. During winter, the correlation is positive across the majority of the United States, with areas of significance in the southeast and adjacent to and in the Gulf of Mexico, although not extending into the SCUSA (Figure 7). The implication is that zonal (i.e., west-east) flow hinders the meridional transport of Arctic and polar air masses into the United States. In MAM, areas of significant positive correlations include the Gulf of Mexico and adjacent peninsular Florida, and much of the West, with simultaneous negative correlations across the Northeast and adjacent Canada, but no significant areas in the SCUSA (Figure 7). In summer, correlations are negative, but insignificant across the SCUSA, excepting significant negative correlations in Arkansas and down the Mississippi River valley into Louisiana, extending from the Ohio River Valley, with insignificant correlations between temperature and the NAO in the SCUSA and most of the rest of the United States during SON (Figure 7).

The literature suggests that largest and most significant precipitation anomalies associated with the NAO tend to occur along the North Atlantic storm tracks, the Midwest, northeastern United States, and Europe (e.g., Bradbury et al., 2003; Weaver and Nigam, 2008). For example, strong correlations have been observed between central United States precipitation and the NAO index due to the influence of the GPLLJ in the summer. Ruiz-Barradas and Nigam (2005) and Weaver and Nigam (2008) found that negative phases of the NAO coincided with anomalously strong influx of moist Gulf of Mexico air into the United States interior and unseasonably high precipitation in the Midwest. Villarini et al. (2013) also found that in Iowa, the magnitude of the NAO index was a useful predictor in determining the occurrence of floods. However, because the positive NAO is tied to a strengthening of the North Atlantic Subtropical High, also known as the Bermuda-Azores anticyclone (BAA), which strengthens the northeast trade winds and promotes evaporation in the Caribbean Sea and Gulf of

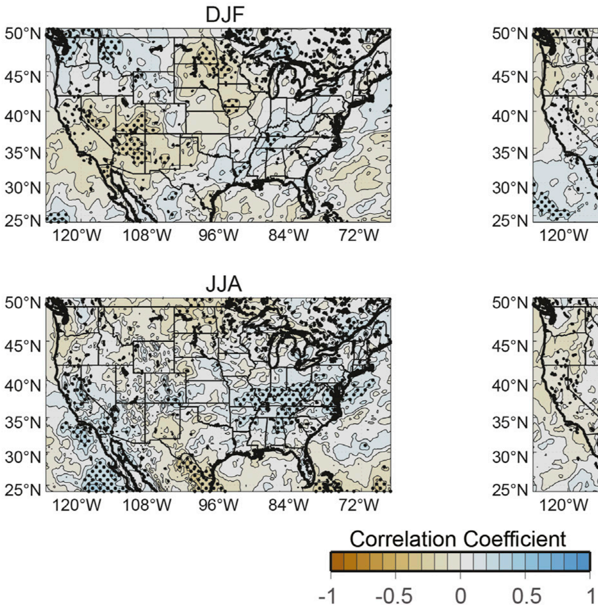

FIGURE 8
As in Figure 7, but for precipitation.

Mexico, with the opposite effects during the negative NAO phase (Kapala et al., 1998; Mächel et al., 1998), the effect of the NAO on the SCUSA is opposite to that farther north. Specifically, the approach of the trade winds to the northwestern Gulf of Mexico, after turning northward, advects increased moisture to the SCUSA during the positive NAO phase and reduced moisture during the negative NAO, thereby contributing to the precipitation anomalies in that area (Oglesby and Erickson, 1989).

The correlations in ERA5 between precipitation and the NAO index are shown in Figure 8, which illustrates the generally weak relationships in the SCUSA, as with temperature (Figure 7). The most extensive areas of significant correlations in the SCUSA occur in spring, when much of Oklahoma and Texas southward along the Texas-Louisiana border and adjacent coastal areas show a positive association between precipitation and the NAO index (Figure 8). In spring, zonality in the NAO is linked with above-normal precipitation, and meridionality brings drier air southward, suppressing precipitation totals, in these areas.

These positive correlations are consistent with the prior studies showing increased streamflow in the Midwest and into the Lower Mississippi River basin during the positive NAO phase. Some negative correlations occur in the westernmost SCUSA in DJF and the Texas-Mexico border in JJA (Figure 8). The NAO's positive phase is linked to significantly greater streamflow than its negative phase in eastern Texas and western Louisiana (middle Mississippi River basin), which aligns prominently with the Ohio, Missouri, and Upper Mississippi basin (Tootle et al., 2005), thereby affecting Lower Mississippi stream discharge. Coleman and Budikova (2010) found that the significant 1993 and 2008 Midwest flood events were both associated with a positive NAO phase preceding the events, but the NAO was in a negative phase during the flooding events. The NAO is also known to alter the effects of ENSO on tropical cyclone activity by modulating SLP associated with the BAA and associated vertical wind shear (Lim et al., 2016).

Impacts of the AMV in the south-central United States

Previous research has identified linkages between the AMV and SCUSA temperatures, through the positive correlation between tropical Atlantic SST and high cloud cover, the latter of which is indicative of convection (Vaideanu et al., 2018). This cloud-cover connection is corroborated by the observation of positive correlations between minimum daily temperatures and the AMV in much of North America, including the SCUSA (Gan et al., 2019).

However, more emphasis has been placed on understanding the hydrometeorological and hydrological impacts of the AMV in the SCUSA. The AMV has been tied to precipitation variability in the United States primarily through its influence on the position and intensity of the BAA. A warm-phase AMV tends to weaken the BAA, which reduces low-level “back of high” moisture advection into the SCUSA (Kushnir et al., 2010). The relationship between tropical cyclone frequency and broad-scale teleconnections seems to be most robust in the Atlantic, particularly regarding the AMV at the interannual to decadal scales (Vimont and Kossin, 2007). The most complete picture is provided through the synergistic effects of ENSO and the AMV (Mo et al., 2009), as the combination of La Niña and AMV warm phase supports Atlantic-Gulf tropical cyclone activity and accumulated cyclone energy (Patricola et al., 2014). A paleoclimate reconstruction from a coral in eastern Caribbean suggests connection between AMV and tropical cyclone activity for 1923–1998 (Hetzinger et al., 2008). Other coral-based reconstructions find strong correlation with AMV and temperature proxies that extend this record back to 1751 (Kilbourne et al., 2008) and central Caribbean coral hydroclimate reconstruction varies with the AMV back to 1887 (von Reumont et al., 2018). However, Gulf of Mexico and Bahamian coral-based reconstructions suggest mixed results with no direct AMO relationship (DeLong et al., 2014) to coral-SST lagging the AMO by 6–9 years with a decreased relationship before ~1800 (Saenger et al., 2009; Flannery et al., 2017). Sea surface temperature in the Caribbean Sea and the Gulf of Mexico plays a vital role in weather, hydroclimate, and extreme events in the SCUSA (Wang et al., 2006, 2008a, 2008b; Martin and Schumacher, 2011a, 2011b, 2012; Misra et al., 2014).

The positive mode of the AMV also appears to favor drought in the SCUSA (Enfield et al., 2001; Rogers and Coleman, 2003; McCabe et al., 2004; Mo et al., 2009). More recently, Torbenson and Stahle (2018) confirmed this relationship using tree-ring reconstructions by finding that the positive (warm) AMV phase is strongly associated with central United States negative precipitation anomalies in autumn (confirmed by Knight et al., 2006), and also in spring and summer (confirmed by Nigam et al., 2011), and with negative streamflow anomalies along the northern and western Gulf of Mexico coast (Tootle et al., 2005). Cook et al. (2014) found that while drought in the SCUSA is positively correlated to the AMV index, drought in the westernmost SCUSA is linked more strongly to La Niña events. The mechanism responsible for such anomalies is the diversion of westward trade wind-associated moisture flow southward of the Gulf of Mexico (Méndez and Magaña, 2010). Perhaps the most striking example of impacts from the AMV on SCUSA drought is the evidence from a tree-ring reconstruction of the 1838 drought, which is likely to have contributed to many deaths during the so-called Trail of Tears (Torbenson and Stahle, 2018). Recent work supports these general findings, as long-term future decreases in streamflow associated with the AMV is projected for the southeastern United States, including Louisiana (Sadeghi et al., 2019), although synergistic impacts between the AMV and ENSO must also be considered (Torbenson et al., 2019).

Results from ERA5 analysis on the extended study period confirm a statistically significant positive relationship between the AMV index and the SCUSA temperature for most of the year (Figure 9), particularly summer and autumn, and weak, insignificant correlations in spring. When combined with results from the previous studies, it appears likely that Atlantic tropical cyclone season would be impacted strongly by AMV-related variability through its impacts on Gulf of Mexico SSTs (Poore et al., 2009). Other paleoclimate-based research has suggested that cool North Atlantic SSTs, El Niño-like conditions, and the negative phase of the NAO were associated with fewer hurricanes during the Maunder Minimum (Trouet et al., 2016). AMV-precipitation relationships, on the other hand, are weaker in the SCUSA, with negative correlations strongest in autumn in the interior SCUSA (Figure 10) when Gulf of Mexico and Caribbean SSTs peak. Perhaps the coastal areas display the weaker relationship due to the influence of tropical cyclones that are energized by the warmer waters in the summer and autumn months.

Impacts of the PDO in the south-central United States

The role of the PDO in the observed cooler period over the central United States, including the SCUSA, in the last quarter of the 20th century amid substantial warming elsewhere, has been noted (Kumar et al., 2013; Pan et al., 2013; Pan et al., 2017). Responses to PDO-related temperature variability in the SCUSA are stronger in winter and spring than summer and autumn, with a tendency for negative temperature anomalies (Figure 11), as represented by anomalously low geopotential height fields, during warm-phase PDO, and vice versa (Mills and Walsh, 2013). Winter precipitation (Kurtzman and Scanlon, 2007) and extreme precipitation (Zhang et al., 2010) have been shown to be greater in the SCUSA during the positive (warm) PDO phase than during the negative (cold) phase. The PDO-like IPO has also been linked to precipitation anomalies of opposing sign between China and the southwestern U.S., including the SCUSA, with particular amplification of the relationship when the AMV is in the opposite phase (Yang et al., 2019). McCabe et al. (2004) identified the linkage between cooling associated with the cold- (i.e., negative) phase PDO and drought across the conterminous United States, including the SCUSA. Ford et al. (2017) found that below-normal precipitation in the SCUSA is forced by a negative PDO, which had already been associated with a prolonged Medieval megadrought (MacDonald and Case, 2005), accompanied by a positive AMV. Barlow et al. (2001) recognized the synergistic influence of the cold phase of both ENSO and the PDO on the historic drought of the early to middle 1950s in the SCUSA. ERA5 analysis on the extended study period confirms the negative correlation between PDO

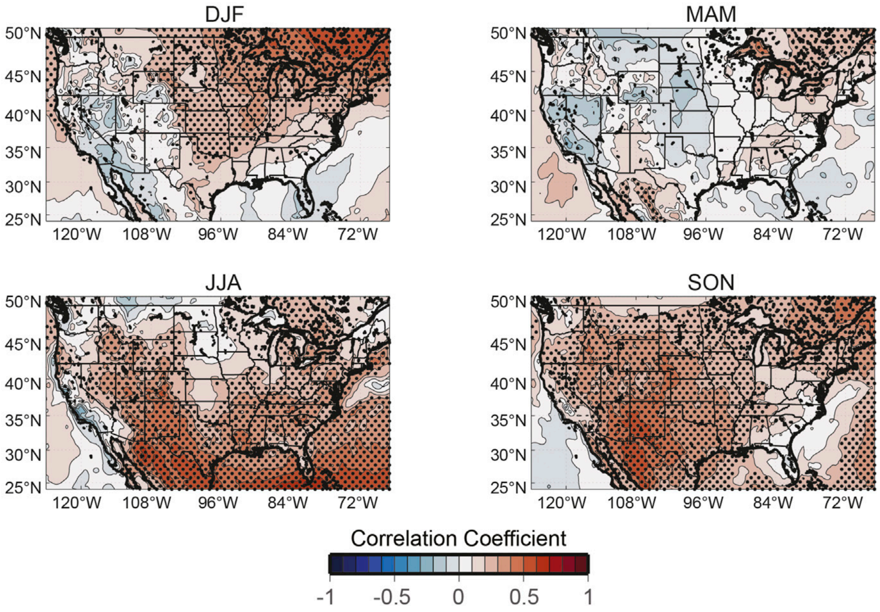

FIGURE 9
Correlation coefficients between the AMV index and seasonal temperature across the continental United States (1950–2020); stippling indicates statistical significance ($p < 0.05$).

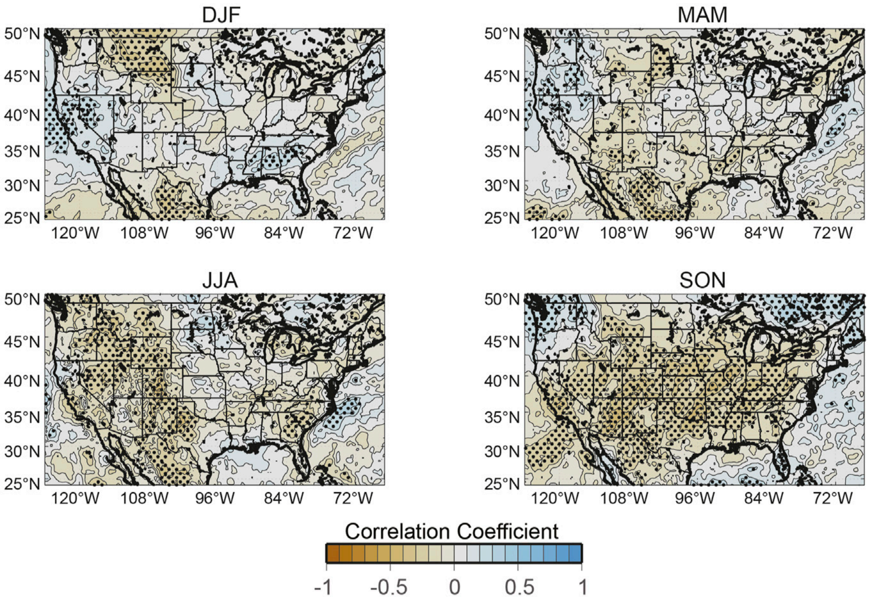

FIGURE 10
As in Figure 9, but for precipitation.

phase and SCUSA temperature, with the relationship statistically significant across large swaths of the SCUSA in winter, spring, and summer and in the Gulf of Mexico in winter and spring months (Figure 11). Anomalously warm Pacific waters associated with the PDO produce positive precipitation anomalies (and vice versa) in the western and coastal SCUSA in all seasons and in the Gulf of Mexico in all seasons except autumn (Figure 12).

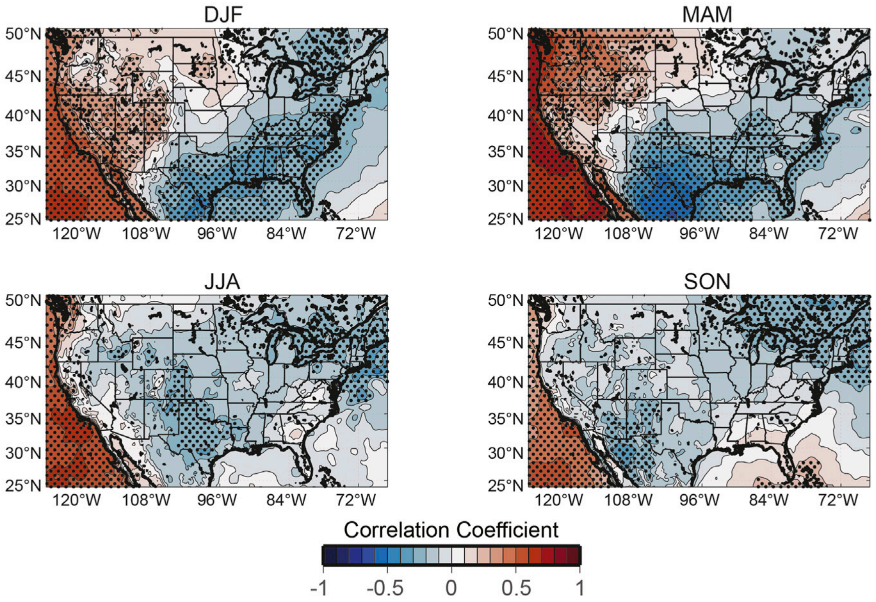

FIGURE 11
Correlation coefficients between the PDO index and seasonal temperature across the continental United States (1950–2020); stippling indicates statistical significance ($p < 0.05$).

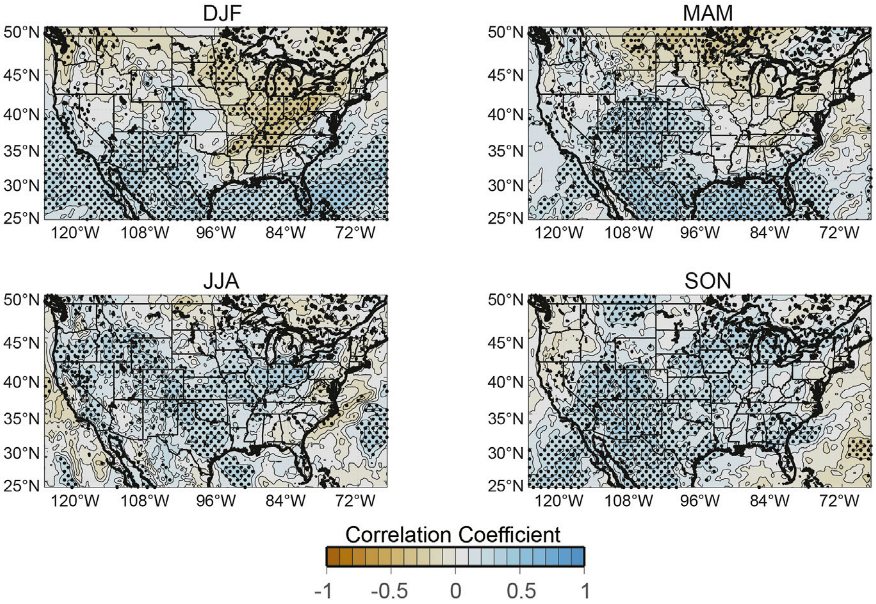

FIGURE 12
As in Figure 11, but for precipitation.

Tootle et al. (2005) linked the PDO's warm phase with significantly enhanced streamflow along the eastern Texas and Louisiana coast, and in eastern Oklahoma, with Sagarika et al. (2015) and Rodgers et al. (2020) concurring with these findings in the SCUSA but with low explained variance (Mantua et al., 1997). Khedun et al. (2012) elaborated on the distinction between the PDO's winter and spring influence (particularly when working in tandem with El Niño) on the upper vs. lower Rio Grande, thereby somewhat mitigating extremes in water availability. Pascolini-Campbell et al. (2017) showed the importance of the positive PDO (and negative

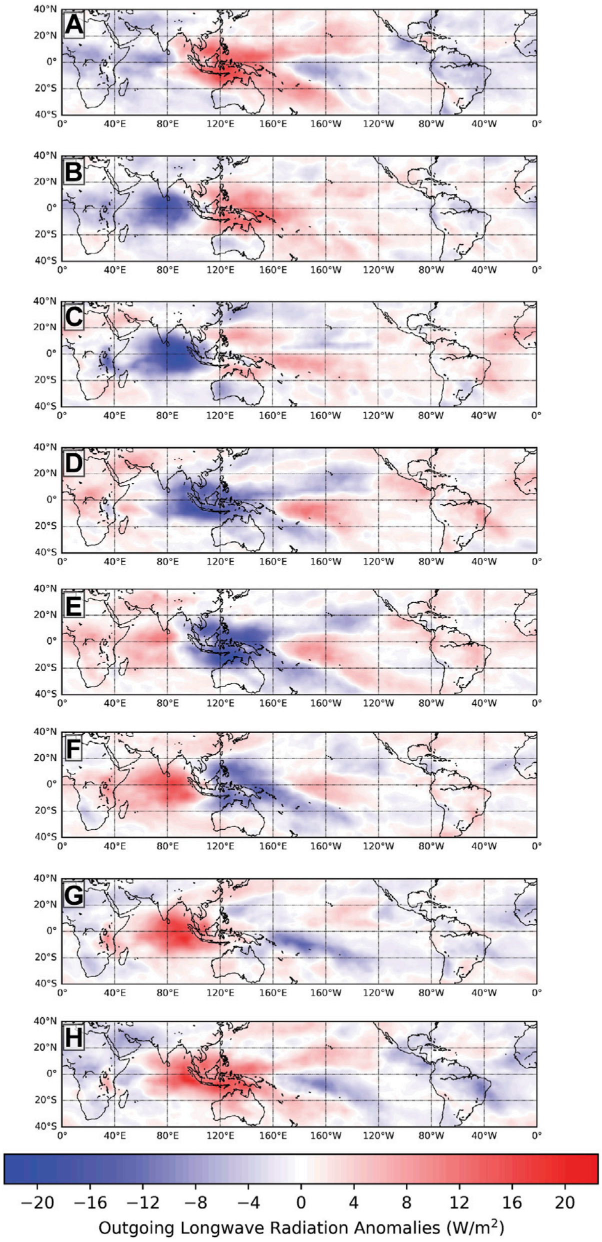

FIGURE 13
Outgoing longwave radiation anomalies by Madden-Julian Oscillation phase, using data from 1979 to 2014. Source: Caparotta (2018). **(A–H)** represent MJO Phase 1 through 8 respectively..

AMV) as a driver of anomalously positive streamflow in the Upper Rio Grande basin.

Intraseasonal variability: The madden-julian oscillation

Whereas the focus of this research is on seasonal-scale modes of climate variability and their teleconnections, the intra-seasonal tropical Madden-Julian Oscillation (MJO; Zhang, 2005) deserves mention because of its proximity to and influence on the SCUSA and because teleconnections are now recognized to exert an untapped source of weather predictability at the intraseasonal scale (Stan et al., 2017). Also known in earlier literature as the 30–60-day Oscillation (e.g., Tokioka et al., 1988; Ferranti et al., 1990) or 40–50-day Oscillation (e.g., Madden and Julian, 1994), Roland Madden and Paul Julian discovered the oscillation when analyzing zonal wind anomalies in the tropical Pacific Ocean (Madden and Julian, 1971). The MJO is characterized by a geographically-propagating sequence of convective pulses as revealed by spatial and temporal fluctuations in outgoing longwave radiation (Figure 13). The location of MJO- induced convective bursts define the eight MJO phases, which are represented by an index developed by Wheeler and Hendon (2004) based on a pair of empirical orthogonal functions of the combined fields of near-equatorially averaged 850-hPa zonal wind, 200-hPa zonal wind, and satellite-observed outgoing longwave radiation. Phase 1 has relatively benign convection ubiquitously, while Phases 2 through 6 support vigorous convection in a west-to-east direction proceeding from the equatorial central Indian Ocean to New Guinea, and Phases 7 and 8 have milder convective clusters from the central to eastern equatorial Pacific.

The MJO phase has been linked to extratropical atmospheric variability, forced largely by convection in the western tropical Pacific (Lukens et al., 2017) through the modulation of circulation, including through other teleconnections including ENSO (Lee et al., 2019), the PNA pattern (Schreck et al., 2013; Zhou et al., 2020; Toride and Hakim, 2021) and the NAO (Cassou, 2008; Lin et al., 2009). Moon et al. (2011) recognized the interplay between ENSO and MJO in modulating MJO impacts.

Regardless of the extent to which other teleconnections exacerbate or mitigate the effects, the MJO is known to be related to North American weather and climate through its impact on circulation. Research has related the MJO to variability in the jet stream (Barrett, 2019) and associated storm tracks (Grise et al., 2013; Zheng et al., 2018) and snowstorms (Moon et al., 2012), temperatures (Zhou et al., 2012), precipitation (Jones, 2000; Martin and Schumacher, 2011b), extreme precipitation (Jones et al., 2011), moisture in atmospheric rivers (Jones and Carvalho, 2014; Baggett et al., 2017), and tropical cyclones (Vitart, 2009) impacting North America. As periods of active MJO activity have been identified as important modes of cold-season circulation predictability in the Northern Hemisphere extratropics (Jones et al., 2004), it is not surprising that improvements in forecast skill for extreme precipitation were found with MJO active Phases 1, 2, 7, and 8, and in strong-magnitude cases of Phases 3, 4, 7, and 8 (Jones et al., 2011).

Somewhat less predictability for SCUSA temperature and precipitation is afforded by MJO phase than in most other areas of North America (Rodney et al., 2013). There is a suggestion of positive winter temperature anomalies in the SCUSA during Phase 4, and in the eastern SCUSA during Phase 6, and positive precipitation anomalies in the northern SCUSA during Phase 5 (Zhou et al., 2012), with Phases 4, 5, and 6 characterized by convective clusters that move across the Maritime Continent into the western tropical Pacific, respectively. Caparotta (2018) observed increased storminess in the Gulf of Mexico region during Phases 7, 8, and 1, which show relatively weak convective clusters, propagating from the central to eastern Pacific. Gulf of Mexico tropical cyclones have also been identified to be modulated by the MJO, with westerly low-level winds in the eastern Pacific far more supportive of cyclogenesis than easterly (Maloney and Hartmann, 2000; Klotzbach and Oliver, 2015), and with Phase 8 associated with enhanced likelihoods for Gulf tropical cyclogenesis (Klotzbach, 2014).

While causes of MJO-influenced intraseasonal precipitation variability in the SCUSA have been investigated thoroughly, including due to mesoscale convective systems (Fritsch et al., 1986) and most recently using isotopic data (Sun et al., 2019), relatively few studies have isolated the regional impact of the MJO. Thompson and Roundy (2013) observed a robust link between March-May violent tornado days in the United States, with strong representation in the SCUSA, and Phase 2, which is manifested as a deep trough over the western and central United States and veering wind anomalies from the south to the southwest with increasing height. Guo et al. (2017) noted the dominance of frequency over intensity of MJO-related cyclonic activity, including over the SCUSA. MJO influences on cyclogenesis and severe convective storms with damaging winds, hail, and/or tornadoes in the United States. Gulf Coastal region, including parts of SCUSA, have also been identified (Caparotta, 2018).

Recent research has begun to suggest possible future changes in the MJO. Zhou et al. (2020) proposed that an eastward shift in the subtropical jet exit region will extend the MJO influence more strongly eastward, toward the SCUSA. Despite the potential, little research exists connecting the MJO beyond atmospheric conditions to other human and environmental systems in the SCUSA.

Discussion and summary/conclusions

Multiple ocean-atmosphere modes of variability and their teleconnections explain a significant amount of variability in low-frequency atmospheric flow at seasonal and longer time scales in the south-central United States (SCUSA). While a rich literature about these teleconnections has been amassed, the use of different data sets over different periods of record with results compiled over different temporal units (i.e., months, seasons, years) complicates comparison of those results. A thorough review of recent research through 2021 regarding the environmental impacts of the teleconnections from each major mode of climate variability in the SCUSA, with a focus on temperature and precipitation, is conducted here, independently of that put forth in the Intergovernmental Panel on Climate Change (IPCC) Fifth and Sixth Assessment Reports (IPCC 2014; IPCC 2022) and the United States. National Climate Assessments. Correlation fields are then generated for each climate mode's index vs. seasonal temperature and (separately) precipitation using a modern, high-resolution data set from 1950 to 2020. Qualitative comparison reveals consistencies and a few differences between the literature and this analysis. In general, the teleconnections associated with the modes of climate variability examined have different degrees of impact seasonally and spatially across the SCUSA, with the spatial impact in the SCUSA varying particularly in the west-east direction. The ERA5 reanalysis product provides a more complete data set for our analysis, but because it is not comprised of direct observations, differences may occur from earlier assessments that used other data sets.

El Niño-Southern Oscillation (ENSO) is found here to have different impacts on the SCUSA than has been revealed in previous work. The fact that ENSO events, particularly Modoki (or central-Pacific ENSO), which may play an increasing role in the future, differ substantially from each other in terms of their physical characteristics and their impacts may explain the discrepancies with and among the previous studies. The most prominent temperature relationship in the SCUSA is in Texas in spring, when anomalously cool conditions occur in the El Niño phase and warm conditions occur in La Niña. Precipitation anomalies are also most prominent in Texas in spring, with El Niño associated with anomalously wet conditions and La Niña having drier-than-normal conditions in the spring.

As in most of the rest of the United States, the Pacific-North American (PNA) pattern relates to temperature only in winter and spring in the SCUSA, where a negative relationship exists in meteorological winter (DJF). This suggests that mid-tropospheric ridging over the Rocky Mountain cordillera is linked to anomalously warm temperatures and mid-tropospheric troughing in the same area is associated with anomalously cold conditions. Regarding precipitation, the positive relationship in much of the western coastal SCUSA and adjacent Gulf of Mexico means that Rocky Mountain ridging brings more precipitation than average, as that region tends to be under the influence of a downstream trough, while Rocky Mountain troughing makes this area drier than usual.

Although the relationship between the North Atlantic Oscillation (NAO) and temperature is weak in the SCUSA, some extensive areas of significant correlations to precipitation occur in spring, when much of Oklahoma and Texas southward along the Texas-Louisiana border and adjacent coastal areas show a relationship. More specifically, with strongly zonal flow associated with the NAO associated with increased precipitation in those areas and weaker zonality linked to suppressed precipitation.

The two large, amorphous climate modes frequently defined based on sea-surface temperatures in the Atlantic and Pacific Oceans also have teleconnections and impacts on the SCUSA. Unlike most other modes of climate variability, the Atlantic Multidecadal Oscillation (AMO; also known as the Atlantic Multidecadal Variability (AMV)) shows its strongest influence in the SCUSA in summer. The warm-phase AMV is tied to anomalously warm SCUSA temperatures, and vice versa. AMV-precipitation relationships, on the other hand, are weaker in SCUSA, with negative correlations strongest in autumn in the interior SCUSA. This analysis verifies the existing literature regarding the impacts of the Pacific Decadal Oscillation (PDO) on the SCUSA. A slight tendency for below-normal temperatures, especially in the cold season, and above-normal precipitation in the SCUSA are apparent during the warm phase, with generally opposite results in the cold-phase PDO. The AMV influences the northern Gulf of Mexico temperatures in summer and autumn whereas the PDO has greater influence in the winter and spring. The AMV has little influence over northern Gulf of Mexico precipitation but the PDO influences precipitation for all seasons except autumn, suggesting a quasi-persistent atmospheric teleconnection between the Gulf of Mexico and the North Pacific Ocean.

Collectively, the SO, NAO, NAM (AO), PNA pattern, AMV, PDO, and MJO ocean-atmosphere teleconnections set up a cascade of linkages (Terjung, 1976) that vary seasonally across the SCUSA that can ripple across environmental, economic, and social systems. One example of such cascading influence is the future impacts of atmospheric and land-use land-cover variability in forest ecosystems (Sohngen and Brown, 2006). Trigo et al. (2002) conducted a similar analysis on effects of the NAO on Europe and the adjacent North Atlantic waters. In general, the teleconnection information collected in previous studies and summarized here could be directed toward more human-environmental systems research. To date, most such work has focused on ENSO but utility exists for connecting other teleconnection-based forcing patterns, particularly the PNA pattern, AMV, and PDO, with human-environmental systems in the SCUSA.

Moreover, whereas the climate modes and their teleconnections described here are important modulators of atmospheric and hydroclimatic variability in the SCUSA, other teleconnections, particularly those identified by Barnston and Livezey (1987) and/or the circumglobal (Branstator, 2002) and extratropical Asian-Bering-North American (Yu et al., 2018) patterns, may also exert an influence on weather and climate in this region, as these latter two modes have been shown to have a comparable influence to the PNA pattern on North American climate (e.g., Yu et al., 2019). It is also possible that other identified or as-yet-unidentified teleconnection patterns could also be important for understanding SCUSA climate and cascading climatic impacts. These modes and their impacts could change in a changing climate. For example, non-stationarity associated with the eastward shift of the NAO, particularly in summer (Sun and Wang, 2012), has likely been associated with changes in its influence over the SCUSA.

Author contributions

The four authors contributed equally to the development of the idea and project planning. RR led the research, writing, and editing effort, but with contributions from all four authors. GS conducted statistical analyses of the reanalysis data sets and produced and revised the figures.

Funding

This research is supported by the Department of the Interior South Central Climate Adaptation Science Center Cooperative Agreement G19AC00086 and the USGS Ecosystems Mission Area facilitated interactions. KD and EM supported by NSF Award Number 2102931.

Acknowledgments

The authors appreciate the support of the South Central Climate Adaptation Science Center and the Teleconnection Working Group for their contributions to the development of this study. We thank our students and postdocs, particularly Kylie Palmer, for their contributions to this study and its development. Any use of trade, firm, or product names is for descriptive purposes only and does not imply endorsement by the United States Government.

Conflict of interest

The authors declare that the research was conducted in the absence of any commercial or financial relationships that could be construed as a potential conflict of interest.

Publisher's note

References

Ahn, S. E., Plantinga, A. J., and Alig, R. J. (2002). Determinants and projections of land use in the South Central United States. *South. J. Appl. For.* 26 (2), 78–84. doi:10.1093/sjaf/26.2.78

Alexander, M. A., Bladé, I., Newman, M., Lanzante, J. R., Lau, N-. C., and Scott, J. D. (2002). The atmospheric bridge: The influence of ENSO teleconnections on air–sea interaction over the global oceans. *J. Clim.* 15 (16), 2205–2231. doi:10.1175/1520-0442(2002)015<2205:TABTIO>2.0.CO;2

Alexander, M. A., Kilbourne, K. H., and Nye, J. A. (2014). Climate variability during warm and cold phases of the Atlantic Multidecadal Oscillation (AMO) 1871–2008. *J. Mar. Syst.* 133, 14–26. doi:10.1016/j.jmarsys.2013.07.017

Alig, R. J., Kline, J. D., and Lichtenstein, M. (2004). Urbanization on the US landscape: Looking ahead in the 21st century. *Landsc. Urban Plan.* 69 (2–3), 219–234. doi:10.1016/j.landurbplan.2003.07.004

Ashok, K., Behera, S. K., Rao, S. A., Weng, H., and Yamagata, T. (2007). El Niño Modoki and its possible teleconnection. *J. Geophys. Res.* 112 (C11), C11007. doi:10.1029/2006JC003798

Baggett, C. F., Barnes, E. A., Maloney, E. D., and Mundhenk, B. D. (2017). Advancing atmospheric river forecasts into subseasonal-to-seasonal timescales. *Geophys. Res. Lett.* 44 (14), 7528–7536. doi:10.1002/2017GL074434

Bahaga, T. K., Fink, A. H., and Knippertz, P. (2019). Revisiting interannual to decadal teleconnections influencing seasonal rainfall in the Greater Horn of Africa during the 20th century. *Int. J. Climatol.* 39 (5), 2765–2785. doi:10.1002/joc.5986

Barlow, M., Nigam, S., and Berbery, E. H. (2001). ENSO, Pacific decadal variability, and US summertime precipitation, drought, and stream flow. *J. Clim.* 14 (9), 2105–2128. doi:10.1175/1520-0442(2001)014<2105:EPDVAU>2.0.CO;2

Barnston, A. G., and Livezey, R. E. (1987). Classification, seasonality and persistence of low-frequency atmospheric circulation patterns. *Mon. Weather Rev.* 115 (6), 1083–1126. doi:10.1175/1520-0493(1987)115<1083:CSAPOL>2.0.CO;2

Barrett, B. S. (2019). Connections between the madden–julian oscillation and surface temperatures in winter 2018 over eastern north America. *Atmos. Sci. Lett.* 20 (1), e869. doi:10.1002/asl.869

Bentley, A. M., Bosart, L. F., and Keyser, D. (2019). A climatology of extratropical cyclones leading to extreme weather events over central and eastern North America. *Mon. Weather Rev.* 147 (5), 1471–1490. doi:10.1175/MWR-D-18-0453.1

Biondi, F., Gershunov, A., and Cayan, D. R. (2001). North Pacific decadal climate variability since 1661. *J. Clim.* 14 (1), 5–10. doi:10.1175/1520-0442(2001)014<0005:NPDCVS>2.0.CO;2

Bishop, D. A., Williams, A. P., Seager, R., Fiore, A. M., Cook, B. I., Mankin, J. S., et al. (2019). Investigating the causes of increased twentieth-century fall precipitation over the southeastern United States. *J. Clim.* 32 (2), 575–590. doi:10.1175/JCLI-D-18-0244.1

Bjerknes, J. (1969). Atmospheric teleconnections from the equatorial Pacific[1]. *Mon. Weather Rev.* 97 (3), 163–172. doi:10.1175/1520-0493(1969)097<0163:atftep>2.3.co;2(1969)097<0163:ATFTEP>2.3.CO;2

Bonfils, C., and Santer, B. D. (2011). Investigating the possibility of a human component in various Pacific decadal oscillation indices. *Clim. Dyn.* 37 (7), 1457–1468. doi:10.1007/s00382-010-0920-1

Booth, B. B. B., Dunstone, N. J., Halloran, P. R., Andrews, T., and Bellouin, N. (2012). Aerosols implicated as a prime driver of twentieth-century North Atlantic climate variability. *Nature* 484 (7393), 228–232. doi:10.1038/nature10946

Bove, M. C., Elsner, J. B., Landsea, C. W., Niu, X., and O'Brien, J. J. (1998). Effect of El Niño on US landfalling hurricanes, revisited. *B. Am. Meteorol. Soc.* 9 (11), 2477–2482. doi:10.1175/1520-0477(1998)079<2477:EOENOO>2.0.CO;2

Bradbury, J. A., Keim, B. D., and Wake, C. P. (2003). The influence of regional storm tracking and teleconnections on winter precipitation in the northeastern United States. *Ann. Assoc. Am. Geogr.* 93 (3), 544–556. doi:10.1111/1467-8306.9303002

Branstator, G. (2002). Circumglobal teleconnections, the jet stream waveguide, and the North Atlantic Oscillation. *J. Clim.* 15 (14), 1893–1910. doi:10.1175/1520-0442(2002)015<1893:CTTJSW>2.0.CO;2

Bretherton, C. S., Widmann, M., Dymnikov, V. P., Wallace, J. M., and Bladé, I. (1999). The effective number of spatial degrees of freedom of a time-varying field. *J. Clim.* 12 (7), 1990–2009. doi:10.1175/1520-0442(1999)012<1990:TENOSD>2.0.CO;2

Budikova, D. (2005). Impact of the pacific decadal oscillation on relationships between temperature and the arctic oscillation in the USA in winter. *Clim. Res.* 29 (3), 199–208. doi:10.3354/cr029199

Bunge, L., and Clarke, A. J. (2009). A verified estimation of the El Niño index Niño-3.4 since 1877. *J. Clim.* 22 (14), 3979–3992. doi:10.1175/2009JCLI2724.1

Bushra, N., and Rohli, R. V. (2021). Relationship between atmospheric teleconnections and the Northern Hemisphere's circumpolar vortex. *Earth Space Sci.* 8 (9), e2021EA001802. doi:10.1029/2021EA001802

Cai, W. J., Wang, G. J., Santoso, A., McPhaden, M. J., Wu, L. X., Jin, F.- F., et al. (2015). Increased frequency of extreme La Niña events under greenhouse warming. *Nat. Clim. Chang.* 5 (2), 132–137. doi:10.1038/NCLIMATE2492

Cai, W., Santoso, A., Collins, M., Dewitte, B., Karamperidou, C., Kug, J.- S., et al. (2021). Changing El niño-southern oscillation in a warming climate. *Nat. Rev. Earth Environ.* 2 (9), 628–644. doi:10.1038/s43017-021-00199-z

Callahan, C. W., Chen, C., Rugenstein, M., Bloch-Johnson, J., Yang, S., and Moyer, E. J. (2021). Robust decrease in El Niño/Southern Oscillation amplitude under long-term warming. *Nat. Clim. Chang.* 11 (9), 752–757. doi:10.1038/s41558-021-01099-2

Caparotta, S. P. (2018). *Madden-julian oscillation relationships with cool season cyclogenesis, daily precipitation, and cool season severe weather frequencies in the Gulf of Mexico region* (Baton Rouge, LA: Louisiana State University). Ph.D. Dissertation.

Capotondi, A., Wittenberg, A. T., Newman, M., Di Lorenzo, E., Yu, J.- Y., Braconnot, P., et al. (2015). Understanding ENSO diversity. *Bull. Am. Meteorol. Soc.* 96 (6), 921–938. doi:10.1175/BAMS-D-13-00117.1

Cassou, C. (2008). Intraseasonal interaction between the madden-julian oscillation and the north atlantic oscillation. *Nature* 455 (7212), 523–527. doi:10.1038/nature07286

Ceballos, L. I., Di Lorenzo, E., Hoyos, C. D., Schneider, N., and Taguchi, B. (2009). North Pacific Gyre Oscillation synchronizes climate fluctuations in the eastern and Western boundary systems. *J. Clim.* 22 (19), 5163–5174. doi:10.1175/2009JCLI2848.1

Cellitti, M. P., Walsh, J. E., Rauber, R. M., and Portis, D. H. (2006). Extreme cold air outbreaks over the United States, the polar vortex, and the large-scale circulation. *J. Geophys. Res.* 111 (D2), D02114. doi:10.1029/2005JD006273

Chen, J.- M., Hsieh, C.- M., and Liu, J.- S. (2012). Possible influences of ENSO on winter shipping in the North Pacific. *Terr. Atmos. Ocean. Sci.* 23 (4), 397–411. doi:10.3319/TAO.2012.03.02.01(A

Chiang, J. C. H., and Vimont, D. J. (2004). Analogous Pacific and Atlantic meridional modes of tropical atmosphere-ocean variability. *J. Clim.* 17 (21), 4143–4158. doi:10.1175/JCLI4953.1

Clement, A., Bellomo, K., Murphy, L. N., Cane, M. A., Mauritsen, T., Rädel, G., et al. (2015). The Atlantic Multidecadal Oscillation without a role for ocean circulation. *Science* 350 (6258), 320–324. doi:10.1126/science.aab3980

Coleman, J. S. M., and Budikova, D. (2010). Atmospheric aspects of the 2008 midwest floods: A repeat of 1993? *Int. J. Climatol.* 30 (11), 1645–1667. doi:10.1002/joc.2009

Cook, A. R., Leslie, L. M., Parsons, D. B., and Schaefer, J. T. (2017). The impact of El Niño–Southern Oscillation (ENSO) on winter and early spring US tornado outbreaks. *J. Appl. Meteorol. Climatol.* 56 (9), 2455–2478. doi:10.1175/JAMC-D-16-0249.1

Cook, B. I., Smerdon, J. E., Seager, R., and Cook, E. R. (2014). Pan-continental droughts in North America over the last millennium. *J. Clim.* 27 (1), 383–397. doi:10.1175/JCLI-D-13-00100.1

Copernicus Climate Change Service (2017). ERA5: Fifth generation of ECMWF atmospheric reanalyses of the global climate. Copernicus climate change Service climate data store (CDS). Available at: https://www.ecmwf.int/en/forecasts/datasets/reanalysis-datasets/era5 (Last accessed: April 20, 2022).

D'Arrigo, R., Villalba, R., and Wiles, G. (2001). Tree-ring estimates of Pacific decadal climate variability. *Clim. Dyn.* 18 (3–4), 219–224. doi:10.1007/s003820100177

Danco, J., and Martin, E. R. (2018). Understanding the influence of ENSO on the Great Plains low-level jet in CMIP5 models. *Clim. Dyn.* 51 (4), 1537–1558. doi:10.1007/s00382-017-3970-9

Davis, R. E. (1976). Predictability of sea-surface temperature and sea-level pressure anomalies over North Pacific Ocean. *J. Phys. Oceanogr.* 6 (3), 249–266. doi:10.1175/1520-0485(1976)006<0249:POSSTA>2.0.CO;2

de Chazal, J., and Rounsevell, M. D. A. (2009). Land-use and climate change within assessments of biodiversity change: A review. *Glob. Environ. Change* 19 (2), 306–315. doi:10.1016/j.gloenvcha.2008.09.007

DeLong, K. L., Flannery, J. A., Poore, R. Z., Quinn, T. M., Maupin, C. R., Lin, K., et al. (2014). A reconstruction of sea surface temperature variability in the southeastern Gulf of Mexico from 1734–2008 CE using cross-dated Sr/Ca records from the coral *Siderastrea siderea*. *Paleoceanography* 29 (5), 403–422. doi:10.1002/2013PA002524

DeLong, K. L., Quinn, T. M., Taylor, F. W., Lin, K., and Shen, C.- C. (2012). Sea surface temperature variability in the southwest tropical Pacific since AD 1649. *Nat. Clim. Chang.* 2 (11), 799–804. doi:10.1038/NCLIMATE1583

Deser, C., Alexander, M. A., Xie, S.- P., and Phillips, A. S. (2010). Sea surface temperature variability: Patterns and mechanisms. *Annu. Rev. Mar. Sci.* 2010 (2), 115–143. doi:10.1146/annurev-marine-120408-151453

Deser, C., and Phillips, A. S. (2021). Defining the internal component of Atlantic Multidecadal Variability in a changing climate. *Geophys. Res. Lett.* 48 (22), e2021GL095023. doi:10.1029/2021GL095023

Deser, C., Phillips, A. S., Tomas, R. A., Okumura, Y. M., Alexander, M. A., Capotondi, A., et al. (2012). ENSO and pacific decadal variability in the community climate system model version 4. *J. Clim.* 25 (8), 2622–2651. doi:10.1175/JCLI-D-11-00301.1

Deser, C., Simpson, I. R., Phillips, A. S., and McKinnon, K. A. (2018). How well do we know ENSO's climate impacts over North America, and how do we evaluate models accordingly? *J. Clim.* 31 (13), 4991–5014. doi:10.1175/JCLI-D-17-0783.1

Dethier, E. N., Sartain, S. L., Renshaw, C. E., and Magilligan, F. J. (2020). Spatially coherent regional changes in seasonal extreme streamflow events in the United States and Canada since 1950. *Sci. Adv.* 6 (49), eaba5939. doi:10.1126/sciadv.aba5939

Di Lorenzo, E., and Mantua, N. (2016). Multi-year persistence of the 2014/15 North Pacific marine heatwave. *Nat. Clim. Chang.* 6 (11), 1042–1047. doi:10.1038/nclimate3082

Di Lorenzo, E., Schneider, N., Cobb, K. M., Franks, P. J. S., Chhak, K., Miller, A. J., et al. (2008). North Pacific Gyre Oscillation links ocean climate and ecosystem change. *Geophys. Res. Lett.* 35 (8), L08607. doi:10.1029/2007GL032838

Dima, M., and Lohmann, G. (2007). A hemispheric mechanism for the atlantic multidecadal oscillation. *J. Clim.* 20 (11), 2706–2719. doi:10.1175/JCLI4174.1

Dong, B., Dai, A., Vuille, M., and Timm, O. E. (2018). Asymmetric modulation of ENSO teleconnections by the interdecadal Pacific oscillation. *J. Clim.* 31 (18), 7337–7361. doi:10.1175/JCLI-D-17-0663.1

Dong, X., Xi, B., Kennedy, A., Feng, Z., Entin, J. K., Houser, P. R., et al. (2011). Investigation of the 2006 drought and 2007 flood extremes at the Southern Great Plains through an integrative analysis of observations. *J. Geophys. Res.* 116, D03204. doi:10.1029/2010JD014776

Eichler, T., and Higgins, W. (2006). Climatology and ENSO-related variability of North American extratropical cyclone activity. *J. Clim.* 19 (10), 2076–2093. doi:10.1175/JCLI3725.1

Ellis, A. W., and Marston, M. L. (2020). Late 1990s' cool season climate shift in eastern North America. *Clim. Change* 162 (3), 1385–1398. doi:10.1007/s10584-020-02798-z

Enfield, D. B., Mestas-Nuñez, A. M., and Trimble, P. J. (2001). The Atlantic multidecadal oscillation and its relation to rainfall and river flows in the continental U.S. *Geophys. Res. Lett.* 28 (10), 2077–2080. doi:10.1029/2000GL012745

Fang, S. W., Khodri, M., Timmreck, C., Zanchettin, D., and Jungclaus, J. (2021). Disentangling internal and external contributions to Atlantic multidecadal variability over the past millennium. *Geophys. Res. Lett.* 48 (23), e2021GL095990. doi:10.1029/2021GL095990

Felis, T., Suzuki, A., Kuhnert, H., Rimbu, N., and Kawahata, H. (2010). Pacific Decadal Oscillation documented in a coral record of North Pacific winter temperature since 1873. *Geophys. Res. Lett.* 37 (14). doi:10.1029/2010GL043572

Ferranti, L., Palmer, T. N., Molteni, F., and Klinker, E. (1990). Tropical extratropical interaction associated with the 30-60 day oscillation and its impact on medium and extended range prediction. *J. Atmos. Sci.* 47 (18), 2177–2199. doi:10.1175/1520-0469(1990)047<2177:TEIAWT>2.0.CO;2

Flanagan, P. X., Basara, J. B., Furtado, J. C., Martin, E. R., and Xiao, X. (2019). Role of sea surface temperatures in forcing circulation anomalies driving U.S. Great Plains pluvial years. *J. Clim.* 32 (20), 7081–7100. doi:10.1175/JCLI-D-18-0726.1

Flannery, J. A., Richey, J. N., Thirumalai, K., Poore, R. Z., and DeLong, K. L. (2017). Multi-species coral Sr/Ca-based sea-surface temperature reconstruction using *Orbicella faveolata* and *Siderastrea siderea* from the Florida Straits. *Palaeogeogr. Palaeoclimatol. Palaeoecol.* 466, 100–109. doi:10.1016/j.palaeo.2016.10.022

Folland, C. K., Knight, J., Linderholm, H. W., Fereday, D., Ineson, S., and Hurrell, J. W. (2009). The summer North Atlantic oscillation: Past, present, and future. *J. Clim.* 22 (5), 1082–1103. doi:10.1175/2008JCLI2459.1

Folland, C. K., Renwick, J. A., Salinger, M. J., and Mullan, A. B. (2002). Relative influences of the interdecadal pacific oscillation and ENSO on the south pacific convergence zone. *Geophys. Res. Lett.* 29 (13), 1643. doi:10.1029/2001gl014201

Ford, T. W., Quiring, S. M., and Frauenfeld, O. W. (2017). Multi-decadal variability of soil moisture-temperature coupling over the contiguous United States modulated by Pacific and Atlantic sea surface temperatures. *Int. J. Climatol.* 37 (3), 1400–1415. doi:10.1002/joc.4785

Frederiksen, C. S., Zheng, X., and Grainger, S. (2014). Teleconnections and predictive characteristics of Australian seasonal rainfall. *Clim. Dyn.* 43 (5–6), 1381–1408. doi:10.1007/s00382-013-1952-0

Fritsch, J. M., Kane, R. J., and Chelius, C. R. (1986). The contribution of mesoscale convective weather systems to the warm-season precipitation in the United States. *J. Clim. Appl. Meteor.* 25 (10), 1333–1345. doi:10.1175/1520-0450(1986)025<1333:TCOMCW>2.0.CO;2

Gan, Z., Guan, X., Kong, X., Guo, R., Huang, H., Huang, W., et al. (2019). The key role of Atlantic Multidecadal Oscillation in minimum temperature over North America during global warming slowdown. *Earth Space Sci.* 6 (3), 387–397. doi:10.1029/2018EA000443

Gershunov, A., and Barnett, T. P. (1998). Interdecadal modulation of ENSO teleconnections. *Bull. Am. Meteorol. Soc.* 79 (12), 2715–2725. doi:10.1175/1520-0477(1998)079<2715:IMOET>2.0.CO;2

Gomez, F. A., Lee, S.- K., Hernandez, F. J., Chiaverano, L. M., Muller-Karger, F. E., Liu, Y., et al. (2019). ENSO-induced co-variability of salinity, plankton biomass and coastal currents in the Northern Gulf of Mexico. *Sci. Rep.* 9 (1), 178. doi:10.1038/s41598-018-36655-y

Gray, S. T., Graumlich, L. J., Betancourt, J. L., and Pederson, G. T. (2004). A tree-ring based reconstruction of the Atlantic Multidecadal Oscillation since 1567 AD. *Geophys. Res. Lett.* 31 (12), L12205. doi:10.1029/2004GL019932

Gray, W. M. (1984). Atlantic seasonal hurricane frequency. Part 1: El Niño and 30 mb quasi-biennial oscillation influences. *Mon. Weather Rev.* 112 (9), 1649–1668. doi:10.1175/1520-0493(1984)112<1649:ASHFPI>2.0.CO;2

Grise, K. M., Son, S.- W., and Gyakum, J. R. (2013). Intraseasonal and interannual variability in North American storm tracks and its relationship to equatorial Pacific variability. *Mon. Weather Rev.* 141 (10), 3610–3625. doi:10.1175/MWR-D-12-00322.1

Guo, Y., Shinoda, T., Lin, J., and Chang, E. K. (2017). Variations of northern hemisphere storm track and extratropical cyclone activity associated with the Madden-Julian Oscillation. *J. Clim.* 30 (13), 4799–4818. doi:10.1175/JCLI-D-16-0513.1

Hamamoto, M., and Yasuda, I. (2021). Synchronized interdecadal variations behind regime shifts in the Pacific Decadal Oscillation. *J. Oceanogr.* 77 (3), 383–392. doi:10.1007/s10872-021-00592-8

Hamouda, M. E., Pasquero, C., and Tziperman, E. (2021). Decoupling of the arctic oscillation and north atlantic oscillation in a warmer climate. *Nat. Clim. Change* 11 (2), 137–142. doi:10.1038/s41558-020-00966-8

Han, Z., Luo, F., Li, S., Gao, Y., Furevik, T., and Svendsen, L. (2016). Simulation by CMIP5 models of the Atlantic multidecadal oscillation and its climate impacts. *Adv. Atmos. Sci.* 33 (12), 1329–1342. doi:10.1007/s00376-016-5270-4

Hardy, J. W., and Henderson, K. G. (2003). Cold front variability in the southern United States and the influence of atmospheric teleconnection patterns. *Phys. Geogr.* 24 (2), 120–137. doi:10.2747/0272-3646.24.2.120

He, S., and Wang, H. (2013). Oscillating relationship between the East Asian winter monsoon and ENSO. *J. Clim.* 26 (24), 9819–9838. doi:10.1175/JCLI-D-13-00174.1

Henderson, K. G., and Robinson, P. J. (1994). Relationships between the Pacific/North American teleconnection patterns and precipitation events in the south-eastern USA. *Int. J. Climatol.* 14 (3), 307–323. doi:10.1002/joc.3370140305

Henley, B. J., Gergis, J., Karoly, D. J., Power, S., Kennedy, J., and Folland, C. K. (2015). A tripole index for the interdecadal Pacific oscillation. *Clim. Dyn.* 45 (11–12), 3077–3090. doi:10.1007/s00382-015-2525-1

Hersbach, H., Bell, B., Berrisford, P., Hirahara, S., Horanyi, A., Muñoz-Sabater, J., et al. (2020). The ERA5 global reanalysis. *Q. J. R. Meteorol. Soc.* 146 (730), 1999–2049. doi:10.1002/qj.3803

Hetzinger, S., Pfeiffer, M., Dullo, W. C., Keenlyside, N., Latif, M., and Zinke, J. (2008). Caribbean coral tracks Atlantic Multidecadal Oscillation and past hurricane activity. *Geol.* 36 (1), 11–14. doi:10.1130/G24321A.1

Hoerling, M. P., Kumar, A., and Zhong, M. (1997). El Niño, La Niña, and the nonlinearity of their teleconnections. *J. Clim.* 10 (8), 1769–1786. doi:10.1175/1520-0442(1997)010<1769:ENOLNA>2.0.CO;2

Hopkinson, C. S., Covich, A. P., Craft, C. B., DeLong, K. L., Doyle, T. W., Flanagan, N., et al. (2013). "The effects of climate change on natural ecosystems of the Southeast USA," in *Climate of the southeast United States: Variability, change, impacts, and vulnerability*. Editors K. T. Ingram, K. Dow, L. Carter, and J. Anderson (Washington, D.C.: Island Press), 237–270. Available at: https://link.springer.com/content/pdf/10.5822%2F978-1-61091-509-0.pdf (Last accessed: April 20, 2022).

Horel, J. D., and Wallace, J. M. (1981). Planetary-scale atmospheric phenomena associated with the Southern Oscillation. *Mon. Weather Rev.* 109 (4), 813–829. doi:10.1175/1520-0493(1981)109<0813:PSAPAW>2.0.CO;2

Hsieh, W. W., Wu, A., and Shabbar, A. (2006). Nonlinear atmospheric teleconnections. *Geophys. Res. Lett.* 33 (7), L07714. doi:10.1029/2005GL025471

Hsu, H.- H., and Chen, Y.- L. (2011). Decadal to bi-decadal rainfall variation in the Western pacific: A footprint of south Pacific decadal variability? *Geophys. Res. Lett.* 38 (3), L03703. doi:10.1029/2010GL046278

Huang, B., Thorne, P. W., Banzon, V. F., Boyer, T., Chepurin, G., Lawrimore, J. H., et al. (2017). Extended reconstructed sea surface temperature, version 5 (ERSSTv5): Upgrades, validations, and intercomparisons. *J. Clim.* 30 (20), 8179–8205. doi:10.1175/JCLI-D-16-0836.1

Hurrell, J. W. (1995). Decadal trends in the north atlantic oscillation: Regional temperatures and precipitation. *Science* 269 (5224), 676–679. doi:10.1126/science.269.5224.676

Hurrell, J. W. (1996). Influence of variations in extratropical wintertime teleconnections on Northern Hemisphere temperature. *Geophys. Res. Lett.* 23 (6), 665–668. doi:10.1029/96GL00459

Hurrell, J. W., and van Loon, H. (1997). Decadal variations in climate associated with the north Atlantic oscillation. *Clim. Change* 36 (3–4), 301–326. doi:10.1023/A:1005314315270

IPCC (2014). in *Climate change 2014: Impacts, adaptation, and vulnerability. Part A: Global and sectoral aspects*. Editors Field, C. B., Barros, V. R., Dokken, D. J., Mach, K. J., Mastrandrea, M. D., Bilir, T. E., et al. (Cambridge, United Kingdom and New York, NY, U.S.A.: Cambridge University Press), 1132. Contribution of Working Group II to the Fifth Assessment Report of the Intergovernmental Panel on Climate Change.

IPCC (2022). in *Climate change 2022: Impacts, adaptation, and vulnerability. Contribution of working Group II to the Sixth assessment report of the intergovernmental Panel on climate change*. Editors Pörtner, H.-O., Roberts, D. C., Tignor, M., Poloczanska, E. S., Mintenbeck, K., Alegría, A., et al. (Cambridge, United Kingdom and New York, NY, U.S.A.: Cambridge University Press).

Jones, C., and Carvalho, L. M. (2014). Sensitivity to Madden–Julian oscillation variations on heavy precipitation over the contiguous United States. *Atmos. Res.* 147, 10–26. doi:10.1016/j.atmosres.2014.05.002

Jones, C., Gottschalck, J., Carvalho, L. M., and Higgins, W. (2011). Influence of the Madden-Julian oscillation on forecasts of extreme precipitation in the contiguous United States. *Mon. Weather Rev.* 139 (2), 332–350. doi:10.1175/2010MWR3512.1

Jones, C. (2000). Occurrence of extreme precipitation events in California and relationships with the Madden-Julian oscillation. *J. Clim.* 13 (20), 3576–3587. doi:10.1175/1520-0442(2000)013<3576:OOEPEI>2.0.CO;2

Jones, C., Waliser, D. E., Lau, K. M., and Stern, W. (2004). The Madden-Julian oscillation and its impact on Northern Hemisphere weather predictability. *Mon. Weather Rev.* 132 (6), 1462–1471. doi:10.1175/1520-0493(2004)132<1462:TMOAII>2.0.CO;2

Kao, H.- Y., and Yu, J.- Y. (2009). Contrasting eastern-pacific and central-pacific types of ENSO. *J. Clim.* 22 (3), 615–632. doi:10.1175/2008JCLI2309.1

Kapala, A., Mächel, H., and Flohn, H. (1998). Behaviour of the centres of action above the Atlantic since 1881. Part II: Associations with regional climate anomalies. *Int. J. Climatol.* 18 (1), 23–36. doi:10.1002/(SICI)1097-0088(199801)18:1<23::AID-JOC226>3.0.CO;2-7

Kaplan, A., Cane, M. A., Kushnir, Y., Clement, A. C., Blumenthal, M. B., and Rajagopalan, B. (1998). Analyses of global sea surface temperature 1856-1991. *J. Geophys. Res.* 103 (C9), 18567–18589. doi:10.1029/97JC01736

Karnauskas, M., Schirripa, M. J., Craig, J. K., Cook, G. S., Kelbe, C. R., Agar, J. J., et al. (2015). Evidence of climate-driven ecosystem reorganization in the Gulf of Mexico. *Glob. Chang. Biol.* 21, 2554–2568. doi:10.1111/gcb.12894

Kerr, R. A. (2000). A North Atlantic climate pacemaker for the centuries. *Science* 288 (5473), 1984–1985. doi:10.1126/science.288.5473.1984

Khedun, C. P., Mishra, A. K., Bolten, J. D., Beaudoing, H. K., Kaiser, R. A., Giardino, J. R., et al. (2012). Understanding changes in water availability in the Rio Grande/Rio Bravo del Norte basin under the influence of large-scale circulation indices using the Noah land surface model. *J. Geophys. Res.* 117, D05104. doi:10.1029/2011JD016590

Kilbourne, K. H., Alexander, M. A., and Nye, J. A. (2014). A low latitude paleoclimate perspective on Atlantic multidecadal variability. *J. Mar. Syst.* 133, 4–13. doi:10.1016/j.jmarsys.2013.09.004

Kilbourne, K. H., Quinn, T. M., Webb, R., Guilderson, T., Nyberg, J., and Winter, A. (2008). Paleoclimate proxy perspective on Caribbean climate since the year 1751: Evidence of cooler temperatures and multidecadal variability. *Paleoceanography* 23 (3), PA3220. doi:10.1029/2008PA001598

Kim, H.- M., Webster, P. J., and Curry, J. A. (2009). Impact of shifting patterns of Pacific Ocean warming on North Atlantic tropical cyclones. *Science* 325 (5936), 77–80. doi:10.1126/science.1174062

Klemm, T., and McPherson, R. A. (2018). Assessing decision timing and seasonal climate forecast needs of winter wheat producers in the South-central United States. *J. Appl. Meteorol. Climatol.* 57 (9), 2129–2140. doi:10.1175/JAMC-D-17-0246.1

Klotzbach, P. J., and Oliver, E. C. (2015). Modulation of Atlantic basin tropical cyclone activity by the Madden-Julian Oscillation (MJO) from 1905 to 2011. *J. Clim.* 28 (1), 204–217. doi:10.1175/JCLI-D-14-00509.1

Klotzbach, P. J. (2014). The Madden-Julian Oscillation's impacts on worldwide tropical cyclone activity. *J. Clim.* 27 (6), 2317–2330. doi:10.1175/JCLI-D-13-00483.1

Knight, J. R., Allan, R. J., Folland, C. K., Vellinga, M., and Mann, M. E. (2005). A signature of persistent natural thermohaline circulation cycles in observed climate. *Geophys. Res. Lett.* 32 (20), L20708. doi:10.1029/2005GL024233

Knight, J. R., Folland, C. K., and Scaife, A. A. (2006). Climate impacts of the atlantic multidecadal oscillation. *Geophys. Res. Lett.* 33, L17706. doi:10.1029/2006GL026242

Konapala, G., Veettil, A. V., and Mishra, A. K. (2018). Teleconnection between low flows and large-scale climate indices in Texas River basins. *Stoch. Environ. Res. Risk Assess.* 32 (8), 2337–2350. doi:10.1007/s00477-017-1460-6

Krishnamurthy, L., Vecchi, G. A., Msadek, R., Wittenberg, A., Delworth, T. L., and Zeng, F. (2015). The seasonality of the Great Plains low-level jet and ENSO relationship. *J. Clim.* 28 (11), 4525–4544. doi:10.1175/JCLI-D-14-00590.1

Kumar, S., Kinter, J., Dirmeyer, P. A., Pan, Z., and Adams, J. (2013). Multidecadal climate variability and the "warming hole" in North America: Results from CMIP5 twentieth- and twenty-first-century climate simulations. *J. Clim.* 26 (11), 3511–3527. doi:10.1175/JCLI-D-12-00535.1

Kurtzman, D., and Scanlon, B. R. (2007). El niño–southern oscillation and pacific decadal oscillation impacts on precipitation in the southern and central United States: Evaluation of spatial distribution and predictions. *Water Resour. Res.* 43 (10), W10427. doi:10.1029/2007WR005863

Kushnir, Y., Seager, R., Ting, M., Naik, N., and Nakamura, J. (2010). Mechanisms of tropical Atlantic SST influence on North American precipitation variability. *J. Clim.* 23 (21), 5610–5628. doi:10.1175/2010JCLI3172.1

Lamb, P. J., and Peppler, R. A. (1987). North Atlantic oscillation: Concept and an application. *B. Am. Meteorol. Soc.* 68 (10), 1218–1225. doi:10.1175/1520-0477(1987)068<1218:NAOCAA>2.0.CO;2

Leathers, D. J., and Palecki, M. A. (1992). The Pacific/North American teleconnection pattern and United States climate. Part II: Temporal characteristics and index specification. *J. Clim.* 5 (7), 707–716. doi:10.1175/1520-0442(1992)005<0707:TPATPA>2.0.CO;2

Leathers, D. J., Yarnal, B., and Palecki, M. A. (1991). The Pacific North-American teleconnection pattern and United-States climate. 1. Regional temperature and precipitation associations. *J. Clim.* 4 (5), 517–528. doi:10.1175/1520-0442(1991)004<0517:TPATPA>2.0.CO;2

Lee, R. W., Woolnough, S. J., Charlton-Perez, A. J., and Vitart, F. (2019). ENSO modulation of MJO teleconnections to the north atlantic and Europe. *Geophys. Res. Lett.* 46 (22), 13535–13545. doi:10.1029/2019GL084683

Lee, S. K., Atlas, R., Enfield, D., Wang, C., and Liu, H. (2013). Is there an optimal ENSO pattern that enhances large-scale atmospheric processes conducive to tornado outbreaks in the United States? *J. Clim.* 26 (5), 1626–1642. doi:10.1175/JCLI-D-12-00128.1

Liang, Y.- C., Lo, M.- H., and Yu, J.- Y. (2014). Asymmetric responses of land hydroclimatology to two types of El Niño in the Mississippi River Basin. *Geophys. Res. Lett.* 41, 582–588. doi:10.1002/2013GL058828

Liang, Y.-C., Yu, J.- Y., Lo, M.- H., and Wang, C. (2015). The changing influence of El Nino on the Great Plains low-level jet. *Atmos. Sci. Lett.* 16, 512–517. doi:10.1002/asl.590

Lim, Y. K., Schubert, S. D., Reale, O., Molod, A. M., Suarez, M. J., and Auer, B. M. (2016). Large-scale controls on Atlantic tropical cyclone activity on seasonal time scales. *J. Clim.* 29 (18), 6727–6749. doi:10.1175/JCLI-D-16-0098.1

Lin, H., Brunet, G., and Derome, J. (2009). An observed connection between the north atlantic oscillation and the madden-julian oscillation. *J. Clim.* 22 (2), 364–380. doi:10.1175/2008JCLI2515.1

Linsley, B. K., Zhang, P. P., Kaplan, A., Howe, S. S., and Wellington, G. M. (2008). Interdecadal-decadal climate variability from multicoral oxygen isotope records in the South Pacific Convergence Zone region since 1650 A.D. *Paleoceanography* 23 (2), PA2219. doi:10.1029/2007PA001539

Liu, Y., Li, Z., Lin, X., Yang, J. C., Zhang, T., Luan, M., et al. (2021). Impacts of COVID-19 on black carbon in two representative regions in China: Insights based on online measurement in beijing and tibet. *Geophys. Res. Lett.* 48 (22), e2021GL092770. doi:10.1029/2021GL092770

Liu, Z., Yoshimura, K., Bowen, G. J., and Welker, J. M. (2014). Pacific-North American teleconnection controls on precipitation isotopes ($\delta^{18}O$) across the contiguous United States and adjacent regions: A GCM-based analysis. *J. Clim.* 27 (3), 1046–1061. doi:10.1175/JCLI-D-13-00334.1

Liu, Z., Yoshimura, K., Buenning, N. H., Jian, Z., and Zhao, L. (2017). The response of winter Pacific North American pattern to strong volcanic eruptions. *Clim. Dyn.* 48 (11), 3599–3614. doi:10.1007/s00382-016-3287-0

Loewe, F. (1966). The temperature see-saw between Western Greenland and Europe. *Weather* 21 (7), 241–246. doi:10.1002/j.1477-8696.1966.tb02865.x

Loikith, P. C., and Broccoli, A. J. (2014). The influence of recurrent modes of climate variability on the occurrence of winter and summer extreme temperatures over North America. *J. Clim.* 27 (4), 1600–1618. doi:10.1175/JCLI-D-13-00068.1

Lorenz, E. N. (1951). Seasonal and irregular variations of the northern hemisphere sea-level pressure profile. *J. Meteor.* 8 (1), 52–59. doi:10.1175/1520-0469(1951)008<0052:SAIVOT>2.0.CO;2

Lukens, K. E., Feldstein, S. B., Yoo, C., and Lee, S. (2017). The dynamics of the extratropical response to Madden–Julian Oscillation convection. *Q. J. R. Meteorol. Soc.* 143 (703), 1095–1106. doi:10.1002/qj.2993

MacDonald, G. M., and Case, R. A. (2005). Variations in the pacific decadal oscillation over the past millennium. *Geophys. Res. Lett.* 32 (8), L08703. doi:10.1029/2005GL022478

Mächel, H., Kapala, A., and Flohn, H. (1998). Behaviour of the centres of action above the Atlantic since 1881. Part I: Characteristics of seasonal and interannual variability. *Int. J. Climatol.* 18 (1), 1–22. doi:10.1002/(SICI)1097-0088(199801)18:1<1::AID-JOC225>3.0.CO;2-A

Madden, R. A., and Julian, P. R. (1971). Detection of a 40-50 day oscillation in the zonal wind in the tropical Pacific. *J. Atmos. Sci.* 28 (5), 702–708. doi:10.1175/1520-0469(1971)028<0702:DOADOI>2.0.CO;2

Madden, R. A., and Julian, P. R. (1994). Observations of the 40-50-Day tropical oscillation – a review. *Mon. Weather Rev.* 122 (5), 814–837. doi:10.1175/1520-0493(1994)122<0814:OOTDTO>2.0.CO;2

Maloney, E. D., and Hartmann, D. L. (2000). Modulation of hurricane activity in the Gulf of Mexico by the madden-julian oscillation. *Science* 287 (5460), 2002–2004. doi:10.1126/science.287.5460.2002

Mann, M. E. (2021). Beyond the hockey stick: Climate lessons from the Common Era. *Proc. Natl. Acad. Sci. U. S. A.* 118 (39), e2112797118. doi:10.1073/pnas.2112797118

Mantua, N. J., and Hare, S. R. (2002). The pacific decadal oscillation. *J. Oceanogr.* 58 (1), 35–44. doi:10.1023/A:1015820616384

Mantua, N. J., Hare, S. R., Zhang, Y., Wallace, J. M., and Francis, R. C. (1997). A pacific interdecadal climate oscillation with impacts on salmon production. *Bull. Am. Meteorol. Soc.* 78 (6), 1069–1079. doi:10.1175/1520-0477(1997)078<1069:APICOW>2.0.CO;2

Marshall, J., Kushnir, Y., Battisti, D., Chang, P., Czaja, A., Dickson, R., et al. (2001). North Atlantic climate variability: Phenomena, impacts and mechanisms. *Int. J. Climatol.* 21 (15), 1863–1898. doi:10.1002/joc.693

Martin, E. R., and Schumacher, C. (2011b). Modulation of caribbean precipitation by the madden-julian oscillation. *J. Clim.* 24 (3), 813–824. doi:10.1175/2010JCLI3773.1

Martin, E. R., and Schumacher, C. (2011a). The Caribbean Low-Level Jet and its relationship with precipitation in IPCC AR4 models. *J. Clim.* 24 (22), 5935–5950. doi:10.1175/JCLI-D-11-00134.1

Martin, E. R., and Schumacher, C. (2012). The relationship between tropical warm pool precipitation, sea surface temperature, and large-scale vertical motion in IPCC AR4 models. *J. Atmos. Sci.* 69 (1), 185–194. doi:10.1175/JAS-D-11-0104.1

McCabe, G. J., and Muller, R. A. (2002). Effects of ENSO on weather-type frequencies and properties at New Orleans, Louisiana, USA. *Clim. Res.* 20 (2), 95–105. doi:10.3354/cr020095

McCabe, G. J., Palecki, M. A., and Betancourt, J. L. (2004). Pacific and Atlantic Ocean influences on multidecadal drought frequency in the United States. *Proc. Natl. Acad. Sci. U. S. A.* 101 (12), 4136–4141. doi:10.1073/pnas.0306738101

McGregor, G. (2017). Hydroclimatology, modes of climatic variability and stream flow, lake and groundwater level variability: A progress report. *Prog. Phys. Geogr. Earth Environ.* 41 (4), 496–512. doi:10.1177/0309133317726537

Meehl, G. A., Hu, A., Arblaster, J. M., Fasullo, J., and Trenberth, K. E. (2013). Externally forced and internally generated decadal climate variability associated with the Interdecadal Pacific Oscillation. *J. Clim.* 26 (18), 7298–7310. doi:10.1175/JCLI-D-12-00548.1

Méndez, M., and Magaña, V. (2010). Regional aspects of prolonged meteorological droughts over Mexico and Central America. *J. Clim.* 23 (5), 1175–1188. doi:10.1175/2009JCLI3080.1

Mihunov, V. V., Lam, N. S. N., Zou, L., Rohli, R. V., Bushra, N., Reams, M. A., et al. (2018). Community resilience to drought hazard in the south-central United States. *Ann. Am. Assoc. Geogr.* 108 (3), 739–755. doi:10.1080/24694452.2017.1372177

Mills, C. M., and Walsh, J. E. (2013). Seasonal variation and spatial patterns of the atmospheric component of the Pacific decadal oscillation. *J. Clim.* 26 (5), 1575–1594. doi:10.1175/JCLI-D-12-00264.1

Mishra, A. K., Singh, V. P., and Ozger, M. (2011). Seasonal streamflow extremes in Texas river basins: Uncertainty, trends, and teleconnections. *J. Geophys. Res.* 116, D08108. doi:10.1029/2010JD014597

Misra, V., Li, H., and Kozar, M. (2014). The precursors in the Intra-Americas Seas to seasonal climate variations over North America. *J. Geophys. Res. Oceans* 119 (5), 2938–2948. doi:10.1002/2014JC009911

Mo, K. C. (2010). Interdecadal modulation of the impact of ENSO on precipitation and temperature over the United States. *J. Clim.* 23 (13), 3639–3656. doi:10.1175/2010JCLI3553.1

Mo, K. C., and Livezey, R. E. (1986). Tropical-extratropical geopotential height teleconnections during the northern hemisphere winter. *Mon. Weather Rev.* 114 (12), 2488–2515. doi:10.1175/1520-0493(1986)114<2488:TEGHTD>2.0.CO;2

Mo, K. C., Schemm, J. K. E., and Yoo, S. H. (2009). Influence of ENSO and the atlantic multidecadal oscillation on drought over the United States. *J. Clim.* 22 (22), 5962–5982. doi:10.1175/2009JCLI2966.1

Mokhov, I. I., and Smirnov, D. A. (2006). El niño–southern oscillation drives North Atlantic oscillation as revealed with nonlinear techniques from climatic indices. *Geophys. Res. Lett.* 33 (3), L03708. doi:10.1029/2005GL024557

Moon, J.- Y., Wang, B., and Ha, K.- J. (2011). ENSO regulation of MJO teleconnection. *Clim. Dyn.* 37 (5–6), 1133–1149. doi:10.1007/s00382-010-0902-3

Moon, J.- Y., Wang, B., and Ha, K.- J. (2012). MJO modulation on 2009/10 winter snowstorms in the United States. *J. Clim.* 25 (3), 978–991. doi:10.1175/jcli-d-11-00033.1

Muñoz, E., and Enfield, D. (2011). The boreal spring variability of the Intra-Americas low-level jet and its relation with precipitation and tornadoes in the eastern United States. *Clim. Dyn.* 36, 247–259. doi:10.1007/s00382-009-0688-3

Munroe, R., Crawford, T., and Curtis, S. (2014). Geospatial analysis of space-time patterning of ENSO forced daily precipitation distributions in the Gulf of Mexico. *Prof. Geogr.* 66 (1), 91–101. doi:10.1080/00330124.2013.765291

National Conference of State Legislatures (2018). Federal and state recognized tribes. Available at: http://www.ncsl.org/research/state-tribal-institute/list-of-federal-and-state-recognized-tribes.aspx (Last accessed: April 20, 2022).

Naumann, G., Alfieri, L., Wyser, K., Mentaschi, L., Betts, R. A., Carrao, H., et al. (2018). Global changes in drought conditions under different levels of warming. *Geophys. Res. Lett.* 45 (7), 3285–3296. doi:10.1002/2017GL076521

Newman, M., Alexander, M. A., Ault, T. R., Cobb, K. M., Deser, C., Di Lorenzo, E., et al. (2016). The pacific decadal oscillation, revisited. *J. Clim.* 29 (12), 4399–4427. doi:10.1175/JCLI-D-15-0508.1

Newman, M., Compo, G. P., and Alexander, M. A. (2003). ENSO-Forced variability of the pacific decadal oscillation. *J. Clim.* 16 (23), 3853–3857. doi:10.1175/1520-0442(2003)016<3853:EVOTPD>2.0.CO;2

Nigam, S., Guan, B., and Ruiz-Barradas, A. (2011). Key role of the atlantic multidecadal oscillation in 20th century drought and wet periods over the Great Plains. *Geophys. Res. Lett.* 38, L16713. doi:10.1029/2011GL048650

Ning, L., and Bradley, R. S. (2016). NAO and PNA influences on winter temperature and precipitation over the eastern United States in CMIP5 GCMs. *Clim. Dyn.* 46 (3–4), 1257–1276. doi:10.1007/s00382-015-2643-9

Oglesby, R. J., and Erickson, D. J. (1989). Soil moisture and the persistence of North American drought. *J. Clim.* 2 (11), 1362–1380. doi:10.1175/1520-0442(1989)002<1362:SMATPO>2.0.CO;2

Ó'hUallacháin, B. (2008). Regional growth transition clubs in the United States. *Pap. Reg. Sci.* 87 (1), 33–53. doi:10.1111/j.1435-5957.2007.00151.x

Pan, Z., Liu, X., Kumar, S., Gao, Z., and Kinter, J. (2013). Intermodel variability and mechanism attribution of central and southeastern US anomalous cooling in the twentieth century as simulated by CMIP5 models. *J. Clim.* 26 (17), 6215–6237. doi:10.1175/JCLI-D-12-00559.1

Pan, Z., Shi, C., Kumar, S., and Gao, Z. (2017). North Pacific SST forcing on the central United States "warming hole" as simulated in CMIP5 coupled historical and uncoupled AMIP experiments. *Atmosphere-Ocean* 55 (1), 57–77. doi:10.1080/07055900.2016.1261690

Pascolini-Campbell, M., Seager, R., Pinson, A., and Cook, B. I. (2017). Covariability of climate and streamflow in the Upper Rio Grande from interannual to interdecadal timescales. *J. Hydrol.- Reg. Stud.* 13 (2017), 58–71. doi:10.1016/j.ejrh.2017.07.007

Patricola, C. M., Saravanan, R., and Chang, P. (2014). The impact of the El niño-southern oscillation and atlantic meridional mode on seasonal atlantic tropical cyclone activity. *J. Clim.* 27 (14), 5311–5328. doi:10.1175/JCLI-D-13-00687.1

Piazza, B. P., LaPeyre, M. K., and Keim, B. D. (2010). Relating large-scale climate variability to local species abundance: ENSO forcing and shrimp in Breton sound, Louisiana, USA. *Clim. Res.* 42 (3), 195–207. doi:10.3354/cr00898

Pielke, R. A., and Landsea, C. N. (1999). La Niña, El Niño, and atlantic hurricane damages in the United States. *B. Am. Meteorol. Soc.* 80 (10), 2027–2034. doi:10.1175/1520-0477(1999)080<2027:LNAENO>2.0.CO;2

Poore, R. Z., DeLong, K. L., Richey, J. N., and Quinn, T. M. (2009). Evidence of multidecadal climate variability and the Atlantic Multidecadal Oscillation from a Gulf of Mexico sea-surface temperature-proxy record. *Geo-Mar. Lett.* 29 (6), 477–484. doi:10.1007/s00367-009-0154-6

Power, S., Lengaigne, M., Capotondi, A., Khodri, M., Vialard, J., Jebri, B., et al. (2021). Decadal climate variability in the tropical Pacific: Characteristics, causes, predictability, and prospects. *Science* 374 (6563), eaay9165. doi:10.1126/science.aay9165

Qin, M., Dai, A., and Hua, W. (2020). Quantifying contributions of internal variability and external forcing to Atlantic multidecadal variability since 1870. *Geophys. Res. Lett.* 47 (22), e2020GL089504. doi:10.1029/2020GL089504

Rajagopalan, B., Cook, E., Lall, U., and Ray, B. K. (2000). Spatiotemporal variability of ENSO and SST teleconnections to summer drought over the United States during the twentieth century. *J. Clim.* 13 (24), 4244–4255. doi:10.1175/1520-0442(2000)013<4244:SVOEAS>2.0.CO;2

Rasmusson, E. M., and Carpenter, T. A. (1982). Variations in tropical sea surface temperature and surface wind fields associated with the Southern Oscillation/El Niño. *Mon. Weather Rev.* 110 (5), 354–384. doi:10.1175/1520-0493(1982)110<0354:VITSST>2.0.CO;2

Renwick, J. A., and Wallace, J. M. (1996). Relationships between north Pacific wintertime blocking, El Niño, and the PNA pattern. *Mon. Weather Rev.* 124 (9), 2071–2076. doi:10.1175/1520-0493(1996)124<2071:RBNPWB>2.0.CO;2

Rodgers, K., Roland, V., Hoos, A., Crowley-Ornelas, E., and Knight, R. (2020). An analysis of streamflow trends in the southern and southeastern US from 1950–2015. *Water* 12 (12), 3345. doi:10.3390/w12123345

Rodionov, S., and Assel, R. A. (2003). Winter severity in the Great Lakes region: A tale of two oscillations. *Clim. Res.* 24 (1), 19–31. doi:10.3354/cr024019

Rodney, M., Lin, H., and Derome, J. (2013). Subseasonal prediction of wintertime North American surface air temperature during strong MJO events. *Mon. Weather Rev.* 141 (8), 2897–2909. doi:10.1175/MWR-D-12-00221.1

Rodwell, M. J., Rowell, D. P., and Folland, C. K. (1999). Oceanic forcing of the wintertime North Atlantic oscillation and European climate. *Nature* 398 (6725), 320–323. doi:10.1038/18648

Rogers, J. C., and Coleman, J. S. M. (2003). Interactions between the atlantic multidecadal oscillation, El Niño/La Niña, and the PNA in winter Mississippi valley stream flow. *Geophys. Res. Lett.* 30 (10), 1518. doi:10.1029/2003GL017216

Rogers, J. C. (1990). Patterns of low-frequency monthly sea level pressure variability (1899–1986) and associated wave cyclone frequencies. *J. Clim.* 3 (12), 1364–1379. doi:10.1175/1520-0442(1990)003<1364:POLFMS>2.0.CO;2

Rogers, J. C., and Rohli, R. V. (1991). Florida citrus freezes and polar anticyclones in the Great-Plains. *J. Clim.* 4 (11), 1103–1113. doi:10.1175/1520-0442(1991)004<1103:FCFAPA>2.0.CO;2

Rogers, J. C. (1984). The association between the north atlantic oscillation and the southern oscillation in the Northern hemisphere. *Mon. Weather Rev.* 112 (10), 1999–2015. doi:10.1175/1520-0493(1984)112<1999:TABTNA>2.0.CO;2

Rogers, J., and McHugh, M. J. (2002). On the separability of the north atlantic oscillation and arctic oscillation. *Clim. Dyn.* 19 (7), 599–608. doi:10.1007/s00382-002-0247-7

Rohli, R. V., and Rogers, J. C. (1993). Atmospheric teleconnections and citrus freezes in the southern United States. *Phys. Geogr.* 14 (1), 1–15. doi:10.1080/02723646.1993.10642464

Ropelewski, C. F., and Halpert, M. S. (1987). Global and regional scale precipitation patterns associated with the El-Niño Southern Oscillation. *Mon. Weather Rev.* 115 (8), 1606–1626. doi:10.1175/1520-0493(1987)115<1606:GARSPP>2.0.CO;2

Ropelewski, C. F., and Halpert, M. S. (1986). North American precipitation and temperature patterns associated with the El Niño southern oscillation (ENSO). *Mon. Weather Rev.* 114 (12), 2352–2362. doi:10.1175/1520-0493(1986)114<2352:NAPATP>2.0.CO;2

Ropelewski, C. F., and Halpert, M. S. (1989). Precipitation patterns associated with the high index phase of the Southern Oscillation. *J. Clim.* 2 (3), 268–284. doi:10.1175/1520-0442(1989)002<0268:PPAWTH>2.0.CO;2

Ropelewski, C. F., and Halpert, M. S. (1996). Quantifying southern oscillation-precipitation relationships. *J. Clim.* 9 (5), 1043–1059. doi:10.1175/1520-0442(1996)009<1043:QSOPR>2.0.CO;2

Ropelewski, C. F., and Jones, P. D. (1987). An extension of the Tahiti–Darwin southern oscillation index. *Mon. Weather Rev.* 115 (9), 2161–2165. doi:10.1175/1520-0493(1987)115<2161:AEOTTS>2.0.CO;2

Ruiz-Barradas, A., and Nigam, S. (2005). Warm season rainfall variability over the U.S. Great Plains in observations, NCEP and ERA-40 reanalyses, and NCAR and NASA atmospheric model simulations. *J. Clim.* 18 (11), 1808–1830. doi:10.1175/JCLI3343.1

Sadeghi, S., Tootle, G., Elliott, E., Lakshmi, V., Therrell, M., Kam, J., et al. (2019). Atlantic Ocean sea surface temperatures and southeast United States streamflow variability: Associations with the recent multi-decadal decline. *J. Hydrol. X.* 576, 422–429. doi:10.1016/j.jhydrol.2019.06.051

Saenger, C., Cohen, A. L., Oppo, D. W., Halley, R. B., and Carilli, J. E. (2009). Surface-temperature trends and variability in the low-latitude North Atlantic since 1552. *Nat. Geosci.* 2 (7), 492–495. doi:10.1038/ngeo552

Sagarika, S., Kalra, A., and Ahmad, S. (2015). Interconnections between oceanic–atmospheric indices and variability in the US streamflow. *J. Hydrol. X.* 525, 724–736. doi:10.1016/j.jhydrol.2015.04.020

Salinger, M. J., Renwick, J. A., and Mullan, A. B. (2001). Interdecadal Pacific oscillation and south Pacific climate. *Int. J. Climatol.* 21 (14), 1705–1721. doi:10.1002/joc.691

Sanchez-Rubio, G., Perry, H. M., Biesiot, P. M., Johnson, D. R., and Lipcius, R. N. (2011). Oceanic-atmospheric modes of variability and their influence on riverine input to coastal Louisiana and Mississippi. *J. Hydrol. X.* 396 (1–2), 72–81. doi:10.1016/j.jhydrol.2010.10.034

Schlesinger, M. E., and Ramankutty, N. (1994). An oscillation in the global climate system of period 65–70 years. *Nature* 367 (6465), 723–726. doi:10.1038/367723a0

Schmidt, N., Lipp, E. K., Rose, J. B., and Luther, M. E. (2001). ENSO influences on seasonal rainfall and river discharge in Florida. *J. Clim.* 14 (4), 615–628. doi:10.1175/1520-0442(2001)014<0615:EIOSRA>2.0.CO;2

Schmidt, N., and Luther, M. E. (2002). ENSO impacts on salinity in Tampa Bay, Florida. *Estuaries* 25 (2002), 976–984. doi:10.1007/BF02691345

Schneider, N., and Cornuelle, B. D. (2005). The forcing of the Pacific decadal oscillation. *J. Clim.* 18 (21), 4355–4373. doi:10.1175/JCLI3527.1

Schreck, C. J., III, Cordeira, J. M., and Margolin, D. (2013). Which MJO events affect North American temperatures? *Mon. Weather Rev.* 141 (11), 3840–3850. doi:10.1175/MWR-D-13-00118.1

Schubert, S. M., Suarez, J., Pegion, P. J., Koster, R. D., and Bacmeister, J. T. (2004). Causes of long-term drought in the U.S. Great Plains. *J. Clim.* 17 (3), 485–503. doi:10.1175/1520-0442(2004)017<0485:COLDIT>2.0.CO;2

Shakun, J. D., and Shaman, J. (2009). Tropical origins of North and south pacific decadal variability. *Geophys. Res. Lett.* 36 (19), L19711. doi:10.1029/2009GL040313

Shapiro, L. J. (1987). Month-to-month variability of the Atlantic tropical circulation and its relationship to tropical storm formation. *Mon. Weather Rev.* 115 (11), 1598–1614. doi:10.1175/1520-0493(1987)115<2598:MTMVOT>2.0.CO;2

Sheridan, S., and Lee, C. C. (2012). Synoptic climatology and the analysis of atmospheric teleconnections. *Prog. Phys. Geogr. Earth Environ.* 36 (4), 548–557. doi:10.1177/0309133312447935

Simmons, A. J., Wallace, J. M., and Branstator, G. W. (1983). Barotropic wave propagation and instability, and atmospheric teleconnection patterns. *J. Atmos. Sci.* 40 (6), 1363–1392. doi:10.1175/1520-0469(1983)040<1363:BWPAIA>2.0.CO;2

Smith, S. R., Brolley, J., O'Brien, J. J., and Tartaglione, C. A. (2007). ENSO's impact on regional U.S. hurricane activity. *J. Clim.* 20 (7), 1404–1414. doi:10.1175/JCLI4063.1

Sohngen, B., and Brown, S. (2006). The influence of conversion of forest types on carbon sequestration and other ecosystem services in the South Central United States. *Ecol. Econ.* 57 (4), 698–708. doi:10.1016/j.ecolecon.2005.06.001

Soulard, N., Lin, H., and Yu, B. (2019). The changing relationship between ENSO and its extratropical response patterns. *Sci. Rep.* 9, 6507. doi:10.1038/s41598-019-42922-3

Stahle, D. W., and Cleaveland, M. K. (1988). Texas drought history reconstructed and analyzed from 1698 and 1980. *J. Clim.* 1 (1), 59–74. doi:10.1175/1520-0442(1988)001<0059:TDHRAA>2.0.CO;2

Stan, C., Straus, D. M., Frederiksen, J. S., Lin, H., Maloney, E. D., and Schumacher, C. (2017). Review of tropical-extratropical teleconnections on intraseasonal time scales. *Rev. Geophys.* 55 (4), 902–937. doi:10.1002/2016RG000538

Stenseth, N. C., Ottersen, G., Hurrell, J. W., Mysterud, A., Lima, M., Chan, K. S., et al. (2003). Review article. Studying climate effects on ecology through the use of climate indices: the north atlantic oscillation, El Niño southern oscillation and beyond. *Proc. R. Soc. Lond. B* 270 (1529), 2087–2096. doi:10.1098/rspb.2003.2415

Steptoe, H., Jones, S. E. O., and Fox, H. (2018). Correlations between extreme atmospheric hazards and global teleconnections: Implications for multihazard resilience. *Rev. Geophys.* 56 (1), 50–78. doi:10.1002/2017RG000567

Straus, D. M., and Shukla, J. (2002). Does ENSO force the PNA? *J. Clim.* 15 (17), 2340–2358. doi:10.1175/1520-0442(2002)015<2340:DEFTP>2.0.CO;2

Sun, C. J., Shanahan, T. M., and Partin, J. (2019). Controls on the isotopic composition of precipitation in the south-central United States. *J. Geophys. Res. Atmos.* 124 (14), 8320–8335. doi:10.1029/2018JD029306

Sun, J., and Wang, H. (2012). Changes of the connection between the summer North Atlantic oscillation and the east asian summer rainfall. *J. Geophys. Res.* 117, D08110. doi:10.1029/2012JD017482

Swain, S., Abeysundara, S., Hayhoe, K., and Stoner, A. M. K. (2017). Future changes in summer MODIS-based enhanced vegetation index for the South-Central United States. *Ecol. Inf.* 41 (2017), 64–73. doi:10.1016/j.ecoinf.2017.07.007

Sweet, W. V., and Zervas, C. (2011). Cool-season sea level anomalies and storm surges along the U.S. East Coast: Climatology and comparison with the 2009/10 El Niño. *Mon. Weather Rev.* 139 (7), 2290–2299. doi:10.1175/MWR-D-10-05043.1

Tanimoto, Y., Iwasaka, N., Hanawa, K., and Toba, Y. (1993). Characteristic variations of sea surface temperature with multiple time scales in the North Pacific. *J. Clim.* 6 (6), 1153–1160. doi:10.1175/1520-0442(1993)006<1153:CVOSST>2.0.CO;2

Taschetto, A. S., Rodrigues, R. R., Meehl, G. A., McGregor, S., and England, M. H. (2016). How sensitive are the Pacific–tropical North Atlantic teleconnections to the position and intensity of El Niño-related warming? *Clim. Dyn.* 46 (5), 1841–1860. doi:10.1007/s00382-015-2679-x

Terjung, W. (1976). Climatology for geographers. *Ann. Assoc. Am. Geogr.* 66 (2), 199–220. doi:10.1111/j.1467-8306.1976.tb01086.x

Thompson, D. B., and Roundy, P. E. (2013). The relationship between the Madden-Julian Oscillation and US violent tornado outbreaks in the spring. *Mon. Weather Rev.* 141 (6), 2087–2095. doi:10.1175/MWR-D-12-00173.1

Thompson, D. W. J., and Wallace, J. M. (1998). The Arctic Oscillation signature in the wintertime geopotential height and temperature fields. *Geophys. Res. Lett.* 25 (9), 1297–1300. doi:10.1029/98GL00950

Thompson, D. W., and Wallace, J. M. (2000). Annular modes in the extratropical circulation. Part I: Month-to-month variability. *J. Clim.* 13 (5), 1000–1016. doi:10.1175/1520-0442(2000)013<1000:AMITEC>2.0.CO;2

Thompson, D. W., Wallace, J. M., and Hegerl, G. C. (2000). Annular modes in the extratropical circulation. Part II: Trends. *J. Clim.* 13 (5), 1018–1036. doi:10.1175/1520-0442(2000)013<1018:AMITEC>2.0.CO;2

Ting, M., Kushnir, Y., and Li, C. (2014). North Atlantic multidecadal SST oscillation: External forcing versus internal variability. *J. Mar. Syst.* 133, 27–38. doi:10.1016/j.jmarsys.2013.07.006

Ting, M., Kushnir, Y., Seager, R., and Li, C. (2009). Forced and internal twentieth-century SST trends in the North Atlantic. *J. Clim.* 22 (6), 1469–1481. doi:10.1175/2008JCLI2561.1

Tokioka, T., Yamazaki, K., Kitoh, A., and Ose, T. (1988). The equatorial 30–60 day oscillation and the Arakawa-Schubert penetrative cumulus parameterization. *J. Meteorological Soc. Jpn.* 66 (6), 883–901. doi:10.2151/jmsj1965.66.6_883

Tolan, J. M. (2007). El niño-southern oscillation impacts translated to the watershed scale: Estuarine salinity patterns along the Texas Gulf coast, 1982 to 2004. *Estuar. Coast. Shelf Sci.* 72 (1–2), 247–260. doi:10.1016/j.ecss.2006.10.018

Tootle, G. A., Piechota, T. C., and Singh, A. (2005). Coupled oceanic-atmospheric variability and U.S. streamflow. *Water Resour. Res.* 41 (12), W12408. doi:10.1029/2005WR004381

Torbenson, M. C. A., Stahle, D. W., Howard, I. M., Burnette, D. J., Villanueva-Diaz, J., Cook, E. R., et al. (2019). Multidecadal modulation of the ENSO teleconnection to precipitation and tree growth over subtropical North America. *Paleoceanogr. Paleoclimatology* 34 (5), 886–900. doi:10.1029/2018PA003510

Torbenson, M. C. A., and Stahle, D. W. (2018). The relationship between cool and warm season moisture over the central United States, 1685–2015. *J. Clim.* 31 (19), 7909–7924. doi:10.1175/JCLI-D-17-0593.1

Toride, K., and Hakim, G. J. (2021). Influence of low-frequency PNA variability on MJO teleconnections to North American atmospheric river activity. *Geophys. Res. Lett.* 48, e2021GL094078. doi:10.1029/2021GL094078

Tranchant, B., Pujol, I., Di Lorenzo, E., and Legeais, J.- F. (2019). the North pacific gyre oscillation. *J. Oper. Oceanogr.* 12 (S1), s29–s31.

Trenberth, K. E. (1984). Signal versus noise in the southern oscillation. *Mon. Weather Rev.* 112 (2), 326–332. doi:10.1175/1520-0493(1984)112<0326:SVNITS>2.0.CO;2

Trenberth, K. E. (1976). Spatial and temporal variations of the southern oscillation. *Q. J. R. Meteorol. Soc.* 102 (433), 639–653. doi:10.1002/qj.49710243310

Trenberth, K. E., and Stepaniak, D. P. (2001). Indices of El Niño evolution. *J. Clim.* 14 (8), 1697–1701. doi:10.1175/1520-0442(2001)014<1697:LIOENO>2.0.CO;2

Trenberth, K. E. (1997). The definition of El Niño. *B. Am. Meteorol. Soc.* 78 (12), 2771–2777. doi:10.1175/1520-0477(1997)078<2771:TDOENO>2.0.CO;2

Trigo, R. M., Osborn, T. J., and Corte-Real, J. M. (2002). The North Atlantic Oscillation influence on Europe: Climate impacts and associated physical mechanisms. *Clim. Res.* 20 (1), 9–17. doi:10.3354/cr020009

Trouet, V., Harley, G. L., and Domínguez-Delmás, M. (2016). Shipwreck rates reveal Caribbean tropical cyclone response to past radiative forcing. *Proc. Natl. Acad. Sci. U. S. A.* 113 (12), 3169–3174. doi:10.1073/pnas.1519566113

Vaideanu, P., Dima, M., and Voiculescu, M. (2018). Atlantic Multidecadal Oscillation footprint on global high cloud cover. *Theor. Appl. Climatol.* 134 (3–4), 1245–1256. doi:10.1007/s00704-017-2330-3

van Loon, H., and Rogers, J. C. (1978). Seesaw in winter temperatures between Greenland and northern Europe. Part I: General description. *Mon. Weather Rev.* 106 (3), 296–310. doi:10.1175/1520-0493(1978)106<0296:TSIWTB>2.0.CO;2

van Loon, H., and Rogers, J. C. (1981). The Southern Oscillation. Part II: Associations with changes in the middle troposphere in the northern winter. *Mon. Weather Rev.* 109 (6), 1163–1168. doi:10.1175/1520-0493(1981)109<1163:TSOPIA>2.0.CO;2

Vega, A. J., Rohli, R. V., and Henderson, K. G. (1998). The Gulf of Mexico mid-tropospheric response to El Niño and La Niña forcing. *Clim. Res.* 10 (2), 115–125. doi:10.3354/cr010115

Villarini, G., Smith, J. A., Vitolo, R., and Stephenson, D. B. (2013). On the temporal clustering of US floods and its relationship to climate teleconnection patterns. *Int. J. Climatol.* 33 (3), 629–640. doi:10.1002/joc.3458

Vimont, D. J., and Kossin, J. P. (2007). The Atlantic meridional mode and hurricane activity. *Geophys. Res. Lett.* 34 (7), L07709. doi:10.1029/2007GL029683

Visbeck, M. H., Hurrell, J. W., Polvani, L., and Cullen, H. M. (2001). the North atlantic oscillation: Past, present, and future. *Proc. Natl. Acad. Sci. U. S. A.* 98 (23), 12876–12877. doi:10.1073/pnas.231391598

Vitart, F. (2009). Impact of the Madden Julian Oscillation on tropical storms and risk of landfall in the ECMWF forecast system. *Geophys. Res. Lett.* 36, L15802. doi:10.1029/2009GL039089

von Reumont, J., Hetzinger, S., Garbe-Schönberg, D., Manfrino, C., and Dullo, C. (2018). Tracking interannual-to multidecadal-scale climate variability in the Atlantic Warm Pool using central Caribbean coral data. *Paleoceanogr. Paleoclimatology* 33 (4), 395–411. doi:10.1002/2018PA003321

Walker, G. T., and Bliss, E. W. (1932). "World weather V," in *Memoirs of the Royal Meteorological Society*. Berks, England: Royal Meteorological Soc, 44, 53–84.

Wallace, J. M., and Gutzler, D. S. (1981). Teleconnections in the geopotential height field during the Northern Hemisphere winter. *Mon. Weather Rev.* 109 (4), 784–812. doi:10.1175/1520-0493(1981)109<0784:TITGHF>2.0.CO;2

Wallace, J. M. (2000). North Atlantic Oscillation/annular mode: Two paradigms – one phenomenon. *Q. J. R. Meteorol. Soc.* 126 (564), 791–805. doi:10.1256/smsqj.56401

Walsh, J. E., Phillips, A. S., Portis, D. H., and Chapman, W. L. (2001). Extreme cold outbreaks in the United States and Europe, 1948–99. *J. Clim.* 14 (12), 2642–2658. doi:10.1175/1520-0442(2001)014<2642:ECOITU>2.0.CO;2

Wang, C., Enfield, D. B., Sang-ki, L., and Landsea, C. W. (2006). Influences of the atlantic warm pool on western hemisphere summer rainfall and atlantic hurricanes. *J. Clim.* 19 (12), 3011–3028. doi:10.1175/JCLI3770.1

Wang, C., Lee, S.- K., and Enfield, D. B. (2008a). Atlantic warm pool acting as a link between atlantic multidecadal oscillation and atlantic tropical cyclone activity. *Geochem. Geophys. Geosyst.* 9 (5), Q05V03. doi:10.1029/2007GC001809

Wang, C., Lee, S.- K., and Enfield, D. B. (2008b). Climate response to anomalously large and small Atlantic warm pools during the summer. *J. Clim.* 21 (11), 2437–2450. doi:10.1175/2007JCLI2029.1

Wang, J., Yang, B., Ljungqvist, F. C., Luterbacher, J., Osborn, T. J., Briffa, K. R., et al. (2017). Internal and external forcing of multidecadal Atlantic climate variability over the past 1, 200 years. *Nat. Geosci.* 10 (7), 512–517. doi:10.1038/NGEO2962

Wang, L., and Robertson, A. W. (2019). Week 3–4 predictability over the United States assessed from two operational ensemble prediction systems. *Clim. Dyn.* 52 (9–10), 5861–5875. doi:10.1007/s00382-018-4484-9

Wang, S.- Y. S., Huang, W.- R., Hsu, H.- H., and Gillies, R. R. (2015). Role of the strengthened El Niño teleconnection in the may 2015 floods over the southern Great Plains. *Geophys. Res. Lett.* 42 (19), 8140–8146. doi:10.1002/2015GL065211

Wang, X., Brown, P. M., Zhang, Y., and Song, L. (2011). Imprint of the atlantic multidecadal oscillation on tree-ring widths in northeastern Asia since 1568. *PloS One* 6 (7), e22740. doi:10.1371/journal.pone.0022740

Wang, Y., Hu, K., Huang, G., and Tao, W. (2021). Asymmetric impacts of El Niño and La Niña on the Pacific–North American teleconnection pattern: The role of subtropical jet stream. *Environ. Res. Lett.* 16 (11), 114040. doi:10.1088/1748-9326/ac31ed

Watanabe, M., and Tatebe, H. (2019). Reconciling roles of sulphate aerosol forcing and internal variability in Atlantic multidecadal climate changes. *Clim. Dyn.* 53 (7), 4651–4665. doi:10.1007/s00382-019-04811-3

Weaver, S. J., and Nigam, S. (2008). Variability of the Great Plains low-level jet: Large-scale circulation context and hydroclimate impacts. *J. Clim.* 21 (7), 1532–1551. doi:10.1175/2007JCLI1586.1

Weaver, S. J., Schubert, S., and Wang, H. (2009). Warm season variations in the low-level circulation and precipitation over the central United States in observations, AMIP simulations, and idealized SST experiments. *J. Clim.* 22 (20), 5401–5420. doi:10.1175/2009JCLI2984.1

Wheeler, M. C., and Hendon, H. H. (2004). An all-season real-time multivariate MJO index: Development of an index for monitoring and prediction. *Mon. Weather Rev.* 132 (8), 1917–1932. doi:10.1175/1520-0493(2004)132<1917:AARMMI>2.0.CO;2

Wise, E. K., Wrzesien, M. L., Dannenberg, M. P., and McGinnis, D. L. (2015). Cool-season precipitation patterns associated with teleconnection interactions in the United States. *J. Appl. Meteorol. Climatol.* 54 (2), 494–505. doi:10.1175/JAMC-D-14-0040.1

Wolter, K., and Timlin, M. S. (2011). El Niño/Southern Oscillation behaviour since 1871 as diagnosed in an extended multivariate ENSO index (MEI.ext). *Int. J. Climatol.* 31 (7), 1074–1087. doi:10.1002/joc.2336

Wu, S., Liu, Z., Zhang, R., and Delworth, T. L. (2011). On the observed relationship between the pacific decadal oscillation and the atlantic multi-decadal oscillation. *J. Oceanogr.* 67 (1), 27–35. doi:10.1007/s10872-011-0003-x

Yang, Q., Ma, Z., Wu, P., Klingaman, N. P., and Zhang, L. (2019). Interdecadal seesaw of precipitation variability between North China and the southwest United States. *J. Clim.* 32 (10), 2951–2968. doi:10.1175/JCLI-D-18-0082.1

Yeh, S.- W., Kug, J.- S., Dewitte, B., Kwon, M.- H., Kirtman, B. P., and Jin, F.- F. (2009). El Niño in a changing climate. *Nature* 461 (7263), 511–514. doi:10.1038/nature08316

Yu, B., Lin, H., and Soulard, N. (2019). A comparison of North American surface temperature and temperature extreme anomalies in association with various atmospheric teleconnection patterns. *Atmos. (Basel).* 10 (4), 172. doi:10.3390/atmos10040172

Yu, B., Lin, H., Wu, Z. W., and Merryfield, W. J. (2018). The Asian-Bering-North American teleconnection: Seasonality, maintenance, and climate impact on North America. *Clim. Dyn.* 50 (5–6), 2023–2038. doi:10.1007/s00382-017-3734-6

Yu, J.-Y., Lu, M.- M., and Kim, S. T. (2012a). A change in the relationship between tropical central Pacific SST variability and the extratropical atmosphere around 1990. *Environ. Res. Lett.* 7, 034025. doi:10.1088/1748-9326/7/3/034025

Yu, J. -Y., Zou, Y. H., Kim, S. T., and Lee, T. (2012b). The changing impact of El Niño on US winter temperatures. *Geophys. Res. Lett.* 39, L15702. doi:10.1029/2012GL052483

Yu, L. J., Zhong, S. Y., Heilman, W. E., and Bian, X. D. (2017). A comparison of the effects of El Niño and El Niño Modoki on subdaily extreme precipitation occurrences across the contiguous United States. *J. Geophys. Res.–Atmos.* 122 (14), 7401–7415. doi:10.1002/2017JD026683

Yu, L., Zhong, S., Bian, X., Heilman, W. E., and Andresen, J. A. (2014). Temporal and spatial variability of frost-free seasons in the Great Lakes region of the United States. *Int. J. Climatol.* 34 (13), 3499–3514. doi:10.1002/joc.3923

Zhang, C. D. (2005). Madden-julian oscillation. *Rev. Geophys.* 43 (2), RG2003. doi:10.1029/2004RG000158

Zhang, J., Liu, Y. S., Sun, C., Li, J. P., Ding, R. Q., Xie, F., et al. (2021). On the connection between AMOC and observed land precipitation in northern hemisphere: A comparison of the AMOC indicators. *Clim. Dyn.* 56 (1–2), 651–664. doi:10.1007/s00382-020-05496-9

Zhang, R., and Delworth, T. L. (2007). Impact of the atlantic multidecadal oscillation on North pacific climate variability. *Geophys. Res. Lett.* 34 (23), L23708. doi:10.1029/2007GL031601

Zhang, R., Sutton, R., Danabasoglu, G., Kwon, Y. O., Marsh, R., Yeager, S. G., et al. (2019). A review of the role of the Atlantic meridional overturning circulation in Atlantic multidecadal variability and associated climate impacts. *Rev. Geophys.* 57 (2), 316–375. doi:10.1029/2019RG000644

Zhang, W. J., Jin, F. F., Ren, H. L., Li, J. P., and Zhao, J. X. (2012). Differences in teleconnection over the North Pacific and rainfall shift over the USA associated with two types of El Niño during boreal autumn. *J. Meteorological Soc. Jpn.* 90 (4), 535–552. doi:10.2151/jmsj.2012-407

Zhang, X., Wang, J., Zwiers, F. W., and Groisman, P. Y. (2010). The influence of large-scale climate variability on winter maximum daily precipitation over North America. *J. Clim.* 23 (11), 2902–2915. doi:10.1175/2010JCLI3249.1

Zhang, Y. C., and Liang, X. S. (2021). The causal role of South China Sea on the Pacific-North American teleconnection pattern. *Clim. Dyn.* doi:10.1007/s00382-021-06070-7

Zheng, C., Chang, E. K.- M., Kim, H.- M., Zhang, M., and Wang, W. (2018). Impacts of the Madden–Julian oscillation on storm-track activity, surface air temperature, and precipitation over North America. *J. Clim.* 31 (15), 6113–6134. doi:10.1175/JCLI-D-17-0534.1

Zhou, S. T., L'Heureux, M., Weaver, S., and Kumar, A. (2012). A composite study of the MJO influence on the surface air temperature and precipitation over the continental United States. *Clim. Dyn.* 38 (7–8), 1459–1471. doi:10.1007/s00382-011-1001-9

Zhou, W., Yang, D., Xie, S.- P., and Ma, J. (2020). Amplified Madden–Julian oscillation impacts in the Pacific–North America region. *Nat. Clim. Chang.* 10 (7), 654–660. doi:10.1038/s41558-020-0814-0

Zhou, Y., Wu, D., Lau, W. K.- M., and Tao, W.- K. (2016). Scale dependence of land-atmosphere interactions in wet and dry regions as simulated with NU-WRF over the southwestern and south-central United States. *J. Hydrometeorol.* 17 (8), 2121–2136. doi:10.1175/JHM-D-16-0024.1

frontiers | Frontiers in Earth Science

TYPE Original Research
PUBLISHED 07 September 2022
DOI 10.3389/feart.2022.997586

OPEN ACCESS

EDITED BY
Meng Gao,
Hong Kong Baptist University, Hong Kong, SAR, China

REVIEWED BY
Jinhui Gao,
Chengdu University of Information Technology, China
Jiawei Li,
Institute of Atmospheric Physics (CAS), China

*CORRESPONDENCE
Tianliang Zhao,
tlzhao@nuist.edu.cn

SPECIALTY SECTION
This article was submitted to Atmospheric Science, a section of the journal Frontiers in Earth Science

RECEIVED 19 July 2022
ACCEPTED 09 August 2022
PUBLISHED 07 September 2022

CITATION
Zhang L, Guo X, Zhao T, Xu X, Zheng X, Li Y, Luo L, Gui K, Zheng Y and Shu Z (2022), Effect of large topography on atmospheric environment in Sichuan Basin: A climate analysis based on changes in atmospheric visibility.
Front. Earth Sci. 10:997586.
doi: 10.3389/feart.2022.997586

Effect of large topography on atmospheric environment in Sichuan Basin: A climate analysis based on changes in atmospheric visibility

Lei Zhang[1], Xiaomei Guo[2,3], Tianliang Zhao[4]*, Xiangde Xu[1], Xiaobo Zheng[5], Yueqing Li[2], Lei Luo[2], Ke Gui[1], Yu Zheng[1] and Zhuozhi Shu[4]

[1]State Key Laboratory of Severe Weather & Key Laboratory of Atmospheric Chemistry of CMA, Chinese Academy of Meteorological Sciences, Beijing, China, [2]Heavy Rain and Drought—Flood Disasters in Plateau and Basin Key Laboratory of Sichuan Province, Chengdu, China, [3]Weather Modification Office of Sichuan Province, Chengdu, China, [4]CMA-Key Lab for Aerosol-Cloud-Precipitation, Nanjing University of Information Science & Technology, Nanjing, China, [5]Guizhou Institute of Mountainous Climate and Environment, Guizhou Key Laboratory of Mountainous Climate and Resource, Guiyang, China

Using 51 years (1960–2010) of observations from meteorological stations in the Sichuan-Chongqing region, including atmospheric visibility as a proxy for aerosol concentration, relative humidity, air temperature, wind speed and FNL reanalysis data (1°×1°) of air temperature, pressure and wind, and the altitude of each station, a linear trend and multivariate fitting approach was used to explore the effects of the large topography on the atmospheric environment in the Sichuan-Chongqing region. The region mainly consists of two areas: Sichuan Basin (SCB) and Western Sichuan Plateau (WSP; eastern part of the Tibetan Plateau). Visibility was relatively low in the SCB and high in the WSP, indicating the high and low levels of aerosols respectively in the SCB and the WSP. Additionally, visibility and wind speed were positively correlated within the basin (altitude below 750 m), while negatively correlated at stations above 1,500 m, such as on the WSP, indicating that the topography had an influence on the atmospheric environment of the basin. On the one hand, the vertical structures of the wind fields and the vertical profiles of latitudinal deviations in wind speed and air temperature in the basin show that the unique large topography causes a “harbour” effect on the leeward-slope of the WSP, with the SCB being a weak wind region, while the descending air currents in the upper westerlies of the basin form a huge “vault” of air. On the other hand, topographic effects can make the basin more susceptible to the formation of inversion structures near the surface and at high altitudes, thus stabilising the atmosphere. The topographic effects, which is not conducive to horizontal diffusion and convective transport of pollutants, were the most significant in winter, followed by autumn and spring.

KEYWORDS

Sichuan Basin, atmospheric environment, visibility, climate, topographic effects

1 Introduction

The industrialization and urbanization of China over the past few decades have caused serious air pollution problems (Sun et al., 2016; Gui et al., 2020; Zheng et al., 2021), characterized of high loading of fine particulate matter $PM_{2.5}$ (particulate matter with an aerodynamic diameter equal to or less than 2.5 μm) in ambient air and low horizontal visibility (Che et al., 2007; Deng et al., 2008; Sun et al., 2016), with likely consequences on the human health (Kampa and Castanas, 2008; Shang et al., 2013; Feng et al., 2016; Xing et al., 2016; Liu et al., 2017), ecosystems (Carslaw et al., 2010; Allen et al., 2019), and climate (Carslaw et al., 2013; Kelly and Zhu, 2016). In addition to factors such as high emissions, the role of meteorological conditions associated with large topography is also considered to be a crucial factor (Wang et al., 2013; Wang X. et al., 2018; Liao et al., 2018; Ning et al., 2019; Zhang et al., 2019; Shu et al., 2022b; Hu et al., 2022). It is generally accepted that topography has an important influence on synoptic circulation, atmospheric boundary layer, and local meteorology (Poulos and Pielke, 1994; Hu et al., 2014; Wang X. et al., 2018; Liu et al., 2018; Zhu et al., 2018; Zhang et al., 2019), and therefore alter chemical and physical processes of pollutants.

Topography can alter the thermodynamic and dynamic structure of the atmosphere, resulting in flows representing a systematic characteristic of large topography weather and climate (Zardi and Whiteman, 2013; Wagner et al., 2015; Giovannini et al., 2017), and thus affects the exchange of energy and mass in the atmosphere (Wang H. et al., 2018; Wang et al., 2019; Shu et al., 2022b). One of the main effects is the thermodynamic forcing caused by inhomogeneous surface properties, disturbing horizontal wind flows and altering vertical momentum mixing (Schmidli and Rotunno, 2010). In addition, topographic effects can cause strong temperature inversions (Whiteman et al., 1999), low-level jets (Ting and Wang, 2006; Tuononen et al., 2015), lee-side vortices (Gao and Ping, 2005), and gusts (Letson et al., 2019). These phenomena are of worldwide significance, as nearly a quarter of the Earth's land mass can be classified as mountainous (Blyth, 2002), such as the European Alps, the Tibetan Plateau (TP) and the Qinling and Taihang Mountains in China, and the Rocky Mountains in North America. Especially, eastern China has been identified as more climatically stable than Europe and the United States in terms of air conditions, partly due to the country's larger size and more complex terrain (Wang X. et al., 2018).

Among the mountainous areas, atmospheric environment in the Sichuan Basin (SCB) is of particular interest in recent years (Yin et al., 2020; Chang et al., 2021; Kong et al., 2021; Wu et al., 2022), due to both its unique bowl-shaped topography and its high levels of air pollution. The SCB is flanked by mountains-that is, bordered to the west by the TP, to the north by the Daba Mountains, to the east by the Wu mountains, and to the south by the Yunnan-Guizhou Plateau, which together serve to shield the basin from external winds and trap air penetrating the basin via large-scale weather disturbances (Zhang et al., 2019; Guo et al., 2022). The basin is one of the regions with the highest values of atmospheric aerosols and clouds in China (Li et al., 2015; Qiao et al., 2015), with an annual average AOD (550 nm) value of 0.848 from 2000 to 2010, which is very significantly different from that in the TP (about 0.1) (Luo et al., 2014), which is immediately to the west of the basin. Previous studies showed that the average visibility in the SCB from 1973 to 2010 was basically no higher than 20 km, and below 10 km for most of the time in the central and southern regions, while the visibility on the western Sichuan Plateau (WSP) in the immediate west of the region remained above 25 km all year round (Chen and Xie, 2012). The principal causes of the visibility impairment in SCB were identified to be high levels of aerosol concentrations, as well as low wind speed and high relatively humidity conditions due to terrain effects (Wang et al., 2017). Previous studies have examined the influence of terrain effects on haze pollution in the SCB using individual cases of $PM_{2.5}$ pollution and seasonal $PM_{2.5}$ pollution aspects (Ning et al., 2018; Ning et al., 2019; Zhang et al., 2019; Shu et al., 2022b). Using sensitivity simulations of topography, Zhang et al. (Zhang et al., 2019) found that the topography could increase near-surface $PM_{2.5}$ concentrations in the SCB by close to 50 μg/m^3 during a severe haze episode in winter 2014, corresponding to an increase of roughly 45%. Shu et al. (Shu et al., 2022b) then went on to investigate the three-dimensional distribution of terrain-induced $PM_{2.5}$ concentrations over the SCB in different seasons, and they found that the increases in $PM_{2.5}$ concentrations can increase from 30 μg/m^3 in summer to 90 μg/m^3 in winter at surface layer and increase from summertime 10 μg/m^3 to wintertime 30 μg/m^3 in the lower free troposphere.

Although previous studies have manifested the terrain effects of the SCB on regional atmospheric environments, the current understanding is still inadequate, especially from a long-term climate perspective. In the context of the westerly wind belt, the dynamic and thermal effects of the TP significantly influence the regional weather and climate characteristics of China, particularly the SCB region. Therefore, there is a great need for an in-depth analysis of the large topographic dynamics and thermal effects on the long-term spatial and temporal distribution changes of aerosols in the SCB. Due to the lack of long-term aerosol concentration observations, this study uses visibility as a proxy for analysis, and a description of data and method used are presented in Section 2. Section 3 describes the spatial and temporal variability of visibility in relation to topography and analyses the mechanisms by which topography affects it using reanalysis data. Finally, the major conclusions are summarized in Section 4.

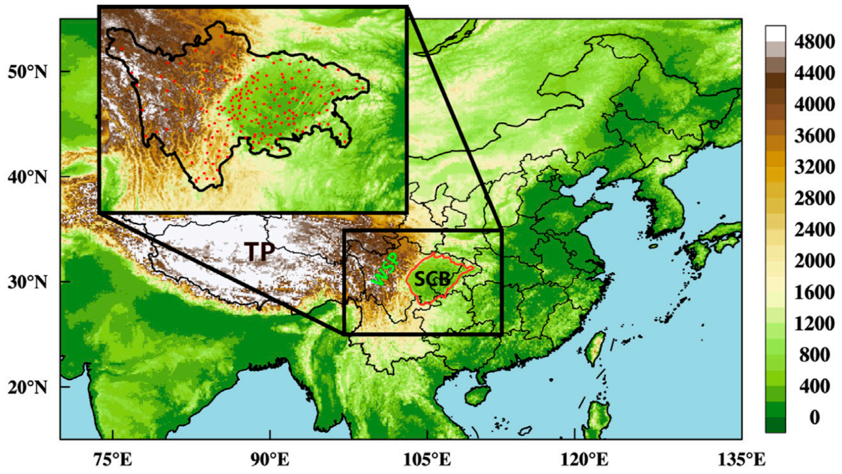

FIGURE 1
Topography map (shading, unit: m) with the locations of TP, WSP, and SCB. The solid red line marks the basin boundary with a topographic elevation of 750 m. The 191 meteorological stations used to collect visibility and wind speed are marked with red dots.

2 Materials and methods

This paper uses observations from meteorological stations in the SCB and its surrounding areas (191 stations in total as shown in Figure 1) for a period of 51 years (1960-2010). The meteorological selected for analysis includes atmospheric visibility as a proxy for aerosol concentration, relative humidity, air temperature, and wind speed, as well as the air temperature, pressure, and wind in the FNL reanalysis data from 1999 to 2010. The AOD from MODIS remote sensing data were used. Data from 2010 onwards is avoided because of the substantial impact on air pollution due to the large number of emission reduction measures undertaken in SCB (Liu et al., 2021; Shu et al., 2022a). Visibility observations in China were classified according to 10 classes before 1980, after which they were expressed in kilometers. In order to make the visibility data comparable before and after 1980, we adopt the method of Qin (Qin et al., 2010) to homogenize the data. With the method, the day-by-day visibility data of all stations from 1980 to 2005 are accurately converted into visibility classes, and the visibility distances are averaged under the limits of each visibility class to obtain a more suitable proxy for the visibility distances corresponding to the 10 visibility classes (Table 1).

The Chinese meteorological stations conduct at least three regular visibility observations per day, i.e., 08:00, 14:00, and 20:00 Beijing time (BJT), with an additional observation at 02:00 BJT for the base meteorological stations. Since the visibility observation at 02:00 BJT and 20:00 BJT are carried out at night, the targets selected for observation are different from those during the daytime (i.e., 14:00 BJT), resulting in inconsistent observation data. In addition, the visibility at 08:00 BJT is easily affected by early morning radiation fog. Therefore, only the observations at 14:00 BJT were selected for analysis. Observations of visibility under weather conditions such as fog, high winds, precipitation, and high humidity (relative humidity RH> 90%), which may affect visibility, have been excluded. The filtered visibility data was then revised for humidity according to the method of Rosenfeld (Rosenfeld et al., 2007) to obtain “dry visibility”, based on which the climatic characteristics of atmospheric visibility in the SCB and its surrounding areas were analyzed. In conjunction with the wind, air temperature, humidity, etc. from FNL, the effects of meteorological elements and the potential impact mechanism on the transport and dispersion of pollution in the special topography were investigated.

3 Results and discussion

3.1 Variation in dry visibility and AOD

Figure 2 shows the spatial distribution of the AOD over China, aggregated over the years 2001–2010. It can be seen that the SCB is one of the several most polluted regions in China, with the AOD comparable with those in NCP and PRD, and that the interior of the basin (marked with white line in Figure 2) is more polluted than the peripheral areas around the basin.

The higher the AOD, the stronger the extinction of the atmosphere. Therefore, visibility is generally inversely proportional to AOD. Atmospheric visibility data can be used to indirectly evaluate the optical properties of aerosols, although the effects of aerosols, air molecules and water vapor on light attenuation should be considered in the calculation. According to the annual average of atmospheric

TABLE 1 Visibility ranges and estimations for visibility levels.

Visibility level	Visibility distance range (km)	Visibility distance estimates (km)
0	< 0.05	0.025
1	0.05–0.2	0.1
2	0.2–0.5	0.28
3	0.5–1.0	0.7
4	1.0–2.0	1.41
5	2.0–4.0	2.67
6	4.0–10.0	6.77
7	10.0–20.0	13.58
8	20.0–50.0	29.04
9	≥50.0	54.27

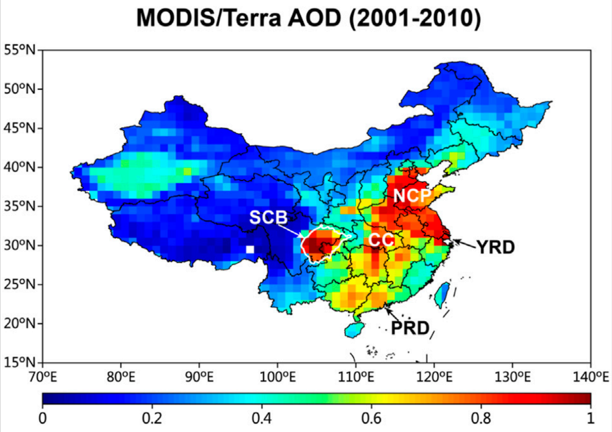

FIGURE 2
Spatial distribution of the AOD over China, aggregated over the years 2001–2010. Regions with relatively high AOD are marked, i.e., the SCB, the North China Plain (NCP), the Yangtze River Delta (YRD), the Central China (CC), and the Pearl River Delta (PRD).

visibility over the past 51 years in Figure 3A, it can be seen that there is a sharp contrast between the visibility in the SCB and its western plateau region. Visibility within the basin, averaged at 18.9 km, is significantly lower than that in the WSP where the visibility mostly falls within 40–50 km, with the average visibility of about 46.0 km in areas above 1.5 km in altitude. The lowest visibility and highest AOD simultaneously occur in the southern part of the basin, with the former showing a gradual increase from east to west, and the maximum visibility occurs on the WSP, reaching 58.1 km.

According to the distribution of atmospheric visibility variability in Figure 3B, 116 of the 191 stations (60.7% of the total number of stations) showed a decreasing trend in visibility, with 77 stations (66.4%) passing the 99% confidence test, indicating a clear trend of decreasing visibility. The stations with reduced visibility were mainly located in the basin, concentrated in southwest of the basin area and the southeast of Chongqing (Figure 3B). The most significant reduction in visibility is in Panzhihua, with a climatic tendency of about -7.73 km per decade. Panzhihua is an important industrial city in the south Sichuan province, where highly developed industries emitting a large amount of air pollutants may be the main reason for the reduction in high visibility. On the other hand, 74 stations (38.7% of the total number of stations), mainly located on WSP, showed an increasing trend in visibility, with 39 stations (52.7%) passing the 99% confidence test. The most significant increase reached about 6.39 km per decade.

3.2 Visibility in relation to terrain height and wind speed

According to the linear correlation between the average visibility and altitude of each station from 1960 to 2010 (Figure 4), it can be seen that visibility and altitude are positively correlated, and the correlation coefficient is about 0.90 (R^2=0.81, p<0.01), indicating that there is a close relationship between visibility and altitude, and the higher the altitude, the greater the visibility. When the altitude is less than 750 m, the visibility is mostly less than 25 km, while when the altitude is greater than 1500 m, the visibility is mostly more than 40 km. A linear correlation between the visibility and terrain altitude is also given for the different interdecadal periods (Figure 5). The visibility and terrain height in different periods are highly positive correlated as well, with all the correlation coefficients exceeding 0.8 (p<0.01).

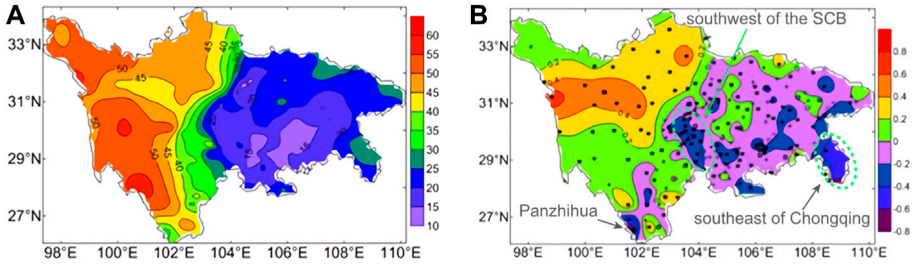

FIGURE 3
Distribution of **(A)** atmospheric visibility and **(B)** atmospheric visibility variability in the SCB and its surrounding areas over the 51 years (1960-2010). The makers *, ●, and ○ indicate passing the 99%, 95% and 90% confidence tests, respectively.

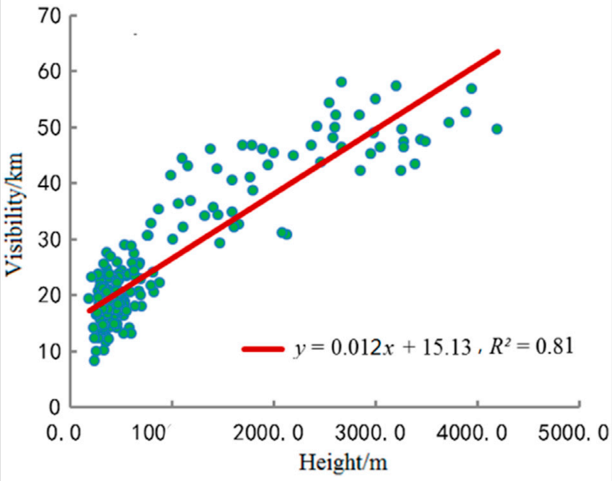

FIGURE 4
Scatter plots and correlation coefficient (*R*) of the visibilities and terrain heights over the years from 1960 to 2010. There are 191 scattered points in the figure, representing the values of 191 meteorological observation stations.

As the relationship between visibility and wind speed is relatively complex, it is discussed here separately for the SCB (below 750 m elevation) and the WSP (above 1500 m elevation). It reveals that visibility in the SCB was positively correlated with the wind speed (Figure 6A), with a correlation coefficient of 0.57 ($p < 0.1$), indicating that wind speed is an important factor influencing visibility changes within the basin. On the contrary, visibility and wind speed on the WSP region are basically negatively correlated (Figure 6B), i.e., visibility decreases with increasing wind speed. As a rule of thumb, in heavily emitting areas such as the SCB, higher wind speeds are more conducive to the dispersion and outward transport of pollutants, while in relatively clean areas, higher wind speeds are more conducive to the transport of external pollutants into the local area causing local pollution.

3.3 The mechanism of topography on visibility

According to the analysis of visibility and altitude correlation for 1960-2010 and for each inter-decade period (1960-1970, 1980-1990, 2000-2010), it can be seen that visibility and altitude do not vary with the inter-decade period, but show a significant positive correlation, indicating that there is indeed a close influence effect between atmospheric environment and topography, and it can be inferred that the conclusions of this study would be still valid if the data are extended to present. In addition, visibility and wind speed are significantly positively correlated in the SCB area, while are weakly negatively correlated in the WSP area, demonstrating the regional differences in visibility variability, and its relationship with influencing factors, which are tightly affected by the topography. It is needed to understand how topography affects the atmospheric environment. In this section, the characteristics of atmospheric dynamic and thermal characteristics (reflected by wind and temperature, respectively) under the influence of the special topography are studied.

Figure 7 illustrates the vertical profile distribution of the latitudinal zone average (28°N-32°N) of horizontal and vertical wind speeds for different seasons. It can be seen that the atmospheric circulation structure over the region is relatively similar in winter, spring and autumn. During the three seasons, the low-level atmosphere in the SCB, where harbored by the Tibetan Plateau (TP) with its impact on midlatitude westerly winds, is characterized by weak winds and updrafts, while the high-level atmosphere is generally characteristic of strong winds and downdrafts, forming a “harbor” effect over the basin on the leeward slopes of the TP (Xu et al., 2015; Xu et al., 2016). On the contrary, the surface wind speed in the WSP area is substantially higher than those within the basin. A minimal horizontal wind

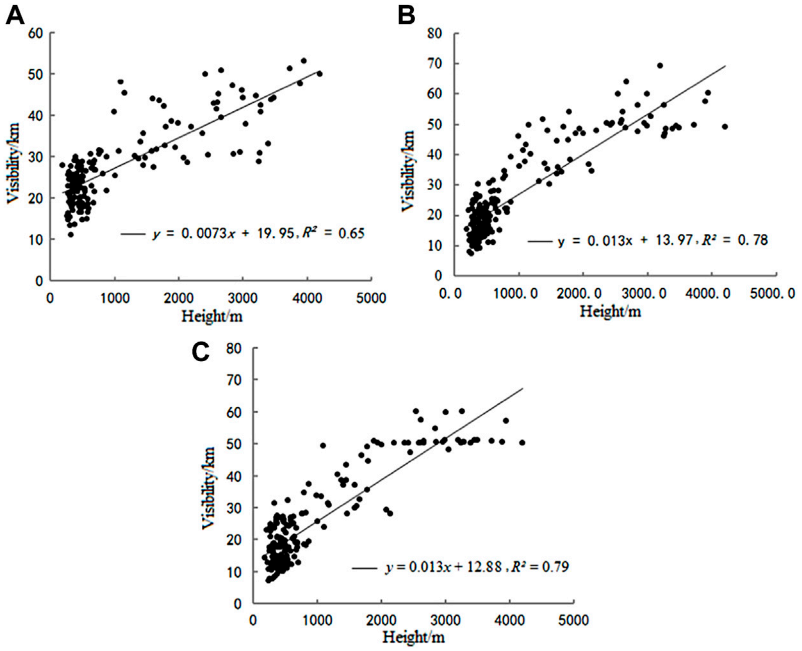

FIGURE 5
Scatter plots and correlation coefficients (*R*) of the visibilities and terrain heights over the years from **(A)** 1960 to 1970, **(B)** 1980 to 1990, and **(C)** 2000 to 2010, respectively. There are 191 scattered points in each of the three subplots, representing the values of 191 meteorological observation stations.

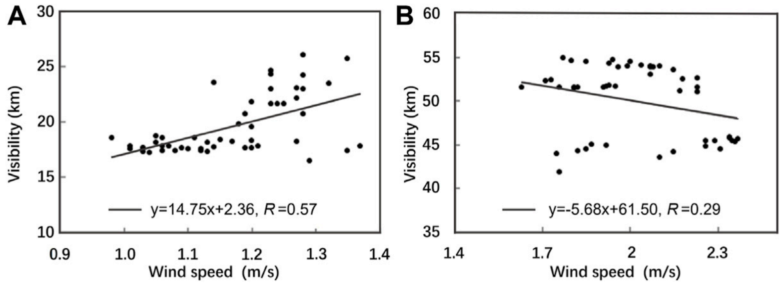

FIGURE 6
Scatter plots and correlation coefficients (R) of the visibilities and wind speeds in the stations with the altitude **(A)** below 750 m and **(B)** above 1,500 m.

speed zone exists between 700 hPa and 850hPa, where is typically the center of a lee-side vortex of immediately upstream TP (Zhang et al., 2019; Shu et al., 2021). The zero vertical velocity layer is at approximately the same altitude as the WSP. It is worth noting that sinking air aloft is stronger in winter than those in spring and autumn, with the updrafts being suppressed within a lower altitude range and at their weakest strength, forming a more unfavourable vertical structure for the transport and dispersion of pollutants. In contrast, although there are also areas of weak winds over the basin in summer, the atmosphere is almost entirely in upward motion, which is more conducive to the upward transport of pollutants. The pronounced difference in the vertical movement of the atmosphere in winter and summer should be related to the thermal effect of the TP, i.e., acting as a cold source in winter and heat source in summer (Zhang et al., 2000). The dynamical structure of the atmosphere under the influence of large topography may partly explain why haze is the most

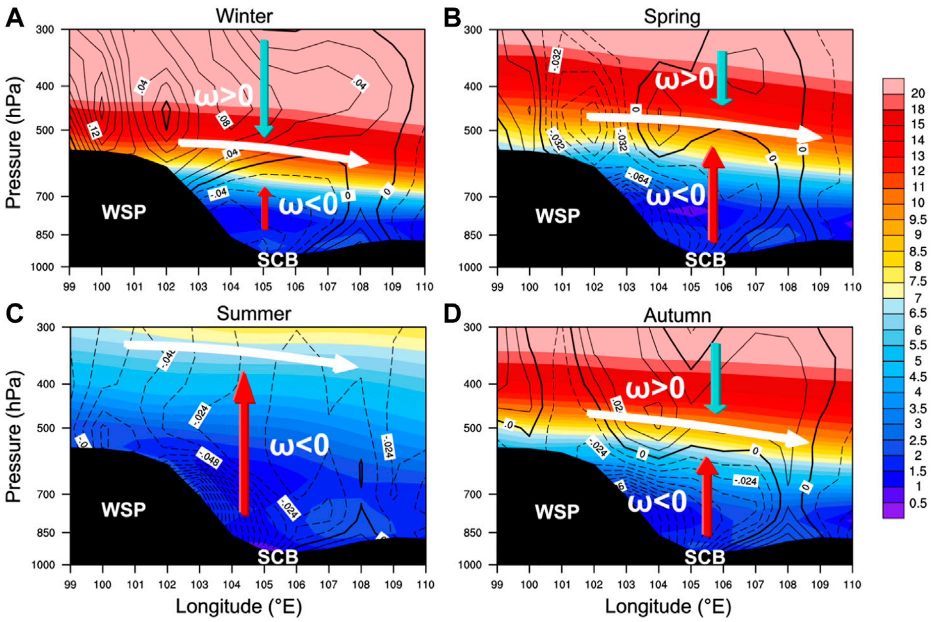

FIGURE 7
Vertical west–east cross–sections of horizontal (shading) and vertical (contour) wind speed averaged from 28°N to 31°N in **(A)** winter, **(B)** spring, **(C)** summer, and **(D)** autumn for the period 1999 to 2010. The solid and dashed lines indicate rise (ω<0) and descend (ω>0) of the airflow, respectively.

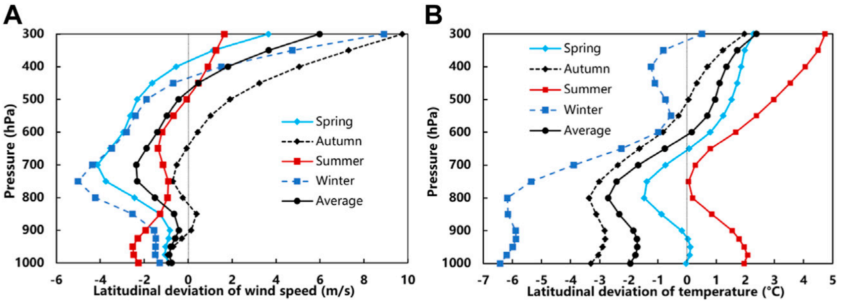

FIGURE 8
Overall and seasonal deviations of wind speed **(A)** and temperature **(B)** from the same latitudinal band for the period 1999 to 2010 in the range 104°E–109°E and 28°N–31°N (corresponding to the SCB region).

severe in the basin in winter, followed by spring and autumn, and least severe in summer (Cai et al., 2018). Overall, on the basis of the preceding analysis, diffusion conditions for pollution are poor in the SCB under the particular large topography, and become progressively better with increasing altitude. Besides, higher anthropogenic emissions within the basin would further reduced the visibility in the basin areas.

In order to isolate the effect of large topography on the atmospheric dynamic and thermal structure of the SCB, the latitudinal deviations in wind speed and temperature within the basin area (28°N~31°N, 104°E-109°E) were calculated. As shown in Figure 8, in terms of average wind speed deviations, the topography reduced the wind speed below 500 hPa in the basin by about 0.5–2 m/s, while increased the wind speeds above 500 hPa significantly. The topography causes the most significant decrease in wind speed over the basin at 700-800 hPa, especially in winter and spring (Figure 8A), which are not conducive to the transport and dispersion of pollutants and tend to cause the accumulation of pollutants in the basin. The large topographic dynamic effects described above are present in different seasons, only to varying degrees. Based on the overall temperature-latitude deviation, it can be seen that, compared with other regions in the same latitudinal zone, the topography reduces the atmospheric temperature below 600 hPa over the basin, with the largest drop of 2.5–3°C at 800 hPa (Figure 8B), which is about the same as the height at which the topography reduces the wind speed over the basin most significantly. This suggests that the topography tends to make this layer of the basin more susceptible to off-ground inversions, which may be closely related to the overall downward warming of the leeward flow over the Tibetan Plateau (Xu et al., 2014). Under the warming effect of the leeward-slope airflow, inversions aloft are prone to form over the basin, with the highest likelihood and frequency of occurrence in winter (Figure 8B). The inversions would make the atmospheric stratification in the basin region more stable and the vertical transport of pollutants would be weakened, leading to the accumulation of pollutants in the basin and thus deteriorating air quality. There is a large seasonal variation in the effect of topography on temperature, with an overall decrease in temperature of a more pronounced magnitude in autumn and winter, and a relatively more pronounced inversion effect at 800-600 hPa. Combining the above analysis of the terrain effects on the wind-temperature structure over the basin shows that the most significant effects are experienced in winter, with both wind speed and temperature changing considerably due to the topography, and that an inversion layer is more likely to be generated than those in the other seasons. It is therefore important to pay more attention to the deteriorating effect of topography on air quality when developing pollution prevention and control in winter.

4 Conclusion

The topography of the Sichuan-Chongqing region is very complex, i.e. the SCB and the surrounding mountains are highly undulating, especially the TP that lies immediately to the west, resulting in a significant topography-dependent atmospheric environment. Studies have been conducted to quantify the influence of topography on atmospheric pollution in the SCB. In this study, the atmospheric environmental effects of topography in the Sichuan-Chongqing region are examined in terms of long-term changes in visibility, a proxy of aerosol concentration, and its connections with topography.

Visibility in the Sichuan-Chongqing region is significantly and positively correlated with the terrain height. Visibility in the SCB (defined as altitude less than 750 m) shows a significant positive correlation with wind speed, while at higher altitudes (larger than 1,500 m), visibility shows a negative correlation with wind speed. The effects of the large topography on the atmospheric environment of the region are mainly manifested in the following ways: The SCB is located on the leeward slope of the WSP. Under the influence of its special large topography, the leeward-slope effect leads to a weak wind area accompanied by ascending motions at low altitude, and descending motions with westerly winds at high altitude during the winter, spring, and autumn. A zone of minimal wind speed exists between 700 and 800 hPa in winter, spring and autumn, which corresponds to the height of the centre of the leeward-slope vortex. The descending motions could form a huge "vault" over the basin, which are not conducive to vertical transport and dispersion of pollutants. The "vault" effect is strongest in winter, followed by autumn and spring, and disappears in summer, being one of the key factors for the worst winter pollution in the basin. Therefore, more attention should be paid to the exacerbating effect of topography on pollution during winter pollution control. In addition, topography has a significant effect on the temperature structure over the basin, leading to a tendency for inversions to form near the surface of the basin as well as at high altitudes above 800 hPa, particularly at the high altitudes where the intensity of the off-ground inversion is very strong in the winter, autumn, and spring. The inversions will further lead to a more stagnant atmosphere over the basin, which is not conducive to the upward transport and dispersion of pollutants.

This study attempts to investigate the atmospheric effects of topography around the SCB from a long-term climatic perspective, which is important for furthering the understanding of the effects of topography on the atmospheric environment and the protection of the atmospheric environment within the basin. There may exist uncertainties in this study, such as the fact that most of the analysis in this study was carried out using statistical methods, such as the difference in meteorological conditions between areas within the basin and the same latitude zone was used in studying the role of topography, in which the interference of some other factors, such as differences in underlying surface and/or climatic background, may not be excluded. Therefore, future studies could combine a variety of methods, such as conducting long time scale topographic sensitivity tests in conjunction with chemical transport models, to reduce uncertainties and improve the quantitative understanding of the effects of topography in the SCB.

Data availability statement

The raw data supporting the conclusion of this article will be made available by the authors, without undue reservation.

Author contributions

LZ and TZ conceived of the presented idea and designed the research framework with support from XG, XX, XZ, YL and LL. LZ and XG reviewed the literature and drafted the manuscript. LZ and YZ led the data analysis and interpreted the results together with KG. ZS provided critical feedback and constructive comments. All authors were involved in the discussion of the results.

Funding

This research was funded by National Key Research and Development Program of China (No. 2019YFC0214604), National Natural Science Foundation of China project (grant no. 42030608, 42090030, 41320714, 41975131), the National Key Foundation Study Developing Programs (grant no. 2019YFC0214601, 2019YFC0214801), and the CAMS Basis Research Project (Grant no. 2020Y001).

Acknowledgments

We are grateful to Sichuan Meteorological Bureau for providing the meteorological data used in this study.

Conflict of interest

The authors declare that the research was conducted in the absence of any commercial or financial relationships that could be construed as a potential conflict of interest.

Publisher's note

References

Allen, S., Allen, D., Phoenix, V. R., Le Roux, G., Durántez Jiménez, P., Simonneau, A., et al. (2019). Atmospheric transport and deposition of microplastics in a remote mountain catchment. *Nat. Geosci.* 12, 339–344. doi:10.1038/s41561-019-0335-5

Blyth, S. (2002). *Mountain watch: environmental change & sustainable developmental in mountains*. Kenya: UNEP/Earthprint.

Cai, H., Gui, K., and Chen, Q. (2018). Changes in haze trends in the sichuan-chongqing region, China, 1980 to 2016. *Atmosphere* 9, 277. doi:10.3390/atmos9070277

Carslaw, K., Boucher, O., Spracklen, D., Mann, G., Rae, J., Woodward, S., et al. (2010). A review of natural aerosol interactions and feedbacks within the Earth system. *Atmos. Chem. Phys.* 10, 1701–1737. doi:10.5194/acp-10-1701-2010

Carslaw, K., Lee, L., Reddington, C., Pringle, K., Rap, A., Forster, P., et al. (2013). Large contribution of natural aerosols to uncertainty in indirect forcing. *Nature* 503, 67–71. doi:10.1038/nature12674

Chang, L., Wu, Z., and Xu, J. (2021). Contribution of Northeastern Asian stratospheric warming to subseasonal prediction of the early winter haze pollution in Sichuan Basin, China. *Sci. Total Environ.* 751, 141823. doi:10.1016/j.scitotenv.2020.141823

Che, H., Zhang, X., Li, Y., Zhou, Z., and Qu, J. J. (2007). Horizontal visibility trends in China 1981–2005. *Geophys. Res. Lett.* 34, L24706. doi:10.1029/2007gl031450

Chen, Y., and Xie, S. (2012). Temporal and spatial visibility trends in the Sichuan Basin, China, 1973 to 2010. *Atmos. Res.* 112, 25–34. doi:10.1016/j.atmosres.2012.04.009

Deng, X., Tie, X., Wu, D., Zhou, X., Bi, X., Tan, H., et al. (2008). Long-term trend of visibility and its characterizations in the Pearl River Delta (PRD) region, China. *Atmos. Environ.* 42, 1424–1435. doi:10.1016/j.atmosenv.2007.11.025

Feng, S., Gao, D., Liao, F., Zhou, F., and Wang, X. (2016). The health effects of ambient PM2. 5 and potential mechanisms. *Ecotoxicol. Environ. Saf.* 128, 67–74. doi:10.1016/j.ecoenv.2016.01.030

Gao, S., and Ping, F. (2005). An experiment study of lee vortex with large topography forcing. *Chin. Sci. Bull.* 50, 248–255. doi:10.1360/03wd0550

Giovannini, L., Laiti, L., Serafin, S., and Zardi, D. (2017). The thermally driven diurnal wind system of the Adige Valley in the Italian Alps. *Q. J. R. Meteorol. Soc.* 143, 2389–2402. doi:10.1002/qj.3092

Gui, K., Che, H., Zeng, Z., Wang, Y., Zhai, S., Wang, Z., et al. (2020). Construction of a virtual PM2. 5 observation network in China based on high-density surface meteorological observations using the Extreme Gradient Boosting model. *Environ. Int.* 141, 105801. doi:10.1016/j.envint.2020.105801

Guo, Q., Wu, D., Yu, C., Wang, T., Ji, M., and Wang, X. (2022). Impacts of meteorological parameters on the occurrence of air pollution episodes in the Sichuan basin. *J. Environ. Sci.* 114, 308–321. doi:10.1016/j.jes.2021.09.006

Hu, J., Zhao, T., Liu, J., Cao, L., Wang, C., Li, Y., et al. (2022). Exploring the ozone pollution over the western Sichuan Basin, Southwest China: The impact of diurnal change in mountain-plains solenoid. *Sci. Total Environ.* 839, 156264. doi:10.1016/j.scitotenv.2022.156264

Hu, X. M., Ma, Z., Lin, W., Zhang, H., Hu, J., Wang, Y., et al. (2014). Impact of the loess plateau on the atmospheric boundary layer structure and air quality in the north China plain: a case study. *Sci. Total Environ.* 499, 228–237. doi:10.1016/j.scitotenv.2014.08.053

Kampa, M., and Castanas, E. (2008). Human health effects of air pollution. *Environ. Pollut.* 151, 362–367. doi:10.1016/j.envpol.2007.06.012

Kelly, F. J., and Zhu, T. (2016). Transport solutions for cleaner air. *Science* 352, 934–936. doi:10.1126/science.aaf3420

Kong, D., Ning, G., Wang, S., Cong, J., Luo, M., Ni, X., et al. (2021). Clustering diurnal cycles of day-to-day temperature change to understand their impacts on air quality forecasting in mountain-basin areas. *Atmos. Chem. Phys.* 21, 14493–14505. doi:10.5194/acp-21-14493-2021

Letson, F., Barthelmie, R. J., Hu, W., and Pryor, S. C. (2019). Characterizing wind gusts in complex terrain. *Atmos. Chem. Phys.* 19, 3797–3819. doi:10.5194/acp-19-3797-2019

Li, Y., Chen, Q., Zhao, H., Wang, L., and Tao, R. (2015). Variations in PM10, PM2. 5 and PM1. 0 in an urban area of the Sichuan Basin and their relation to meteorological factors. *Atmosphere* 6, 150–163. doi:10.3390/atmos6010150

Liao, T., Gui, K., Jiang, W., Wang, S., Wang, B., Zeng, Z., et al. (2018). Air stagnation and its impact on air quality during winter in Sichuan and Chongqing, southwestern China. *Sci. Total Environ.* 635, 576–585. doi:10.1016/j.scitotenv.2018.04.122

Liu, H., Yan, R., and Yang, J. (2021). Credibility and statistical characteristics of CAMSRA and MERRA-2 AOD reanalysis products over the Sichuan Basin during 2003–2018. *Atmos. Environ.* 244, 117980. doi:10.1016/j.atmosenv.2020.117980

Liu, M., Huang, Y., Ma, Z., Jin, Z., Liu, X., Wang, H., et al. (2017). Spatial and temporal trends in the mortality burden of air pollution in China: 2004–2012. *Environ. Int.* 98, 75–81. doi:10.1016/j.envint.2016.10.003

Liu, Q., Ding, D., Huang, M., Tian, P., Zhao, D., Wang, F., et al. (2018). A study of elevated pollution layer over the North China Plain using aircraft measurements. *Atmos. Environ.* 190, 188–194. doi:10.1016/j.atmosenv.2018.07.024

Luo, Y., Zheng, X., Zhao, T., and Chen, J. (2014). A climatology of aerosol optical depth over China from recent 10 years of MODIS remote sensing data. *Int. J. Climatol.* 34, 863–870. doi:10.1002/joc.3728

Ning, G., Wang, S., Yim, S. H. L., Li, J., Hu, Y., Shang, Z., et al. (2018). Impact of low-pressure systems on winter heavy air pollution in the northwest Sichuan Basin, China. *Atmos. Chem. Phys.* 18, 13601–13615. doi:10.5194/acp-18-13601-2018

Ning, G., Yim, S. H. L., Wang, S., Duan, B., Nie, C., Yang, X., et al. (2019). Synergistic effects of synoptic weather patterns and topography on air quality: a case of the Sichuan Basin of China. *Clim. Dyn.* 53, 6729–6744. doi:10.1007/s00382-019-04954-3

Poulos, G. S., and Pielke, R. A. (1994). A numerical analysis of Los Angeles basin pollution transport to the Grand Canyon under stably stratified, southwest flow conditions. *Atmos. Environ.* 28, 3329–3357. doi:10.1016/1352-2310(94)00127-7

Qiao, X., Jaffe, D., Tang, Y., Bresnahan, M., and Song, J. (2015). Evaluation of air quality in Chengdu, Sichuan Basin, China: are China's air quality standards sufficient yet? *Environ. Monit. Assess.* 187, 250–311. doi:10.1007/s10661-015-4500-z

Qin, S., Shi, G., Chen, L., Wang, B., Zhao, J., Yu, C., et al. (2010). Long-term variation of aerosol optical depth in China based on meteorological horizontal visibility observations. *Chin. J. Atmos. Sci.* 34, 449–456.

Rosenfeld, D., Dai, J., Yu, X., Yao, Z., Xu, X., Yang, X., et al. (2007). Inverse relations between amounts of air pollution and orographic precipitation. *Science* 315, 1396–1398. doi:10.1126/science.1137949

Schmidli, J., and Rotunno, R. (2010). Mechanisms of along-valley winds and heat exchange over mountainous terrain. *J. Atmos. Sci.* 67, 3033–3047. doi:10.1175/2010jas3473.1

Shang, Y., Sun, Z., Cao, J., Wang, X., Zhong, L., Bi, X., et al. (2013). Systematic review of Chinese studies of short-term exposure to air pollution and daily mortality. *Environ. Int.* 54, 100–111. doi:10.1016/j.envint.2013.01.010

Shu, Z., Liu, Y., Zhao, T., Xia, J., Wang, C., Cao, L., et al. (2021). Elevated 3D structures of PM<sub>2.5</sub> and impact of complex terrain-forcing circulations on heavy haze pollution over Sichuan Basin, China. *Atmos. Chem. Phys.* 21, 9253–9268. doi:10.5194/acp-21-9253-2021

Shu, Z., Liu, Y., Zhao, T., Zhou, Y., Habtemicheal, B. A., Shen, L., et al. (2022a). Long-term variations in aerosol optical properties, types, and radiative forcing in the Sichuan Basin, Southwest China. *Sci. Total Environ.* 807, 151490. doi:10.1016/j.scitotenv.2021.151490

Shu, Z., Zhao, T., Liu, Y., Zhang, L., Ma, X., Kuang, X., et al. (2022b). Impact of deep basin terrain on PM2.5 distribution and its seasonality over the Sichuan Basin, Southwest China. *Environ. Pollut.* 300, 118944. doi:10.1016/j.envpol.2022.118944

Sun, K., Liu, H-N., Ding, A-J., and Wang, X-Y. (2016). WRF-Chem simulation of a severe haze episode in the Yangtze River Delta, China. *Aerosol Air Qual. Res.* 16, 1268–1283. doi:10.4209/aaqr.2015.04.0248

Ting, M., and Wang, H. (2006). The role of the North American topography on the maintenance of the Great Plains summer low-level jet. *J. Atmos. Sci.* 63, 1056–1068. doi:10.1175/jas3664.1

Tuononen, M., Sinclair, V., and Vihma, T. (2015). A climatology of low-level jets in the mid-latitudes and polar regions of the Northern Hemisphere. *Atmos. Sci. Lett.* 16, 492–499. doi:10.1002/asl.587

Wagner, J., Gohm, A., and Rotach, M. (2015). The impact of valley geometry on daytime thermally driven flows and vertical transport processes. *Q. J. R. Meteorol. Soc.* 141, 1780–1794. doi:10.1002/qj.2481

Wang, D., Miao, J., and Tan, Z. (2013). Impacts of topography and land cover change on thunderstorm over the Huangshan (Yellow Mountain) area of China. *Nat. Hazards (Dordr).* 67, 675–699. doi:10.1007/s11069-013-0595-0

Wang, H., Shi, G., Tian, M., Zhang, L., Chen, Y., Yang, F., et al. (2017). Aerosol optical properties and chemical composition apportionment in Sichuan Basin, China. *Sci. Total Environ.* 577, 245–257. doi:10.1016/j.scitotenv.2016.10.173

Wang, H., Tian, M., Chen, Y., Shi, G., Liu, Y., Yang, F., et al. (2018a). Seasonal characteristics, formation mechanisms and source origins of PM<sub>2.5</sub> in two megacities in Sichuan Basin, China. *Atmos. Chem. Phys.* 18, 865–881. doi:10.5194/acp-18-865-2018

Wang, X., Dickinson, R. E., Su, L., Zhou, C., and Wang, K. (2018b). $PM_{2.5}$ pollution in China and how it has been exacerbated by terrain and meteorological conditions. *Bull. Am. Meteorological Soc.* 99, 105–119. doi:10.1175/bams-d-16-0301.1

Wang, X-C., Klemeš, J. J., Dong, X., Fan, W., Xu, Z., Wang, Y., et al. (2019). Air pollution terrain nexus: A review considering energy generation and consumption. *Renew. Sustain. Energy Rev.* 105, 71–85. doi:10.1016/j.rser.2019.01.049

Whiteman, C. D., Bian, X., and Zhong, S. (1999). Wintertime evolution of the temperature inversion in the Colorado Plateau Basin. *J. Appl. Meteor.* 38, 1103–1117. doi:10.1175/1520-0450(1999)038<1103:weotti>2.0.co;2

Wu, K., Wang, Y., Qiao, Y., Liu, Y., Wang, S., Yang, X., et al. (2022). Drivers of 2013–2020 ozone trends in the Sichuan Basin, China: Impacts of meteorology and precursor emission changes. *Environ. Pollut.* 300, 118914. doi:10.1016/j.envpol.2022.118914

Xing, Y-F., Xu, Y-H., Shi, M-H., and Lian, Y-X. (2016). The impact of PM2. 5 on the human respiratory system. *J. Thorac. Dis.* 8, E69–E74. doi:10.3978/j.issn.2072-1439.2016.01.19

Xu, X., Wang, Y., Zhao, T., Cheng, X., Meng, Y., and Ding, G. (2015). "Harbor" effect of large topography on haze distribution in eastern China and its climate modulation on decadal variations in haze. *Chin. Sci. Bull.* 60, 1132–1143. doi:10.1360/N972014-00101

Xu, X., Zhao, T., Liu, F., Gong, S. L., Kristovich, D., Lu, C., et al. (2016). Climate modulation of the Tibetan Plateau on haze in China. *Atmos. Chem. Phys.* 16, 1365–1375. doi:10.5194/acp-16-1365-2016

Xu, X., Zhao, T., Lu, C., Guo, Y., Chen, B., Liu, R., et al. (2014). An important mechanism sustaining the atmospheric "water tower" over the Tibetan Plateau. *Atmos. Chem. Phys.* 14, 11287–11295. doi:10.5194/acp-14-11287-2014

Yin, D., Zhao, S., Qu, J., Yu, Y., Kang, S., Ren, X., et al. (2020). The vertical profiles of carbonaceous aerosols and key influencing factors during wintertime over western Sichuan Basin, China. *Atmos. Environ.* 223, 117269. doi:10.1016/j.atmosenv.2020.117269

Zardi, D., and Whiteman, C. D. (2013). "Diurnal mountain wind systems," in *Mountain weather research and forecasting* (Dordrecht: Springer), 35–119.

Zhang, D., Fengquan, L., and Jianmin, B. (2000). Eco-environmental effects of the qinghai-tibet plateau uplift during the quaternary in China. *Environ. Geol.* 39, 1352–1358. doi:10.1007/s002540000174

Zhang, L., Guo, X., Zhao, T., Gong, S., Xu, X., Li, Y., et al. (2019). A modelling study of the terrain effects on haze pollution in the Sichuan Basin. *Atmos. Environ.* 196, 77–85. doi:10.1016/j.atmosenv.2018.10.007

Zheng, Y., Che, H., Xia, X., Wang, Y., Yang, L., Chen, J., et al. (2021). Aerosol optical properties and its type classification based on multiyear joint observation campaign in north China plain megalopolis. *Chemosphere* 273, 128560. doi:10.1016/j.chemosphere.2020.128560

Zhu, W., Xu, X., Zheng, J., Yan, P., Wang, Y., and Cai, W. (2018). The characteristics of abnormal wintertime pollution events in the Jing-Jin-Ji region and its relationships with meteorological factors. *Sci. Total Environ.* 626, 887–898. doi:10.1016/j.scitotenv.2018.01.083

frontiers | Frontiers in Earth Science

TYPE Original Research
PUBLISHED 23 September 2022
DOI 10.3389/feart.2022.1012085

Check for updates

OPEN ACCESS

EDITED BY
Duanyang Liu,
Chinese Academy of Meteorological Sciences, China

REVIEWED BY
Jianming Xu,
Shanghai Meteorological Bureau, China
Dai Zhujun,
China Meteorological Administration, China
Yong Huang,
Anhui Provincial Meteorological Bureau, China

*CORRESPONDENCE
Wei Xia-lu,
526098803@qq.com

SPECIALTY SECTION
This article was submitted to Atmospheric Science, a section of the journal Frontiers in Earth Science

RECEIVED 05 August 2022
ACCEPTED 02 September 2022
PUBLISHED 23 September 2022

CITATION
Cheng-gang W, Xia-lu W, Jia-de Y and Ting N (2022), Observational study of the influences of thermal and dynamic boundary layer on the vertical distribution of black carbon aerosol in ShouXian county in wintertime, 2016. *Front. Earth Sci.* 10:1012085.
doi: 10.3389/feart.2022.1012085

Observational study of the influences of thermal and dynamic boundary layer on the vertical distribution of black carbon aerosol in ShouXian county in wintertime, 2016

Wang Cheng-gang[1], Wei Xia-lu[2]*, Yang Jia-de[1] and Ni Ting[3]

[1]Nanjing University of Information Science and Technology School of Atmospheric Physics, Nanjing, China, [2]Fujian Meteorological Information Center, Fuzhou, China, [3]ShouXian National Climate Observatory, Huaihe River Basin Typical Farmland Eco-Meteorology Field Scientific Experiment Base of China Meteorological Administration, Xian, China

Using vertical observation data of black carbon aerosol and meteorological parameters in the ShouXian area of Anhui Province from 14 December 2016 to 3 January 2017, the thermal and dynamic effects of the boundary layer on the vertical distribution structure of black carbon were studied. The results show that 1) of 82 vertical sounding profiles obtained during the observation period, there were 72 boundary layer sounding profiles dominated by heat and 10 profiles dominated by dynamics. 2) When thermal effects were dominant, the concentration of black carbon aerosol was significantly affected by diurnal changes in the boundary layer. In the unstable boundary layer, black carbon aerosol was uniformly distributed in the vertical direction; during the transition from an unstable to a stable boundary layer, the concentrations of black carbon aerosol were significantly higher in the lower layer than in the upper layer; in the stable boundary layer, the concentrations of black carbon aerosol decreased continuously with height; and during the transition from a stable to an unstable boundary layer, the black carbon aerosol concentrations exhibited high values in the upper layer, with the concentration difference reaching 4 μg m^{-3}. 3) When the dynamic effect was dominant, the structure of the vertical distribution of black carbon aerosol was affected by wind and by diurnal changes in the boundary layer simultaneously. The high winds (>4 m/s) removed the black carbon aerosol. In the unstable boundary layer, the black carbon aerosol uniformly distributed in the vertical direction had significantly lower concentrations in the high-wind range; when stable boundary layers occurred and during transitions from stable to unstable boundary layers, the black carbon aerosol concentrations were higher in the lower layer and lower in the upper layer. The stratification was more obvious than that observed under thermal control.

KEYWORDS

black carbon, vertical observation of boundary layer, thermal effect, dynamic effect, shouxian

Introduction

Black carbon (BC) aerosols not only pose a great threat to human health (Zhang et al., 2007), but also play an important role in environmental pollution, climate change, and extreme weather occurrences (Raunemaa et al., 1994; Ramanathan et al., 2002; Ramanathan and Carmichael 2008; Wang Y. et al., 2018a; Slater et al., 2021; Xiao et al., 2011).

The analysis of observational data is a direct means of understanding the spatial and temporal distributions of BC aerosol. Since the 1970s, a series of field observation experiments have been carried out in the United States (Waggoner and Charlson, 1976; Countess et al., 1980; Cass et al., 1982; Wolff et al., 1982), the United Kingdom (Singh et al., 2018), Switzerland (Herich et al., 2011), Finland (Pakkanen et al., 2000), and China (Luan and Mao, 1987; Tang et al., 1999; Weng et al., 2001; Zhang et al., 2015; Lu et al., 2015), leading to an in-depth understanding of the spatial and temporal distribution characteristics, source resolution and formation mechanisms of BC aerosol. However, these works are mostly based on near-surface analyses.

An increasing number of studies have indicated that the vertical distribution characteristics of BC aerosol have important effects on both atmospheric radiative forcing and physical processes in the boundary layer (Corrigan et al., 2008; Ramanathan and Carmichael, 2008; Li et al., 2015; Zhao et al., 2019; Zhang et al., 2015; Ding et al). Gordon (1997) and Duforet et al. (2007) showed that the absorptive heating of BC aerosols by shortwave radiation depends on their vertical distribution characteristics. Slater et al. (2021) used models to quantify this effect. When BC aerosol is concentrated at the top of the boundary layer, a “dome effect” is formed. That is, BC aerosol absorbs shortwave radiation at the top of the boundary layer and heats up the surrounding atmosphere, leading to a decrease in the turbulence intensity and inhibiting the development of the boundary layer, thus increasing ground pollution (Tian et al., 1997; Ding A. J. et al., 2016b; Huang et al., 2018; Y. Wang et al., 2018a; Z. Wang et al., 2018b; Liu et al., 2019; Zhao et al., 2020). At the same time, the cloud condensation nuclei (CCN) capability of BC is significantly enhanced (Ding AJ. et al., 2016a), which further affects indirect radiation. When BC aerosol is concentrated near the ground, its heating effect will, in turn, enhance turbulent motion and promote the development of an unstable boundary layer (Petj et al., 2016; Tian et al., 2019).

Li and Liang et al. (Li et al., 2015; Liang et al., 2016) found that the vertical structure of BC aerosol concentrations differed significantly throughout the day using outfield experimental data. Under stable conditions, BC aerosol concentrations were found to be significantly higher in the lower layers than in the upper layers (Zhang et al., 2012). The shallower boundary layer and temperature inversion layer increase the mass concentration of BC (Zhao et al., 2020). Under unstable conditions, the vertical distribution of BC aerosol is relatively uniform (Lu et al., 2019). When the wind speed is high, ground transport may either remove or exacerbate pollution, depending on the level of pollution in the upstream atmosphere (Zhao et al., 2020). In addition, BC aerosol concentrations are also influenced by the combination of the turbulent motion, temperature stratification, and wind field characteristics in the boundary layer. That is, physical processes in the boundary layer play important roles in the vertical distribution of BC aerosol.

At present, there are many individual case studies on the vertical distribution of BC aerosol (Altstdter et al., 2019; Lu et al., 2019). Zhao et al. (2019) and Shi et al. (2020) found BC aerosol through observations. Zhao et al. (2019) and Shi et al. (2020) found that the vertical structure of BC aerosol is strongly affected by local meteorological conditions, local pollution sources, land types, and atmospheric thermal and dynamic effects. However, when most studies are only 3–5 days, this article has been observed for 21 days and obtained 82 usable profiles. What’s more, there are the profiles under different stability conditions, which is more representative.

Table 1 lists a series of vertical sounding measurements conducted by researchers in China in recent years. Through comparison, these studies mainly discuss the physical characteristics of BC aerosols and their effects on radiation, and lack the influence of boundary layer physical processes on BC profile. However, the distribution of BC mass concentration in the boundary layer is strongly affected by the thermal and dynamic effects of the atmosphere, so research in this area is indispensable.

With this foundation as a starting point, ground-based observations and vertical observations of the boundary layer in ShouXian County, Anhui Province, in winter 2016 were used, among other data, to compare and analyze the effects of dynamic and thermal processes within the atmospheric boundary layer on the vertical distribution characteristics of BC aerosol under different stability conditions.

Experiment

Observation experiment

To understand in detail the variation characteristics of the vertical structure of BC aerosol in a typical rural area in eastern China, Nanjing University of Information Science and

TABLE 1 Comparison of research contents of BC vertical sounding in different regions of China.

Observation area	Observation time	Observation height	Research content	References
Shouxian	14.12.2016-03.01.2017	0–1000 m	Thermal and dynamic effects of boundary layer on the vertical distribution of BC	This article
Beijing	25.11.2018-27.11.2018	0–3000 m	Physical properties of BC vertical profile during heavy pollution and its effect on radiation	Zhao et al., 2020
Beijing	late spring and winter	500–2500 m	Physical characteristics and parameterization of tropospheric vertical BC discuss the influence of BC on radiation	Zhao et al., 2019
Beijing and Europe	Beijing: 09.04-2018; 12.11-2018 Europe: 09.04-2008; 12.11-2008	0–10000 m	The physical properties related to the particle size of BC. The relationship between BC and CCN, radiation is discussed	Ding et al., 2016b
Xuzhou	13.07.2018-15.07.2018	0–3000 m	The effect of BC on radiation	Liu et al., 2019
Nanjing	2016-2019	0–1000 m	BC profile classification. Assess the effect of BC on radiative forcing and heating rate	Shi et al., 2020

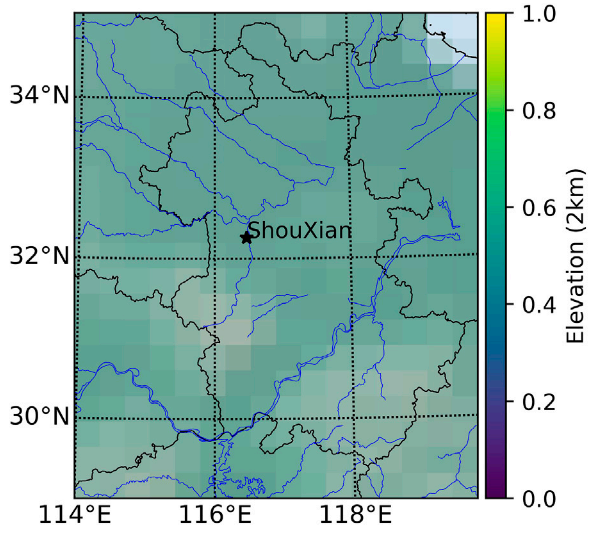

FIGURE 1
The location of the observation point. The black asterisk in the figure refers to ShouXian.

Technology (NUIST), together with Anhui Institute of Meteorological Science, conducted a 21-days comprehensive atmospheric boundary layer observation experiment in ShouXian County, Anhui Province, China, from 14 December 2016 to 3 January 2017. The observation site was the ShouXian National Climate Observatory (116.47E, 32.26N), the specific position is shown in Figure 1, located 9 km from the county, with flat surrounding terrain, homogeneous farmland in the subsurface, and no obvious pollution sources (Yang et al., 2017; Wang et al., 2020).

This experiment focused on the simultaneous observations of the three-dimensional structure of BC aerosol, PM2.5 and meteorological parameters. The ground observation instruments included a microAeth® AE-33 micro-aethalometer (Maggee, United States), a CAWSD600 automatic weather station (Huayun Technology Development, China), and a GRIMM180 particulate matter concentration monitor (GRIMM, Germany). The sampling frequency is 0.02HZ.

The vertical observation system mainly included a tethered balloon (XLS-II type, volume 5.25 m3; payload 5 kg, Supplementary Figure S1), a meteorological sensor (Institute of Atmospheric Physics, Chinese Academy of Sciences, Supplementary Figure S1) and a microAeth® AE-51 micro-aethalometer (Maggee, United States). Vertical observations were conducted eight times a day at 02, 05, 08, 11, 14, 17, 20, and 23 h (local time, local time = UTC + 8, same below). The collection frequency of meteorological data is 1HZ, while the collection frequency of BC and PM2.5 data is 0.2HZ. Due to the observation condition limitations, the observations were suspended when the wind speed was high (>7 m/s) or when precipitation occurred, so there were missing data in the later analysis.

The balloon ascent/descent rate (approximately 0.8 m/s) was controlled by an electric winch. Considering that the fish-shaped balloon was well balanced, the air flow disturbance was largely reduced during launch. Together with consideration of the timing accuracy of the observations, the ascent was chosen for the subsequent analysis.

Data processing

AE-51 has a measuring range of 0–1 mg m−3, a resolution of 1 ng m−3, an accuracy of 5%, and a sensitivity of < 0.1 μg m−3. The collected data were processed using the optimized noise-reduction averaging (ONA) algorithm (Hagler et al., 2011), and the light attenuation (ATN) of the averaging time window increments was determined by the internal filter of the instrument, reducing the light attenuation of the instrument(ΔATN), which in turn reduces the effect of instrument noise on the data. This expression is shown in Eq. 1 as follows:

$$BC_i = \frac{A_s}{Q \cdot E_{atn}} \times \frac{\Delta ATN_i}{\Delta t_i} \tag{1}$$

Where BC_i is the average mass concentration of black carbon (BC) aerosol in the i-th time interval (μg m−3);A_s is the sampling point area (7.1×10−6 m2); Q is the sampling flow rate (100 ml min−1);Δt_i is the sampling time interval (10s); andE_{atn} is the sampling time interval whenΔt_i is the effective mass absorption rate within the sampling interval.

AE-33 has an accuracy of 5% and a sensitivity of < 0.1 μg m−3. The dynamic zero-point test was performed at 00: 00 h in January of each month, and each test lasted for 20 min with a time resolution of 1 s. The average BC value of the zero-point test in this study was 0.01 ± 0.09 μg m−3; the BC values showed a normal distribution, and the expected value was 0.01 after fitting with the Gaussian distribution function, indicating that the instrument we used performed well during the observation period.

The data were measured using a dual-point measurement method (Virkkula et al., 2007; Cheng et al., 2018), and the BC aerosol mass concentration was calculated from the optical attenuation (ATN1 and ATN2) caused by two sampling points with different loading levels, as shown in Eqs 2, 3:

$$BC1_{raw} = BC_{zero\,loading} \times (1 - k \times ATN1) \tag{2}$$

$$BC2_{raw} = BC_{zero\,loading} \times (1 - k \times ATN2) \tag{3}$$

where BC1raw and BC2raw are the mass concentrations of BC aerosol at different flow rates through the sampling point (μg m−3), and BCzero loading is the revised value after removing the loading effect (μg m−3).

Considering that BC aerosol data measurements are affected by temperature, with the measured BC aerosol decreasing by 0.25 μg-m−3 for every 1°C increase in temperature within the sensor (Altstdter et al., 2019), this paper also applies a temperature revision to the BC data. Before the study, we verified the data quality of AE-33 and AE-51, see the attachment for details.

In addition, the sampling frequency of the meteorological data was 1 s/group. The collection frequency of AE-51 was 10 s/group. To eliminate mismatches between the meteorological data and BC data in the vertical direction, a 60-s averaging was performed for both datasets during the data processing. At the same time, unreasonable data from instrument malfunction or human factors were excluded. Variance tests, extreme value tests, and continuity tests were applied to control the quality of all observations and ensure data reliability and accuracy (Ren et al., 2015). The wind direction is divided into 16 directions, e.g., 348.75–360° and 0–11.25° are recorded as due north. 60-s mean wind direction is the most frequent wind direction occurring in the time frame.

In addition to the barometric pressure (P), temperature (T), relative humidity (RH), wind speed (WS) and wind direction (WD) data collected by the meteorological sensors, the atmospheric stability was calculated using the virtual potential temperature (VPT). For the calculation of VPT, see Eq. 4 (Wang, 1987) below:

$$VPT = T \times \left(\frac{P_0}{P}\right)^{\frac{R_d}{C_{pd}}} \left(1 + 6.08 \times 10^4 \left(\varepsilon \times \frac{e}{P - (1-\varepsilon)e} \times 1000\right)\right) \tag{4}$$

Where T is the measured air temperature (K);P andP_0 are the measured air pressure (hPa) and standard sea level pressure (hPa), respectively;R_d is the specific gas constant of dry air (287 J kg−1 K−1); C_{pd} is the specific heat capacity of dry air at a constant pressure and standard temperature (1005 J kg−1 K−1); ε is the mass ratio of water vapor molecules in air to dry air (0.622); and e is the water vapor pressure (hPa), which is the product of the saturation water vapor pressure at a given temperature (T) and relative humidity (RH).

The time series of ground pollutant concentrations and meteorological parameters during the observation period are shown in Figure 2. The solid lines and dotted lines in Figure 2A are the daily variations of BC aerosol and PM2.5, respectively. The solid lines and bars in Figure 2B are the relative humidity and precipitation, respectively. The solid line and arrows show the temperature and wind distribution respectively in Figure 2C, where the length of the arrow indicates the wind speed magnitude. During this period, the atmospheric circulation situation in the ShouXian area was relatively stable, with mainly cloudy weather, low surface wind speeds, high relative humidity, and small amounts of precipitation on 19-21 and 25-26 December. Under the influence of meteorological conditions, the BC aerosol and PM2.5 concentration trends were consistent, and there were 2 complete heavy pollution formation-dissipation processes (PM2.5 ≥ 150 μg m−3) during this period. That is, the first heavy pollution process on 18-20 December 2016, after which pollutants were rapidly cleared on the 21st under continuous precipitation flushing. The second heavy pollution process on 1–2 January 2017. After 13:00 on 2 January, the concentration of BC began to decrease, which was due to the elevation of the

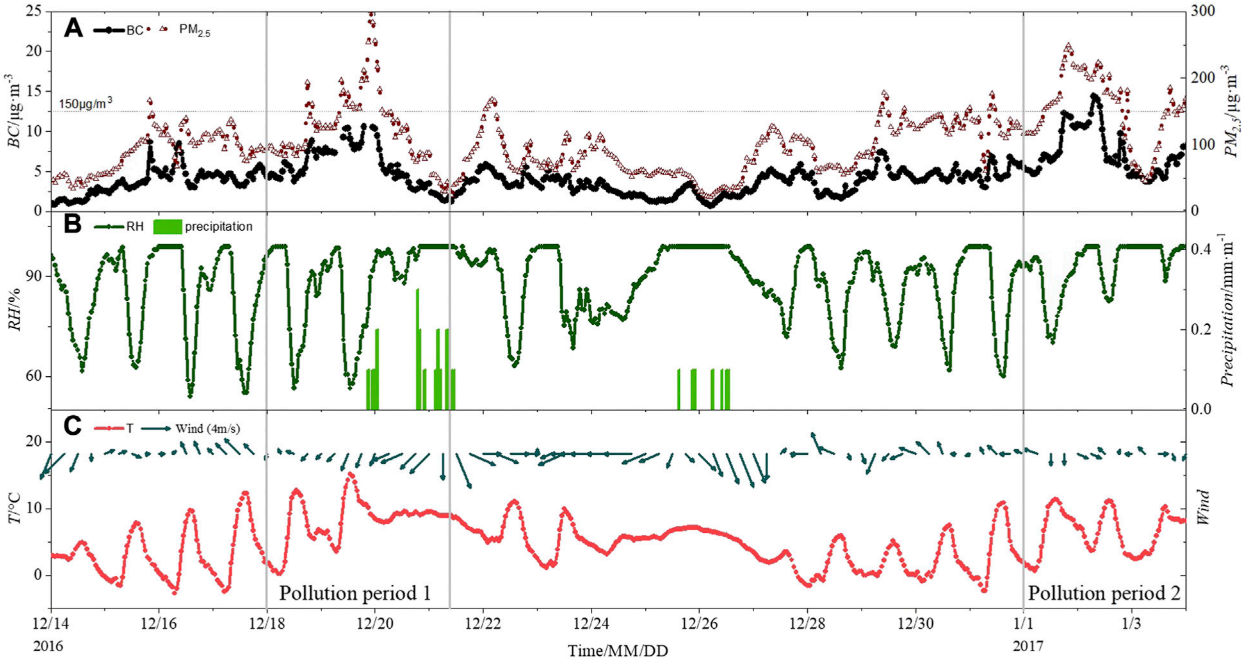

FIGURE 2
From 14 December2016 to 3 January 2017: the changes in ground pollutants and meteorological parameters over time **(A)** BC aerosol, $PM_{2.5}$; **(B)** relative humidity, precipitation; **(C)** temperature, wind).

boundary layer with the increase of solar radiation. The strong turbulent mixing effect caused BC to mix in the boundary layer, and combined with the clearing effect of high wind (Figure 10), the surface concentration decreased. After that, with the decrease of solar radiation and human activities, the pollutants gradually increased until the precipitation on the 4th (see Supplementary Figure S5 in the attachment), and the pollutants were removed.

Results and discussion

The atmospheric boundary layer structure has distinctive daily variation in its distribution characteristics due to the sunrise and sunset (Stull, 1988, See Supplementary Figures S3, S4 in the appendix). The boundary layer evolution process can be roughly divided into four periods according to differences in the vertical structure of the boundary layer: the unstable boundary layer period in the daytime, the unstable-to-stable boundary layer transition period in the evening (referred to as transition period 1), the stable boundary layer period at night, and the stable-to-unstable boundary layer transition period (transition period 2). Location of the maximum vertical gradient of virtual potential temperature was used to determine the height of the boundary layer by calculating the virtual potential temperature profile based on the temperature, humidity and wind speed profiles observed by the sounding. According to the Richardson number, the atmospheric stability is judged; the virtual potential temperature profile is compared with the typical profile (not shown here) of Stull (1988) to finally determine the boundary layer structure and type.

Atmospheric stability varies highly in the boundary layer at different times of the day. The ability of turbulence to disperse pollutants vertically varies, depending on the stability. Atmospheric stability also directly affects the vertical and horizontal transport of pollutants by changing the thermal and dynamic effects in the boundary layer. At this stage, the Richardson number (R_f) is used to determine the atmospheric stability (Vogelezang and Holslag, 1996; Seidel et al., 2012; Guo et al., 2016).R_f is defined as the ratio of buoyancy-related turbulence to mechanical shear-induced turbulence; when$R_f < 1$, the system is dynamically unstable, and when$R_f > 1$, the dynamics are stable (Stull, 1988). Due to the discontinuity of the observed height, the overall Richardson number is commonly used in practical calculations (R_B, Eq. 5). The Richardson number can be calculated as follows:

$$R_B = \frac{g \Delta \overline{VPT} \Delta Z}{\overline{VPT} (\Delta u)^2} \tag{5}$$

where g is the acceleration of gravity; VPT is the virtual potential temperature; Z is the height; and u is the horizontal wind speed. The data of two adjacent layers are used in the paper, and the Richardson number is calculated every 50 m.

TABLE 2 Profile statistics under different boundary layer conditions.

Boundary layer type	Total	Thermal effects dominate the profile	Dynamic effects dominate the profile
Unstable boundary layer	34	31	3
Transformation of unstable to stable boundary layer(Transition period 1)	8	8	0
Stable boundary layer	33	27	6
Transformation of stable to unstable boundary layer(Transition period 2)	7	6	1

In addition to atmospheric stability, wind speed is another important factor that affects the atmospheric dispersion capacity (Li, 1985). A study by Guiqin et al. (2016), Liu et al. (2002) and Sun et al. (2016) pointed out that wind speeds greater than 4 m/s in the boundary layer are favorable for pollutant dispersion. Therefore, in this paper, wind speeds (>4 m/s) and the vertical shear of horizontal wind speeds between two height layers (>1 m/s/50 m) are considered, with $R_B < 1$ as the judgment condition of the boundary layer dominated by dynamic action. The rest of the stability is attributed to the thermally controlled boundary layer.

Based on the above criteria, Table 2 counts the number of contour lines in each of the four boundary layers under the dominant dynamics and thermal controls. A comparative analysis showing the effects of dynamic and thermal processes within the atmospheric boundary layer on the vertical distribution characteristics of BC under different stability conditions was conducted. Due to the limitation of the tethered balloon sounding conditions, 82 effective profiles were obtained because observations could not be made under adverse weather conditions such as precipitation or high winds. Among the obtained cases, more cases were observed under unstable boundary layer and stable boundary layer conditions, with 34 and 33 cases, respectively; fewer cases were obtained for Transition 1 and Transition 2, with only 8 and 7 cases, respectively. Among all boundary layer types, the share of thermodynamic dominance was as high as 87.8%, especially in Transition1, where only thermodynamic dominance data were observed. The number of boundary layers dominated by dynamics was small, with a percentage of only 12.2%. However, previous studies have shown that wind plays an important role in the diffusion and three-dimensional transport of BC (Wang et al., 2001; Liu et al., 2002). Therefore, the influence of dynamics on variations in BC concentrations in the boundary layer cannot be ignored.

Figure 3 shows the vertical profile distribution of the average value of BC, temperature, virtual potential temperature, wind speed and wind direction obtained during the winter observation period. According to Figure 3A, the concentration of BC is the highest at the ground, about 11.01 $\mu g\ m^{-3}$, and decreases rapidly with height. The concentration of BC at 150 m decreases to 4.09 $\mu g\ m^{-3}$. In 150–800 m BC decreases only 2.20 $\mu g\ m^{-3}$ with height. Above 800 m, the BC concentration remains unchanged. The short blue line is the standard deviation line, and the standard deviation also decreases with the height, indicating that the concentration of BC changes higher at the low altitude, but few at the high altitude. The temperature profile in Figure 3B shows that from the ground to 150 m, the inversion is weak to the ground, but in the position temperature profile (Figure 3C), the virtual potential temperature increases slowly with the height, indicating a weak stable stratification ($\partial VPT/\partial z$=0.77K/100 m), and the wind speed gradually increases from 1 m/s to 3.3 m/s. Under the superposition of stratification conditions and wind, the concentration of BC decreases with height.

Although the BC concentration is generally high on the ground and low in the upper air, the shape of the BC profile is different under different boundary layer conditions. The influence of dynamic and thermal conditions on the BC concentration under different boundary layer conditions will be discussed in detail below.

Influence of the thermal effects of the boundary layer on the vertical structure of black carbon

Figures 4–7 show the distributions of BC, temperature, virtual potential temperature, wind speed and wind direction over the vertical profile under the four boundary layer conditions. Among them, a-e are the vertical distribution maps of each element under unstable boundary layer conditions. In the evolution process of boundary layer, due to the influence of weather, advection and other factors, sometimes the imaginary virtual potential temperature profile of each stage is not exactly the same as the diurnal cycle evolution profile of boundary layer of Stull. Under normal conditions, thermal action is the main reason for the formation of an unstable boundary layer. In particular, turbulent activity is strong in boundary layers due to the thermal forcing of the surface at noon. The vertical distribution of meteorological parameters within a boundary layer is more uniform under the effect of turbulent mixing. The virtual potential temperature profiles at 11:00 and 14:00 on 18 December 2016 basically meet the conditions that $\partial VPT/\partial z < 0$ near the ground and $\partial VPT/\partial z \approx 0$ in the middle and

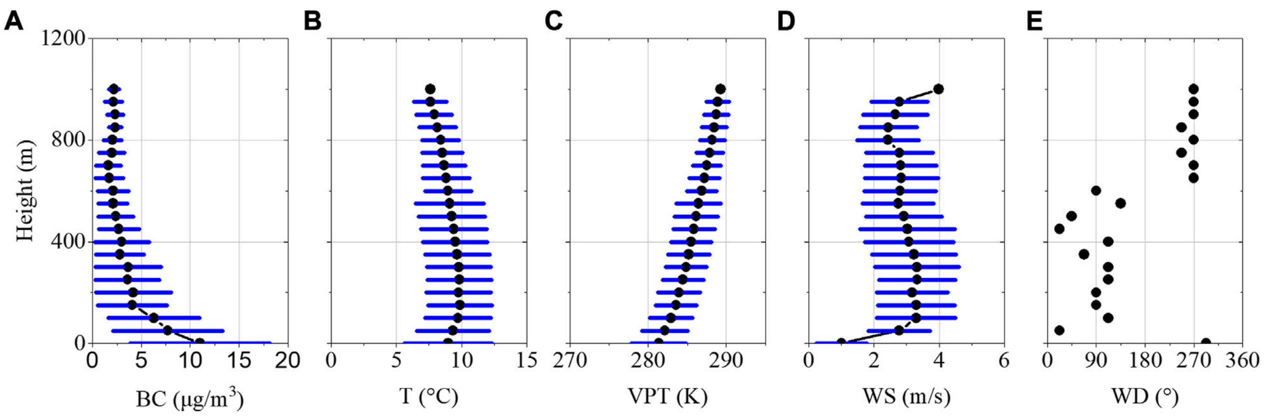

FIGURE 3
During winter observation period, BC, T, VPT, WS and WD contours. Blue lines are BC standard deviation line. **(A)** black carbon aerosol vertical profile, **(B)** temperature vertical profile, **(C)** virtual potential temperature vertical profile, **(D)** wind speed vertical profile, **(E)** wind direction vertical profile.

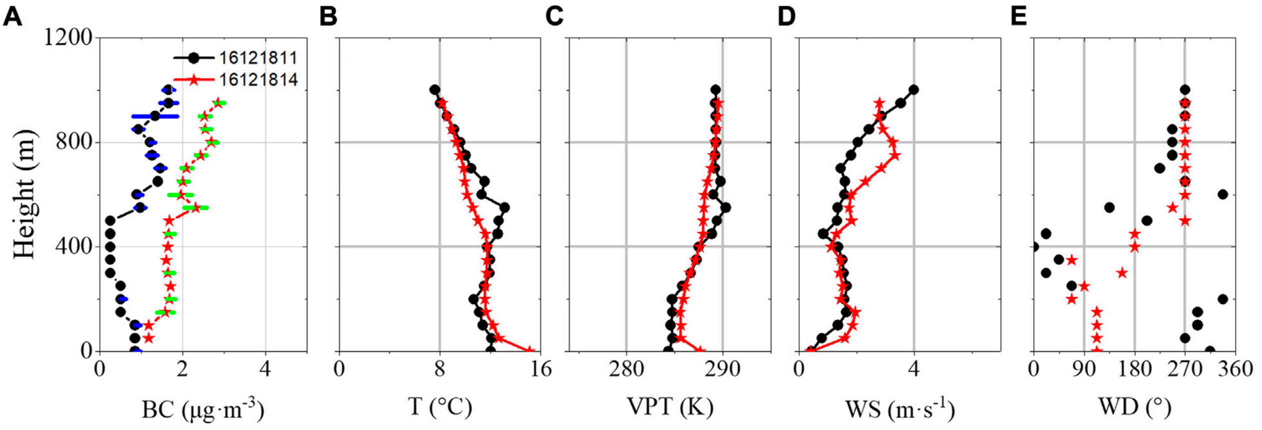

FIGURE 4
Thermally controlled unstable boundary layer BC, T, VPT, WS and WD contours. The black line indicates the contours of each element at 2016121811 and the red line indicates the contours of each element at 2016121814. Green and blue lines are BC error bars. **(A)** black carbon aerosol vertical profile, **(B)** temperature vertical profile, **(C)** virtual potential temperature vertical profile, **(D)** wind speed vertical profile, **(E)** wind direction vertical profile.

upper layers. In this paper, two times were used as typical individual cases among many samples for analysis. As seen in Figure 4A, the BC concentrations throughout the vertical profile (black dotted lines) at 11:00 on 18 December 2016 have slight differences among the three altitude ranges. The profiles below 200 m and above 550 m have large concentration values, 0.86 μg m^{-3} and 1.95 μg m^{-3}, respectively. Figure 4B and Figure 4C show the vertical profiles of temperature and virtual potential temperature. The temperature profile at the moment shown in the Figure indicates an overall decreasing trend, with a hanging inversion (intensity of 0.66°C/100 m) in the range of 200–550 m. The corresponding virtual potential temperature profile also shows a strong stable structure. The wind speed below 700 m (Figure 4D) is less than 1.5 m/s, and the wind direction (Figure 4E) is variable. In summary, the height of the mixed layer is approximately 200 m. The turbulent transport effect is strong, and horizontal transport is weak in the mixed layer. BC is more uniformly distributed in the lower layer, 200–550 m, and due to the existence of top inversion, turbulent mixing is suppressed. The vertical transport of BC is blocked and BC cannot enter the inversion layer, so the BC concentration is lower in this height interval.

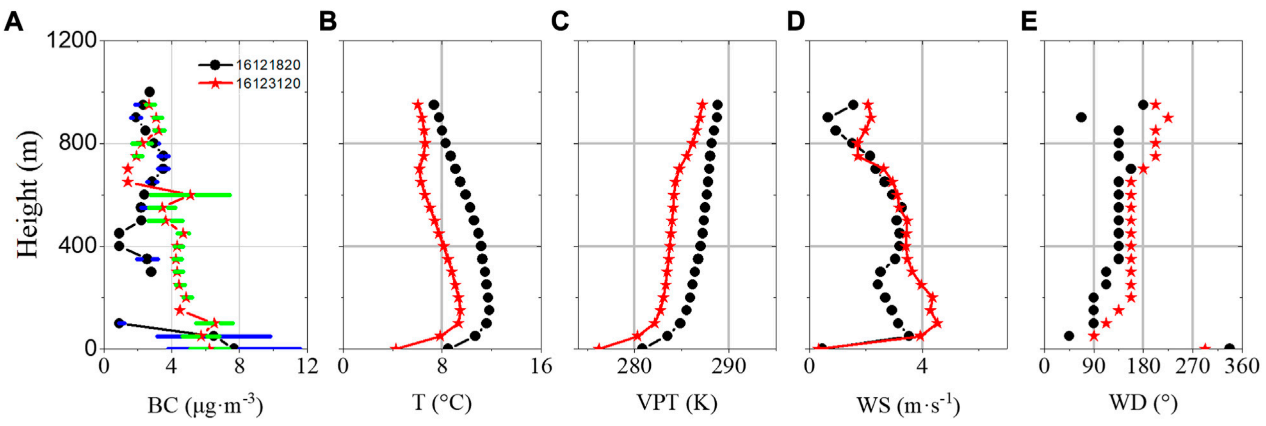

FIGURE 5
Thermally controlled transformation of unstable to stable boundary BC, T, VPT, WS and WD contours. The black line indicates the contours of each element at 2016121820 and the red line indicates the contours of each element at 2016123120. Green and blue lines are BC error bars. **(A)** black carbon aerosol vertical profile, **(B)** temperature vertical profile, **(C)** virtual potential temperature vertical profile, **(D)** wind speed vertical profile, **(E)** wind direction vertical profile.

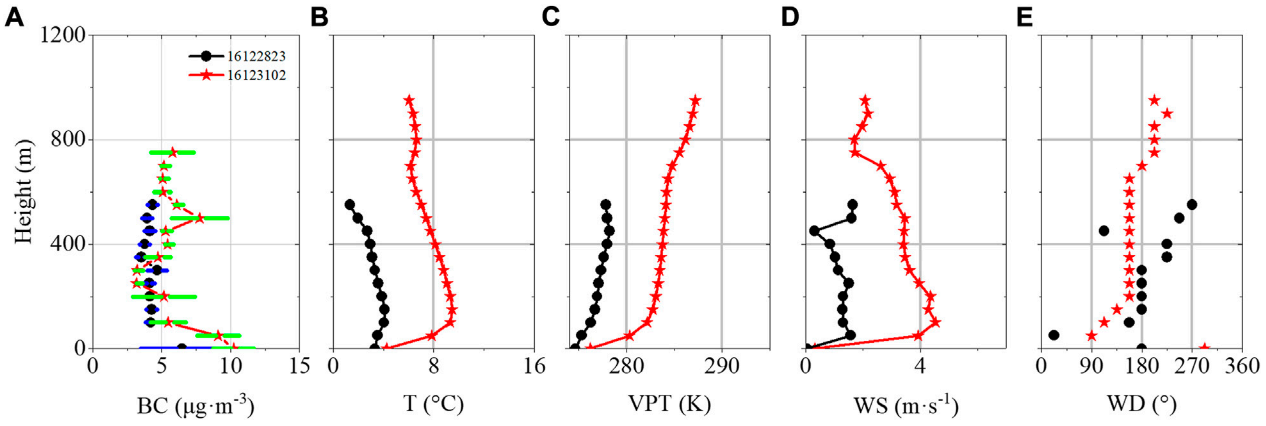

FIGURE 6
Thermally controlled stable boundary BC, T, VPT, WS and WD contours. The black line indicates the contours of each element at 2016122823 and the red line indicates the contours of each element at 2016122302. Green and blue lines are BC error bars. **(A)** black carbon aerosol vertical profile, **(B)** temperature vertical profile, **(C)** virtual potential temperature vertical profile, **(D)** wind speed vertical profile, **(E)** wind direction vertical profile.

The thermal effect is more obvious at 14:00 than at 11:00 on 18 December 2016. As seen in the figure, the suspended inversion disappears at 200 m. Turbulent activity within the mixed layer is stronger at this time than at other times. The vertical distribution of BC (red dotted line) is more uniform, with an average concentration of 2.19 μg m^{-3}. From the ground to a height of 50 m is a superadiabatic layer with a decreasing temperature rate of up to 4.85°C/100 m. The layer junction is in a strongly unstable state ($\partial VPT/\partial z = -4.11K/100m$). The vertical wind speed profile is similar to that seen at 11:00, with a slight shift in the wind direction. Therefore, in such a boundary layer, the layer junction is extremely unstable. Turbulent activity caused by the thermal effect is strong. Convection in the vertical direction is strong. The influence of the dynamic effect on BC remains small, and BC is uniformly mixed in the vertical direction with concentration fluctuations <0.5 μg m^{-3}.

Figure 5A–E shows the structures of the vertical distributions of the parameters during transition 1. In the evening, surface radiation cools as solar radiation disappears. Ground inversion occurs, with the lower layers showing stable boundary layer

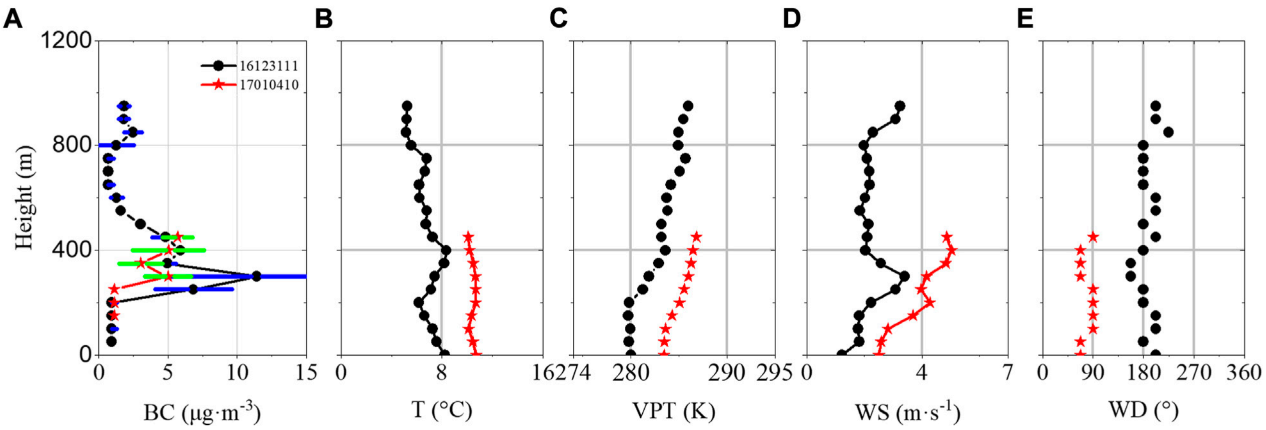

FIGURE 7
Thermally controlled transformation of stable to unstable boundary BC, T, VPT, WS and WD contours. The black line indicates the contours of each element at 2016122311 and the red line indicates the contours of each element at 2017010410. Green and blue lines are BC error bars. **(A)** black carbon aerosol vertical profile, **(B)** temperature vertical profile, **(C)** virtual potential temperature vertical profile, **(D)** wind speed vertical profile, **(E)** wind direction vertical profile.

characteristics, and pollutants decrease with height. The upper layers retaining unstable boundary layer characteristics from the previous moment, the vertical distribution of pollutants is relatively uniform. The temperature profiles of 20:00 on 18 December 2016 and 20:00 on 31 December 2016 are the closest to the standard profile, so they are analyzed as typical cases in this period. From the BC concentration profile obtained at 20:00 on the 18th (Figure 5A; black dotted line), it can be seen that the concentration of BC in the lower layer is significantly larger than that in the upper layer. The near-surface mean concentration is approximately 7.7 μg m^{-3}, which decreases rapidly with increasing height (BC data are missing at 150–250 m). The BC concentration above 300 m is approximately 2.3 μg m^{-3}. In Figures 5A,B strong ground inversion occurs below 100 m, with an intensity of approximately 3.1°C/100 m. The virtual potential temperature profile also shows a strong stable structure (see Figure 5C). The temperature and virtual potential temperature profiles above 100 m are similar to those at 17:00 (omitted), which reflect the atmospheric characteristics of the upper layers retained at the peak of the mixed layer development after turbulence disappears. At 20:00, due to the weak vertical transport of turbulence in the ground inversion layer combined with the effect of evening peak motor vehicle emissions, BC in the near-earth layer cannot be transported upward, and the upper layers retain their concentrations from the previous time period. The BC concentrations in the lower layers are significantly larger than those in the upper layers.

The profiles of each element (red dotted lines) at 20:00 on the 31 December 2016 are similar to those seen at 20:00 on the 18th. Additionally, the characteristics of the two boundary layer types at the time of Transition 1 are shown. The BC profile is distributed in two segments. From the surface to 550 m, the BC concentration slowly decreases from 6.2 μg $m^{-3}$to 3.2 μg m^{-3}. Above 550 m, the average BC concentration is 1.9 μg m^{-3}. A strong ground inversion occurs below 100 m at this time, with an intensity of approximately 5.06°C/100 m. The virtual potential temperature profile also shows a strong stable structure. The temperature and temperature profiles above 100 m still retain the characteristics of the atmosphere at the peak mixed layer development. It can be seen from the above that during Transition 1, an inversion appears close to the ground, and the turbulence-induced vertical transport is weak. The BC concentration values decrease continuously with height inside the inversion layer. However, outside the inversion layer, the BC concentration is still characterized by an unstable boundary layer.

Figure 6A–E shows the structures of the vertical distributions of the parameters of stable boundary layers. The stratification is more stable here than Transition 1 due to continued radiative surface cooling, weak turbulent activity and increased ground inversion thickness, which often occurs from night to early morning. The near-ground $\partial VPT/\partial z>0$ at 23:00 on 28 December and at 0:00 on 31 December 2016 is an obvious virtual temperature profile characteristic at the stable boundary. Therefore, this paper takes it as a typical case for analysis. During the high ground level BC concentrations seen at 23:00 on the 28th, ground level concentration was 6.5 μg m^{-3}. The data are missing for the layer from 50–100 m, and the concentrations above 100 m fluctuate around approximately 4.1 μg m^{-3}. In the temperature profile (Figure 6B), the inverted temperature is close to the ground below 100 m, while the corresponding virtual potential temperature (Figure 6C) increases with height. The wind speed and direction (Figure 6D,E) have less effects on the BC concentration than does temperature. In the stable boundary layer, the turbulent vertical transport is weak. Near-surface BC cannot reach high altitudes, and high altitudes are still characterized by daytime mixed layers. The BC profile is clearly stratified.

At 02:00 on 31 December 2016, the stable boundary layer characteristics were still obvious. Due to the thermal effect, the BC profile could be divided into two segments. Below 200 m, the average BC concentration is larger than above, at approximately 9.3 μg m^{-3}. Above 200 m, the BC concentration fluctuates at approximately 3.0 μg m^{-3}. The ground inversion temperature ranges from 0 to 200 m, and the intensity is 1.36°C/100 m. The virtual potential temperature profile also shows a strong stable structure. The wind speed of the whole layer is less than 3 m/s. In summary, stable boundary layers where thermodynamic effects dominate often have strongly stable structures with inversion temperatures. The wind speed is small; the turbulence activity is weak; BC diffuses poorly in the vertical direction; and the profile shows a two-segment distribution of with the lower level characterized by high BC and the upper level characterized by low BC.

Figure 7A–E shows the vertical structure profile of each element during Transition 2. The stable boundary layer is transitioning to an unstable boundary layer, which often occurs during the morning hours. The surface is heated by the solar radiation that it receives. The thermal effect strengthens the turbulent activity, and the heat is transferred upward. The ground inversion in the lower part of the boundary layer disappears, while the upper part remains a stable layer junction. At 11:00 on 31 December 2016 and 10:00 on 4 January 2017, the virtual potential temperature profile satisfies the conditions that the near ground $\partial VPT/\partial z$ is slightly less than 0, the middle layer $\partial VPT/\partial z > 0$, and the upper layer $\partial VPT/\partial z \approx 0$, which is most similar to the standard profile. In this paper, we choose 11:00 on 31 December 2016 and 10:00 on 4 January 2017 as typical cases for analysis. The BC (Figure 7A) profile shows a nose-like structure at 11:00 on 31 December. The concentration remains at a constant value of 0.9 μg m-3 below 200 m. At heights of 200–300 m, the concentration of BC increases with height up to 11.4 μg m^{-3}, followed by reduced concentration at 300–500 m. Above500 m, the concentration fluctuates between 0.7 and 2.1 μg m^{-3}. The ground inversion (Figure 7B) disappears due to solar radiation, and an overhanging inversion develops at 200–400 m. The virtual potential temperature profile (Figure 7C) hardly varies with height below 200 m, and above 200 m, it shows a stable layer junction. The wind speed and direction (Figure 7D,E) indicate a small southerly wind. Because the wind speed at 400 m reached 7 m/s on 30 December (figure omitted), the wind direction was southerly, Hefei urban area transmitted a large number of pollutants to Shouxian. BC accumulates in the suspended inversion layer, where the turbulent activity inside the overhanging inversion layer is weak, and BC cannot be exchanged with the outside layers. The concentration is 5.2 μg m^{-3} higher inside than outside the inversion layer.

At 10:00 on 4 January 2017, the profile distribution of each element was similar to that at 11:00 on 31 December. The near-surface turbulent activity is strong, the ground inversion disappears and an unstable boundary layer appears. However, the turbulent activity aloft is weak, and there is an overhanging inversion at heights of 100–250 m. The decreasing rate of the virtual potential temperature below 100 m ($\partial VPT/\partial z$=0.15 K/100 m) is less than the increasing rate of the upper level ($\partial VPT/\partial z$=0.85 K/100 m). Under this layer condition, the BC profile is divided into two segments. At 150 m–250 m, there is a constant BC concentration of 0.9 μg m^{-3}. At 250 m–450 m, the concentration increases to 5.4 μg m^{-3}. During the transition from a stable to unstable boundary layer, the ground inversion disappears. However, the upper layers still retain its inversion structure. When the stable boundary layer changes to the unstable boundary layer, the ground-level inversion disappears, but the inversion structure still remains in the upper layer. Weak turbulent transport makes it impossible for black carbon to break through the bottom of the suspended inversion layer, resulting in the difference of BC concentration inside and outside the inversion layer.

Sometimes, in the unstable boundary layer, the ground is superadiabatic, and turbulent activity caused by thermal effects is strong. Under these conditions, BC is mixed uniformly in the vertical direction, and the fluctuation range of the concentration is less than 2.5 μg m^{-3}. In Transition 1, a ground inversion of temperature appears. The turbulence-induced vertical transport capacity is weak. The BC concentration decreases continuously with height. The intensity of the ground inversion in the stable boundary layer strengthens continuously with time, and BC accumulates near the ground. In Transition 2, due to the emergence of solar radiation, the near-surface turbulence activity is enhanced. The ground inversion disappears, but the upper layers still retain their inversion structure. The BC profile is split by the overhanging inversion, and high BC concentrations appear in the upper layers, with concentration differences up to 4 μg m^{-3}.

Effect of boundary layer dynamics on the vertical structure of black carbon

From January 1st to 2 January 2017, the surface $PM_{2.5}$ increased rapidly from 116.42 μg m^{-3} to 227.65 μg m^{-3} from 04:00 to 18:00 on 1 January. From 16:00 on 1 January to 13:00 on 2 January, surface $PM_{2.5}$ fluctuated at 214.25 μg m^{-3}. After 13:00 on 2 January, $PM_{2.5}$ concentration began to decrease. The diurnal variation of air temperature decreased with the increase

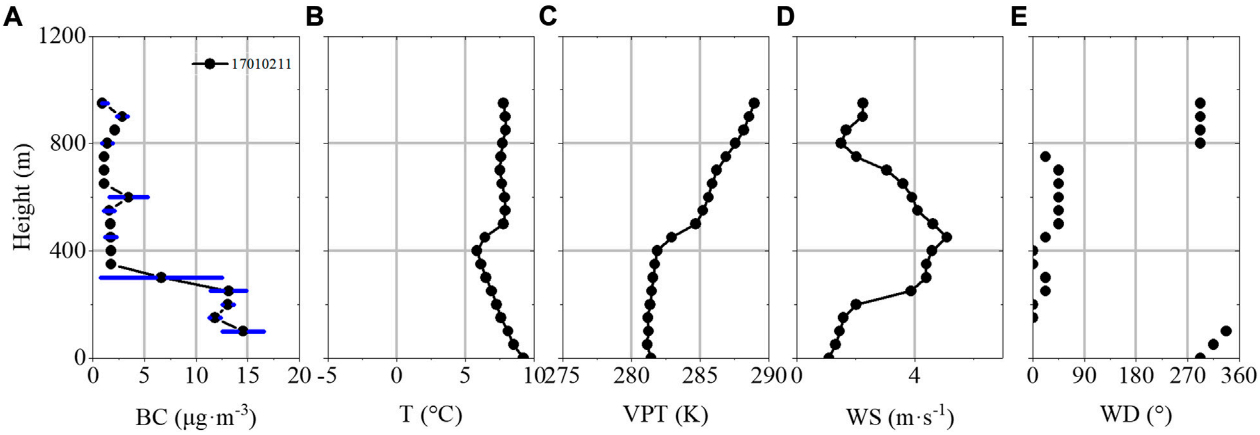

FIGURE 8
Dynamic controlled unstable boundary BC, T, VPT, WS and WD contours. The black line indicates the contours of each element at 2017010211. Blue lines are BC error bars. **(A)** black carbon aerosol vertical profile, **(B)** temperature vertical profile, **(C)** virtual potential temperature vertical profile, **(D)** wind speed vertical profile, **(E)** wind direction vertical profile.

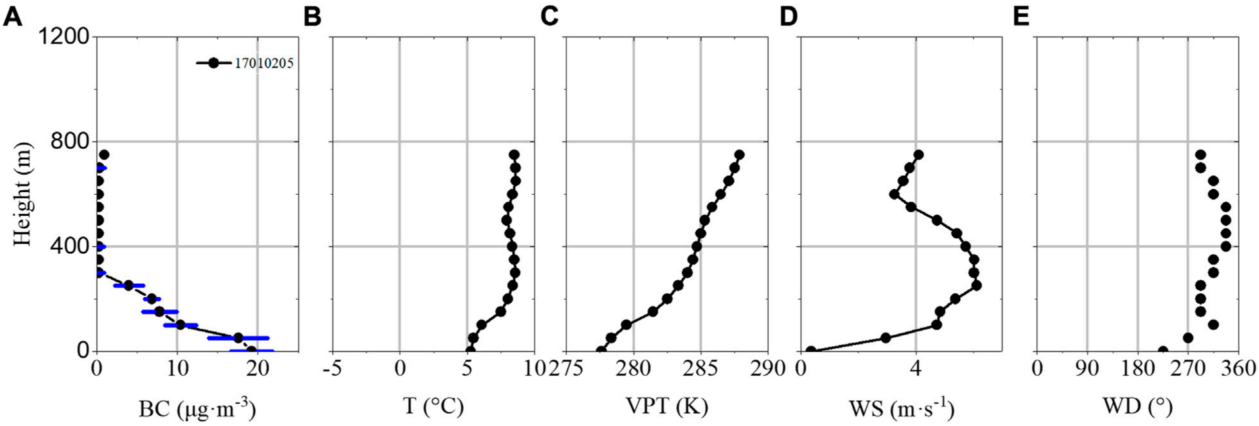

FIGURE 9
Dynamic controlled stable boundary BC, T, VPT, WS and WD contours. The black line indicates the contours of each element at 2017010205. Blue lines are black carbon error bars. **(A)** black carbon aerosol vertical profile, **(B)** temperature vertical profile, **(C)** virtual potential temperature vertical profile, **(D)** wind speed vertical profile, **(E)** wind direction vertical profile.

of $PM_{2.5}$ concentration, and the relative humidity was always above 70%. The surface wind speed is between 0.35 m/s and 2.95 m/s, and the dominant wind direction is north and northwest. There is weak northerly wind pollution transport. Meanwhile, the track 24 h after 00:00 on 2 January, (Supplementary Figure S6), also shows that there is weak northerly wind cold transport.

The selection of typical profiles under different boundary layer conditions when the dynamic action is dominant is consistent with that when the thermal effect is dominant. The time when the temperature profile is most similar to the standard profile is selected as a typical case. Figures 8–10 the vertical profiles of BC, temperature, virtual potential temperature, wind speed and wind direction for different boundary layer conditions when the dynamic effects dominate. Only three boundary layer types are available due to the lack of data for Transition 1, when dynamic effects dominate. At 11:00 on 2 January 2017, the dynamically controlled unstable boundary layer (Figure 8A–E) is characterized by some similarities to the thermally controlled layer, such as high turbulent activity. However, when high wind speeds occur, high winds have a powerful transport effect on material at the corresponding heights. As seen in Figure 8A, below 200 m, the BC concentration is high, approximately 12.9 μg m^{-3}. Then, it decreases slowly with height to

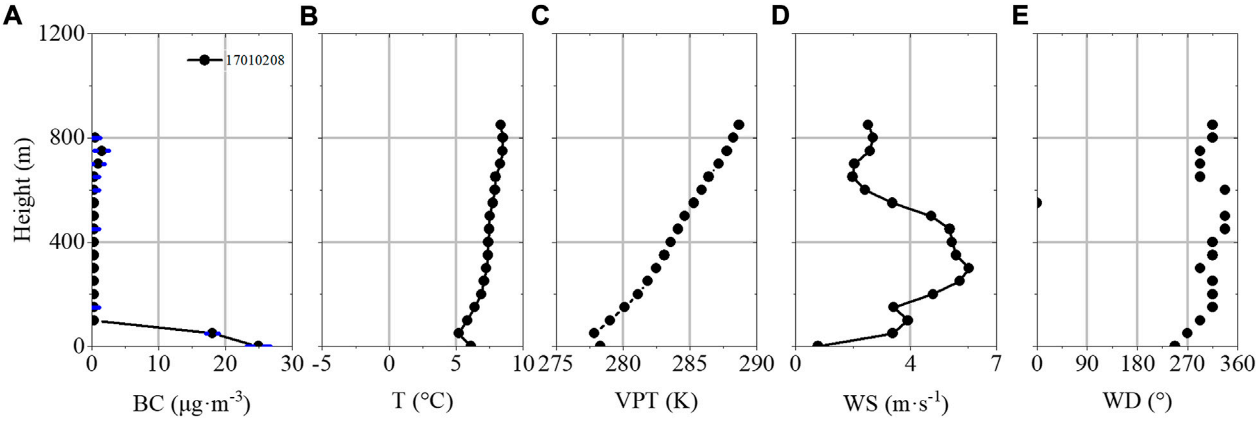

FIGURE 10
Dynamic controlled transformation of stable to unstable boundary BC, T, VPT, WS and WD contours. The black line indicates the contours of each element at 2017010208. Blue lines are BC error bars. **(A)** black carbon aerosol vertical profile, **(B)** temperature vertical profile, **(C)** virtual potential temperature vertical profile, **(D)** wind speed vertical profile, **(E)** wind direction vertical profile.

1.2 μg m^{-3} at 350 m. Above 350 m, the concentration fluctuates at approximately 1.4 μg m^{-3}. Below 400 m, the temperature (Figure 8B) decreases with height, and the corresponding virtual potential temperature (Figure 8C) is almost constant. The wind speed (Figure 8D) has a nose-like structure in the profile. From 200–450 m, the wind speed increases rapidly from 2 m/s to 5 m/s. Above 450 m, the wind speed decreases with height. From the ground to an altitude of 700 m, westerly winds change clockwise to northerly winds (Figure 8E). In summary, when the wind speed is small, the characteristics of the thermally controlled boundary layer are more obvious. For instance, below 200 m, the turbulence activity is strong, and the BC concentration is uniformly distributed. As the wind speed increases, gales play a diffusion and removing role for BC. For example, above 200 m, the BC concentration decreases slowly with height.

Figure 9A–E show the vertical structure profiles for each element of stable boundary layers under dynamic control. In this paper, we choose 05:00 on 2 January 2017 as typical cases for analysis. BC (Figure 9A) has the highest concentration at the ground level, reaching 19 μg m^{-3}. From the ground to 300 m, BC decreases rapidly with height. Then fluctuating at approximately 0.3 μg m^{-3} above 300 m. In Figure 9B and Figure 9C, there is a ground inversion below 300 m with an intensity of approximately 1.11°C/100 m, exhibiting a strong stable structure ($\partial VPT/\partial z$ = 2.12 K/100 m). The wind speed (Figure 9D) profile shows an obvious nose-like structure in the height range from 50–600 m. The maximum wind speeds appear at 300 m and 6 m/s, and the wind direction is northwest (Figure 9E). Above 300 m, the wind speed remains >4 m/s. It is thus clear that the wind speed is high in the whole layer, and the gusty wind plays a scavenging role on BC. The BC concentration decreases with height at the lower level (300 m) under the combined effect of the ground inversion and gusty winds. The BC concentration is still low at high altitudes due to high winds. Therefore, the BC profile shows a clear structure of low-level high concentrations and upper-level low concentrations.

During Transition 2 (Figure 10A–E, 08:00 on 2 January 2017), the unstable boundary layer starts to disappear due to solar radiation. The BC (Figure 10A) concentration is highest fluctuated around the surface (25.0 μg m^{-3}) and fluctuates at approximately 0.38 μg m^{-3} above 100 m. Turbulence activity is intense from 0–100 m, and the layer junction is extremely unstable (Figure 10B,C, $\partial VPT/\partial z$ = -0.92 K/100 m). The top inversion temperature remains above 100 m. The wind speed at 50–600 m (Figure 10D) is higher than 4 m/s, and the nose-like structure is obvious. The wind direction (Figure 10E) is a uniform northwest wind. During Transition 2, the BC concentration decreases rapidly at heights of 50–100 m due to the effect of the top cover inversion. Above 50 m, high winds can significant lower BC concentration. Therefore, the BC concentration is high in the lower layer and low in the upper layer, and the high and low air stratification is more obvious under these conditions than that under thermal control.

Clearly, under dynamically dominated boundary layer conditions, high winds play a diffuse removing role for BC, in agreement with Altstdter et al. (2019), Wei et al, (2020), Caputi et al., 2018, Miao et al., 2019, and others. However, due to the small amount of data in this study, there may still be some errors in the vertical profile distribution of BC in the actual winter boundary layer, and more data are needed to further validate definitive conclusions. In addition, due to the small amount of data used in this study, there may still be some errors within the vertical profile distribution of black carbon in the actual winter boundary layer. More data are needed to further verify this conclusion.

Conclusion

In this study, vertical observations of BC and meteorological parameters in the ShouXian County area during the winter of 2016 were used to analyze and discuss the influence of the thermal and dynamic characteristics of the boundary layer on the vertical distribution of BC. The results are as follows.

1) A total of 82 effective profiles were obtained during the observation period, with a small proportion, 12.2%, dominated by dynamic effects, and the rest representing boundary layer profiles dominated by thermal effects. Among the four boundary layer types, the unstable boundary layer and stable boundary layer appeared more frequently, 34 and 33 times, respectively; the occurrence numbers of Transition 1 and Transition 2 cases were 8 and 7, respectively.

2) When thermodynamics dominate, in the unstable boundary layer, turbulence activity is strong, convection in the vertical direction is strong, and BC is evenly distributed in the vertical direction. During Transition 1, the ground inversion temperature appears, and the turbulence activity is weak. The BC concentrations in the near-ground layer cannot be transported upward. The BC concentrations in the unstable boundary layer are retained in the upper layers, and the BC concentrations in the lower layers are significantly larger than those in the upper layers. In the stable boundary layer, the ground inversion is deeper than that in the unstable layer, and the layer junction is more stable. Under these conditions, turbulence activity is further suppressed, and the BC concentration decreases continuously with height. During Transition 2, an overhanging inversion appears, turbulence activity in the inversion layer is weaker, BC cannot be exchanged with the outside world, the profile is divided by the overhanging inversion, and the concentrations show high values in the upper layers.
3) The BC profiles are similar to that of the thermodynamically dominated profile when these dynamics are dominant. The BC concentrations are evenly distributed in regions of low wind speeds in unstable boundary layers and decrease significantly in regions of high wind speeds (>4 m/s). In stable boundary layers and during Transition 2, the wind removal effect is significant, the BC concentration is higher in the lower layer and lower in the upper layer, and stratification is more obvious than that observed under thermal control.

This study did not consider the influence of regional transport on the BC profile, and there are still many shortcomings. Meanwhile, BC has a strong absorption effect on solar shortwave radiation. If further studies confirm the relationship between BC aerosol profile distribution and boundary layer evolution, this paper can provide a profile reference for subsequent radiation simulations and can provide a feasible idea for air pollution control.

Data availability statement

The raw data supporting the conclusions of this article will be made available by the authors, without undue reservation.

Author contributions

WC-G and WX-L are responsible for data processing and thesis writing. YJ-D is responsible for observing instrument maintenance. NT is responsible for the observation test.

Funding

This study was supported by the National Natural Science Foundation of China (Grant 41975011).

Acknowledgments

We thank the ShouXian County National Climate Observatory for providing ground-level meteorological data and pollutant data and the hard-working teachers and students who conducted the observation experiments.

Conflict of interest

The authors declare that the research was conducted in the absence of any commercial or financial relationships that could be construed as a potential conflict of interest.

Publisher's note

Supplementary material

The Supplementary Material for this article can be found online at: https://www.frontiersin.org/articles/10.3389/feart.2022.1012085/full#supplementary-material

SUPPLEMENTARY FIGURE S1

A tethered balloon and a meteorological sensor. In this observation test, AE-33 micro-Aethalometer measured ground BC data and AE-51 measured high-altitude BC data. In order to verify the consistency of data quality measured by the two instruments, the two kinds of BC data are compared and verified in this paper. In the preparation stage for the moored motorboat to lift off, we turn on the AE-51 collector, so we have a period of time to measure on the ground. We use the ground data during this period of time to compare and verify the ground black carbon data measured by AE-33. Supplementary Figure S1 shows the comparison of ground black carbon concentration observed by AE-33 and AE-51 black carbon measuring instruments. The results show that, the correlation coefficient of the black carbon mass concentration data after correction by the two instruments reached 0.92, the value difference was small, and the change trend was the same. Therefore, it is believed that the observation results of AE-33 and AE-51 in this observation test are consistent.

SUPPLEMENTARY FIGURE S2

Comparison of ground black carbon concentration observations between AE-33 and AE-51 black carbon measuring instruments.

SUPPLEMENTARY FIGURE S3

Schematic diagram of the evolution of the boundary layer (Stull, 1988).

SUPPLEMENTARY FIGURE S4

Average virtual potential temperature profile of a typical profile (Stull, 1988). Stull R. B. An introduction to boundary layer meteorology. Klumer Academic Publishers, Dordretch, 665pp, 1988.

SUPPLEMENTARY FIGURE S5

Changes of surface pollutants and meteorological parameters over time from 1 January to 4, 2017 Relative humidity, precipitation, temperature **(B)** BC aerosol, wind direction, wind speed.

SUPPLEMENTARY FIGURE S6

Backward trajectory diagram of 00:00 on 2 January forward 24 h.

References

Altstdter, B., Deetz, K., Vogel, B., Babi, K., Lohou, F., Pacifico, F., et al. (2020). The vertical variability of black carbon observed in the atmospheric boundary layer during dacciwa. *Atmos. Chem. Phys.* 20 (13), 7911–7928. doi:10.5194/acp-20-7911-2020

Caputi, D. J., Faloona, I., Trousdell, J., Smoot, J., and Conley, S. (2018). Residual layer ozone, mixing, and the nocturnal jet in California's San Joaquin Valley. *Atmos. Chem. Phys.* 19, 4721–4740. doi:10.5194/acp-2018-854

Cass, G. R., Boone, P. M., and Macias, E. S. (1982). *Emissions and air quality relation-ships for atmospheric carbon particles in los angeles*. New York: Wolff, 207–244. doi:10.1007/978-1-4684-4154-3_13

Cheng, D., Wu, C., Wu, D., Liu, J., and Tian, Z. (2018). Characteristics of black carbon aerosols in urban guangzhou: Influencing factors in dry and rainy seasons. *Acta Sci. Circumstantiae* 38 (6), 2223–2232. doi:10.13671/j.hjkxxb.2018.0010

Corrigan, C. E., Roberts, G. C., Ramana, M. V., Kim, D., and Ramanathan, V. (2008). Capturing vertical profiles of aerosols and black carbon over the Indian Ocean using autonomous unmanned aerial vehicles. *Atmos. Chem. Phys.* 7 (4), 737–747. doi:10.5194/acp-8-737-2008

Countess, R. J., Wolff, G. T., and Cadle, S. H. (1980). The denver winter aerosol: A comprehensive chemical characterization. *J. Air Pollut. Control Assoc.* 30 (11), 1194–1200. doi:10.1080/00022470.1980.10465167

Delong, Z., Xuexi, T., Yang, G., Qiang, Z., Haijun, T., Kai, B., et al. (2015). In-situ aircraft measurements of the vertical distribution of black carbon in the lower troposphere of beijing, China, in the spring and summer time. *Atmosphere* 6 (5), 713–731. doi:10.3390/atmos6050713

Ding, A. J., Huang, X., Nie, W., Sun, J. N., Kerminen, V., Petaja, T., et al. (2016a). Enhanced haze pollution by black carbon in megacities in China. *Geophys. Res. Lett.* 43 (6), 2873–2879. doi:10.1002/2016GL067745

Ding, A. J., Huang, X., Nie, W., Sun, J. N., Kerminen, V. M., Petäjä, T., et al. (2016b). Size-related physical properties of black carbon in the lower atmosphere over beijing and europe. *Environ. Sci. Technol.* 53 (19), 11112–11121. doi:10.1021/acs.est.9b03722

Duforêt, L., Frouin, R., and Dubuisson, P. (2007). Importance and estimation of aerosol vertical structure in satellite ocean-color remote sensing. *Appl. Opt.* 46 (7), 1107–1119. doi:10.1364/AO.46.001107

Gordon, H. R. (1997). Atmospheric correction of ocean color imagery in the Earth Observing System era. *J. Geophys. Res.* 102 (D14), 17081–17106. doi:10.1029/96JD02443

Guiqin, F. U., Zhang, X., You, F., Tian, Y., and Erjie, L. I. (2016). Effect of meteorological conditions on PM2.5 concentration in shijiazhuang of hebei. *J. Arid Meteorology* 34 (02), 349–355. doi:10.11755/j.issn.1006-7639(2016)-02-0349

Guo, J., Miao, Y., Zhang, Y., Liu, H., Li, Z., Zhang, W., et al. (2016). The climatology of planetary boundary layer height in China derived from radiosonde and reanalysis data. *Atmos. Chem. Phys.* 16 (20), 13309–13319. doi:10.5194/acp-16-13309-2016

Hagler, G. S. W., Yelverton, T. L. B., Vedantham, R., Hansen, A. D. A., and Turner, J. R. (2011). Post-processing method to reduce noise while preserving high time resolution in aethalometer real-time black carbon data. *Aerosol Air Qual. Res.* 11 (5), 539–546. doi:10.4209/aaqr.2011.05.0055

Herich, H., Hueglin, C., and Buchmann, B. (2011). A 2.5 year's source apportionment study of black carbon from wood burning and fossil fuel combustion at urban and rural sites in Switzerland. *Atmos. Meas. Tech.* 4 (7), 1409–1420. doi:10.5194/amt-4-1409-2011

Huang, X., Wang, Z., and Ding, A. (2018). Impact of aerosol-PBL interaction on haze pollution: Multiyear observational evidences in north China. *Geophys. Res. Lett.* 45 (16), 8596–8603. doi:10.1029/2018GL079239

Li, J., Fu, Q. Y., Huo, J. T., Wang, D. F., Yang, W., Bian, Q. G., et al. (2015). Tethered balloon-based black carbon profiles within the lower troposphere of Shanghai in the 2013 East China smog. *Atmos. Environ. X.* 123, 327–338. doi:10.1016/j.atmosenv.2015.08.096

Li, Z. K. (1985). *Principles and applications of air pollution Meteorology*. Beijing: Meteorological Press, 0195.

Liang, R., Deng, Z. Z., Xu, X. B., Yan, P., Lin, W. L., Wang, Y., et al. (2016). Vertical profiles of black carbon measured by a micro-aethalometer in summer in the North China Plain. *Atmos. Chem. Phys.* 16 (16), 10441–10454. doi:10.5194/acp-16-10441-2016

Liu, D., Zhao, D., Xie, Z., Yu, C., Ding, D., Tian, P., et al. (2019). Enhanced heating rate of black carbon above the planetary boundary layer over megacities in summertime. *Environ. Res. Lett.* 14 (12), 124003. doi:10.1088/1748-9326/ab4872

Liu, Y., Wang, S., Shang, K., Yang, D., and Bin, Q. I. (2002). Time-space changing character of low-level wind in lanzhou city and its correlation with air pollution. *Plateau Meteorol.* 21 (3), 322. doi:10.3321/j.issn:1000-0534.2002.03.015

Lu, Y., Wang, Q. G., and Zhang, Y. Y. (2015). Remediation of PAH-contaminated soil by the combination of tall fescue, arbuscular mycorrhizal fungus and epigeic earthworms. *J. Hazard. Mat.* 51 (3), 535–541. doi:10.1016/j.jhazmat.2014.07.021

Lu, Y., Zhu, B., Huang, Y., Shi, S., Wang, H., An, J., et al. (2019). Vertical distributions of black carbon aerosols over rural areas of the Yangtze River Delta in winter. *Sci. Total Environ.* 661 (APR.15), 1–9. doi:10.1016/j.scitotenv.2019.01.170

Luan, S., and Mao, J. (1987). Measurements of the absorption coefficient of atmospheric aerosols. *J. Meteorological Res.* 44 (3), 198–205.

Miao, Y., Liu, S., Sheng, L., and Huang, S. (2019). Influence of boundary layer structure and low-level jet on PM2.5 pollution in beijing: A case study. *Int. J. Environ. Res. Public Health* 16 (4), 616. doi:10.3390/ijerph16040616

Pakkanen, T. A., Kerminen, V. M., Ojanen, C. H., Hillamo, R. E., Aarnio, P., and Koskentalo, T. (2000). Atmospheric black carbon in Helsinki. *Atmos. Environ. X.* 34 (9), 1497–1506. doi:10.1016/S1352-2310(99)00344-1

Petj, T., Jrvi, L., Kerminen, V. M., Ding, A. J., Kulmala, M., Nie, W., et al. (2016). Enhanced air pollution via aerosol-boundary layer feedback in China. *Sci. Rep.* 6, 18998. doi:10.1038/srep18998

Ramanathan, V., and Carmichael, G. (2008). Global and regional climate changes due to black carbon. *Nat. Geosci.* 36 (4), 221–227. doi:10.1038/ngeo156

Ramanathan, V., Crutzen, P. J., Kiehl, J. T., and Rosenfeld, D. (2002). Aerosols, climate, and the hydrological cycle. *Science* 294 (5549), 2119–2124. doi:10.1126/science.1064034

Raunemaa, T., Kikas, U., and Bernotas, T. (1994). Observation of submicron aerosol, black carbon and visibility degradation in remote area at temperature range from 24 to 20°C. *Atmos. Environ. X.* 28 (5), 865–871. doi:10.1016/1352-2310(94)90245-3

Ren, Z., Zhang, Z., Sun, C., Liu, Y., Jun, L. I., Xiaohui, J. U., et al. (2015). Development of three-step quality control system of real-time observation data from aws in China. *Meteorol. Mon.* 41 (10), 1268–1277. doi:10.7519/j.issn.1000-0526.2015.10.010

Seidel, D. J., Zhang, Y., Beljaars, A., Golaz, J. C., Jacobson, A. R., and Medeiros, B. (2012). Climatology of the planetary boundary layer over the continental United States and Europe. *J. Geophys. Res.* 117 (D17). doi:10.1029/2012JD018143

Shi, S., Zhu, B., Lu, W., Yan, S., Liu, C., Liu, X., et al. (2020). Estimation of radiative forcing and heating rate based on vertical observation of black carbon in Nanjing, China. *Sci. Total Environ.* 756, 144135. doi:10.1016/j.scitotenv.2020.144135

Singh, V., Ravindra, K., Sahu, L., and Sokhi, R. (2018). Trends of atmospheric black carbon concentration over the United Kingdom. *Atmos. Environ. X.* 178 (APR), 148–157. doi:10.1016/j.atmosenv.2018.01.030

Slater, J., Coe, H., Mcfiggans, G., Tonttila, J., and Romakkaniemi, S. (2021). The effect of black carbon on aerosol-boundary layer feedback: Potential implications for Beijing haze episodes. *Atmos. Chem. Phys.* 22, 2937–2953. doi:10.5194/acp-2021-139

Stull, R. B. (1988). *An introduction to boundary layer Meteorology*. Netherlands: Springer. doi:10.1007/978-94-009-3027-8

Sun, Z. B., Liao, X. N., Wang, Z. S., Li, Z. M., and Hua, C. (2016) Scavenging effect of rime and east wind on PM2.5 under air heavy pollution in beijing. *Huan jing ke xue= Huanjing kexue/[bian ji, Zhongguo ke xue yuan huan jing ke xue wei yuan hui "Huan jing ke xue" bian ji wei yuan hui.]* 37 (10), 3679–3685. doi:10.13227/j.hjkx.2016.10.001

Tang, J., Wen, Y. P., Zhou, L. X., and Ling, X. (1999). Observational study of black carbon in clean air area of Western China. *Q. J. Appl. Meteorology* 10 (2), 160–170. doi:10.3969/j.issn.1001-7313.1999.02.004

Tian, P., Liu, D., Huang, M., Liu, Q., Zhao, D., Ran, L., et al. (2019). The evolution of an aerosol event observed from aircraft in Beijing: An insight into regional pollution transport. *Atmos. Environ. X.* 206, 11–20. doi:10.1016/j.atmosenv.2019.02.005

Tian, W., Chen, C., Huang, J., and Zhang, L. (1997). The solar heating effect of the winter aerosol in LaZhou and its influence on evolution of the mixed layer. *Q. J. Appl. Meteorology* 8 (3), 292–301. doi:10.1007/s00376-997-0061-6

Virkkula, A., Maekelae, T., Hillamo, R., Yli-Tuomi, T., Hirsikko, A., HaemeriKoponen, K. I. K., et al. (2007). A simple procedure for correcting loading effects of aethalometer data. *J. air & waste Manag. Assoc.* 57 (10), 1214–1222. doi:10.3155/1047-3289.57.10.1214

Vogelezang, D. H. P., and Holtslag, A. A. M. (1996). Evaluation and model impacts of alternative boundary-layer height formulations. *Bound. Layer. Meteorol.* 81 (3-4), 245–269. doi:10.1007/BF02430331

Waggoner, A. P., and Charlson, R. J. (1976). *Measurements of aerosol optical parameters*. Cambridge, Massachusetts: Academic Press, 511–533. doi:10.1016/B978-0-12-452950-2.50027-0

Wang, K. H., Shen, L., and Zhao, R. D. (2020). Anthropogenie ammonia emission invertory and its spatial distribution in Anhui Province from 2006 to 2017. *Trans. Atmos. Sci.* 43 (03), 547–556. doi:10.13878/j.cnki.dqkxxb.20191109006

Wang, X. Q., Yang, T., and Wang, Z. F. (2001). Impact of dust-haze episode from one air pollution control region to the other-one case study. *Clim. Environ. Res.* 16 (6), 690–696. doi:10.3878/j.issn.1006-9585.2011.06.02

Wang, Y. S. (1987). *Atmospheric physics [M]*. Beijing: Meteorological Press, 6–29.

Wang, Y., Vogel, J. M., Lin, Y., Pan, B., Zhang, R., Liu, Y., et al. (2018a). Aerosol microphysical and radiative effects on continental cloud ensembles. *Adv. Atmos. Sci.* 35 (2), 234–247. doi:10.1007/s00376-017-7091-5

Wang, Z., Huang, X., and Ding, A. (2018b). Dome effect of black carbon and its key influencing factors: Aone-dimensional modelling study. *Phys. Chem. A* 18, 1–29. doi:10.5194/acp-2017-967

Wei, W., Zhang, H., Cai, X., Song, Y., Zhang, H., Xiao, K., et al. (2020). Influence of intermittent turbulence on air pollution and its dispersion in winter 2016/2017 over beijing, China. *J. Meteorol. Res.* 34 (1), 176–188. doi:10.1007/s13351-020-9128-4

Weng, Y. P., Xu, X. B., Tang, J., Zhang, X. C., and Zhao, Y. C. (2001). Enrichment characteristics and origin of atmospheric aerosol elements at mt. *WaLiGuan. Q. J. Appl. Meteorology* 12 (4), 400–408. doi:10.3969/j.issn.1001-7313.2001.04.003

Wolff, G. T., Groblicki, P. J., Cadle, S. H., and Countess, R. J. (1982). *Particulate carbon at various locations in the United States*. US: Springer, 297–315. doi:10.1007/978-1-4684-4154-3_17

Xiao, X. Z., Liu, P. F., Geng, F. H., Gao, W., and Zhao, C. S. (2011). Comparison of black carbon aerosols in urban and suburban areas of Shanghai. *Q. J. Appl. Meteorology* 22 (2), 158–168. doi:10.3969/j.issn.1001-7313.2011.02.005

Yang, Y., Wang, L., Yong, H., Shi, C., and Tao, S. (2017). Impact of urbanization on meteorological observation and its environment representativeness: A case study of shouxian national climate station. *Ann. N. Y. Acad. Sci.* 45 (1), 7–14. doi:10.1111/nyas.13558

Zhang, D., Chen, B., Yamada, M., Niu, H., Wang, B., Iwasaka, Y., et al. (2012). Elevated soot layer in polluted urban atmosphere: A case study in beijing. *J. Meteorological Soc. Jpn.* 90 (3), 361–375. doi:10.2151/jmsj.2012-302

Zhang, R. J., Shi, L., and Liu, Y. (2007). High resolution observation and source identification of carbonaceous aerosols in PM10 in beijing in winter. *China Powder Sci. Technol.* 13 (6), 1–4. doi:10.3969/j.issn.1008-5548.2007.06.001

Zhang, X., Tang, J., Yunfei, W. U., Jian, W. U., Yan, P., and Zhang, R. (2015). Variations of black carbon aerosol observed in beijing and surrounding area during 2006—2012. *China Powder Sci. Technol.* 43, 6. doi:10.13732/j.issn.1008-5548.2015.04.006

Zhao, D., Huang, M., Tian, P., He, H., Lowe, D., Zhou, W., et al. (2019). Vertical characteristics of black carbon physical properties over Beijing region in warm and cold seasons. *Atmos. Environ. X.* 213, 296–310. doi:10.1016/j.atmosenv.2019.06.007

Zhao, D., Liu, D., Yu, C., Tian, P., Hu, D., Zhou, W., et al. (2020). Vertical evolution of black carbon characteristics and heating rate during a haze event in Beijing winter. *Sci. Total Environ.* 709, 136251. doi:10.1016/j.scitotenv.2019.136251

frontiers | Frontiers in Earth Science

TYPE Original Research
PUBLISHED 29 September 2022
DOI 10.3389/feart.2022.995843

OPEN ACCESS

EDITED BY
Yi Li,
Intel, United States

REVIEWED BY
Yu Hao,
Henan Normal University, China
Chao-Tung Yang,
Tunghai University, Taiwan
Dien Wu,
California Institute of Technology,
United States

*CORRESPONDENCE
Huan Li,
lihuan@hainanu.edu.cn

SPECIALTY SECTION
This article was submitted to
Atmospheric Science,
a section of the journal
Frontiers in Earth Science

RECEIVED 16 July 2022
ACCEPTED 14 September 2022
PUBLISHED 29 September 2022

CITATION
Mo X, Li H and Zhang L (2022), Design a regional and multistep air quality forecast model based on deep learning and domain knowledge.
Front. Earth Sci. 10:995843.
doi: 10.3389/feart.2022.995843

Design a regional and multistep air quality forecast model based on deep learning and domain knowledge

Xinyue Mo[1,2], Huan Li[1]* and Lei Zhang[2]

[1]School of Cyberspace Security, Hainan University, Haikou, China, [2]College of Atmospheric Sciences, Lanzhou University, Lanzhou, China

Air pollution is an issue across the world. It not only directly affects the environment and human health, but also influences the regional and even global climate by changing the atmospheric radiation budget, resulting in extensive and serious adverse effects. It is of great significance to accurately predict the concentration of pollutant. In this study, the domain knowledge of Atmospheric Sciences, advanced deep learning methods and big data are skillfully combined to establish a novel integrated model TSTM, derived from its fundamental features of Time, Space, Type and Meteorology, to achieve regional and multistep air quality forecast. Firstly, Expectation Maximization and Min-Max algorithms are used for the interpolation and normalization of data. Secondly, feature selection and construction are accomplished based on domain knowledge and correlation coefficient, and then Sliding Time Window algorithm is employed to build the supervised learning task. Thirdly, the features of pollution source and meteorological condition are learned and predicted by CNN-BiLSTM-Attention model, the integrated model of convolutional neural network and Bidirectional long short-term memory network based on Sequence to Sequence framework with Attention mechanism, and then Convolutional Long Short-Term Memory Neural Network (ConvLSTM) integrates the two determinant features to obtain predicted pollutant concentration. The multiple-output strategy is also employed for the multistep prediction. Lastly, the forecast performance of TSTM for pollutant concentration, air quality and heavy pollution weather is tested systematically. Experiments are conducted in Beijing-Tianjin-Hebei Air Pollution Transmission Channel (“2+26” cities) of China for multistep prediction of hourly concentration of six conventional air pollutants. The results show that the performance of TSTM is better than other benchmark models especially for heavy pollution weather and it has good robustness and generalization ability.

KEYWORDS

air quality forecast, deep learning, domain knowledge, big data, heavy pollution weather

1 Introduction

With the rapid development of industrialization and urbanization, more and more fossil fuels are burned, resulting in the deterioration of air quality and frequent haze weather (Jerrett, 2015; Mo et al., 2021; Mu et al., 2021). As a serious environmental problem air pollution has attracted worldwide attention. Air pollution is the single greatest environmental risk to human health and one of the main avoidable causes of death and disease globally, with some estimated 6.5 million premature deaths (2016) across the world attributed to indoor and outdoor air pollution (United Nations Environment Programme, 2022). Predicting air pollution in advance is of great significance to the health guide of the public and the pollution control of government (Li et al., 2019).

Numerical forecast and statistical forecast are mainstream methods for air quality forecast. The numerical forecast model predicts the concentration of air pollutants by simulating the transmission and diffusion of pollutants in the atmosphere. Numerical forecast has more advantages in regional pollution forecast and analysis, but it has higher demands on input data and computation power. Commonly used models are based on the Weather Research and Forecasting Model (WRF). Spiridonov et al. (Spiridonov et al., 2019) configured and designed an air quality system based on the WRF coupled with chemistry (WRF-Chem) for Macedonia. A generalized additive model was also developed to predict the concentration of $PM_{2.5}$ by using the WRF to obtain the input of the prediction model (Sahu et al., 2020). And Cheng et al. (Cheng et al., 2021) proposed an air quality forecasting system composed of WRF and Community Multiscale Air Quality Modeling System (CMAQ) and a bias-correction method to improve the accuracy of forecast. The statistical forecast model obtains predicted pollutant concentration in the basis of statistical analysis on historical data of pollutant and meteorology. Statistical forecast is relatively more efficient and practical, while it has limitations for the prediction of hourly concentration and heavy pollution. Common statistical models are multiple linear regression model (MLR) and autoregressive integrated moving average model (ARIMA). Ng et al. established a MLR based on meteorological factors and air pollutants to predict the daily average concentration of PM_{10}, and obtained good prediction performance (Ng and Awang, 2018). Pohoata et al. used the ARIMA to predict pollutants, and the results showed that the prediction performance of PM and CO was poor, but the prediction of NO_X and O_3 achieved relatively good results (Pohoata and Lungu, 2017).

In recent years artificial intelligence (AI) has acquired the rapid development, especially machine learning has been applied in various fields and great success was achieved. Machine learning technologies effectively serve air pollution forecast too, and there are relatively more applications of traditional machine learning algorithms. Perisic et al. (Perišić et al., 2017) used the boosted decision tree model to predict the hourly concentration of PM_{10} at different stations, and found that the prediction performance of the model at different stations was affected by emission sources, topography and local climate. Chen (Chen, 2018) applied Back Propagation Neural Network combined with $PM_{2.5}$ concentration, temperature, humidity, wind force and satellite remote sensing data of aerosol optical thickness, and realized the high-precision prediction of $PM_{2.5}$ in the next 3 hours. Cheng et al. (Cheng et al., 2019) combined Empirical Mode Decomposition (EMD) with Support Vector Regression (SVR) to forecast daily air quality index (AQI) of Xingtai in China. Li et al. (Li et al., 2020) designed a geographically and temporally weighted generalized regression neural network (GTW-GRNN) to estimate ground NO_2 concentrations by integrating ground NO_2 station measurements. Mo et al. (Mo et al., 2019) combined Improved Complete Ensemble Empirical Mode Decomposition with Adaptive Noise (ICEEMDAN), Whale Optimization Algorithm (WOA) and Extreme Learning Machine (ELM) to design prediction model and acquired superior effect in daily concentration prediction of conventional air pollutants. The applications of deep learning to air quality forecast attract increasingly more attention. Chakma et al. (Chakma et al., 2017) collected street view photos containing sky, buildings and pollution category labels in Beijing from 2013 to 2017 to train convolutional neural network (CNN), and the accuracy of the model in predicting air pollution category through photos can reach 68.74%. Kim et al. (Kim et al., 2018) compared the performance of traditional machine learning model multilayer perceptron, deep learning model Elman neural network and long-short term memory network (LSTM) in predicting ozone concentration, and the experiment shows that the performance of LSTM is better and the error growth rate of LSTM is smaller with the increase of prediction time. Pak et al. (Pak et al., 2020) combined CNN, LSTM and the historical data of air quality and meteorological elements related to the target based on mutual information (MI), and realized the one-step prediction of the daily average concentration of $PM_{2.5}$ in Beijing. Convolutional Long Short-Term Memory Neural Network (ConvLSTM) was used by Wen et al. (Wen et al., 2019) to predict hourly $PM_{2.5}$ concentration of all monitoring stations in China. Wang et al. (Wang et al., 2020) predicted hourly ozone concentration of 35 monitoring stations in Beijing by Sequence to Sequence model (Seq2Seq). In addition, other forecast methods based on AI have also been proposed in recent years (Zhao et al., 2019; Mo et al., 2020; Ulpiani et al., 2022; Yu et al., 2022).

However, there are still shortages in previous studies, and air quality forecast based on AI needs to be further improved. Previous studies always focus on single pollutant, but actually six conventional air pollutants $PM_{2.5}$, PM_{10}, CO, NO_2, SO_2, O_3 are essential for air quality prediction and early warning. For example, AQI must rely on predicted concentrations of the six pollutants to report future air quality level and chief pollutant. This deficiency also leads to an incomplete evaluation of model performance. Missing data is a common problem and can cause serious impacts to data-driven model, but it is usually neglected. Besides data, algorithm and computing power, domain knowledge plays a critical role in the application of AI algorithm, but the modeling of air quality forecast always ignores this point. Furthermore, the application of deep learning to air quality forecast is an important research direction, and it is urgent to conduct numerous studies to comprehensively explore the applicability of deep learning algorithms to air pollution prediction and develop appropriate models[1].

To overcome shortcomings of previous studies, we introduce the domain knowledge of Atmospheric Sciences to design a novel integrated model based on deep learning to perform regional and multistep forecast of six air pollutants in this study. Our model is called TSTM because of its four key features including Time, Space, Type and Meteorology. It is worth mentioning that TSTM is the result of combining the theories of Atmospheric Sciences and deep learning technologies. First of all, the theories of Atmospheric Sciences help grasp the evolution mechanism of air pollution and determinants of pollutant concentration, and then the forecast framework are also designed based on related domain knowledge. Secondly, it is needed to find solutions from deep learning models to dispose important factors for prediction. It can be seen from previous studies that CNN and LSTM are preferred in air pollution prediction because of their superiority in feature extraction and learning long and short-term correlations in big data (Ian et al., 2017). Therefore, CNN and advanced versions of LSTM, namely Bidirectional long short-term memory network (BiLSTM) and ConvLSTM, are applied. Moreover, Seq2Seq framework is used to establish integrated model, and Attention mechanism is helpful to multiple-feature task. At last, a comprehensive evaluation plan is proposed from the perspective of Atmospheric Sciences too. Besides common statistical indicators, more practical evaluation is conducted involving air quality level, chief pollutant, heavy pollution weather and so on, which is the focus of the public and government.

The workflow of TSTM can be summarized as follows. Firstly, Expectation Maximization algorithm (EM) efficiently deals with missing data and Min-Max normalization can improve the convergence speed and accuracy of model. Secondly, domain knowledge of Atmospheric Sciences helps us decide preliminary features and effective features are further selected by correlation coefficient, and then feature decomposition and combination as well as the sliding time window algorithm is applied to transform the original time series into the supervised learning task. Thirdly, CNN-BiLSTM-Attention, an integrated model of CNN and BiLSTM by Seq2Seq with Attention mechanism, is used to learn and forecast pollution source and meteorological condition features separately, and then ConvLSTM couples them to obtain predicted pollutant concentration. Furthermore, multiple-output strategy is employed for multi-step prediction, which achieves high efficiency and low cost. Finally, a comprehensive performance evaluation scheme is designed referencing "Technical guideline for numerical forecasting of ambient air quality (HJ 1130-2020)" issued by China's Ministry of Ecology and Environment (The Ministry of Ecology and Environment of China, 2022a). Evaluation involves three aspects, namely, pollutant concentration forecast, air quality forecast and heavy pollution weather forecast. TSTM is tested on two independent test sets for the multi-step prediction of the hourly concentration of six conventional air pollutants in Beijing-Tianjin-Hebei Air Pollution Transmission Channel ("2+26" cities) of China.

2 Data and methods

2.1 Study area

Recently regional and compound air pollution is increasingly notable. Beijing-Tianjin-Hebei and surrounding regions belong to the core economic zone of China but the most polluted region with prominent cross-region air pollution, which has caused serious concern from the public and government. The Ministry of Ecology and Environment of China determined Beijing-Tianjin-Hebei Air Pollution Transmission Channel ("2+26" cities) involving 6 provinces in 2017 and established its special emission limits of air pollutants in 2018. Therefore, Beijing-Tianjin-Hebei Air Pollution Transmission Channel ("2+26" cities) as Figure 1 shows is chosen as study area for its important strategic position and space correlation of air pollution.

2.2 Data

Six conventional air pollutants ($PM_{2.5}$, PM_{10}, CO, NO_2, SO_2, O_3) are necessary items for air quality forecast and evaluation, especially AQI must rely all of them. As to meteorological elements, we collect data of wind speed, temperature, relative humidity and precipitation based on the domain knowledge of Atmospheric Science. Hourly monitoring data of 6 air pollutants and 4 meteorological elements during 2017.12–2019.2 of 28 cities are collected from The Ministry of Ecology and Environment of China[2]

---

[1] https://www.nsfc.gov.cn/publish/portal0/tab934/info79588.htm.

[2] https://www.mee.gov.cn/

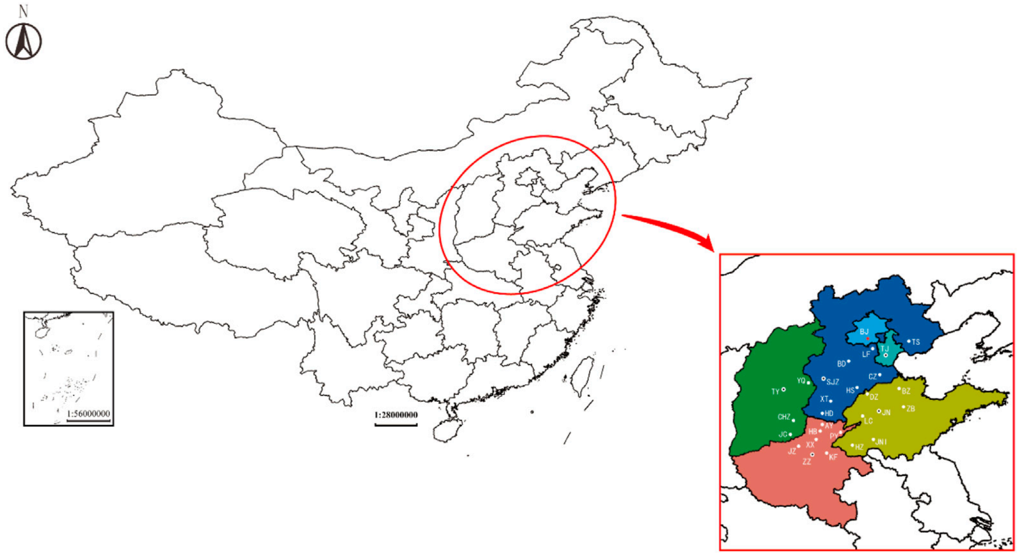

FIGURE 1
The Beijing-Tianjin-Hebei Air Pollution Transmission Channel (“2+26” cities).

and China Meteorological Administration[3]. Same architecture of forecast model is shared, while the model for each pollutant in each city needs to be trained and evaluated separately. The total number of data participating in modeling is approximately 100 million, which means actually big data. Data from 2017.12 to 2018.12 are used as training set, and the data of 2019.1 are used as validation set while the data of 2019.2 are selected as test set. The hyperparameters are tuned manually and determined based on the performance of model on validation set. In addition, in order to test the generalization ability of the model, the data of 2019.6 are supplemented as an additional test set.

2.3 Methods

2.3.1 Convolutional neural network

Convolutional neural network (CNN) is a feedforward neural network with convolution operation and depth structure (Lecun, 1989). It is a classical deep learning algorithm. The research on CNN began in the 1980s. After the 21st century, with the proposal of deep learning theory and the improvement of numerical computing ability, it has developed rapidly. Based on the visual perception of biology, it has been successfully used in computer vision, natural language processing and so on because of its sparse connection and weight sharing. CNN is usually composed of input layer, convolutional layer, pooling layer, fully-connected layer and output layer (Figure 2).

2.3.2 Long short-term memory network

Long Short-Term Memory Network (LSTM) (Hochreiter and Schmidhuber, 1997) is an improved model of Recurrent Neural Network (RNN). It replaces hidden node with memory block to solve the problem of gradient disappearance or explosion after many time steps. Memory block is made up of memory cell, forget gate, input gate and output gate. Figure 3 presents the architecture of LSTM. LSTM is skilled in learning from experience and processing time series with unknown time delay between important events. It has been successfully applied to handwritten character recognition, machine translation and so forth.

2.3.3 Bidirectional long short-term memory network

The traditional recurrent neural network can only predict the output of the current time according to the historical information. However, in some cases, the output of the current moment is closely related to the history and future state, so considering the context information at the same time is conducive to comprehensive judgment. Bidirectional long short-term memory network (BiLSTM) solves this problem. It consists of two unidirectional LSTM (Schuster and Paliwal, 1997) (Figure 4). The input at each time will be provided to the forward and backward LSTM at the same time. The two hidden layers calculate the state and output independently. The final output of the BiLSTM is jointly determined by the outputs of the two LSTM.

---

[3] http://www.cma.gov.cn/

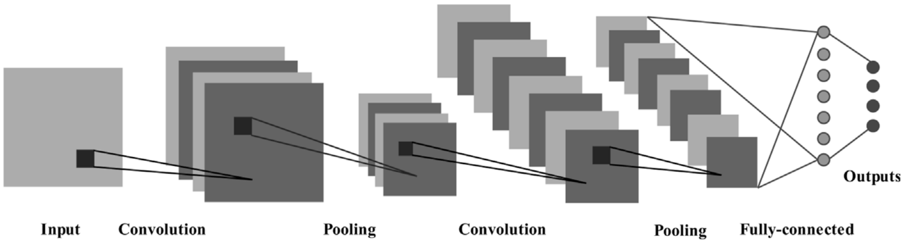

FIGURE 2
The architecture of CNN.

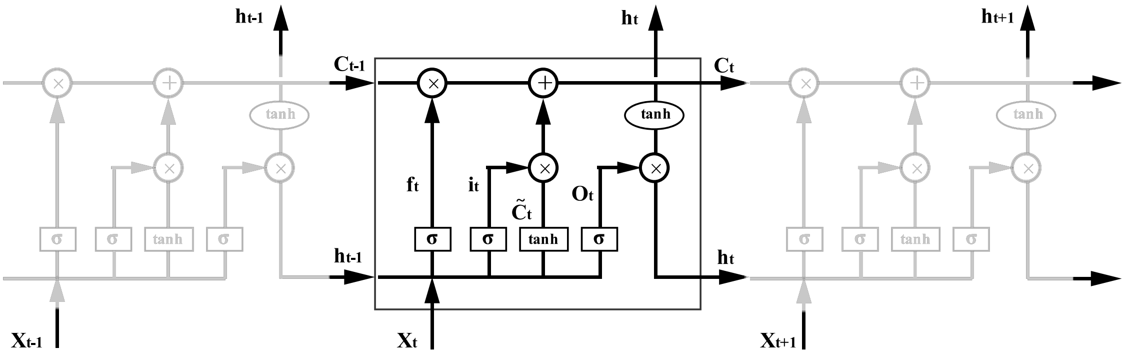

FIGURE 3
The architecture of LSTM.

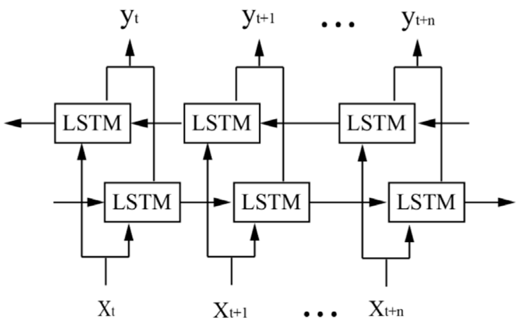

FIGURE 4
The architecture of BiLSTM.

2.3.4 Convolutional long short-term memory network

Convolutional long short-term memory network (ConvLSTM) is a variant of LSTM (Shi et al., 2015). The conventional LSTM belongs to the fully connected LSTM (FC-LSTM), that is, the input to state and state to state connections are calculated by feedforward neural network. ConvLSTM replaces this connection with convolution, which not only has the time series processing advantage of LSTM, but also obtains the feature extraction ability of CNN.

2.3.5 Sequence to sequence

Sequence to Sequence (Seq2Seq) is a variant of RNN, and Encoder and Decoder are its main parts. This framework is proposed for the case that the length of input sequence and output sequence is unequal. Two neural networks are treated as Encoder and Decoder respectively, and Encoder reads and compresses input sequence to a vector C with fixed length which is then read and processed by Decoder according to target sequence (Cho et al., 2014).

However, experiments show that the performance of this method will deteriorate sharply with the increase of input length, which is mainly because it is very difficult to summarize all features of long input sequence by vector C with fixed length. Therefore, Attention Mechanism is proposed for this problem (Bahdanau et al., 2014) (Figure 5). In each step of decoding, the hidden state of the encoder will be queried. Calculate the correlation between each part of the input sequence and the

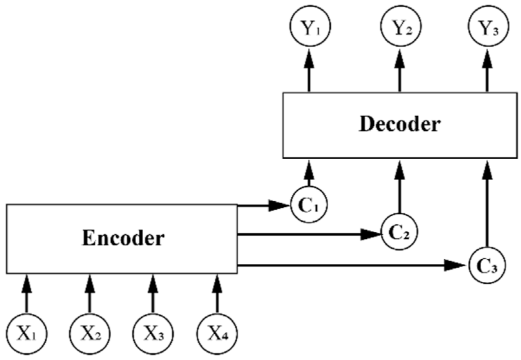

FIGURE 5
The architecture of Encoder-Decoder-Attention.

current output (weight). Then the hidden state of each part of input is weighted and averaged to get the vector C which contains most relevant information of input to the current output.

3 The design of TSTM

3.1 Domain knowledge

The introduction of domain knowledge is helpful to the application of deep learning algorithms to modeling. For pollutant concentration prediction, it is necessary to know which factors actually affect concentration, and then proper methods are applied to learn their correlations.

3.1.1 Pollution source

Type and property of air pollutant are decided by pollution source, so comprehensive information of pollution source is crucial in pollutant concentration forecast. Air pollution sources of a city can be divided into two categories from the perspective of source apportionment, namely internal source and external source, which refer to local emission and regional transmission respectively.

For local generation, it is necessary to consider the primary emission and secondary generation of pollutants. The pollutant directly discharged into the air by the pollution source and whose physical and chemical properties has not changed is primary pollutant (Xue et al., 2020). The primary pollutant is usually affected by the emission source with obvious periodicity, and the high-time resolution monitoring data of pollutant contain the change law of the emission of pollution source. For example, the bimodal mode of NO_2 hourly concentration in city corresponds to the morning and evening peak of traffic. Primary pollutant can change under the influence of physical and chemical factors or react with other substances in the air to produce secondary pollutant with different properties (Drozd et al., 2018). The formation and transformation mechanism of secondary pollutant involves complex physical and chemical reactions between different pollutants, and its harm to the environment and biology is also greater than that of primary pollutant (Kong et al., 2019; Menares et al., 2020). For example, SO_2 and NO_2, as precursors, can undergo photochemical oxidation reaction and gas-solid conversion to form sulfate and nitrate, becoming secondary particles. NOx, VOCs and CO can participate in atmospheric photochemical reaction to produce O_3. In addition, particles and O_3 also have complex interactions (Chen et al., 2019). Particles reduce the solar shortwave radiation reaching the ground through absorption and scattering, thereby reducing the photochemical reaction rate of O_3. O_3 will lead to the enhancement of atmospheric oxidation, which is conducive to the formation of secondary particles. Therefore, when predicting the concentration of pollutant, we should not only pay attention to the change law of pollutant with time, but also consider the complex interaction between different pollutants.

Air pollutants can be transported over long distances across regions, making air pollution affect each other among cities. This problem is particularly prominent in area with dense cities and heavy pollution, and sometimes the contribution of regional transmission even exceeds that of local generation (Sun et al., 2017). For air pollution prevention and control, the actions of a single city cannot fundamentally solve the problem, and regional joint prevention and control is an effective way.

When carrying out urban air pollutant concentration prediction, the introduction of pollution sources should consider the primary emission, secondary generation and regional transmission of pollutants. Based on the above analysis, the predicted pollutant, the related pollutants in the same city, and the same pollutants in related cities can be used as prediction factors. The time series of the above variables are mined by deep learning algorithm to learn their complex interactions and spatial-temporal variations.

3.1.2 Meteorological condition

In addition to the root cause of pollution source, meteorological conditions are also main factors affecting the change of pollutant concentration, which is mainly reflected in the migration and transformation process of pollutant (Dong et al., 2020). Diffusion condition represents the ability of the atmosphere to dilute, diffuse, accumulate and remove air pollutants. Under different diffusion conditions, even the same pollution source will cause significant differences in pollutant concentration (Liu et al., 2019). Wind speed, temperature, humidity and weather phenomenon are the main meteorological factors that determine the diffusion condition (Wang et al., 2019; Jury, 2020; Pérez et al., 2020; The Standardization administration of China, 2022). The wind can transport pollutant along the horizontal direction, and the wind speed determines the speed and distance of pollutant migration.

The irregular change of wind will form turbulence, which will fully mix the pollutant with the surrounding clean air and promote the dilution and diffusion of pollutant. However, excessive wind speed will also blow the dust on the ground into the air, causing particle pollution. The temperature and humidity of the atmosphere are closely related to the stability of the atmosphere and affect the vertical diffusion of pollutant. At the same time, high temperature and humidity are conducive to the photochemical reaction of ozone and the hygroscopic growth of particles, respectively. Precipitation is an important way to remove air pollutants. During the falling process, raindrops absorb solid particles through collision, and gaseous pollutants can also be dissolved in water or chemically reacted with water and brought to the ground.

Referring to the instruction of the "Air pollution diffusion condition index" from the China Meteorological Administration[4] and above research, the change of air pollutant concentration is closely related to wind speed, temperature, relative humidity and precipitation. Therefore, in the prediction of urban air pollutant concentration, the above four meteorological elements in the same city are introduced as prediction factors.

3.2 Data preprocessing

The problem of missing data is common but always overlooked. For the data-driven deep learning model, its performance is directly related to the integrity and accuracy of data. Deletion or simple interpolation method is incompetent for the data of air pollutant and meteorological element which are highly nonlinear and nonstationary. Thus, the dataset is processed by advanced Expectation Maximization (EM) algorithm. EM (Neal and Hinton, 1998) algorithm is an iterative algorithm to calculate maximum likelihood estimation of posterior distribution in the case of incomplete data. Two steps are performed alternately in each iteration cycle: E step (Expectation), calculate the conditional expectation of log likelihood function by the estimated parameters from previous iteration; M step (Maximization), maximize the log likelihood function to determine the parameters which are used in next iteration. The algorithm iterates between E step and M step until convergence. It has good convergence and is suitable for large sample.

The normalization of data is an important procedure of deep learning, which can eliminate the influence of magnitude among different features and further improve convergence speed and accuracy of model. So Min-Max normalization is applied to input data and then output data are processed by reverse normalization for the evaluation of model's performance (Jin et al., 2015).

3.3 Feature selection

For the prediction of air pollutant concentration, based on the domain knowledge of Atmospheric Sciences, the preliminary features are conventional air pollutants ($PM_{2.5}$, PM_{10}, CO, NO_2, SO_2, O_3) and meteorological elements (wind speed, temperature, relative humidity, precipitation) of all cities in the region. In order to eliminate irrelevant features and improve computational efficiency, effective features are further selected through statistical methods. For pollution source, besides predicted pollutant itself, Spearman rank correlation coefficient and Pearson correlation coefficient are used to screen the related pollutants in the same city and the related cities on the same pollutant, and the threshold value is 0.6 (strong correlation). For meteorological condition, four meteorological elements of the same city are selected as effective features to predict pollutant concentration.

Feature decomposition and combination are used in this study. From the perspective of deep learning, the predicted pollutant, the related cities on the same pollutant, the related pollutants in the same city and the meteorological elements in the same city can be classified into four types of features: time, space, type and meteorology. Pollution source and meteorological condition are the two main factors that determine the change of pollutant concentration. Pollution source can be learned based on the first three types of features. With reference to the "Grades of air pollution diffusion meteorological conditions (QX/T 413-2018)" issued by the China Meteorological Administration, the meteorological condition in the future can be estimated based on the historical data of air pollutant concentration and meteorological elements without considering the pollution source (China Meteorological Administration, 2022). Therefore, meteorological condition can be learned based on time and meteorology features. In this study, the features of pollution source and meteorological condition are studied and predicted respectively, and then the final prediction result are obtained by integrating the two features. In addition, the hourly concentration of air pollutant has significant diurnal variation (24 h), so the time lag is 24, which is also consistent with previous studies (Wang et al., 2020). Finally, the sliding time window algorithm is applied to divide the data, and the original time series is transformed into supervised learning tasks.

3.4 Forecast strategy

On the basis of domain knowledge of atmospheric science, deep learning algorithms are employed to learn pollution source and meteorological condition, which contain time, space, type

---

[4] http://www.cma.gov.cn/2011qxfw/2011qqxkp/2011qqxzs/201110/t20111027_126331.html.

and meteorology features, namely four important correlations. Time correlation: air pollutant concentration has prominent periodicity and hourly monitoring data can reflect this variation over time. Space correlation: air pollution of different cities affects each other because of regional transmission, and Pearson correlation coefficient is used to select highly related cities for target city on the same pollutant. Type correlation: in view of the transformation mechanism of secondary pollutant, it is necessary to learn complex interactions among air pollutants, and Spearman's rank correlation coefficient is used to find highly related pollutants for target pollutant. Meteorology correlation needs to be considered in forecast too. Attention mechanism can give each variable distinct weight, so integrated model CNN-BiLSTM-Attention with advantages of different deep learning algorithms is applied to learn and forecast pollution source (time, space, type) and meteorological condition (time, meteorology) features respectively. And then the advanced ConvLSTM is adopted to integrate the two features to forecast air pollutant concentration. Moreover, in this study multiple-output strategy is employed to obtain multistep prediction results simultaneously, which has greater efficiency and lower cost when compared with recursive strategy or multi-independent models.

3.5 Performance evaluation

Besides pollutant concentration, the forecast performance of model for air quality and heavy pollution weather are also evaluated to form a comprehensive evaluation plan.

3.5.1 Pollutant concentration forecast

TSTM's performance is evaluated by three representative indicators including normalized mean bias (NMB), root mean square error (RMSE), and correlation coefficient (r). The prediction performance of the model is evaluated from the deviation, error and correlation between the predicted value and the observed value. Their equations are as follows:

$$NMB = \frac{\sum_{i=1}^{n}(X_i - Y_i)}{\sum_{i=1}^{n} Y_i} \tag{1}$$

$$RMSE = \sqrt{\frac{1}{n}\sum_{i=1}^{n}(X_i - Y_i)^2} \tag{2}$$

$$r = \frac{\sum_{i=1}^{n}(X_i - \bar{X})(Y_i - \bar{Y})}{\sqrt{\sum_{i=1}^{n}(X_i - \bar{X})^2}\sqrt{\sum_{i=1}^{n}(Y_i - \bar{Y})^2}} \tag{3}$$

where X_i and Y_i are the predicted value and observed value of air pollutant concentration; n is the number of test samples; $\bar{X}$ and $\bar{Y}$ are the average value of the predicted value and the observed value respectively.

3.5.2 Air quality forecast

1) Air quality index range

Based on the predicted concentrations of six conventional air pollutants, the predicted value of AQI is calculated, and that it plus/minus 25% is taken as the prediction range. If the actual value of AQI is within the prediction range, the prediction is accurate. The calculation equation of prediction accuracy of AQI range is as follow:

$$A_{AQI} = \frac{n_{AQI}}{N} \tag{4}$$

Where A_{AQI} is the prediction accuracy of AQI range; n_{AQI} is the number of samples with accurate AQI range prediction; N is the total number of samples.

2) Air quality level

The range of predicted air quality level can be obtained through AQI prediction range. If the actual value of the level is within the prediction range, the prediction is accurate. The calculation equation of the prediction accuracy of the air quality level is as follow:

$$A_{AQL} = \frac{n_{AQL}}{N} \tag{5}$$

Where A_{AQL} is the prediction accuracy of air quality level; n_{AQL} is the number of samples with accurate air quality level prediction; N is the total number of samples.

3) Chief pollutant

When the actual air quality level is greater than or equal to level II, if the prediction is the same as the actual chief pollutant, the prediction is accurate. The calculation equation of the prediction accuracy of the chief pollutant is as follow:

$$A_{CP} = \frac{n_{CP}}{N} \tag{6}$$

Where $A_{CP}$is the prediction accuracy of chief pollutants; n_{CP} is the number of samples with accurate chief pollutant prediction in the evaluation period; N is the number of samples whose actual air quality level is greater than or equal to level II.

3.5.3 Heavy pollution weather forecast

1) Prediction accuracy

The prediction accuracy of air quality level when the actual AQI is greater than 200 is calculated as follow:

$$HA_{AQL} = \frac{n_{AQL}}{N_{OH}} \tag{7}$$

Where HA_{AQL} is the prediction accuracy of heavy pollution weather; n_{AQL} is the number of samples with accurate prediction in the evaluation period; N_{OH} is the actual number of heavy pollution weather samples.

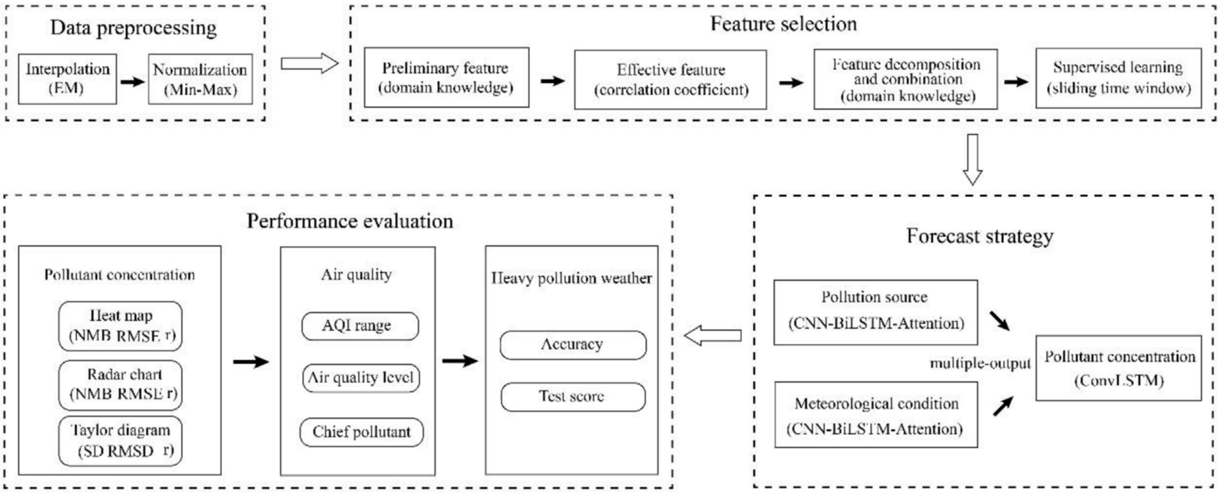

FIGURE 6
The architecture of TSTM.

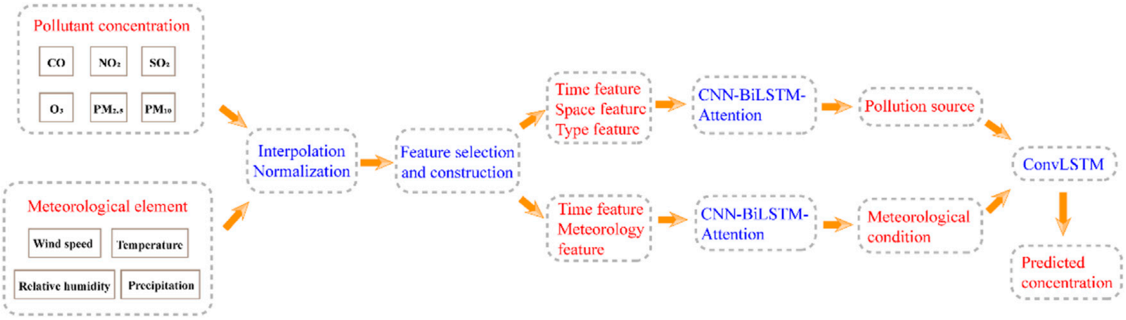

FIGURE 7
The workflow of TSTM.

2) Prediction test score

The prediction accuracy of air quality level when the predicted or actual AQI is greater than 200 is calculated as follow:

$$HS_{AQL} = \frac{n_{AQL}}{N_{FOH}} \tag{8}$$

Where HS_{AQL} is the prediction test score of heavy pollution weather; n_{AQL} is the number of samples with accurate prediction in the evaluation period; N_{FOH} is the number of predicted or actual heavy pollution weather samples.

Based on above all, we proposed a novel integrated model TSTM based on the theory and methods of Atmospheric Sciences and deep learning for regional and multistep air quality forecast. The architecture and workflow of TSTM can be seen in Figure 6 and Figure 7, respectively.

4 Results and discussion

4.1 Pollutant concentration forecast

The performance of TSTM for regional (e.g. BJ and TJ) and multistep (e.g. CO_1, CO_2 and CO_3) air quality prediction is tested on the hourly concentrations of six conventional air pollutants in study area, and independent test sets (e.g. BJ 1 and BJ 2) are used. In view of a large number of experimental results, the heat map is used to present the performance of TSTM on all cities and pollutants. NMB in Figure 8 reflects the deviation between prediction and observation. A positive value indicates that the predicted concentration is generally higher than actual concentration, while a negative value indicates that the predicted result is

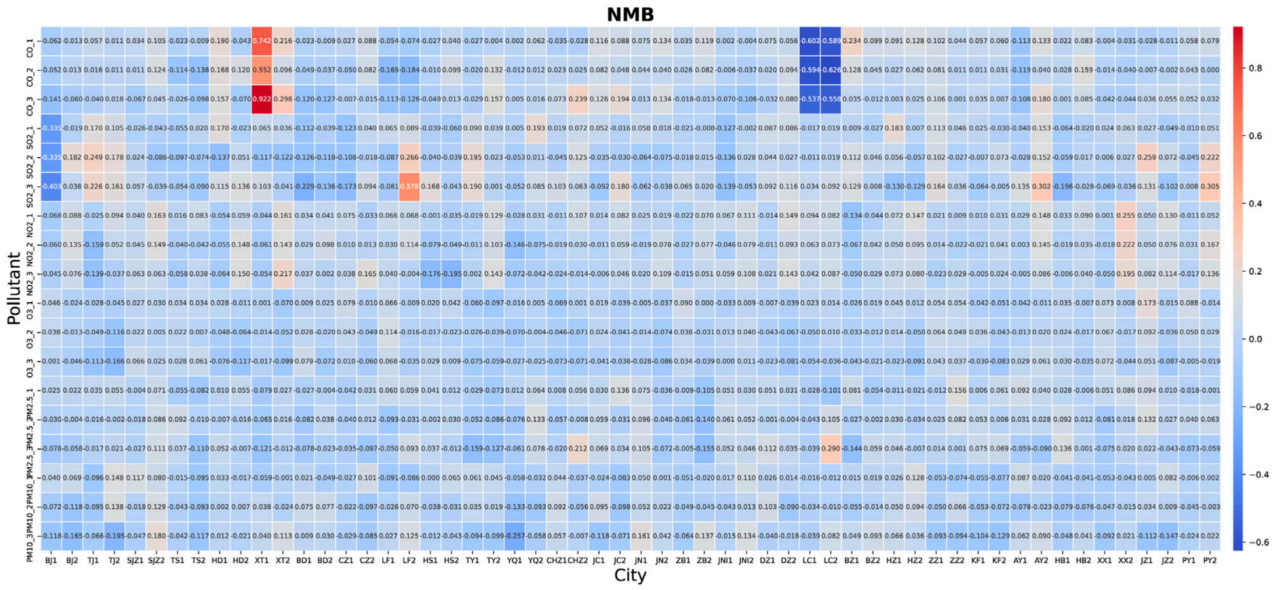

FIGURE 8
The NMB of pollutant concentration prediction of TSTM in “2+26” cities.

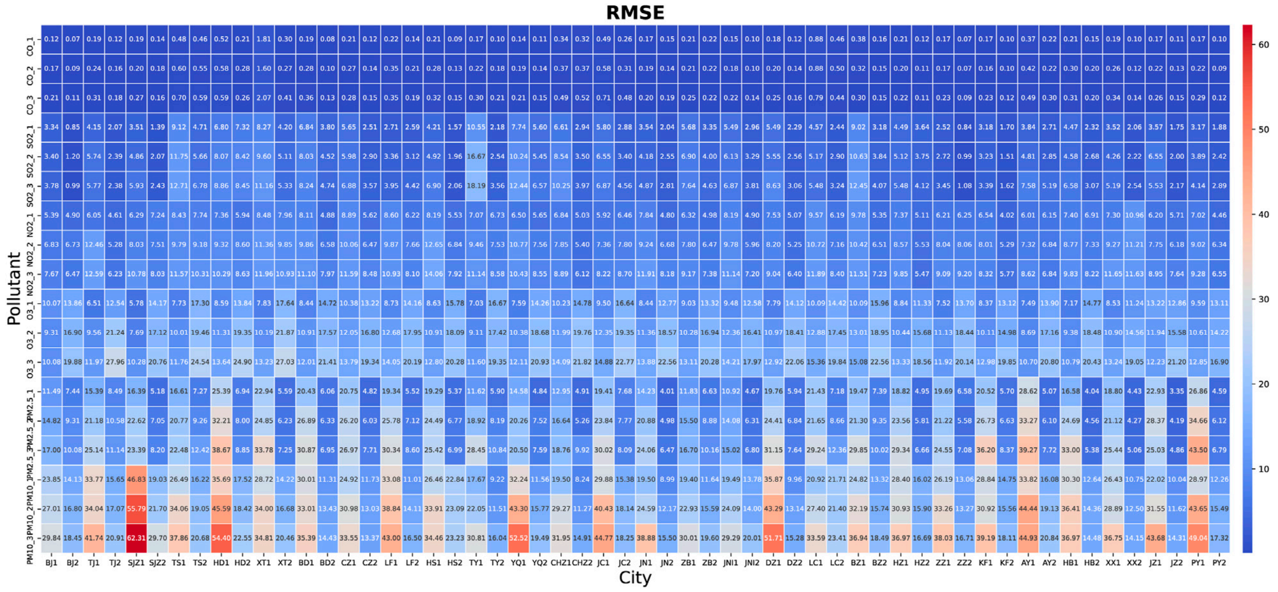

FIGURE 9
The RMSE of pollutant concentration prediction of TSTM in “2+26” cities (unit: mg/m^3 for CO, μg/m^3 for other pollutants).

lower. According to all results, the number of positive values is equal to that of negative values. Generally, the NMB does not show obvious correlation with city, pollutant, prediction step and test set, and there is no systematical deviation shown by these experiments.

Figure 9 shows the RMSE of TSTM under different conditions. RMSE can not only reflect the average error of the prediction, but also is very sensitive to outliers, which is the focus of deep learning in the application for air quality prediction. The experimental results show a certain regularity. The accuracy of

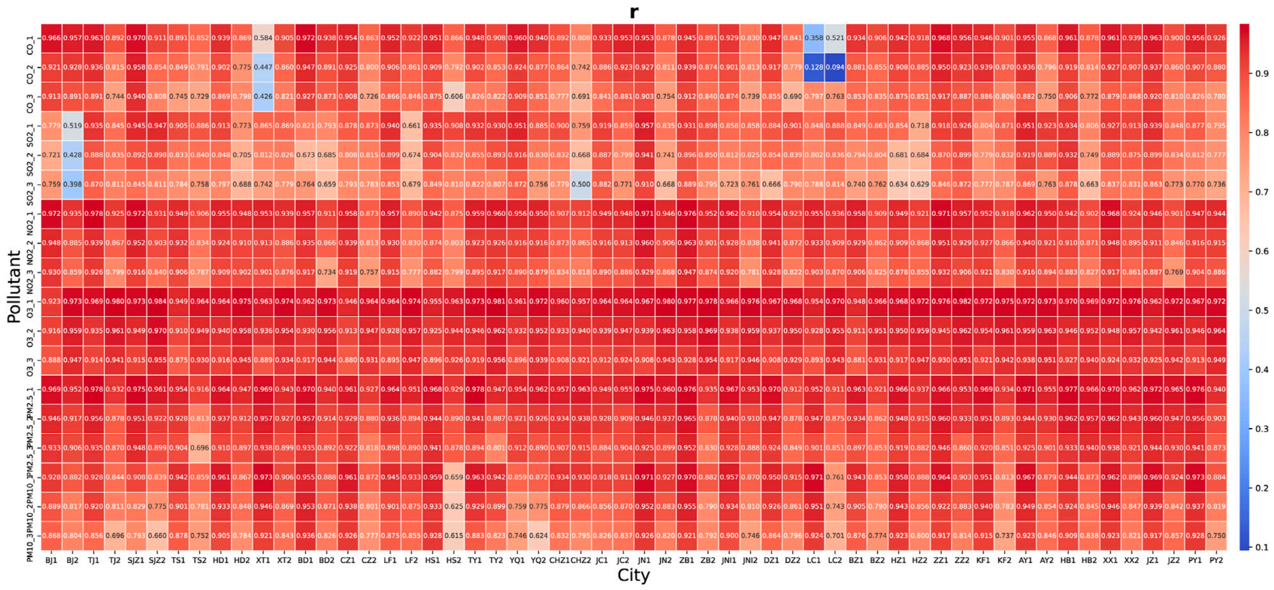

FIGURE 10
The r of pollutant concentration prediction of TSTM in "2+26" cities.

the model is mainly affected by the data themselves. Generally, the higher the concentration value, the higher the RMSE value. On test set 1, the six conventional air pollutants are arranged according to the increasing order of the average concentration value, namely CO, SO_2, NO_2, O_3, $PM_{2.5}$ and PM_{10}, which is consistent with the order of RMSE value. For 1-step prediction, the results of PM_{10} on test set 1 show that the RMSE and concentration of Shijiazhuang is 46.83 μg/m^3 and 194 μg/m^3, while the 19.49 μg/m^3 and 138 μg/m^3 of Jining. In Anyang, the concentration of $PM_{2.5}$ on test set 1 and 2 are 162 μg/m^3 and 36 μg/m^3 respectively, while the RMSE are 28.62 μg/m^3 and 5.07 μg/m^3. For multistep prediction, based on the same historical data, it is obviously more difficult to predict multistep result at the same time than one-step result. The experimental results show that the accuracy decreases slightly with the increase of prediction steps. Take the O_3 on test set 2 as an example, in Taiyuan, the RMSE of 1 step, 2 steps and 3 steps are 16.67 μg/m^3, 17.42 μg/m^3 and 19.35 μg/m^3 respectively.

Figure 10 shows the correlation between the predicted value and the actual value, that is, whether the model can accurately capture the change trend of air pollution. The results show that TSTM has a good performance in almost all experiments. The predicted value is strongly correlated with the actual value ($r > 0.6$), and the correlation coefficient decreases slightly with the increase of prediction steps. Very few experimental results show weak correlation, the pollutants with low concentration value such as CO and SO_2 are further explored. There are random deviations from deep learning model. Compared with pollutants with high concentration value, the correlation of pollutants with low concentration value are more affected, but the uncertainty only exists in very few cases.

In view of a large number of experimental results and similar forecast effects in all cities, it is necessary to select representative city and further carry out detailed comparative analysis. Beijing is the capital of China and has an important strategic position, but it is under considerable strain in air pollution prevention and control. Beijing is also the central city of this study area, and it is a common target in previous studies. Therefore, Beijing is selected as the representative, and the radar chart is used to analyze the prediction effects of TSTM in all experiments.

Figure 11 shows the results of TSTM's multistep prediction for six conventional air pollutants in Beijing, involving three evaluation indicators (NMB, RMSE, r) and two independent test sets (winter and summer). TSTM adopts the multi-output strategy for multistep prediction, and the prediction error usually increases with the increase of prediction step. In addition, the random deviation is shown by NMB.

In winter (Test 1), the air pollution is relatively heavier and there are more negative values of NMB. The NMB of high concentration value PM_{10} (72.19 μg/m^3) and $PM_{2.5}$ (51.76 μg/m^3) increases with the increase of prediction step. For medium concentrations value of O_3 (44.70 μg/m^3) and NO_2 (33.80 μg/m^3), the NMB for one-step and two-steps prediction are close, while the NMB of three-steps decreases. The NMB of low concentration value SO_2 (6.33 μg/m^3) and CO (0.79 mg/m^3) for one-step and two-steps prediction are close, while the NMB of three-steps increases. In summer (Test 2), except for the increased concentration of O_3, the concentration of other

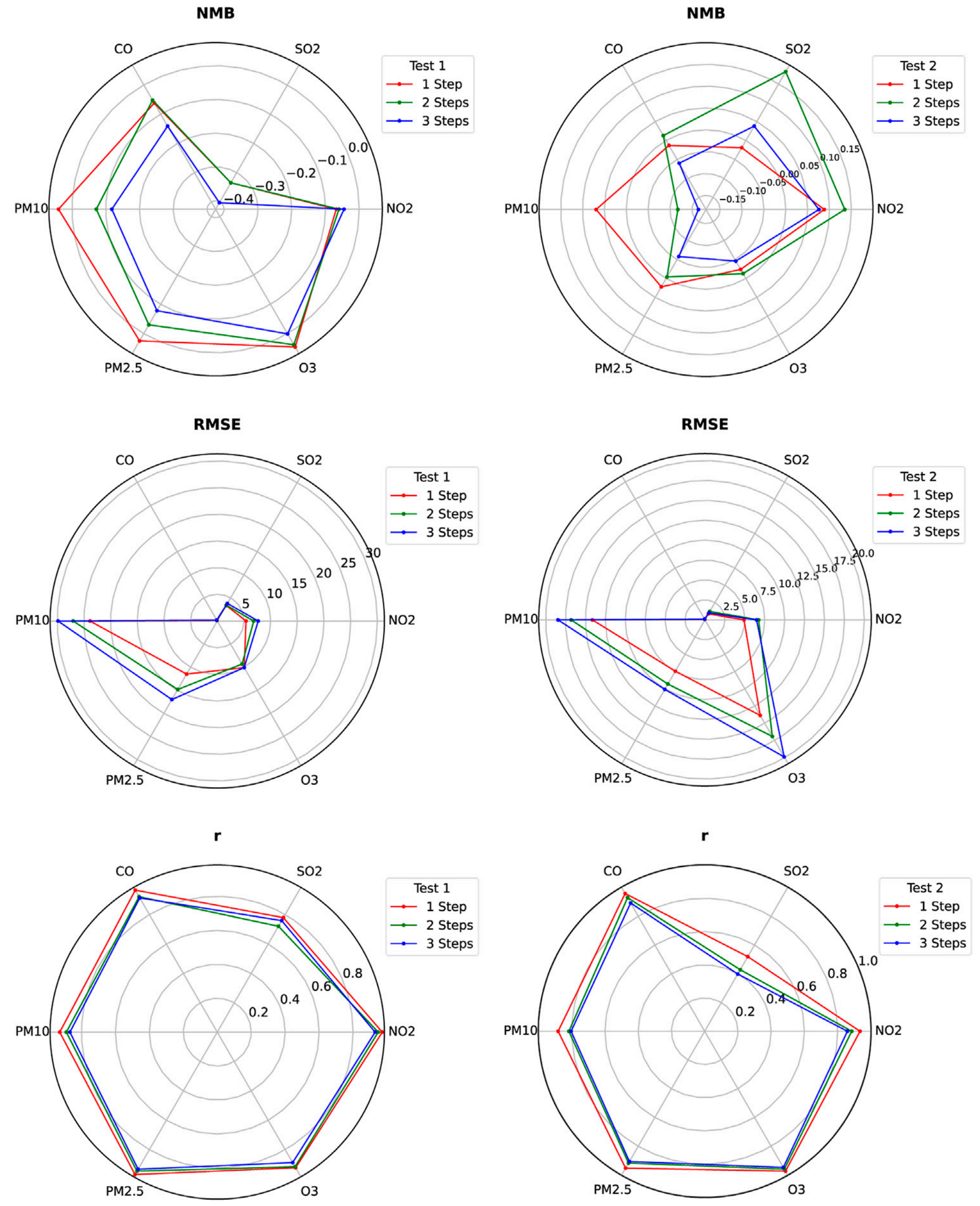

FIGURE 11
The radar chart of pollutant concentration prediction of TSTM in Beijing.

pollutants decreases, and the number of positive and negative values of NMB are approximate. The NMB of high concentration value PM_{10} (52.82 μg/m^3) increases with the increase of prediction step; The NMB of high concentration value O_3 (102.78 μg/m^3), medium concentration value $PM_{2.5}$ (36.35 μg/m^3) and low concentration value CO (0.66 mg/m^3) first decrease and then increase with the increase of prediction step. The NMB of lower concentration values of NO_2 (26.05 μg/m^3) and SO_2 (2.70 μg/m^3) first increase and then decrease with the increase of prediction step. Compared with NMB, the laws of RMSE and r of model are more obvious. Considering the current air pollution in China, CO and SO_2 are not the main pollutants, while O_3 (summer) and PM (winter) pollution are more serious, that is, they have higher frequency of pollution process (maximum value of concentration). The weak ability to predict the peak value of data is a common problem for models based on machine learning. And it can be seen from Figure 11 that the RMSE value of PM_{10}, $PM_{2.5}$ and O_3 is always greater than that of the other three pollutants. In general, RMSE value increases with the increase of pollutant concentration value and prediction step. r decreases with the increase of prediction step, and is affected by random deviation. For the same pollutant, r is positively correlated with the concentration.

Taylor diagram can compare the performance of multiple models from different aspects in single map (Taylor, 2001). It is recommended by Intergovernmental Panel on Climate Change (IPCC) and is widely favored in the field of Geoscience. Taylor diagram skillfully presents the cosine relationship of the three evaluation indicators of the model, namely, the central root mean square difference (RMSD), standard deviation and correlation coefficient. In this study, this data visualization method is applied for model comparison.

The traditional root mean square error E can be decomposed into overall deviation $\bar{E}$and central root mean square difference E'. The smaller the E', the better the prediction precision.

$$E = \left[\frac{1}{N}\sum_{n=1}^{N}\left(f_n - r_n\right)^2\right]^{1/2} \tag{9}$$

$$\bar{E} = \bar{f} - \bar{r} \tag{10}$$

$$E' = \left\{\frac{1}{N}\sum_{n=1}^{N}\left[\left(f_n - \bar{f}\right) - \left(r_n - \bar{r}\right)\right]^2\right\}^{1/2} \tag{11}$$

$$E^2 = \bar{E}^2 + E'^2 \tag{12}$$

Where N is the number of samples; f_n and r_n are the predicted and actual value of the nth sample; $\bar{f}$ and $\bar{r}$ are the average of the predicted sequence and the actual sequence.

The standard deviation σ can be used to judge whether the prediction sequence of the model reflects the dispersion of the actual sequence.

$$\sigma_A = \left[\frac{1}{N}\sum_{n=1}^{N}\left(A_n - \bar{A}\right)^2\right]^{1/2} \tag{13}$$

Where A_n and $\bar{A}$ are the nth value and average value of the sequence respectively.

The closer the correlation coefficient R is to 1, the better the prediction performance of the model.

$$R = \frac{\frac{1}{N}\sum_{n=1}^{N}\left(f_n - \bar{f}\right)\left(r_n - \bar{r}\right)}{\sigma_f \sigma_r} \tag{14}$$

Where f_n and r_n are the predicted and actual value of the nth sample; $\bar{f}$ and $\bar{r}$ are the average of the forecast sequence and the actual sequence; $\sigma_f$and σ_r are the standard deviation of the forecast sequence and the actual sequence.

Three indicators can form a cosine relationship:

$$E'^2 = \sigma_f^2 + \sigma_r^2 - 2\sigma_f\sigma_r R \tag{15}$$

$$c^2 = a^2 + b^2 - 2abcos\phi \tag{16}$$

Referring to the "Technical guide for ambient air quality prediction and early-warning methods" from the China National Environmental Monitoring Centre (China National Environmental Monitoring Centre, 2017), three classical benchmark models, Radial basis function network (RBF) of traditional machine learning, Deep Belief Network (DBN) and Elman neural network (Elman) of deep learning, are selected to compare with the proposed model TSTM.

Figure 12 and Figure 13 are Taylor diagrams of the prediction performance of four models on two test sets in Beijing. The results of Test 1 show that they are TSTM, Elman, RBF and DBN in descending order according to the prediction accuracy. Although the deep learning model has more complex structure and algorithm, it does not mean that it must obtain better effect than traditional machine learning. It is necessary to explore the applicability of different deep learning algorithms by practice, and establish an effective model for air quality prediction. In this study, DBN cannot capture the characteristics of high oscillation of air pollutant concentration, and its three indicators of all pollutants are poor. RBF has worse robustness, and the prediction accuracy is obviously affected by outlier (PM_{10}). Elman belongs to recurrent neural network and has short-term memory ability. Its prediction effect for most pollutants is second only to TSTM, but it has the same problem as RBF. TSTM not only combines CNN, BiLSTM and other advanced deep learning algorithms suitable for time series prediction, but also considers varieties of related features based on domain knowledge. As shown in experiments, TSTM obtains better results especially in the face of outliers. In addition, the multistep effects of recurrent neural network TSTM and Elman with memory ability are generally more stable, and the prediction error increases slightly with the increase of prediction step.

The experimental results of Test 2 are similar to that of Test 1. TSTM still maintains the highest precision. Take $PM_{2.5}$ in winter and O_3 in summer as examples, the RMSD (r) of the three-steps prediction are 16.52 μg/m^3 (0.93) and 19.31 μg/m^3 (0.95) respectively. The experimental results show that TSTM has good robustness and generalization ability.

4.2 Air quality forecast

The purpose of pollutant concentration prediction is to release air pollution information in advance, providing the guidance for the public in production and life as well as the basis for government in pollution prevention and control. Therefore, based on the predicted concentration of six conventional air pollutants, the performance of four models for air quality forecast is further compared and analyzed according to the "Technical Regulation on Ambient Air Quality Index (HJ 633-2012)" issued by the Ministry of Ecology and Environment of China (The Ministry of Ecology and Environment of China, 2022b). Table 1 reflects the accuracy of the four models for different tasks of air quality prediction. According to the "Technical guideline for numerical forecasting of ambient air quality (HJ 1130-2020)", the requirement for air quality level is 60%, which can be used as a reference. The results show that there is a large gap in the performance of the four

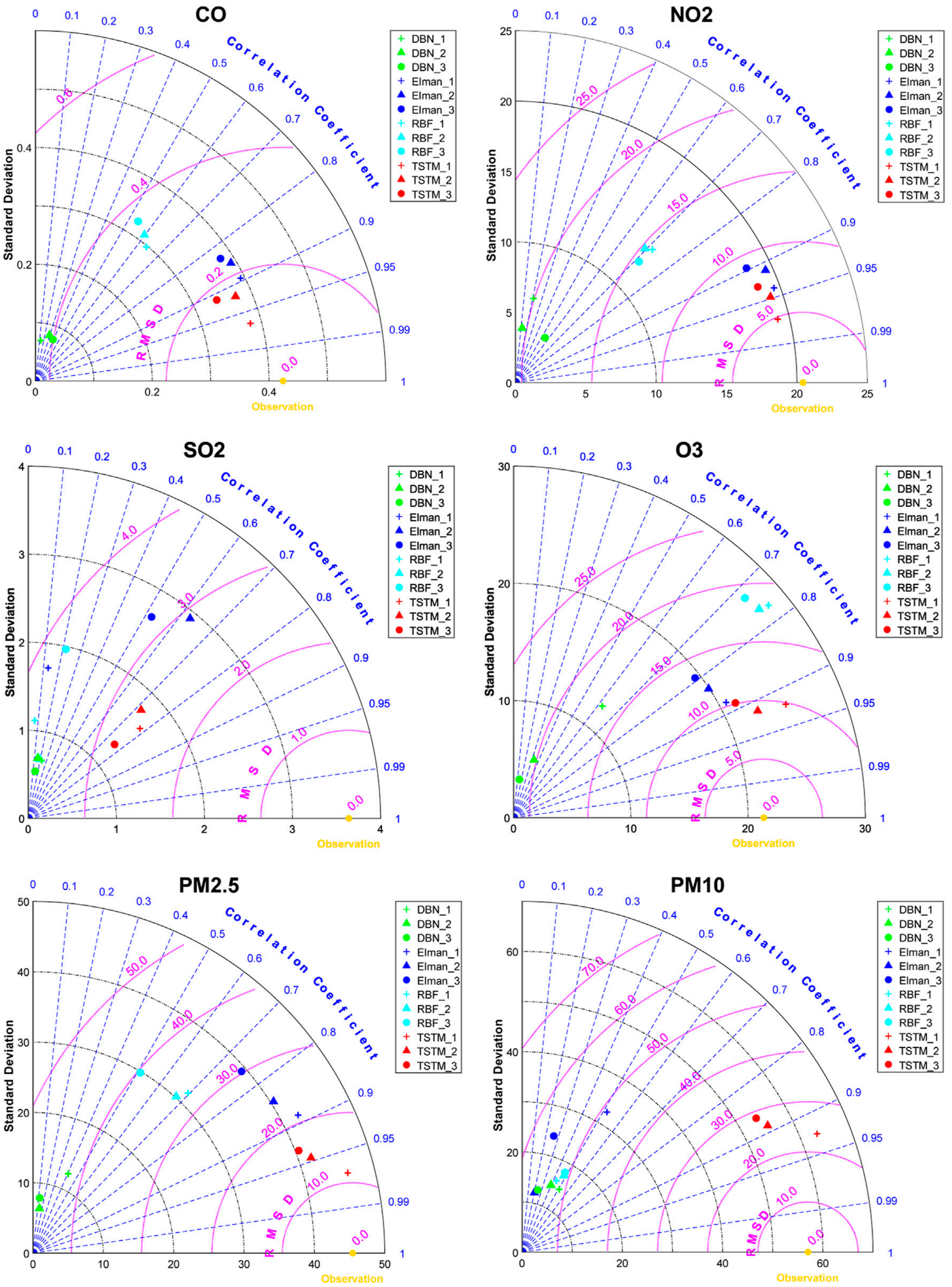

FIGURE 12
The Taylor diagram of pollutant concentration prediction in Beijing (Test 1).

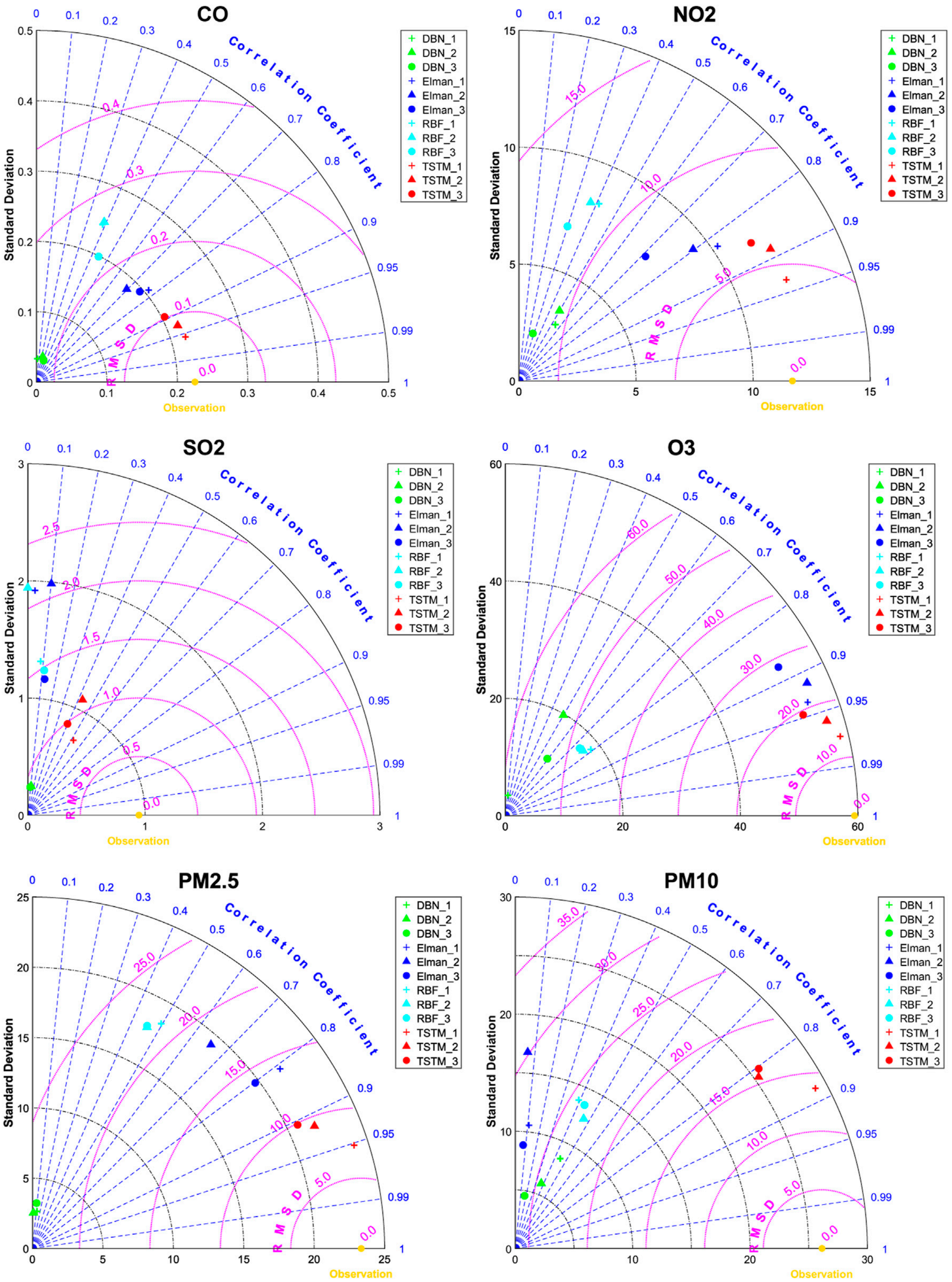

FIGURE 13
The Taylor diagram of pollutant concentration prediction in Beijing (Test 2).

TABLE 1 Accuracy of four models for air quality forecast in Beijing.

		AQI range	Air quality level	Chief pollutant
TSTM	1 step	0.88	0.98	0.91
	2 steps	0.79	0.95	0.88
	3 steps	0.69	0.92	0.86
RBF	1 step	0.30	0.71	0.67
	2 steps	0.32	0.70	0.66
	3 steps	0.33	0.67	0.62
DBN	1 step	0.32	0.73	0.46
	2 steps	0.29	0.76	0.38
	3 steps	0.29	0.77	0.40
Elman	1 step	0.50	0.87	0.73
	2 steps	0.46	0.83	0.70
	3 steps	0.45	0.80	0.70

models for air quality prediction. RBF and DBN have similar prediction accuracy for AQI range and air quality level, but DBN has poor prediction effect for chief pollutant. TSTM and Elman with recurrent neural network structure always rank in the top two. Their effects of multistep prediction are more stable, and the accuracy decreases slightly with the increase of steps. The accuracy of one-step prediction of the three benchmark models are all lower than 0.6, but the performance of TSTM is the best, reaching 0.88. The accuracy for air quality level of the four models can all meet the national requirement. TSTM has the best performance, its one-step and three-steps prediction can reach 0.98 and 0.92, respectively.

4.3 Heavy pollution weather forecast

For air pollution prevention and control, heavily polluted weather has always been the focus of attention. In order to reduce pollution and protect human health, all cities issue the emergency plan for heavy air pollution and take measures according to the air quality forecast results. Therefore, it is crucial to ensure the prediction accuracy in heavy pollution weather. At the same time, the prediction ability for peak values has always been a difficulty and challenge for machine learning model, and the heavy pollution weather contains more concentration maximum values, which is a “touchstone” to test the robustness of the model. Table 2 reveals great differences of the four models under extreme conditions. Deep learning has a higher upper limit than traditional machine learning, and the prediction accuracy of RBF for heavy pollution weather is lower than that of three deep learning models. Elman still maintains the second position. However, with the increase of prediction steps, the performance decreases significantly, and the accuracy for air quality level of three-steps prediction is lower than 0.6. TSTM widens the gap with other models in heavy pollution weather forecast. The accuracy and test score of one-step prediction are close to the full score, although the performance decreases slightly with the steps, the results of three-steps prediction are also above 0.86.

TABLE 2 Performance of four models for heavy pollution weather forecast in Beijing.

		Prediction accuracy	Prediction test score
TSTM	1 step	1	0.97
	2 steps	0.93	0.94
	3 steps	0.87	0.86
RBF	1 step	0.07	0.07
	2 steps	0	0
	3 steps	0	0
DBN	1 step	0.32	0
	2 steps	0.29	0
	3 steps	0.29	0
Elman	1 step	0.80	0.82
	2 steps	0.73	0.71
	3 steps	0.50	0.49

5 Conclusion

Accurate prediction of pollutant concentration is significant to air pollution prevention. To overcome the shortcomings of present studies, a novel integrated model TSTM is proposed to achieve regional and multistep air quality prediction. The domain knowledge of Atmospheric Sciences is innovatively introduced to design the model architecture, and advanced deep learning algorithms including ConvLSTM, Seq2Seq, *etc.* are applied to learn important correlations of time, space, type, meteorology. “Beijing-Tianjin-Hebei air pollution transmission channel (2+26 cities)" is selected as the study area, and the prediction of hourly concentrations for six conventional air pollutants in all cities are carried out. And then the detailed performance evaluation and analysis are conducted based on two independent test sets (winter and summer) and three benchmark models (RBF, DBN, Elman).

Pollutant concentration prediction results show that TSTM has small NMB and RMSE as well as large r, which is similar in all cities. As for air quality prediction, there are similar prediction effects as pollutant concentration prediction. TSTM is obviously better than other comparison models, and the prediction accuracy only decreases slightly with the increase of prediction step. The tests under heavy pollution weather show that TSTM and Elman with recurrent neural network structure have better results, but the accuracy of Elman with short-term memory decreases significantly with the increase of prediction step. In general, comprehensive experiments and detail evaluations prove TSTM's feasibility on regional and multistep air quality prediction especially in heavy pollution weather. In future, we will continue improving our model, which is hoped to provide effective supports for the daily health guide of the public and the air pollution control of government.

Data availability statement

The data can be downloaded from http://www.cma.gov.cn/ and http://www.mee.gov.cn. Basic models can be called from the Keras of Python. And other materials will be provided when requested.

Author contributions

All authors listed have made a substantial, direct, and intellectual contribution to the work and approved it for publication.

Funding

This work was supported by the Scientific Research Fund of Hainan University (grant number: KYQD (ZR)-22097, KYQD (ZR)-22096).

Conflict of interest

The authors declare that the research was conducted in the absence of any commercial or financial relationships that could be construed as a potential conflict of interest.

Publisher's note

References

Bahdanau, D., Cho, K., and Bengio, Y. (2014). *Neural machine translation by jointly learning to align and translate[J]*. arXiv preprintarXiv:1409.0473).

Chakma, A., Vizena, B., Cao, T., Lin, J., and Zhang, J. (2017). "Image-based air quality analysis using deep convolutional neural network[C]," in *2017 IEEE international conference on image processing (ICIP), 17-20 sept*, 3949–3952.

Chen, J., Shen, H., Li, T., Peng, X., Cheng, H., and Ma, C. (2019). Temporal and spatial features of the correlation between PM2.5 and O3 concentrations in China. *Int. J. Environ. Res. Public Health* 16 (23), 4824. doi:10.3390/ijerph16234824

Chen, Y. (2018). Prediction algorithm of PM2.5 mass concentration based on adaptive BP neural network. *Computing* 100 (8), 825–838. doi:10.1007/s00607-018-0628-3

Cheng, F., Feng, C., Yang, Z., Hsu, C. H., Chan, K. W., Lee, C. Y., et al. (2021). Corrigendum to "Evaluation of real-time PM2.5 forecasts with the WRF-CMAQ modeling system and weather-pattern-dependent bias-adjusted PM2.5 forecasts in Taiwan". *Atmos. Environ.* 354, 118263. doi:10.1016/j.atmosenv.2021.118263

Cheng, Y., Zhang, H., Liu, Z., Chen, L., and Wang, P. (2019). Hybrid algorithm for short-term forecasting of PM2.5 in China[J]. *Atmos. Environ.* 200, 264–279.

China Meteorological Administration. 2022. *Grades of air pollution diffusion meteorological conditions*. Beijing: QX/. T 413-2018) [EB/OL]. [2022-07-15] Availabla at: http://cmastd.cmatc.cn/standardView.jspx?id=2875.

China National Environmental Monitoring Centre (2017). *Technical guide for ambient air quality prediction and early-warning methods[M]*. Beijing: China Environmental Science Press.

Cho, K., Merrienboer, B. V., Gulcehre, C., Bahdanau, D., Bougares, F., Schwenk, H., et al. (2014). Learning phrase representations using RNN encoder-decoder for statistical machine translation[J]. *Comput. Sci.* 338, 1724–1734.

Dong, Z., Wang, S., Xing, J., Chang, X., Ding, D., and Zheng, H. (2020). Regional transport in Beijing-Tianjin-Hebei region and its changes during 2014–2017: The impacts of meteorology and emission reduction. *Sci. Total Environ.* 737, 139792. doi:10.1016/j.scitotenv.2020.139792

Drozd, G. T., Zhao, Y., Saliba, G., Frodin, B., Maddox, C., Oliver Chang, M. C., et al. (2018). Detailed speciation of intermediate volatility and semivolatile organic compound emissions from gasoline vehicles: Effects of cold-starts and implications for secondary organic aerosol formation. *Environ. Sci. Technol.* 53 (3), 1706–1714. doi:10.1021/acs.est.8b05600

Hochreiter, S., and Schmidhuber, J. (1997). Long short-term memory. *Neural Comput.* 9 (8), 1735–1780. doi:10.1162/neco.1997.9.8.1735

Ian, G., Yoshua, B., and Aaron, C. (2017). *Deep learning[M]*. MIT Press.

Jerrett, M. (2015). Atmospheric science: The death toll from air-pollution sources [J]. *Nature* 525 (7569), 330–331. doi:10.1038/525330a

Jin, J., Li, M., and Jin, L. (2015). Data normalization to accelerate training for linear neural net to predict tropical cyclone tracks. *Math. Problems Eng.* 2015, 1–8. doi:10.1155/2015/931629

Jury, M. R. (2020). Meteorology of air pollution in los angeles. *Atmos. Pollut. Res.* 11 (7), 1226–1237. doi:10.1016/j.apr.2020.04.016

Kim, K., Kim, D., Noh, J., and Kim, M. (2018). Stable forecasting of environmental time series via long short term memory recurrent neural network. *IEEE Access* 6, 75216–75228. doi:10.1109/access.2018.2884827

Kong, L., Hu, M., Tan, Q., Feng, M., Qu, Y., An, J., et al. (2019). Key role of atmospheric water content in the formation of regional haze in southern China. *Atmos. Environ.* 216, 116918. doi:10.1016/j.atmosenv.2019.116918

Lecun, Y. (1989). Generalization and network design strategies[J]. *Connect. perspective* 19.

Li, T., Wang, Y., and Yuan, Q. (2020). Remote sensing estimation of regional NO2 via space-time neural networks. *Remote Sens.* 12, 2514. doi:10.3390/rs12162514

Li, X., Jin, L., and Kan, H. (2019). Air pollution: A global problem needs local fixes. *Nature* 570 (7762), 437–439. doi:10.1038/d41586-019-01960-7

Liu, Z., Wang, H., Shen, X., Peng, Y., Shi, Y., Che, H., et al. (2019). Contribution of meteorological conditions to the variation in winter PM2.5 concentrations from 2013 to 2019 in middle-eastern China. *Atmosphere* 10 (10), 563. doi:10.3390/atmos10100563

Menares, C., Gallardo, L., Kanakidou, M., Seguel, R., and Huneeus, N. (2020). Increasing trends (2001–2018) in photochemical activity and secondary aerosols in Santiago, Chile. *Tellus B Chem. Phys. Meteorology* 72 (1), 1821512–1821518. doi:10.1080/16000889.2020.1821512

Mo, X., Li, H., Zhang, L., and Qu, Z. (2020). A novel air quality evaluation paradigm based on the fuzzy comprehensive theory. *Appl. Sci. (Basel).* 10 (23), 8619. doi:10.3390/app10238619

Mo, X., Li, H., Zhang, L., and Qu, Z. (2021). Environmental impact estimation of PM2.5 in representative regions of China from 2015 to 2019: Policy validity, disaster threat, health risk, and economic loss. *Air Qual. Atmos. Health* 14 (10), 1571–1585. doi:10.1007/s11869-021-01040-8

Mo, X., Zhang, l., Li, H., and Qu, Z. (2019). A novel air quality early-warning system based on artificial intelligence. *Int. J. Environ. Res. Public Health* 16 (19), 3505. doi:10.3390/ijerph16193505

Mu, L., Su, J., Mo, X., Peng, N., Xu, Y., Wang, M., et al. (2021). The temporal-spatial variations and potential causes of dust events in xinjiang basin during 1960–2015. *Front. Environ. Sci.* 9, 727844. doi:10.3389/fenvs.2021.727844

Neal, R. M., and Hinton, G. E. (1998). "A view of the em algorithm that justifies incremental, sparse, and other variants[M]," in *Learning in graphical models*.(Dordrecht: Springer Netherlands), 355–368.

Ng, K. Y., and Awang, N. (2018). Multiple linear regression and regression with time series error models in forecasting PM10 concentrations in Peninsular Malaysia. *Environ. Monit. Assess.* 190 (2), 63. doi:10.1007/s10661-017-6419-z

Pak, U., Ma, J., Ryu, U., Ryom, K., Juhyok, U., Pak, K., et al. (2020). Deep learning-based PM2.5 prediction considering the spatiotemporal correlations: A case study of beijing, China. *Sci. Total Environ.* 699, 133561. doi:10.1016/j.scitotenv.2019.07.367

Pérez, I. A., García, M., Sánchez, M. L., Pardo, N., and Fernández-Duque, B. (2020). Key points in air pollution meteorology. *Int. J. Environ. Res. Public Health* 17 (22), 8349. doi:10.3390/ijerph17228349

Perišić, M., Maletić, D., Stojić, S. S., Rajšić, S., and Stojić, A. (2017). Forecasting hourly particulate matter concentrations based on the advanced multivariate methods. *Int. J. Environ. Sci. Technol. (Tehran).* 14 (5), 1047–1054. doi:10.1007/s13762-016-1208-8

Pohoata, A., and Lungu, E. (2017). A complex analysis employing ARIMA model and statistical methods on air pollutants recorded in ploiesti, Romania. *Rev. Chim.* 68, 818–823. doi:10.37358/rc.17.4.5559

Sahu, S. K., Sharma, S., Zhang, H., Chejarla, V., Guo, H., Hu, J., et al. (2020). Estimating ground level PM2.5 concentrations and associated health risk in India using satellite based AOD and WRF predicted meteorological parameters. *Chemosphere* 255, 126969. doi:10.1016/j.chemosphere.2020.126969

Schuster, M., and Paliwal, K. K. (1997). Bidirectional recurrent neural networks. *IEEE Trans. Signal Process.* 45 (11), 2673–2681. doi:10.1109/78.650093

Shi, X., Chen, Z., Wang, H., Yeung, D-Y., Wong, W. K., and Woo, W-C. (2015). "Convolutional LSTM network: A machine learning approach for precipitation nowcasting[C]," in *Proc.eedings of the 28th Int.ernational Conf.erence on Neural Inf.ormation Processing Syst.ems* 06/121 (Cambridge, MA, USA: MIT Press), 802–810.

Spiridonov, V., Jakimovski, B., Spiridonova, I., and Pereira, G. (2019). Development of air quality forecasting system in Macedonia, based on WRF-Chem model. *Air Qual. Atmos. Health* 12 (7), 825–836. doi:10.1007/s11869-019-00698-5

Sun, J., Huang, L., Liao, H., Li, J., and Hu, J. (2017). Impacts of regional transport on particulate matter pollution in China: A review of methods and results. *Curr. Pollut. Rep.* 3 (3), 182–191. doi:10.1007/s40726-017-0065-5

Taylor, K. E. (2001). Summarizing multiple aspects of model performance in a single diagram. *J. Geophys. Res.* 106 (D7), 7183–7192. doi:10.1029/2000jd900719

The Ministry of Ecology and Environment of China. 2022. Technical guideline for numerical forecasting of ambient air quality. HJ 1130-2020) [EB/OL]. [2022-07-15] Availabla at: https://www.mee.gov.cn/ywgz/fgbz/bz/bzwb/jcffbz/202005/t20200518_779714.shtml.

The Ministry of Ecology and Environment of China. 2022. Technical regulation on ambient air quality index. HJ 633-2012) [EB/OL]. [2022-07-15] Availabla at: https://www.mee.gov.cn/ywgz/fgbz/bz/bzwb/jcffbz/201203/W020120410332725219541.pdf.

The Standardization administration of China 2022. Grades of atmospheric purification capability. GB/T 34299-2017) [EB/OL]. [2022-07-15] Availabla at: http://ah.cma.gov.cn/zfxxgk/zwgk/flfgbz/dfbz/202102/t20210210_2720010.html.

Ulpiani, G., Duhirwe, P., Yun, G., and Lipson, M. (2022). Meteorological influence on forecasting urban pollutants: Long-term predictability versus extreme events in a spatially heterogeneous urban ecosystem. *Sci. Total Environ.* 814, 152537. doi:10.1016/j.scitotenv.2021.152537

United Nations Environment Programme. 2022. International Day of Clean Air for blue skies. [EB/OL].[2022-07-05] Availabla at: https://www.un.org/en/observances/clean-air-day.

Wang, H., Li, X., Wang, D., Zhao, J., He, H., and Peng, Z-R. (2020). Regional prediction of ground-level ozone using a hybrid sequence-to-sequence deep learning approach. *J. Clean. Prod.* 253, 119841. doi:10.1016/j.jclepro.2019.119841

Wang, P., Guo, H., Hu, J., Kota, S. H., Ying, Q., and Zhang, H. (2019). Responses of PM2.5 and O3 concentrations to changes of meteorology and emissions in China. *Sci. Total Environ.* 662, 297–306. doi:10.1016/j.scitotenv.2019.01.227

Wen, C., Liu, S., Yao, X., Peng, L., Li, X., Hu, Y., et al. (2019). A novel spatiotemporal convolutional long short-term neural network for air pollution prediction. *Sci. Total Environ.* 654, 1091–1099. doi:10.1016/j.scitotenv.2018.11.086

Xue, Y., Cao, X., Ai, Y., Xu, K., and Zhang, Y. (2020). Primary air pollutants emissions variation characteristics and future control strategies for transportation sector in beijing, China. *Sustainability* 12 (10), 4111. doi:10.3390/su12104111

Yu, T., Wang, Y., Huang, J., Liu, X., Li, J., and Zhan, W. (2022). Study on the regional prediction model of PM2.5 concentrations based on multi-source observations. *Atmos. Pollut. Res.* 13 (4), 101363. doi:10.1016/j.apr.2022.101363

Zhao, S., Yu, Y., Qin, D., Yin, D., Dong, L., and He, J. (2019). Analyses of regional pollution and transportation of PM2.5 and ozone in the city clusters of Sichuan Basin, China. *Atmos. Pollut. Res.* 10 (2), 374–385. doi:10.1016/j.apr.2018.08.014

frontiers | Frontiers in Earth Science

TYPE Original Research
PUBLISHED 06 October 2022
DOI 10.3389/feart.2022.1018661

OPEN ACCESS

EDITED BY
Jianqi Sun,
Institute of Atmospheric Physics (CAS),
China

REVIEWED BY
Eduardo Zorita,
Helmholtz Centre for Materials and
Coastal Research (HZG), Germany
Huopo Chen,
Institute of Atmospheric Physics (CAS),
China

*CORRESPONDENCE
Eva Holtanová,
Eva.Holtanova@matfyz.cuni.cz

SPECIALTY SECTION
This article was submitted to
Atmospheric Science,
a section of the journal
Frontiers in Earth Science

RECEIVED 13 August 2022
ACCEPTED 21 September 2022
PUBLISHED 06 October 2022

CITATION
Holtanová E, Belda M and Halenka T
(2022), Projected changes in mean
annual cycle of temperature and
precipitation over the Czech Republic:
Comparison of CMIP5 and CMIP6.
Front. Earth Sci. 10:1018661.
doi: 10.3389/feart.2022.1018661

Projected changes in mean annual cycle of temperature and precipitation over the Czech Republic: Comparison of CMIP5 and CMIP6

Eva Holtanová*, Michal Belda and Tomáš Halenka

Department of Atmospheric Physics, Faculty of Mathematics and Physics, Charles University, Prague, Czechia

The multi-model ensembles like CMIP5 or CMIP6 provide a tool to analyze structural uncertainty of climate simulations. Currently developed regional and local climate change scenarios for the Czech Republic assess the uncertainty based on state-of-the-art Global Climate Model (GCM) and Regional Climate Model (RCM) ensembles. Present study focuses on multi-model spread of projected changes in long-term monthly means and inter-annual variability of monthly mean minimum, mean and maximum daily air temperature and monthly mean precipitation. We concentrate in more detail on the simulation of CNRM-ESM2-1, the driving GCM for the convection permitting ALADIN-Climate/CZ simulation contributing to the local scenarios in very high resolution. For this GCM, we also analyze a mini-ensemble with perturbed initial conditions to evaluate the range of internal climate variability. The results for the Czech Republic reveal minor differences in model performance in the reference period whereas quite substantial inter-generation shift in projected future change towards higher air temperature and lower summer precipitation in CMIP6 comparing to CMIP5. One of the prominent features across GCM generations is the pattern of summer precipitation decrease over central Europe. Further, projected air temperature increase is higher in summer and autumn than in winter and spring, implying increase of thermal continentality of climate. On the other hand, slight increase of winter precipitation and tendency towards decrease of summer precipitation lead to projected decrease of ombric continentality. The end of 21st century projections also imply higher probability of dry summer periods, higher precipitation amounts in the cold half of the year and extremely high temperature in summer. Regarding the CNRM-ESM2-1, it is often quite far from the multi-model median. Therefore, we strictly recommend to accompany any analysis based on the simulation of nested Aladin-CLIMATE/CZ with proper uncertainty estimate. The range of uncertainty connected to internal climate variability based on one GCM is often quite large in comparison to the range of whole CMIP6 ensemble. It implies that when constructing climate change scenarios for the Central Europe region, attention should be paid not only to structural uncertainty represented by inter-model differences and scenario uncertainty, but also to the influence of internal climate variability.

KEYWORDS

climate change projections, uncertainty, air temperature, precipitation, central Europe, annual cycle, inter-annual variability

Introduction

The climate change is an essential problem of the planet Earth and associated global changes affect natural ecosystems as well as human activities. As a basis for the assessment of its effects across many Earth Science disciplines, global climate models (GCMs) are commonly used providing the tool for projections of these changes and impacts. Thus, the outputs of GCMs have become an indispensable source of information to many sectors and research fields, most prominently for studying climate system dynamics (e.g. Dai and Deng, 2022; Yang et al., 2022), evolution of past climates (e.g. Otto-Bliesner et al., 2017) and climate change projections (e.g. Belda et al., 2017; Coppola et al., 2021a; Thomas et al., 2022). However, model simulations of climate are subject to many uncertainties. Generally, the uncertainties in model outputs come from the inaccuracies of initial and boundary conditions, the parameterization of small-scale processes, and the structure of the model (Tebaldi and Knutti, 2007; Abramowitz et al., 2019). Additionally, in the case of future climate simulations, the unknown development of forcings that influence the climate system also plays a role (e.g. Meinshausen et al., 2020). Ensembles of simulations of one model with perturbed initial conditions are designed to provide an estimate of uncertainty stemming from internal climate variability, which is inevitably different in models and in the real world (e.g. Deser et al., 2012; Deser, 2020). The relative importance of uncertainty connected to internal climate variability increases with shorter temporal scale and smaller spatial scale of studied phenomena (e.g. Bassett et al., 2020; Poschlod and Ludwig, 2021). The multi-model ensembles provide a tool to analyze structural uncertainty (connected to choices of numerical schemes, spatial resolution, etc.), even though the interpretation of multi-model spread is not simple. However, the design of available ensembles in terms of model choice is not systematic and thus the commonly used model ensembles such as CMIP (Coupled Model Intercomparison Project) or CORDEX (Coordinated Regional Climate Downscaling Experiment) do not represent an independent estimate of the overall uncertainty (Abramowitz et al., 2019).

Czech Republic has joined the United Nations Framework Convention on Climate Change (UNFCCC). One of the obligations connected with the UNFCCC ratification is to observe the ongoing climate change and its impacts and to support research in the fields of climate change, its impacts, adaptation and impact mitigation. In present, this goal is approached within the project PERUN (https://www.perun-klima.cz/indexENG.html), connecting the study of local climate changes and impacts with preparation of adaptation options in several other disciplines and sectors, like hydrology, agriculture, etc. Regional and local climate change scenarios for the Czech Republic that are currently being developed within this project will try to distill all the available information, with CMIP6 GCMs (Eyring et al., 2016) being the straightforward resource. However, for regional and local applications, RCMs provide better information with added value coming from the higher resolution (Torma and Giorgi, 2020), eventually more detailed description of some processes, e.g. convection (Kendon et al., 2017). Regional climate models (RCMs) have become widely accepted as physically consistent tool for downscaling spatially coarse GCM simulations (Giorgi, 2019). RCMs inevitably need inputs from their driving GCMs and the RCM simulations are substantially influenced by the driving fields (Takayabu et al., 2016; Crhová and Holtanová, 2018; Holtanová et al., 2019; Prein et al., 2019). For the purpose of the project, EURO-CORDEX RCM simulations (e.g. Jacob et al., 2020) downscaling the CMIP5 GCMs (Taylor et al., 2012) that are available up to now are very useful. In addition, there is strong effort within the PERUN project to use convection permitting RCM ALADIN-Climate/CZ (Termonia et al., 2018; Wang et al., 2018) in very high horizontal resolution of 2.3 km and to analyze its results within uncertainty estimates derived from available ensembles of GCM and RCM simulations. Therefore, to provide a basis for further uncertainty estimate, we first analyze available GCM outputs from both the CMIP6 project and their predecessors from CMIP5 project.

In the present study, we focus on multi-model spread of projected changes in long-term monthly means and inter-annual variability of selected variables. The analysis is based on CMIP5 and CMIP6 multi-model ensembles. It is done for monthly mean minimum, mean and maximum daily air temperature and monthly mean precipitation as basic variables characterizing climate of studied area. The annual cycle of these characteristics has an important impact in various sectors of human activities as well as natural ecosystems. Some recent studies (e.g. Coppola et al., 2021a; Coppola et al., 2021b; Palmer et al., 2021) have already analyzed the CMIP5 and CMIP6 projections for Europe, but in the present study we provide a more detailed information about the expected changes focusing on Central Europe and climatic characteristics relevant for various end-users.

Besides the analysis and comparison of the whole GCM ensembles, we concentrate in more detail on the simulation of CNRM-ESM2-1 (Séférian et al., 2019) because this model (specifically the run denoted as r1i1p1f2) is used as the driving GCM in above mentioned project PERUN. For this model, we also analyze a mini-ensemble consisting of simulations with perturbed initial conditions (see *Data and methods* Section).

The paper is structured as follows. The data and methods used for the analysis are described in *Data and methods* Section. The results are described and illustrated in *Results* Section. *Discussion* Section discusses the results and *Conclusion* Section provides conclusions with future prospects and possible usage of our results.

Data and methods

A suite of CMIP5 and CMIP6 GCM simulations is employed here. List of all model simulations incorporated is presented in Supplementary Tables S1, S2 (in the Supplementary material). Further information and references can be found in Tebaldi et al. (2021) for CMIP6 and at PCMDI website (https://pcmdi.llnl.gov/mips/cmip5/availability.html) for CMIP5. The data were approached *via* Deutsches Klimarechenzentrum (DKRZ); we used monthly means of daily mean air temperature (further abbreviated as TAS), daily maximum air temperature (TX), daily minimum air temperature (TN) and daily precipitation (PR). For both CMIP5 and CMIP6, the outputs from the experiment denoted as 'historical' were used for the reference period 1961–1990. For the future time period of 2070–2099, we considered simulations for two alternative socio-economic and emission scenarios. For CMIP5, the representative concentration pathways (RCPs, Moss et al., 2010) RCP4.5 and RCP8.5 were used. For CMIP6, two shared socio-economic pathways (SSPs, Meinshausen et al., 2020) SSP2-4.5 and SSP5-8.5 were chosen.

The GCMs were selected based on the availability of data for selected scenarios in the time of analysis preparation. In total, there are 47 CMIP5 GCMs and 57 CMIP6 GCMs with varying number of available simulations for individual variables and time periods (Supplementary Tables S1, S2). We decided not to choose only corresponding simulations for each ensemble as we wanted to include as many model simulations as possible to gain as wide uncertainty range as possible. Where more ensemble members were available, we used only r1i1p1 simulations for CMIP5. For CMIP6 we used preferably r1i1p1f1, but where "f1" is not available, we used "f2". The "f" index distinguishes simulations run under the same CMIP6 experiment protocol, but with different forcing. For more detailed explanation of the notation "ripf" please see CMIP protocol and associated documentation. In case of CNRM-ESM2-1 from CMIP6 ensemble we also used other available realizations (technically, ensemble members with different "r" values), varying from r1 to r10 in case of historical and SSP2-4.5, and from r1 to r5 in case of SSP5-8.5. These mini-ensembles provide a rough view of the uncertainty connected to perturbed initial conditions, e.i. representing internal climate variability, and are further denoted as "CNRM_INI". We especially focus on the simulation of CNRM-ESM2-1 r1i1p1f2, which is the driving simulation for the Aladin-Climate/CZ as described in the *Introduction* Section. This simulation is denoted as CNRM_r1 in the rest of the text.

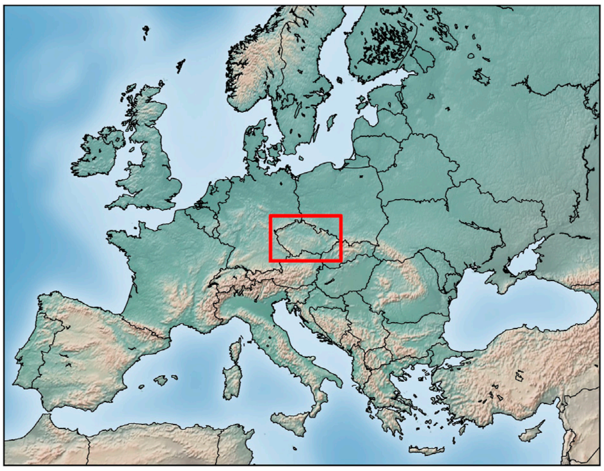

FIGURE 1
The orography of Europe with red box denoting the area studied here.

We concentrate on mean annual cycle of monthly mean values of studied variables (TAS, PR, TN, TX) and on annual cycle of standard deviation of the monthly values for both time periods 1961–1990 (further denoted as reference) and 2070–2099 (further denoted as future). Standard deviation was chosen as a basic measure of inter-annual variability of studied variables. For its calculation we used "(n-1)" in the denominator, and the data for each 30-year period were linearly detrended.

Further, we also used several observed datasets. For all incorporated variables, we used EOBS v.23.1e (Cornes et al., 2018) in two spatial resolutions (0.25° and 0.11°). For TAS and PR we also used two versions of Climatic Research Unit (CRU) datasets: TS 3.22 dataset (Harris et al., 2014) and TS 4.05 dataset (Harris et al., 2020). For PR we further used the dataset created by GPCC Global Precipitation Climatology Centre (https://www.dwd.de/EN/ourservices/gpcc/gpcc.html) version 7 in two spatial resolutions (1° and 0.5°) (Becker et al., 2013). The spread between individual observed datasets provides a benchmark for the evaluation of multi-model spread.

The GCM simulations were interpolated to a common grid corresponding to the grid used by Climatic research unit with horizontal resolution of 0.5° × 0.5°. A simple bilinear interpolation method was used for this purpose (similarly like in Belda et al., 2015). The purpose of this interpolation is to avoid the influence of different gridbox sizes which could result in

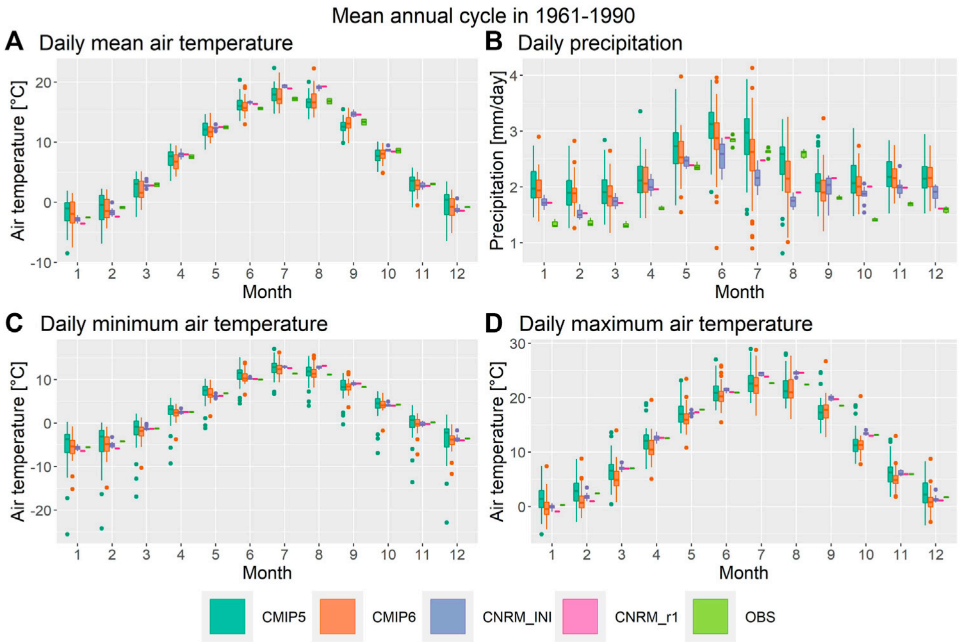

FIGURE 2
Mean annual cycle of monthly means of daily mean air temperature **(A)**, daily precipitation amount **(B)**, daily minimum air temperature **(C)** and daily maximum air temperature **(D)** in the period 1961–1990 averaged over the studied area (see Figure 1). Boxplots show intra-ensemble statistical distribution (median, lower and upper quartiles, whiskers representing 1.5 * IQR, and outliers as dots) of CMIP5 (green), CMIP6 (orange), perturbed initial conditions mini-ensemble of CNRM-ESM2-1 model (CNRM_INI, 10 members, blue) and observations (consisting of EOBS v. 23.1 in both 0.1° and 0.25° resolutions, for daily mean air temperature and precipitation also CRU TS 3.22 and CRU TS 4.05 datasets, for precipitation also GPCC version 7 datasets in two spatial resolutions (1° and 0.5°), green). The CNRM-ESM2-1 r1i1p1f2 simulation is plotted as a pink line.

different size of studied area. The observed datasets were used with their original grids.

The area used for the analysis covers the region between 11.85° and 19.15° E of longitude and 48.25° and 51.25° N of latitude (Figure 1). We concentrate on the values averaged over this region, which covers the area of the Czech Republic. The effective spatial resolution does not allow GCMs to resolve details of climate over orographically complex area of the Czech Republic (effective spatial resolution depends on numerical methods incorporated in the models but is generally several times coarser than the nominal spatial resolution), therefore we focus on areal averages over the region of interest.

The results are presented in the form of boxplots that show median, lower and upper quartiles with whiskers extending no more than 1.5*IQR (inter-quartile range) from the hinges, and outliers plotted as points.

For the comparison of model performance between corresponding pairs of CMIP5 and CMIP6 GCMs we use the root mean square error (RMSE) of monthly values plotted in Figure 2. As reference data we use the EOBS data in 0.25°. The RMSE was used for RCM evaluation over the Czech Republic by Holtanová et al. (2012), on global scale by e.g. Gleckler et al. (2008).

Results

The results are described separately for the reference period of 1961–1990 (*Mean annual cycle in 1961–1990* Section) and for future time period of 2070–2099 (*Projected changes* Section).

Mean annual cycle in 1961–1990

Figure 2 shows the results for monthly mean values of studied variables, whereas Figure 3 shows the results for annual cycle of standard deviation of the monthly values.

Results for monthly means of daily mean air temperature (TAS) are displayed in Figure 2A. Generally, both CMIP6 and CMIP5 GCMs represent the mean annual cycle quite well. Except for August, September and October, the CMIP6 multi-model median gives lower temperatures than CMIP5 median, which otherwise tend to overestimate observed values. Regarding the multi-model ensemble spread (both IQR and the minimum-maximum range) it cannot be concluded that in all months it is smaller or larger in CMIP6 than CMIP5, even though there is a different number of simulations in CMIP6 (57 vs 42, see Supplementary Tables S1, S2), so it could be expected that the range of CMIP6 was larger. There are a couple of outliers in both

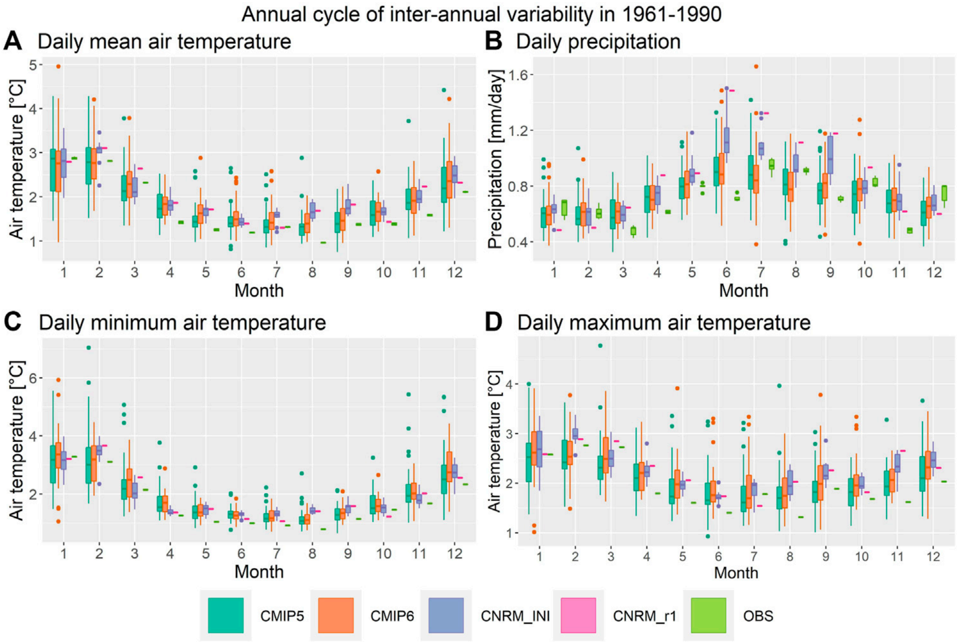

FIGURE 3
Same as Figure 2, but for standard deviation of monthly mean values.

ensembles in some months, but these are different models in different months. Therefore we cannot mark any of the GCMs to be systematically worse than the others. CNRM_INI ensemble members have mean annual amplitude of TAS higher than observed with winter temperatures lower and summer temperatures higher than observed and simulated by most of the GCMs. CNRM_r1 lies in the lower part of the multi-model distribution in January and in higher part in July and August (Figure 2A).

Both CMIP5 and CMIP6 ensembles tend to overestimate observed values of monthly mean precipitation (pr), especially in the cold half of the year (Figure 2B). Only in May, June, July and September the CMIP6 multi-model median is close to observed monthly mean precipitation. In the rest of months the differences between CMIP5 and CMIP6 are small, with CMIP6 giving slightly lower precipitation amounts (and thus being closer to observations). CNRM-INI mini-ensemble lies within the lowest quartile of CMIP6 in most months. In winter, the range of CNRM-INI mini-ensemble is comparable to the range of different observed values (from six different datasets), whereas in the rest of the year the differences between observed precipitation are much less than the range of CNRM-INI. CNRM_r1 simulation tends to be in the lower part of the CMIP6 ensemble distribution, except for May, June and July, being quite close to the observed precipitation amounts in these months (Figure 2B).

There are a few GCMs outlying strongly from both multi-model ensembles severely underestimating EOBS values of daily minimum air temperature (TN, Figure 2C, note that only EOBS dataset includes TN and TX). In CMIP5 these are all three IPSL GCMs, in CMIP6 the most outlying simulation is AWI-CM-1-1-MR, the other outliers vary between months. If we do not take these outliers into account the patterns of GCMs distributions of TN are very similar to TAS.

In case of daily maximum air temperature (TX) mean annual cycle, contrarily to TAS and TN, CMIP6 GCMs give worse results than CMIP5 in most of the months (Figure 2D). CMIP6 underestimate observed TX, whereas CMIP5 correspond well to EOBS except for August–October, where it underestimates EOBS similarly to CMIP6. A few outliers from both muti-model ensembles overestimate TX. In most of the months, these outliers correspond to the simulations that underestimate TN (see above), i.e., “IPSL” models from CMIP5 and AWI-CM-1-1-MR from CMIP6. However, it is not possible to conclude that these models would be the worst in general, because according to simulated annual cycle of TAS and PR they give better results.

Both CMIP5 and CMIP6 ensembles capture the shape of annual cycle of standard deviation of TAS quite well with respect to the observed values, with slight overestimation especially in spring and autumn (Figure 3A). Again, the outlying simulations differ between months. CNRM_INI tend to overestimate observed standard deviation of TAS, lying mostly in higher part of the CMIP6 distribution, except for January, March, April and June.

In case of standard deviation of PR one of the prominent features in Figure 3B is that the differences between observed datasets are comparable to multi-model spread in winter (DJF), the simulated annual amplitude is lower than observed and the shape of the annual cycle is not captured very well by neither of the multi-model ensembles. CNRM_INI tend to overestimate observed values with CNRM_r1 lying mostly on the edges of the multi-model spread (Figure 3B).

Mean annual cycle of standard deviation of TN is relatively well reproduced with CMIP6 having tendency to rather higher values and more overestimation than CMIP5 (Figure 3C). Similarly to mean annual cycle of TN (Figure 2C), there are a few distinct outliers, with the “IPSL” CMIP5 GCMs being within them in most of the months. CNRM_r1 overestimates observed standard deviation of TN throughout the year, sometimes being close to the CMIP6 multi-model median, sometimes in the upper part of the distribution (Figure 3C).

CMIP6 GCMs tend to simulate higher standard deviation of TX with multi-model median being thus further from observations than CMIP5 GCMs (Figure 3D). This feature is quite similar to mean values of TX in the sense that CMIP6 give slightly worse results than CMIP5 (Figure 2D). CNRM_r1 also tends to overestimate observed standard deviation of TX, except for July (Figure 3D).

For standard deviation of all studied variables, the spread of CNRM_INI is comparable to multi-model spread of CMIP6, at least in some months (Figure 3). Similar conclusion can be inferred for mean annual cycle of PR (Figure 2B). For monthly mean TAS, TN and TX the contrary is true (Figures 2A,C,D). Thus, the magnitude of uncertainty resulting from internal climate variability is large in case of variability of studied variables and also for mean values of precipitation.

For TAS and PR, observational uncertainty can be evaluated. Regarding monthly mean air temperature, there are visible differences between CRU and EOBS up to 0.9°C. However, the values of standard deviation of TAS differ much less, the differences in individual months are up to 0.2°C. For mean precipitation the uncertainty connected to observations is up to 0.1 mm/day, i.e., 3 mm per month. Generally, in comparison to multi-model spread the observational uncertainty of TAS and PR is small, except for standard deviation of precipitation in winter, where the differences between observed datasets are comparable to multi-model spread. For TN and TX only EOBS in 0.25° and 0.11° datasets are available and they give practically identical values, therefore the observational uncertainty cannot be evaluated in the present study.

To investigate more the difference in model performance between CMIP5 and CMIP6 ensembles, we compare a simple performance metric RMSE of the mean annual cycle of four studied variables for ten pairs of GCMs from both ensembles for which the CMIP5 GCM can be considered as predecessor of corresponding CMIP6 GCM (Table 1). For most of these ten pairs, the CMIP6 RMSE is lower than RMSE of corresponding CMIP5 GCM. In some cases the progress is not very high, there are also pairs with higher CMIP6 RMSE (worse performance than CMIP5). Generally, for annual cycle of PR the differences in RMSE are lower. The better CMIP6 performance is most visible for TN and TX (Table 1).

Projected changes

Figure 4 shows the results for projected changes in monthly mean values of studied variables, whereas Figure 5 shows results for standard deviation of the monthly values. Changes in annual mean of monthly mean values of studied variables are also shown in Figure 4.

Projected changes in TAS, TN and TX are positive indicating expected increase of air temperature in studied area in all months (Figures 4A,C,D). The increase is naturally larger for stronger forcing scenarios (RCP8.5, SSP5-8.5) in all months, and in most cases the changes in summer and autumn months are higher than in winter and spring. CMIP6 project generally higher air temperature changes than CMIP5. The difference between CMIP5 and CMIP6 is higher in summer and autumn, especially for TAS. Regarding changes of TAS, TN and TX simulated by CNRM_r1, the annual mean values are very close to the CMIP6 median (Figure 4). In winter, this simulation tends to be in the upper part of CMIP6 distribution and in summer in the lower part.

Projected mean annual change of PR shows slight increase of precipitation amount with 75% of GCMs giving positive annual mean change and multi-model medians projecting change of approximately 5% for both CMIP5 and CMIP6 under both forcing scenarios (Figure 4B). CNRM_INI mini-ensemble gives higher changes around 10% (Figure 4B). However, the change is not distributed uniformly throughout the year. From November to May all GCM simulations agree on precipitation increase. During summer season, the results differ for both GCM ensembles and forcing scenarios. For CMIP5 under RCP4.5 the multi-model median change is close to zero (corresponding to value of 100% in Figure 4B, with the term “zero change” meaning no increase nor decrease of PR) and the spread between lower and upper quartiles includes zero change from June to October. Similar conclusion applies for CMIP5 under RCP8.5, with lower (more negative) multi-model median change and larger spread in July and August (Figure 4B). Under SSP2-4.5 CMIP6 projected median precipitation change is near zero in June, and from July to September slightly negative with multi-model inter-quartile spread including zero change. Under SSP5-8.5 CMIP6 GCMs project precipitation decrease from June to September with maximum median decrease of 25% in August. In October CMIP6 projected precipitation changes do not practically differ between scenarios with median changes indicating

TABLE 1 Comprasion of root mean square error (RMSE) of the mean annual cycle of studied variables between selected CMIP6 and CMIP5 GCM pairs. The differences are shown relatively, values lower than 100 implying better performance of CMIP6 GCM than its CMIP5 counterpart.

		RMSE(CMIP6)/RSME(CMIP5)*100			
CMIP5	**CMIP6**	**tas**	**Tasmin**	**Tasmax**	**pr**
CanESM2	CanESM5	36	60	85	152
CNRM-CM5	CNRM-CM6-1-HR	62	69	94	139
EC-EARTH	EC-Earth3	177	227	91	53
FGOALS-g2	FGOALS-g3	51	32	165	96
GFDL-CM3	GFDL-CM4	188	117	87	98
GFDL-ESM2M	GFDL-ESM4	187	89	97	70
IPSL-CM5A-LR	IPSL-CM6A-LR	74	19	58	90
MIROC5	MIROC6	88	95	101	206
MPI-ESM-LR	MPI-ESM1-2-LR	94	30	85	103
NorESM1-M	NorESM2-LM	108	—	—	173

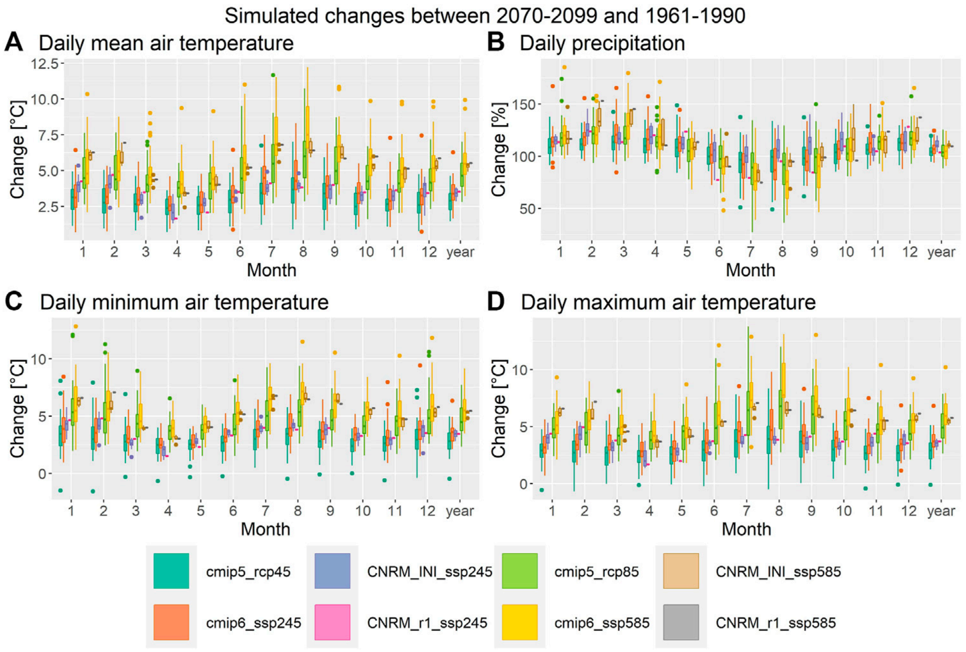

FIGURE 4
Projected changes of monthly means of daily mean air temperature **(A)**, daily precipitation amount **(B)**, daily minimum air temperature **(C)** and daily maximum air temperature **(D)** for the period of 2070–2099 in comparison to 1961–1990 averaged over the area of the Czech Republic, "year" denotes annual mean change. Boxplots show intra-ensemble statistical distribution (median, lower and upper quartiles, whiskers representing 1.5 * IQR, and outliers as dots) of CMIP5 under RCP4.5 (dark green), CMIP6 under SSP2-4.5 (orange), perturbed initial conditions mini-ensemble of CNRM-ESM2-1 GCM under SSP2-4.5 (10 members, blue), CMIP5 under RCP8.5 (light green), CMIP6 under SSP5-8.5 (yellow), perturbed initial conditions mini-ensemble of CNRM-ESM2-1 GCM under SSP5-8.5 (5 members, brown). The CNRM-ESM2-1 r1i1p1f2 simulation is plotted as a pink line for SSP2-4.5 and as grey line for SSP5-8.5.

increase of approximately 5% but MME spread between quartiles involving zero change (Figure 4B). CNRM_INI gives more positive precipitation changes than most of other GCMs in all months, with practically zero median change in July and rather positive changes in other months. CNRM_r1 projects precipitation decrease of 10–25% from June to September, and precipitation increase of similar magnitude range in other months, with only minor differences between forcing scenarios.

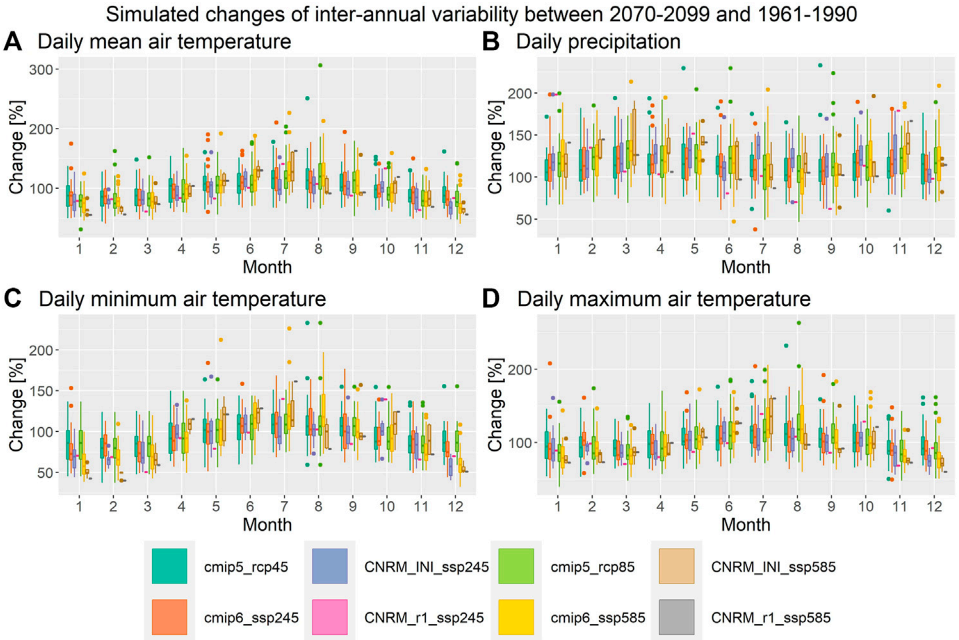

FIGURE 5
Same as Figure 4, but for relative changes in standard deviation of studied variables.

Regarding the projected changes in inter-annual variability of TAS, TN, TX and PR, which were evaluated based on relative changes in standard deviation (Figure 5), the differences between CMIP5 and CMIP6 and individual emission scenarios are smaller than in case of changes in mean values of studied variables (compare to Figure 4). Further, the spread of CNRM_INI mini-ensemble is comparable to the spread of the whole CMIP5 and CMIP6 ensembles. This implies that the internal variability seems to play an important role in changes of inter-annual variability of studied variables. Standard deviation of TAS, TN and TX is expected to increase in summer and decrease in winter. Standard deviation of PR is projected to increase, but the multi-model spread includes zero in some months. CNRM_r1 tend to be rather far from the multi-model median of CMIP6, especially for changes in standard deviation of PR.

Furthermore, regarding the changes in standard deviation of studied variables, there are some severely outlying points visible in Figure 5, with changes up to 150–200% in several extreme cases. The outlying models vary. It is not possible to depict several particular models. However, we have to note that the CNRM_r1 is also in some cases among these outlying simulations, especially for standard deviation of PR, as already noted above.

Similarly like in *Mean annual cycle in 1961–1990* Section, to investigate more the difference between air temperature changes projected by CMIP5 and CMIP6 ensembles, we compare changes in daily mean air temperature for ten pairs of GCMs from both ensembles for which the CMIP5 GCM can be considered as predecessor of corresponding CMIP6 GCM (Table 2). For the sake of easier interpretation, we only show the differences for summer and annual means of projected TAS changes. We choose summer season because the results in Figure 4 show that for this season the differences in TAS changes between the two multi-model ensembles are largest. For six out of these ten pairs, the CMIP6 signal is higher for both forcing scenarios. For "MIROC", "FGOALS" and "GFDL-CM" pairs the difference between generations is zero or CMIP5 version gives higher TAS change than CMIP6. Also for "NorESM" pair under the lower radiative forcing the CMIP5 projected annual mean TAS change is slightly higher than CMIP6 (Table 2). Therefore, we cannot conclude that all CMIP6 GCMs give higher TAS changes than their CMIP5 predecessors do.

Discussion

Most of the results are presented in the form of boxplots for individual ensembles. When comparing the boxplots we have to keep in mind that each ensemble has different number of members. So for example in some cases higher number of simulations included can cause larger spread. On the other

TABLE 2 Differences in TAS projected changes (°C) between selected CMIP6 a CMIP5 GCM pairs for two forcing scenarios. Positive values imply higher projected changes in CMIP6 than in CMIP5. JJA denotes mean over June-July-August season, Y denotes annual mean.

		RCP45/SSP2-4.5		**RCP85/SSP5-8.5**	
CMIP5	**CMIP6**	**JJA**	**Y**	**JJA**	**Y**
CanESM2	CanESM5	0,9	1,2	0,8	1,7
CNRM-CM5	CNRM-CM6-1-HR	1,2	0,5	2,4	1,2
EC-EARTH	EC-Earth3	2,3	2,4	3,9	3,9
FGOALS-g2	FGOALS-g3	−0,7	−0,4	−1,1	−1,3
GFDL-CM3	GFDL-CM4	−1,4	0,1	−2,6	−0,7
GFDL-ESM2M	GFDL-ESM4	0,8	0,6	1,1	0,5
IPSL-CM5A-LR	IPSL-CM6A-LR	1,0	0,5	2,4	0,9
MIROC5	MIROC6	0,0	−0,7	0,0	−1,0
MPI-ESM-LR	MPI-ESM1-2-LR	0,7	0,9	1,0	0,6
NorESM1-M	NorESM2-LM	0,4	−0,2	1,3	0,4

hand, we can conclude that higher number of models in CMIP6 comparing to CMIP5 does not automatically lead to larger spread, which implies higher convergence in CMIP6.

Differences in model performance and changes projected by CMIP6 simulations in comparison to previous CMIP5 GCMs are hard to attribute to one particular feature or difference between the multi-model ensembles, because the ensembles differ in various aspects. These include different number of contributing models, differences in model complexity, e.g., inclusion of wider scale of bio-geo-chemical processes in some CMIP6 earth-system models, differences in forcing scenarios etc. Regarding the forcing scenarios, according to Gidden et al. (2019) there are slight differences in emission and concentration pathways between corresponding SSP-RCP pairs in the course of the 21st century. As discussed in Tebaldi et al. (2021) there are only minor differences in the radiative forcing according to more traditional definition established by IPCC AR5 (Myhre et al., 2013). However, when considering effective radiative forcing (Smith et al., 2020), some differences arise, due to above mentioned differences in emission pathways (for detailed discussion see Tebaldi et al., 2021, Section 3.1.3).

Another important issue potentially contributing to revealed differences in projected climate changes is higher effective climate sensitivity in some of the CMIP6 GCMs (e.g., Zelinka et al., 2020) leading to higher projected temperature changes especially in summer (e.g., Palmer et al., 2021). Moreover, a number of recent studies have shown that there is a certain relationship between model performance in recent decades and the magnitude of projected future changes (e.g., Tokarska et al., 2020; Hegerl et al., 2021). When some kind of constraint is applied based on the historical simulations then the constrained CMIP6 projected changes get more in line with CMIP5 constrained projections (e.g., Tokarska et al., 2020; Tebaldi et al., 2021). However, most of relevant studies concentrate on global mean surface air temperature (e.g., Brunner et al., 2020; Tokarska et al., 2020), so the effect of such constraints over Central Europe needs to be assessed. Analysis of possible constraints is out of scope of the present study, the authors are working on a follow-up study focusing on this issue. Preliminary results for the reference period analyzed here do not show any difference in simulated air temperature trends between CMIP5 and CMIP6. Nevertheless, we can make a note, that both GCM generations tend to overestimate observed air temperature trends, with observed trends of monthly mean air temperature being mostly statistically insignificant and simulated trends statistically significant in approximately half of studied cases (not shown).

Regarding model performance, some previous studies compared the GCMs contributing to both CMIP5 and CMIP6 in order to evaluate explicitly the progress between the generations. For example, Cannon (2020) evaluated 15 such pairs of GCMs according to their skill in simulating observed patterns of atmospheric circulation over six selected continental regions based on daily values of sea-level pressure. They concluded that the simulated atmospheric circulation is substantially improved in the new generation of models. Similarly, Fernandez-Granja et al. (2021) also report a progress to better results in CMIP6 when evaluating atmospheric circulation based on Lamb classification over Europe for nine pairs of GCMs. Evaluation of model performance is not the main goal of this study, as we evaluate mainly multi-model characteristics rather than individual model performance. Anyway, our results for the reference period are quite inconclusive; there are not large differences in the resemblance with observed values between CMIP5 and CMIP6 (Figures 2, 3). On the other, the simple comparison of

RMSE of mean annual cycle of studied variables for selected CMIP5-CMIP6 pairs show general tendency towards better performance in the new GCM generation.

One of the prominent features visible in our results across GCM generations is the pattern of summer precipitation decrease over central Europe. It has already been described based on both GCM and RCM projections (e.g., Coppola et al., 2021a) and has been reported to get even more prominent in CMIP6 (Palmer et al., 2021). Another noticeable feature is that projected air temperature increase is higher in summer and autumn than in winter and spring (Figure 4A). This implies a possible change in the annual air temperature amplitude and hence thermal continentality of climate. Continentality of climate generally characterizes the influence of the distance of ocean on the climate of a place (Driscoll and Yee Fong, 1992). Previous studies based on Köppen-Trewartha climatic classification showed projected transition from continental temperate climate to oceanic temperate climate over Central Europe (Feng et al., 2012; Belda et al., 2017). This is seemingly in contrast to our results. However, Köppen-Trewartha climatic classification distinguishes the continental and oceanic temperate climates based solely on a numerical threshold for air temperature of the coldest month (Belda et al., 2014). However, thermal continentality indices are generally based on annual air temperature amplitude (e.g., Gorczynski, 1922). Hence, as our results for both CMIP5 and CMIP6 show increasing annual temperature amplitude, it implies increase of continentality of climate over Central Europe. On the other hand, a different view on continentality can be based on the annual course of precipitation (e.g., Brázdil et al., 2009). More uniform annual course implies ombric oceanity, whereas increasing differences between seasonal precipitation amounts imply increasing ombric continentality. Our results show slight increase of winter precipitation and tendency towards decrease of summer precipitation (Figure 4B). Combining these projections with observed annual course of precipitation (Figure 2B), we can conclude that our results indicate projected decrease of ombric continentality over Central Europe, contrasting with expected increase of thermal continentality of climate.

Regarding projected changes in inter-annual variability of studied parameters, our results indicate increase of variability of precipitation, except for summer months, where the results are inconclusive with multi-model ranges including zero changes (Figure 5B). Together with projected decrease of summer precipitation (Figure 4B), this might lead to higher probability of dry summer periods. Increased inter-annual variability together with increased mean precipitation in winter, spring and autumn leads to higher probability of extreme precipitation that might point toward higher probability of floods. Inter-annual variability of studied temperature characteristics in summer is expected to increase (Figures 5A,C,D) which together with projected increase of monthly mean values (Figures 4A,C,D) leads to even higher probability of extremely high temperatures with possible more frequent heat waves in summer. Higher probability of high temperature extremes in future has also been concluded in previous studies, most recently e.g., in Coppola et al. (2021b).

Conclusion

We have evaluated differences between CMIP5 and CMIP6 GCM multi-model ensembles with regard to mean annual cycle of four basic climatic variables and their inter-annual variability in the 1961–1990 reference period and projected changes in 2070–2099 under two forcing scenarios. The reference period of 1961–1990 was selected to represent relatively stable recent climate over the Czech Republic. More recent reference period would be more influenced by contemporary anthropogenic climate changes (e.g., Brázdil et al., 2022). A special attention has been paid to the simulation of CNRM-ESM2-1, one of the CMIP6 GCMs, and its perturbed-initial conditions mini-ensemble. The results for the area centered on the Czech Republic reveal minor differences in model performance in the reference period whereas quite substantial inter-generation shift in projected future change towards higher air temperature and lower summer precipitation in the new GCM generation. Based on our simple comparison of selected predecessor-successor pairs it cannot be concluded that all CMIP6 GCMs project systematically higher air temperature changes (Table 2). However, the multi-model characteristics imply generally higher changes for CMIP6 GCMs, especially in summer.

Regarding the consistency of GCM simulations with observed values in the reference period, we can conclude that based on the multi-model characteristics the GCMs are capable of capturing the main features of annual cycles of studied climatic elements. Even though the model performance does not automatically imply reliability of future climate change projections (e.g., Abramowitz et al., 2019), it is a necessary condition for the process of climate change scenario creation.

Regarding the CNRM-ESM2-1, the driving GCM simulation of Aladin-CLIMATE/CZ, which is the core simulation for the PERUN climate change scenarios, its results are often quite far from the multi-model median. Therefore, we strictly recommend accompanying any analysis based on the simulation of Aladin-CLIMATE/CZ with proper uncertainty estimate using available GCMs and RCMs. On the other hand, the nested RCM does not automatically inherit the manner of behavior from the driving GCM, even the climate change signal is often substantially modified (e.g., Sørland et al., 2018; Crhová and Holtanová, 2019). We concentrated here on the CNRM-ESM2-1 simulation for the area of the Czech Republic, which lies in the center of the Aladin-CLIMATE/CZ integration domain. However, for the resulting RCM simulation, the input from GCM in the form of boundary conditions is very important (e.g., Christensen and Kjellström, 2020; Ahrens and Leps, 2021). Therefore, in an upcoming study, we will concentrate on evaluation of CNRM-ESM2-1 with regard to the boundary conditions provided to Aladin-CLIMATE/CZ, i.e., the upper-air parameters over the boundaries of the integration domain.

The range of CNRM_INI mini-ensemble represents a rough estimate of uncertainty related with internal climate variability. It is relatively larger in case of inter-annual variability of studied air temperature variables than for the mean values, in both the reference period and with regard to projected changes. For precipitation, the role of internal variability is more pronounced than for air temperature, in both reference and future time periods. The CNRM_INI mini-ensemble includes only ten or five simulations for only one model, and therefore provided uncertainty estimate must be considered as a lower bound. With regard to this fact, we can conclude that the CNRM_INI range is often quite large in comparison to the range of whole CMIP6 ensemble. It implies that when constructing climate change scenarios for Central Europe, attention must be paid not only to structural uncertainty represented by inter-model differences and scenario uncertainty, but also to the influence of internal climate variability.

Our results and above discussion lead us to the conclusion that it is necessary to explore possible constraints on simulated changes before the CMIP6 GCM outputs are used for any kind of further analysis, including uncertainty estimates for impact and adaptation studies on regional and local scales. Therefore, within the project PERUN, a further analysis of possible links between simulated changes, model performance and model climate sensitivity will be performed to tackle this issue appropriately.

Data availability statement

Publicly available datasets were analyzed in this study. This data can be found here: https://esgf-node.llnl.gov/projects/esgf-llnl/.

Author contributions

EH designed the study and wrote the paper. MB participated in data processing and calculation of the results. MB and TH helped write the paper and interpret the results. All authors contributed to the article and approved the submitted version.

Funding

The research was funded by the Technology Agency of the Czech Republic (Grant No. SS02030040, PERUN and Grant No. SS04030013 SEEPIA).

Acknowledgments

This work used resources of the Deutsches Klimarechenzentrum (DKRZ) granted by its Scientific Steering Committee (WLA) under project MCS LOVE CCS in framework of IS-ENES3 Analysis Platform activity. We acknowledge the World Climate Research Programme's Working Group on Coupled Modelling, which is responsible for CMIP, and we thank the climate modeling groups for producing and making available their model outputs. For CMIP the US Department of Energy's Program for Climate Model Diagnosis and Intercomparison provides coordinating support and led development of software infrastructure in partnership with the Global Organization for Earth System Science Portals. We acknowledge the E-OBS dataset from the EU-FP6 project UERRA (https://www.uerra.eu) and the Copernicus Climate Change Service, and the data providers in the ECA&D project (https://www.ecad.eu). We acknowledge the Climatic Research Unit (CRU) for creation of datasets TS 3. 22 dataset (Harris et al., 2014) and TS 4.05 dataset (Harris et al., 2020). We also acknowledge the GPCC Global Precipitation Climatology Centre (https://www.dwd.de/EN/ourservices/gpcc/gpcc.html) version 7 (Becker et al., 2013).

Conflict of interest

The authors declare that the research was conducted in the absence of any commercial or financial relationships that could be construed as a potential conflict of interest.

Publisher's note

Supplementary material

The Supplementary Material for this article can be found online at: https://www.frontiersin.org/articles/10.3389/feart.2022.1018661/full#supplementary-material

References

Abramowitz, G., Herger, N., Gutmann, E., Hammerling, D., Knutti, R., Leduc, M., et al. (2019). ESD reviews: Model dependence in multi-model climate ensembles: Weighting, sub-selection and out-of-sample testing. *Earth Syst. Dyn.* 10 (1), 91–105. doi:10.5194/esd-10-91-2019

Ahrens, B., and Leps, N. (2021). Sensitivity of convection permitting simulations to lateral boundary conditions in idealized experiments. *J. Adv. Model. Earth Syst.* 13, e2021MS002519. doi:10.1029/2021MS002519

Bassett, R., Young, P. J., Blair, G. S., Samreen, F., and Simm, W. (2020). A large ensemble approach to quantifying internal model variability within the WRF numerical model. *J. Geophys. Res. Atmos.* 125 (7), e2019JD031286. doi:10.1029/2019JD031286

Becker, A., Finger, P., Meyer-Christoffer, A., Rudolf, B., Schamm, K., Schneider, U., et al. (2013). A description of the global land-surface precipitation data products of the Global Precipitation Climatology Centre with sample applications including centennial (trend) analysis from 1901–present. *Earth Syst. Sci. Data* 5 (1), 71–99. doi:10.5194/essd-5-71-2013

Belda, M., Holtanová, E., Halenka, T., and Kalvová, J. (2014). Climate classification revisited: From Köppen to Trewartha. *Clim. Res.* 59, 1–13. doi:10.3354/cr01204

Belda, M., Holtanová, E., Halenka, T., Kalvová, J., and Hlávka, Z. (2015). Evaluation of CMIP5 present climate simulations using the Köppen-Trewartha climate classification. *Clim. Res.* 64, 201–212. doi:10.3354/cr01316

Belda, M., Holtanová, E., Kalvová, J., and Halenka, T. (2017). Global warming-induced changes in climate zones based on CMIP5 projections. *Clim. Res.* 71 (1), 17–31. doi:10.3354/cr01418

Brázdil, R., Trnka, M., Dobrovolný, P., Chromá, K., Hlavinka, P., and Žalud, Z. (2009). Variability of droughts in the Czech republic, 1881–2006. *Theor. Appl. Climatol.* 97 (3), 297–315. doi:10.1007/s00704-008-0065-x

Brázdil, R., Zahradníček, P., Dobrovolný, P., Řehoř, J., Trnka, M., Lhotka, O., et al. (2022). Circulation and climate variability in the Czech republic between 1961 and 2020: A comparison of changes for two "normal" periods. *Atmosphere* 13 (1), 137. doi:10.3390/atmos13010137

Brunner, L., Pendergrass, A. G., Lehner, F., Merrifield, A. L., Lorenz, R., and Knutti, R. (2020). Reduced global warming from CMIP6 projections when weighting models by performance and independence. *Earth Syst. Dyn.* 11 (4), 995–1012. doi:10.5194/esd-11-995-2020

Cannon, A. J. (2020). Reductions in daily continental-scale atmospheric circulation biases between generations of global climate models: CMIP5 to CMIP6. *Environ. Res. Lett.* 15 (6), 064006. doi:10.1088/1748-9326/ab7e4f

Christensen, O. B., and Kjellström, E. (2020). Partitioning uncertainty components of mean climate and climate change in a large ensemble of European regional climate model projections. *Clim. Dyn.* 54 (9), 4293–4308. doi:10.1007/s00382-020-05229-y

Coppola, E., Nogherotto, R., Ciarlo, J. M., Giorgi, F., van Meijgaard, E., Kadygrov, N., et al. (2021a). Assessment of the European climate projections as simulated by the large EURO-CORDEX regional and global climate model ensemble. *JGR. Atmos.* 126, e2019JD032356. doi:10.1029/2019JD032356

Coppola, E., Raffaele, F., Giorgi, F., Giuliani, G., Xuejie, G., Ciarlo, J. M., et al. (2021b). Climate hazard indices projections based on CORDEX-CORE, CMIP5 and CMIP6 ensemble. *Clim. Dyn.* 57 (5), 1293–1383. doi:10.1007/s00382-021-05640-z

Cornes, R., van der Schrier, G., van den Besselaar, E. J. M., and Jones, P. D. (2018). An ensemble version of the E-OBS temperature and precipitation datasets. *J. Geophys. Res. Atmos.* 123, 9391–9409. doi:10.1029/2017JD028200

Crhová, L., and Holtanová, E. (2018). Simulated relationship between air temperature and precipitation over Europe: Sensitivity to the choice of RCM and GCM. *Int. J. Climatol.* 38 (3), 1595–1604. doi:10.1002/joc.5256

Crhová, L., and Holtanová, E. (2019). Temperature and precipitation variability in regional climate models and driving global climate models: Total variance and its temporal-scale components. *Int. J. Climatol.* 39 (3), 1276–1286. doi:10.1002/joc.5876

Dai, A., and Deng, J. (2022). Recent Eurasian winter cooling partly caused by internal multidecadal variability amplified by Arctic sea ice-air interactions. *Clim. Dyn.* 58, 3261–3277. doi:10.1007/s00382-021-06095-y

Deser, C. (2020). Certain uncertainty: The role of internal climate variability in projections of regional climate change and risk management. *Earth's. Future* 8, e2020EF001854. doi:10.1029/2020EF001854

Deser, C., Phillips, A., Bourdette, V., and Teng, H. (2012). Uncertainty in climate change projections: The role of internal variability. *Clim. Dyn.* 38, 527–546. doi:10.1007/s00382-010-0977-x

Driscoll, D. M., and Fong, J. M. Y. (1992). Continentality: A basic climatic parameter re-examined. *Int. J. Climatol.* 12 (2), 185–192. doi:10.1002/joc.3370120207

Eyring, V., Bony, S., Meehl, G. A., Senior, C. A., Stevens, B., Stouffer, R. J., et al. (2016). Overview of the coupled model intercomparison project phase 6 (CMIP6) experimental design and organization. *Geosci. Model. Dev.* 9 (5), 1937–1958. doi:10.5194/gmd-9-1937-2016

Feng, S., Ho, C. H., Hu, Q., Oglesby, R. J., Jeong, S. J., and Kim, B. M. (2012). Evaluating observed and projected future climate changes for the Arctic using the Köppen-Trewartha climate classification. *Clim. Dyn.* 38, 1359–1373. doi:10.1007/s00382-011-1020-6

Fernandez-Granja, J. A., Casanueva, A., Bedia, J., and Fernandez, J. (2021). Improved atmospheric circulation over Europe by the new generation of CMIP6 Earth system models. *Clim. Dyn.* 56 (11), 3527–3540. doi:10.1007/s00382-021-05652-9

Gidden, M. J., Riahi, K., Smith, S. J., Fujimori, S., Luderer, G., Kriegler, E., et al. (2019). Global emissions pathways under different socioeconomic scenarios for use in CMIP6: A dataset of harmonized emissions trajectories through the end of the century. *Geosci. Model. Dev.* 12 (4), 1443–1475. doi:10.5194/gmd-12-1443-2019

Giorgi, F. (2019). Thirty years of regional climate modeling: Where are we and where are we going next? *J. Geophys. Res. Atmos.* 124, 2018JD030094–5723. doi:10.1029/2018JD030094

Gleckler, P. J., Taylor, K. E., and Doutriaux, C. (2008). Performance metrics for climate models. *J. Geophys. Res.* 113 (D6), D06104. doi:10.1029/2007JD008972

Gorczynski, L. (1922). The calculation of the degree of continentality. *Mon. Weather Rev.* 50, 369–370.

Harris, I., Jones, P. D., Osborn, T. J., and Lister, D. H. (2014). Updated high-resolution grids of monthly climatic observations—The CRU TS3.10 dataset. *Int. J. Climatol.* 34, 623–642. doi:10.1002/joc.3711

Harris, I., Osborn, T. J., Jones, P., and Lister, D. (2020). Version 4 of the CRU TS monthly high-resolution gridded multivariate climate dataset. *Sci. Data* 7, 109. doi:10.1038/s41597-020-0453-3

Hegerl, G. C., Ballinger, A. P., Booth, B. B., Borchert, L. F., Brunner, L., Donat, M. G., et al. (2021). Toward consistent observational constraints in climate predictions and projections. *Front. Clim.* 3, 678109. doi:10.3389/fclim.2021.678109

Holtanová, E., Mendlik, T., Koláček, J., Horová, I., and Mikšovský, J. (2019). Similarities within a multi-model ensemble: Functional data analysis framework. *Geosci. Model. Dev.* 12, 735–747. doi:10.5194/gmd-12-735-2019

Holtanová, E., Mikšovský, J., Kalvová, J., Pišoft, P., and Motl, M. (2012). Performance of ENSEMBLES regional climate models over Central Europe using various metrics. *Theor. Appl. Climatol.* 108, 463–470. doi:10.1007/s00704-011-0542-5

Jacob, D., Teichmann, C., Sobolowski, S., Katragkou, E., Anders, I., Belda, M., et al. (2020). Regional climate downscaling over Europe: Perspectives from the EURO-CORDEX community. *Reg. Environ. Change* 20 (2), 51–20. doi:10.1007/s10113-020-01606-9

Kendon, E. J., Ban, N., Roberts, N. M., Fowler, H. J., Roberts, M. J., Chan, S. C., et al. (2017). Do convection-permitting regional climate models improve projections of future precipitation change? *Bull. Am. Meteorol. Soc.* 98 (1), 79–93. doi:10.1175/BAMS-D-15-0004.1

Meinshausen, M., Nicholls, Z. R., Lewis, J., Gidden, M. J., Vogel, E., Freund, M., et al. (2020). The shared socio-economic pathway (SSP) greenhouse gas concentrations and their extensions to 2500. *Geosci. Model. Dev.* 13 (8), 3571–3605. doi:10.5194/gmd-13-3571-2020

Moss, R. H., Edmonds, J. A., Hibbard, K. A., Manning, M. R., Rose, S. K., van Vuuren, D. P., et al. (2010). The next generation of scenarios for climate change research and assessment. *Nature* 463, 747–756. doi:10.1038/nature08823

Myhre, G., Shindell, D., Bréon, F.-M., Collins, W., Fuglestvedt, J., et al. (2013). "Anthropogenic and natural radiative forcing," in *Climate change 2013: The physical science basis. Contribution of working group I to the fifth assessment report of the intergovernmental panel on climate change*. Editors T. F. Stocker, D. Qin, G.-K. Plattner, M. Tignor, S. K. Allen, J. Boschung, et al. (Cambridge, United Kingdom and New York, NY, USA: Cambridge University Press).

Otto-Bliesner, B. L., Brady, E. C., Fasullo, J., Jahn, A., Landrum, L., Stevenson, S., et al. (2016). Climate variability and change since 850 C.E.: An ensemble approach with the community earth system. *Model. Bull. Amer. Met. Soc.* 97, 735–754. doi:10.1175/BAMS-D-14-00233.1

Palmer, T. E., Booth, B. B. B., and McSweeney, C. F. (2021). How does the CMIP6 ensemble change the picture for European climate projections? *Environ. Res. Lett.* 16 (9), 094042. doi:10.1088/1748-9326/ac1ed9

Poschlod, B., and Ludwig, R. (2021). Internal variability and temperature scaling of future sub-daily rainfall return levels over Europe. *Environ. Res. Lett.* 16 (6), 064097. doi:10.1088/1748-9326/ac0849

Prein, A. F., Bukovsky, M. S., Mearns, L. O., Bruyère, C. L., and Done, J. M. (2019). Simulating North American weather types with regional climate models. *Front. Environ. Sci.* 7, 36. doi:10.3389/fenvs.2019.00036

Séférian, R., Nabat, P., Michou, M., Saint-Martin, D., Voldoire, A., Colin, J., et al. (2019). Evaluation of CNRM earth-system model, CNRM-ESM2-1: Role of earth system processes in present-day and future climate. *J. Adv. Model. Earth Syst.* 11, 4182–4227. doi:10.1029/2019MS001791

Smith, C. J., Kramer, R. J., Myhre, G., Alterskjær, K., Collins, W., Sima, A., et al. (2020). Effective radiative forcing and adjustments in CMIP6 models. *Atmos. Chem. Phys.* 20, 9591–9618. doi:10.5194/acp-20-9591-2020

Sørland, S. L., Schär, C., Lüthi, D., and Kjellström, E. (2018). Bias patterns and climate change signals in GCM-RCM model chains. *Environ. Res. Lett.* 13 (7), 074017. doi:10.1088/1748-9326/aacc77

Takayabu, I., Kanamaru, H., Dairaku, K., Benestad, R., von Storch, H., and Christensen, J. H. (2016). Reconsidering the quality and utility of downscaling. *J. Meteorological Soc. Jpn.* 94, 31–45. doi:10.2151/jmsj.2015-042

Taylor, K., Stouffer, R. J., and Meehl, G. A. (2012). An overview of CMIP5 and the experiment design. *Bull. Am. Meteorol. Soc.* 93, 485–498. doi:10.1175/BAMS-D-11-00094.1

Tebaldi, C., Debeire, K., Eyring, V., Fischer, E., Fyfe, J., Friedlingstein, P., et al. (2021). Climate model projections from the scenario model intercomparison project (ScenarioMIP) of CMIP6. *Earth Syst. Dyn.* 12 (1), 253–293. doi:10.5194/esd-12-253-2021

Tebaldi, C., and Knutti, R. (2007). The use of the multi-model ensemble in probabilistic climate projections. *Phil. Trans. R. Soc. A* 365 (1857), 2053–2075. doi:10.1098/rsta.2007.2076

Termonia, P., Fischer, C., Bazile, E., Bouyssel, F., Brožková, R., Benard, P., et al. (2018). The ALADIN System and its canonical model configurations AROME CY41T1 and ALARO CY40T1. *Geosci. Model. Dev.* 11 (1), 257–281. doi:10.5194/gmd-11-257-2018

Thomas, T. S., Schlosser, C. A., Strzepek, K., Robertson, R. D., and Arndt, C. (2022). Using a large climate ensemble to assess the frequency and intensity of future extreme climate events in Southern Africa. *Front. Clim.* 79. doi:10.3389/fclim.2022.787721

Tokarska, K. B., Stolpe, M. B., Sippel, S., Fischer, E. M., Smith, C. J., Lehner, F., et al. (2020). Past warming trend constrains future warming in CMIP6 models. *Sci. Adv.* 6 (12), eaaz9549. doi:10.1126/sciadv.aaz9549

Torma, C., and Giorgi, F. (2020). On the evidence of orographical modulation of regional fine scale precipitation change signals: The Carpathians. *Atmos. Sci. Lett.* 21 (6), e967. doi:10.1002/asl.967

Wang, Y., Belluš, M., Ehrlich, A., Mile, M., Pristov, N., Smolikova, P., et al. (2018). 27 years of regional cooperation for limited area modelling in central Europe. *Bull. Am. Meteorol. Soc.* 99 (7), 1415–1432. doi:10.1175/BAMS-D-16-0321.1

Yang, H., Lu, J., Wang, Q., Shi, X., and Lohmann, G. (2022). Decoding the dynamics of poleward shifting climate zones using aqua-planet model simulations. *Clim. Dyn.* 58, 3513–3526. doi:10.1007/s00382-021-06112-0

Zelinka, M. D., Myers, T. A., McCoy, D. T., Po-Chedley, S., Caldwell, P. M., Ceppi, P., et al. (2020). Causes of higher climate sensitivity in CMIP6 models. *Geophys. Res. Lett.* 47 (1), e2019GL085782. doi:10.1029/2019GL085782

frontiers | Frontiers in Earth Science

TYPE Original Research
PUBLISHED 04 January 2023
DOI 10.3389/feart.2022.1073885

Check for updates

OPEN ACCESS

EDITED BY
Duanyang Liu,
Chinese Academy of Meteorological Sciences, China

REVIEWED BY
Chunsong Lu,
Nanjing University of Information Science and Technology, China
Dai Zhujun,
China Meteorological Administration, China
Min Xie,
Nanjing University, China

*CORRESPONDENCE
Yong Huang,
✉ hy121_2000@126.com

SPECIALTY SECTION
This article was submitted to Atmospheric Science, a section of the journal Frontiers in Earth Science

RECEIVED 19 October 2022
ACCEPTED 12 December 2022
PUBLISHED 04 January 2023

CITATION
Zhang H, Wang X, Hong X, Wang S and Huang Y (2023), Observational study of river-land breeze and its influence on distribution of PM_{10} concentrations over a main mining city in the Yangtze River Delta, China.
Front. Earth Sci. 10:1073885.
doi: 10.3389/feart.2022.1073885

Observational study of river-land breeze and its influence on distribution of PM_{10} concentrations over a main mining city in the Yangtze River Delta, China

Hong Zhang[1], Xinqi Wang[1], Xingyuan Hong[1], Shuibin Wang[1] and Yong Huang[2,3]*

[1]Anhui Environment Science Institute, Hefei, Anhui, China, [2]Anhui Meteorology Institute, Anhui Key Lab of Atmospheric Science and Satellite Remote Sensing, Hefei, Anhui, China, [3]Shouxian National Climate Observatory, Shouxian, China

Wind data from air pollutant observation networks and meteorological stations are used to analyze the characteristics of river-land breeze near Tongling city (a main mining city in the Yangtze River Delta). The inhomogeneous distribution of pollutant matters near Tongling city due to river-land breeze is also investigated. Our results show the following conclusions. 1) The river breeze during the daytime is stronger than the land breeze at night. And the speed of river-land breeze is increased rapidly from 7:00 and arrived at the maximum at 12:00. After 15:00, the speed is slowed rapidly. 2) The river-land breeze in city area (east of Yangtze River, speed is .07 m/s) is weaker than the natural area (west of Yangtze River, speed is 0.18 m/s). Furthermore, the seasonal variations of breeze both in the west and east sides are different. In west side, the breeze is strongest in spring. And in the east side, the breeze is strongest in summer. 3) Under a weak breeze (≤0.45 m/s), the PM_{10} is moved by the breeze within the region and causes the heterogeneity. While with a strong breeze (>0.45 m/s), the PM_{10} is transported out of the region, and the PM_{10} concentration becomes homogenous. 4) The river breeze leads to a reduction of the pollutant concentration near the Yangtze River, but an increase in the city due to the transportation of pollutant particles from coast to city at daytime.

KEYWORDS

river-land breeze, the distribution of air pollutant, inhomogeneity, PM10, Yangtze River Delta

Highlights

Weak river-land breezes caused spatial heterogeneity of PM_{10}. And strong breezes produced spatial homogeneity.

1 Introduction

The Yangtze River Delta (YRD) is one of the most important economic zones in China, including 26 cities in Shanghai, Jiangsu, Zhejiang and Anhui provinces. It is a region has not only heavy industries such as machinery industry, chemical industry, automobile manufacturing and mining, but also has agricultural products like wheat, rice and corn. It is also a hub of transportation. With the significant economic growth of the YRD, environmental problems become more and more prominent in that region. Hu et al. (2014) pointed out some atmospheric environmental problems including increase of particle concentration, more haze weather and the deterioration of air quality. Fu et al. (2013) also showed that the average emission intensities in the YRD for some air pollutants (SO_2, NO_X, $PM_{2.5}$, PM_{10}, NMVOCs and NH_3) were 2–7 times higher than the national average value in 2010. The annual average concentrations of $PM_{2.5}$ in the cities of Shanghai, Nanjing and Hangzhou in 2013 were 5–7 times higher than the World Health Organization (WHO) Air Quality Guidelines (Wang et al., 2014). These problems of air pollution may cause loss of both human health and Economic wealth (Wang et al., 2015). Therefore, the atmospheric environmental problem in the YRD is one of the most important issues that researchers should pay a close attention to.

Tongling city, a major mining city, is located in the west of YRD and near the Yangtze River. There are various industries, such as ore mining, metal smelting and Energy-Chemical industry. And the source of air pollution is a complicated problem in Tongling. In addition, complex topography (the Yangtze River, hills, cities, *etc.*) also creates special regional meteorological conditions. Particularly the specific geographic distribution of water and urban land use will have a certain effect on regional climate. Previous studies indicate that physical property differences between water and land may cause local atmospheric motion, form weather phenomenon with significant diurnal variation such as Sea-Land Breeze, land-lake breeze, and river-land wind (Avissar and Pielke, 1989; Oliveira and Fitzjarrald, 1993; Porson et al., 2007; Crosman and Horel, 2010; Crosman and Horel, 2012; Choi et al., 2015). Local atmospheric motion can change wind direction and speed, and thus influence the distribution of air pollutants in the area (Clappier et al., 2000; Melas et al., 2006). For example, air pollutant could be transported from coast to land due to the effect of sea breeze (Alexandra et al., 2016).

Despite that the spatial scale of river-land breeze is smaller (about 20 km) than sea breeze, it can bring remarkable influences on local weather and air quality (Wang et al., 2010). Silva Dias et al. (2004) studied the Amazon basin and found that river-land breeze could induce local convergence and divergence and create a local climate with distinct geographical features. The contrast between the wide surface of the Yangtze River and the land is prone to the formation of river-land breezes under a certain condition, which creates local climate regime and corresponding distribution features of atmospheric pollutant concentration. Therefore, in this study, we analyze river-land breeze and its influence on regional air pollution in Tongling city.

We analyze the characteristics of river-land breeze and the influence on distribution of PM_{10} in the Yangtze River Delta, China. The remainder of this paper is organized as follows: The study area, observations, and data quality control methods used are described in Section 2. We analyze the results in Section 3. The Discussion are given in Section 4 and the conclusions are given in Section 5.

2 Materials and methods

2.1 Meteorological and air quality data

In this study, we focus on Tongling city and the area surrounding it. The study region (117.5E-118E, 30.8–31.1N) is shown in Figure 1. In this domain, the Yangtze River passes through from south to north and is almost perpendicular to the latitude in all lines. Therefore, the river breeze caused by the difference of land and surface contrast is mainly in east-west direction. Observation data from all meteorological stations (total 22 stations) and air quality monitoring stations (total four stations) in study region are collected for analyzing river breeze and its influences on pollutant particles distribution. These four air quality monitoring stations are located at the ninth middle school (NS), the wastewater factory (WF), the fourth middle school (FS) and the road bureau (RB).

The data from air pollutant observation stations (national stations of Ministry of Ecology and Environment, PRC) and meteorological observation stations (regional stations of China Meteorological Administration) in the whole year of 2011 (observation experiment period in Tongling) are used in this study, include concentration of PM_{10}, the wind speed and direction. The time frequency of these observation data is 1 h. Those concentration of PM_{10} were observed by the LGH-01B PM_{10} air particulate matter monitoring instrument (produced by Anhui Landun Photoelectron CO., LTD., Anhui, PRC). The wind speed was observed by the three-cup wind speed sensor (EL15-1A) and the wind direction was observed by the sensor of EL15-2A (produced by Zhonghuan TIG, Tianjin, PRC).

The data of PM_{10} are disposed according to the technical specifications of Ministry of Ecology and Environment, PRC (Technical Specifications for Installation and Acceptance of Continuous Automatic Monitoring System for Ambient Air Particulate Matter (PM_{10} and $PM_{2.5}$), HJ 655–2013). And the supplemental quality control of all these datasets had been carried out before analysis. The primary purpose of quality control is to eliminate the outliers. However, it is also assumed 10% of air pollutant data are unreliable. The quality control aims to eliminate not only the outliers, but also those unreliable data. So, first step is

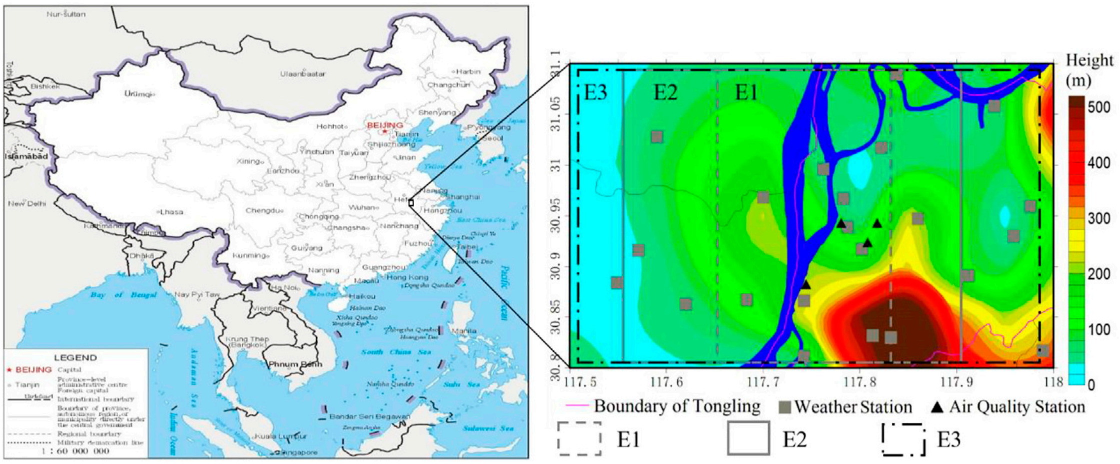

FIGURE 1
Map of the study region (squares are weather stations, and triangles are air quality stations, color shadow is altitude, blue is Yangtze River).

to calculate its probability distribution, then, a threshold is obtained to eliminate those 10% data.

2.2 River-land breeze calculation

According to formulas (1), it is clear that total wind ($\vec{V}$)can be decomposed into zonal ($u\vec{i}$), meridional ($v\vec{j}$) and vertical component ($w\vec{k}$). Because only horizontal wind data are collected in meteorological stations, and only zonal and meridional wind data are available. And for our case, the river-land breeze mainly affects the winds in east-west direction; therefore, only zonal winds (positive for westerly wind and negative for easterly wind) are analyzed. In addition, since river-land breeze is local deviated wind from environmental background wind, we further decompose zonal wind into environmental background wind ($\bar{u}$) and local deviated wind (Δu) as shown in formulas (2).

$$\vec{V} = u\vec{i} + v\vec{j} + w\vec{k} \tag{1}$$

$$u = \bar{u} + \Delta u \tag{2}$$

$$\bar{u} = \frac{1}{n}\sum\nolimits_{i=1}^{n} u_i \tag{3}$$

n is the number of weather stations in the study region, u_i is the zonal wind of the weather station i for the per hour observation data.

As the environment background wind ($\bar{u}$) is calculated with domain average method as formula (3) shown, the local deviated wind (Δu) is subtracted from the total zonal as formula (2). As the local deviated wind (Δu) is caused by the local geomorphic characteristics (river and land), and it is used to express river-land breeze in the following articles.

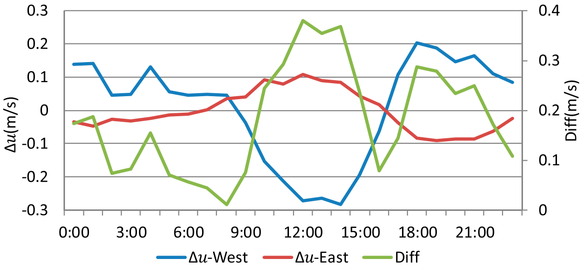

FIGURE 2
Diurnal variation of annual mean local deviated wind speed (Δu) in both sides of the Yangtze River and their difference in 2011 year.

Environment background wind ($\bar{u}$) is calculated with domain average method, and the formula is showed in formula (3). The difference (Diff) between the local deviated wind in the east (Δu_{east}) and west (Δu_{west}) bank of the Yangtze River is also calculated as formula (4).

$$\mathrm{Diff} = |\Delta u_{west} - \Delta u_{east}| \tag{4}$$

3 Results

3.1 Analysis of yangtze river breeze

Diurnal variation of annual mean local deviated wind (Δu) is shown in Figure 2. Generally, A “change inversely” relationship can be noticed between the west and east side of the river. During

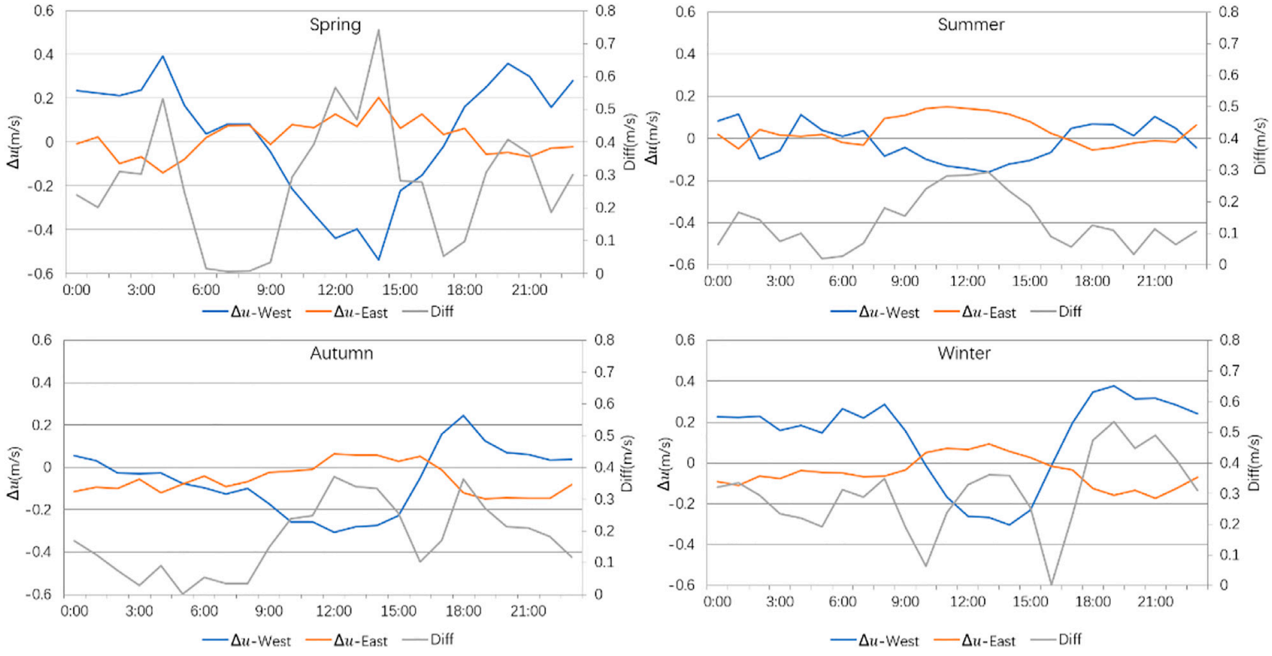

FIGURE 3
Diurnal variation of local deviated wind (Δu) in both sides of Yangtze River and their differences for different seasons.

8:00–16:00 (local time, and same hereafter), It is easterly wind in the west of the Yangtze River and westerly wind in the east, exhibiting a divergence pattern. In contrast, during 16:00–1:00, the local winds reverse the direction, which forms a convergence pattern. It can also be noticed that the local deviated zonal wind speed Δu in both east and west sides of the Yangtze River increases from 8:00a.m., reaching the maximum between 12:00–14:00, and gradually decreases afterwards. According to the difference between Δu in the east and west (Diff), there are two maximums in a diurnal cycle. The first one occurs between 12:00–14:00 when both u' and Diff reach their maximums (the largest Δu is 0.28 m/s and occurs in the west side of the Yangtze River, while the largest Diff is 0.37 m/s). The second maximum occurs between 16:00–22:00, and both Δu and Diff (0.2 m/s and 0.29 m/s respectively) are smaller in magnitude compared with the first maximum.

The diurnal variation of local deviated wind (Δu) in the east and west side of Yangtze River and their difference for different seasons are shown in Figure 3. It shows the following information. 1) For the pairs of Δu maximum at any season, in the daytime, it is always negative in the west side and positive in the east side of the Yangtze River. The only difference about this aspect for different seasons is the strength of Δu and the duration time of strong wind reversal. 2) In the daytime, the difference between the winds in either side of the Yangtze River is most significant in spring, followed by autumn, winter and summer. 3) In the nighttime, the difference between the winds in either side of the Yangtze River is the most obvious in winter, followed by spring and autumn, and the smallest difference occurs in summer too. 4) "Diff" is larger in the

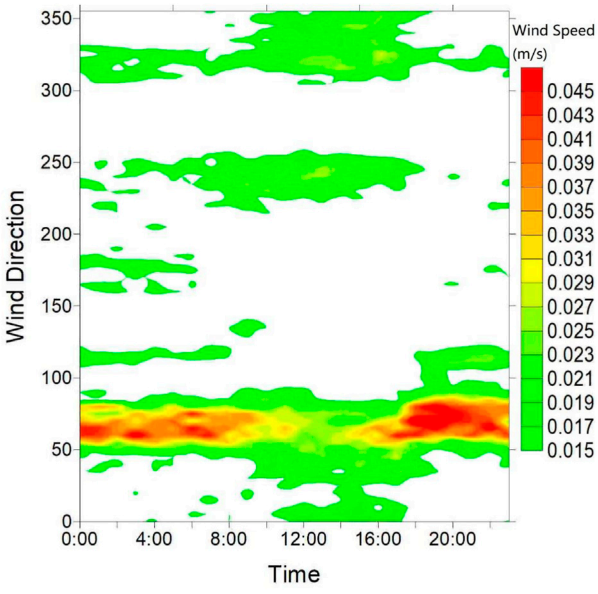

FIGURE 4
Diurnal variation of wind direction in east side of the Yangtze River.

TABLE 1 The mean of local deviated wind Δu in the west and east side of the Yangtze River (negative value indicates easterly wind; positive value indicates westerly wind).

		West (m/s)	East (m/s)
annual	day	−0.18(±0.09)	0.07(±0.03)
	night	0.13(±0.05)	−0.06(±0.03)
spring	day	−0.29(±0.16)	0.09(±0.06)
	night	0.27(±0.07)	−0.05(±0.05)
summer	day	−0.11(±0.04)	0.11(±0.04)
	night	0.03(±0.08)	0.00(±0.04)
autumn	day	−0.23(±0.08)	0.04(±0.05)
	night	0.03(±0.05)	−0.06(±0.05)
winter	day	−0.14(±0.16)	0.04(±0.04)
	night	0.26(±0.07)	−0.10(±0.04)

nighttime than daytime in winter, while *vice versa* for other seasons. For the Diff represents the difference of wind between the east and west sides of the Yangtze River, as formula (4), it can be used to represent the speed of river-land breeze. As Figure 3 shown, the speed of river-land breeze at night is greater than that in daytime in winter, and it is just the opposite in other seasons.

The mean local deviated wind speed and standard deviations are calculated during daytime (9:00–16:00) and nighttime (19:00–04:00). As shown in Table 1, the land breeze in the west side of Yangtze River is stronger than that in the east. The mean Δu in the west and east are −0.18 m/s (negative sign indicates easterly wind) and .07 m/s (positive sign indicates westerly wind) respectively. In the west side, the river-land breeze is strongest in spring. And the average easterly/westerly wind speed is 0.29/0.27 m/s. However, in the east side, the river breeze in summer is the most prominent (0.11 m/s), so is the land breeze in winter. For the wind different between the west and east side, the maximum occurs during daytime in spring, and the minimum occurs during nighttime in summer.

As shown in Figure 4, the results from this analysis support that easterly winds (land breezes) are dominant during nighttime, but westerly winds (river breezes) appear during 10:00–16:00, which has crucial impacts on dominant winds over Tongling. During the diurnal cycle, when the maximum occurs with westerly winds in the east and easterly winds in the west during 10:00–16:00, the river breezes are dominant winds; when the maximum occurs with westerly winds in the west and easterly winds in the east during 16:00–22:00, the land breezes are dominant winds. The difference is more significant in the daytime than nighttime.

3.2 The origin and effects of river breeze

The main cause of river-land breeze is the different heat capacity between river and land. Suppose Q (J/m^2) is solar radiation flux, C is specific heat capacity of surface (land and water), dT represents the change of temperature due to radiation, and m indicates unit mass of atmosphere. Then the formula of solar radiation flux is as following:

$$Q = C \cdot dT \cdot m \tag{5}$$

Because specific heat capacity of land (denoted as CL) is smaller than that of water (denoted as CW), for same solar radiation, temperature change of water (denoted as dTW) is less than that of land (denoted as dTL). In the daytime, temperatures of both land and the Yangtze River rise because of solar radiation, but the land is heated much quicker than the river, resulting in warm land and cold water. In contrast, during the night, temperatures of both land and the Yangtze River decrease due to radiation cooling, but the land cools much quicker than the river, resulting in cold land and warm water. A pressure gradient is generated due to the temperature difference between the Yangtze River, which leads to airflow movement.

According to atmospheric state equation $p = \rho RT$, if there is a difference between the temperatures in two regions, their corresponding atmospheric pressure (p) will respond to the change of temperature gradient by increasing their gradient accordingly. Based on equation of atmospheric motion [formula (6)], wind speed as well as the change rate of the wind speed with time will follow the changes of the pressure gradient, resulting in an increase of the local deviated wind speed. In another word, the river-land breeze increases the amplitude of the perturbed wind component, which further aggravate the inhomogeneity of the wind fields. Therefore, river-land breeze increases the change rate of the wind with time, amplifies the perturbations of the total wind and finally effects the diffusion of the atmospheric polluted matters.

$$\begin{cases} \frac{du}{dt} - fv = -\frac{1}{\rho}\frac{\partial p}{\partial x} + F_x \\ \frac{dv}{dt} + fu = -\frac{1}{\rho}\frac{\partial p}{\partial y} + F_y \\ \frac{dw}{dt} = -\frac{1}{\rho}\frac{\partial p}{\partial z} - g + F_z \end{cases} \tag{6}$$

Diurnal variation of the speed of Δu and the regional average concentration of PM_{10} are shown in Figure 5. We can find that the Δu is generally low speed (<0.35 m/s) from 0:00 to 7:00. A quick increase can be noticed after 7:00, and it reaches maximum around 16:00 and then decreases abruptly afterwards. Also, it is obvious that the speed of Δu is small during the night, and less than 0.4 m/s after 20:00.

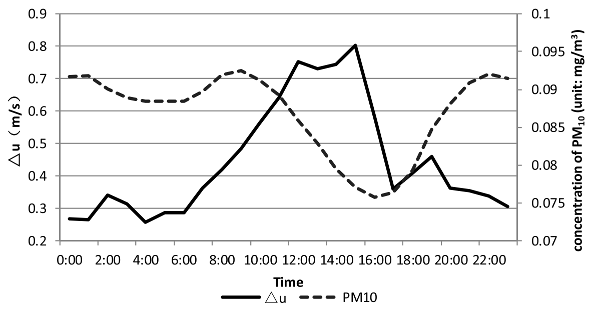

FIGURE 5
Diurnal variation of Δu (unit: m/s) and regional average concentration of PM_{10} (unit: mg/m^3).

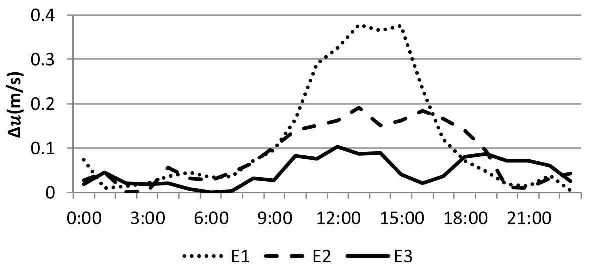

FIGURE 7
Diurnal variation of the local deviated wind speed (Δu) in three regions east side of the Yangtze River (E1: close to the Yangtze River; E2: moderate distance from the Yangtze River; E3: far from the Yangtze River).

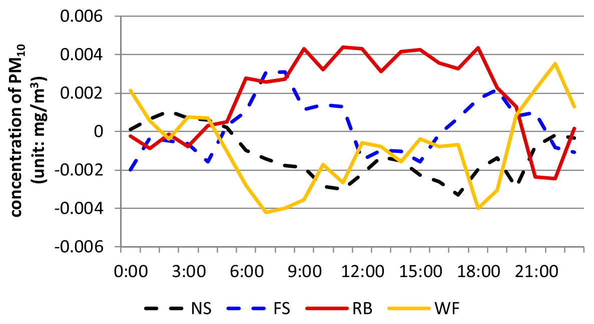

FIGURE 6
Diurnal variation of PM_{10} anomalies at individual stations.

4 Discussion

Unlike the variation of PM_{10} concentration which is primarily determined by the meteorological conditions, the variation of the NO_2 and SO_2 concentrations is much more complicated and subjected to combined effects from multiple factors. Therefore, we use PM_{10} as a representative of air pollutant to study the impact of river-land breeze on its spatial distribution.

We first calculate the domain-averaged concentration of the PM_{10}, then the PM_{10} anomalies at each observation station can be obtained by subtracting the averaged PM_{10} value from the observed PM_{10}. Those anomalies reflect the inhomogeneity of the PM_{10} spatial distribution.

According to the diurnal variation of averaged PM_{10} concentration from four stations, the main period of reduced concentration is 9:00–16:00. During that period, the speed of Δu is larger than 0.45 m/s. This implies the local perturbed winds can effectively enhance the diffusion of atmospheric pollutants for the concentration of PM_{10} is decreased significant. We can also notice from Figure 6 that the PM_{10} concentrations at stations FS and RB are larger than those at station NS and WF, and the former two stations are the farthest from the Yangtze River while the latter are the closest. This indicates the PM_{10} concentration is lower near the Yangtze River. Diurnal variation of local deviated wind in three different regions from the east side of the Yangtze River is depicted in Figure 7. E1, E2 and E3 respectively represent the region whose distance from the Yangtze River is less than 10km, between 10 and 20 km and more than 20 km. It is clear that u' varies inversely with the distance from the Yangtze River. As a result, the local deviated wind speed is stronger and pollutant concentration is less near the Yangtze River.

The diurnal variation of pollutant concentration is also obvious in Figure 6. The anomalous PM_{10} concentration at those four stations gradually increase starting from 6:00 and decrease after 20:00. This period corresponds to the exact time frame when the local deviated winds are enhanced (Figure 7), indicating a strong correlation between the pollutant concentration and the local deviated winds. In addition, there are also remarkable diurnal variation for the differences of averaged Δu in E1, E2 and E3. The difference of averaged Δu between E1 and E2 reaches maximum (0.21 m/s) around 14:00 and the ratio is 2.4. The difference of averaged Δu between E2 and E3 reaches maximum (0.16 m/s) around 16:00 and the ratio is 9.2. In general, u' increases rapidly after 6:00, which causes stronger winds in the areas along the Yangtze River.

There are strong correlations about the diurnal variation of pollutant concentration between the stations. The correlation coefficient is -0.75 between stations NS and RB and -0.71 between stations WF and FS. The strong negative correlations between these two pairs of stations imply a plausible scenario that the pollutants are transported between stations: the concentration of pollutant in one observation point is increased, while the concentration of pollutant in the other point is decreased.

Figure 8 is the scatter diagram of local deviations of PM_{10} concentration (SD-PM_{10}) and the speed of Δu. As the speed less

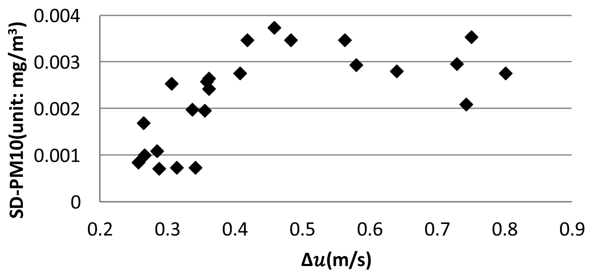

FIGURE 8
Scatter diagram of the local deviations of PM_{10} concentration ($SD\text{-}PM_{10}$) and the local deviated wind (Δu).

than 0.45 m/s, the SD-PM10 increases quickly with the speed of u'. However, after the speed of Δu more than 0.45 m/s, the SD-PM_{10} decreases gradually with the 0.45 m/s. That is to say, the PM_{10} distribution generally becomes homogenous after Δu more than 0.45 m/s.

The above analysis shows: 1) river-land breeze causes strong local wind in the area near the Yangtze River and helps to spread the air pollutants, which results in a low concentration of pollutant in this area; 2) in the daytime, river breeze transports the pollutants away from the Yangtze River, leading to a negative correlation of the pollutant concentration between the areas close to and far away from the river. 3) Under a weak river breeze ($\Delta u \leq 0.45$ m/s) scenario, the PM_{10} is transported by the breeze within the study region and causes the heterogeneity of PM_{10} concentration. While under a strong river breeze ($\Delta u > 0.45$ m/s) scenario, the PM_{10} is transported out of the study region, and the PM_{10} concentration becomes homogenous.

5 Conclusion

A river-land breeze is a regional meteorological phenomenon caused by the difference of heat capacity between water and land. As one of the major mining cities near the Yangtze River, Tongling is subjected to significant influences from the river-land breezes. The river-land breezes in Tongling have the following characteristics:

1) During the spring, the local deviated wind (river-land breeze) is more prominent, and the speed of breeze in daytime is stronger than the speed at night.
2) Although the dominant winds in Tongling are easterlies, they frequently turn to westerlies due to the influences of breezes.
3) The river-land wind component is large for area near the Yangtze River and small for those far from, and it exhibits a significant non-linear decreasing relation with the increase of the distance from Yangtze River.

Under the influence of the river-land breezes, the spatial distribution of PM_{10} concentration in Tongling has the following characteristics:

1) PM_{10} concentration is lower at the stations near the Yangtze River and higher at the stations far away. The discrepancies of concentration between different stations gradually increase after 6:00.
2) In the daytime, river breeze transports the pollutants away from the Yangtze River, leading to a negative correlation of the pollutant concentration between the areas close to and far away from the river.

Data availability statement

The raw data supporting the conclusions of this article will be made available by the authors, without undue reservation.

Author contributions

For research articles with several authors, a short paragraph specifying their individual contributions must be provided. The following statements should be used "Conceptualization, HZ; methodology, YH; software, XW; validation, XH; formal analysis, SW; investigation YH; resources, HZ; data curation, YH; writing—original draft preparation, HZ; writing—review and editing, YH; visualization, YH; supervision, YH; project administration, HZ; funding acquisition, HZ. All authors have read and agreed to the published version of the manuscript. Authorship must be limited to those who have contributed substantially to the work reported.

Acknowledgments

The authors acknowledge support from the Natural Science Foundation of Anhui Province (2108085MD138), the National Key R&D Program (2018YFC0213806), and the Anhui Public Welfare Technology Application Research Linkage Project (1604f0804002). We acknowledge editors and reviewers for improving the language of the paper and for in-depth discussions. We would like to thank LetPub (www.letpub.com) for providing linguistic assistance during the preparation of this manuscript.

Conflict of interest

The authors declare that the research was conducted in the absence of any commercial or financial relationships that could be construed as a potential conflict of interest.

Publisher's note

References

Alexandra, M., Carla, G., Marta, C., Isabel, R., David, C., and Myriam, L. (2016). Investigating ozone high levels and the role of sea breeze on its transport. *Atmos. Pollut. Res.* 7 (2), 339–347. doi:10.1016/j.apr.2015.10.013

Avissar, R., and Pielke, R. A. (1989). A parameterization of heterogeneousl and surfaces for atmospheric numerical models and its impact on regional meteorology. *Mon. Weather Rev.* 117, 2113–2136. doi:10.1175/1520-0493(1989)117<2113:apohls>2.0.co;2

Choi, S-Y., Young-Hee, L., Cho, C., and Kim, K. R. (2015). Analysis of local wind induced by surface heterogeneity and sloping terrain near nakdong river, asia-pac. *J. Atmos. Sci.* 51 (3), 249–257. doi:10.1007/s13143-015-0075-4

Clappier, A., Martilla, A., Grossi, P., Thunis, P., Pasi, F., Krueger, B. C., et al. (2000). Effect of sea breeze on air pollution in the greater athens area. Part I: Numerical simulations and field observations. *J. Appl. Meteorology* 39 (4), 546–562. doi:10.1175/1520-0450(2000)039<0546:eosboa>2.0.co;2

Crosman, E. T., and Horel, J. D. (2010). Sea and lake breezes: A review of numerical studies. *Boundary-Layer Meteorol.* 137, 1–29. doi:10.1007/s10546-010-9517-9

Crosman, E. T., and Horel, J. D. (2012). Idealized large-eddy simulations of sea and lake breezes: Sensitivity to lake diameter, heat flux and stability. *Boundary-Layer Meteorol.* 144, 309–328. doi:10.1007/s10546-012-9721-x

Fu, X., Wang, S. X., Zhao, B., Xing, J., Cheng, Z., Liu, H., et al. (2013). Emission inventory of primary pollutants and chemical speciation in 2010 for the Yangtze River Delta region, China. *Atmos. Environ.* 70 (0), 39–50. doi:10.1016/j.atmosenv.2012.12.034

Hu, J., Wang, Y., Qi, Y., and Zhang, H. (2014). Spatial and temporal variability of PM2.5 and PM10 over the north China plain and the Yangtze River Delta, China. *Atmos. Environ.* 95, 598–609. doi:10.1016/j.atmosenv.2014.07.019

Melas, D., Kioustioukis, I., and Lazaridis, M. (2006). "The impact of sea breeze on air quality in the Athens area," in *Advances in air pollution modelling for environmental security*. Editors L. Farago, K. Georgiev, and Á. Havasi (Netherlands: Springer), Vol. 54, 285–295.

Oliveira, A. P., and Fitzjarrald, D. R. (1993). The Amazon river breeze and the local boundary layer: I – observations. *Bound. Layer. Meteorol.* 63 (1–2), 141–162. doi:10.1007/bf00705380

Porson, A., Steyn, D. G., and Schayes, G. (2007). Sea-breeze scaling from numerical model simulations, Part I: Pure sea breezes. *Boundary-Layer Meteorol.* 122, 17–29. doi:10.1007/s10546-006-9090-4

Silva Dias, M. A. F., Silva Dias, P. L., Longo, M., Fitzjarrald, D. R., and Denning, A. S. (2004). river breeze circulation in eastern amazonia: Observations and modeling results. *Theor. Appl. Climatol.* 78, 111–121.

Wang, J., Wang, S., Scott, V. A., Zhao, B., Jang, C., Jiang, J., et al. (2015). Assessment of short-term PM2.5-related mortality due to different emission sources in the Yangtze River Delta, China. *Atmos. Environ.* 123, 440–448. doi:10.1016/j.atmosenv.2015.05.060

Wang, X-H., Lu, E., and Xiao, Y. (2010). River-land wind features in Yangtze River Ma'anshan Branch and countermeasures for air pollution. *J. Central South Univ. Forestry& Technol.* 30 (1), 120–124.

Wang, Y., Ying, Q., Hu, J., and Zhang, H. (2014). Spatial and temporal variations of six criteria air pollutants in 31 provincial capital cities in China during 2013-2014. *Environ. Int.* 73 (0), 413–422. doi:10.1016/j.envint.2014.08.016

frontiers | Frontiers in Earth Science

TYPE Original Research
PUBLISHED 06 January 2023
DOI 10.3389/feart.2022.1036692

Influence of key parameters of ice accretion model under coexisting rain and fog weather

Yue Zhou[1], Rong Wan[1]*, Jing Sun[1], Zhengxu Gao[2] and Jialun Yang[3]

[1]Hubei Key Laboratory for Heavy Rain Monitoring and Warning Research, Institute of Heavy Rain, China Meteorological Administration, Wuhan, China, [2]Wuhan Regional Climate Center, Wuhan, China, [3]China Electric Power Research Institute, Beijing, China

OPEN ACCESS

EDITED BY
Honglei Wang,
Nanjing University of Information Science and Technology, China

REVIEWED BY
Ying Wang,
Gansu Meteorological Bureau, China
Pengguo Zhao,
Chengdu University of Information Technology, China

*CORRESPONDENCE
Rong Wan,
wanrong@whihr.com.cn

SPECIALTY SECTION
This article was submitted to Atmospheric Science, a section of the journal Frontiers in Earth Science

RECEIVED 05 September 2022
ACCEPTED 16 September 2022
PUBLISHED 06 January 2023

CITATION
Zhou Y, Wan R, Sun J, Gao Z and Yang J (2023), Influence of key parameters of ice accretion model under coexisting rain and fog weather.
Front. Earth Sci. 10:1036692.
doi: 10.3389/feart.2022.1036692

Based on 30 complete wire icing processes lasted longer than 24 h observed from the Enshi, Jinsha, Dacaoping and Shennongding of Shennongjia in mountainous areas of Hubei province during the winter of 2008–2016, the macroscopic effects of rain–fog weather on the ice accretion process were analyzed. Furthermore, the distribution characteristics of key simulation parameters in supercooled fog (SF) and freezing rain (FR) were discussed according to the physical model of icing process. Finally, the evolution characteristics of the simulated ice thickness in rain–fog weather were proposed. Results showed that the duration of ice accretion in mountainous areas is the key factor affecting the maximum ice thickness; the freezing rain is most frequent during the glaze icing process, which leads to the substantial growth of ice thickness. The average growth rates of ice thickness with and without freezing rain are 1.26 mm h–1 and -0.11 mm h–1, respectively. Collision rate is the main parameter for inhibiting ice accretion of SF, with an average value of ~ 0.1, while freezing rate is the main parameter for inhibiting ice accretion of FR, with an average value of ~ 0.6. The ice accretion of SF shows the characteristics of periodic growth, while the ice accretion of FR shows the explosive growth of ice thickness, which makes the simulated values of icing closer to the observations. The ice formation efficiency of FR was more than twice that of SF, with a negative feedback mechanism to the ice accumulation of SF.

KEYWORDS

supercooled fog mixed with freezing rain, icing model, collision rate, freezing rate, wire icing

Introduction

Since the first 500 kV high-voltage transmission line with the length of 595 km from Pingdingshan to Wuhan in China was put into operation in 1981, seven inter-provincial power grids as well as the five independent provincial (regional) power grids have been put into operation one after another; the total length of 500 kV lines is >20,000 km. As high-voltage transmission lines are usually erected in high-altitude mountainous areas, they are highly vulnerable to freezing rain (FR) and supercooled fog (SF); the cooling droplets condensed on the cable or snow slush frozen on the cable will cause ice coating on cable, which is usually called as "wire icing". Wire icing will not only affect the normal operation of the transmission network but also cause serious insulator flashover, cable breaking after galloping, damage to the fittings and insulators, tilt and collapse of poles towers, and other accidents (Adhikari and Liu, 2019; Deng et al., 2012; Lu et al., 2022). Since the deployment of China's 330 and 500 kV high-voltage transmission lines, wire icing disasters have increased and seriously affected the safe and stable operation of the power grid (Wang and Jiang, 2012; Hu et al., 2016; Huang et al., 2021). There were four severe low-temperature snowstorm and ice freezing events hitting the 20 provinces and cities in South China during 10 January 2008–2 February 2008, causing severe influence to the development of economy and security of humans. However, widespread icing disasters are not frequently seen. In winter, high-altitude mountainous areas become icing-prone areas due to low temperature and sufficient water vapor (Lamraoui et al., 2014; Neil et al., 2014), therefore, the local icing disaster has become the focus of attention in the field of power communications.

According to the icing density, ice accretion mainly includes three types: glaze, rime, and mixed-phase of glaze and rime. The glaze is more commonly observed in the South China than in the North China, whereas the rime is more frequently observed in the North China than in the South China; both types of icing are more frequently observed in the mountainous areas than on the plains (Wang, 2011; 2014a; 2014b). Zhao et al. (2010) revealed the spatial distribution and climate change characteristics of freezing weather in China from 1961 to 2008, and demonstrated that the frequency of freezing weather in most areas of China decreased, but the intensity has increased. The continuous invasion of cold air and transportation of large amount of water vapor due to the combined anomalies of atmospheric circulation are the key reasons for the widespread freezing weather (Ding et al., 2008; Kuang et al., 2019; Wang et al., 2020; Zhao et al., 2022). Bernstein (2000) studied the meteorological conditions like temperature, relative humidity, wind speed, wind direction, and precipitation during glaze and rime icing processes, and indicated that the glaze icing requires more stringent meteorological conditions than rime-type icing, whereas the mixed-phase icing has more relaxed requirement on meteorological condition. The FR caused by the "melting process" depends on altitude, thickness, and temperature of the near-surface cold and warm layers (Rauber et al., 2000). Therefore, glaze icing mainly occurs in the plains, with low frequency, while the FR formed by the "supercooled warm-rain process" has looser requirement on the cold layer and warm layer, and is often accompanied by the rime icing in mountainous areas; this makes the mixed-phase icing the most frequently seen in this regions (Gultepe et al., 2014), imposing great safety threat to the transmission lines and communication towers.

The wire icing is essentially the coagulation of supercooled droplets on the surface of the cable. Changes in the number concentration of droplets, average particle size and liquid water content, and other physical parameters dominate the ice accretion intensity, where the rain intensity is the key factor affecting the intensity of glaze icing, has the similar droplet spectrum characteristics with stratiform cloud precipitation (Chen et al., 2011), while the liquid water content determines the intensity of rime icing, with the similar droplet spectrum characteristics to that of advection fog (Niu et al., 2012). The particle size of FR droplets is much larger than that of SF droplets; when it approaches the ground, it not only provides more supercooled water to the icing process but also affects the microphysical process of SF near the ground (Wang et al., 2019a), thereby indirectly affecting the ice accretion process. For the simulation of FR ice accretion processes, Jones (1998) developed a relatively simple ice accretion model of FR, which primarily considers raindrops falling vertically and those blown by wind. Szilder (1994) proposed an ice accretion model considering icicle occurrence, and obtained the size and shape of FR icing by using comprehensive analysis and stochastic theory. However, the magnitude of FR icing mainly depends on the number of supercooled raindrops coagulated on the cable surface (Makkonen, 1998), and the empirical model cannot describe the whole process of icing accurately. Contrarily, the simulation on the SF icing is relatively mature. Makkonen (1984; 2000) proposed the ice accretion model considering collision, capture, and freezing rates of supercooled droplets, and the model can describe the evolution of SF icing. Drage and Hauge (2008) and Nygaard et al. (2011) used this ice accretion model to simulate the icing process of power lines in mountainous areas, and obtained better simulation results compared with the measured values.

In summary, the ice accretion model of SF is highly correlated to the microphysical characteristics of liquid droplets. The occurrence of FR increases supercooled liquid water content in the atmosphere and enhance its contribution to ice accretion. However, it would also affect the microphysical characteristics of SF, which in turn will change the contribution of SF to the development of icing process. To this end, our paper explored the occurrence characteristics of SF and FR in the process of ice accretion in mountainous areas, the influence of the coexistence of FR and SF on the process of ice accretion is analyzed, and the ice thickness during rain–fog weather in mountainous areas is simulated through the physical model of ice accretion, which provides a reference for the meteorological sector to carry out targeted wire icing early warning and disaster assessment and the power sector in decision-making.

Data and methods

In the winter of 2008 and 2009, for the macro-micro characteristics of cloud-precipitation affecting the ice accretion

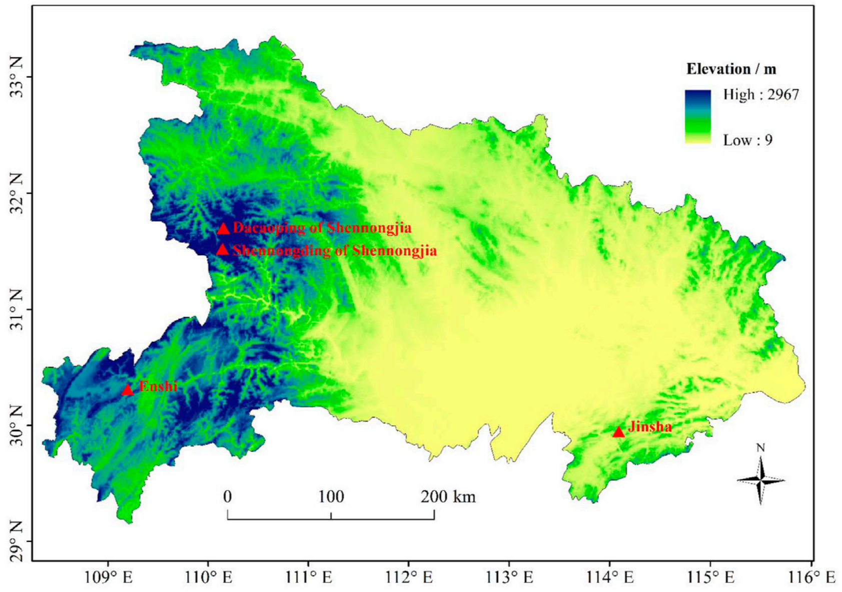

FIGURE 1
Map of study area and distribution of observation sites of wire icing (red triangles) in Hubei in the winter of 2008–2009 and 2012–2016.

process, two consecutive comprehensive observations were conducted at Enshi (109.27°E, 30.28°N; altitude 1722 m), Jinsha (114.21°E, 29.63°N; altitude 751 m), and Dacaoping of Shennongjia (110.33°E, 31.63°N; altitude 2,593 m) in Hubei (Niu et al., 2012). In addition, five consecutive observations of wire icing were conducted at Enshi, Jinsha, and Shennongding of Shennongjia (110.31°E, 31.45°N; altitude 3,100 m) in the winter of 2012–2016, and a total of 30 complete wire icing processes lasting longer than 24 h were obtained in 7-year field observations. The distribution of the above four sites is shown in Figure 1. The four stations are located in the intermediate and high-altitude mountainous areas in the southwest, southeast, and west of Hubei Province, which basically cover the three main heavy ice areas in Hubei Province (Zhou et al., 2013, 2018); the southwest and southeast areas have Gezhouba Power Plant, Three Gorges Power Station Transmission Project and West-to-East Power Transmission Project, representing the ice accretion process in mountainous areas under the joint action of cold front system and southwest warm-humid airflow. The Shennongjia in the west is a typical representative of ice accretion in high-altitude mountains.

The observations mainly included icing photos, ice thickness and weight, cloud amount, weather phenomena, and meteorological elements. The ice accretion observations were made every 1 h in the winter of 2008 and 2009, and every 6 h in the winter of 2012–2016. Icing photos were taken at the same time as ice thickness measured, and icing was weighted once or twice during each ice accretion process when ice thickness reached its maximum. The microphysical characteristics of SF and FR were observed in the winter of 2008 and 2009 using the FM-100 fog droplet spectrometer and the Parsivel raindrop spectrometer, and the specific observation design is described in Reference (Zhou et al., 2013). The temporal resolution of the meteorological elements (temperature, barometric pressure, humidity and wind) is 1 h.

In this study, the evolutions of ice thickness formed by SF and FR are simulated using a physical model based on the collision, capture, and freezing rates of supercooled droplets (Makkonen, 1984) as follows:

$$\frac{\mathrm{d}M}{\mathrm{d}t} = E_1 E_2 E_3 w v A \tag{1}$$

where, dM is the icing amount per unit time and dt is the unit time, E1 is the collision rate; E2 is the freezing rate; E3 is the capture rate; v is the effective particle velocity (approximated as the wind speed); w is the liquid water content of supercooled droplets; and A is the effective cross section of icing. Based on the analysis of the distribution characteristics of key simulation parameters, combining with their influence on the ice accretion model, the simulation was conducted on the three ice accretion processes in winter 2008 and 2009 (Table 1), and the macro and microphysical characteristics of the ice accretion process are shown in the literature (Niu et al., 2012). The capture rate in the icing simulation can usually be considered as a constant of 1, and the effect of ice thickness on the collision rate and capture rate of supercooled droplets was also considered to achieve a normalized simulation of ice thickness in rain–fog weather.

TABLE 1 Overview of the Three Icing Processes at Enshi in winter 2008 and 2009.

Cases	Duration	Icing type	Relative humidity/%	Minimum temperature/°C	Initial temperature (shedding temperature)/°C
Case1	26 February 2009–04 March 2009	Mixed-phase	100	−5.9	−0.3 (−0.2)
Case2	09 January 2010–11 January 2010	Mixed-phase	100	−5.8	−1.6 (−0.5)
Case3	21 January 2010–24 January 2010	Mixed-phase	100	−4.6	−0.3 (−0.6)

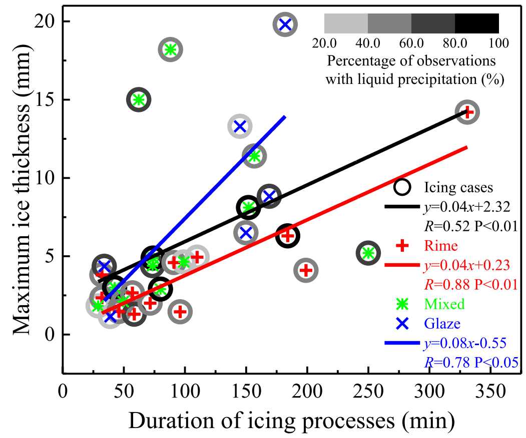

FIGURE 2
The correlation characteristics between the duration and maximum ice thickness of rime (red plus), glaze (blue cross), and mixed-phase (green star) icing during 30 ice accretion processes, with the percentage of observations with liquid precipitation (gray scale; %).

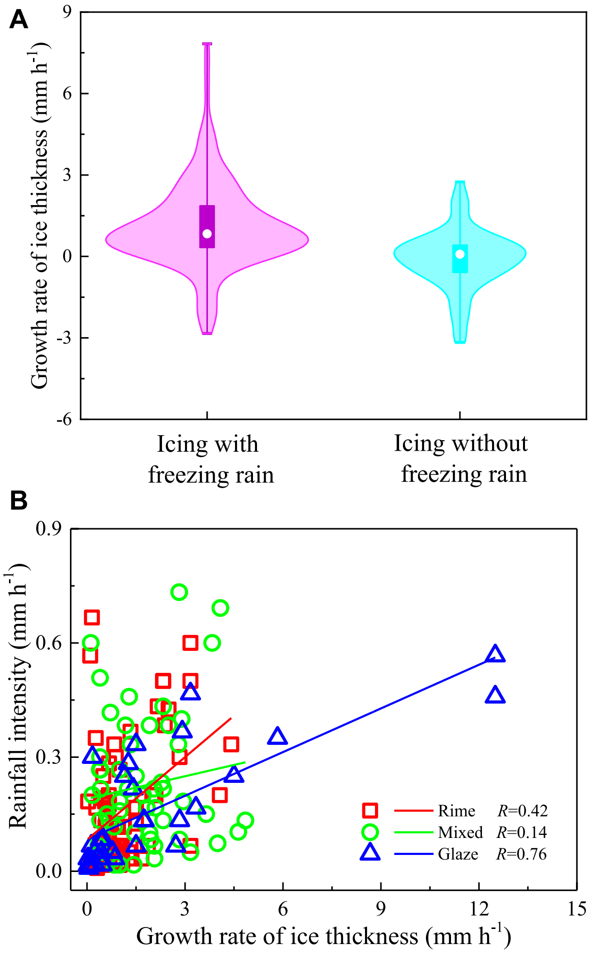

FIGURE 3
Relationship between the FR and growth rate of ice thickness during the 30 ice accretion processes. **(A)** Violin and box-whisker plots of the growth rate of ice thickness with and without FR. The central box represents the values from the lower to upper quartiles (25th to 75th percentiles), and the vertical line extends from the minimum to the maximum. The middle hollow square represents the mean value. **(B)** The correlations between the rainfall intensity and growth rate of ice thickness during the rime (red square), glaze (blue triangle), and mixed-phase (green circle) icing processes.

Influence of rain–fog weather on the ice accretion process

The FR lasts for a relatively short period, but has a heavier rain intensity, leading to a higher icing density, while the duration of SF is longer, the rain intensity is lower or even no precipitation occurs, leading to a lower icing density (Makkonen and Ahti, 1995; Ikeda et al., 2007). Figure 2 presents the correlation characteristics between the duration of icing process and maximum ice thickness of rime, glaze, and mixed-phase icing during 30 ice accretion processes at Enshi, Jinsha, and Shennongjia in 7-year field observations, with the percentage of observations with liquid precipitation. It can be seen that, regardless of the type of ice accretion, the duration of icing in mountainous areas is positively correlated with the maximum ice thickness, with a correlation coefficient of 0.52. The increase rate of ice accretion in mountainous areas is usually smaller than that in plain areas, and the long duration is an important characteristic and disaster-causing property (Jasinski et al., 1998; Frohboese and Anders, 2007). The increase rate of maximum ice thickness with the duration during the rime icing cases is similar to the relationship between the two in all cases, with a higher correlation coefficient of 0.88. The correlation coefficient between the two in the cases of glaze icing also reaches 0.78, but the slope of the fitted curve is about twice as high as that in the case of rime icing, which indicates that the duration determines the maximum ice thickness of rime and glaze icing, and that the increase rate of ice thickness in glaze icing is significantly higher than that of the rime icing. The correlation between the maximum ice thickness and the duration is not stable for the mixed-phase icing due to the alternative effect of SF and FR.

The periods with liquid precipitation to the total observed periods for the entire ice accretion process is calculated as the percentage of liquid precipitation. From Figure 2, we can see that the percentage of liquid precipitation in either type of ice accretion is above 20%, and the average percentage can reach 57% of the total number of observations, which indicates that the intermittent FR is a typical feature of the ice accretion in mountainous areas. At the same time, further analysis of the percentage of observations with liquid precipitation in different icing types revealed that the glaze icing has the lowest percentage of liquid precipitation, with the most concentrated percentage values; while the hard rime ice accretion has the highest percentage of liquid precipitation, with the most scattered percentage values.

The growth rate of ice thickness with and without FR is further compared in Figure 3A, showing that the occurrence of FR does not guarantee a positive ice thickness growth rate. Ice melting as well as breaking off and shedding were observed in both situation, but the cases with a negative ice thickness growth rate without FR was 2.5 times higher than that with FR. In addition, the occurrence of FR made the growth rate of ice thickness reach the maximum value of 7.83 mm·h−1, and the ice thickness growth rate was positive in more than 75% of the observations, and the average ice thickness growth rate was 1.26 mm·h−1; while in the observation without FR, the growth rate of ice thickness was more evenly distributed between −3.0 and 3.0 mm·h−1, centered on 0. The average growth rate was −0.11 mm·h−1, and the variation of ice thickness under the influence of SF was mainly stable, without explosive growth. The correlation characteristics between the rainfall intensity and growth rate of ice thickness deeply illustrate the importance of FR to the ice accretion (Figure 3B). Whether it is the rime icing, glaze icing, or mixed-phase icing, the growth rate of ice thickness is positively correlated with the rainfall intensity, with the correlation coefficient of 0.42, 0.76, and 0.14, respectively, showing the rainfall intensity has the most significant effect on the growth rate of glaze icing.

Distributions of the key parameters of ice accretion model under rain–fog weather

The different effects of SF and FR on the icing process are given in terms of macro-features in the above section. Then, to reveal the reasons for this difference from the perspective of the physical mechanism of ice accretion, it needs to be quantitatively determined that whether the droplets of SF and FR collide and freeze on the cable. Therefore, in this section, the distributions of the collision rate (E1) and freezing rate (E2) of SF and FR and their correlation characteristics with key physical parameters are analyzed using the observations of microphysical properties of fog/cloud and precipitation during icing processes in Hubei Province in winter of 2008 and 2009.

Figure 4 presents the distributions of the collision and freezing rates of SF and FR during the three icing cases. It can be seen that E1 and E2 show opposite distribution patterns, where the collision rate of SF (Figure 4A) is mostly below 0.15, with a mean value of about 0.1, while the freezing rate (Figure 4B) is mostly above 0.9, with a mean value greater than 0.8. The droplet size of SF on the order of 101 μm prevents them from colliding with the cable due to the ambient flow, while their small size makes them easier to freeze on the cable (Farzaneh, 2008). The collision rate of FR (Figure 4C) is close to 1, while the freezing rate (Figure 4D) vary the most (more than 75% of the values are distributed within the range of 0.2–1), with the average value is still around 0.6, and the droplet size of FR on the order of 101 mm makes almost all of them collide with the cable, while raindrops also tend to flow down along the cable to form into icicles (Makkonen, 2000), which in turn leads to reduce the direct contribution of raindrops to ice accretion. Since the ice thickness simulation is obtained by multiplying the multiple parameters, the extremely low collision rate of SF makes its contribution to ice accretion significantly lower than that of FR in similar scenarios.

In order to explore the key physical properties affecting the icing process, the correlation characteristics between liquid water content (Clw), median volume diameter (Dmv), wind speed (V), the collision rate (E1), and the freezing rate (E2) during the SF and FR process are given in Figure 5. It is seen that the key physical properties affecting the ice accretion of SF are Dmv, V and Clw in order, with correlation coefficients of 0.66, 0.41 and 0.22 with E1, respectively. Meanwhile, based on the average values of relevant variables with the E1 intervals of the value of 0.05, and the E2 intervals of the value of 0.1, the correlation coefficients increase to more than 0.8, which indicates that these meteorological properties have an obvious impact on E1 and E2 in general, but the degree is different. The droplet size of the SF has the greatest effect on E1 (Figure 5B), especially after

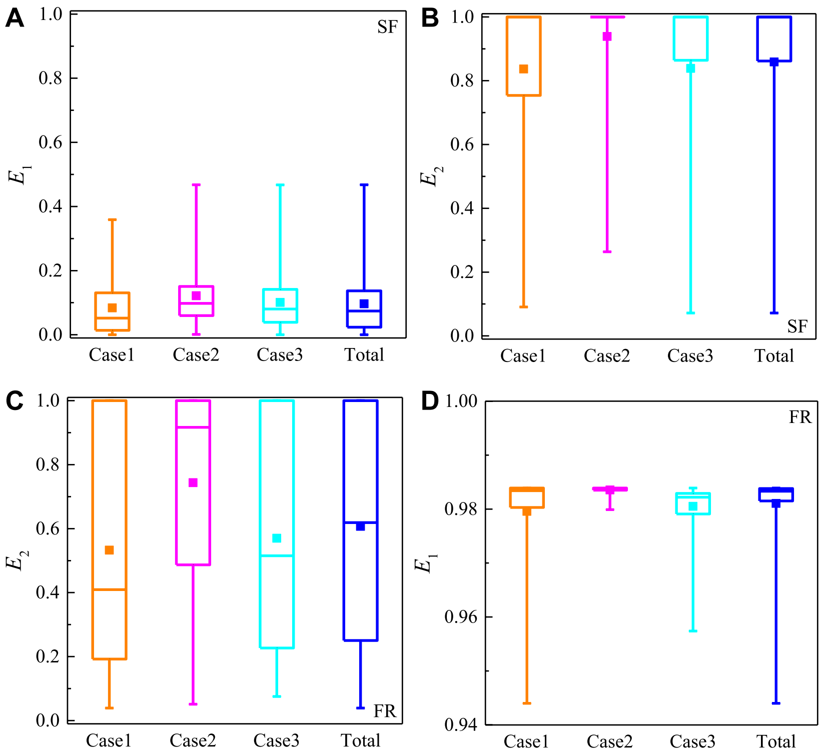

FIGURE 4
Distribution characteristics of collision rates (E1) of supercooled fog **(A)** and freezing rain **(C)**, and freezing rates (E2) of supercooled fog **(B)** and freezing rain **(D)** of the three ice accretion cases in winter of 2008 and 2009. The central box represents the values from the lower to upper quartiles (25th to 75th percentiles), and the vertical line extends from the minimum to the maximum. The middle solid square and line represents the mean value and median value, respectively.

Dmv > 15 μm, and the increase of Dmv significantly increases the value of E1, which is similar to the results of ice accretion processes in a Swiss wind farm (Davis et al., 2014); The increase of V leads to the decrease of E1 (Figure 5C), especially when V > 3.5 m·s−1, the mean value of E1 basically remains below 0.1, and only a small number of supercooled droplets will collide with the cable. The correlation between Clw and E1 is the lowest (Figure 5A), even when the value of Clw is greater than 0.2 g·m−3, E1 is mainly distributed within 0.3, which indicates that the increase of liquid water content during the ice accretion of SF in mountainous areas mainly relies on the increase of the number concentration and overall size of fog droplets. The mechanism of significantly increasing liquid water content by forming big droplets through collision-growth process are relatively weak, which is consistent with the microphysical characteristics of SF during these icing cases (Zhou et al., 2013).

For the FR process, the freezing rate (E2) is the key parameter that inhibits the increase of ice thickness. It is seen that E2 exponentially decreases with the increase of Clw (Figure 5C) and Dmv (Figure 5D), and the correlation coefficients are 0.77 and 0.82, respectively. When Clw > 0.5 g·m−3, E2 is maintained below 0.2, the corresponding raindrop size is about 1.0 mm; when both the value of Clw and Dmv are small, E2 is distributed within the range of 0–1, and the simulation to ice accretion of FR has higher uncertainty. Similarly, larger wind speed also inhibits the E2 value (Figure 5D), and when the wind speed is 2.5–3.0 m·s−1, E2 has higher uncertainty and mainly distributed within 0–1; when the wind speed is smaller than this value range, E2 is larger than 0.9, and almost all the raindrops can freeze on the cable; while when the wind speed is larger than this value range, E2 is below 0.3, which is significantly lower than its average value.

Simulation of the ice accretion process under rain–fog weather

Figure 6 presents the evolution of the simulated ice thickness during the above three ice accretion processes (Case1, Case2, and Case3) under the joint effect of SF and FR. It can be seen that the ice accretion of SF shows a periodic variation. And Case1 (Figure 6A) showed three significant

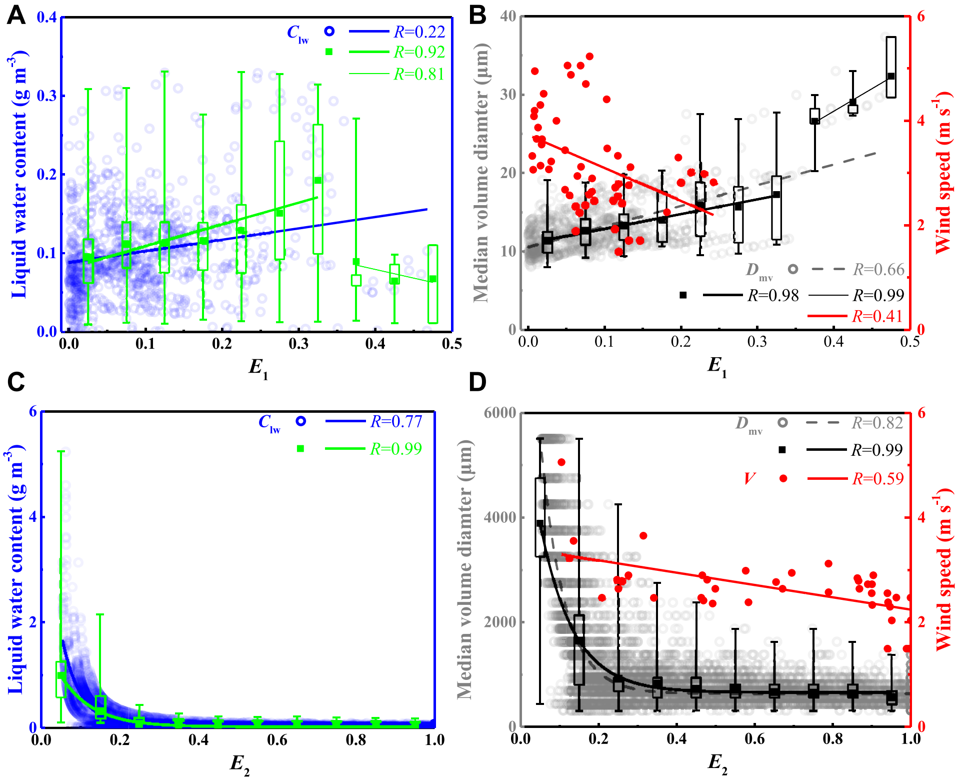

FIGURE 5
Scatter plots comparing collision rate E1 with liquid water content Clw **(A)**, median volume diameter Dmv, and wind speed V **(B)** during SF process, and freezing rate E2 with liquid water content Clw **(C)**, median volume diameter Dmv, and wind speed V **(D)** during FR process. The corresponding least-square fitting lines and correlation coefficient (R) are given in the corner of each panel. Box plots also show **(A)** Clw, **(B)** Dmv of SF process, and **(C)** Clw, **(D)** Dmv of FR process with the E1 intervals of the value of 0.05, and the E2 intervals of the value of 0.1. The central box represents the values from the lower to upper quartiles (25th to 75th percentiles), and the vertical line extends from the minimum to the maximum. The middle solid square represents the mean value.

increases in ice thickness, with an increase of about 7.6 mm, Case2 (Figure 6B) showed three significant ice thickness increases lasting about 200 h during the ice accretion process, with an increase of about 9.1 mm, Case3 (Figure 6C) showed a significant ice thickness increase lasting 160 h during the ice accretion process, with an increase of about 12.2 mm. The significant increase in ice thickness occurred mainly at the initial stage of the ice accretion, and the change in ice thickness during the growth period accounted for more than 90% of the total ice thickness during the process, which was mainly limited by the collision rate of the SF droplets. The effective cross section at the initial stage of the ice accretion was the smallest in the whole process, and more droplets can fall on the cable easily, while with the increase of ice thickness, the effective cross section is amplified significantly, making supercooled droplets that can collide with the cable originally can no longer collide with the cable, which is also the main reason for the relatively stable and unobvious increase of ice thickness in later stage of ice accretion (Wang et al., 2019b). Unless a stronger SF process occurs in the later stage of ice accretion, there are more and bigger droplets to make the ice thickness continue to increase again.

Meanwhile, it can be clearly seen that the duration of FR is short, with the ratio of duration of FR to SF is 6.60, 21.01, and 5.48%, respectively. Although the freezing rate of FR was significantly smaller than the collision rate, the bigger size and larger liquid water content of the raindrops can ensure that enough liquid water is frozen on the cable, promoting the increase of ice thickness significantly.

Statistical analysis of the ratio of the simulated icing of FR to SF was also illustrated in Figure 6. For Case2 and Case3 with weak FR, the ice accretion efficiency of FR to SF which is calculated by the ratio of duration and simulated ice thickness, was about 2.69, and 3.19, respectively, while for Case1, where the FR is stronger, the ice accretion efficiency can reach the value of 6.81. Also, the total ice thickness simulated by the comprehensive consideration of FR and SF can reflect the explosive growth of icing process obviously, and make the simulations closer to the numerical range of observations. Meanwhile, the occurrence of FR leads to the rapid growth of ice

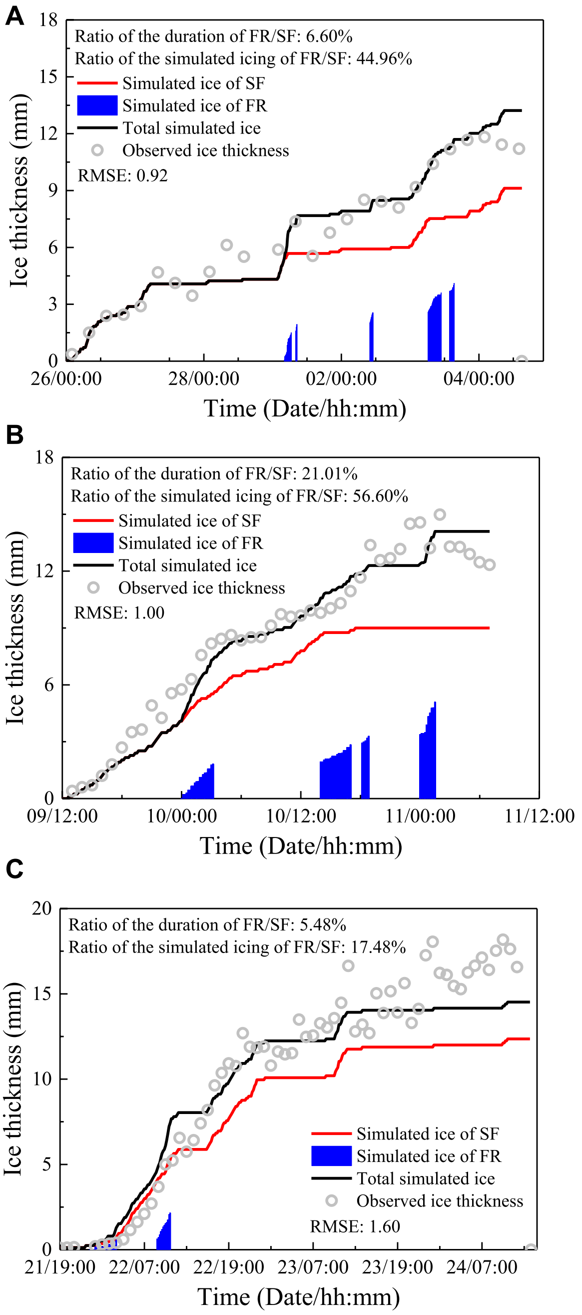

FIGURE 6
Temporal variations of observed ice thickness (gray hollow circle), simulated ice thickness under the effect of supercooled fog (red line), freezing rain (blue column), and joint effect of the both (black line) during ice accretion of Case1 **(A)**, Case2 **(B)**, and Case3 **(C)** in Hubei Province in winter of 2008 and 2009.

thickness during this period, significantly reduce the collision rate of SF droplets, which in turn inhibit the ice accretion efficiency of SF. Generally speaking, there is a negative feedback mechanism of the occurrence of FR on the ice accretion of SF.

Conclusion

During the winter of 2008–2016, the icing properties and key influence factors of 30 complete wire icing processes observed at Enshi, Jinsha, Dacaoping, and Shennongding of Shennongjia in Hubei are investigated, the collision rate and freezing rate of supercooled droplets under rain–fog weather is also analyzed, and the simulation of ice accretion processes is conducted considering the joint effect of FR and SF. The conclusions are as follows:

1) The duration of ice accretion in mountainous areas determined the maximum ice thickness of the process, and the two variables were positively correlated with a correlation coefficient of 0.52. There was the highest increase rate of ice thickness during the glaze icing processes. FR occurred in more than 50% of the icing processes.
2) The occurrence of FR could lead to an explosive increase in ice thickness, with a maximum value of 7.83 mm·h−1 and an average growth rate of 1.26 mm·h−1, while the variation of ice thickness was relatively stable during the icing processes without FR, with the growth rate mainly distributed within the range of −3–3 mm·h−1, and an average growth rate of −0.11 mm·h−1. The growth rate of ice thickness was positively correlated with the rainfall intensity, with the correlation coefficient of 0.42, 0.76, and 0.14, respectively, showing the rainfall intensity had the most significant effect on the growth rate of glaze icing.
3) The collision rate (E1) was the main parameter inhibiting the ice accretion in SF, with the mean value of about 0.1. The median volume diameter (Dmv) of SF had the greatest influence on E1, and when it was larger than 15 μm, the increase of Dmv would significantly increase E1. The increase of wind speed (V) would reduce the value of E1, and when it was larger than 3.5 m·s−1, the mean value of E1 basically stays below 0.1. The correlation between liquid water content (Clw) and E1 was the weakest. The freezing rate (E2), on the other hand, was the main covariate that inhibited the ice accretion of FR, with the mean value of about 0.6. The Dmv, V, and Clw of FR were all negatively correlated with E2, and the distribution range of E2 values was wide (0–1), with large uncertainty.
4) The ice accretion of SF showed the characteristics of periodic growth, with increase of ice thickness of the growth period accounts for more than 90% of the total ice thickness of the process. However, the ice accretion of FR showed the explosive growth of ice thickness, which made the simulated values of icing closer to the observations. The ice formation efficiency of FR was more than twice that of SF, with a negative feedback mechanism to the ice accumulation of SF.

Although the research in this manuscript is helpful to reveal the physical mechanism of the explosive growth of icing process in mountainous areas, the ice accretion properties are mainly obtained through manual observation, which is featured by low temporal resolution, and does not match the macro–microscopic physical quantity observations of cloud and precipitation. These problems are yet to be solved through further researches on the response of ice accretion to changes in physical properties of supercooled droplets by using the automated icing observation equipment in the future.

Data availability statement

Publicly available datasets were analyzed in this study. This data can be found here: http://hb.cma.gov.cn/qxfw/index.html.

Author contributions

YZ and RW conducted the study design. YZ, ZG, and JY provided the observational data. JS and ZG assisted with data processing. YZ wrote the paper with the help of RW and JS. RW, ZG, and JY were involved in the scientific interpretation and discussion. All authors provided commentary on the paper.

Funding

This research was funded by the National Key R&D Program of China (Grant No. 2018YFC1507201), the National Natural Science Foundation of China (Grant No. 41875170), and the Natural Science Foundation of Hubei Province (Grant No. 2021CFB571).

Conflict of interest

The authors declare that the research was conducted in the absence of any commercial or financial relationships that could be construed as a potential conflict of interest.

Publisher's note

References

Adhikari, A., and Liu, C. (2019). Remote sensing properties of freezing rain events from space. *J. Geophys. Res. Atmos.* 124, 10385–10400. doi:10.1029/2019jd030788

Bernstein, B. (2000). Regional and local influences on freezing drizzle, freezing rain, and ice pellet events. *Weather Forecast.* 15, 485–508. doi:10.1175/1520-0434(2000)015<0485:raliof>2.0.co;2

Chen, B., Hu, W., and Pu, J. (2011). Characteristics of the raindrop size distribution for freezing precipitation observed in southern China. *J. Geophys. Res.* 116, D06201. doi:10.1029/2010jd015305

Davis, N., Hahmann, A., Clausen, N., and Žagar, M. (2014). Forecast of icing events at a wind farm in Sweden. *J. Appl. Meteorol. Climatol.* 53, 262–281. doi:10.1175/jamc-d-13-09.1

Deng, D., Gao, S., Du, X., and Wu, W. (2012). A diagnostic study of freezing rain over Guizhou, China, in January 2011. *Q. J. R. Meteorol. Soc.* 138 (666), 1233–1244. doi:10.1002/qj.981

Ding, Y., Wang, Z., Song, Y., and Zhang, J. (2008). Causes of the unprecedented freezing disaster in January 2008 and its possible association with the global warming. *Acta. Meteor. Sin.* 66, 808–825. doi:10.11676/qxxb2008.074

Drage, M., and Hauge, G. (2008). Atmospheric icing in a coastal mountainous terrain: Measurements and numerical simulations, a case study. *Cold Reg. Sci. Technol.* 53, 150–161. doi:10.1016/j.coldregions.2007.12.003

Farzaneh, M. (2008). *Atmospheric icing of power networks*. Quebec: Springer.

Frohboese, P., and Anders, A. (2007). Effects of icing on wind turbine fatigue loads. *J. Phys. Conf. Ser.* 75, 012061. doi:10.1088/1742-6596/75/1/012061

Gultepe, I., Isaac, G., Joe, P., Kucera, P., Theriault, J., and Fisico, T. (2014). Roundhouse (RND) mountain top research site: Measurements and uncertainties for winter alpine weather conditions. *Pure Appl. Geophys.* 171, 59–85. doi:10.1007/s00024-012-0582-5

Hu, Q., Wang, S., Yang, H., Shu, L., Jiang, X., Li, H., et al. (2016). Effects of icing degree on ice growth characteristics and flashover performance of 220kV composite insulators. *Cold Reg. Sci. Technol.* 128, 47–56. doi:10.1016/j.coldregions.2016.04.010

Huang, Y., Jiang, X., and Virk, M. (2021). Ice accretion study of FXBW4–220 transmission line composite insulators and anti–icing geometry optimization. *Electr. Power Syst. Res.* 194, 107089. doi:10.1016/j.epsr.2021.107089

Ikeda, K., Rasmussen, R., Hall, W., and Thompson, G. (2007). Observations of freezing drizzle in extratropical cyclonic storms during IMPROVE–2. *J. Atmos. Sci.* 64, 3016–3043. doi:10.1175/jas3999.1

Jasinski, W., Noe, S., Selig, M., and Bragg, M. (1998). Wind turbine performance under icing conditions. *J. Sol. Energy Eng.* 120, 60–65. doi:10.1115/1.2888048

Jones, K. (1998). A simple model for freezing rain ice loads. *Atmos. Res.* 46, 87–97. doi:10.1016/s0169-8095(97)00053-7

Kuang, X., Zhang, Y., Wang, Z., Huang, D., and Huang, Y. (2019). Characteristics of boreal winter cluster extreme events of low temperature during recent 35 years and its future projection under different RCP emission scenarios. *Theor. Appl. Climatol.* 138, 569–579. doi:10.1007/s00704-019-02850-8

Lamraoui, F., Fortin, G., Benoit, R., Perron, J., and Masson, C. (2014). Atmospheric icing impact on wind turbine production. *Cold Reg. Sci. Technol.* 100, 36–49. doi:10.1016/j.coldregions.2013.12.008

Lu, Z., Han, Y., and Liu, Y. (2022). Occurrence of warm freezing rain: Observation and modeling study. *JGR. Atmos.* 127, e2021JD036242. doi:10.1029/2021jd036242

Makkonen, L., and Ahti, K. (1995). Climatic mapping of ice loads based on airport weather observations. *Atmos. Res.* 36, 185–193. doi:10.1016/0169-8095(94)00034-b

Makkonen, L. (1984). Modeling of ice accretion on wires. *J. Clim. Appl. Meteor.* 23, 929–939. doi:10.1175/1520-0450(1984)023<0929:moiaow>2.0.co;2

Makkonen, L. (1998). Modeling power line icing in freezing precipitation. *Atmos. Res.* 46, 131–142. doi:10.1016/s0169-8095(97)00056-2

Makkonen, L. (2000). Models for the growth of rime, glaze, icicles and wet snow on structures. *Philosophical Trans. R. Soc. Lond. Ser. A Math. Phys. Eng. Sci.* 358, 2913–2939. doi:10.1098/rsta.2000.0690

Neil, D., Hahmann, A. N., Clausen, N. E., and Zagar, M. (2014). Forecast of icing events at a wind farm in Sweden. *J. Appl. Meteorol. Climatol.* 53 (2), 262–281. doi:10.1175/jamc-d-13-09.1

Niu, S., Zhou, Y., Jia, R., Yang, J., Lü, J., Ke, Y., et al. (2012). The microphysics of ice accretion on wires: Observations and simulations. *Sci. China Earth Sci.* 55, 428–437. doi:10.1007/s11430-011-4325-8

Nygaard, B., Kristjánsson, J., and Makkonen, L. (2011). Prediction of in–cloud icing conditions at ground level using the WRF model. *J. Appl. Meteorol. Climatol.* 50, 2445–2459. doi:10.1175/jamc-d-11-054.1

Rauber, R., Olthoff, L., Ramamurthy, M., and Kunkel, K. (2000). The relative importance of warm rain and melting processes in freezing precipitation events. *J. Appl. Meteor.* 39, 1185–1195. doi:10.1175/1520-0450(2000)039<1185:triowr>2.0.co;2

Szilder, K. (1994). Simulation of ice accretion on a cylinder due to freezing rain. *J. Glaciol.* 40, 586–594. doi:10.1017/s0022143000012478

Wang, S., and Jiang, X. (2012). Progress in research on ice accretions on overhead transmission lines and its influence on mechanical and insulating performance. *Front. Electr. Electron. Eng.* 7 (3), 326–336. doi:10.1007/s11460-012-0197-8

Wang, T., Niu, S., Lü, J., and Zhou, Y. (2019a). Observational study on the supercooled fog droplet spectrum distribution and icing accumulation mechanism in Lushan, Southeast China. *Adv. Atmos. Sci.* 36, 29–40. doi:10.1007/s00376-018-8017-6

Wang, T., Niu, S., Lü, J., Zhou, Y., and Wang, Y. (2019b). Observation and simulation studies of three types of wire icing. *Atmosphere* 10, 234. doi:10.3390/atmos10050234

Wang, Z. (2011). Climatic characters and changes of ice freezing days in China. *Chin. J. Atmos. Sci.* 35, 411–421. doi:10.3878/j.issn.1006-9895.2011.03.03

Wang, Z., Ding, Y., Zhou, B., and Chen, L. (2020). Comparison of two severe low-temperature snowstorm and ice freezing events in China: Role of Eurasian mid-high latitude circulation patterns. *Int. J. Climatol.* 40, 3436–3450. doi:10.1002/joc.6406

Wang, Z., Xing, H., Liao, L., Su, B., Zhao, Q., Feng, Y., et al. (2014a). The development of drug resistance mutations K103N Y181C and G190A in long term Nevirapine-containing antiviral therapy. *AIDS Res. Ther.* 33, 36–48. doi:10.1186/1742-6405-11-36

Wang, Z., Yang, S., Ke, Z., and Jiang, X. (2014b). Large–scale atmospheric and oceanic conditions for extensive and persistent icing events in China. *J. Appl. Meteorol. Climatol.* 53, 2698–2709. doi:10.1175/jamc-d-14-0062.1

Zhao, P., Xiao, H., Liu, J., and Zhou, Y. (2022). Precipitation efficiency of cloud and its influencing factors over the Tibetan plateau. *Int. J. Climatol.* 42 (1), 416–434. doi:10.1002/joc.7251

Zhao, S., Gao, G., Zhang, Q., Wang, Z., and Yin, S. (2010). Climate characteristics of freezing weather in China. *Meteor. Mon.* 36, 34–38.

Zhou, Y., Niu, S., Gao, Z., and Yang, J. (2018). Research to the influence factors on shedding processes of three–types icing. *Cold Reg. Sci. Technol.* 155, 300–307. doi:10.1016/j.coldregions.2018.08.024

Zhou, Y., Niu, S., and Lü, J. (2013). The influence of freezing drizzle on wire icing during freezing fog events. *Adv. Atmos. Sci.* 30, 1053–1069. doi:10.1007/s00376-012-2030-y

frontiers | Frontiers in Earth Science

TYPE Original Research
PUBLISHED 10 January 2023
DOI 10.3389/feart.2022.1123747

OPEN ACCESS

EDITED BY
Honglei Wang,
Nanjing University of Information Science and Technology, China

REVIEWED BY
Chao You,
Nanjing University of Aeronautics and Astronautics, China
Chao Wang,
Civil Aviation Flight University of China, China

*CORRESPONDENCE
Ning Yang,
✉ yangn@czust.edu.cn

SPECIALTY SECTION
This article was submitted to Atmospheric Science, a section of the journal Frontiers in Earth Science

RECEIVED 14 December 2022
ACCEPTED 29 December 2022
PUBLISHED 10 January 2023

CITATION
Yang N, Jiang W, Jin C, Zhang S and Hou W (2023), Numerical simulation of the effect of atmospheric condition on the lightning strike for wind turbine.
Front. Earth Sci. 10:1123747.
doi: 10.3389/feart.2022.1123747

Numerical simulation of the effect of atmospheric condition on the lightning strike for wind turbine

Ning Yang[1]*, Wei Jiang[1], Chenlu Jin[2], Shuqin Zhang[1] and Wenhao Hou[3]

[1]Changzhou Institute of Technology, Changzhou, China, [2]Nanjing Meteorological Bureau, Nanjing, China, [3]Jiangsu Provincial Meteorological Bureau, Nanjing, China

The risk of lightning exposure increases as wind turbine size increases, and lightning accidents have grown up to be a severe threat to wind turbines. The present paper focuses on the influence of the changes in atmospheric conditions around the rotating blade for the upward leader initiation. A 2D computational fluid dynamics model was established to obtain the air pressure distribution around the blades, and the simplified inception model was used to determine the initiation of the upward leader mechanism. In this paper, two significant factors of velocity and attack angle were studied. The results show that the trigger height is about an 11.2% difference for 120 m/s with the peak current of return stroke at 30 kA; the difference has reached about 28% for the attack angle of 10°. The research indicates that the area with higher air pressure is exposed to a greater risk of lightning strikes, and the probability of lightning strikes will increase as the blade attack angle increases.

KEYWORDS

lightning strike, wind turbine, air pressure distribution, upward leader inception, positive streamer

Introduction

In recent years, wind energy has grown to be a significant source of sustainable energy to reach emission reduction. Wind turbine installation capacity has increased rapidly in order to meet carbon peak and neutrality targets, which have become common sustainability goals around the world. Based on GWEC (Global Wind Energy Council. 2022) reports, the global wind power total installed capacity reached 837 GW by the end of 2021, about 12.4% growth compared to 2020. With the progress of material technology (such as carbon and glass fiber-reinforced polymers), wind turbine blades have experienced an enormous development due to the new material. Therefore, the size of wind turbines has tremendously increased in recent decades. A large percentage of wind turbines are likely to be installed in places with significant lightning activity [SArajcev et al., 2013]. Lightning strikes on wind turbines are strongly influenced by topological factors, wind turbines installed in mountainous areas are riskier to lightning damage than wind turbines installed in coastal regions [McNiff et al., 2002]. Thus, it is expected that wind turbines need to suffer greater lightning strikes (Agoris, 2002; Cotton et al., 2001; Sorensen, 1998).

Lightning is a tremendous nature phenomenon, the number of lightning strikes increases with structure height, posing significant challenges to wind turbines of growing size (Beckers, 2016). The threat posed by lightning strikes has increased, and caused significant damage due to both direct and indirect effects. According to the insurance company report, lightning strikes cause 23.4% of wind turbine failures in the United States (Gcube-insurance, 2012). Damages to the wind turbine occurred to the blades, rotor, and generator. The blades are the key components that convert wind energy to mechanical energy, and it is also one of the wind turbine's most vulnerable parts. According to a report from the ECN (Energy Research Centre of the Netherlands), the blades have the highest frequency of lightning strikes (approximately 75%), as well as the most extended downtime (about 10 days per lightning incident) (Rademakers et al., 2002). About 118 lightning strike accidents were recorded, the research has shown that 88.1% were attached to the blade tips. (Madsen et al., 2006). Garolera analyzed 304 cases of lightning-striking accidents in the USA and noted that most of the lightning strike is located at the blade tip, with about 90% of incidents located at the last 4 m of the blade (Garolera et al., 2014). Furthermore, 739 lightning incidents were observed during 7 years, but more than 1032 failures were found. That were indicating a single lightning strike can cause multiple component damage (Rademakers et al., 2002). Despite the fact that wind turbine being equipped with lightning protection equipment, lightning strikes have occurred nevertheless. This is because the manufacturers' design lightning protection devices mainly regard lightning strikes occurring at the place of the maximum electric field strength, for wind turbines that are the tip of blades. Remarkably, the lightning statistics data for wind turbines shows that only about 60% of lightning strikes occur at the blade tip (maximum electric field strength). However, there are still close to half of the lightning strikes occurring outside the vulnerable lightning strike area. The considerable number of existing protection failures indicates this direction is worth further study.

Different researchers have conducted some experiments with the scaled models to investigate the lightning characteristics. Radicevic presented a study with the reduced-size model, and the result shows the rotation of the blades decreases the number of direct lightning strikes. (Radicevic et al., 2012). Wen experimented with a scaled model and switching impulses (250/2500 μs), and the result indicates that the rotation of the blades improves lightning triggering ability (Wen et al., 2016). Furthermore, A comparison between current parameters from stationary and rotating wind turbines was carried out, and it reveals there is no substantial difference between the two operational modes (Yu et al., 2022). From the above study, some ambiguous and even conflicting conclusions have been obtained, and these results are confusing.

The blades of wind turbine generate periodic electric discharges indicating that the effect of rotation plays a critical role [Montanya et al., 2013]. Meanwhile, the lightning development and attachment mechanism considering space charge density distribution were carried out by some researchers. Gu discovered the electric field distortion produced by the space charge and discussed the variation of the streamer during the discharge process [Gu et al., 2020]. To determine the mechanisms of corona and leader initiation for rotating wind turbines, Yu established a three-dimensional drift and diffusion model. The results reveal that as the spinning speed increases, it becomes more sensitive to initiating corona discharge (Yu et al., 2017). Qu proposed a model to investigate the distribution of charged particle migration. It was further discovered that the rotation effect reduces positive ion concentration (Qu et al., 2019). Wang conducted long-gap discharge experiments to determine the difference in lightning triggering ability between rotating and stationary blades. According to the study, rotation increases its capacity to generate lightning strikes [Wang et al., 2017]. However, the space charge distribution is not the only factor that can influence the upward leader initiation when the blades are rotating. These studies have been limited to the shielding effect of space charges generated by thundercloud electric fields. The effect of the change of atmospheric conditions around the blades due to the rotation is neglected. Nevertheless, this factor is strong enough to influence the initiation process of the upward leader. But very few existing studies have paid attention to this point. M. Ramirez carried out a research to investigate the impact of air density on the discharge process [M. Ramirez et al., 1990]. The influence of pressure and humidity on the corona onset performance was studied, and a mathematical model to evaluate the corona onset voltages was proposed (Hu et al., 2011). Yu examined the corona discharge at low atmospheric pressure and discovered that the corona inception voltage drops as atmospheric pressure falls. (Yu et al., 2006). However, the above studies are concentrated on static conditions, and no further research has been proposed for dynamic systems. Therefore, it is necessary to conduct a numerical simulation to analyze the lightning strike characteristics for rotating blades considering the atmospheric conditions. In this paper, a 2D numerical model of air pressure distribution was established. Combining the inception model of upward leaders, the relevant sensitive factors were examined. Furthermore, the vulnerable strike areas of the blade were analyzed. The study will give a theoretical foundation for wind turbine lightning strike performance.

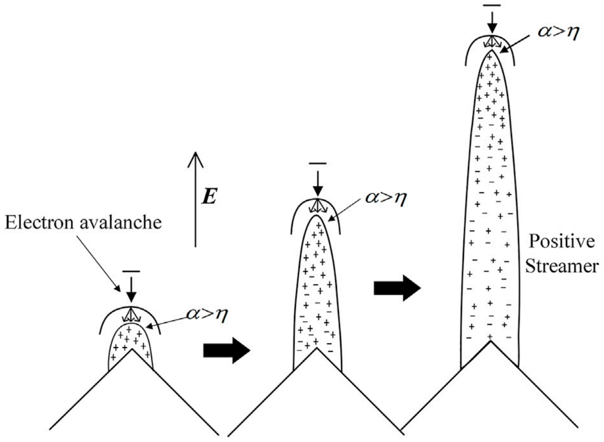

FIGURE 1
Formation of a positive streamer in the enhanced electric field.

Methods

In the second or subsequent streamer bursts, the streamer-leader transform condition is equal to or greater than approximately 1 μC (Gallimberti, 1979; Lalande et al., 2002). Once the requirement is reached, the ionization process provides the energy and current to sustain the thermal transition. At the same time, the upward leader channel expansion generates the electric field to enable the ionization process (Goelian et al., 1997). If this process reaches a dynamic equilibrium, the upward leader–streamer system can develop continuously and steadily.

According to the streamer criterion, free electrons are accelerated under electric field E. The impact ionization of neutral gas particles

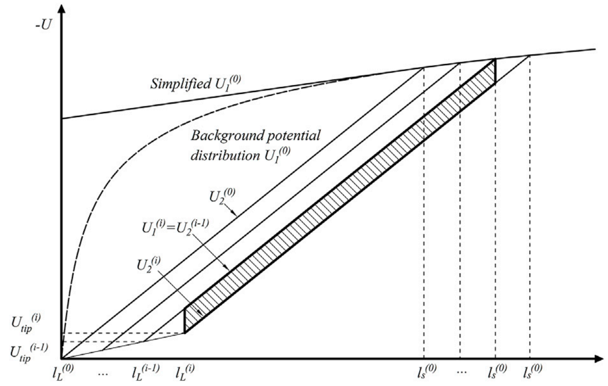

FIGURE 2
The background potential distribution.

increases the electrons. A net ionization coefficient α' can be defined as:

$$\alpha' = \alpha(E) - \eta(E) \tag{1}$$

Where $\alpha(E)$ and $\eta(E)$ are functions of E representing ionization and attachment coefficient, respectively. Defining the distance between $\alpha(E)$ and $\eta(E)$ where they are equal (α' =0) is l. The criterion from the conversion of electron avalanche to streamer is given below:

$$\int_0^l (\alpha(E) - \eta(E))dl \geq \ln\ (N_{stab}) \tag{2}$$

Where, N_{stab} is the critical number of positive ions, taken as 55×10^8 γ is the absolute humidity, P_w is the partial pressure of water vapor, α_w and α_d are ionization coefficients in water vapor and dry air, η_w and η_d are attachment coefficients.

Eq. 1 is only valid for $\alpha' > 0$. The electronic avalanche process is formed with the number of electrons increasing exponentially. The electric field gets greater ahead of the space charge zone, resulting in more positive space charges enter to the electrode gap to neutralize the positive space charges, as shown in Figure 1. When the stability number of positive ions or electrons at the head of the avalanche exceeds N_{stab}, the streamer is assumed to be formed. The average electric field of the streamers E_{str} is affected by the air humidity and the relative air density according to (Eriksson et al., 1986)

$$E_{str} = 425\delta^{1.5} + (4 + 5\delta)\gamma \tag{3}$$

$$P(z) = P_0 \exp\ (-z/z_0) \tag{4}$$

$$T = T_0 - 6H_L \tag{5}$$

$$\gamma = \gamma_0 \exp\ (-H_L/z_H) \tag{6}$$

Where γ is the absolute humidity, δ is the relative air density given by $\delta = (P/P_0)(T_0/T)$, in which P is the atmospheric pressure, T is the temperature, P_0 is the standard atmospheric pressure (1013.25 hPa), H_L is the altitude (km), and T_0 is 293 K; E_{str} is equal to 52 MV/m under the standard atmospheric condition ($P=P_0$, $T=T_0$; $\gamma = 11 g/m^3$). It is worth noting that it can be considered as a constant value for stationary objects, but it is necessary to make the corrections for a dynamic system.

In order to determine the stable upward leader's inception, the positive upward-leader inception theory is adopted (Becerra and Cooray, 2006a; Becerra and Cooray, 2006b). The method of approximate geometric based on the background potential distribution was presented. When $\triangle Q$ is greater than 1 μC, it is considered that the unstable upward leader has been generated since the background potential is strong enough to create a second corona charge. Furthermore, if the leader length exceeds the maximum value of 2 m, the steady leader inception criterion is considered satisfied. Otherwise, the development of the upward leader is considered to be terminated.

Charge conservation theory states that the quantity of charge entering the leader should be equal to the number of space charges remaining in the corona zone. The background potential distribution $U_1^{(0)}$ shift to $U_2^{(0)}$ for the reason of space charge existence and expressed as a straight line, the slope is E_1 and the intercept of the vertical axis Is U_0', as Figure 2 shows. Accordingly, the distribution of background potential can represented as:

$$U_1^{(0)} \approx E_1 \cdot l + U_0' \tag{7}$$

According to the approximate geometric method, the second corona charge defines as:

$$\Delta Q^{(0)} \approx K_Q \cdot \frac{l_s^2}{2} \cdot (E_{str} - E_1) \tag{8}$$

When thermal ionization is completed (temperature above 1500 K), the stem is transited to the leader with increased conductivity and energy as $\Delta Q^{(0)} \geq 1\,\mu C$. The potential for the tip of leader can be computed with:

$$U_{tip}^{(i)} = l_L^{(i)} \cdot E_\infty + x_0 \cdot E_\infty \cdot ln\left[\frac{E_{str}}{E_\infty} - \frac{E_{str} - E_\infty}{E_\infty} \cdot e^{-l_L^{(i)}/x_0}\right] \tag{9}$$

The charge ΔQ can be calculated as:

$$\Delta Q \approx K_Q\left[\left(E_{str} \cdot \left(l_L^{(i)} - l_l^{(i-1)}\right) + U_{tip}^{(i-1)} - U_{tip}^{(i)}\right) \cdot \left(l_s^{(i-1)} - l_L^{(i)}\right)\right] \tag{10}$$

The developed distance of the upward leader and the corona can be expressed with:

$$l_s^{(i)} = l_s^{(0)} + \frac{E_{str} \cdot l_L^{(i)} - U_{tip}^{(i)}}{E_{str} - E_1} \tag{11}$$

$$l_L^{(i+1)} = l_L^{(i)} + \Delta l_L^{(i)} = l_L^{(i)} + \frac{\Delta Q}{q_L} \tag{12}$$

When l_L reaches 2 m, the stable upward leader requirement is satisfied. Once $\Delta l_L^{(i)} < 0$, the development of the upward leader is terminated. The relevant parameters are shown in Table 1. In a previous study, the validity of model was examined by comparing simulated results with optically observed data which shows great agreement. (Yang et al., 2017).

The positive streamer gradient is affected by the atmospheric conditions (air humidity and air pressure), which make significant changes to lightning strike performance. Hence, it can obtain a method to determine the initiation of the upward leader by taking the atmospheric condition as an essential factor from the above correlating formulas. It is important to note that the lightning strike is assumed to be taken place successfully when the inception condition of the upward leader is satisfied in this study. The initial point is considered the subsequent strike point.

Results

The geometry of the wind turbine increases with the installed capacity, and the blade length also increases accordingly, which leads

TABLE 1 The parameters.

Parameter	Description	Value	Units
$I_L^{(1)}$	Initial leader length	5×10^{-2}	m
E_{str}	Positive streamer gradient	4.5×10^{5}	V/m
E_{∞}	Final quasi-stationary leader gradient	3×10^{4}	V/m
x_0	Constant given by the ascending positive leader speed and the leader time constant	.75	m
q_L	Charger per unit length necessary for thermal transition	6.5×10^{-7}	C/m
K_Q	Geometrical constant	4×10^{-11}	C/Vm

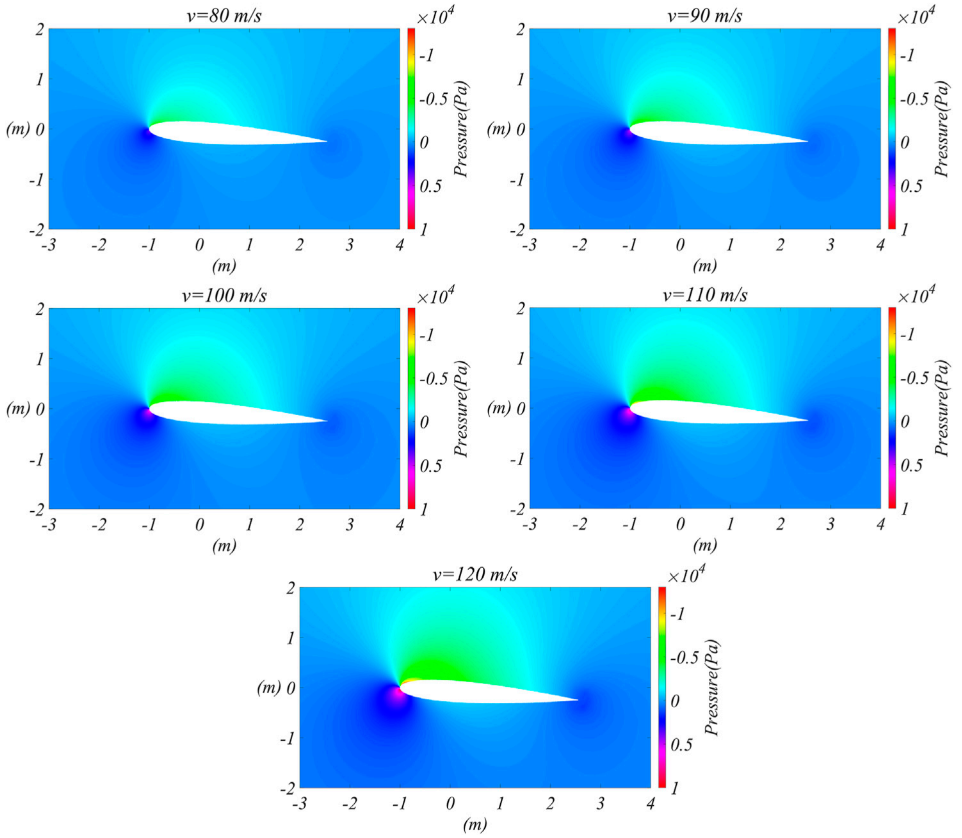

FIGURE 3
The air pressure distribution at different velocities around wind turbine blade.

to the blade tip speed becoming higher. As a result, precisely predicting a lightning strike to a wind turbine is critical. The study applies the geometry of a 2 MW wind turbine model with a 95 m hub and 54 m blades, with rotational speeds ranging from 8.1 rpm to 19 rpm according to the wind. The linear velocity of the blade tip is between 45 and 110 m/s. It is faster than wind speed, but much slower than the downward stepped leader (approximately 10^5–10^6 m/s). For the sake of a quantitative study, a symmetric wing NACA0012 was used in this research. Different speeds and attack angles were used as variables in this study to discuss the lightning strike characteristics of wind turbines under different conditions.

According to Bernoulli's theory, the air velocity on the top surface of the airfoil is greater than on the bottom. Hence, the atmospheric pressure on the blade surface is unequal (the pressure on the lower surface is high and the upper surface is low), and it depends on the two factors of velocity and attack angle. To analyze the lightning striking characteristics of the wind turbine, the air pressure distribution around the blade must be obtained. In this paper, a commercial finite element method (FEM) program based on the COMSOL software (Comsol Group, 2014) is used to analyze the pressure distribution. A two-dimensional model is made for the sake of achieving a balance between computational speed and accuracy.

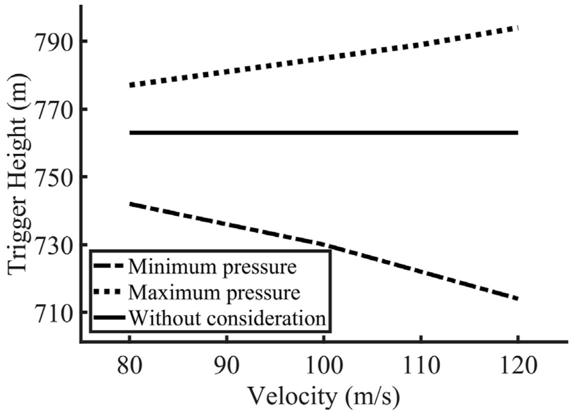

FIGURE 4
The trigger height at different velocities for minimum and maximum air pressure area.

From the above, it is known that the inception of the upward leader is a necessary condition for the object to be struck by lightning. The major factors must be identified to investigate the upward leader development process. Firstly, the effect of the velocity of the blade is considered. Figure 3 shows the simulated result of air pressure distribution for several different velocities of the blade, the attack angle is set to 4°. As can be seen, the difference in air pressure increases while the blade speeds up. Several velocities between 80 m/s to 120 m/s are simulated, respectively. The simulation result shows that the minimum pressure (relative pressure) is close to -1.22×10^4 Pa when the blade speed is at 120 m/s, while the maximum pressure (relative pressure) reaches 8.93×10^3 Pa. Therefore, the difference of pressure could cause a huge change in the positive streamer gradient, which can lead to a considerable change in lightning strike characteristics according to Eq. (3). Based on the simulation results, the positive streamer gradient varies between 4.43×10^5 V/m and 5.87×10^5 V/m in this case.

This study makes the assumption that the downward stepped leader channel is vertical with branch-free and non-uniform charge density distribution, which can be expressed as a function of the return stroke peak current (Cooray et al., 2007). In this case study, the return stroke peak current is taken as a typical value with 30 kA. As the downward-stepped leader moves toward the ground, an upward leader can be initiated when downward-stepped leader descends to a certain height. There is a decreasing trend with the increasing velocity at minimum pressure area, which equals 742 m at the velocity of 80 m/s, while it is approximately 714 m for the

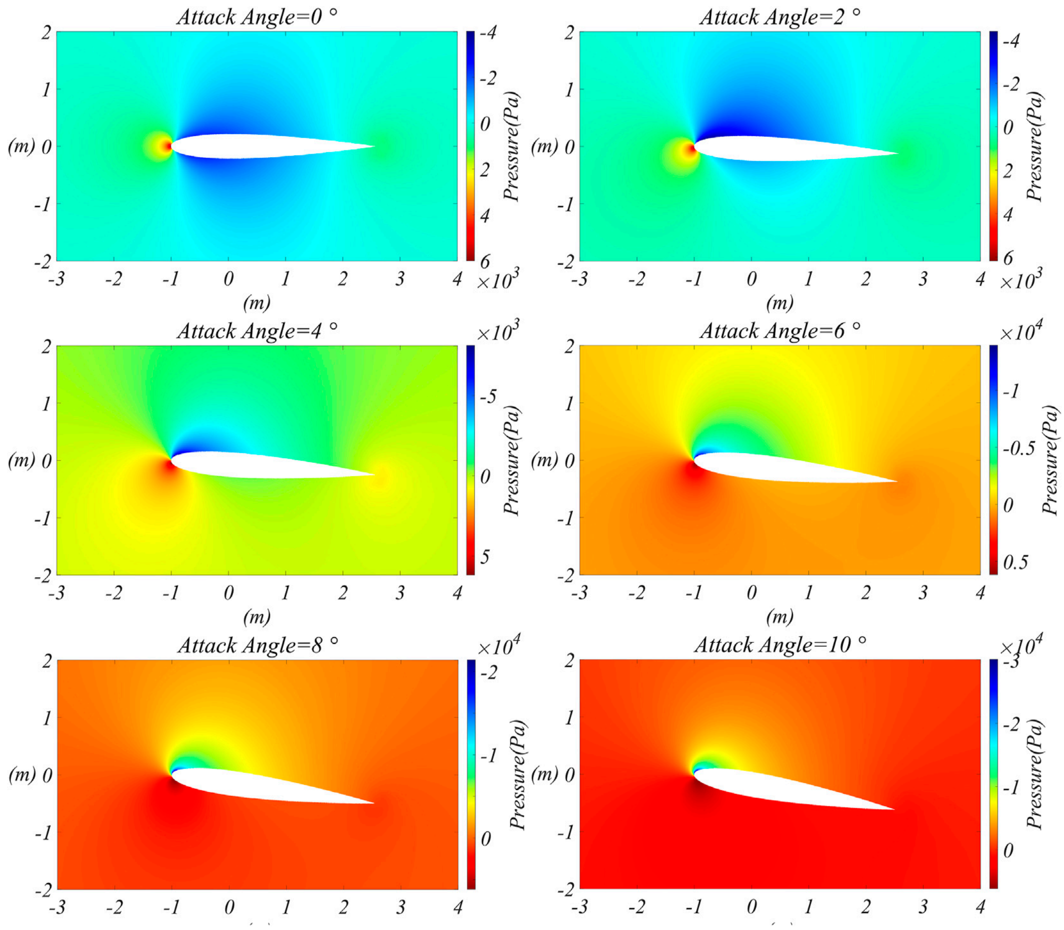

FIGURE 5
The air pressure distribution for different attack angles around wind turbine blade.

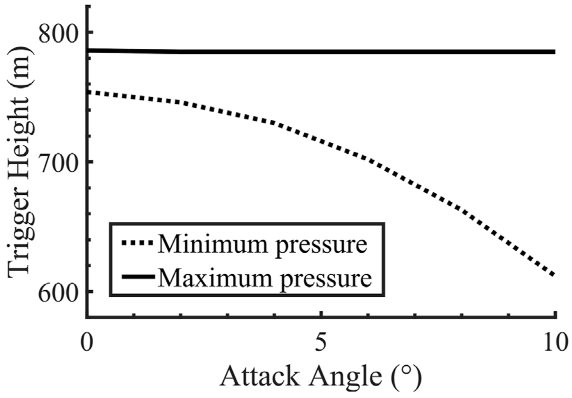

FIGURE 6
The trigger height of different attack angles for minimum and maximum air pressure area.

velocity at 120 m/s. However, the maximum pressure area shows the opposite trend. Note that if the effect of air pressure change is not considered, the downward-stepped leader trigger height is a fixed value of 763 m regardless of how fast the blade rotates. From the above results, it can be seen that the region where the air pressure is higher will be more likely to trigger a lightning strike than the lower-pressure region. The trigger height for the two different regions reaches 714 m and 794 m at 120 m/s, respectively. There is about an 11.2% difference between the two regions, as shown in Figure 4.

On the other hand, the attack angle is also regarded as an important factor. A similar method is adopted, the simulation result of pressure distribution for different attack angles is obtained, represented in Figure 5. In this case study, the obtained result is simulated with different attack angles from 0 to 10° at 100 m/s (the airflow separation effect occurs as the angle of attack increases, there are no more discussion for larger attack angles), respectively. The change in the pressure result in a considerable variation of the positive streamer gradient, which varies between 3.19×10^5 V/m and 5.67×10^5 V/m in this case. The trigger height that makes the upward leader successfully initiated was correspondingly changed. The simulation results are depicted in Figure 6. It is shown that the trigger height decreases dramatically with increased attack angle for the low-pressure area (0°–10°). But this trend in the high-pressure area is not significant. The trigger height is 785 m for the high-pressure area, and is reduced to 612 m in the low-pressure area (−28% reduction) for the case of 10°. The difference in trigger height tends to increase gradually with the increase of the attack angle. According to the simulated results, it can be concluded that the probability of lightning strikes in the low-pressure area will be reduced as the attack angle increases for the blade.

Conclusion and discussion

According to the statistics, lightning strikes have already become a severe threat to wind turbines that could cause enormous damage. The size of the wind turbine is getting increasingly larger, which faces more potential threats. As a result, it is expected that the wind turbines would be suffered more lightning strikes. In this paper, a 2D computational fluid dynamics model was established to obtain the distribution of the air pressure field around the blade. Aside from that, an upward leader inception model was established as well, and the initiation process of the upward leader on the blade for different velocities and attack angles was calculated. It can be found that there is a severe shortage without considering the changes in air pressure. The related conclusions are given as follows.

1 The difference between the maximum and minimum air pressure values increases as the blade accelerates, which can reach 2.11×10^4 Pa at 120 m/s. The changes result in the positive streamer gradient varying between 4.43×10^5 V/m and 5.87×10^5 V/m, which leads to a considerable difference in the lightning strike characteristics for the wind turbines.
2 The trigger height decreases with the increasing velocity at the minimum pressure area. However, the maximum pressure area shows the opposite trend. The trigger height for the two regions reaches 714 m and 794 m at 120 m/s with a typical return stroke peak current of 30 kA respectively, there is about 11.2% difference between the two regions. It can be inferred that the region where the blade pressure is higher will face more risk of lightning strikes than the lower-pressure region. The lightning protection device is recommended to be installed at the high pressure area of the blade.
3 The attack angle has a more significant impact than velocity on the positive streamer gradient, and the tends to increase gradually as the attack angle increases. It is noteworthy that the difference has reached about 28% for the attack angle of 10°. According to the simulated results, it can be concluded that the probability of lightning strikes in the low-pressure area of the blade will be reduced as the attack angle increases.

When the downward stepped leader is descending to a certain height, the upward leader will be initiated at the areas where the conditions are satisfied. After the height of the developing stepped leader decreases further, other places will also meet the conditions of the upward leader initiation. Therefore, more than one upward leader could be generated in the process of the downward stepped leader development. In general, the upward leader that initiates in the first place gets more time to develop an extended channel and has a higher probability of eventually connecting with the downward stepped leader to discharge. Nevertheless, according to the observation data, although the upward leader is successfully initiated and developed subsequently, there are still cases where the initiation point fails to become a lightning strike point. However, in this paper, it is still considered that the successful initiation of the upward leader is an important indication of the lightning strike, ignoring the development process after the initiation.

Data Availability statement

The raw data supporting the conclusion of this article will be made available by the authors, without undue reservation.

Author contributions

NY and WH, contributed to conception and design of the study. WJ and CJ organized the database. NY performed the analysis. NY wrote the first draft of the manuscript. SZ verify the manuscript. All authors contributed to manuscript revision, read, and approved the submitted version.

Funding

This work is supported by Natural Science Foundation of Jiangsu Province (Grants No: BK20200175); Major Basic Research Project of Natural Science Foundation of Jiangsu Higher Education (1KJA460001).

Conflict of interest

The authors declare that the research was conducted in the absence of any commercial or financial relationships that could be construed as a potential conflict of interest.

Publisher's note

References

Agoris, D. (2002). "Analysis of lightning incidents on wind turbines in Greece," in Proceedings of the 26th International Conference on Lightning Protection (ICLP 2002), Cracow, Poland, 2nd - 6th September 2002, 717–721.

Becerra, M., and Cooray, V. (2006a). A self-consistent upward leader propagation model. *J. Phys. D Appl. Phys.* 39 (16), 3708–3715. doi:10.1088/0022-3727/39/16/028

Becerra, M., and Cooray, V. (2006b). A simplified physical model to determine the lightning upward connecting leader inception. *IEEE Trans. Power Deliv.* 21 (2), 897–908. doi:10.1109/tpwrd.2005.859290

Beckers, R. (2016). Lightning protection. Available at: http://www.solacity.com/lightning-protection/.

Comsol Group (2014). *User's guide.* Stockholm, Sweden: Comsol Group.

Cooray, V., Rakov, V., and Theethayi, N. (2007). The lightning striking distance—Revisited. *J. Electrost.* 65 (5-6), 296–306. doi:10.1016/j.elstat.2006.09.008

Cotton, I., Jenkins, N., and Pandiaraj, K. (2001). Lightning protection for wind turbine blades and bearings. *Wind Energy Int. J. Prog. Appl. Wind Power Convers. Technol.* 4 (1), 23–37. doi:10.1002/we.44

Eriksson, A. J., Le Roux, B. C., Geldenhuys, H. J., and Meal, D. V. (1986). Study of airgap breakdown characteristics under ambient conditions of reduced air density. *IEE Proc. A Phys. Sci. Meas. Instrum. Manag. Educ. Rev.* 133 (8), 485–492. doi:10.1049/ip-a-1.1986.0067

Gallimberti, I. (1979). The mechanism of the long spark formation. *Le J. de Physique Colloques* 40 (C7), C7. doi:10.1051/jphyscol:19797440

Garolera, A. C., Madsen, S. F., Nissim, M., Myers, J. D., and Holboell, J. (2014). Lightning damage to wind turbine blades from wind farms in the US. *IEEE Trans. Power Deliv.* 31 (3), 1043–1049. doi:10.1109/tpwrd.2014.2370682

Gcube-insurance (2012). GCube top 5 US wind energy insurance claims report. Available at: http://www.gcube-insurance.com/en/press/gcube-top-5-us-wind-energy-insurance-claims-report/.

Global Wind Energy Council (2022). *Global wind report 2022.* Belgium: GWEC.

Goelian, N., Lalande, P., Bondiou-Clergerie, A., Bacchiega, G. L., Gazzani, A., and Gallimberti, I. (1997). A simplified model for the simulation of positive-spark development in long air gaps. *J. Phys. D Appl. Phys.* 30 (17), 2441–2452. doi:10.1088/0022-3727/30/17/010

Gu, J., Huang, S., Fu, Y., Chen, W., Cheng, D., Shi, W., et al. (2020). Morphological characteristics of streamer region for long air gap positive discharge. *J. Phys. D Appl. Phys.* 54 (2), 025205. doi:10.1088/1361-6463/abbeb3

Hu, Q., Shu, L., Jiang, X., Sun, C., Zhang, S., and Shang, Y. (2011). Effects of air pressure and humidity on the corona onset voltage of bundle conductors. *IET generation, Transm. distribution* 5 (6), 621–629. doi:10.1049/iet-gtd.2010.0560

Lalande, P., Bondiou-Clergerie, A., Bacchiega, G., and Gallimberti, I. (2002). Observations and modeling of lightning leaders. *Comptes Rendus Phys.* 3 (10), 1375–1392. doi:10.1016/s1631-0705(02)01413-5

Madsen, S. F., Holbøll, J., Henriksen, M., and Sørensen, T. (2006). "Interaction between electrical discharges and materials for wind turbine blades particularly related to lightning protection," in *Ørsted–DTU, electric power engineering* (Lyngby, Denmark: Technical University of Denmark). PhD thesis.

Qu, L., Wang, Y., Liu, G., Liao, M., Cai, H., Zhang, T., et al. (2019). Simulation study on positive corona discharge of receptors on rotating wind turbine blade tips under thundercloud electric fields. *Energies* 12 (24), 4696. doi:10.3390/en12244696

Rademakers, L. W., Braam, H., Ramakers, S. G., Wessels, H. R., Prins, R. K., Lok, R., et al. (2002). Netherlands: Energy research Centre of the Netherlands.Lightning damage of OWECS. Part 1.'Parameters relevant for cost modelling

Radičević, B. M., Savić, M. S., Madsen, S. F., and Badea, I. (2012). Impact of wind turbine blade rotation on the lightning strike incidence–A theoretical and experimental study using a reduced-size model. *Energy* 45 (1), 644–654. doi:10.1016/j.energy.2012.07.032

Ramirez, M., Moreno, M., Pigini, A., Rizzi, G., and Garbagnati, E. (1990). Air density influence on the strength of external insulation under positive impulses: Experimental investigation up to an altitude of 3000 m asl. *IEEE Trans. power Deliv.* 5 (2), 730–737. doi:10.1109/61.53076

Sorensen, T. (1998). *Lightning damages to power generating wind turbines*. Birmingham, UK: ICLP-98.

Wen, X., Qu, L., Wang, Y., Chen, X., Lan, L., Si, T., et al. (2016). Effect of wind turbine blade rotation on triggering lightning: An experimental study. *Energies* 9 (12), 1029. doi:10.3390/en9121029

Yang, N., Zhang, Q., Hou, W., and Wen, Y. (2017). Analysis of the lightning attractive radius for wind turbines considering the developing process of positive attachment leader. *J. Geophys. Res. Atmos.* 122, 3481–3491. doi:10.1002/2016JD026073

Yu, D., Farzaneh, M., Zhang, J., Shu, L., Sima, W., and Sun, C. (2006). "Properties of corona discharge under positive DC voltage at low atmospheric pressure," in Proceedings of the 2006 IEEE Conference on Electrical Insulation and Dielectric Phenomena, Denver, CO, USA, 15-18 Oct. 2006 (IEEE), 393–396.

Yu, W. A. N. G., Lu, Q. U., Tianjun, S. I., Yang, N. I., Jianwei, X. U., and Xishan, W. E. N. (2017). Experimental study of rotating wind turbine breakdown characteristics in large scale air gaps. *Plasma Sci. Technol.* 19 (6), 064016. doi:10.1088/2058-6272/aa6743

Yu, W., Li, Q., Zhao, J., and Siew, W. H. (2022). Numerical simulation of the lightning leader development and upward leader initiation for rotating wind turbine. *Machines* 10 (2), 115. doi:10.3390/machines10020115

frontiers | Frontiers in Earth Science

TYPE Original Research
PUBLISHED 17 January 2023
DOI 10.3389/feart.2022.1066610

Aircraft observations on a continuous haze pollution event in Shijiazhuang area

Xuesi Zhou[1,2], Xiaoshen Sun[2], Yang Yang[1,2]*, Xiaorui Zhang[2], Zhaochu Huang[2], Yi Cui[2] and Yi Huang[2]

[1]Key Laboratory of Meteorology and Ecological Environment of Hebei Province, Shijiazhuang, China, [2]Hebei Weather Modification Center, Shijiazhuang, China

OPEN ACCESS

EDITED BY
Honglei Wang,
Nanjing University of Information Science and Technology, China

REVIEWED BY
Ruiguang Xu,
Hebei University of Engineering, China
Ping Tian,
Beijing weather modification center, China

*CORRESPONDENCE
Yang Yang,
yangyang@hebwmo.cn

SPECIALTY SECTION
This article was submitted to Atmospheric Science, a section of the journal Frontiers in Earth Science

RECEIVED 11 October 2022
ACCEPTED 03 November 2022
PUBLISHED 17 January 2023

CITATION
Zhou X, Sun X, Yang Y, Zhang X, Huang Z, Cui Y and Huang Y (2023), Aircraft observations on a continuous haze pollution event in Shijiazhuang area.
Front. Earth Sci. 10:1066610.
doi: 10.3389/feart.2022.1066610

A continuous haze event was recorded on November 14th~17th, 2020 over Shijiazhuang. Two flights of King-air 350 meteorological research aircraft were performed on November 14th and 16th for the retrieval and observations of meteorological elements, aerosols, and black carbon. In this study, we combined airborne data with air pollution data ($PM_{2.5}$), ground meteorological data, and ERA-5 reanalysis data to describe the vertical distribution of aerosols (namely 0.1–3.0 μm) and black carbon. We further explicated the formation of this haze event. $PM_{2.5}$ pollution dominated this haze event, and the highest concentration of $PM_{2.5}$ was 209 μg/m^3. The intensity and height of thermal layers highly linked with the vertical transport of pollution. The highest number concentration of aerosols and black carbon was found below the thermal layers on both airborne sounding days. On the 14th, both BC and aerosol concentrations showed unimodal distribution, and the highest concentrations of BC and aerosols were 12683 ng/m^3 and 6965.125#/L at 250 m within layer I. The intensity of the thermal layer near-ground was weaker on the 16th that the number concentrations of BC and aerosols also remained at high levels in layer II. Backward trajectories of air mass indicated the long-range transport of pollution contributed to the high level of pollution on the 16th. Vapor conditions were more favorable for aerosols growth through moisture absorption. The maximum concentration of 943.58#/L was recorded at particles with a diameter of 0.4 μm on the 16th, while 749.26#/L was reached at 0.14 μm on the 14th. The corresponding height was consistent with the height of maximum concentration in the vertical distribution.

KEYWORDS

aerosols, black carbon, vertical distribution, airborne observation, particle size distribution

1 Introduction

Aerosols are the key components in earth-atmosphere system, affecting the global and regional climate (Anderson et al., 2003; Shi et al., 2008; Li et al., 2015), they can also severely harm the ecological environment and human health (Haywood and Boucher, 2000; Bond et al., 2013; Rao et al., 2013; Lei et al., 2016). They lay important forces on atmospheric circulation, precipitation distribution, and weather forecast (Jacobson, 2001). Through absorbing or scattering solar radiation (shortwave radiation), aerosols can heat the atmosphere or cool down the surface. Changing the thermal condition of the atmosphere, aerosols can further affect the vertical dynamic structure of the atmosphere. Therefore, to assess and calculate the direct and indirect radiation forcing from aerosols, we must form a clear picture of the vertical concentration distribution and particle size distribution of aerosols (Haywood and Boucher, 2000; Gobbi et al., 2004; Landman, 2010).

Black carbon (BC) is one of the key components of atmospheric aerosols (Janssen et al., 2012). As a strong absorbing component, BC can only absorb the visible wavelengths (Bond et al., 2013). They warm up the surrounding atmosphere, and to a great extent, this warming can offset the cooling caused by the scattering of atmospheric aerosols, in which BC will further influence local and global climate (Jacobson, 2001; Ramanathan and Carmichael, 2008).

Current instrumentation has been mainly mounted on sounding platforms, such as meteorological towers (Han et al., 2015), tethered balloons (Ran et al., 2016), remote sensing (Strawbridge and Snyder, 2004), and aircraft (Ding et al., 2009). Among, aircraft can collect data of the spatial distribution of aerosols and BC in real time. More importantly, the *in-situ* detection can reach higher altitudes and cover larger areas. The vertical distribution of aerosol showed a great correlation with the atmospheric structure (Johnson et al., 2000). The accumulation of aerosol particles was often found with thermal layers and high values of relative humidity (Sun et al., 2012; You et al., 2015). The number concentration of aerosols was distinct under different weather conditions and atmospheric structures (Yao et al., 2016). The vertical number concentration of aerosols followed a unimodal distribution (Fan et al., 2007), and the spectral width narrowed with increasing height (You et al., 2015). Li et al., 2014 found the spectral width of aerosols broadened with increasing height over the middle of Shanxi Province, China. In a stable atmosphere, BC concentration was higher in lower layers (Zhang et al., 2012), but evenly distributed in an unstable atmosphere (Lu et al., 2019). Besides, the vertical distribution of BC was different throughout the day (Li et al., 2015), and in different regions (Tan et al., 2022).

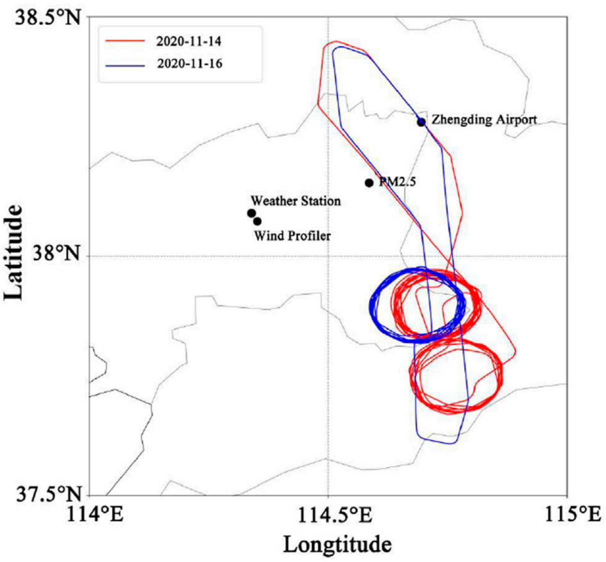

FIGURE 1
Flight trajectory on November 14th (red) and 16th (blue), 2020, and locations of observation stations.

Zhang et al. (2013) have found that China was the main contributor to global BC emissions up to a quarter. Shijiazhuang is the capital of Hebei province and is located in the middle and southern parts of Hebei Province. Due to rapid economic growth and accelerated urbanization, this region has been facing severe pollution for past decades. Recent researches have been focused on the aerosols in this region but rarely refers to the BC. Zhai et al. (2011) analyzed the number concentration and particle spectrum of aerosols in the atmosphere based on near-ground aerosols data, as well as the causes of it. During 2005–2007autumn seasons in the Hebei region, Zhang et al. (2011) concluded that high values of aerosol number concentration near the ground were often found under different synoptic weather conditions with records of small wind speed, high relative humidity, and thermal invasion, or on haze days. Sun et al. (2013) analyzed airborne observations of aerosols over the middle and west of North China Plain during the 2010 autumn. They found that the main source of aerosols was from the underlying transport, and the transport efficiency was determined by thermal inversion layers and the wind shear within the boundary layer.

Air quality has been improved over Shijiazhuang region for the past years, however, heavily polluted events still occurred every now and then. Therefore, it is still needed to explore the vertical characteristics and the transport of pollution. We focused on the analysis of both ground and airborne observations for a continuous haze event recorded during November 14th~ 17th, 2020 over Shijiazhuang. Specifically, we concluded the vertical distribution of both aerosols and BC based on two flights of airborne data, including the concentration, mean diameter, and particle spectrum of aerosols and BC. Potential sources of near-ground aerosols were also discussed.

Data and flight sounding description would be in “Data”. The following sections are in the order of “Weather and Pollution Background”, “Vertical Distribution of Pollutant Concentration”, “Backward Trajectory”, “Aerosol Spectrum Density Distribution”, and “Discussion”.

2 Data

Ground hourly meteorological data was acquired from Zhengding station (38.15°N, 114.34°E), ground $PM_{2.5}$ data was sourced from Zhengding (38.15°N, 114.59°E), wind profiler data was from Shijiazhuang (38.07°N, 114.35°E), and the geological distribution was illustrated in Figure 1.

2.1 Airborne observation

King Air-350 meteorological aircraft was carried out for the vertical observations and the true airspeed was around 250–300 km/h. Two sounding flights were on November 14th 18:50 and 16th 18:00, 2020 (Beijing time). The time in this article would be Beijing Time unless specifically highlighted. The flight tracks were drawn in Figure 1. Under the left flight wing, PCASP-100X (Passive Cavity Aerosol Spectrometer Probe-100X) was mounted for aerosol observations. Meanwhile, the AE-33 model of the aethalometer was mounted for the black carbon acquisition.

2.1.1 Aerosol observation

The Passive Cavity Aerosol Spectrometer Probe 100-X (PCASP) is manufactured by Droplet Measurement Technologies (DMT). The PCASP-100X is an optical particle counter for measuring aerosol size distributions from 0.1μm to 3 μm in diameter. It uses the Mie scattering theory to derive aerosol particle size distribution (Zhao et al., 2018). The size is divided into 15 bins and the sampling frequency is 1 Hz. The sample flow volume in the PCASP-100X is set to 1 cm^3/s. The details and detecting uncertainties of PCASP-100X can be found in Zhao et al. (2018) and Rosenberg et al. (2012).

2.1.2 Black carbon observation

In this study, Magee Scientific Aethalometer® Model AE33 is used to observe black carbon concentration. Two sample spots are collected from the same input air stream with different accumulation rates and the analysis of air is conducted simultaneously. The two results are combined mathematically to eliminate the “Filter Loading Effect” nonlinearity and accurately measure the aerosol concentration. The analysis will be performed at seven optical wavelengths spanning from the near-infrared (950 nm) to the near-ultraviolet (370 nm). The sequencing of illumination and analysis is performed on a 1Hz time base. This will present a complete spectrum of aerosol optical absorption with one data line every second.

2.2 Wind profiler data

Wind profiler is Doppler radars that have five antenna beams. The radar transmits electromagnetic pulses in five directions, in the order of north, east, south, west, and vertical direction. A wind profiler radar can derive atmospheric motion and wind information from the Doppler shift in the echoes produced under different atmospheric conditions (Wang et al., 2022). We use hourly wind data from the wind profiler manufactured by the China Aerospace Science & Industry Corporation (Liu et al., 2020).

2.3 Backward trajectory analysis

The HYSPLIT-4 model is an open-access model from NOAA’s Air Resources Laboratory and can compute atmospheric transport, dispersion, and deposition of pollutants and hazardous materials (Stein et al., 2015). The model has been widely used in the analysis of air parcel trajectories and atmospheric pollution transportation (Li et al., 2019). The backward trajectory model meteorological background data input from the NCEP GDAS dataset, 4 times daily including 00, 06, 12, and 18UTC (08, 14, 20, 02 as in Beijing Time) output. The geological resolution of the GDAS dataset is 1°×1°.

3 Result and discussion

3.1 Weather and pollution background

3.1.1 Weather analysis

During November 14th ~ 17th 2020, a continuous haze event was recorded over the Shijiazhuang region. At 500 h Pa, the meridional circulation spanned over the mid-and high altitudes regions in East Asia. The cold air was impeded from moving southward. On the 13th, (first stage, Figures 2A, 3A), the atmospheric water vapor content was underprovided. The synoptic settings included a high-level ridge, a weak anticyclonic circulation lower level at 850 hPa, and a ground high-pressure field. The atmosphere was clear and cloudless, in favor of radiative cooling. As a result, water moisture and pollutants gradually accumulated near the ground, marking the beginning of this haze event. The second stage lasted from the 13th evening to the 14th daytime as a weak upper-level trough was passing through North China. In mid-to-low levels, moisture was brought by the weak southwest air flow. Near the ground, the uniform pressure field behind the high-pressure

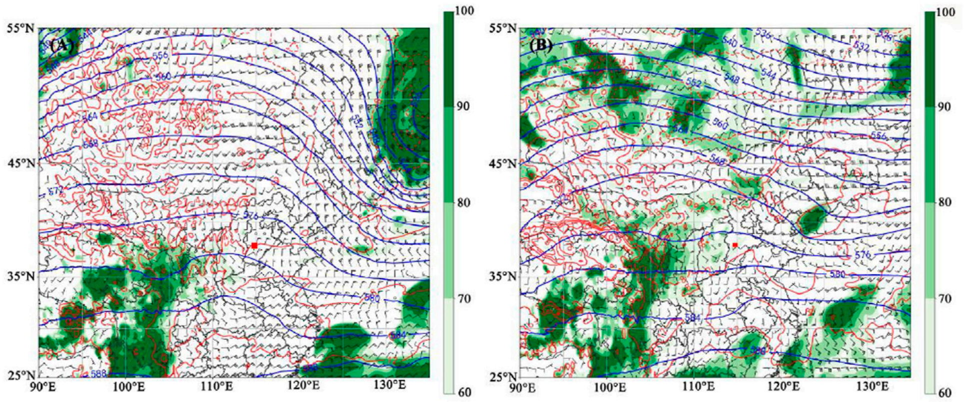

FIGURE 2
Upper-level synoptic weather at 08:00 2020 November 13th **(A)** and 08:00 2020 November 15th**(B)**, among, blue lines denote 500 hPa geopotential height, red lines denote 850 hPa isothermals, and wind barbs represent wind field at 850 hPa. The red square is Shijiazhuang area.

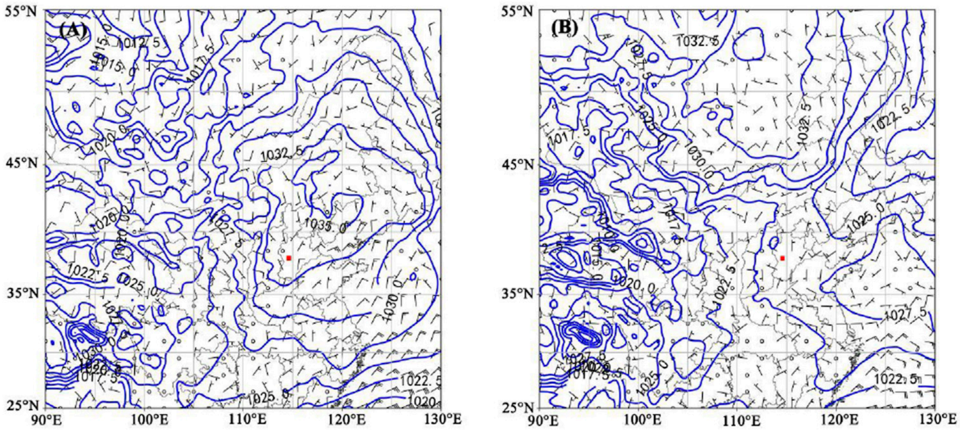

FIGURE 3
Sea level pressure at 08:00 2020 November 13th **(A)** and 08:00 2020 November 15th **(B)**. The red square is Shijiazhuang area.

ridge further aggravated the pollution level. The synoptic background in the third stage was similar to the first stage, from the 14th nighttime to the 15th morning (Figures 2B, 3B), where the high level was under the control of a high-pressure ridge. The pressure field from high to low levels was even more stable during this time which reinforced the pollution event. The fourth stage was from the 15th afternoon to the 16th. The high-level field was under the control of westerly flows behind the high-pressure ridge. Near the ground, the wind speed was low. The continuous moisture supply facilitated the haze development. The highest concentration of $PM_{2.5}$ was reached on the 16th at midnight. Afterward, southerly airflow at 850 hPa was getting stronger, and the low-pressure field took over near the ground. However, the cold air was rather to the west and the high-level trough slowly was moving to the east. Near the ground, the wind speed was rather low that cannot disperse atmospheric pollutants. On the 17th, atmospheric pollutants were removed due to the precipitation and the air quality improved.

During this haze event, stable westerly air was dominated at high levels. In the early stage of this pollution event, water vapor was inadequate in the atmosphere but more sufficient in later stages. In the seal level pressure fields, the cold air was rather weak and located to the North (Figure 3), which was favorable for southwesterly air to transport moisture. Horizontal winds were small near the ground that pollutants were hardly dispersed.

3.1.2 Characteristics of air pollutants and surface meteorological elements

The temporal variation of meteorological elements and pollution levels were shown in Figure 4, covering the whole

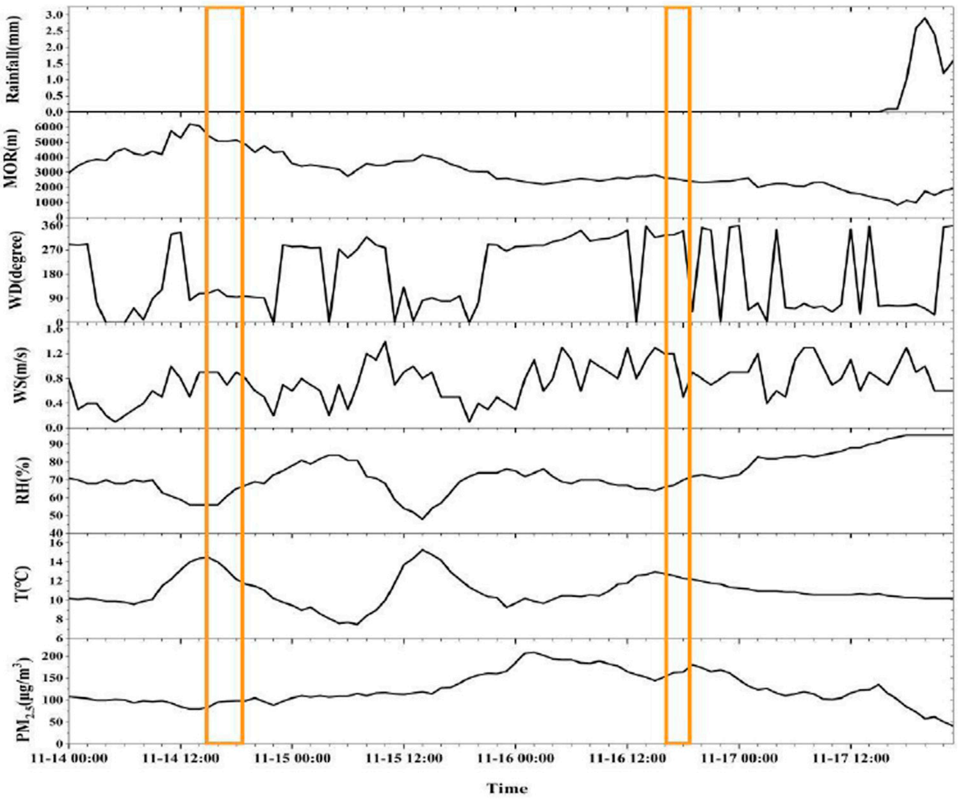

FIGURE 4
Time series of $PM_{2.5}$, temperature (T), relative humidity (RH), wind speed (WS), wind direction (WD), visibility (MOR), and precipitation during the pollution event. The yellow boxes cover the periods of flight sounding.

polluted period between November 14th and 17th. The $PM_{2.5}$ concentration remained above 75 μg/m^3 on the 14th (early stage of the pollution event). It reached the highest concentration on the 16th (pollution accumulated and worsen) with a value of 209 μg/m^3 and dramatically dropped below 50 μg/m^3 on the 17th (pollution ended). During the 14th and 15th, the diurnal changes of temperature and relative humidity were quite the opposite. Temperature rose during the day but relative humidity decreased, and *vice versa* at night. Ground winds were mostly easterly and northwesterly and varied around 0.8~1 m/s. In the afternoon, temperature dropped and the altitude of the boundary layer decreased. Meanwhile, pollution concentration near the ground increased. After the 15th at 14:00, the $PM_{2.5}$ concentration started increasing from 119 μg/m^3 to 209 μg/m^3 on the 16th at 02:00. On the 16th, relative humidity remained at 65–75%, and the $PM_{2.5}$ concentration varied around 150–209 μg/m^3. A precipitation event occurred on the 17th. Due to the wet removal, the concentration of $PM_{2.5}$ dropped dramatically and this pollution event came to an end.

As shown in Figure 5, no wind shear was recorded by the ground wind profiler radar before the 15th at 14:00. After that, wind shear was near 700 m and existed till the 17th at 04:00. As mentioned, ground $PM_{2.5}$ concentration continued rising to the highest value (Figure 4). Afterward, the altitude of wind shear elevated and the pollution level was reduced. During the whole pollution event, the vertical motion of atmospheric air was rather weak which hinders the vertical transportation of pollutants.

3.2 Vertical distribution of pollutant concentration

King-Air 350 meteorological aircraft was employed on the 14th and 16th to investigate the vertical distribution of pollutants over Shijiazhuang. The properties of air mass can determine the declining rate of potential temperature ($\partial\theta/\partial z$). Therefore, different layers were drawn based on the variation of $\partial\theta/\partial z$ (Yang et al., 2020), and we analyzed the distribution of pollutants in each layer. When the declining rate of potential temperature is zero ($\partial\theta/\partial z=0$), the declining rate ($\gamma$) is the same as the dry adiabatic declining rate (Γ), define as the neutral layer; When $\partial\theta/\partial z>0$, $\Gamma<\gamma$, defines as a stable layer; Otherwise as an unstable layer.

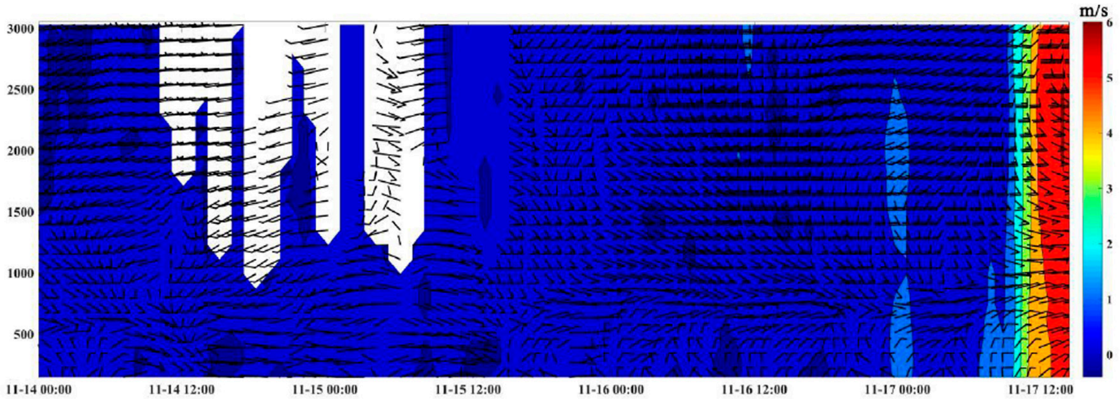

FIGURE 5
Time series of wind profiler data with atmospheric vertical motion contoured.

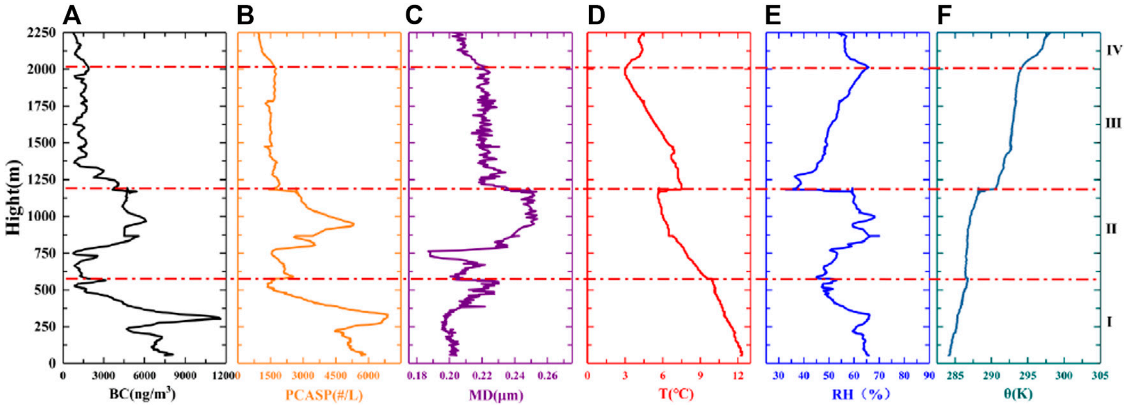

FIGURE 6
The vertical distribution of black carbon (BC) mass concentration **(A)**, PCASP number concentration **(B)**, PCASP mean diameter (MD, **(C)**, temperature (T, **(D)**, relative humidity (RH, **(E)**, and potential temperature (θ, **(F)** during aircraft descending on 14 Nov 2020.

The vertical distribution of BC mass concentration, aerosol number concentration, mean diameter of aerosols, temperature, relative humidity, and the potential temperature was presented in Figure 6. According to the $\partial\theta/\partial z$, we defined four layers including ground to 600 m, 600–1,200 m, 1,200–2,000 m, and 2,000 m above (labeled from Ⅰ to Ⅳ in Figure 6). For all four layers, the number of $\partial\theta/\partial z$ was positive with little variation. During this period, the vertical velocity was less than 1 m/s (Figure 5). All four layers were stable with weak atmospheric convection. Two thermal inversion layers were 1,150–1230m and 2,000–2,300 m, where the 1,150–1230 m layer was stronger with a variation of 2.7°C/100 m.

Layer Ⅰ and Ⅱ were within the same thermal inversion layer (Figure 6D). In layer Ⅰ, both BC and aerosol concentration showed unimodal distribution. The peak concentration of BC and aerosol were 12683 ng/m^3 and 6965.125#/L, respectively. The mean particle diameter was around 0.2–0.225 μm. Near the ground, accumulated particles were mostly small particles. As shown in the backtrack trajectory (Figure 8A), pollution transportation from the underlying surface contributed to this heavily polluted layer. Our results accorded with what Sun et al. (2013) previously concluded. Within layer Ⅱ, the BC concentration fluctuated around 4,000–6,000 ng/m^3 and the aerosol concentration peaked at 950 m with a value of 5438.416#/L. The mean diameter decreased from the top of layer Ⅰ to 800 m, and the minimum value was 0.188 μm. Near the top of layer Ⅱ (1,000–1200 m), the mean diameter was enlarged up to 0.25 μm. Thermal inversion can restrain the vertical transportation of pollution to the higher atmosphere, and hence, pollutants were accumulated below the thermal

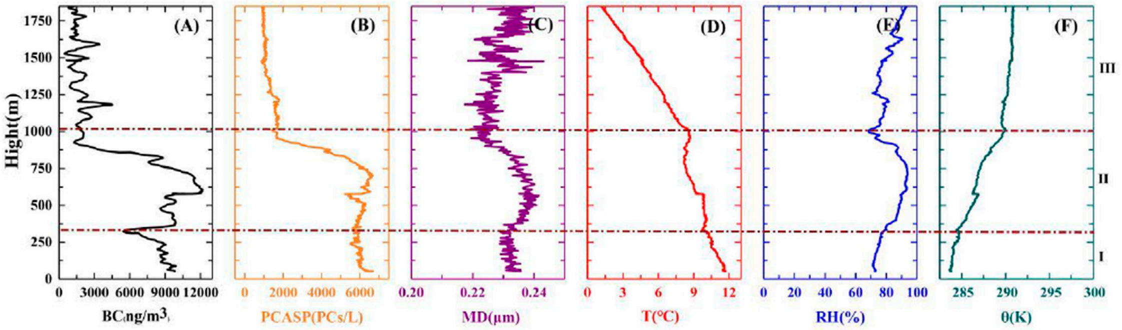

FIGURE 7
The vertical distribution of BC mass concentration **(A)**, PCASP number concentration **(B)**, PCASP mean diameter (MD, **(C)**, temperature (T, **(D)**, relative humidity (RH, **(E)**, and potential temperature (θ, **(F)** during aircraft descending on 16 Nov 2020.

inversion layer. The peak values of both relative humidity and pollutant concentration appeared almost at the same altitude. For both layers Ⅰ and Ⅱ, aerosol concentration shows a better correlation result with relative humidity than BC concentration. The correlation coefficient of BC and aerosol concentration in layer Ⅰ is 0.66 and 0.92, respectively, and 0.74 and 0.9 in layer Ⅱ.

A distinct dropping in pollutant concentration was noted within the 1,150–1,200 m inversion layer. The upward transport of pollutants was impeded by this strong thermal inversion. The concentrations of BC and aerosol at 1150 m were 4292 ng/m^3 and 2855.219#/L, respectively. At 1200m, the concentrations of BC and aerosol dropped to 537 ng/m^3 and 1757.318#/L. Again, due to the thermal inversion, pollutants in layer Ⅱ cannot be transported into layer Ⅲ. Therefore, the concentrations of both BC and aerosol was comparatively low in layer Ⅲ. The concentrations range of BC and aerosol were 500–1500 ng/m^3 and 1,200–1800#/L. Meanwhile, the mean diameter of aerosols was 0.22 μm with slight variation. Since the pollution concentration was already low in layers Ⅲ and Ⅳ, the thermal inversion at 2,000 m hardly affected the pollutant concentration.

The vertical profiling on the 16th was dived into three layers, including ground to 350 m, 350–1,000 m, and 1,000–1980 m (labeled as Ⅰ, Ⅱ, and Ⅲ in Figure 7). Two thermal inversion layers were defined in 350–400 m, and 800–1000 m. The 350–400 m inversion was relatively weak with a value of 0.43°C/100 m. Below each inversion layer, the relative humidity increased with height.

The layer Ⅰ was below the 350–400 m inversion layer. Above this inversion layer, the temperature remained almost unchanged around 400–500 m. This will block the vertical transportation of pollutants, and the pollutant concentration hardly changed with height within layer Ⅰ. The average mass concentration of BC and number concentration of aerosol are 8857.9 ng/m^3 and 5964.458#/L. Near the inversion layer (350 m), the BC concentration dramatically dropped to 4000 ng/m^3. Within this inversion layer, BC concentration rapidly increased to 9,633 ng/m^3 at 400 m. Underlying pollutants can be transported to this altitude and upwards since the thermal inversion was weak (Figure 7D). Meanwhile, the number concentration of aerosols barely changed below and above the inversion layer. The weak thermal inversion near the ground hardly affected the vertical transport of aerosols but affected the BC distribution. Both BC and aerosols concentrations were maintained at relatively high levels in layer Ⅱ. The bottom isothermal layer (400–500 m) and the top inversion layer (800–1,000 m) were responsible for pollutant accumulation in this layer. The peak concentrations of BC and aerosol in the isothermal layer were 10422 ng/m^3 and 6283.851#/L. Below the thermal inversion layer, the highest concentrations were 12873 ng/m^3 and 6612.291#/L, respectively.

The intensity of thermal inversion in layer 800–1,000 m was 1°C/100 m and the pollutant concentration dropped rapidly within the inversion layer. At 800 m, BC and aerosol concentrations were 9379 ng/m^3 and 5466.911#/L, and the concentrations dropped to 960 ng/m^3 and 1,494.99#/L at 1,000 m, respectively. The mean diameter of aerosol particles varied around 0.21–0.22 μm in layers Ⅰ and Ⅱ. The aerosol concentration in layer Ⅲ decreased with height while BC concentration fluctuated at a low level. The thermal inversion at 800–1,000 m blocked the vertical transport of pollutants from layer Ⅱ.

On both the 14th and 16th, values of ∂θ/∂z in all layers were higher than zero, which were all defined as stable layers. Hence, within these layers, thermal conditions were not favorable for the vertical transportation of pollution. Aerosol particles were enlarged through moisture absorption, which was confirmed by the increasing relative humidity. As a result, the aerosol concentration increased. On the 16th, the heights of thermal inversion layers were lower compared to the 14th. This led to pollution accumulation below the inversion layers and the peak concentrations were closer to the ground. Compared to the 14th,

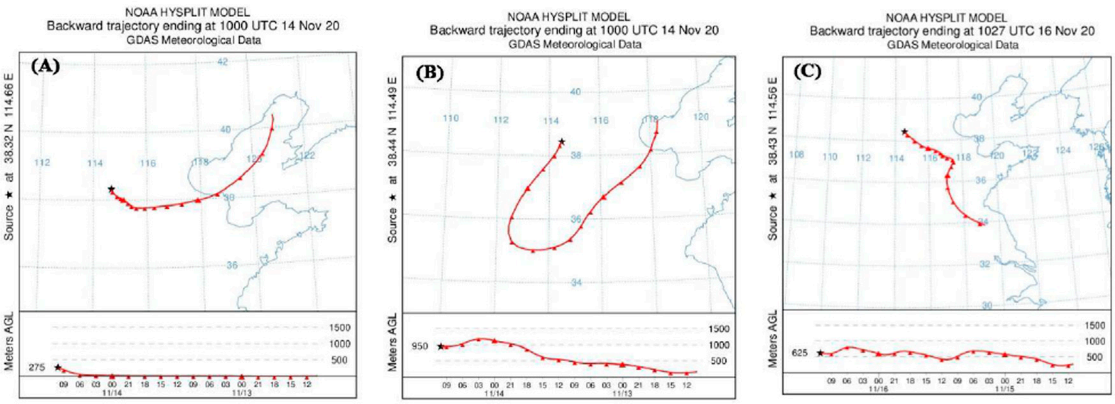

FIGURE 8
Backward trajectory of air mass during aircraft sounding period at 275 m **(A)** and 950 m **(B)** on 14 Nov 2020, and 625 m **(C)** on Nov16th, 2020.

the BC concentration increased more significantly than the aerosol concentration on the 16th. At 55 m, the BC and aerosol concentrations were 9861 ng/m^3 and 6662.823#/L on the 16th, but 6519 ng/m^3 and 5797.351#/L on the 14th.

3.3 Backward trajectory

Regional transport has an important effect on the distribution of pollutants (Shen et al., 2022). To investigate the effect of regional transport on the vertical distribution of pollution, we chose the altitude with peak concentration values of and aerosols for backward trajectory simulation, which was 275m and 950 m on the 14th, and 625 m on the 16th, namely. The 48-h backward trajectories (UTC Time) were presented in Figure 8.

On the 14th, the air masses at 275 m and 950 m both originated from the Bohai Sea but moved in different trajectories (Figures 8A,B). Before the 14th 14:00, the 275 m air mass was first moving towards the southwest and then northwest, close to the ground. Afterward, the air mass elevated till arriving at 275 m above the observation location. The concentration of $PM_{2.5}$ in Hengshui and Cangzhou exceeded 110 μg/m^3. This indicated that air at 275 m was mostly polluted from the underlying surfaces. The air mass at 950 m first moved further to the southwest and then to the northeast. After the 13th 20:00, the air mass rose from the ground till reaching 950 m. The high level of the polluted level at 950 m was a result of both thermal inversion blocking and distant transport of pollution. This trajectory detour was considered highly linked to atmospheric circulation. On the 16th (Figure 8C), the air mass originated from the Shanghai region and kept moving northwards to the observation location. After the 15th 08:00, the air mass reached the height of 500 m and stayed at this height. This indicated a relatively stable atmosphere, not favorable for pollution dispersal. To conclude, ground pollution was mostly from local sources but pollution in the higher air also came from distant regional sources. Besides, the southerly air was responsible for the distant transport of pollution.

3.4 Aerosol spectrum density distribution

The particle size distribution is one of the determining factors for aerosols' transportation, lifetime, and optical properties in the atmosphere. Particles from different sources will show different features of spectral distribution. Besides, the atmospheric condition will largely affect the microphysical processes of moisture absorption and particle coagulation, and as a result of particle size spectrum will be changed (Sheng et al., 2003).

The aerosol spectral density distribution in the vertical observation phase was stratified with the same height according to the potential temperature. As shown in Figure 9A, aerosols were mostly dispersed in layers Ⅰ and Ⅱ on the 14th. From ground to 250 m, aerosol particles were distributed within the range of 0.12–0.45 μm. Around 250–400 m, high values were found at 0.125–0.15 μm and 0.2 μm. The corresponding height was consistent with the height of maximum concentration (Figure 6B). A diameter of 0.14 μm was recorded with the highest concentration of 749.26#/L. Since aerosols in layer Ⅰ were mostly from the underlying surface (Figure 8A), small particles took the majority in the transportation.

Compared to layer Ⅰ, aerosols in layer Ⅱ were larger with higher number concentrations. The diameter range was between 0.2 and 0.5 μm. Below the thermal inversion layer, the relative humidity was relatively high and aerosols can grow through moisture absorption (Figure 6E). The aerosol concentration peaked at 950 m and around this height particle within

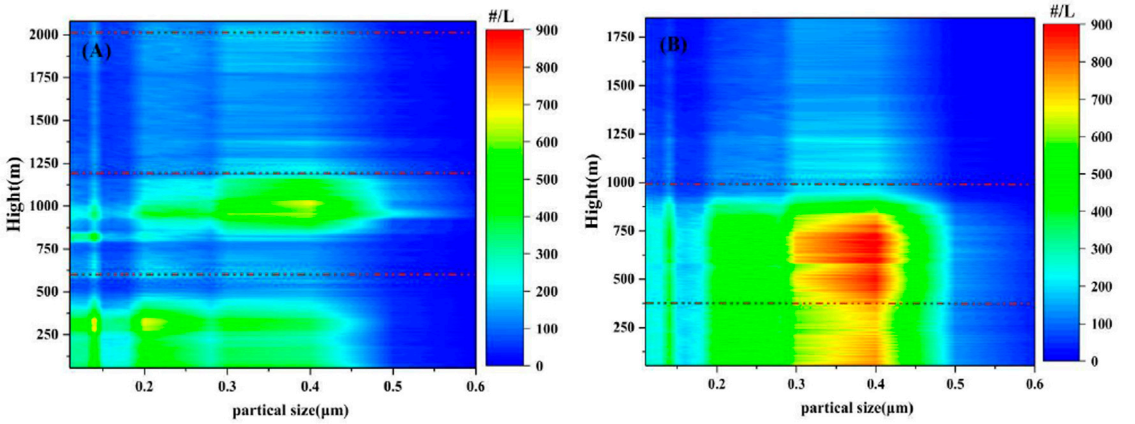

FIGURE 9
The particle size distribution of aerosols from PCASP probe during vertical soundings on November 14th **(A)** and 16th **(B)**, 2020. The black dotted lines divide the vertical altitudes into four layers based on ∂θ/∂z.

0.35–0.45 μm also had the highest number concentration. The thermal inversion layer can block the vertical transport of pollutants, and thus, aerosol number concentrations were rather low in both layers Ⅲ and Ⅳ.

On the 16th, the aerosols were also mainly spread in layers Ⅰ and Ⅱ but the particle diameter enlarged into 0.35–0.4 μm (Figure 9B). Among, particles of 0.4 μm was found with a maximum concentration of 943.58#/L. The lapse rate of temperature in layers Ⅰ and Ⅱ was relatively small, indicating a stable atmosphere. Aerosols with concentrations higher than 600#/L were less in layer Ⅰ than in layer Ⅱ. Aerosols around 0.3–0.4 μm, the number concentration of particles were also less in layer Ⅰ than in layer Ⅱ. Again, the thermal inversion prevented the vertical transportation of pollutants to layer Ⅲ.

The relative humidity was higher on the 16th than the 14th, which was more favorable for particles growing through moisture absorption. On the 16th, both wind shear and thermal inversion exacerbated the pollution accumulation. Therefore, the diameters of aerosol particles were larger with higher number concentrations. The height of the thermal inversion layer was lower on the 16th. This also explained the higher aerosol concentration on the 16th below 800 m.

4 Conclusion

In this article, we analyzed a heavily polluted event that occurred in Shijiazhuang on November 14th~17th, 2020. Ground and airborne meteorological and pollutant monitoring data were combined for the analysis of this heavily polluted event, specifically the meteorological causes and the vertical distribution of pollutants.

This heavy pollution event was dominated by $PM_{2.5}$ with a highest concentration of 209 μg/m^3. During the whole polluted period, the Shijiazhuang region was under the control of a high-pressure ridge. Winds were mostly westerly winds in the upper air but northerly near the ground. Ground winds were lower than 1 m/s and convergences were found in the ground wind field. The atmosphere maintained a stable status and the vertical motion was weak.

Pollutants were accumulated below the thermal inversion layer and the highest concentration was found on both the 14th and 16th just below the inversion layer. On the 14th, both BC and aerosol concentrations showed unimodal distribution, and the highest concentrations of BC and aerosols were 12683 ng/m^3 and 6965.125#/L at 250 m within layer Ⅰ. In layer Ⅱ, the concentrations of BC and aerosols were distinctly low due to the transport inhibition of the thermal layer. On the 16th, the thermal layer near ground was rather weak that pollutants in layer Ⅰ can be transported into layer Ⅱ.

Distant transport of pollutants also contributed to this continuous haze event. On the16th, before reaching the Shijiazhuang region, air mass in layer Ⅰ was moving close to the ground. Apart from the vertical transport of the underlying surfaces, the continuous high-level pollution in layer Ⅱ was also sourced from regional transport.

Aerosols were mostly dispersed in layers Ⅰ and Ⅱ on both 14th and 16th. On the 14th, small particles within 0.125–0.15 μm were the most particles near the ground where below the inversion layer 1,150–1230 m large aerosols around 0.4 μm had the highest concentration. On the 16th, the thermal and vapor conditions were more favorable for aerosol accumulation.

Data availability statement

The raw data supporting the conclusions of this article will be made available by the authors, without undue reservation.

Author contributions

XUZ was the main contributor. XS contributed to analysis and translation. YY was for peer-review. XIZ contributed to weather analysis. YH and ZH contributed to data analysis. YC contributed to the graphics.

Funding

This work was supported by the National Key Research and Development Program of China (Grant 2019YFC1510301), the Hebei province Key Research and Development project (Grants 20375402D and 19275420D), Key Laboratory for Cloud Physics of China Meteorological Administration supported by (KDW 1904), Hebei Meteorological Service Scientific Research and Development Project (20ky28 and 21ky12).

Conflict of interest

The authors declare that the research was conducted in the absence of any commercial or financial relationships that could be construed as a potential conflict of interest.

Publisher's note

References

Anderson, T. L., Charlson, R. J., Schwartz, S. E., Knutti, R., Boucher, O., Rodhe, H., et al. (2003). Climate forcing by aerosols-a hazy picture. *Science* 300 (20), 1103–1104. doi:10.1126/science.1084777

Bond, T. C., Doherty, S. J., Fahey, D. W., Forster, P. M., Berntsen, T., DeAngelo, B. J., et al. (2013). Bounding the role of black carbon in the climate system: A scientific assessment. *J. Geophys. Res. Atmos.* 118 (11), 5380–5552. doi:10.1002/jgrd.50171

Ding, A., Wang, T., Xue, L., Gao, J., Stohl, A., Lei, H., et al. (2009). Transport of north China air pollution by midlatitude cyclones: Case study of aircraft measurements in summer 2007. *J. Geophys. Res.* 114 (D8), D08304. doi:10.1029/2008JD011023

Fan, Y., Guo, X. L., Fu, D. H., and Li, H. Y. (2007). Observational studies on aerosol distribution during August to September in 2004 over Beijing and its surrounding areas. *Clim. Environ. Res.* 12 (1), 49–62. doi:10.3969/j.issn.1006-9585.2007.01.006

Gobbi, G. P., Barnaba, F., and Ammannato, L. (2004). The vertical distribution of aerosols, Saharan dust and cirrus clouds in Rome (Italy) in the year 2001. *Atmos. Chem. Phys.* 4 (2), 351–359. doi:10.5194/acp-4-351-2004

Han, S., Zhang, Y., Wu, J., Zhang, X., Tian, Y., Wang, Y., et al. (2015). Evaluation of regional background particulate matter concentration based on vertical distribution characteristics. *Atmos. Chem. Phys.* 15 (19), 11165–11177. doi:10.5194/acp-15-11165-2015

Haywood, J., and Boucher, O. (2000). Estimates of the direct and indirect radiative forcing due to tropospheric aerosols: A review. *Rev. Geophys.* 38 (4), 513–543. doi:10.1029/1999RG000078

Jacobson, M. Z. (2001). Strong radiative heating due to the mixing state of black carbon in atmospheric aerosols. *Nature* 409 (6821), 695–697. doi:10.1038/35055518

Janssen, N. A., Gerlofs-Nijland, M. E., Lanki, T., Salonen, R. O., Cassee, F., Hoek, G., et al. (2012). *Health effects of black carbon*. Copenhagen, Denmark: World Health Organization.

Johnson, D. W., Osborne, S., Wood, R., Suhre, K., Quinn, P. K., Bates, T., et al. (2000). Observations of the evolution of the aerosol, cloud and boundary-layer characteristics during the 1st ACE-2 Lagrangian experiment. *Tellus B Chem. Phys. Meteorology* 52 (2), 348–374. doi:10.3402/tellusb.v52i2.16118

Landman, W. (2010). Climate change 2007: The physical science basis. *South Afr. Geogr. J.* 92 (1), 86–87. doi:10.1080/03736245.2010.480842

Lei, X., Xiu, G., Li, B., Zhang, K., and Zhao, M. (2016). Individual exposure of graduate students to $PM_{2.5}$ and black carbon in Shanghai, China. *Environ. Sci. Pollut. Res.* 23 (12), 12120–12127. doi:10.1007/s11356-016-6422-x

Li, J., Fu, Q., Huo, J., Wang, D., Yang, W., Bian, Q., et al. (2015). Tethered balloon-based black carbon profiles within the lower troposphere of Shanghai in the 2013 East China smog. *Atmos. Environ.* 123 (B), 327–338. doi:10.1016/j.atmosenv.2015.08.096

Li, J. X., Yin, Y., Li, P. R., Li, R. J., Jin, L. J., and Li, J. (2014). Aircraft measurements of aerosol spatial distribution properties in Shanxi Province in summer. *China Environ. Sci.* 34 (8), 1950–1959.

Li, P. R., Xiao, T. G., and Wang, M. Y. (2019). Study on typical continuous heavily polluted weather in Chengdu area based on wind profiler radar. *Acta Sci. Circumstantiae* 39 (12), 4174–4186. doi:10.13671/j.hjkxxb.2019.0332

Li, Y. J., Lee, B. P., Su, L., Fung, J. C. H., and Chan, C. K. (2015). Seasonal characteristics of fine particulate matter (PM) based on high resolution time-of-flight aerosol mass spectrometric (HR-ToF-AMS) measurements at the HKUST Supersite in Hong Kong. *Atmos. Chem. Phys.* 15, 37–53. doi:10.5194/acp-15-37-2015

Liu, B., Guo, J., Gong, W., Shi, L., and Ma, Y. (2020). Characteristics and performance of vertical winds as observed by the radar wind profiler network of China. *Atmos. Meas. Tech.* 13, 4589–4600. doi:10.5194/amt-2020-75

Lu, Y., Zhu, B., Huang, Y., Shi, S. S., Wang, H. L., An, J., et al. (2019). Vertical distributions of black carbon aerosols over rural areas of the Yangtze River Delta in winter. *Sci. Total Environ.* 661 (APR.15), 1–9. doi:10.1016/j.scitotenv.2019.01.170

Ramanathan, V., and Carmichael, G. (2008). Global and regional climate changes due to black carbon. *Nat. Geosci.* 1 (4), 221–227. doi:10.1038/ngeo156

Ran, L., Deng, Z., Xu, X., Yan, P., Lin, W., Wang, Y., et al. (2016). Vertical profiles of black carbon measured by a micro-aethalometer in summer in the North China Plain. *Atmos. Chem. Phys.* 16 (16), 10441–10454. doi:10.5194/acp-16-10441-2016

Rao, S., Pachauri, S., Dentener, F., Kinney, P., Klimont, Z., Riahi, K., et al. (2013). Better air for better health: Forging synergies in policies for energy access, climate change and air pollution. *Glob. Environ. Change* 23 (5), 1122–1130. doi:10.1016/j.gloenvcha.2013.05.003

Rosenberg, P. D., Dean, A. R., Williams, P. I., Dorsey, J. R., Minikin, A., Pickering, M. A., et al. (2012). Particle sizing calibration with refractive index correction for light scattering optical particle counters and impacts upon pcasp and cdp data collected during the fennec campaign. *Atmos. Meas. Tech.* 5, 1147–1163. doi:10.5194/amt-5-1147-2012

Shen, L., Zhao, T., Liu, J., Wang, H., Bai, Y., Kong, A., et al. (2022). Regional transport patterns for heavy $PM_{2.5}$ pollution driven by strong cold airflows in Twain-Hu Basin, Central China. *Atmos. Environ.* 269 (15), 118847. doi:10.1016/j.atmosenv.2021.118847

Sheng, P. X., Mao, J. T., Li, J. G., Zhang, A. C., Sang, J. G., and Pan, N. X. (2003). *Atmospheric physics*.

Shi, G. Y., Wang, B., Zhang, H., Zhao, J. Q., Tan, S. C., and Wen, T. X. (2008). The radiative and climatic effects of atmospheric aerosols. *Chin. J. Atmos. Sci.* 32 (4), 826–840. doi:10.3878/j.issn.1006-9895.2008.04.11

Stein, A. F., Draxler, R. R., Rolph, G. D., Stunder, J. B., Cohen, M. D., and Ngan, F. (2015). NOAA's HYSPLIT atmospheric transport and dispersion modeling system. *Bull. Am. Meteorol. Soc.* 96 (12), 2059–2077. doi:10.1175/BAMS-D-14-00110.1

Strawbridge, K. B., and Snyder, B. J. (2004). Daytime and nighttime aircraft lidar measurements showing evidence of particulate matter transport into the Northeastern valleys of the Lower Fraser Valley, BC. *Atmos. Environ.* 38 (34), 5873–5886. doi:10.1016/j.atmosenv.2003.10.036

Sun, Y. W., Sun, X., Yin, Y., Han, Y., Dong, X. B., Jiang, Y., et al. (2012). Aerosol distribution in North China Plain under different weather conditions. *China Environ. Sci.* 32 (10), 1736–1743.

Sun, Y. W., Sun, X., Yin, Y., and Han, Y. (2013). Observation study of aerosol over mid-western north China plain in autumn (October). *Plateau Meteorol.* 32 (5), 1308–1320. doi:10.7522/j.issn.1000-0534.2012.00123

Tan, Y., Wang, H., Zhu, B., Zhao, T., Shi, S., Liu, A., et al. (2022). The interaction between black carbon and planetary boundary layer in the Yangtze River Delta from 2015 to 2020: Why O_3 didn't decline so significantly as PM2. 5. *Environ. Res.* 214, 114095. doi:10.1016/j.envres.2022.114095

Wang, C., Chen, M., and Chen, Y. D. (2022). Impact of combined assimilation of wind profiler and Doppler radar data on a convective-scale cycling forecasting system. *Mon. Weather Rev.* 150 (2), 431–450. doi:10.1175/MWR-D-20-0383.1

Yang, Y. M., Zhou, Y. Q., and Cai, Z. X. (2020). A case study of aircraft observation of aerosol vertical distribution and activation characteristics. *Meteorol. Mon.* 46 (9), 1199–1209. doi:10.7519/j.issn.1000-0526.2020.09.007

Yao, Q., Liu, J. L., Han, S. Q., and Fan, W. Y. (2016). Pollution characteristics and number concentration of atmospheric aerosol during spring festival in Tianjin. *Meteorol. Mon.* 42 (4), 443–449. doi:10.7519/j.issn.1000-0526.2016.04.007

You, J. P., Gao, J. Q., Huang, M. Y., Zhang, X. X., Zhao, B., Lin, J. J., et al. (2015). Analysis of the characteristics of the aircraft-observed atmospheric aerosols in Pearl River Delta. *J. Trop. Meteorology* 31 (1), 71–77. doi:10.16032/j.issn.1004-4965.2015.01.008

Zhai, Q. F., Jin, L. J., Lin, Z. Y., Wu, Z. H., and Kuang, S. S. (2011). Observational characteristic of aerosol number concentration and size distribution at Shijiazhuang in spring season. *China Environ. Sci.* 31 (6), 886–891.

Zhang, D. Z., Chen, B., Yamada, M., Niu, H. Y., Wang, B., Iwasaka, Y., et al. (2012). Elevated soot layer in polluted urban atmosphere: A case study in beijing. *J. Meteorological Soc. Jpn.* 90 (3), 361–375. doi:10.2151/jmsj.2012-302

Zhang, N., Qin, Y., and Xie, S. D. (2013). Spatial distribution of black carbon emissions in China. *Chin. Sci. Bull.* 58 (19), 3830–3839. doi:10.1007/s11434-013-5820-4

Zhang, Y., Yin, Y., Shi, L. X., Duan, Y., and Wu, Z. H. (2011). An observational study of the aerosol distributions over Hebei area during autumn. *J. Meteorological Sci.* 31 (6), 755–762. doi:10.3969/j.issn.1009-0827.2011.06.013

Zhao, C. F., Qiu, Y. M., Dong, X. B., Wang, Z. E., Peng, Y. R., Li, B. D., et al. (2018). Negative Aerosol-Cloud r_e Relationship From Aircraft Observations Over Hebei, China. *Earth Space Sci.* 5 (1), 19–29. doi:10.1002/2017ea000346

Frontiers in Earth Science

TYPE Original Research
PUBLISHED 01 March 2023
DOI 10.3389/feart.2023.1105140

EDITED BY
Yi Li,
Intel, United States

REVIEWED BY
Haofei Yu,
University of Central Florida, United States
Xueying Yu,
Stanford University, United States
Xiao He,
Shenzhen University, China
Ruizi Shi,
Tsinghua University, China
Yimeng Song,
Yale University, United States

*CORRESPONDENCE
Xiefei Zhi,
✉ zhi@nuist.edu.cn

SPECIALTY SECTION
This article was submitted to Atmospheric Science, a section of the journal Frontiers in Earth Science

RECEIVED 22 November 2022
ACCEPTED 14 February 2023
PUBLISHED 01 March 2023

CITATION
Ji Y, Zhi X, Wu Y, Zhang Y, Yang Y, Peng T and Ji L (2023), Regression analysis of air pollution and pediatric respiratory diseases based on interpretable machine learning.
Front. Earth Sci. 11:1105140.
doi: 10.3389/feart.2023.1105140

Regression analysis of air pollution and pediatric respiratory diseases based on interpretable machine learning

Yan Ji[1,2], Xiefei Zhi[1,2]*, Ying Wu[3], Yanqiu Zhang[4], Yitong Yang[4], Ting Peng[3] and Luying Ji[5]

[1]Collaborative Innovation Center on Forecast and Evaluation of Meteorological Disasters (CIC-FEMD)/Key Laboratory of Meteorological Disasters, Ministry of Education (KLME), Nanjing University of Information Science and Technology, Nanjing, China, [2]Weather Online Institute of Meteorological Applications, Wuxi, China, [3]Taizhou Environmental Monitoring Center, Taizhou, China, [4]Department of Environmental Occupational Hygiene, Taizhou Center for Disease Control and Prevention, Taizhou, China, [5]Key Laboratory of Transportation Meteorology of China Meteorological Administration, Nanjing Joint Institute for Atmospheric Sciences, Nanjing, China

Air pollution is of high relevance to human health. In this study, multiple machine-learning (ML) models—linear regression, random forest (RF), AdaBoost, and neural networks (NNs)—were used to explore the potential impacts of air-pollutant concentrations on the incidence of pediatric respiratory diseases in Taizhou, China. A number of explainable artificial intelligence (XAI) methods were further applied to analyze the model outputs and quantify the feature importance. Our results demonstrate that there are significant seasonal variations both in the numbers of pediatric respiratory outpatients and the concentrations of air pollutants. The concentrations of NO_2, CO, and particulate matter (PM_{10} and $PM_{2.5}$), as well as the numbers of outpatients, reach their peak values in the winter. This indicates that air pollution is a major factor in pediatric respiratory diseases. The results of the regression models show that ML methods can capture the trends and turning points of clinic visits, and the non-linear models were superior to the linear ones. Among them, the RF model served as the best-performing model. The analysis on the RF model by XAI found that AQI, O_3, PM_{10}, and the current month are the most important predictors affecting the numbers of pediatric respiratory outpatients. This shows that the number of outpatients rises with an increasing AQI, especially with the increasing of particulate matter. Our study indicates that ML models with XAI methods are promising for revealing the underlying impacts of air pollution on the pediatric respiratory diseases, which further assists the health-related decision-making.

KEYWORDS

air pollutants, respiratory diseases in children, explainable artificial intelligence (XAI), feature importance analysis, Taizhou city

1 Introduction

Since the reform and opening up of China from the 1980s, there have been significant achievements in its economy and the construction of infrastructure. However, the environmental problems caused by the extensive development model in the early stages is becoming a serious issue (Xu et al., 2013; Qi et al., 2020), especially regarding air pollution.

Due to the rapid development of heavy industry, the continuous expansion of urbanization, and the sudden surge in the number of motor vehicles, the increasing emission of air pollutants is being monitored (Kan et al., 2012; Xu et al., 2013; Gu et al., 2020). In recent years, air pollution has been considered by the World Health Organization (WHO) as the greatest environmental risk to health (World Health Organization, 2021). Reports show that 90% of people are breathing polluted air every day (World Health Organization, 2018a). There are nearly 7 million premature deaths from cancer, strokes, and cardiopulmonary diseases caused by air pollution, and 90% of these deaths occur in low- and middle-income countries (World Health Organization, 2018b).

Studies have shown that the content of air pollutants significantly affects human health, both in the short and long term (Shahi et al., 2014; Khaniabadi et al., 2017; Song et al., 2018; Wang L. et al., 2018a; Song et al., 2019). The short-term effects are characterized by a rapid increase in the incidence of respiratory diseases, especially in vulnerable groups such as the elderly, children, and pregnant women (Sarnat et al., 2012; MacIntyre et al., 2014; Zhu et al., 2017; Li et al., 2018). WHO points it out that the particulate matter can penetrate into the lungs and enter the bloodstream, which further cause cardiovascular and respiratory impacts (World Health Organization, 2021). Besides, There is emerging evidence that NO_2 is associated with respiratory diseases, i.e. asthma, coughing, and difficulty breathing (World Health Organization, 2022). Long-term chronic effects of air pollution are also seen on human health (Zhang et al., 2014; Islam et al., 2017). The Global Burden of Disease Study 2015 showed that chronic respiratory diseases ranked third among the fatal diseases in China, second only to cardiovascular and cerebrovascular diseases and tumors; all three of these types of disease are highly related to air pollution (Prüss-Üstün et al., 2016).

It is clear that air pollution is becoming one of the most important risk factors affecting human health. Specifically, a large number of studies have been performed examining the impact of air pollutants on the incidence of respiratory diseases in major cities across China (Wang and Chau, 2013; Wang L. et al., 2018a). It has been found that the air quality index (AQI) is positively correlated with bronchial infections, upper respiratory-tract infections, and lung diseases in Tianjin (Guo et al., 2010). Yin et al. (2011) pointed out that levels of particulate matter ($PM_{2.5}$ and PM_{10}), NO_2, SO_2, and carbon monoxide (CO) have positive correlations with the number of pediatric outpatients with respiratory diseases in Shanghai, while the correlation with ozone (O_3) was negative. A case study by Zhang et al. (2014) showed that short-term exposure to air pollutants can cause explosive increases in pediatric patients with pneumonia in Guangzhou. The results of the study by Shen et al. (2017) showed that sulfur dioxide (SO_2) is the main pathogenic factor for respiratory-tract infections in Henan Province, and this has synergistic effects with the particulate matter and nitrogen oxides (NO_x). A study in Beijing further showed that air pollution is one of the important causes of the increase in the number of elderly patients with allergic rhinitis (Zhang et al., 2016).

The above studies clearly point out that the content of air pollutants can significantly affect the incidence of respiratory diseases. However, these studies were mainly based on parametric linear models, i.e., multiple linear regression, (Ruckerl et al., 2006; Wang M. et al., 2018b), or they relied on semi-parametric generalized linear models and generalized additive models (Dominici et al., 2002; Terzi and Cengiz, 2009; Ravindra et al., 2019). Unfortunately, these linear models are not very efficient for capturing the non-linear dependence among the complex data. Furthermore, although the regression coefficient can be simply used for evaluating the feature importance, it is incapable of quantifying the synergy of multiple variables and performing a local analysis for a given sample with the linear models.

The development of machine learning (ML) and deep learning has led to technological innovations in numerous areas, including autonomous driving (Bojarski et al., 2016; Badue et al., 2021), facial recognition (Hu et al., 2015; Parkhi et al., 2015), weather forecasting (McGovern et al., 2017; Reichstein et al., 2019), and smart healthcare (Litjens et al., 2017; Hesamian et al., 2019). Using a variety of linear and non-linear computational units, ML approaches are able to learn complex representative features from high-dimension data to establish models projecting from predictors to predictands. In the field of the atmospheric environment, a number of studies have been performed considering time-series prediction of atmospheric pollutants (Freeman et al., 2018; Wang et al., 2020; Kleinert et al., 2022), spatial and temporal downscaling (Yu and Liu, 2021; Geiss et al., 2022), and modal classification (Harrou et al., 2018). However, there have still been few studies using ML models with explainable artificial intelligence (XAI) methods to analyze the correlations between air-pollutant concentrations and human health. Because ML models have higher non-linearity and stronger robustness, it is of great significance to simulate how the morbidity rates of respiratory diseases are affected by the concentrations of different air pollutants. Furthermore, XAI methods can further quantitatively analyze the feature importance of each air-pollutant input and help to reveal the underlying impacts of air pollution on human health.

Taizhou is an important part of the Yangtze River Delta Economic Zone in East China, with inland ports and mature industries. However, it still suffers from the growing problem of air pollution in its main urban area. This is largely caused by the chemical industry, automobile exhaust emissions, construction-site dust, and transmission of pollutants. More seriously, measurements further show that the air pollution issue in Taizhou is more prominent among the surrounding cities and few studies are performed for assessing the impacts of air pollution on human health in Taizhou city. In this context, exploring the impact of air quality on the incidence of pediatric respiratory diseases is of great social significance. In this study, we aimed to carry out a risk assessment of air pollution on children's health in Taizhou with ML models and provide a scientific basis for taking effective intervention measures. In this work, the impact of the air pollution was characterized by changes in the number of pediatric patients visiting respiratory departments; furthermore, XAI methods were used to analyze the contribution of the content of the air pollutants. The main contributions of our study can be summarized as follows: 1. A detailed statistical analysis is performed between the air-pollutant concentrations and the number of pediatric respiratory outpatients in Taizhou, i.e. detrended correlation analysis, stratified analyses by seasons, air-pollution levels, and types of primary pollutant. 2. XAI methods are introduced to evaluate the ML model performance in simulating the number of the clinic visits, by quantifying the feature importance of the air-pollutant factors. 3. It is a useful complement to the research of regional air quality and pediatric respiratory diseases using XAI and ML methods in Taizhou city.

The remainder of this manuscript is organized as follows. Section 2 introduces the clinical and air-pollutant monitoring data used in our work, as well as the ML models and XAI methods. Summary and detailed results are presented in Section 3, and this is followed by conclusions and future outlook in Section 4.

2 Data and methods

2.1 Data and preprocessing

The datasets used in this work included daily air-pollutant monitoring data from the Taizhou Environmental Monitoring Center and daily clinical data from the pediatric department of a comprehensive Grade 3A hospital in the urban area of Taizhou, spanning from 2018 to 2020. The air-pollutant data covers measurements of the content of $PM_{2.5}$, PM_{10}, CO, NO_2, SO_2, and O_3, as well as the AQI, the level of air pollution, and the type of primary pollutant. The clinical data is the total number of outpatients visiting the pediatric department each day. Since the daily number of outpatients was found to follow a Poisson distribution using the Kolmogorov–Smirnov test, a log transform was further applied to the raw clinical data. Given the raw clinical data as C_t, the preprocessed predicant Y_t is:

$$Y_t = \log C_t \tag{1}$$

where the subscript t is the timestamp of the sample.

In this study, in addition to the measurements of air pollutants, temporal information was also used as an additional predictor. Hence, the candidate predictors X_t consist of $PM_{2.5}$, PM_{10}, CO, NO_2, SO_2, and O_3, as well as AQI, the level of air pollution (AQI_level), the type of primary pollutant (Major_pollutant), and temporal information (Month). AQI_level consists of four categories from I to IV; the higher the AQI_level, the worse the air quality. Major_pollutant indicates the type of primary pollutant. In our study, Major_pollutant I means that there is no air pollution. Major_pollutant values from II to VII were defined as the cases of O_3, CO, NO_2, SO_2, PM_{10}, and $PM_{2.5}$, respectively being the primary pollutant. The temporal information is the month of the given sample.

2.2 ML models

The ML models used in this study included linear regression, ridge regression, Huber regression, random forest (RF), adaptive boosting (AdaBoost), and a neural network (NN). Among these, linear regression, ridge regression, and Huber regression are considered as weakly non-linear models, while RF, AdaBoost, and NN are more robust and complex.

Linear regression is one of the most basic statistical models. Given predictors $X = \{x_1, x_2, \ldots, x_k\}$, the prediction $\hat{y}$ of linear regression is written as:

$$\hat{y}(w, x) = w_0 + w_1 x_1 + \cdots + w_k x_k \tag{2}$$

where $W = \{w_0, w_1, w_2, \ldots, w_k\}$ are the regression coefficients (weights) of the corresponding predictors. The weights are usually estimated by optimizing the $L2$ loss:

$$\|\hat{y}(w, x) - y\|_2^2 \tag{3}$$

where y is the ground truth. However, linear regression models are sensitive to outliers and are hence highly dependent on reliable feature engineering. To build a more robust model, ridge regression (Hoerl and Kennard, 1970) and Huber regression (Huber, 1973) further add regularization terms into the loss function. The loss function of ridge regression can be written as:

$$\|\hat{y}(w, x) - y\|_2^2 + \alpha \|w\|_2^2 \tag{4}$$

where $\alpha \geq 0$ is the penalty coefficient. A larger α means stronger regularization on the model. Huber regression pays more attention to handling outliers. The loss is given as:

$$\sum_{i=1}^{n} \left(\delta + H\left(\frac{\hat{y}(w, x) - y}{\delta} \right) \delta \right) + \alpha \|w\|_2^2 \tag{5}$$

where

$$H(z) = \begin{cases} z^2, & |z| < \epsilon \\ 2\epsilon |z| - \epsilon^2, & |z| \geq \epsilon \end{cases} \tag{6}$$

in which δ and ϵ are the non-negative constant parameters.

A decision tree is a classic non-parametric supervised learning approach; a tree-like model is built to learn the simple rules inferred from the data features, and this has multiple nodes and branches. The clear structure of a decision tree makes it easy to understand, and it is hence commonly used in data science and decision-making. An RF (Breiman, 2001) is an ensemble of decision trees. It consists of a number of independent decision trees; each decision tree is trained with random bootstrapped samples, and each node of the decision tree is estimated using random combinations of predictor variables. The ensemble mean of the decision trees is used as the prediction of the RF model, and this helps to improve accuracy and mitigate overfitting problems.

AdaBoost (Freund and Schapire, 1997) is another commonly used ensemble machine model. It starts with an initial weak learner, i.e., a linear model, and this weak learner is trained with the complete dataset to obtain an accuracy that is slightly higher than random guessing. Then, AdaBoost reweights the training samples and assigns higher weights to the samples misclassified by the initial weak learner. Subsequently, the goal of AdaBoost is to build another weak learner to complement the previous one with these reweighted training samples. In this adaptive strategy, the training samples misclassified by the previous weak learner will contribute more to the model performance, and hence the subsequent weak learners are forced to improve the misclassified samples. The final AdaBoost model is an ensemble of all the individual weak learners that converges to a strong learner.

As a more flexible and non-linear ML method, NNs (Rumelhart et al., 1986) have been widely used in multiple fields including computer vision, earth science, and biological science.

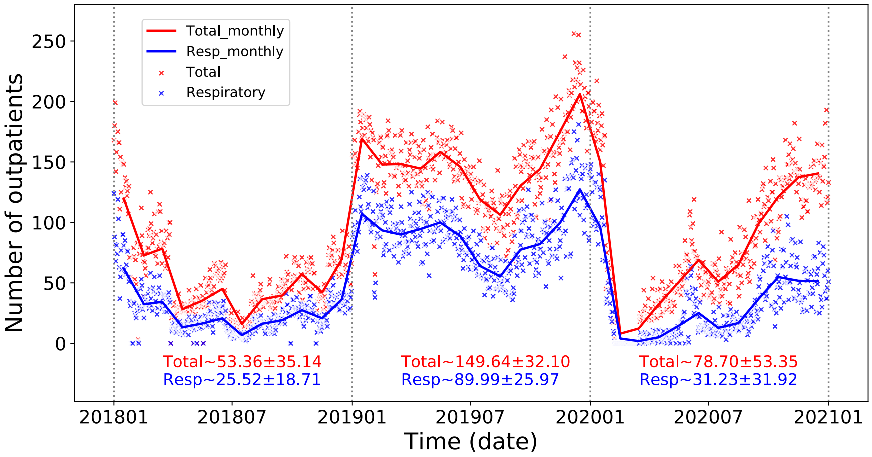

FIGURE 1
Time series of the numbers of patients visiting the pediatric department of a comprehensive Grade 3A hospital in Taizhou from 2018 to 2020. The scatter points show the number of pediatric outpatients (red) and outpatients visiting for respiratory diseases (blue) in a single day. The solid lines are the monthly average respectively. The mean and standard deviation for each year are shown at the bottom of the plot.

These are built from multiple layers, and each layer consists of a number of neural nodes with non-linear activation functions. The prediction of an NN model is generated through forward propagation. A loss function is applied to quantify the distance between the model output and the ground truth. A series of optimizers have been designed to minimize the loss function using backward propagation with the training samples. Hence, NNs are highly non-linear and they have advantages in learning representative features from the data. However, a decrease in model performance is seen when handling a small dataset with an NN.

2.3 Explainable artificial intelligence methods

Although ML models show great potential for improved performance, there are always questions relating to how their decisions are made and how much we can rely on them. Hence, it is of great importance to understand the results of ML models rather than them simply being "black boxes." In this study, four XAI methods—permutation feature importance (PFI), the partial dependence plot (PDP), local interpretable model-agnostic explanations (LIME), and Shapley additive explanations (SHAP)—are used to gain a well-grounded understanding of the established ML models and explore the feature importance of their predictors.

The PFI method (Breiman, 2001) computes the contribution of a single feature by randomly shuffling its values among the validation/testing samples with a trained model while keeping the other features unchanged. The decrease in the model score, i.e., R^2 for regression, with the permuted data is defined as the importance of the selected feature. Since the model and the remaining features are unchanged, the change in the model's score is seen as the contribution of that feature to the model performance. It can be seen that the PFI strategy can be applied to any ML model because it gives the feature importance by simply permuting the data without internal knowledge of model that has been used. Given an ML model f trained with data containing K features, the model score evaluated on the unpermuted testing data D is s. Then, a random permutation is performed on feature k among the testing samples to obtain the permuted data $\tilde{D}_k$. The new model score evaluated on the permuted data $\tilde{D}_k$ is s_k. The importance I_k of feature k is defined as:

$$I_k = s - s_k \tag{7}$$

In practice, I_k is computed multiple times on different perturbed data, and the average value is used as the feature importance. The larger the value of I_k, the more significant the impact of the feature on the prediction and the more important the feature.

The PDP (Friedman, 2001) is used to assess the marginal effects of one or two features in an ML model. The idea is similar to the PFI method, in that the feature importance is defined as the drop in the model score that occurs when breaking the relationship between the given feature and targets. The strategy of the PDP is to calculate the importance of the given feature by marginalizing over the distribution of the other features among the training data. Given an ML model f trained with data D containing K features, the set of features we are interested in is k (usually one or two features) and the set of remaining features is c. The partial dependence function is then given as:

$$\hat{f}_k(D_k) = \int \hat{f}(D_k, D_c)\, d\mathbb{P}(D_c) \tag{8}$$

In practice, the partial dependence function is estimated as:

$$\hat{f}_k(x_k) = \frac{1}{n}\sum_{i=1}^{n} \hat{f}(x_k, x_c^i) \tag{9}$$

where n is the number of instances in the training data, x_k is the value of feature k, and x_c is the actual values of the remaining features in set c. The partial dependence $\hat{f}_k(x_k)$ shows the marginal effect of the given value x_k of feature k on the prediction.

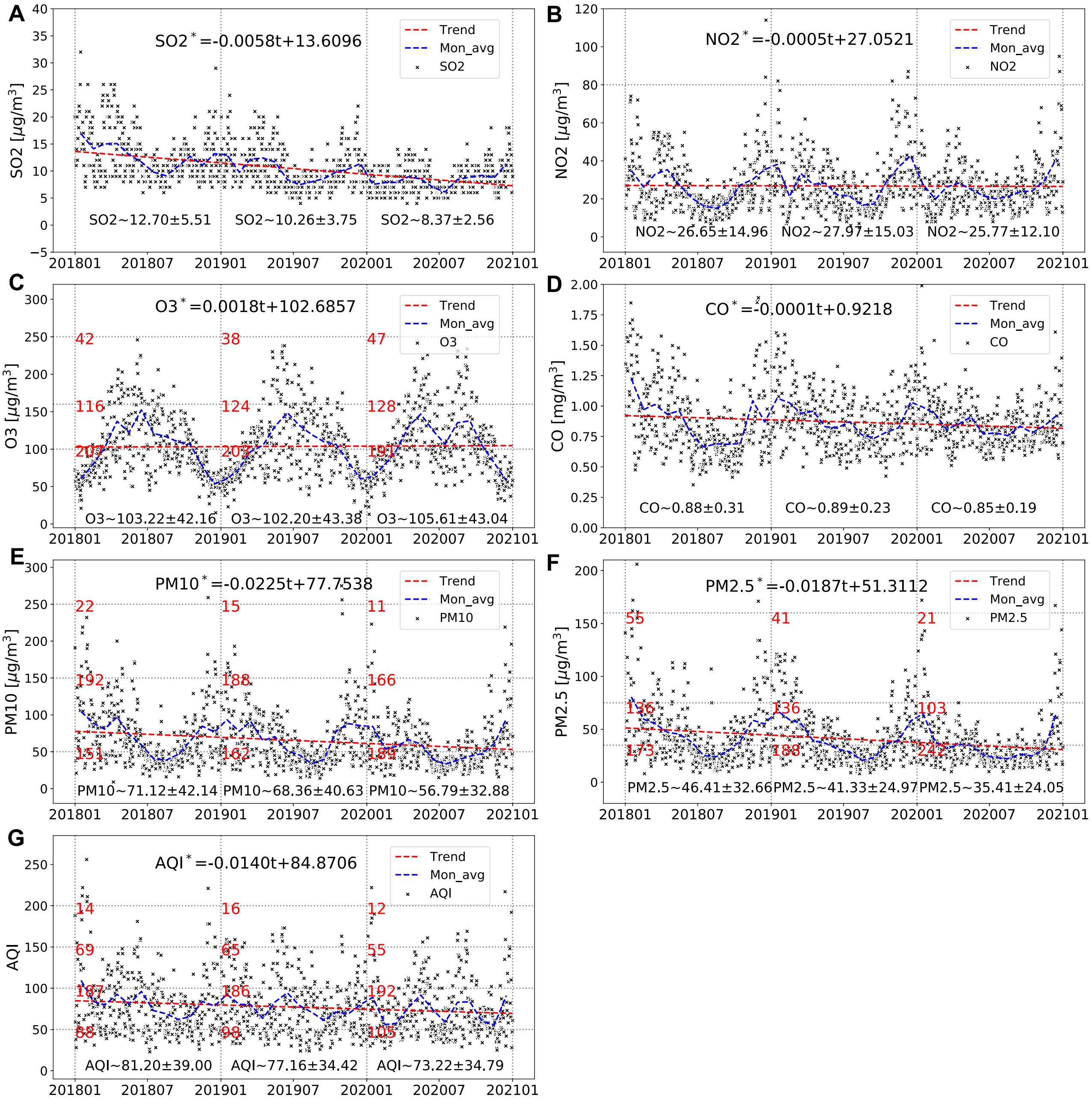

FIGURE 2

Time series of air-pollutant concentrations and AQI in Taizhou from 2018 to 2020: **(A)** SO_2, **(B)** NO_2, **(C)** O_3, **(D)** CO, **(E)** PM_{10}, **(F)** $PM_{2.5}$, and **(G)** AQI. The scatter points show the daily data, the blue dashed lines are the monthly averages, and the red dashed lines are trend lines. Unitary linear regression models for each air pollutant are given at the top of each plot, and the mean and standard deviation for each year are shown at the bottom. The horizontal dotted lines show the thresholds of air-pollutant concentrations for the different levels of pollution. The numbers below the horizontal dotted lines show the number of days in each year that exceeded these pollution thresholds.

Both the PFI and PDP methods evaluate the global contribution of a feature to the model prediction. However, in many cases, we are more interested in how the features affect the model's decision in a given instance. Here, LIME (Ribeiro et al., 2016) serves as an XAI method for the local explanations for agnostic models; this further helps to understand the ways in which ML models make their predictions. The basic idea of LIME is to train an interpretable model as a good approximation of the original ML model locally. Given an ML model f trained with data D containing K features, the predictions of f for sample D_i are $f(D_i)$. To understand the prediction $f(D_i)$, LIME generates a new dataset $\tilde{D}_i$ from the sample D_i by perturbation, and this consists of the perturbed features and the corresponding predictions of the trained model f. With this generated dataset, LIME then trains an interpretable model f', i.e., linear regression and decision trees, as a local substitution for the black-box model f. Hence, the explanation of the agnostic model f

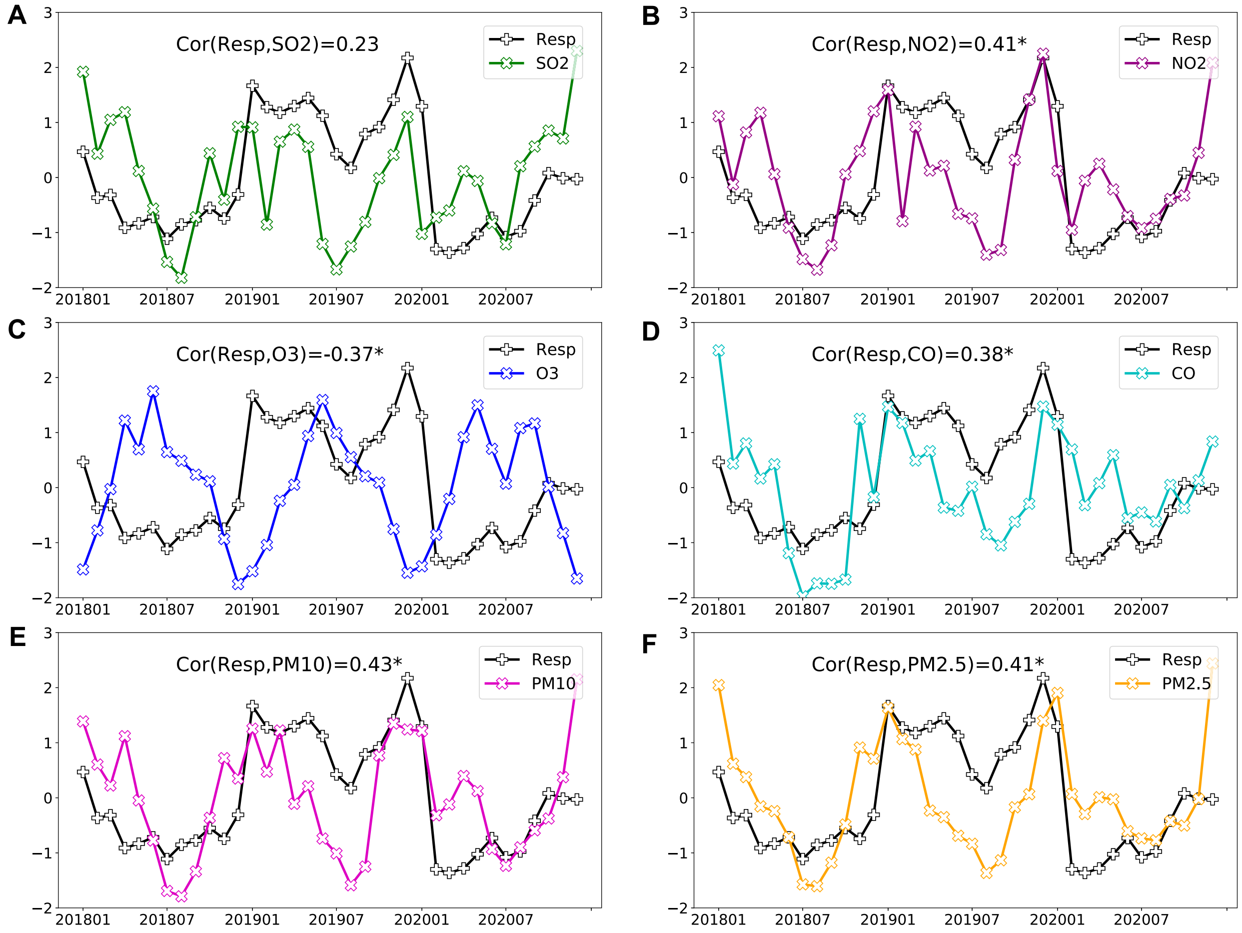

FIGURE 3
Normalized time series of detrended monthly air-pollutant concentrations **(A)** SO_2, **(B)** NO_2, **(C)** O_3, **(D)** CO, **(E)** PM_{10}, and **(F)** $PM_{2.5}$, as well as the number of detrended pediatric respiratory outpatients from 2018 to 2020. The detrended Pearson correlation coefficients between the air-pollutant concentrations and the number of outpatients are listed at the top; the symbol * indicates that the correlation passes the 95% significance test.

is given by the understanding of the interpretable model f' for the given instance D_i.

SHAP (Lundberg and Lee, 2017) gives another solution to explain the individual predictions of ML models based on the Shapley values (Shapley, 1997) in coalitional game theory. The Shapley values are used to fairly assess the contribution of each feature to the model prediction. In coalitional game theory, the effect of a feature should not be evaluated alone but on all the possible coalitions of features. Given an ML model f with training data D containing K features, the number of possible combinations of features is $2^K - 1$. Using each combination as the input of the trained model f, there are $2^K - 1$ predictions, and the differences between these predictions and the original predictions using the complete set of features are calculated as the contributions of the combined features. The average marginal effect of a feature across all possible coalitions is defined as the Shapley value. However, in real applications, it is very time-consuming to calculate all these coalitions. Hence, Lundberg and Lee (2017) combined the LIME and Shapley values and further proposed an alternative estimation method, SHAP, based on the kernel and tree models. SHAP is computationally efficient and can be used for both global and local interpretation.

3 Results

3.1 Overview of the air-pollutant concentrations and the number of pediatric respiratory outpatients in Taizhou

Figure 1 shows the distribution and the trend in the number of patients visiting the pediatric department of a comprehensive Grade 3A hospital in Taizhou from 2018 to 2020. It can be seen that respiratory-related diseases account for over 60% of all diseases in the pediatric department, and there are clear interannual and seasonal variations. In particular, the number of pediatric respiratory outpatients in 2019 was significantly higher than in 2018 and 2020, with a peak occurring in the winter. Could this difference be related to the emission of air pollution?

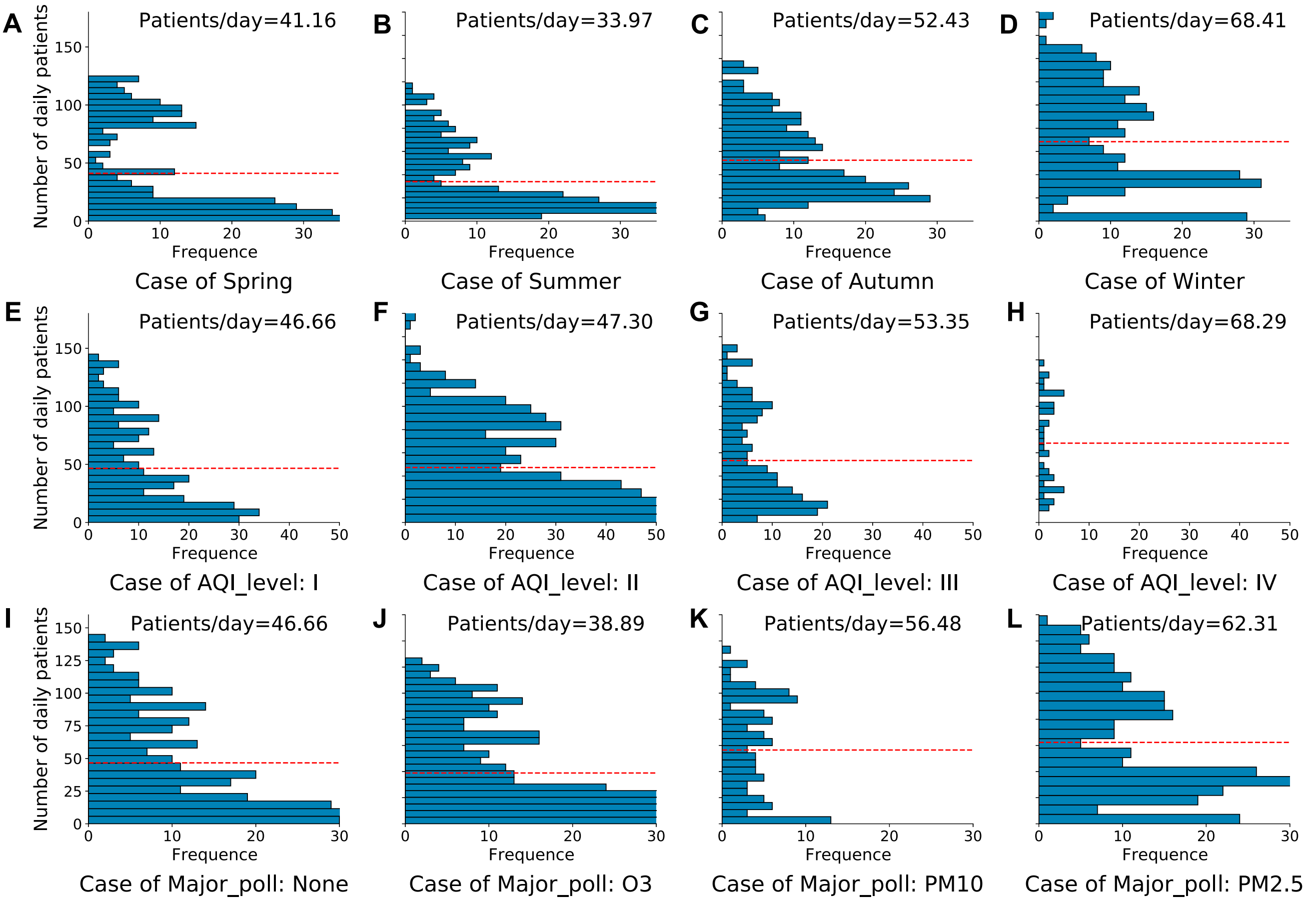

FIGURE 4
Frequency histograms of the total numbers of pediatric respiratory outpatients from 2018 to 2020 in different cases: **(A–D)** different seasons, **(E–H)** different levels of air pollution, and **(I–L)** different types of primary pollutant. The red dashed lines show the daily averages of the numbers of outpatients in each case.

The statistics of the air-pollutant concentrations are shown in Figure 2. A remarkable decline is seen in most of the air-pollutant concentrations from 2018 to 2020, although there is a slight increase in O_3. This indicates that the measures implemented to control air pollution in Taizhou have resulted in some progress, especially for the emission of SO_2, $PM_{2.5}$, and PM_{10}. The results also show that there is significant seasonal variation in the relative proportions of the air pollutants. The concentrations of NO_2, CO, $PM_{2.5}$, and PM_{10} are at their peak in winter and low in summer, which is opposite to the trend for O_3. The main reason for the high concentrations of NO_2, CO, and PM in winter is the increased heating needs of residents; this causes an increase in the amount of coal being burned. The high concentration of O_3 in summer is mainly related to the high temperature and strong sunshine, which act as a catalyst in O_3 production.

The results in Figures 1, 2 show that there is significant seasonal variation in both the number of pediatric respiratory outpatients and the air-pollutant concentrations. The inference is drawn that there is a certain correlation between them, and a quantitative assessment of this is now presented.

3.2 Possible factors affecting the number of pediatric respiratory outpatients

Figure 3 presents the detrended monthly time series of air-pollutant concentrations and the number of pediatric respiratory outpatients. The monthly data is used here because there is often a lag of a few days between a heavy air-pollution event and patients visiting the respiratory department. We use these data to explore the basic mechanism of how air-pollution-related factors affecting the pediatric respiratory diseases. The results demonstrate that the main air pollutants—NO_2, CO, O_3, $PM_{2.5}$, and PM_{10}—have significant correlations with the numbers of outpatients, with detrended Pearson correlation coefficients exceeding 0.35 (passing the 95% significance test). It also shows that the trends in the air-pollutant concentrations, aside from O_3, are highly consistent with the outpatient visits; an increasing (decreasing) number of pediatric respiratory outpatients is seen with an increasing (decreasing) concentration of air pollutants. This indicates that the pediatric respiratory diseases are highly related to the air-pollutant factors, at least in statistics. A stratified analyse is further given as follows to confirm the point.

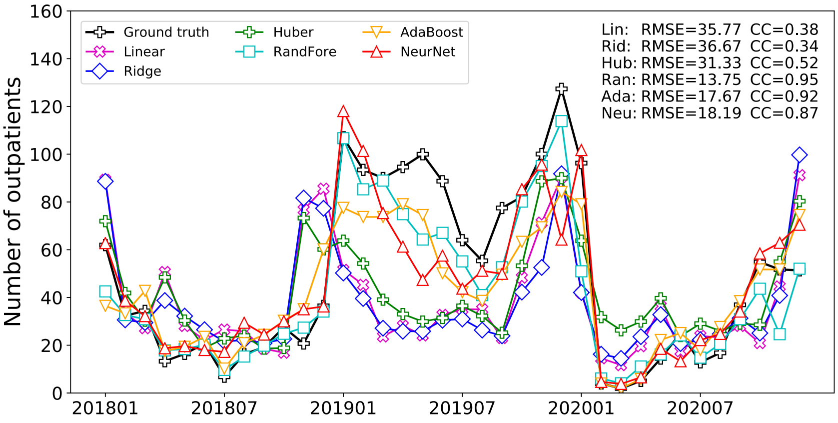

FIGURE 5
Monthly numbers of pediatric respiratory outpatients simulated by different ML models. The evaluation metrics, RMSE and CC, are given at the top.

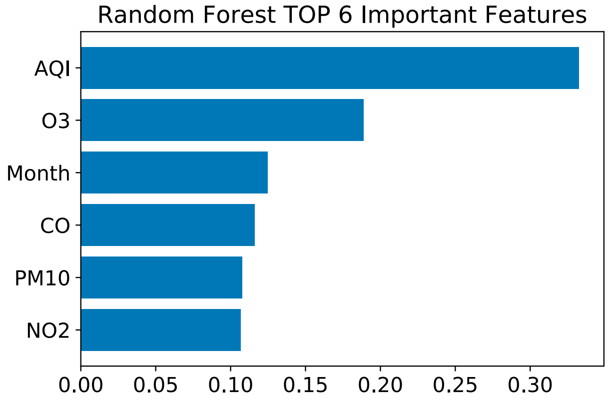

FIGURE 6
Feature importance for the trained RF model obtained using the PFI method.

The impacts of the seasons, the level of air pollution, and the type of primary pollutant on the clinic visits are presented in Figure 4. These histograms show that all three of these factors have significant effects on the incidence of pediatric respiratory diseases. Figures 4A–D show that the daily number of clinic visits in winter is almost twice that in the summer, which quantitatively demonstrates that there is remarkable seasonal variation. The comparisons in the levels of air pollution in Figures 4E–H show that the daily clinic visits gradually increase with increasing AQI level (i.e., with worse air quality). The daily number of pediatric respiratory outpatients increased from 47 in AQI I to 69 in AQI IV, which indicates that the air quality can significantly affect the incidence of pediatric respiratory disease. The results in Figures 4I–L show that the type of primary pollutant is another factor affecting the daily numbers of clinic visits. The excessive emission of $PM_{2.5}$ and PM_{10} can lead to a notable increase in the number of pediatric respiratory outpatients. Conversely, the O_3 concentration has a negative correlation with clinic visits. One of the reasons for this is that ozone-related pollution usually occurs in summer when the concentration of PM is at a low level.

3.3 ML regression models of air pollutants and pediatric respiratory outpatients

A number of ML methods were used to explore the statistical relationships among the air-pollutant concentrations and the numbers of pediatric respiratory outpatients. A monthly average was performed on the raw daily data to show the long-term impact. As noted in Section 2.1, the candidate predictors cover the concentrations of major air pollutants, the AQI, the level of air pollution, the type of primary pollutant, and temporal information. The log-transformed number of outpatients was used as the predictand. Hence, the regression model can be written as:

$$\ln\mathrm{Resp} \sim \mathrm{ML}\left(PM_{2.5},\ PM_{10},\ CO,\ NO_2,\ SO_2,\ \text{and}\ O_3,\ AQI,\ AQI\_level,\ Major\_pollutant,\ Month\right) \tag{10}$$

where Resp is the number of monthly clinic visits, ML() is the ML model, AQI_level is the level of air pollution, Major_pollutant is the type of primary pollutant and Month is the index of month.

Figure 5 presents the results of the simulation of the clinic visits by using ML models. The corresponding scores, root mean square error (RMSE), and correlation coefficient (CC) are listed at the top. These results show that all the ML models are able to capture the trend of the clinic visits and turning points. However, an underestimate is also seen in simulating the number of outpatients in 2019. Results in terms of RMSE and CC show that the non-linear models significantly outperform the linear ones. The RMSE values of the linear models, i.e., linear regression, ridge regression, and Huber regression, are greater than 30 persons/day, and their correlation coefficients are less than 0.6. The non-linear models, especially the RF, show superior performance, with RMSE values of less than 20 persons/day and CC values greater than 0.85.

It is noted that the purpose of this study was not to establish a high-quality prediction model for the number of pediatric respiratory outpatients but to explore the potential impact of the

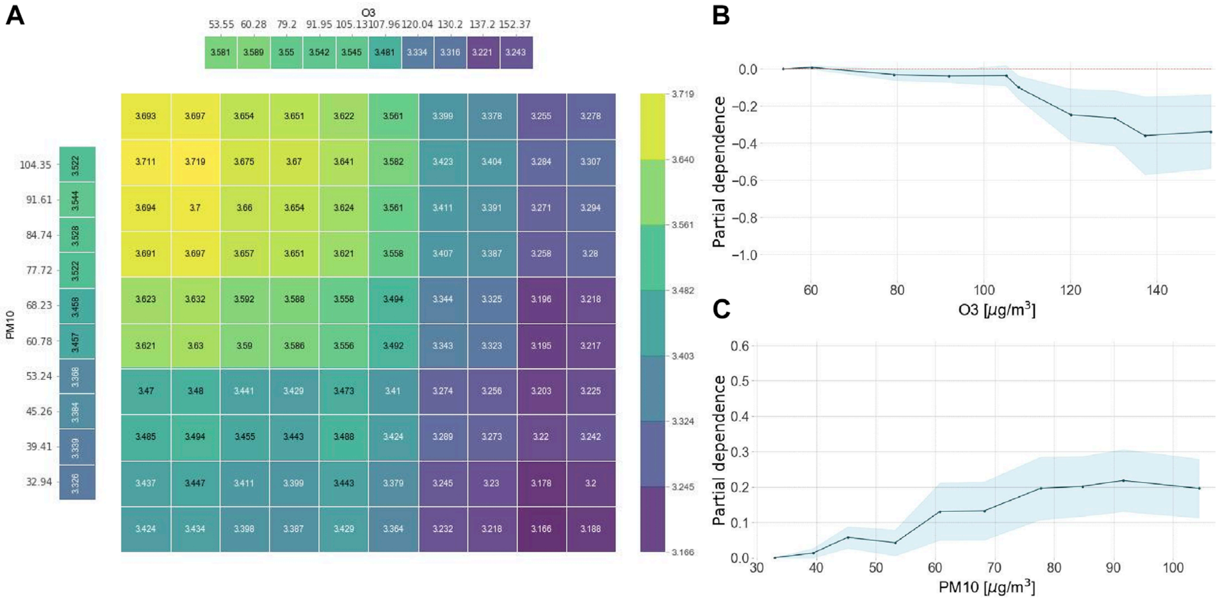

FIGURE 7
Feature importance of the O_3 and PM_{10} concentrations for the trained RF model using a PDP. **(A)** Heat map showing the synergistic impact of O_3 and PM_{10} on the number of outpatients, where the legend is the number of outpatients after the logarithm; PDPs showing the impacts of **(B)** O_3 and **(C)** PM_{10}.

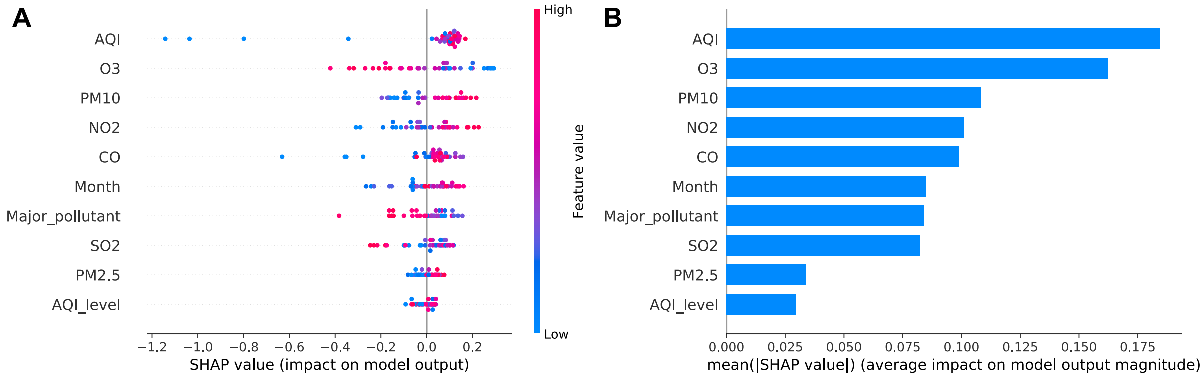

FIGURE 8
SHAP feature importance for the trained RF model. **(A)** SHAP values of each feature; **(B)** mean of absolute SHAP values of each feature.

air pollutants on this number. The next section details the results of the application of a number of XAI methods to understanding the regression models built by the best-performing model, the RF.

3.4 Explanations of the RF model

The feature importance for the RF model, as obtained using the PFI method, is plotted in Figure 6. This shows that the AQI, the O_3 concentration, and the month index are the three most important factors correlating with clinic visits. As noted earlier, the PFI method evaluates the global impact of each feature on the model prediction. However, it can only assess a single feature at a time, and it cannot show whether the impact is positive or negative. Hence, Figure 7 further presents an analysis of the contributions of O_3 and PM_{10} using the PDP method.

Figure 7A shows how O_3 and PM_{10} synergistically affect the number of clinic visits. The values in the heat map are the logarithm of the clinic visits, in which the warm (cold) tones indicate more (fewer) clinic visits. The impact of PM_{10} is given in the bar on the left side. An increasing number of clinic visits is seen from bottom to top as the concentration of PM_{10} increases. Similarly, the impact of O_3 is presented at the top: an increase in the O_3 concentration is correlated with a decrease in clinic visits. The heat map shows the joint impact of the O_3 and PM_{10} concentrations on the number of pediatric respiratory

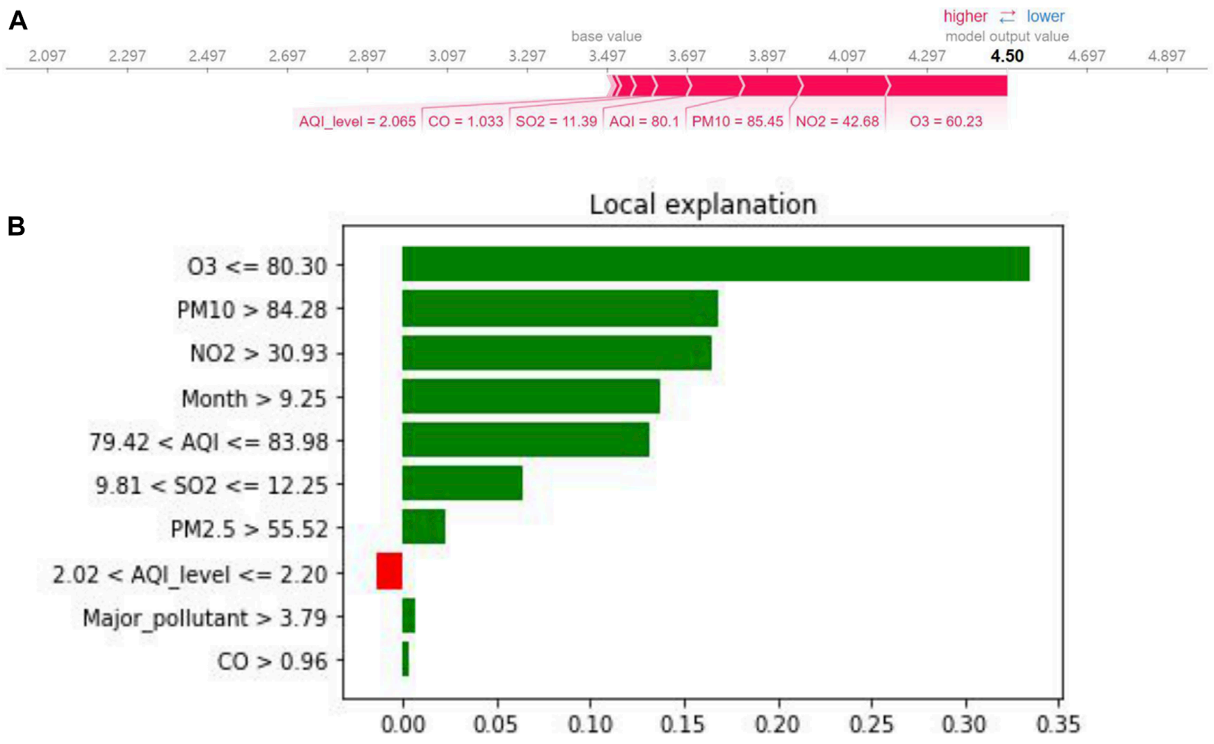

FIGURE 9
Case study of feature importance for the trained RF model with **(A)** SHAP and **(B)** LIME.

outpatients. This indicates that increasing PM_{10} concentration and decreasing O_3 concentration correlate with increasing clinic visits. The partial dependences of O_3 and PM_{10} are respectively given in **Figures 7B, C**. These plots show that with increasing O_3 concentration—especially when it exceeds 100 $\mu g/m^3$—a clear decrease in the number of clinic visits is seen. The results for PM_{10} show that increasing PM_{10} concentration is correlated with a rapid increase in the number of clinic visits. It's noted that the feature importance only gives the contribution of the factors on the model simulation in statistics. The underlying mechanism requires further experiments. Here, the contribution of PM_{10} is clear as pointed out in the WHO reports (World Health Organization, 2021; World Health Organization, 2022), while that of O_3 is likely a statistical correlation. Nevertheless, the O_3 concentration is an important indicator of respiratory disease in the view of feature importance.

The feature importance was further assessed using the SHAP method for the trained RF model, as shown in **Figure 8**. The colored scatter plot in **Figure 8A** shows the SHAP values of different features; the larger the SHAP value, the more important the feature for the model prediction. The color of each scatter point indicates the value of each feature. Taking AQI as an example, higher SHAP values for AQI values are generally positive, which indicates that AQI has a significant positive impact on the model results. Conversely, the SHAP values of higher O_3 values are negative, which indicates a negative impact. Among the pollutants, NO_2, CO, $PM_{2.5}$, and PM_{10} show a promoting impact on clinic visits. Our results are in line with previous research (Yin et al., 2011; Shen et al., 2017; Song et al., 2018). Particulate matter can penetrate deep into the lungs and exposure to NO_2 can irritate the respiratory tract, where both can further lead to respiratory symptoms. **Figure 8B** presents the feature importance as obtained using SHAP. The overall results are consistent with that assessed by the PFI method, which indicates that the interpretations of both of these XAI methods are credible.

Local explanations of a given sample by SHAP and LIME are presented in **Figure 9**. The selected case happens in December 2019, which has the most clinic visits in a single month. **Figure 9A** shows the impacts of different predictors on the predictand with the SHAP method. A red (blue) arrow to the right (left) indicates that a factor has a positive (negative) contribution to the model to generate a high-value (low-value) prediction. The length of each arrow shows the degree of the contribution. The feature values are listed at the bottom, and the model prediction (after logarithm) is given in bold on the axis. In this case, almost all the predictors contribute to generating a high-value prediction, especially the joint effects of O_3, NO_2, and PM_{10}. **Figure 9B** shows the assessment given by the LIME method. Similar to the results of SHAP, LIME shows that most of the predictors have positive contributions, except the AQI_level being a slightly inhibitory factor. Moreover, LIME can provide additional explanations using binary trees. For instance, the concentration of O_3 in this case is 60.23 $\mu g/m^3$ (see in **Figure 9A**), which is less the threshold 80.3 $\mu g/m^3$ and causes the model to predict a higher value. The result is consistent with the PDP analysis in **Figure 7B**, which indicates that the model explanations given by LIME are reliable and easy to understand. It further assists the decision-making and the selection of important factors.

4 Conclusion and discussion

4.1 Conclusion

In this study, air pollution was found to be a major factor correlating with the incidence of pediatric respiratory diseases. Multiple ML models were used to explore the relationships between the air-pollutant concentrations and the numbers of pediatric respiratory outpatients in Taizhou, China. Different XAI methods were applied to explain the constructed model and analyze the feature importance. The main conclusions are as follows.

1. There is a significant seasonal variation in the number of clinic visits for pediatric respiratory diseases, and the peak value happens in the winter. Seasonal variation is seen in the concentrations of air pollutants. The concentrations of NO_2, CO, $PM_{2.5}$, and PM_{10} are higher in the winter, while that of O_3 is higher in the summer. Among the air pollutants, NO_2, CO, O_3, $PM_{2.5}$, and PM_{10} are significantly correlated with the numbers of clinic visits, with Pearson correlation coefficients greater than 0.35. Furthermore, comparisons between groups showed that the seasons, the level of air pollution, and the type of primary pollutant significantly affected the incidence of respiratory diseases in children. The concentration of PM was found to be the most important factor.
2. ML models are capable of well simulating the monthly clinic visits. The RMSE and CC results show that the non-linear models significantly outperform the linear ones. Among them, RF served as the best-performing model.
3. Four different XAI methods—PFI, PDP, SHAP, and LIME—were used for the explanation of the best-performing model, RF. The results showed that AQI, O_3, PM, and the month were the four most important features. Among the air pollutants, increases in the concentrations of NO_2, CO, $PM_{2.5}$, and PM_{10} were correlated with increases in clinic visits. A case study in December 2019 showed that the SHAP and LIME methods are credible and easy to understand for local explanations of the RF model.

4.2 Discussion

The incidence of pediatric respiratory diseases is affected by a variety of factors, and air pollution is certainly one of the major causes. For instance, PM_{10} can penetrate deep in the lungs and $PM_{2.5}$ can even enter the bloodstream, both leading to the respiratory symptoms (World Health Organization, 2021). Exposure to NO_2 can irritate airways and aggravate respiratory diseases (World Health Organization, 2022). In this study, this incidence is characterized as the number of pediatric patients visiting the respiratory department of a single hospital in Taizhou. Comprehensive collection of clinic-visit information could further help to improve the reliability of the model. The purpose of the study was to explore the potential impact of air-pollutant concentrations on the incidence of pediatric respiratory diseases using ML models and XAI methods. Here, the monthly data was used which helped to abstract a clear and basic pattern of how air-pollution-related factors affecting the pediatric respiratory diseases. However, the small datasets could cause the over-fitting issue when training the ML models. Hence, interpretable ML models that prove still efficient for small datasets were adopted in this study, i.e. Adaboost and random forest. With this preliminary exploration, a prediction model for daily clinic visits will be investigated in future studies, where sufficient daily data can be used for training and validation. Furthermore, more factors should be taken into account aside from the air pollutants. The meteorological data, i.e. temperature and relative humidity (moisture), are commonly used to adjust the effects of weather on hospital outpatients (Song et al., 2018). The time lags between the air-pollution events and the patients visiting the hospital should also be included as additional factors.

Data availability statement

The raw data supporting the conclusion of this article will be made available by the authors, without undue reservation.

Author contributions

The study was conceived by YJ and YW. YJ and YZ contributed to the model development and maintained the code. YJ, TP, and LJ wrote the original draft. All authors reviewed and edited the manuscript. XZ supervised the entire project.

Funding

The work was jointly funded by the National Key Research and Development Program of China (Grant Nos. 2018YFC1507305, 2018YFC1507200, and 2017YFC1502000).

Conflict of interest

The authors declare that the research was conducted in the absence of any commercial or financial relationships that could be construed as a potential conflict of interest.

Publisher's note

References

Badue, C., Guidolini, R., Carneiro, R. V., Azevedo, P., Cardoso, V. B., Forechi, A., et al. (2021). Self-driving cars: A survey. *Expert Syst. Appl.* 165, 113816. doi:10.1016/j.eswa.2020.113816

Bojarski, M., Del Testa, D., Dworakowski, D., Firner, B., Flepp, B., Goyal, P., et al. (2016). *End to end learning for self-driving cars. arXiv preprint arXiv:1604.07316.*

Breiman, L. (2001). Random forests. *Mach. Learn.* 45, 5–32. doi:10.1023/a:1010933404324

Dominici, F., McDermott, A., Zeger, S. L., and Samet, J. M. (2002). On the use of generalized additive models in time-series studies of air pollution and health. *Am. J. Epidemiol.* 156, 193–203. doi:10.1093/aje/kwf062

Freeman, B. S., Taylor, G., Gharabaghi, B., and Thé, J. (2018). Forecasting air quality time series using deep learning. *J. Air Waste Manag. Assoc.* 68, 866–886. doi:10.1080/10962247.2018.1459956

Freund, Y., and Schapire, R. E. (1997). A decision-theoretic generalization of on-line learning and an application to boosting. *J. Comput. Syst. Sci.* 55, 119–139. doi:10.1006/jcss.1997.1504

Friedman, J. H. (2001). Greedy function approximation: A gradient boosting machine. *Ann. Stat.* 29, 1189–1232. doi:10.1214/aos/1013203451

Geiss, A., Silva, S. J., and Hardin, J. C. (2022). Downscaling atmospheric chemistry simulations with physically consistent deep learning. *Geosci. Model. Dev.* 15, 6677–6694. doi:10.5194/gmd-15-6677-2022

Gu, H., Yan, W., Elahi, E., and Cao, Y. (2020). Air pollution risks human mental health: An implication of two-stages least squares estimation of interaction effects. *Environ. Sci. Pollut. Res.* 27, 2036–2043. doi:10.1007/s11356-019-06612-x

Guo, Y., Barnett, A. G., Zhang, Y., Tong, S., Yu, W., and Pan, X. (2010). The short-term effect of air pollution on cardiovascular mortality in Tianjin, China: Comparison of time series and case–crossover analyses. *Sci. Total. Environ.* 409, 300–306. doi:10.1016/j.scitotenv.2010.10.013

Harrou, F., Dairi, A., Sun, Y., and Kadri, F. (2018). Detecting abnormal ozone measurements with a deep learning-based strategy. *IEEE Sensors J.* 18, 7222–7232. doi:10.1109/jsen.2018.2852001

Hesamian, M. H., Jia, W., He, X., and Kennedy, P. (2019). Deep learning techniques for medical image segmentation: Achievements and challenges. *J. Digit. Imaging* 32, 582–596. doi:10.1007/s10278-019-00227-x

Hoerl, A. E., and Kennard, R. W. (1970). Ridge regression: Applications to nonorthogonal problems. *Technometrics* 12, 69–82. doi:10.1080/00401706.1970.10488635

Hu, G., Yang, Y., Yi, D., Kittler, J., Christmas, W., Li, S. Z., et al. (2015). “When face recognition meets with deep learning: An evaluation of convolutional neural networks for face recognition,” in Proceedings of the IEEE International Conference on Computer Vision Workshops (Santiago, Chile: IEEE), 142–150. doi:10.1109/ICCVW.2015.58

Huber, P. J. (1973). Robust regression: Asymptotics, conjectures and Monte Carlo. *Ann. Stat.* 1, 799–821. doi:10.1214/aos/1176342503

Islam, M. S., Chaussalet, T. J., and Koizumi, N. (2017). Towards a threshold climate for emergency lower respiratory hospital admissions. *Environ. Res.* 153, 41–47. doi:10.1016/j.envres.2016.11.011

Kan, H., Chen, R., and Tong, S. (2012). Ambient air pollution, climate change, and population health in China. *Environ. Int.* 42, 10–19. doi:10.1016/j.envint.2011.03.003

Khaniabadi, Y. O., Goudarzi, G., Daryanoosh, S. M., Borgini, A., Tittarelli, A., and De Marco, A. (2017). Exposure to PM_{10}, NO_2, and O_3 and impacts on human health. *Environ. Sci. Pollut. Res.* 24, 2781–2789. doi:10.1007/s11356-016-8038-6

Kleinert, F., Leufen, L. H., Lupascu, A., Butler, T., and Schultz, M. G. (2022). Representing chemical history in ozone time-series predictions–a model experiment study building on the MLAir (v1.5) deep learning framework. *Geosci. Model. Dev. Discuss.* 15, 8913–8930. doi:10.5194/gmd-15-8913-2022

Li, Y., Xiao, C., Li, J., Tang, J., Geng, X., Cui, L., et al. (2018). Association between air pollution and upper respiratory tract infection in hospital outpatients aged 0–14 years in hefei, China: A time series study. *Public Health* 156, 92–100. doi:10.1016/j.puhe.2017.12.006

Litjens, G., Kooi, T., Bejnordi, B. E., Setio, A. A. A., Ciompi, F., Ghafoorian, M., et al. (2017). A survey on deep learning in medical image analysis. *Med. Image Anal.* 42, 60–88. doi:10.1016/j.media.2017.07.005

Lundberg, S. M., and Lee, S. I. (2017). A unified approach to interpreting model predictions. *Adv. Neural Inf. Process. Syst.* 30, 4768. doi:10.5555/3295222.3295230

MacIntyre, E. A., Gehring, U., Mölter, A., Fuertes, E., Klümper, C., Krämer, U., et al. (2014). Air pollution and respiratory infections during early childhood: An analysis of 10 European birth cohorts within the ESCAPE Project. *Environ. Health Perspect.* 122, 107–113. doi:10.1289/ehp.1306755

McGovern, A., Elmore, K. L., Gagne, D. J., Haupt, S. E., Karstens, C. D., Lagerquist, R., et al. (2017). Using artificial intelligence to improve real-time decision-making for high-impact weather. *Bull. Am. Meteorol. Soc.* 98, 2073–2090. doi:10.1175/bams-d-16-0123.1

Parkhi, O. M., Vedaldi, A., and Zisserman, A. (2015). “Deep face recognition,” in Proceedings of the British Machine Vision Conference 2015 (Durham, DH1, UK: British Machine Vision Association), 1–12. doi:10.5244/C.29.41

Prüss-Üstün, A., Wolf, J., Corvalán, C., Bos, R., and Neira, M. (2016). *Preventing disease through healthy environments: A global assessment of the burden of disease from environmental risks.* Geneva, Switzerland: World Health Organization.

Qi, J., Ruan, Z., Qian, Z., Yin, P., Yang, Y., Acharya, B. K., et al. (2020). Potential gains in life expectancy by attaining daily ambient fine particulate matter pollution standards in mainland China: A modeling study based on nationwide data. *PLoS Med.* 17, e1003027. doi:10.1371/journal.pmed.1003027

Ravindra, K., Rattan, P., Mor, S., and Aggarwal, A. N. (2019). Generalized additive models: Building evidence of air pollution, climate change and human health. *Environ. Int.* 132, 104987. doi:10.1016/j.envint.2019.104987

Reichstein, M., Camps-Valls, G., Stevens, B., Jung, M., Denzler, J., Carvalhais, N., et al. (2019). Deep learning and process understanding for data-driven Earth system science. *Nature* 566, 195–204. doi:10.1038/s41586-019-0912-1

Ribeiro, M. T., Singh, S., and Guestrin, C. (2016). ““Why should I trust you?” explaining the predictions of any classifier,” in Proceedings of the 22nd ACM SIGKDD International Conference on Knowledge Discovery and Data Mining, 1135–1144. doi:10.1145/2939672.2939778

Ruckerl, R., Ibald-Mulli, A., Koenig, W., Schneider, A., Woelke, G., Cyrys, J., et al. (2006). Air pollution and markers of inflammation and coagulation in patients with coronary heart disease. *Am. J. Respir. Crit. Care Med.* 173, 432–441. doi:10.1164/rccm.200507-1123oc

Rumelhart, D. E., Hinton, G. E., and Williams, R. J. (1986). Learning representations by back-propagating errors. *Nature* 323, 533–536. doi:10.1038/323533a0

Sarnat, S. E., Raysoni, A. U., Li, W.-W., Holguin, F., Johnson, B. A., Luevano, S. F., et al. (2012). Air pollution and acute respiratory response in a panel of asthmatic children along the US–Mexico border. *Environ. Health Perspect.* 120, 437–444. doi:10.1289/ehp.1003169

Shahi, A. M., Omraninava, A., Goli, M., Soheilarezoomand, H. R., and Mirzaei, N. (2014). The effects of air pollution on cardiovascular and respiratory causes of emergency admission. *Emergency* 2, 107–114.

Shapley, L. S. (1997). A value for n-person games. *Cl. Game Theory* 69. doi:10.7249/P0295

Shen, F., Ge, X., Hu, J., Nie, D., Tian, L., and Chen, M. (2017). Air pollution characteristics and health risks in Henan Province, China. *Environ. Res.* 156, 625–634. doi:10.1016/j.envres.2017.04.026

Song, J., Lu, M., Zheng, L., Liu, Y., Xu, P., Li, Y., et al. (2018). Acute effects of ambient air pollution on outpatient children with respiratory diseases in Shijiazhuang, China. *BMC Pulm. Med.* 18, 150. doi:10.1186/s12890-018-0716-3

Song, Y., Huang, B., He, Q., Chen, B., Wei, J., and Mahmood, R. (2019). Dynamic assessment of pm2. 5 exposure and health risk using remote sensing and geo-spatial big data. *Environ. Pollut.* 253, 288–296. doi:10.1016/j.envpol.2019.06.057

Terzi, Y., and Cengiz, M. (2009). Using of generalized additive model for model selection in multiple Poisson regression for air pollution data. *Sci. Res. Essays* 4, 867–871.

Wang, H. W., Li, X. B., Wang, D., Zhao, J., He, H. D., and Peng, Z. R. (2020). Regional prediction of ground-level ozone using a hybrid sequence-to-sequence deep learning approach. *J. Clean. Prod.* 253, 119841. doi:10.1016/j.jclepro.2019.119841

Wang, K. Y., and Chau, T. T. (2013). An association between air pollution and daily outpatient visits for respiratory disease in a heavy industry area. *PLoS One* 8, e75220. doi:10.1371/journal.pone.0075220

Wang, L., Liu, C., Meng, X., Niu, Y., Lin, Z., Liu, Y., et al. (2018a). Associations between short-term exposure to ambient sulfur dioxide and increased cause-specific mortality in 272 Chinese cities. *Environ. Int.* 117, 33–39. doi:10.1016/j.envint.2018.04.019

Wang, M., Zheng, S., Nie, Y., Weng, J., Cheng, N., Hu, X., et al. (2018b). Association between short-term exposure to air pollution and dyslipidemias among type 2 diabetic patients in northwest China: A population-based study. *Int. J. Environ. Res. Public Health* 15, 631. doi:10.3390/ijerph15040631

World Health Organization (2018a). *9 out of 10 people worldwide breathe polluted air, but more countries are taking action (news release).* Geneva, Switzerland: World Health Organization. Available at: https://www.who.int/news-room/detail/02-05-2018-9-out-of-10-people-worldwide-breathe-polluted-air-but-more-countries-are-taking-action.

World Health Organization (2018b). *Ambient (outdoor) air quality and health (news release).* Geneva, Switzerland: World Health Organization. Available at: https://www.who.int/zh/news-room/fact-sheets/detail/ambient-(outdoor)-air-quality-and-health.

World Health Organization (2022). *Billions of people still breathe unhealthy air: New who data (news release)*. Geneva, Switzerland: World Health Organization. Available at: https://www.who.int/news/item/04-04-2022-billions-of-people-still-breathe-unhealthy-air-new-who-data.

World Health Organization (2021). *WHO global air quality guidelines: Particulate matter (PM2.5 and PM10), ozone, nitrogen dioxide, sulfur dioxide and carbon monoxide*. Geneva, Switzerland: World Health Organization.

Xu, P., Chen, Y., and Ye, X. (2013). Haze, air pollution, and health in China. *Lancet* 382, 2067. doi:10.1016/s0140-6736(13)62693-8

Yin, Y., Chen, J., Duan, Y., Wei, H., Ji, R. X., Yu, J. L., et al. (2011). Correlation analysis between the PM2.5, PM10 which were taken in the hazy day and the number of outpatient about breathing sections, breathing sections of pediatrics in Shanghai. *Environ. Sci. Chin.* 32, 1894–1898.

Yu, M., and Liu, Q. (2021). Deep learning-based downscaling of tropospheric nitrogen dioxide using ground-level and satellite observations. *Sci. Total. Environ.* 773, 145145. doi:10.1016/j.scitotenv.2021.145145

Zhang, H., Wang, S., Hao, J., Wang, X., Wang, S., Chai, F., et al. (2016). Air pollution and control action in Beijing. *J. Clean. Prod.* 112, 1519–1527. doi:10.1016/j.jclepro.2015.04.092

Zhang, Z., Wang, J., Chen, L., Chen, X., Sun, G., Zhong, N., et al. (2014). Impact of haze and air pollution-related hazards on hospital admissions in Guangzhou, China. *Environ. Sci. Pollut. Res.* 21, 4236–4244. doi:10.1007/s11356-013-2374-6

Zhu, L., Ge, X., Chen, Y., Zeng, X., Pan, W., Zhang, X., et al. (2017). Short-term effects of ambient air pollution and childhood lower respiratory diseases. *Sci. Rep.* 7, 4414–4417. doi:10.1038/s41598-017-04310-7

Frontiers in Earth Science

TYPE Original Research
PUBLISHED 11 April 2023
DOI 10.3389/feart.2023.1147848

Surface impacts and associated mechanisms of a moisture intrusion into the Arctic observed in mid-April 2020 during MOSAiC

Benjamin Kirbus[1]*, Sofie Tiedeck[2], Andrea Camplani[3], Jan Chylik[4], Susanne Crewell[4], Sandro Dahlke[2], Kerstin Ebell[4], Irina Gorodetskaya[5,6], Hannes Griesche[7], Dörthe Handorf[2], Ines Höschel[2], Melanie Lauer[4], Roel Neggers[4], Janna Rückert[8], Matthew D. Shupe[9], Gunnar Spreen[8], Andreas Walbröl[4], Manfred Wendisch[1] and Annette Rinke[2]

[1]Leipzig Institute for Meteorology, University of Leipzig, Leipzig, Germany, [2]Alfred Wegener Institute, Helmholtz Centre for Polar and Marine Research, Potsdam, Germany, [3]Institute of Atmospheric Sciences and Climate, National Research Council of Italy, Rome, Italy, [4]Institute for Geophysics and Meteorology, University of Cologne, Cologne, Germany, [5]Centre for Environmental and Marine Studies, Department of Physics, University of Aveiro, Aveiro, Portugal, [6]Interdisciplinary Centre of Marine and Environmental Research, University of Porto, Matosinhos, Portugal, [7]Leibniz-Institute for Tropospheric Research, Leipzig, Germany, [8]Institute of Environmental Physics, University of Bremen, Bremen, Germany, [9]Cooperative Institute for Research in Environmental Sciences (CIRES), University of Colorado and NOAA Physical Sciences Laboratory, Boulder, CO, United States

EDITED BY
Andreas Franz Prein,
National Center for Atmospheric Research (UCAR), United States

REVIEWED BY
Priscilla Mooney,
Norwegian Research Institute (NORCE), Norway
Alex Crawford,
University of Manitoba, Canada

*CORRESPONDENCE
Benjamin Kirbus,
✉ benjamin.kirbus@uni-leipzig.de

SPECIALTY SECTION
This article was submitted to Atmospheric Science, a section of the journal Frontiers in Earth Science

RECEIVED 19 January 2023
ACCEPTED 27 March 2023
PUBLISHED 11 April 2023

CITATION
Kirbus B, Tiedeck S, Camplani A, Chylik J, Crewell S, Dahlke S, Ebell K, Gorodetskaya I, Griesche H, Handorf D, Höschel I, Lauer M, Neggers R, Rückert J, Shupe MD, Spreen G, Walbröl A, Wendisch M and Rinke A (2023), Surface impacts and associated mechanisms of a moisture intrusion into the Arctic observed in mid-April 2020 during MOSAiC. *Front. Earth Sci.* 11:1147848. doi: 10.3389/feart.2023.1147848

Distinct events of warm and moist air intrusions (WAIs) from mid-latitudes have pronounced impacts on the Arctic climate system. We present a detailed analysis of a record-breaking WAI observed during the MOSAiC expedition in mid-April 2020. By combining Eulerian with Lagrangian frameworks and using simulations across different scales, we investigate aspects of air mass transformations *via* cloud processes and quantify related surface impacts. The WAI is characterized by two distinct pathways, Siberian and Atlantic. A moist static energy transport across the Arctic Circle above the climatological 90th percentile is found. Observations at research vessel Polarstern show a transition from radiatively clear to cloudy state with significant precipitation and a positive surface energy balance (SEB), i.e., surface warming. WAI air parcels reach Polarstern first near the tropopause, and only 1–2 days later at lower altitudes. In the 5 days prior to the event, latent heat release during cloud formation triggers maximum diabatic heating rates in excess of 20 K d^{-1}. For some poleward drifting air parcels, this facilitates strong ascent by up to 9 km. Based on model experiments, we explore the role of two key cloud-determining factors. First, we test the role moisture availability by reducing lateral moisture inflow during the WAI by 30%. This does not significantly affect the liquid water path, and therefore the SEB, in the central Arctic. The cause are counteracting mechanisms of cloud formation and precipitation along the trajectory. Second, we test the impact of increasing Cloud Condensation Nuclei concentrations from 10 to 1,000 cm^{-3} (pristine Arctic to highly polluted), which enhances cloud water content. Resulting stronger longwave cooling at cloud top makes entrainment more efficient and deepens the atmospheric boundary layer. Finally, we show the strongly positive effect of the WAI on the SEB. This is mainly driven by turbulent heat fluxes over the ocean, but radiation over sea ice. The WAI also contributes a large fraction to precipitation in the Arctic, reaching 30% of total precipitation in a 9-day period at the MOSAiC site. However, measured precipitation varies substantially between different platforms. Therefore, estimates of total precipitation are subject to considerable observational uncertainty.

KEYWORDS

warm and moist air intrusions, moisture transport, Arctic air mass transformation, Arctic Ocean, MOSAiC, trajectory analysis

1 Introduction

The Arctic has warmed nearly four times faster than the globe (Rantanen et al., 2022), a phenomenon termed Arctic amplification. The main underlying mechanisms have been reviewed recently (Previdi et al., 2021; Taylor et al., 2022; Wendisch et al., 2022). The poleward atmospheric transport of dry-static and latent energy plays a critical role for the seasonality and magnitude of Arctic air temperatures, and long-term changes in this transport are likely one of the driving forces of Arctic amplification (e.g., Graversen and Burtu, 2016; Mewes and Jacobi, 2019; Naakka et al., 2019). These poleward energy transports are tightly coupled to local feedback mechanisms. Of particular importance are those related to cloud formation/dissipation, thermodynamic phase partitioning, and liquid-water-to-ice phase transitions within atmospheric boundary layer clouds during air mass transformation processes (Pithan et al., 2018).

Besides long-term transport and its changes, episodic variability is also crucial. Such variability is particularly caused by distinct events of warm and moist air intrusions (WAIs) from the mid-latitudes into the Arctic. In fact, 60%–90% of poleward moisture transport occurs during only 10% of the time (Johansson et al., 2017; Nash et al., 2018; Pithan et al., 2018). WAIs take place throughout the year, move along season-dependent pathways, and are associated with specific large-scale atmospheric circulation patterns and individual weather events (Henderson et al., 2021), such as synoptic cyclones and the occurrence of atmospheric blocking (e.g., Binder et al., 2017; Fearon et al., 2021; Murto et al., 2022; Papritz et al., 2022).

The related heat and moisture transport into the Arctic contributes to the so-called water vapor triple effect, i.e., warming caused by condensation, the greenhouse effect of water vapor, and the mostly warming effect due to clouds, in particular during polar night (Taylor et al., 2022). This directly and indirectly impacts the surface energy budget (SEB) by cloud-radiation feedbacks (e.g., Wendisch et al., 2019; You et al., 2021; 2022; Bresson et al., 2022). Cloud radiative forcing especially of liquid-water containing clouds (Shupe et al., 2022) causes surface warming (e.g., Woods and Caballero, 2016; Dahlke and Maturilli, 2017; Graham et al., 2017; Messori et al., 2018) and can trigger sea-ice melt in spring-summer or retarded sea-ice growth in winter seasons (e.g., Park et al., 2015; Tjernström et al., 2015; Boisvert et al., 2016; Mortin et al., 2016; Persson et al., 2016; Li et al., 2022; Liang et al., 2022). WAIs also cause precipitation in different phases (rain and/or snow) in the Arctic (e.g., Viceto et al., 2022). This topic has rarely been studied, even though precipitation further influences the sea ice, for example, by modifying the thermal insulation or surface albedo (Webster et al., 2018).

Because of the important role of WAIs for the Arctic climate in general, and for Arctic amplification in particular, a better quantification of the impacts of WAIs on the SEB and precipitation is required. For this purpose, moisture sources, pathways into the Arctic and related large-scale flow need to be investigated; the air mass transformations along the flow and involved processes have to be better understood (Pithan et al., 2018; Henderson et al., 2021; Wendisch et al., 2021; Taylor et al., 2022).

To pursue the aims discussed above, we follow the approach of combining both i) observations and process modeling, as well as ii) Eulerian and Lagrangian approaches. In this study, we apply this strategy to a case study of a WAI observed during the Multidisciplinary drifting Observatory for the Study of Arctic Climate (MOSAiC) expedition, which provides unique observations from aboard the research vessel (RV) Polarstern as well as from the surrounding of it in the central Arctic (Nicolaus et al., 2022; Rabe et al., 2022; Shupe et al., 2022). The selected WAI occurred in mid-April 2020. This event is particularly interesting because of three aspects: i) It consisted of two separate intrusions within about a week, connected to different synoptic circulation patterns (Magnusson et al., 2020), ii) It was a record-breaking event, i.e., extreme with regard to moisture, air temperature, and longwave downward radiation at the surface, all being the highest for this location and time of year in the past 40 years (Rinke et al., 2021), and iii) It carried air pollutants from northern Eurasia and caused drastic changes in the atmospheric composition, aerosol characteristics, and cloud condensation nuclei concentrations in the central Arctic (Dada et al., 2022). This study aims to explore in detail this WAI event with respect to the following three specific objectives: (O1) Quantify the synoptic situation and transport, (O2) Understand air mass transformation *via* cloud processes, and (O3) Investigate related surface impacts in terms of the SEB and precipitation.

2 Complementary analysis methods

We apply a number of different research tools to thoroughly analyze this WAI event in unprecedented detail. These tools provide highly complementary perspectives, including a detailed examination of ERA5 reanalysis data to provide a large-scale context, trajectory calculations to track air mass evolution, Lagrangian Large-Eddy Simulations (LES) to demonstrate the involved atmosphere-cloud processes in detail, regional limited-area modeling (LAM) to explore the sensitivity of the intrusion to moisture parameters, and finally MOSAiC and novel satellite observations to verify model results and offer insight into atmosphere-surface interactions.

TABLE 1 **Overview of MOSAiC measurements used in this study. For all analyses, the original data was averaged to hourly means.**

Variable	Instrument	Sampling	References
Near-surface temperature, relative humidity, air pressure, atmospheric SEB components (turbulent and radiative fluxes)	Met Tower and two autonomous Atmospheric Surface Flux Stations	1 min	Shupe et al. (2022)
			Riihimaki (2022)
			Cox et al. (2021a); Cox et al. (2021b); Cox et al. (2021c); Cox et al. (2021d)
Integrated water vapor, liquid water path	HATPRO microwave radiometer	1 s	Walbröl et al. (2022)
Vertical profiles of cloud liquid and ice water content, ice water path	Cloudnet algorithm: combination of cloud radar, lidar and microwave radiometer	30 s	Illingworth et al. (2007)
Snowfall rate	SLALOM-CT algorithm: based on satellite-borne microwave radiometers	1 h	Sanó et al. (2022)
			Camplani et al. (2021)
	KAZR Ka-Band Zenith Radar	30 s	Matrosov et al. (2022)
	Pluvio weighing bucket precipitation gauge	1 min	Cromwell and Bartholomew (2022)

2.1 Observations

We use the MOSAiC measurements listed in Table 1 for the evaluation of the simulations. For details of the observational data, we refer to the references given in the table. Near-surface temperature, relative humidity, air pressure, and atmospheric SEB observations (consisting of radiative, turbulent sensible and latent heat fluxes) are obtained from the Met Tower and two autonomous Atmospheric Surface Flux Stations (Shupe et al., 2022). Data from the Humidity and Temperature Profiler (HATPRO) is used (Walbröl et al., 2022), from which Integrated Water Vapor (IWV) and Liquid Water Path (LWP) data are derived. Remote sensing measurements from cloud radar, lidar and microwave radiometer at RV Polarstern are combined *via* the Cloudnet algorithm to investigate the vertical distribution of cloud liquid and ice water content (LWC and IWC) (Illingworth et al., 2007). The ice water path (IWP) is calculated by vertical integration of the IWC profiles. As Cloudnet does not differentiate between suspended and falling solid hydrometeors, it actually outputs the combined ice and snow water path (IWP + SWP).

Due to the high uncertainty of snowfall measurements, we base our analysis on ERA5 reanalysis data and on three additional observational sources. i) Satellite data: The surface snowfall rate estimates are obtained from the Advanced Technology Microwave Sounder observations (ATMS) by using the Snow retrievaL ALgorithm fOr gpM–Cross Track (SLALOM-CT) (Sanó et al., 2022). The ATMS instrument provides global coverage and a relatively short revisit time at high latitudes of about one hour. The high frequency channels are the most sensitive to the presence of snow in the atmosphere (Weng et al., 2012). ATMS observations from the near-polar orbiting satellites Suomi National Polar-orbiting Partnership (SNPP) and NOAA-20 are used in this work. ii) Ka-Band Zenith Radar (KAZR): The snowfall rate has been calculated at the MOSAiC site using the radar reflectivity (Matrosov et al., 2022). iii) Pluvio: This is a weighing bucket precipitation gauge (Cromwell and Bartholomew, 2022). During MOSAiC, Pluvio was installed at the ice camp and sheltered by a double windshield to reduce the influences of blowing snow.

2.2 Reanalysis data

We use the European Centre for Medium-range Weather Forecast's (ECMWF) fifth generation reanalysis data set ERA5 (Hersbach et al., 2020), which is appropriate here because of its high resolution, both horizontally (ca. 30 km) and temporally (1-hourly), and the advanced 4D-var assimilation scheme. Compared to observations and other reanalyses, ERA5 offers an improved performance over the Arctic (Graham et al., 2019a; b). The ERA5 data is used to characterize the integrated water vapor transport (IVT), IWV, air temperature at 2 m height (T_{2m}), equivalent potential temperature at 850 hPa (θ_e 850 hPa), mean sea level pressure (SLP), precipitation, snowfall, cloud properties, and SEB components.

2.3 Lagrangian trajectories

Lagrangian trajectories are calculated using LAGRANTO (Sprenger and Wernli, 2015). The required wind fields are retrieved from ERA5 reanalysis on 137 model levels and its native spatiotemporal resolution. ERA5 wind fields have been used in many recent studies relying on trajectory analysis in the Arctic (e.g., Ali and Pithan, 2020; You et al., 2021; 2022; Papritz et al., 2022). Notably, during the WAI period in mid-April 2020, 4 radiosondes were launched daily at different locations upstream of RV Polarstern, and additional 7 radiosondes daily directly from RV Polarstern. All of those were assimilated by ECMWF, which greatly helped to improve the Arctic forecast (ECMWF, 2020) as well as reliability of trajectory calculations.

To study the origin of the air masses that arrive at RV Polarstern, an extensive ensemble of trajectories is computed. The trajectories are initiated throughout the vertical column above the hourly position of RV Polarstern and calculated 5 days backward. Vertically, they are spaced from 0.1 km to 12 km above ground in 0.5 km steps. Horizontally, trajectory starting points are evenly spaced every 3 km in a circle of 20 km radius around RV Polarstern. For further analysis, statistics of ERA5-derived meteorological parameters during the previous 5 days along the trajectories are extracted. In a first step, the following statistics are calculated for each individual trajectory:

- lat_{med} (°N) Median latitude the air masses resided at.
- z_{min} (km) Minimum altitude the air masses resided at.
- $\Delta\theta$ K) Maximum change in potential temperature. This is calculated with respect to the final state above RV Polarstern. $\Delta\theta$ is positive (negative) if diabatic heating (cooling) dominated.
- Δq (g kg^{-1}) Maximum change in specific humidity. Δq is positive (negative) if moistening (loss of moisture) is the dominating mechanism along air mass drift towards RV Polarstern.
- WVT_{max} (g kg^{-1} m s^{-1}) Maximum water vapor transport. This is calculated as the product of specific humidity and scalar wind speed, and is not to be confused with IVT (which is vertically integrated WVT).
- $\partial T/\partial t_{\mathrm{lhr,max}}$ (K d^{-1}) Maximum temperature tendency due to latent heat release during cloud formation. This is extracted from ERA5 model physics similarly as described by You et al. (2021).

In order to depict mean air mass properties, for each ensemble set started at an individual time and location, these statistics are then averaged (mean value).

We calculate further trajectories to investigate the large-scale flow. For this, the air parcels are started in a box evenly spaced every 30 km along latitude/longitude, spanning 5°W to 30°E and 81–87°N (i.e., centered around RV Polarstern; see Supplementary Figure S1). Calculations are started on 19 April 2020, 12 UTC, and extended 24 h backward and 30 h forward in time. Vertically, air parcels are started at pressure levels between 700 hPa and 950 hPa in 10 hPa steps. Similar to others (e.g., You et al., 2021), we extract ensemble averages of meteorological parameters along the trajectories.

2.4 Atmospheric river detection

To estimate the precipitation caused by the WAIs, the spatial shape of the WAIs is approximated by applying the atmospheric river detection algorithm of Guan et al. (2018) and using ERA5 reanalysis data. In this algorithm, the shape of the atmospheric river component of the WAI is constrained by the following characteristics: i) For each grid point, IVT must at least exceed the local 85th percentile from climatology, ii) The overall length must be a minimum of 2,000 km, and iii) The length/width ratio must be greater than 2. If an IVT object obtained *via* the 85th percentile threshold fails to fulfill geometric requirements, IVT thresholds are incrementally increased. A maximum 95th percentile threshold is used.

2.5 Large-scale energy transport and circulation regimes

The vertically integrated atmospheric horizontal energy transport (*IET*) is calculated and split into latent and dry static components following Graversen and Burtu (2016):

$$\boldsymbol{IET} = \underbrace{\overbrace{\int_{p_s}^{0} \vec{v} q \mathrm{L_v} \frac{\mathrm{d}p}{\mathrm{g}}}^{\text{latent}} + \overbrace{\int_{p_s}^{0} \vec{v} \left(\mathrm{c_p} T + \mathrm{g}z\right) \frac{\mathrm{d}p}{\mathrm{g}}}^{\text{dry static}}}_{\text{moist static}} + \int_{p_s}^{0} \vec{v} \frac{1}{2} (\vec{v})^2 \frac{\mathrm{d}p}{\mathrm{g}}$$

where p is pressure (hPa), p_s surface pressure (hPa), $\vec{v} = (u,v)$ horizontal wind vector with components u and v (m s^{-1}), $\mathrm{L_v}$ = 2,260 kJ kg^{-1} the latent heat of vaporization, q specific humidity (kg kg^{-1}), $\mathrm{c_p}$ = 1.005 kJ kg^{-1} K^{-1} specific heat capacity at constant pressure, T temperature (K), g = 9.81 m s^{-2} gravitational acceleration, and z height (m).

Horizontal energy transport is calculated from 6-hourly data of ERA5 reanalysis on model levels before vertical integration and daily averaging is performed. As suggested by Trenberth (1991) and used in several recent publications (e.g., Lembo et al., 2019; Liu et al., 2020), a barotropic wind-field correction is applied to the wind before the calculations of the energy transport is done to account for spurious mass-fluxes due to the assimilation procedure of reanalyses. Climatological values are calculated from all April days of the years 1979–2020. The net energy transport across the Arctic Circle is derived from the meridional component of the vertically integrated energy transport and integration along 66.3°N.

To identify preferred states of the large-scale atmospheric circulation, the regime analysis described in Crasemann et al. (2017) is applied to daily ERA5 SLP anomalies of spring (March to June) 1979–2020 over the North-Atlantic/European region. In order to determine five atmospheric circulation regimes, a k-means clustering algorithm is carried out in a reduced phase space spanned by the five leading empirical orthogonal functions (Hannachi et al., 2017; Falkena et al., 2020).

2.6 High-resolution process modeling

2.6.1 Large-Eddy simulations (LES)

The transformation of an Arctic air mass is studied using targeted LES experiments at turbulence- and cloud-resolving resolutions similar to Bretherton et al. (1999, 2010). In this method, the upper-level profile above the boundary layer and the surface boundary condition remain tightly constrained by reanalysis or observational data. In contrast, the resolved turbulence and associated mixed-phase clouds inside the LES domain are free to develop, and can respond to the changing meteorological conditions along the trajectory. In this setting the transformation can be investigated at process level, for example, through targeted sensitivity experiments on conditions of interest.

Lagrangian LES are performed with the DALES code (Heus et al., 2010) and forced by ERA5 data, following the method introduced by Van Laar et al. (2019) and Neggers et al. (2019). Nudging is applied above the thermal inversion, which marks the boundary layer top. Nudging linearly increases in intensity across a 1 km deep transition layer towards full nudging above, at a relaxation timescale of 30 min. Below the inversion, no nudging is applied, leaving the turbulence and clouds free to develop. For radiation, a multi-waveband transfer model is used in combination with a Monte Carlo approach (Pincus and Stevens, 2009). The microphysics follow a two-moment scheme with the five hydrometeor types of Seifert and Beheng (2006), albeit with the following modification: The Cloud Condensation Nuclei (CCN) concentration (N_{CCN}) is prognostic, meaning it can evolve from its initial value as a result of processes such as advection, diffusion, and microphysical transformations. Simulations with three different N_{CCN} are conducted, with the following rationale: i) $N_{CCN} = 10$ cm^{-3} represents very clean conditions, ii) $N_{CCN} = 100$ cm^{-3} is typical for the wintertime Arctic, and iii) $N_{CCN} = 1{,}000$ cm^{-3} is a highly polluted state; latter order of magnitude has recently been reported for the first half of the WAI event observed in mid-April 2020 (Dada et al., 2022). The simulations are initialized upstream of RV Polarstern at 0 UTC on 19 April. The LES domain is a cube with a length of 12.8 km in all three directions. The resolution of the simulation is 50 m in both horizontal directions. To prevent reflection of gravity waves from the domain top, a sponge layer is applied in the top 25% of the domain. The vertical resolution is telescopic, starting with 20 m at the bottom of the boundary layer and extending with altitude to 140 m at the top of the domain.

2.6.2 Limited area modeling (ICON-LAM)

To study the moisture intrusion event on a large scale with high resolution, we use the German weather and climate model ICON (Icosahedral Non-hydrostatic Model; Zängl et al., 2014) in the limited area mode (ICON-LAM). Simulations are performed over a circum-Arctic domain (covering 65–90°N) at a 6 km horizontal resolution (R03B08 in ICON terminology). The simulations are initialized from global ICON analysis at 13.15 km resolution (R03B07), which also serves as the 3-hourly lateral and lower boundary forcing. Our setup uses the single-moment microphysics scheme (Doms et al., 2011), which predicts the specific mass content of five hydrometeor categories (cloud liquid water, rain water, cloud ice, snow, graupel), and is recommended for LAM simulations (Prill et al., 2020). For radiation, the ecRad from ECMWF (Hogan and Bozzo, 2018) and for shallow convection the Tiedtke–Bechtold convection scheme (Tiedtke, 1989; Bechtold et al., 2008) are applied. A bulk-thermodynamic sea-ice model (Mironov et al., 2012) is applied with an adjusted heat capacity as introduced by Littmann (2022). For more details on the ICON model and its LAM setup we refer to Prill et al. (2020) and Bresson et al. (2022).

ICON-LAM is used to explore the sensitivity of the WAI with respect to the moisture inflow. In a sensitivity run, the amount of moisture at the lateral boundaries is reduced by a maximum of 30% (Supplementary Figure S1). To ensure that the reduction is only applied at the longitudes where the WAI penetrates into the Arctic, the specific humidity at the boundaries is multiplied by a Gaussian distribution centered at 330°E with a standard deviation of 15°. The reduction by a maximum of 30% is chosen as the event was characterized by about 30% higher IWV than climatology during this time and region, based on ERA5. The ICON-LAM simulations are initialized on 17 April at 18 UTC and run until 21 April, 0 UTC. We analyze hourly output at a latitude-longitude-grid with 0.054° spacing.

3 Results and discussion

We bring the broad range of observational and modeling tools together to describe key aspects of the mid-April 2020 WAI. The analysis first addresses the large-scale setting of the event (Section 3.1). Next, it focuses on the characteristics of the WAI as it passed over RV Polarstern, using the unique MOSAiC observations (Section 3.2). Expanding the Eulerian viewpoint with Lagrangian trajectory analysis, the evolution of the air masses along their drift into the Arctic is discussed (Section 3.3). We examine how the air masses observed at RV Polarstern relate to their origin, and how variations in the initial conditions, such as CCN concentration or lateral moisture influx, may impact the atmospheric state as observed at the shipborne site, and further downstream in the central Arctic. Finally, the impacts of this WAI on the surface are quantified (Section 3.4).

3.1 Large-scale setting of the event

3.1.1 Synoptic overview and circulation regimes

The WAI event consists of two distinct, consecutive intrusions characterized by record-breaking anomalies in T_{2m} as well as in IWV (Rinke et al., 2021; Section 3.2). In terms of preferred atmospheric circulation regimes (Figure 1A), the initiation of these intense transport events is characterized by a transition from an Icelandic high - Siberian low dipole to a positive North Atlantic Oscillation pattern persisting between 13–19 April.

For the first intrusion, which peaks at the MOSAiC site on 16 April, a corridor of increased IVT and IWV (Figures 1B, D) originating in northwestern Russia and passing the Barents Sea is found (Supplementary Figure S2). In the Barents Sea region, the event is associated with T_{2m} anomalies exceeding climatological mean values (1979–2020, ERA5) by 8 K. Synoptically, a low-pressure system just west of Svalbard and a high-pressure system to the northeast of Novaya Zemlya facilitate this transport. The resulting pressure dipole pushes warm and moist air northwards. Observations of high aerosol particle concentrations at the MOSAiC site support an origin in the vicinity of industrial activities in northwestern Russia (Dada et al., 2022).

Three days later, on 19 April and during the second intrusion peak recorded by MOSAiC (Figures 1C, E), the low pressure system shifts towards the northeast of Greenland while two high pressure systems evolve, centered around Novaya Zemlya and Norway. Accordingly, the 20–21 April circulation is classified as Scandinavian blocking (Figure 1A), which favors warm and moist air transport across the Fram Strait. This agrees with previous findings that episodes of WAIs to the Arctic are often related to Scandinavian/Ural blocking (Henderson et al., 2021). As a result, a corridor of IVT above 300 kg m^{-1} s^{-1} forms from the North Atlantic over Iceland towards the central Arctic. Our trajectory analyses show that the corridor during 2020 is initially positioned over Greenland, and only later shifts to the Fram Strait/Iceland region (Section 3.2). In springtime, the North Atlantic WAI corridor is climatologically favored and has been reported to yield the most intense events (e.g., Mewes and Jacobi, 2019; Nygård et al., 2020; Papritz et al., 2022).

3.1.2 Meridional energy transport

The WAI is characterized by an increased horizontal transport of moist static energy (Figure 2A). The transport anomalies occur along two pathways: While the first intrusion (16 April) shows a connection to the West-Siberian

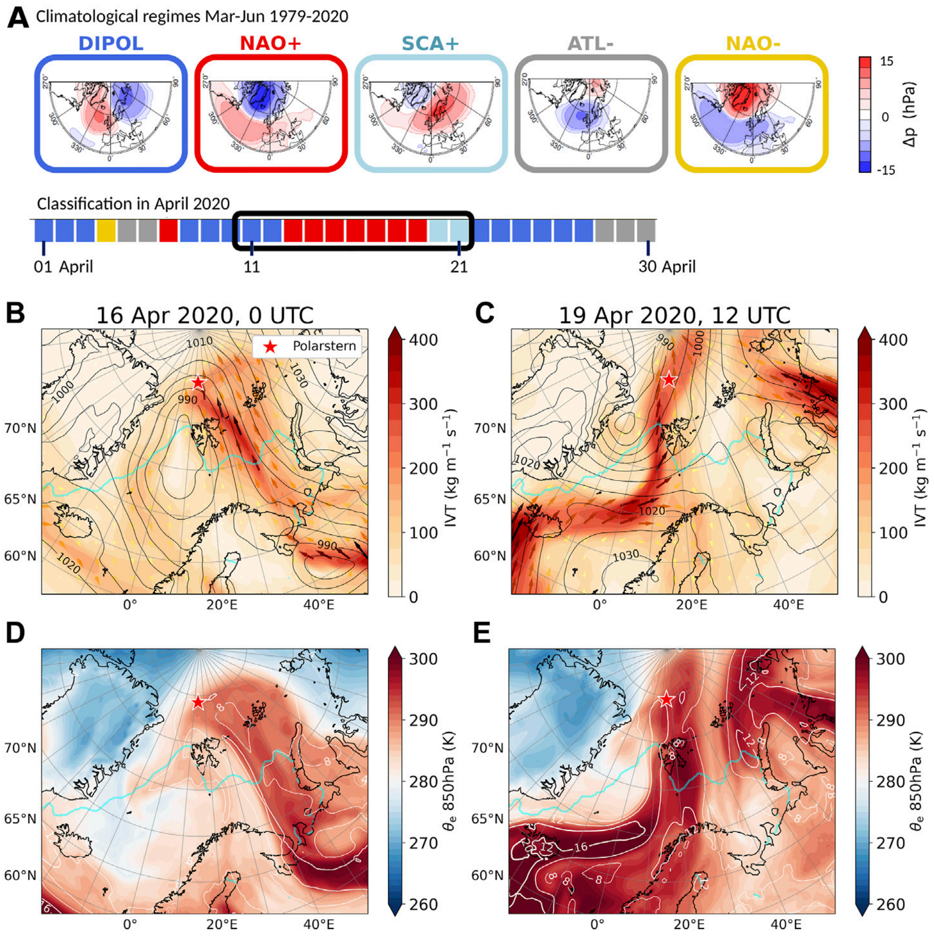

FIGURE 1
(A) Spring circulation regimes in ERA5 reanalysis. Upper panel: five preferred circulation regime patterns during spring time (MAMJ) identified as dipole (DIPOL), positive and negative North Atlantic Oscillation (NAO+, NAO-), Scandinavian blocking (SCA+) and Atlantic low (ATL-). Lower panel: classification during April 2020, with 11–21 April 2020 marked by a black frame. **(B–E)** Synoptic overview based on ERA5 centered on 16 April 2020, 0 UTC and 19 April 2020, 12 UTC. **(B,C)** IVT (color shading and arrows), sea level pressure (black isobars; hPa); **(D,E)** 850 hPa equivalent potential temperature θ_e (color shading), IWV (white isolines; kg m^{-2}). In each graph the red star shows the locations of RV Polarstern and the cyan line indicates the sea-ice margin based on 15% sea-ice concentration from ERA5.

lowlands, the second one (19 April) is linked with an enhanced energy transport from the North Atlantic. This agrees with the already discussed large-scale flow. In this section, we focus on the latent energy transport, which strongly influences water vapor content and cloud formation. Compared to the April climatology, where the meridional latent energy transport has maxima over the Pacific and western North Atlantic/Eastern North America and is rather weak at higher latitudes, the two episodes in April 2020 stand out as intense poleward energy transport events.

The analysis of the daily net meridional transport of moist static energy and its latent energy component across the Arctic Circle shows that all days within 15–20 April exhibit strong poleward transport of energy (Figure 2B). The total moist static energy transport into the Arctic exceeds the 90th percentile of the April climatology for April 17, 19 and 20. While the moist static transport is dominated by the dry static component, the latent energy component shows the strongest anomalies. Here, all days between 15–19 April exceed the 90th percentile of the April climatology.

Splitting this further up into the Siberian lowland and Atlantic sections, even stronger anomalies emerge. The first intrusion episode with the pathway from West Siberia is exceptional, with the latent energy transport on 17 April above the 95th percentile of the climatology in that area. Indeed, studies have shown that this Siberian pathway is gaining importance in recent decades (Komatsu et al., 2018; Mewes and Jacobi, 2019). To explain this, several studies have linked the marked retreat of sea ice in the Barents Sea to enhanced local evaporation, moistening, and cyclone-associated precipitation (e.g., Rinke et al., 2019; Crawford et al., 2022), while Pithan and Jung (2021) have questioned the role of local sea-ice changes for the atmospheric moisture budget.

During the second intrusion episode (18–20 April), which occurred along the North Atlantic pathway, the daily mean net latent energy transports range within the 90th-95th percentile of climatology in this area.

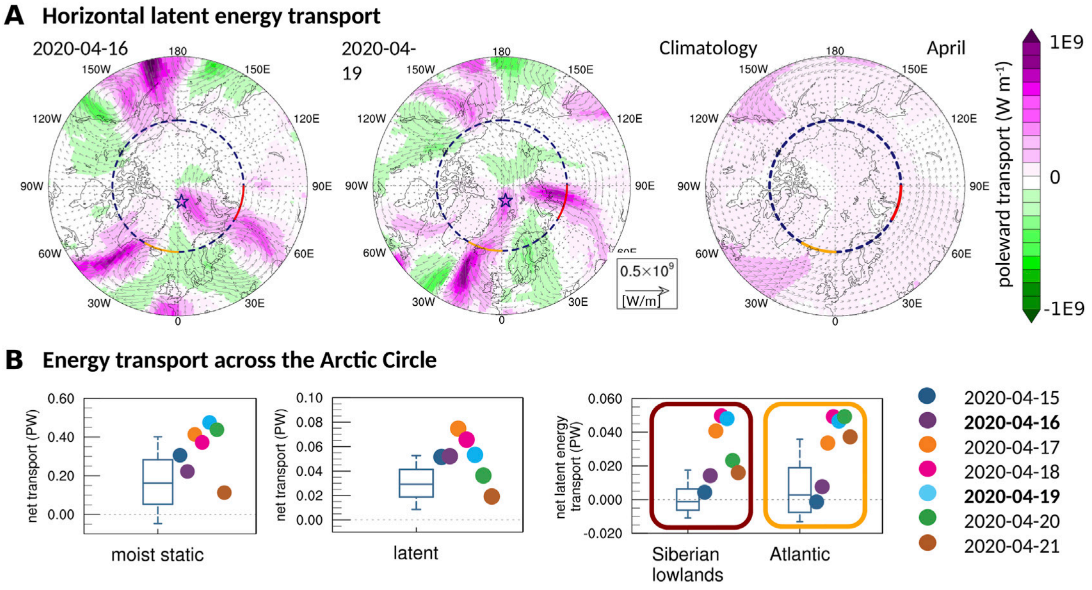

FIGURE 2
(A) Vertically integrated horizontal latent energy transport (arrows), poleward component (pink) and equatorward component (green) on 16 April (left), 19 April (middle), and April climatology from 1979–2020 (right), based on ERA5 reanalysis. The Arctic Circle is marked with a stippled line, the Atlantic segment in orange, the Siberian lowlands segment in red, the position of RV Polarstern with a star. **(B)** Daily mean net transport across the Arctic Circle in April; moist static energy (left), latent energy (middle), latent energy of Atlantic and Siberian lowlands segments (right). Box plots show the climatology of days in April 1979–2020 from ERA5 reanalysis. Whiskers show the lower decile, lower quartile, median, upper quartile, and upper decile. Colored dots indicate the days of April 2020, from 15 to 21 April.

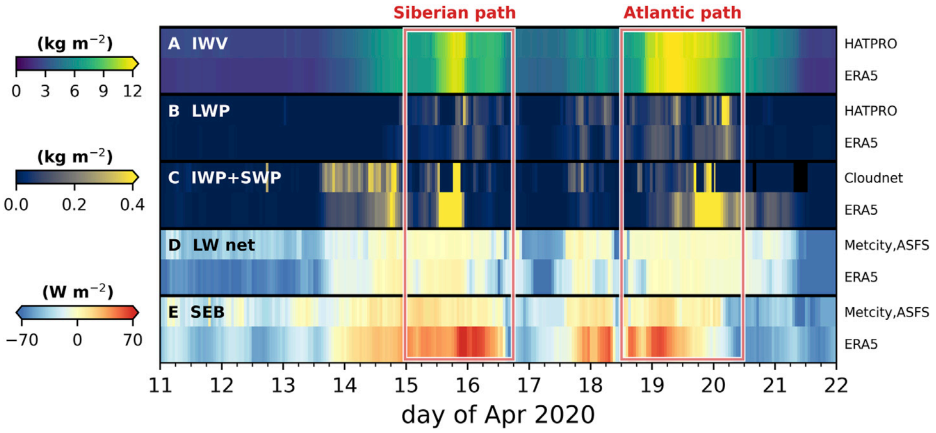

FIGURE 3
Comparison between observed and ERA5-extracted cloud and moisture parameters at RV Polarstern during mid-April 2020. The red boxes denote the peak time periods of the two subsequent episodes of the WAI, with their Siberian and Atlantic pathways. Shown are the hourly means of **(A)** IWV from HATPRO, **(B)** LWP from HATPRO, **(C)** IWP+SWP based on Cloudnet observations, **(D)** longwave net radiation (LW_{net}) from measurements at Met City and autonomous Atmospheric Surface Flux Stations (ASFS), **(E)** SEB, derived at Met City and ASFS. For LW_{net} and the SEB, downward fluxes are defined as positive. Included in each graph is also the ERA5 reference. Data sources are indicated on the right side.

3.2 Warm air intrusion as seen at RV Polarstern and its origin

The WAI was record-breaking and influenced the meteorological conditions in the central Arctic (Rinke et al., 2021; Walbröl et al., 2022). This is illustrated by the MOSAiC measurements at RV Polarstern, which show noticeable features during this event (Figure 3, Supplementary Figure S3). The pre-WAI background period of 11–13 April is characterized by low IWV ≅ 3 kg m^{-2} (Figure 3A), very little or no clouds (Figures 3B, C), strong radiative cooling of the surface with $LW_{net} \cong -50$ W m^{-2} (Figure 3D), and overall negative (neutral) SEB during night (day) (Figure 3E).

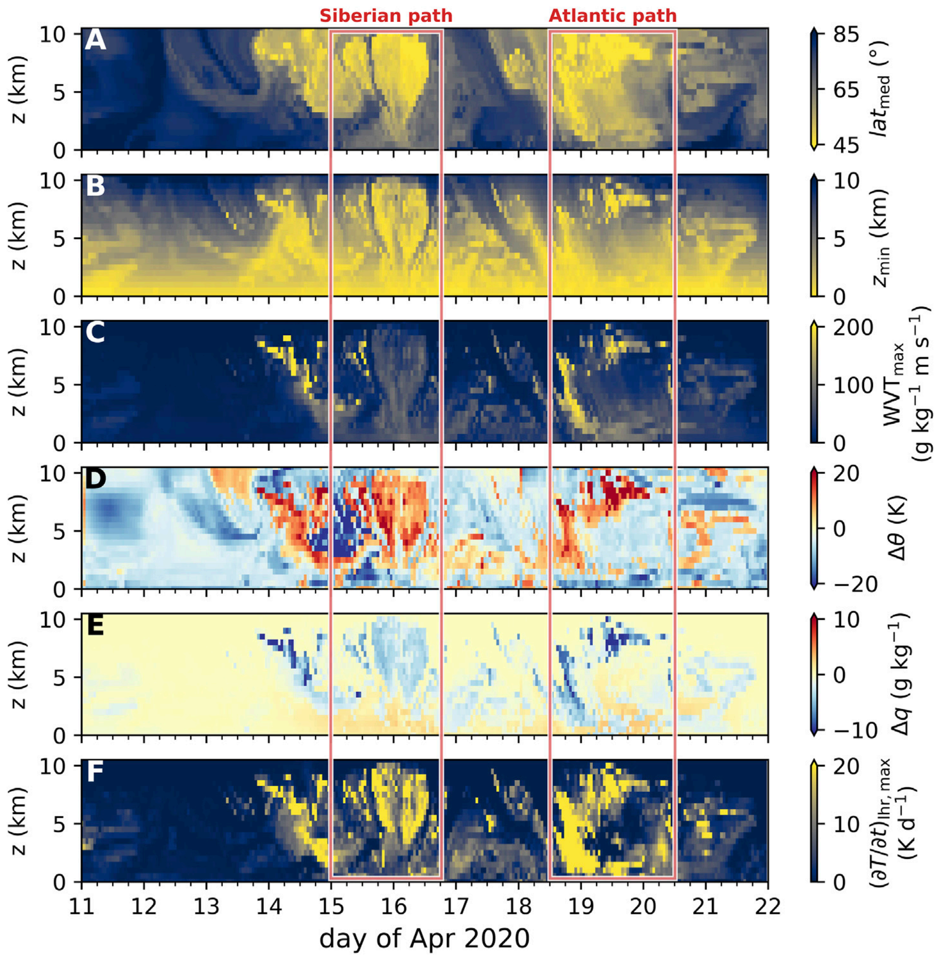

FIGURE 4
Characteristics of 5-day backward trajectories based on ERA5 starting at RV Polarstern for altitudes from the surface up to 10 km, mid-April 2020. Shown are **(A)** median latitude that the air masses occupied in the previous 5 days, **(B)** the lowest altitude at which air masses had resided, **(C)** maximum water vapor transport, **(D)** maximum change of potential temperature θ with respect to the final state, **(E)** maximum change of specific humidity q with respect to the state, and **(F)** maximum temperature tendency due to latent heat release during cloud formation.

Correspondingly, T_{2m} exhibits typical values of around −30°C (Supplementary Figure S3), with a weak diurnal cycle. Beginning on 14 April, this state is notably disturbed. A remarkable increase of IWV up to 12 kg m^{-2} is observed, with two maxima on 16 April 0 UTC and 19 April 12 UTC. This high IWV is accompanied by large amounts of cloud liquid and ice water and a transition towards a positive SEB (i.e., surface-heating). T_{2m} first approaches −2°C and finally 0°C. The surface is now effectively heated by the atmosphere, a crucial prerequisite for snow and ice melt. Interestingly, the largest deviations of the SEB in ERA5 from observations are dominated by biases in the LW_{net} under pristine conditions, but by turbulent fluxes during the WAI (Supplementary Figure S3). A bias of ERA5 in estimating LW_{net} has been explained by ERA5's assumption of a constant sea-ice thickness in combination with a missing insulating snow layer on sea ice (Batrak and Müller, 2019). This causes excessive near-surface air and skin temperatures, and thus overexaggerated upward longwave radiative fluxes. The partially quite strong offset in turbulent fluxes during the WAI period seems not to be caused by errors in wind speeds, as these are mostly reproduced well by ERA5 (Supplementary Figure S3). General errors in representing the vertical thermodynamic boundary layer structure and/or in turbulence parametrizations seem more likely, but a further investigation is beyond the scope of this study.

As discussed above, the air mass origin for the two consecutive intrusions differs quite remarkably (see Section 3.1). To provide more detailed insight, 5-day backward trajectories are calculated (Supplementary Figure S2). Figure 4A shows the median latitude that air parcels resided at in the previous 5 days before arriving at RV Polarstern in different altitudes. During the background period of 11–13 April, air masses at all altitudes are of Arctic origin ($lat_{\mathrm{med}} \geqq$ 70°N). On 14 April, this slowly changes. At first, only air masses at high altitudes (approx. 7 km–11 km above ground) originate from the mid-latitudes, with median latitudes within the previous 5 days partly below 45°N. With every additional hour, starting from the top of the troposphere, more air masses also at lower altitudes stem from the mid-latitudes. This reflects typical behavior of warm fronts. On 16 April at 0 UTC, the whole atmospheric column above RV Polarstern originates from latitudes below 50°N within the past

5 days. This large-scale link is disturbed on 17 April, with the arrival of more regional Arctic air masses. On 18 April, with the onset of the intrusion from the Atlantic pathway, a new link to lower latitudes is established, starting again at higher altitudes. As this second intrusion begins to recede on 20 April, some links to lower latitudes persist at medium to high altitudes.

To investigate the vertical movement of air masses, Figure 4B depicts the minimum altitude that air parcels occupied in the prior 5 days. During the pre-WAI background period, air masses typically remain relatively close to their arrival height throughout their 5-day drift, which implies the absence of strong vertical displacement. With the arrival of mid-latitude air masses around 14 April, this pattern abruptly changes. Some air parcels observed at 8 km–9 km above RV Polarstern originate close to the surface, i.e., they ascended 8 km–9 km within 5 days. Interestingly, some of these ascended air parcels previously contributed strongly to water vapor transport within the WAI (Figure 4C). In fact, the most extreme values for water vapor transport occur for air masses ending at high altitudes above the MOSAiC site (z>6 km; 14 April, 0–24 UTC and from 18 April, 12 UTC to 19 April, 24 UTC). These are altitudes at which MOSAiC radiosondes observe only very little water vapor (Supplementary Figure S3). This highlights the dynamic nature of WAIs, where air masses constantly enter and exit the corridor of moisture transport convergence.

To further study key mechanisms during air mass transport as related to thermodynamics, the maximum changes of potential temperature ($\Delta\theta$) and specific humidity (Δq) along trajectories with respect to the final state at RV Polarstern are traced (Figures 4D, E). Generally, air masses arriving in the Arctic are dominantly subjected to diabatic cooling ($\Delta\theta$<0 K), mostly *via* longwave radiation (not shown). This pattern is broken for the strongly ascending air masses, where diabatic heating dominates ($\Delta\theta$>0 K), and extreme $\Delta\theta$ up to +20 K in 5 days are found. Here, a strong loss of water vapor occurred (Δq partly below −10 g kg^{-1}). This triggered intense latent heat release during cloud formation (Figure 4F), causing the extreme diabatic heating. Such heated air parcels show elevated buoyancy and therefore a greatly accelerated further ascent with or without the presence of a polar dome (Komatsu et al., 2018). In our case, this allowed some air masses to ascend over the steep Greenland orography before reaching the central Arctic (now shown). Furthermore, the lifting and moist-diabatic heating introduces negative potential vorticity anomalies to upper tropospheric levels, a fundamental prerequisite for atmospheric blocking and therefore WAI formation (You et al., 2021; 2022; Murto et al., 2022). Lifting typically occurs 1–6 days before blocking formation in rising branches of mid-latitude cyclones, often over the Atlantic basin. Our values for $\Delta\theta$ and Δq both roughly equal the upper 90th climatological percentile as reported by Murto et al. (2022) for the 50 most extreme high-Arctic wintertime WAIs 1979–2016. Similarly, we also detect the ascent region in close vicinity to Atlantic cyclones south of Greenland (not shown), and likewise find two subsequent warm extremes in short succession, which can be caused by a single blocking. Finally, in contrast to the strongly ascending air masses, the air arriving at RV Polarstern near the surface (z<3 km) typically experienced slight moistening and only medium water vapor transport and continuous longwave cooling on their path northwards.

To summarize this chapter, the observed double-episode WAI impacts not only the lowest layers of the Arctic atmosphere, but leaves its fingerprints on air masses reaching up to 10 km. Thus, the whole troposphere is influenced by the intrusion (Figure 4, Supplementary Figure S3A).

3.3 Air mass transformation

In this section, the evolution of the air mass along its poleward trajectory is analyzed, with focus on cloud formation and development. To estimate the role of two key cloud-determining factors, namely, CCN concentration and moisture availability, we set up dedicated LES and ICON-LAM simulation experiments (Section 2.6). In the following detailed analysis, we focus on the 19 April episode with the Atlantic pathway, centered around 12 UTC. This second intrusion peak is chosen because i) it is characterized by high temperature and moisture extremes (Supplementary Figure S3), ii) it has not been analyzed yet in the literature, and iii) it follows the climatologically more common pathway into the Arctic (as shown in Figure 2).

Figure 5A shows the temporal development of ensemble-averaged cloud LWC and IWC profiles along the trajectories (LAGRANTO calculations based on ERA5 input). In order to indicate environmental boundary conditions, the sea-ice concentration as well as the assumed clear-sky downward solar radiation are additionally depicted at the bottom and top of the graph, respectively. 16 h before encountering RV Polarstern, over the marginal sea ice zone, large amounts of liquid clouds start to form. 12 h–18 h after encountering RV Polarstern, the thick liquid cloud splits into two decks, which hints towards internal decoupling. A comparison with the cloud observations at RV Polarstern (Figure 5C) shows that the ERA5 structure of a low-level liquid-water containing cloud topped by a high-level ice cloud is realistic.

Cloud processes critically depend on moisture availability, and therefore a targeted sensitivity experiment (EXP) with ICON-LAM is set up, where the lateral moisture inflow is reduced by up to 30% (see Section 2.6; Supplementary Figure S1). The calculations with LAGRANTO based on the ICON-LAM output show that the control run (CTRL) reflects the general observed cloud structure (Figure 5C). However, we recognize some differences in the boundary layer, at least for the snapshot around 10–12 UTC. Compared to radiosondes, the model in the lowest ca. 1 km is slightly warmer and moister. We also see differences between the simulated cloud ice content and Cloudnet observations in the boundary layer. These mainly stem from the fact that the model output represents the ice only, while the observations represent the combined ice and snow water. But importantly, the cloud liquid water is simulated realistically by ICON (Figure 5C, Supplementary Figure S3B), and this is the key for the cloud radiative effect, which we discuss in Section 3.4.

Next, the focus is set on the sensitivity of the ICON simulations. The drier atmosphere in EXP naturally generates higher surface moisture fluxes (Section 3.4), serving to mitigate the perturbation. Still, all the way from the ocean to the marginal sea ice zone, the formation of liquid water and ice clouds is strongly delayed in EXP vs. CTRL (Figure 5B). Even more notably, during the drift further into the central Arctic (t>0 h, north of RV Polarstern), similar or

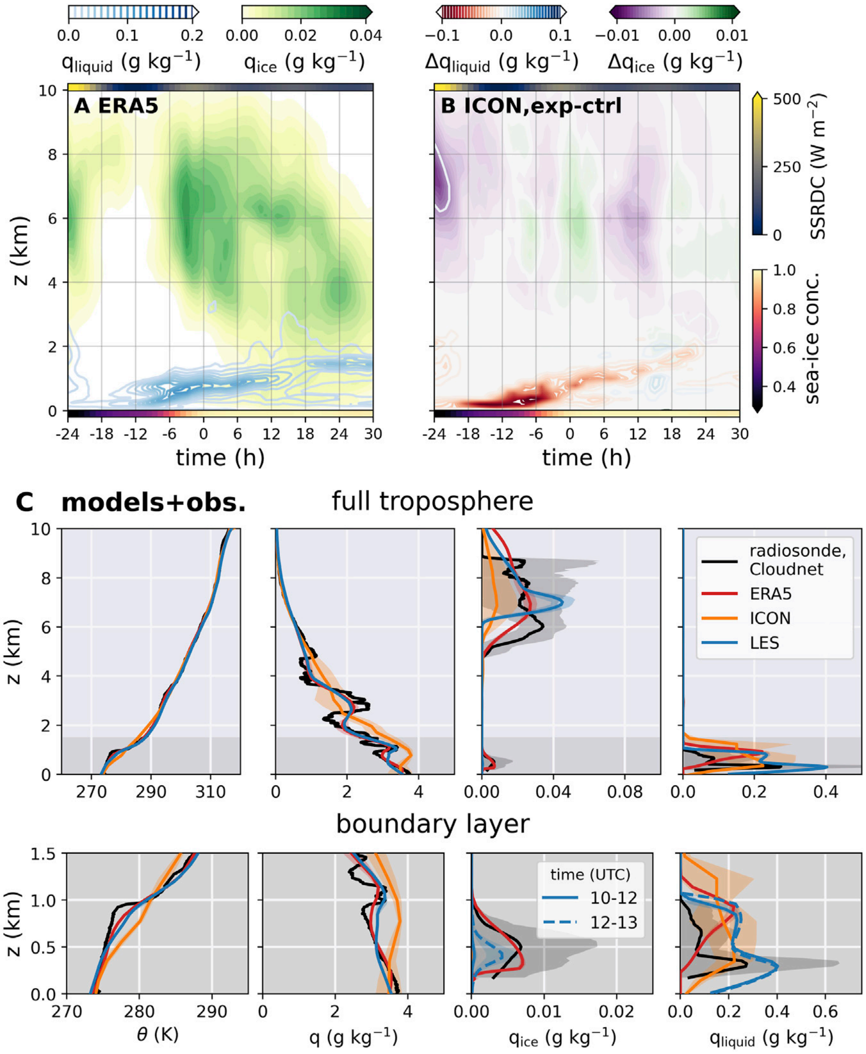

FIGURE 5
(A,B) Height-time cross sections of LWC (q_{liquid}, in blue) and IWC (q_{ice}, in green) along trajectories covering 24 h backward and 30 h forward with time. *t* = 0 h references 19 April 2020, 12 UTC, at RV Polarstern. Colored line at top of graphs: ERA5-based surface shortwave downward radiation under clear-sky conditions (SSRDC), colored line at bottom of graphs: ERA5-based sea-ice concentration. **(A)** LWC and IWC along the air mass trajectories based on ERA5, **(B)** LWC and IWC differences "EXP−CTRL" based on ICON-LAM. **(C)** Vertical thermodynamic and cloud profiles simulated and observed at RV Polarstern on 19 April, averaged for 10–12 UTC. Shown are the outputs from ERA5, control runs of the process models (LES, ICON-LAM) as well as observations from Cloudnet and radiosonde (launched at 11 UTC). Upper panel: profile covering altitudes of 0 km–10 km, bottom panel: zoomed into lowest levels covering 0 km–1.5 km.

shortly even higher cloud water contents are found in the reduced moisture EXP. This occurs because in EXP lower temperatures are required for the air masses temperature to significantly drop below the dew point, and these temperatures are only encountered later during the poleward drift, over sea ice. Here, the CTRL clouds have already experienced significant moisture loss *via* precipitation (see Section 3.4)–a process that takes place later in EXP. Overall, this shift in timing leads to a rather counterintuitive result: While the higher moisture influx of CTRL features much higher cloud water contents over the ocean and marginal sea ice zone, strong precipitation formation over these regions leads to a central Arctic state where the cloud LWC is comparable between CTRL and EXP. Crucially, LWP values larger than 30 g m^{-2}, typically associated with a radiatively opaque state and saturated longwave cloud radiative forcing (Shupe et al., 2022), are maintained for both simulations for the initial 24 h drift into the central Arctic beyond RV Polarstern. The implications of this finding for the SEB will be discussed in Section 3.4.1.

A further factor that strongly impacts cloud formation is the availability of CCNs, a process that is investigated using Lagrangian LES experiments with the DALES model (Section 2.6). The simulations are initialized upstream of RV Polarstern at 0 UTC on 19 April. Following the low-level flow of air masses, the simulated domain arrives at RV Polarstern at 11 UTC, timed to coincide with a radiosonde launch. Figure 6A depicts the cloud LWC and IWC of the control simulations, using an initial N_{CCN} of 100 cm^{-3}. During the approach to the MOSAiC site, a well-defined low-level stratocumulus cloud layer develops. This cloud layer is

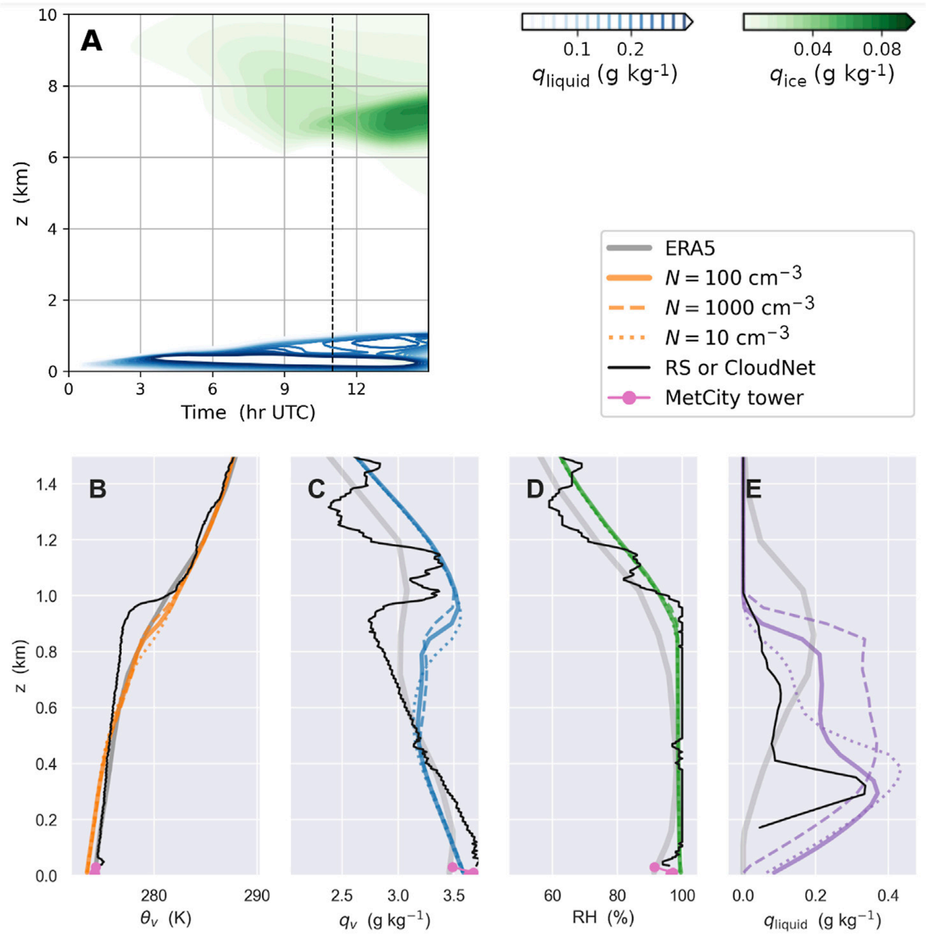

FIGURE 6
Results from Lagrangian LES simulations with the DALES code for 19 April 2020. **Upper panel: (A)** Height-time cross sections of cloud LWC (q_{liquid}, in blue) and IWC (q_{ice}, in green). The dashed black line at 11 UTC indicates the air mass arrival time at RV Polarstern. **Lower panels:** Domain-averaged thermodynamic profiles at 11 UTC of **(B)** virtual potential temperature θ_v, **(C)** water vapor specific humidity q_v, **(D)** relative humidity RH and **(E)** cloud liquid water specific humidity q_{liquid}. Three LES experiments are shown in orange, with *N* indicating the initial CCN concentration in cm^{-3} (dashed, solid and dotted). The radiosonde (RS) and Cloudnet data are shown in black, the 10 m Met Tower data in pink, and ERA5 in gray.

predominantly of liquid phase, due to the unusually high near-surface air temperatures. At higher altitudes, a relatively thick ice layer is present. The comparison to Figure 5A illustrates that this simulated cloud structure resembles that of ERA5 along the trajectory, which is expected since ERA5 is used to force the LES. At RV Polarstern, the LES captures the observed overall cloud structure (Figure 5C). The liquid-water cloud layer constantly deepens during the air mass drift and later develops a double peak in liquid water similar to the Cloudnet observations.

In addition to the control simulation, two sensitivity experiments are performed, in which the initial CCN concentration N_{CCN} is altered (Figures 6B–E). One reflects pristine Arctic conditions (N_{CCN} = 10 cm^{-3}), the other represents the polluted continental concentrations observed at RV Polarstern during this period (N_{CCN} = 1,000 cm^{-3}; Dada et al., 2022). This range reflects the observed variation during the selected days, and thus guides the sensitivity experiment. With the basic observed boundary-layer state already reproduced to a reasonable degree in the control experiment, thus one single aspect (the CCN concentration) is varied in a virtual laboratory setting, to assess its impact while keeping all other factors constant. In doing so, it is possible to gain insight into how the CCN concentration can affect the boundary layer structure on its way to RV Polarstern. When interpreting the outcome of the sensitivity test, it should be considered that the imposed large-scale forcings and boundary conditions still carry significant uncertainty, mainly due to a lack of measurements in upstream areas. We thus do not seek perfect agreement with the observations at RV Polarstern; instead, the main goal is to understand impacts, given the observed CCN range.

Several things can be noted by comparing the different LES runs. The impact of CCN concentrations on the boundary layer, in particular on the inversion height, is evident. The polluted air masses feature a slightly deeper boundary layer, exceeding that of the pristine simulation by approximately 100 m and agreeing best with the radiosonde data. The vertical structure and amount of the low-level liquid water clouds changes substantially as well, such that more liquid water occurs at the top part of the cloud in the polluted simulation. The interrelated mechanisms that take place works as

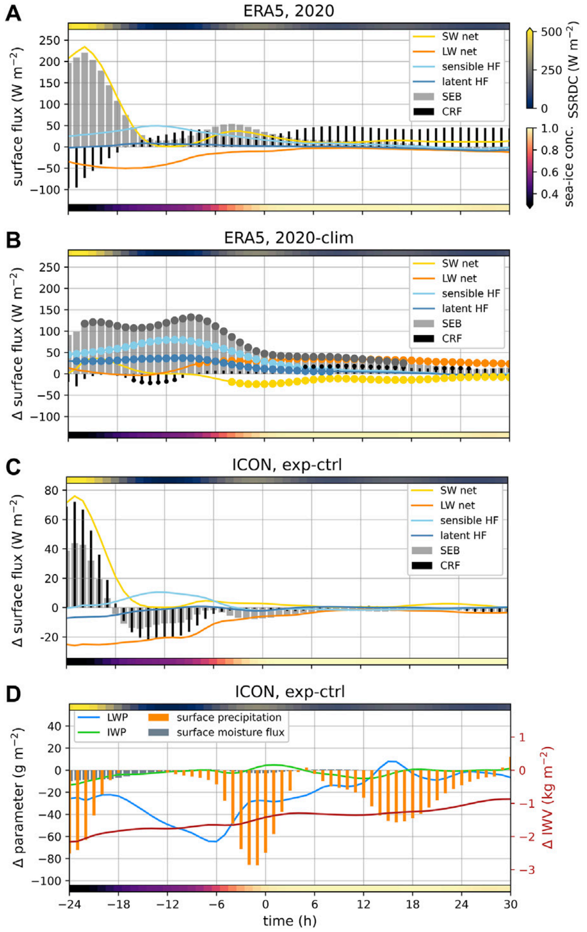

FIGURE 7

(A–C) Time series of the SEB and its components (net short- and longwave SW and LW, sensible and latent heat fluxes HF), as well as CRF along trajectories. At the top of each graph, ERA5-based surface shortwave downward radiation under clear-sky conditions (SSRDC) is depicted. At the bottom of each graph, ERA5-based sea-ice concentration is shown. Time is relative to 19 April, 12 UTC. **(A)** ERA5 reanalysis, 2020 event **(B)** Difference of 2020 WAI minus 1979–2020 climatology, based on ERA5. Dots indicate timesteps where surface fluxes exceed one climatological standard deviation. **(C)** Differences EXP-CTRL based on ICON-LAM simulations. **(D)** As in **(C)** but for LWP and IWP, IWV, surface precipitation and surface moisture flux.

follows: With larger N_{CCN}, the cloud LWC increases. Accordingly, increased longwave cooling at the (now sharper) cloud top makes radiatively driven entrainment more efficient and deepens the boundary layer (Stevens et al., 2005). The intensified entrainment warming partially counteracts the cloud top cooling. These presented mechanisms align well with the findings of Chylik et al. (2021) who employed a LES on a case observed during the ACLOUD field campaign in the Fram Strait (Wendisch et al., 2019).

According to our simulations, this mechanism may also play a role in air mass transformation during WAIs, and may impact the lifetime of cloudy air masses through modification of precipitation. It moreover highlights that accurate observations of N_{CCN} are needed for realistic model simulations of cloud processes in WAIs.

Another finding is the importance of correctly assed cooling rates. The zoom-in to the boundary layer in Figure 5C compares results using data that is extended from the original 10–12 UTC time window to 12–13 UTC. By allowing the air mass to drift and cool just 1 h longer, sufficient cooling triggers the formation of a low-level mixed phase cloud with q_{ice}>0 g kg^{-1}. This is better in line with the Cloudnet observations, which also show a mixed-phase cloud instead of a pure liquid-phase cloud.

3.4 Surface impact

3.4.1 Surface energy budget

The aforementioned cloud changes during the air mass transformation along the WAI path are expected to impact the SEB, which we further discuss in this section. We continue our focus on the 19 April episode. To directly attribute changes in SEB to the intrusion, we again apply the Lagrangian approach and examine the SEB components from ERA5 along the calculated air mass trajectories. We define the SEB as the sum of the radiative and turbulent heat fluxes. Fluxes towards the surface are defined as positive, i.e., warming the surface.

Figure 7A shows the ERA5-LAGRANTO-derived components of the SEB along the trajectory, as well as environmental conditions (sea-ice concentration, surface downward solar radiation under clear sky assumption). In the 24 h preceding its arrival above RV Polarstern, the air mass traverses the ocean and marginal sea ice zone to the east of Greenland, eventually reaching the consolidated ice pack (Supplementary Figures S1, S2). Strongly positive daytime values of the SEB of above +200 W m^{-2} and strong sensible heat fluxes from the atmosphere to the surface of up to + 50 W m^{-2} are found. The surface net cloud radiative forcing (CRF) is strongly negative as large as −100 W m^{-2}, indicating a cooling effect of clouds over the ocean and marginal sea ice zone, in part because of the high shortwave radiation at this time of day. CRF is mediated by thick ice clouds, as liquid-water containing clouds are still mostly absent (see Figure 5A). Furthermore, the absence of liquid cloud water correlates with negligible longwave CRF (i.e., warming) and allows for an efficient surface radiative cooling.

During the course of the next few days with cloud formation and the track over the ice, turbulent heat fluxes decrease. CRF is now exclusively positive in the range from +25 W m^{-2} to +50 W m^{-2} (warming longwave CRF), with slightly reduced values during daytime (cooling shortwave CRF). The longwave net radiation rises to around 0 W m^{-2}, indicating that strong downward longwave fluxes cancel the upward-directed longwave cooling. The resulting net SEB decreases to values around 0 W m^{-2}.

Comparing the event to the 1979–2020 climatology along the drift pathway, shown in Figure 7B, we find that the WAI's impact on the SEB is an overall anomalous warming. However, the main contributions and the absolute effect varies with the surface type. This agrees with other recent studies (e.g., Murto et al., 2022; You et al., 2022). Over open ocean and in the marginal sea ice zone, both latent and sensible heat fluxes are significantly higher than the climatological averages. The WAI leads to a SEB anomaly of up to +140 W m^{-2}. Over sea ice, the anomalies of all four SEB components are reduced, resulting in a SEB anomaly of only about +50 W m^{-2}. The contributions of both latent and sensible

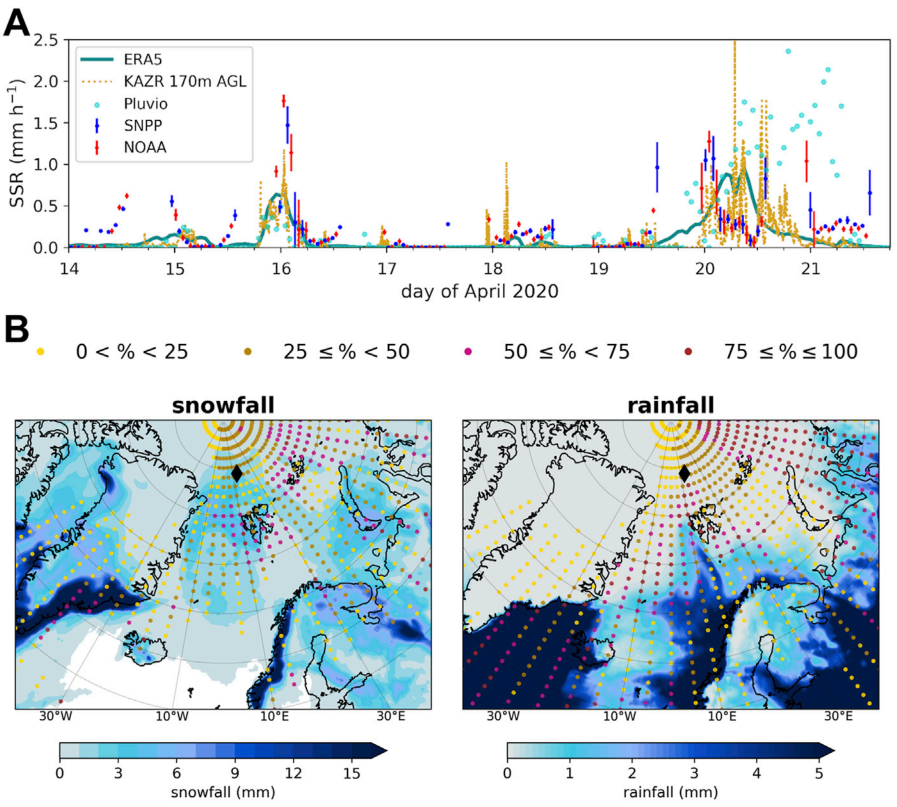

FIGURE 8
(A) Time series of the surface snowfall rate (SSR) at RV Polarstern during the peak intrusion period, from 14 April, 0 UTC until 21 April, 23 UTC. For ERA5 (cyan solid line) the grid cell closest to RV Polarstern position is taken. For satellite ATMS measurements (NOAA-20: red points, SNPP: blue points), SLALOM-CT estimates at RV Polarstern nearest pixel and standard deviations on a 3 × 3 pixel window are shown. In addition, ground-based measurements (Pluvio - turquoise points, KAZR at 170 m above ground - yellow dashed line) are shown. **(B)** Snowfall (left), and rainfall (right) accumulated for the 9-day period mentioned in **(A)**, based on ERA5. The colored dots illustrate the contribution of the two intense episodes of the WAI to precipitation as detected *via* the atmospheric river algorithm during that time period. The location of RV Polarstern is marked by the black diamond.

heat flux are less important in this region, while the longwave radiation anomaly plays a larger role and shows a positive anomaly, i.e., less net longwave radiation loss from the surface happens during the WAI. This is counteracted by a comparable negative shortwave radiation anomaly. Both radiative effects are consistent with enhanced cloud influences during the WAI (Section 3.3, and e.g., Clancy et al., 2022; Finocchio and Doyle, 2021), and the warming CRF effect dominates. Deeper in the central Arctic (t>24 h beyond Polarstern), the short- and longwave contributions add up to only a small anomalous SEB of +20 W m^{-2} and the net CRF anomaly remains positive, but small. Overall, the anomalies of SEB components during the mid-April 2020 event are within the order of magnitude as reported for WAIs in other seasons (recently e.g., Murto et al., 2022; Bresson et al., 2022; You et al., 2022). Furthermore, our reported WAI-related SEB anomalies are consistent with surface energy flux anomalies associated with cyclones and related sea-ice changes (recently, Aue et al., 2022; Clancy et al., 2022; Finoccio et al., 2022).

To better understand the influence of advected atmospheric moisture during this event, we explore the ICON-LAM experiments (Section 2.6). Figure 7C shows the difference of the "SEB in EXP with reduced moisture inflow minus CTRL" along the trajectory. The general ability of the ICON-LAM control run to represent the observed SEB during this WAI can be seen in Supplementary Figure S3B. As depicted in Figures 5B, 7D, the reduced moisture inflow results in reduced cloud LWC and IWC. Therefore, at the lower latitudes in the first 6 h of the drift, the shortwave radiation is not blocked as much and is up to +70 W m^{-2} higher than in the control run. This effect is also reflected in the much more positive CRF at these time steps. Furthermore, the prevented cloud formation also allows for more energy loss *via* longwave radiation. This effect is especially important at the marginal sea ice zone and when the trajectory drifts through the night (negligible incoming shortwave radiation). Here, the CRF is about 20 W m^{-2} lower than in the control run. These radiative processes result in a slightly colder surface, which then increases the surface sensible heat flux relative to the control run. The latent heat flux only changes over the open ocean due to an increased thermodynamically-driven evaporation. After entering the central Arctic, the difference EXP-CTRL is only minimal, i.e., similar SEBs are found for both simulations. For EXP as well as CTRL, LWP values larger than 30 g m^{-2} and thus near-saturated longwave CRF persist into the inner Arctic. Additionally, CTRL has already lost significant amounts of cloud water through precipitation over the ocean and the marginal sea ice zone (Figure 7D), while EXP is able to conserve its cloud water for a longer time. Hence the difference of LWP values narrows.

Overall, the model experiments imply that WAIs with reduced moisture inflow can cause an elevated SEB in the daytime over ocean, but a lowered SEB later when passing the marginal sea ice zone during nighttime, compared to more intense (moister) WAI. Interestingly, as long as a near-saturation of longwave CRF is achieved, for an initially drier WAI the impact on the SEB over the ice-covered central Arctic Ocean might be quite comparable.

3.4.2 Precipitation and snowfall

The time series of hourly snowfall rates at RV Polarstern shows that the mid-April 2020 double-episode WAI event brought considerable amounts of snowfall to the MOSAiC site (Figure 8A). During the first episode (15–16 April), the different measurement platforms observe snowfall rates up to 2 mm h^{-1}. From 16 April noon to 19 April noon, only little precipitation is recorded. Then, on 20 April the precipitation rate increases up to values of 2.5 mm h^{-1}. The figure also highlights the high uncertainty of snowfall estimates. Particularly during the second episode on 20 April, the snowfall rates derived from reanalysis data, satellite and ground-based measurements strongly vary. The temporal evolution of the snowfall rate from ERA5 reanalysis agrees relatively well with the ground-based measurements (KAZR, Pluvio), but shows a tendency to slightly underestimate the snowfall. The snowfall rate estimated from satellites can deviate by up to a factor of two. This deviation can partially be attributed to the fact that the precipitation rates spatially vary significantly across the domain around RV Polarstern, resulting in different precipitation values for the nearest satellite pixels. Moreover, such small-scale variability has an impact on the satellite estimates especially for the large ATMS pixel sizes (viewing angles > 20°) encountered at RV Polarstern's position. Here, the spatial resolution reduces from 16 × 16 km^2 at nadir down to 68 × 30 km^2 at the edges (Weng et al., 2012). Still, the good skill of SLALOM-CT especially on 16 and 19 April warrants further future assessment of this novel algorithm.

Next, precipitation patterns based on ERA5 are investigated on a larger spatial scale. The fraction of precipitation (rain, snow), as directly caused by the WAIs is calculated based on the atmospheric river shape (Section 2.4; Figure 8B). In the slightly shorter mid-April period considered here (14–22 April), the total 9-day snowfall and rainfall are calculated for each grid cell individually. Then, the fraction of precipitation deposited by the detected atmospheric river is extracted. We find that the atmospheric river components of the WAI contribute about 30% to the total precipitation (27% snowfall, 3% rainfall) at the grid cell nearest to RV Polarstern. A similar magnitude of contribution was calculated during two other campaigns in the Arctic (Lauer et al., 2023). Even larger fractions are discovered further east and south, at the marginal sea ice zone. However, it should be stressed that the exact contribution percentages depend on the detection algorithm applied, and might thus vary for different algorithms (Viceto et al., 2022).

The high uncertainty of precipitation estimates has important consequences. As demonstrated, WAIs bring large amounts of rain and snowfall into the central Arctic. These can have major impacts on the sea ice, such as increased insulation (snow on sea ice), modified surface albedo, or altered mass balance. Depending on the season, this can heavily influence longwave cooling efficiency and shortwave surface heating, and thus SEB and sea-ice cover.

4 Summary and conclusion

In our detailed analysis of the record-breaking WAI observed in mid-April 2020 during the MOSAiC expedition, we come to the following conclusion, according to our three objectives:

- (O1) Synoptic situation and transport: The WAI is characterized by two distinct pathways (Siberian, Atlantic) and exceptional moist static energy transports above the 90th percentile of climatology. The strongest anomaly is found in the latent energy transport along the Siberian pathway. This anomalous moisture transport is driven by a persistent positive NAO and later by a Scandinavian blocking pattern. Air masses at all altitudes between the surface and 10 km feature mid-latitude origins with median latitudes during the 5 previous days of 45°N and below.
- (O2) Air mass transformation *via* cloud processes: As measured at the MOSAiC site, the WAI establishes low-level liquid water and high-level ice clouds in the central Arctic. The observed LWP larger than 30 g m^{-2} is typically associated with the radiatively opaque state of the Arctic atmosphere. Model experiments demonstrate that two key cloud-determining factors, namely, moisture inflow and CCN concentration, can significantly affect the vertical cloud structure and especially the amount of the low-level liquid clouds. In the simulations, a reduction of both factors causes a reduction of LWC at the MOSAiC site. Furthermore, we show how modifications in CCN concentrations can trigger complex cloud-boundary layer feedbacks: Higher CCN concentrations lead to higher LWC in low-level liquid clouds and an associated stronger longwave cloud-top cooling. This leads to stronger entrainment and thus a stronger mixing in the boundary layer.
- (O3) Surface impacts: Along the poleward drift, the WAI has a strong and anomalous warming influence on the SEB. It is mostly driven by turbulent heat fluxes over the ocean and by radiation (longwave radiation, cloud radiative forcing) over the sea ice. For a reduced moisture inflow, major SEB impacts are mainly seen at the beginning of the track over the ocean and the marginal sea ice zone, but not the inner Arctic. The WAI contributes to a large, regionally variable fraction in total precipitation over a 9-day period, reaching up to about 30% at the MOSAiC site. We stress the pronounced uncertainty in precipitation and specifically snowfall observational estimates.

With these new insights, follow-up research is emerging. In the future, additional dedicated model experiments can help to further address the (O2) objective touched on here, namely, to better understand how complex aerosol-cloud-precipitation processes affect air mass transformation. For example, further exploration of processes is needed that are involved in controlling the moisture content of air masses. The simulations conducted here suggest counter-intuitive responses of the air mass to reduced moisture content, and further studies are needed to explore the responses and potential thresholds related to the amount of moisture in WAIs. The role of CCN in these processes also warrants further study. To first order, increased CCN should decrease the precipitation efficiency of an air mass, however it is not clear if, or how, such pollution impacts the cloudiness along the trajectory, the rate at which moisture is removed, or the implications for the SEB (O3). The analysis of the relationship between WAIs and sea-ice concentration is complicated as well and calls for follow-up research. No significant reduction of sea ice concentration is reported during mid-April 2020 from the ship during MOSAiC (Krumpen et al., 2021), but false, too low passive microwave satellite sea-ice concentration retrievals due to weather and surface glazing effects (Schreiber and Serreze, 2020) make interpretation difficult (Krumpen et al., 2021). We manually inspected synthetic aperture radar satellite scenes, which are less contaminated by weather influence, and can confirm that some leads opened and closed during the WAI, but sea ice concentration in the vicinity of RV Polarstern stayed high (> 95%). Overall, more in-depth studies are needed to separate retrieval uncertainties from actual sea ice changes and to further divide the latter into dynamic and thermodynamic components.

Finally, we stress that we present results for a specific case study only. It will be informative to extend some of our methods to climatological data sets in order to substantiate the robustness of our findings.

Data availability statement

Publicly available datasets were analyzed in this study. This data can be found here: MOSAiC meteorological data from Met City and the ASFS are available at the Arctic Data Center (Cox et al. 2021a, b, c, d). Radiation data from Met City (Riihimaki, 2022), Pluvio data (Cromwell and Bartholomew, 2022), and KAZR-based snowfall data (Matrosov et al., 2022) are available from the DOE ARM Archive. IWV and LWP as derived from HATPRO (Walbröl et al., 2022) as well as radiosonde data are freely available at PANGEA: https://doi.pangaea.de/10.1594/PANGAEA.941389, https://doi.org/10.1594/PANGAEA.928656. All data related to reanalysis can be found on the ERA5 data repository: https://www.ecmwf.int/en/forecasts/dataset/ecmwf-reanalysis-v5 (last access: 12 January 2023; Hersbach et al., 2020). The main outputs of LES experiments are available at: https://doi.org/10.5281/zenodo.7544108, while the current version of DALES (dales 4.3 with extension for mixed-phase microphysics, https://doi.org/10.5281/zenodo.5642477) is available on github as https://github.com/jchylik/dales/releases/tag/dales4.3sb3cgn. Lastly, the following data is available by contacting the lead author: SLALOM-CT estimates of surface snowfall; mean sea-level pressure fields of ICON-CTRL; cloud liquid and ice water contents along trajectories based on ERA5, ICON-CTRL and ICON-EXP.

Author contributions

AR, BK, RN, SC, and ST contributed to conception and design of the study. Observational data was supplied and interpretation supported by: AC (SLALOM-CT), AR and MS (SEB components, KAZR), AW (HATPRO), HG (Cloudnet). BK performed synoptic analysis based on ERA5, trajectory calculations based on ERA5 and ICON-LAM, and created most figures. IH and DH investigated preferred circulation regimes and large-scale energy transport. ML compared precipitation estimates from different platforms and weather systems, applying the atmospheric river algorithm. RN and JC performed and analyzed LES simulations. ST performed ICON-LAM simulations and analyzed them together with BK. BK, AR, and ST wrote the first draft of the article. BK coordinated the co-author's input. AR, BK, IH, ML, RN, and ST wrote sections of the manuscript. All authors actively discussed the draft, contributed to manuscript revision and approved the submitted version.

Funding

We acknowledge funding by the Deutsche Forschungsgemeinschaft (DFG, German Research Foundation)— project 268020496 TRR 172, within the Transregional Collaborative Research Center "ArctiC Amplification: Climate Relevant Atmospheric and SurfaCe Processes, and Feedback Mechanisms (AC)^3". MS acknowledges support of a Mercator Fellowship as part of (AC)^3, the National Science Foundation (OPP-1724551), and the NOAA Global Ocean Monitoring and Observing Program (*via* NA22OAR4320151). AR and DH were partly supported by the European Union's Horizon 2020 research and innovation framework programme under Grant agreement no. 101003590 (PolarRES). IG thanks FCT/MCTES for financial support to CESAM (UIDP/50017/2020, UIDB/50017/2020, and LA/P/0094/2020), to CIIMAR (UIDB/04423/2020, UIDP/04423/2020) and individual funding 2021.03140.CEECIND through national funds provided by FCT—Fundação para a Ciência e a Tecnologia. Data was collected from the Multidisciplinary drifting Observatory for the Study of the Arctic Climate (MOSAiC) under expedition number MOSAiC20192020 and project identifying AWI_PS122_00. The Gauss Centre for Supercomputing e.V., (www.gauss-centre.eu) is acknowledged for providing computing time on the GCS Supercomputer JUWELS at the Jülich Supercomputing Centre (JSC) under project VIRTUALLAB.The publication of this article was funded by the Open Access Publishing Fund of Leipzig University, supported by the German Research Foundation within the program Open Access Publication Funding.

Acknowledgments

Data was collected from the Multidisciplinary drifting Observatory for the Study of the Arctic Climate (MOSAiC). Some data was obtained from the Atmospheric Radiation Measurement (ARM) User Facility, a U.S. Department of Energy Office (DOE) of Science User Facility managed by the Biological and Environmental Research Program.

Conflict of interest

The authors declare that the research was conducted in the absence of any commercial or financial relationships that could be construed as a potential conflict of interest.

Publisher's note

Supplementary material

The Supplementary Material for this article can be found online at: https://www.frontiersin.org/articles/10.3389/feart.2023.1147848/full#supplementary-material

References

Ali, S. M., and Pithan, F. (2020). Following moist intrusions into the Arctic using SHEBA observations in a Lagrangian perspective. *Q. J. R. Meteorol. Soc.* 146, 3522–3533. doi:10.1002/qj.3859

Aue, L., Vihma, T., Uotila, P., and Rinke, A. (2022). New insights into cyclone impacts on sea ice in the Atlantic sector of the Arctic Ocean in winter. *Geophys. Res. Lett.* 49, e2022GL100051. doi:10.1029/2022GL100051

Batrak, Y., and Müller, M. (2019). On the warm bias in atmospheric reanalyses induced by the missing snow over Arctic sea-ice. *Nat. Commun.* 10, 4170. doi:10.1038/s41467-019-11975-3

Bechtold, P., Köhler, M., Jung, T., Doblas-Reyes, F., Leutbecher, M., Rodwell, M. J., et al. (2008). Advances in simulating atmospheric variability with the ECMWF model: From synoptic to decadal time-scales. *Q. J. R. Meteorol. Soc.* 134 (634), 1337–1351. doi:10.1002/qj.289

Binder, H., Boettcher, M., Grams, C. M., Joos, H., Pfahl, S., and Wernli, H. (2017). Exceptional air mass transport and dynamical drivers of an extreme wintertime Arctic warm event. *Geophys. Res. Lett.* 44, 12028–12036. doi:10.1002/2017gl075841

Boisvert, L. N., Petty, A. A., and Stroeve, J. C. (2016). The impact of the extreme winter 2015/16 Arctic cyclone on the Barents–Kara seas. *Mon. Wea. Rev.* 144, 4279–4287. doi:10.1175/mwr-d-16-0234.1

Bresson, H., Rinke, A., Mech, M., Reinert, D., Schemann, V., Ebell, K., et al. (2022). Case study of a moisture intrusion over the arctic with the ICOsahedral non-hydrostatic (ICON) model: Resolution dependence of its representation. *Atmos. Chem. Phys.* 22, 173–196. doi:10.5194/acp-22-173-2022

Bretherton, C. S., Krueger, S. K., Wyant, M. C., Bechtold, P., Van Meijgaard, E., Stevens, B., et al. (1999). A GCSS boundary-layer cloud model intercomparison study of the first ASTEX Lagrangian experiment. *Boundary-Layer Meteorol.* 93, 341–380. doi:10.1023/A:1002005429969

Bretherton, C. S., Uchida, J., and Blossey, P. N. (2010). Slow manifolds and multiple equilibria in stratocumulus-capped boundary layers. *J. Adv. Model. Earth Syst.* 2 (14). doi:10.3894/JAMES.2010.2.14

Camplani, A., Casella, D., Sanò, P., and Panegrossi, G. (2021). The passive microwave empirical cold surface classification algorithm (PESCA): Application to GMI and ATMS. *J. Hydrometeorol.* 22 (7), 1727–1744. doi:10.1175/jhm-d-20-0260.1

Chylik, J., Chechin, D., Dupuy, R., Kulla, B. S., Lüpkes, C., Mertes, S., et al. (2021). Aerosol-cloud-turbulence interactions in well-coupled Arctic boundary layers over open water. *Atmos. Chem. Phys. Discuss.* [Preprint]. doi:10.5194/acp-2021-888

Clancy, R., Bitz, C. M., Blanchard-Wrigglesworth, E., McGraw, M. C., and Cavallo, S. M. (2022). A cyclone-centered perspective on the drivers of asymmetric patterns in the atmosphere and sea ice during Arctic cyclones. *J. Clim.* 35 (1), 1–47. doi:10.1175/jcli-d-21-0093.1

Cox, C., Gallagher, M., Shupe, M., Persson, O., Solomon, A., Ayers, T., et al. (2021b). *Atmospheric surface flux station #30 measurements (level 1 raw), Multidisciplinary drifting Observatory for the Study of Arctic Climate (MOSAiC), central Arctic, October 2019 - September 2020.* Alexandria, VA, United States: National Science Foundation's Office of Polar Programs. doi:10.18739/A20C4SM1J

Cox, C., Gallagher, M., Shupe, M., Persson, O., Solomon, A., Ayers, T., et al. (2021d). *Atmospheric surface flux station #40 measurements (level 1 raw), Multidisciplinary drifting Observatory for the Study of Arctic Climate (MOSAiC), central Arctic, October 2019 - September 2020.* Alexandria, VA, United States: National Science Foundation's Office of Polar Programs. doi:10.18739/A2CJ87M7G

Cox, C., Gallagher, M., Shupe, M., Persson, O., Solomon, A., Ayers, T., et al. (2021c). *Atmospheric surface flux station #50 measurements (level 1 raw), Multidisciplinary drifting Observatory for the Study of Arctic Climate (MOSAiC), central Arctic, October 2019 - September 2020.* Alexandria, VA, United States: National Science Foundation's Office of Polar Programs. doi:10.18739/A2445HD46

Cox, C., Gallagher, M., Shupe, M., Persson, O., Solomon, A., Blomquist, B., et al. (2021a). *10-meter (m) meteorological flux tower measurements (level 1 raw), Multidisciplinary drifting Observatory for the Study of Arctic Climate (MOSAiC), central Arctic, October 2019 - September 2020.* Alexandria, VA, United States: National Science Foundation's Office of Polar Programs. doi:10.18739/A2VM42Z5F

Crasemann, B., Handorf, D., Jaiser, R., Dethloff, K., Nakamura, T., Ukita, J., et al. (2017). Can preferred atmospheric circulation patterns over the North-Atlantic-Eurasian region be associated with Arctic sea ice loss? *Polar Sci.* 14, 9–20. doi:10.1016/j.polar.2017.09.002

Crawford, A. D., Lukovich, J. V., McCrystall, M. R., Stroeve, J. C., and Barber, D. G. (2022). Reduced sea ice enhances intensification of winter storms over the Arctic Ocean. *J. Clim.* 35 (11), 3353–3370. doi:10.1175/jcli-d-21-0747.1

Cromwell, E., and Bartholomew, M. J. (2022). *Weighing bucket precipitation gauge (WBPLUVIO2).* Atmospheric Radiation Measurement (ARM) User Facility. doi:10.5439/1338194

Dada, L., Angot, H., Beck, I., Baccarini, A., Quéléver, L. L. J., Boyer, M., et al. (2022). A central Arctic extreme aerosol event triggered by a warm air-mass intrusion. *Nat. Commun.* 13, 5290. doi:10.1038/s41467-022-32872-2

Dahlke, S., and Maturilli, M. (2017). Contribution of atmospheric advection to the amplified winter warming in the Arctic North Atlantic region. *Adv. Meteorol.* 2017, 1–8. doi:10.1155/2017/4928620

Doms, G., Forstner, J., Heise, E., Herzog, H.-J., Mironov, D., Raschendorfer, M., et al. (2011). A description of the nonhydrostatic regional COSMO model. Part II: Physical parameterization. Consortium for small-scale modelling. Available at: http://www.cosmo-model.org.

ECMWF (2020). ECMWF newsletter number 164 - summer 2020, European Centre for medium-range weather forecasts (ECMWF). Available at: https://www.ecmwf.int/en/newsletter/164/news/warm-intrusions-arctic-april-2020 (Accessed January 16, 2023).

Falkena, S. K. J., Wiljes, J., Weisheimer, A., and Shepherd, T. G. (2020). Revisiting the identification of wintertime atmospheric circulation regimes in the Euro-Atlantic sector. *Q. J. R. Meteorol. Soc.* 146, 2801–2814. doi:10.1002/qj.3818

Fearon, M. G., Doyle, J. D., Ryglicki, D. R., Finocchio, P. M., and Sprenger, M. (2021). The role of cyclones in moisture transport into the Arctic. *Geophys. Res. Lett.* 48, e2020GL090353. doi:10.1029/2020gl090353

Finocchio, P. M., and Doyle, J. D. (2021). Summer cyclones and their association with short-term sea ice variability in the Pacific sector of the Arctic. *Front. Earth Sci.* 9, 738497. doi:10.3389/feart.2021.738497

Finoccio, P. M., Doyle, J. D., and Stern, D. P. (2022). Accelerated sea ice Loss from late summer cyclones in the New Arctic. *J. Clim.* 35, 4151–4169. doi:10.1175/jcli-d-22-0315.1

Graham, R. M., Cohen, L., Petty, A. A., Boisvert, L. N., Rinke, A., Hudson, S. R., et al. (2017). Increasing frequency and duration of Arctic winter warming events. *Geophys. Res. Lett.* 44, 6974–6983. doi:10.1002/2017gl073395

Graham, R. M., Cohen, L., Ritzhaupt, N., Segger, B., Graversen, R. G., Rinke, A., et al. (2019a). Evaluation of six atmospheric reanalyses over Arctic sea ice from winter to early summer. *J. Clim.* 32, 4121–4143. doi:10.1175/jcli-d-18-0643.1

Graham, R. M., Hudson, S. R., and Maturilli, M. (2019b). Improved performance of ERA5 in Arctic gateway relative to four global atmospheric reanalyses. *Geophys. Res. Lett.* 46, 6138–6147. doi:10.1029/2019gl082781

Graversen, R. G., and Burtu, M. (2016). Arctic amplification enhanced by latent energy transport of atmospheric planetary waves. *Q. J. R. Meteorol. Soc.* 142, 2046–2054. doi:10.1002/qj.2802

Guan, B., Waliser, D. E., and Ralph, F. M. (2018). An intercomparison between reanalysis and dropsonde observations of the total water vapor transport in individual atmospheric rivers. *J. Hydrometeorol.* 19, 321–337. doi:10.1175/JHM-D-17-0114.1

Hannachi, A., Straus, D. M., Franzke, C. L. E., Corti, S., and Woollings, T. (2017). Low-frequency nonlinearity and regime behavior in the Northern Hemisphere extratropical atmosphere. *Rev. Geophys.* 55, 199–234. doi:10.1002/2015rg000509

Henderson, G. R., Barrett, B. S., Wachowicz, L. J., Mattingly, K. S., Preece, J. R., and Mote, T. L. (2021). Local and remote atmospheric circulation drivers of Arctic change: A review. *Front. Earth Sci.* 9. doi:10.3389/feart.2021.709896

Hersbach, H., Bell, B., Berrisford, P., Hirahara, S., Horányi, A., Muñoz-Sabater, J., et al. (2020). The ERA5 global reanalysis. *Q. J. R. Meteorol. Soc.* 146, 1999–2049. doi:10.1002/qj.3803

Heus, T., van Heerwaarden, C. C., Jonker, H. J. J., Siebesma, A. P., Axelsen, S., van den Dries, K., et al. (2010). Formulation of the Dutch atmospheric large-eddy simulation (DALES) and overview of its applications. *Geoph. Model Dev.* 3, 415–444. doi:10.5194/gmd-3-415-2010

Hogan, R. J., and Bozzo, A. (2018). A flexible and efficient radiation scheme for the ECMWF model. *J. Adv. Model. Earth Syst.* 10, 1990–2008. doi:10.1029/2018ms001364

Illingworth, A. J., Hogan, R. J., O'Connor, E. J., Bouniol, D., Brooks, M. E., Delanoé, J., et al. (2007). *Cloudnet. Bull. Am. Meteorol. Soc.* 88, 883–898. doi:10.1175/bams-88-6-883

Johansson, E., Devasthale, A., Tjernström, M., Ekman, A. M. L., and L'Ecuyer, T. (2017). Response of the lower troposphere to moisture intrusions into the Arctic. *Geophys. Res. Lett.* 44, 2527–2536. doi:10.1002/2017gl072687

Komatsu, K. K., Alexeev, V. A., Repina, I. A., and Tachibana, Y. (2018). Poleward upgliding Siberian atmospheric rivers over sea ice heat up Arctic upper air. *Sci. Rep.* 8, 2872. doi:10.1038/s41598-018-21159-6

Krumpen, T., von Albedyll, L., Goessling, H., Hendricks, S., Juhls, B., Spreen, G., et al. (2021). MOSAiC drift expedition from October 2019 to July 2020: Sea ice conditions from space and comparison with previous years. *Cryosphere* 15, 3897–3920. doi:10.5194/tc-15-3897-2021

Lauer, M., Rinke, A., Gorodetskaya, I., Sprenger, M., Mech, M., and Crewell, S. (2023). Influence of atmospheric rivers and associated weather systems on precipitation in the Arctic. *EGUsphere*. [Preprint]. doi:10.5194/egusphere-2023-261

Lembo, V., Messori, G., Graversen, R., and Lucarini, V. (2019). Spectral decomposition and extremes of atmospheric meridional energy transport in the Northern hemisphere midlatitudes. *Geophys. Res. Lett.* 46, 7602–7613. doi:10.1029/2019gl082105

Li, L., Cannon, F., Mazloff, M. R., Subramanian, A. C., Wilson, A. M., and Ralph, F. M. (2022). Impact of atmospheric rivers on Arctic sea ice variations. *EGUsphere*. [Preprint]. doi:10.5194/egusphere-2022-36

Liang, Y., Bi, H., Huang, H., Lei, R., Liang, X., Cheng, B., et al. (2022). Contribution of warm and moist atmospheric flow to a record minimum July sea ice extent of the Arctic in 2020. *Cryosphere* 16, 1107–1123. doi:10.5194/tc-16-1107-2022

Littmann, D.-C. (2022). Large eddy simulations of the Arctic boundary layer around the MOSAiC drift track. Dissertation. Germany: University Potsdam, 87.

Liu, Y., Attema, J., Moat, B., and Hazeleger, W. (2020). Synthesis and evaluation of historical meridional heat transport from midlatitudes towards the Arctic. *Earth Syst. Dyn.* 11, 77–96. doi:10.5194/esd-11-77-2020

Magnusson, L., Day, J., Sandu, I., and Svensson, G. (2020). Warm intrusions into the arctic in April 2020. Shinfield Park, Reading, United Kingdom: European Centre for Medium-Range Weather Forecasts, 164. Available at: https://www.ecmwf.int/en/newsletter/164/news/warm-intrusions-arctic-april-2020.

Matrosov, S. Y., Shupe, M. D., and Uttal, T. (2022). High temporal resolution estimates of Arctic snowfall rates emphasizing gauge and radar-based retrievals from the MOSAiC expedition. *Elem. Sci. Anthr.* 10 (1). doi:10.1525/elementa.202100101

Messori, G., Woods, C., and Caballero, R. (2018). On the drivers of wintertime temperature extremes in the high Arctic. *J. Clim.* 31, 1597–1618. doi:10.1175/jcli-d-17-0386.1

Mewes, D., and Jacobi, C. (2019). Heat transport pathways into the Arctic and their connections to surface air temperatures. *Atmos. Chem. Phys.* 19, 3927–3937. doi:10.5194/acp-19-3927-2019

Mironov, D., Ritter, B., Schulz, J.-P., Buchhold, M., Lange, M., and MacHulskaya, E. (2012). Parameterisation of sea and lake ice in numerical weather prediction models of the German Weather Service. *Tellus A* 64, 17330. doi:10.3402/tellusa.v64i0.17330

Mortin, J., Svensson, G., Graversen, R. G., Kapsch, M.-L., Stroeve, J. C., and Boisvert, L. N. (2016). Melt onset over Arctic sea ice controlled by atmospheric moisture transport. *Geophys. Res. Lett.* 43, 6636–6642. doi:10.1002/2016gl069330

Murto, S., Caballero, R., Svensson, G., and Papritz, L. (2022). Interaction between Atlantic cyclones and Eurasian atmospheric blocking drives wintertime warm extremes in the high Arctic. *Weather Clim. Dynam.* 3, 21–44. doi:10.5194/wcd-3-21-2022

Naakka, T., Nygård, T., Vihma, T., Sedlar, J., and Graversen, R. (2019). Atmospheric moisture transport between mid-latitudes and the Arctic: Regional, seasonal and vertical distributions. *Int. J. Climatol.* 39, 2862–2879. doi:10.1002/joc.5988

Nash, D., Waliser, D., Guan, B., Ye, H., and Ralph, F. M. (2018). The role of atmospheric rivers in extratropical and polar hydroclimate. *J. Geophys. Res. Atmos.* 123, 6804–6821. doi:10.1029/2017jd028130

Neggers, R. A. J., Chylik, J., Egerer, U., Griesche, H., Schemann, V., Seifert, P., et al. (2019). Local and remote controls on Arctic mixed-layer evolution. *J. Adv. Mod. Earth Syst.* 11 (7), 2214–2237. doi:10.1029/2019MS001671

Nicolaus, M., Perovich, D. K., Spreen, G., Granskog, M. A., von Albedyll, L., Angelopoulos, M., et al. (2022). Overview of the MOSAiC expedition: Snow and sea ice. *Elem. Sci. Anthr.* 10 (1). doi:10.1525/elementa.2021.000046

Nygård, T., Naakka, T., and Vihma, T. (2020). Horizontal moisture transport dominates the regional moistening patterns in the arctic. *J. Clim.* 33, 6793–6807. doi:10.1175/JCLI-D-19-0891.1

Papritz, L., Hauswirth, D., and Hartmuth, K. (2022). Moisture origin, transport pathways, and driving processes of intense wintertime moisture transport into the Arctic. *Weather Clim. Dyn.* 3, 1–20. doi:10.5194/wcd-3-1-2022

Park, D.-S. R., Lee, S., and Feldstein, S. B. (2015). Attribution of the recent winter sea ice decline over the atlantic sector of the Arctic Ocean. *J. Clim.* 28, 4027–4033. doi:10.1175/jcli-d-15-0042.1

Persson, P. O. G., Shupe, M. D., Perovich, D., and Solomon, A. (2016). Linking atmospheric synoptic transport, cloud phase, surface energy fluxes, and seasea-ice growth: Observations of midwinter SHEBA conditions. *Clim. Dyn.* 49, 1341–1364. doi:10.1007/s00382-016-3383-1

Pincus, R., and Stevens, B. (2009). Monte Carlo spectral integration: A consistent approximation for radiative transfer in large Eddy simulations. *J. Adv. Model. Earth Syst.* 1, 1. doi:10.3894/JAMES.2009.1.1

Pithan, F., and Jung, T. (2021). Arctic amplification of precipitation changes—the energy hypothesis. *Geophys. Res. Lett.* 48 (21), e2021GL094977. doi:10.1029/2021gl094977

Pithan, F., Svensson, G., Caballero, R., Chechin, D., Cronin, T. W., Ekman, A. M. L., et al. (2018). Role of air-mass transformations in exchange between the Arctic and mid-latitudes. *Nat. Geosci.* 11, 805–812. doi:10.1038/s41561-018-0234-1

Previdi, M., Smith, K. L., and Polvani, L. M. (2021). Arctic amplification of climate change: A review of underlying mechanisms. *Environ. Res. Lett.* 16, 093003. doi:10.1088/1748-9326/ac1c29

Prill, F., Reinert, D., Rieger, D., and Zängl, G. (2020). Working with the ICON model. Offenbach, Germany: *Deutscher Wetterdienst*. Available at: www.dwd.de/EN/ourservices/nwv_icon_tutorial/pdf_volume/icon_tutorial2020_en.pdf.

Rabe, B., Heuzé, C., Regnery, J., Aksenov, Y., Allerholt, J., Athanase, M., et al. (2022). Overview of the MOSAiC expedition: Physical oceanography. *Elem. Sci. Anthr.* 10 (1). doi:10.1525/elementa.2021.00062

Rantanen, M., Karpechko, A. Y., Lipponen, A., Nordling, K., Hyvärinen, O., Ruosteenoja, K., et al. (2022). The Arctic has warmed nearly four times faster than the globe since 1979. *Commun. Earth Environ.* 3, 168. doi:10.1038/s43247-022-00498-3

Riihimaki, L. (2022). *Radiation instruments on ice (ICERAD). Atmospheric radiation measurement (ARM) user facility*. doi:10.5439/1608608

Rinke, A., Cassano, J. J., Cassano, E. N., Jaiser, R., and Handorf, D. (2021). Meteorological conditions during the MOSAiC expedition. *Elem. Sci. Anthr.* 9. doi:10.1525/elementa.2021.00023

Rinke, A., Segger, B., Crewell, S., Maturilli, M., Naakka, T., Nygaard, T., et al. (2019). Trends of vertically integrated water vapor over the Arctic during 1979-2016: Consistent moistening all over? *J. Clim.* 32 (18), 6097–6116. doi:10.1175/JCLI-D-19-0092.1

Sanò, P., Casella, D., Camplani, A., D'Adderio, L. P., and Panegrossi, G. (2022). A machine learning snowfall retrieval algorithm for ATMS. *Remote Sens.* 14, 1467. doi:10.3390/rs14061467

Schreiber, E. A. P., and Serreze, M. C. (2020). Impacts of synoptic-scale cyclones on arctic sea-ice concentration: A systematic analysis. *Ann. Glaciol.* 61, 139–153. doi:10.1017/aog.2020.23

Seifert, A., and Beheng, K. D. (2006). A two-moment cloud microphysics parameterization for mixed-phase clouds. Part 1: Model description. *Meteor. Atmos. Phys.* 92, 45–66. doi:10.1007/s00703-005-0112-4

Shupe, M. D., Rex, M., Blomquist, B., Persson, P. O. G., Schmale, J., Uttal, T., et al. (2022). Overview of the MOSAiC expedition: Atmosphere. *Elem. Sci. Anthr.* 10 (1). doi:10.1525/elementa.2021.00060

Sprenger, M., and Wernli, H. (2015). The LAGRANTO Lagrangian analysis tool – version 2.0. *Model Dev.* 8, 2569–2586. doi:10.5194/gmd-8-2569-2015

Stevens, B., Moeng, C.-H., Ackerman, A. S., Bretherton, C. S., Chlond, A., de Roode, S., et al. (2005). Evaluation of large-eddy simulations via observations of nocturnal marine stratocumulus. *Mon. Wea. Rev.* 133, 1443–1462. doi:10.1175/MWR2930.1

Taylor, P. C., Boeke, R. C., Boisvert, L. N., Feldl, N., Henry, M., Huang, Y., et al. (2022). Process drivers, inter-model spread, and the path forward: A review of amplified Arctic warming. *Front. Earth Sci.* 9. doi:10.3389/feart.2021.758361

Tiedtke, M. (1989). A comprehensive mass flux scheme for cumulus parameterization in large-scale models. *Mon. Weather Rev.* 117, 1779–1800. doi:10.1175/1520-0493(1989)117<1779:acmfsf>2.0.co;2

Tjernström, M., Shupe, M. D., Brooks, I. M., Persson, P. O. G., Prytherch, J., Salisbury, D. J., et al. (2015). Warm-air advection, air mass transformation and fog causes rapid ice melt. *Geophys. Res. Lett.* 42, 5594–5602. doi:10.1002/2015gl064373

Trenberth, K. E. (1991). Climate diagnostics from global analyses: Conservation of mass in ECMWF analyses. *J. Clim.* 4, 707–722. doi:10.1175/1520-0442(1991)004<0707:cdfgac>2.0.co;2

Van Laar, T., Schemann, V., and Neggers, R. A. J. (2019). Investigating the diurnal evolution of the cloud size distribution of continental cumulus convection using multi-day LES. *J. Atmos. Sci.* 76 (3), 729–747. doi:10.1175/JAS-D-18-0084.1

Viceto, C., Gorodetskaya, I. V., Rinke, A., Maturilli, M., Rocha, A., and Crewell, S. (2022). Atmospheric rivers and associated precipitation patterns during the ACLOUD and PASCAL campaigns near svalbard (May–June 2017): Case studies using observations, reanalyses, and a regional climate model. *Atmos. Chem. Phys.* 22, 441–463. doi:10.5194/acp-22-441-2022

Walbröl, A., Crewell, S., Engelmann, R., Orlandi, E., Griesche, H., Radenz, M., et al. (2022). Atmospheric temperature, water vapour and liquid water path from two microwave radiometers during MOSAiC. *Sci. Data* 9, 534. doi:10.1038/s41597-022-01504-1

Webster, M., Gerland, S., Holland, M., Hunke, E., Kwok, R., Lecomte, O., et al. (2018). Snow in the changing sea-ice systems. *Nat. Clim. Change* 8, 946–953. doi:10.1038/s41558-018-0286-7

Wendisch, M., Brückner, M., Crewell, S., Ehrlich, A., Notholt, J., Lüpkes, A., et al. (2022). Atmospheric and surface processes, and feedback mechanisms determining Arctic amplification: A review of first results and prospects of the (AC)3 project. *Bull. Am. Meteorol. Soc.* 104, E208–E242. doi:10.1175/bams-d-21-0218.1

Wendisch, M., Handorf, D., Tegen, I., Neggers, R., and Spreen, G. (2021). Glimpsing the ins and outs of the Arctic atmospheric cauldron. *Eos* 102. doi:10.1029/2021eo155959

Wendisch, M., Macke, A., Ehrlich, A., Lüpkes, C., Mech, M., Chechin, D., et al. (2019). The Arctic cloud puzzle: Using ACLOUD/PASCAL multiplatform observations to unravel the role of clouds and aerosol particles in Arctic amplification. *Bull. Am. Meteorol. Soc.* 100, 841–871. doi:10.1175/bams-d-18-0072.1

Weng, F., Zou, X., Wang, X., Yang, S., and Goldberg, M. D. (2012). Introduction to Suomi national polar-orbiting partnership advanced technology microwave sounder for numerical weather prediction and tropical cyclone applications. *J. Geophys. Res.* 117, D19112. doi:10.1029/2012jd018144

Woods, C., and Caballero, R. (2016). The role of moist intrusions in winter Arctic warming and sea ice decline. *J. Clim.* 29, 4473–4485. doi:10.1175/jcli-d-15-0773.1

You, C., Tjernström, M., and Devasthale, A. (2021). Eulerian and Lagrangian views of warm and moist air intrusions into summer Arctic. *Atm. Res.* 256, 105586. doi:10.1016/j.atmosres.2021.105586

You, C., Tjernström, M., and Devasthale, A. (2022). Warm and moist air intrusions into the winter Arctic: A Lagrangian view on the near-surface energy budgets. *Atmos. Chem. Phys.* 22, 8037–8057. doi:10.5194/acp-22-8037-2022

Zängl, G., Reinert, D., Rípodas, P., and Baldauf, M. (2014). The ICON (ICOsahedral Non-hydrostatic) modelling framework of DWD and MPI-M: Description of the non-hydrostatic dynamical core. *Q. J. R. Meteorol. Soc.* 141, 563–579. doi:10.1002/qj.2378

Frontiers in
Earth Science

Investigates the processes operating within the major spheres of our planet

Advances our understanding across the earth sciences, providing a theoretical background for better use of our planet's resources and equipping us to face major environmental challenges.

Discover the latest Research Topics

See more →

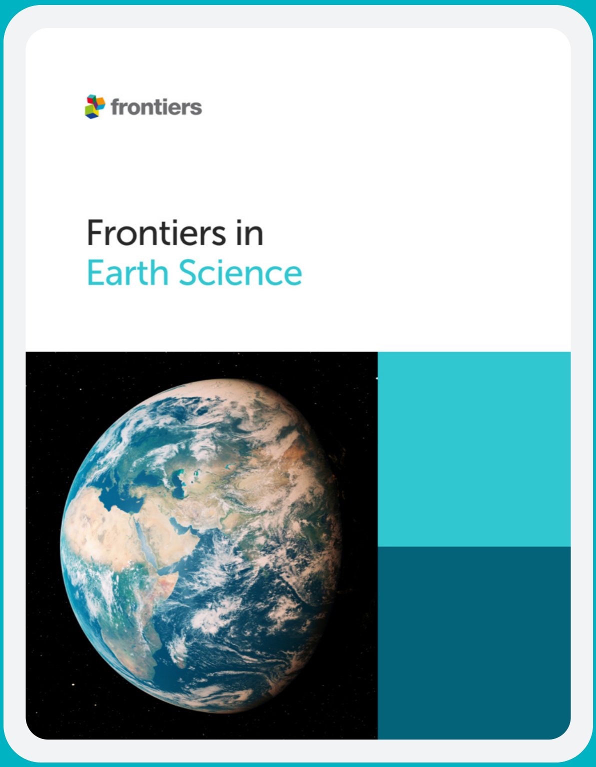

frontiers

Frontiers in
Earth Science

Frontiers

Avenue du Tribunal-Fédéral 34
1005 Lausanne, Switzerland
frontiersin.org

Contact us

+41 (0)21 510 17 00
frontiersin.org/about/contact